Akademiya Nauk Ukrainskoi SSR

PLASMA PHYSICS
AND
CONTROLLED THERMONUCLEAR FUSION

Edited by K. D. Sinel'nikov

Translated from Russian

Published for the National Aeronautics and Space Administration, U.S.A.
and the National Science Foundation, Washington, D.C.
by the Israel Program for Scientific Translations

NASA TT F-433
TT 67-51369
Published Pursuant to an Agreement with
THE NATIONAL AERONAUTICS AND SPACE ADMINISTRATION, U.S.A.
and
THE NATIONAL SCIENCE FOUNDATION, WASHINGTON, D.C.

IPST Cat. No. 1818

Translated by Z. Lerman

Printed in Jerusalem by S. Monson

Binding: Wiener Bindery Ltd., Jerusalem

Price: $ 7.80

Available from the
U.S. DEPARTMENT OF COMMERCE
Clearinghouse for Federal Scientific and Technical Information
Springfield, Va. 22151

XII/13/5

Table of Contents

Section One
HIGH-FREQUENCY PROPERTIES OF PLASMA

Section Two
PLASMA-BEAM INTERACTION

Section Three
GAS DISCHARGE

Section Four
PLASMA STABILITY

Section Five
METHODS AND DIAGNOSTICS OF PLASMOIDS. PLASMA INJECTORS

Section Six
INTERACTION OF PLASMA WITH MAGNETIC FIELDS. SHOCK WAVES IN PLASMA

Section Seven
INJECTION OF PLASMA AND BEAMS OF PARTICLES

Section Eight
MAGNETIC TRAPS

Section Nine
VACUUM TECHNIQUES. LOW-TEMPERATURE PROPERTIES OF METALS

Section Ten
PLASMA DIAGNOSTICS

ANNOTATION

The book is a collection of papers presented at the Fourth Plasma Physics and Controlled Fusion Conference of the Physicotechnical Institute of the Ukrainian Academy of Sciences, held in Kharkov on 20—25 May 1963. [References to papers presented at the previous Plasma Physics and Controlled Fusion Conferences appear in the bibliographies in the following form: full transliteration of the official title of the conference proceedings, followed by the conference (volume) number. Thus, "Fizika plazmy i problemy upravlyaemogo termoyadernogo sinteza", 2 is a reference to the proceedings of the Second Conference.]

The papers deal with the theoretical and the experimental aspects of plasma physics and reflect the state of research at the Institute in the years 1962—1963. The collection is subdivided into several topical sections: high-frequency properties of plasmas, plasma—beam interactions, plasma stability, gas discharge, plasmoid experiments, plasma guns, behavior of plasma in magnetic fields, injection of plasma and plasmoids, magnetic traps and plasma confinement, plasma diagnostics; in addition, special sections are devoted to methods of high-vacuum production and the properties of metals at low temperature, in application to the design of new high-efficiency vacuum pumps.

TRANSLATOR'S NOTE

All the formulas in this text are photographically reproduced from the Russian original, and some of the mathematical notations are slightly different from those currently accepted in the West. This refers mainly to hyperbolic trigonometric functions (ch stands for the hyperbolic cosine, sh for the hyperbolic sine, etc.) and to vector analysis notations (e. g., rot for curl); the Russian lg, tg, and ctg have been retained for the more conventional log, tan, and cot, respectively. It is hoped that this peculiarity of notations will not unduly disturb the reader.

N. I. Nazarov, A. I. Ermakov, and V. T. Tolok

THE BEHAVIOR OF A PLASMA BOUNDARY HEATED BY ION CYCLOTRON WAVES

This study continues the investigation of a plasma generated by resonance excitation of ion cyclotron waves. The equipment and the experimental conditions are identical to those described in /1, 2/.

It has already been observed /2/ that two distinctly different modes of behavior of the plasma density are possible in the resonance excitation of ion cyclotron waves; the actual mode depends on the amount of the r-f energy fed into the plasma. A study of the decay constant τ of the plasma with a microwave interferometer at a wavelength $\lambda = 8$ mm confirms the existence of two different modes of density decay in a plasma. In one of the modes, the decay constant reaches 300 μsec, but as the injected energy increases (i.e., the voltage is increased leaving the pulse length unchanged, or the pulse length is increased leaving the voltage constant), anomalously rapid density decay sets in, with a decay constant τ as low as 20–30 μsec.

Figure 1 plots some characteristic features of the discharge as a function of the confining magnetic field H_0. Figure 1,a gives the variation of the amplitude of the signal of the magnetic probe registering the high-frequency magnetic field, namely the $\widetilde{H}_z$-components of the travelling ion cyclotron wave. The magnetic probe was held at a distance of 25 cm from the edge of the excitation coil. Figure 1,b plots the variation of the plasma decay constant obtained from the interferograms of the 8-mm signal, and Figure 1,c gives the intensity of the spectral line C III ($\lambda = 4647$ Å). We see from these graphs that the decay constant is maximal in the same region of magnetic fields where the amplitude of the ion cyclotron wave reaches its peak. The increase of τ at the time of resonance generation is apparently attributable to the increase in the transverse energy of the plasma ions. Furthermore, the electron temperature of the plasma also increases under resonance conditions, as is evident from the appearance of the line of doubly ionized carbon C III ($\lambda = 4647$ Å) with an excitation potential of ~50 eV in the discharge. Since the energy of the electromagnetic wave is directly transmitted to the ions, the electrons are heated by collision with ions. These collision losses can be reduced in a plasma with hot electrons. The electrons may be heated, say, by means of resonance excitation of high-frequency oscillations effectively interacting with the plasma electrons /3, 4/.

Since in this experiment the density of the plasma was higher than the critical density for the 8-mm signal, additional information on the behavior of the plasma at the time of heating was gained by studying the reflection

of VHF signals from the plasma. It is known that when a plasma is probed with a signal whose frequency if below the critical value, the phase of the reflected signal is indicatory of the position of the critical layer in space /5/.

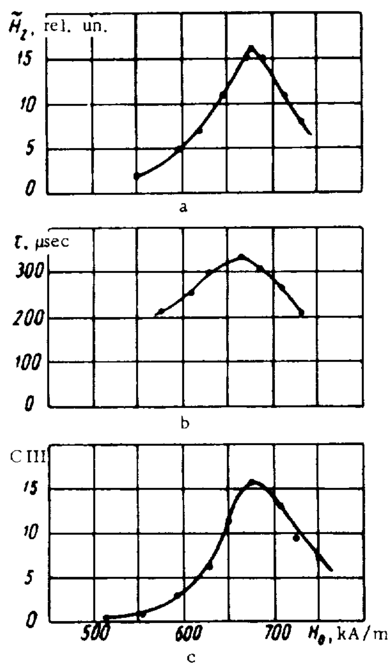

FIGURE 1. Discharge characteristics vs. the confining magnetic field H_0.

Figure 2 shows some oscillograms (a – cutoff of the 8-mm signal, b – reflection of the 8-mm signal) obtained in two magnetic fields, 517 and 675 kA/m. The lower oscillogram of the reflected signal shows that the plasma cylinder oscillates intensely when the amplitude of the ion cyclotron wave in the plasma is maximal. These oscillations are difficult to interpret in view of their irregularity. More definite results on the oscillation of the boundary of the plasma cylinder were obtained by examining the reflection of signals with $\lambda = 3.2$ cm. In magnetic fields below the resonance (Figure 3,a) the reflected signal does not experience noticeable phase shifts if $n > n_{cr.}$, i.e., under these conditions the plasma layer with n_{cr} shows no substantial radial motion. In resonance, the phase of the reflected signal changes considerably (Figure 3,b). The phase shifts range between $3\pi/2$ and 2π, which corresponds to a radial displacement of about $\lambda/2 = 16$ mm for the plasma layer with critical density.

A comparison of the amplitudes and the phases of signals reflected by metal rods of various diameters, in line with the axis of a discharge tube, with the amplitudes and the phases of signals reflected by plasma columns has established that the critical plasma layer moves toward the center of the discharge tube. Since at this instant the density of the plasma increases under the conditions of the experiment, this radial displacement of the plasma cylinder actually points to the formation of a 16-mm gap between the plasma and the walls of the discharge tube. The plasma cylinder is detached from the walls apparently because the resonance radial distribution of the high-frequency fields in the ion cyclotron wave /1/ is conducive to plasma confinement. Figure 4 shows the radial distribution of the magnetic pressure $\left(\frac{\tilde{H}^2}{8\pi}\right)$ set up by the wave. The pressure is maximal at a distance of 15 mm from the wall of the discharge tube ($R = 30$ mm), which is consistent with the measurements of plasma constriction using the 3.2-cm signal.

The ratio of the gas-kinetic pressure and the pressure set up by the alternating magnetic field of the wave $\left(\beta = \frac{8\pi nkT}{\tilde{H}^2}\right)$ is $\beta = 0.3$, which justifies our interpretation of the constriction of the plasma column.

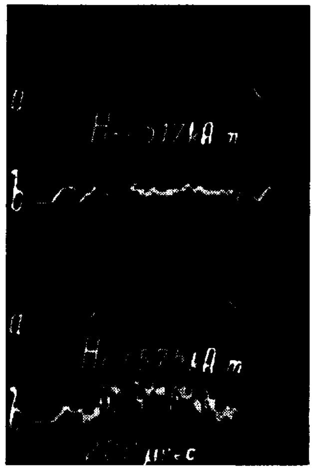

FIGURE 2. Oscillograms of signal cutoff (a) and of the reflected signal (b).

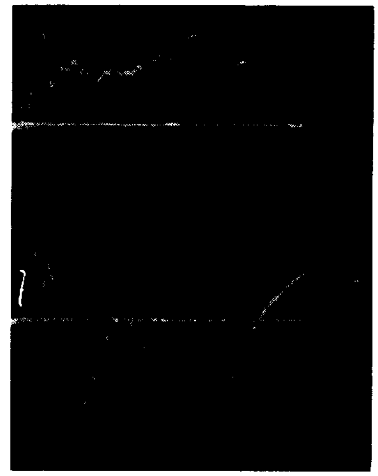

FIGURE 3. Oscillograms of the reflected 3.2-cm signal.

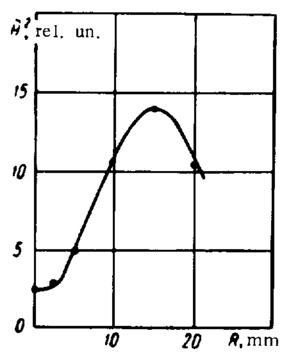

FIGURE 4. Radial distribution of the magnetic pressure set up by the wave in a discharge tube.

BIBLIOGRAPHY

1. NAZAROV, N. I., A. I. ERMAKOV, A. S. LOBKO, V. A. BONDAREV, V. T TOLOK, and K. D. SINEL'NIKOV. - ZhTF, **32**: 537. 1962.

2. NAZAROV, N. I., A. I. ERMAKOV, V. T. TOLOK, and K. D. SINEL'NIKOV. - In: "Fizika plazmy i problemy upravlyaemogo termoyadernogo sinteza", **3**, p.164. Kiev, Izdatel'stvo AN UkrSSR. 1963.

3. NAZAROV, N. I., A. I. ERMAKOV, V. V. DOLGOPOLOV, K. N. STEPANOV, and V. T. TOLOK. - This volume, p. 4.

4. DOLGOPOLOV, V. V., A. I. ERMAKOV, N. I. NAZAROV, K. N. STEPANOV, and V. T. TOLOK. - This volume, p. 9.

5. ANISIMOV, V. A., V. E. GOLANT, B. P. KONSTANTINOV, B. P. POLOSKIN, and O. N. SHERBININ. - ZhTF, 30: 1447. 1960.

N. I. Nazarov, A. I. Ermakov, V. V. Dolgopolov,
K. N. Stepanov, and V. T. Tolok

A STUDY OF RESONANCE EXCITATION AND ČERENKOV DAMPING OF HIGH-FREQUENCY PLASMA OSCILLATIONS

Excitation and propagation of electromagnetic waves in a plasma is of considerable applied significance. Two electromagnetic waves may propagate in a plasma (the ordinary and the extraordinary one), each having its own phase velocity, polarization, and damping. The damping of electromagnetic waves in a plasma is attributable to collisions, as well as to collisionless mechanisms (Čerenkov and cyclotron absorption). In the range of frequencies much less than the gyrofrequency of the electrons and greater than the gyrofrequency of the ions, there exists a long-wave oscillation mode whose phase velocity may be less than the thermal velocity of the electrons. Many electrons will effectively interact with the field of this wave, and its Čerenkov damping is therefore considerable. The ratio of the collisionless damping length to the wavelength in this case is /1/

$$\frac{l_L}{\lambda} = \frac{a_1 \lambda \omega_H}{(2\pi)^2 v_e}, \tag{1}$$

where $\omega_H = \frac{eH_0}{mc}$ is the gyrofrequency of the electrons, H_0 the external magnetic field, $v_e = \sqrt{\frac{2T_e}{m}}$ the thermal velocity of the electrons, a_1 a coefficient depending on the angle ϑ between the direction of propagation of the wave and the magnetic field (with $\vartheta \approx 1$, $a_1 \sim 1$).

The wavelength in a homogeneous plasma cylinder, as in the case of a "cold" plasma, is determined by /2/

$$\lambda = 2\pi \left(\frac{\omega_p \omega}{\omega_H c^2} - \frac{k_r^2}{2} \right)^{-1/2}, \tag{2}$$

where ω_p is the plasma frequency k_r the radial wave number.

The damping length in collisions between electrons and ions is /3/

$$\frac{l_{\text{col}}}{\lambda} = \frac{a_2 \omega_H}{2\pi\nu}, \tag{3}$$

where ν is the effective collision frequency of electrons and ions, $a_2(\vartheta) \sim 1$.

In a rarefied hot plasma, the collisionless damping (1) may be substantially higher than the damping by collisions (3).

Some problems of the excitation of plasma oscillations in the region

$\omega \ll \omega_H$ were considered in /4,5/. A theoretical study of the absorption of these waves in an inhomogeneous plasma cylinder was made in /6/.

In the present work we studied resonance excitation and damping of waves of frequency $\omega \ll \omega_H$ in a plasma cylinder in the presence of a strong longitudinal magnetic field.

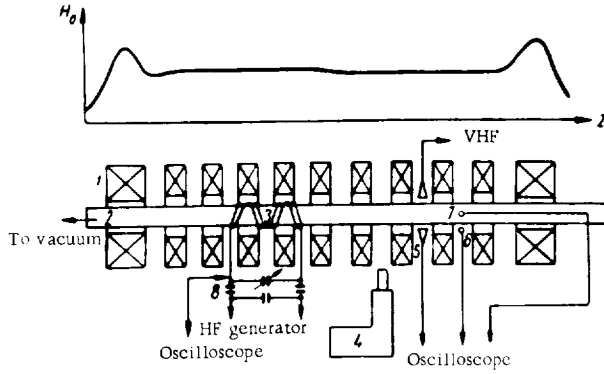

FIGURE 1. The experimental setup:
1) magnetic-field solenoid; 2) discharge tube; 3) excitation coil; 4) ISP-51 spectrograph; 5) VHF measuring channel; 6, 7) internal and external magnetic probes; 8) voltage-measuring circuit; 9) gas-pumping system.

The excitation and the damping of waves with frequencies substantially less than the electron cyclotron frequency $\left(\omega \sim \frac{1}{200}\omega_H\right)$ was studied on the experimental setup previously used in an investigation of the excitation and damping of ion cyclotron waves /7/. A schematic diagram of the equipment is shown in Figure 1. The plasma was generated by high-frequency currents flowing through an excitation coil. The coil, comprising four sections in "head-on" coupling, set up a space-periodic high-frequency field of wavelength $\lambda_0 = 15$ cm. The quasistationary magnetic field would attain its maximum in 6 msec, so that the magnetic field was assumed to be time-independent at the instant of taking readings of the discharge characteristics. The field varied by less than 1% in that time. The high-frequency generator operated at 10 Mc/s. The power generated could be as high as 300 kW with a pulse length of 1 msec. The pulse length varied between wide limits. The experiments were made with hydrogen and helium in a pressure range of 0.13–0.53 N/m^2.

The measurements show that with high-frequency voltages of 30-40 kV, the load in magnetic fields of 25-80 kA/m is high (300-1000 Oe). With 80 kA/m, the electromagnetic wave propagates along the magnetic field. The wave amplitude $\widetilde{H}_z$ measured with a magnetic probe held at a distance of 25 cm from the edge of the coil is shown in Figure 2.

Figure 3 shows that the excitation of these waves clearly follows a resonance curve. The alternating high-frequency fields are maximal ($\widetilde{H}_z \sim 8$ kA/m) when the generator frequency and the excitation coil period are equal to the frequency and the wavelength obtaining from the dispersion relation (2). In the experimental magnetic field of 80 kA/m, resonance

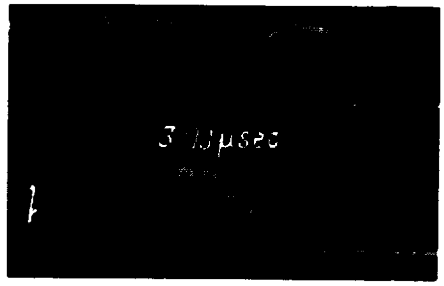

FIGURE 2. Oscillograms of circuit voltage U_c(a) and magnetic probe signal U_p(b).

excitation of waves with $\lambda_z = 15$ cm is observed for plasma densities of $n_e \sim 5 \cdot 10^{13}$ cm^{-3}. This is fully consistent with the densities measured by a microwave interferometer, $n_e \sim (4-8) \cdot 10^{13}$ cm^{-3}. Spectral measurements show that the working gas was virtually fully ionized.

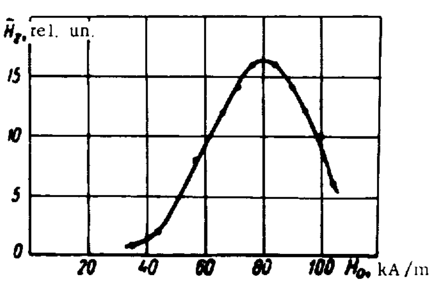

FIGURE 3. The amplitude $\widetilde{H}_z$ vs. the external magnetic field H_0.

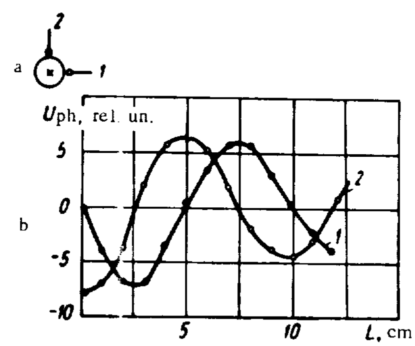

FIGURE 4. The amplitude of the phase-detector signal (U_{ph}) vs. the distance along the magnetic field (L).

The propagation and the damping of the wave was studied in magnetic fields whose strength H_0 was 10% less than the magnetic-field strength on excitation; the field was maintained constant along the plasma column. All the wave-propagation parameters were measured in this length of homogeneous magnetic field.

The travelling electromagnetic wave in a plasma cylinder may be represented as $\sim e^{i(m\varphi + kz - \omega t)}$. Applying a ring phase detector /8/, we measured the phase shift in the wave both in the direction of propagation and at an angle φ. The results of these measurements are plotted in Figure 4,b. Curves 1 and 2 correspond to two positions of the magnetic probe at an angle of 90°(Figure 4,a). The wavelength λ_z in these measurements was 10 cm, $m=1$; the sense of rotation of the wave coincides with the sense of

gyration of electrons in the magnetic field. The longitudinal wavelength can also be determined by measuring the distribution of $\widetilde{H}_z$ outside the plasma $[\widetilde{H}_z \sim K_0(k_r r)]$. The λ_z measured by this technique coincides with the λ_z found from phase measurements.

The angle between the direction of wave propagation and the magnetic field H_0 is given by the relation $\operatorname{tg}\vartheta = \frac{k_r}{k_z}$. The radial wave number k_r is found from boundary conditions. Since the plasma is confined in a conducting enclosure (the excitation coil), then of necessity $J_1(k_1 R) = 0$, where R is the radius of the coil. Hence $k_r R = \alpha_n = 3, 8, \ldots$, α_n being the root of Bessel's function of first order. In our case $R = 3.5$ cm, i.e., $k_r \sim 1$, so that for $\lambda_z = 10$ cm, $\vartheta \sim 30°$.

As we have previously observed, all measurements were made in a virtually constant magnetic field. Figure 2, however, shows that the load U_c and the magnetic-probe signal U_p have a distinct resonance appearance. For given generator frequency, magnetic field strength, and excitation coil period, resonance may occur due to the variation of the plasma density in time. To confirm this suggestion, we measured the wavelength in plasma at different times (Figure 5). A microwave interferometer was simultaneously applied to measure the electron density of the plasma. Figure 6 plots the electron density n_0 measured with the microwave interferometer (curve 1) and the plasma density calculated from the dispersion relation (curve 2) with $k_r = 1$. The two sets of results are in satisfactory agreement. Measuring the time-dependence of the wavelength in plasma, we can thus find the density of the plasma and the nature of its variation.

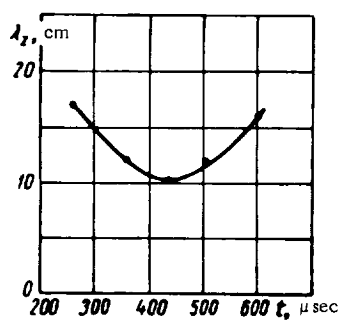

FIGURE 5. The variation of the wavelength λ_z with the length of the high-frequency pulse, t.

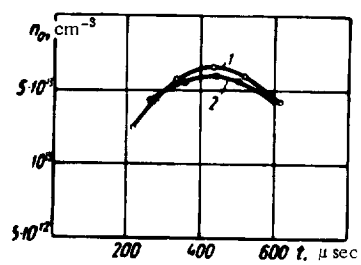

FIGURE 6. The electron density n_0 vs. the length of the high-frequency pulse, t: 1) microwave measurements; 2) calculations with a dispersion relation.

The variation of plasma density after the high-frequency pulse revealed an anomalously rapid decay, similar to that previously described in /9/. Figure 7 plots the plasma decay constant τ against the length of the high-frequency pulse. As the pulse length increases from 200 to 600 μsec, τ grows from 100 to 250 μsec. This points to an increase in plasma energy. However, further increase in the length of the high-frequency pulse results in an anomalously rapid decay of the plasma. The decay constant in this case is as low as 20–30 μsec.

The damping of the wave was studied by tracing, with a magnetic probe, the variation of $\tilde{H}_z$ with the distance along the magnetic field. The reflection of the wave at the end points of the system was virtually nil on account of the high absorption and the considerable length of the system (~2m). We see from Figure 8 that the wave amplitude decreases to 1/2.7 of the original value over a distance of some 40 cm.

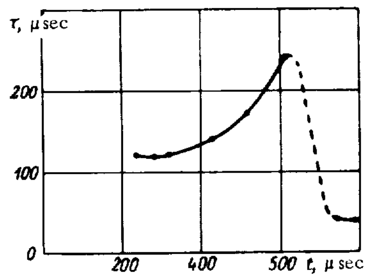

FIGURE 7. The decay constant τ of the plasma vs. the length of the high-frequency pulse, t.

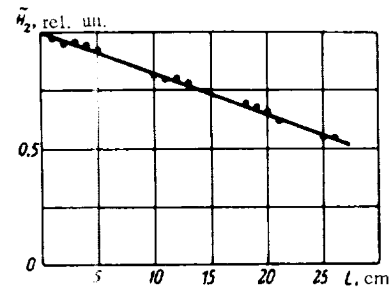

FIGURE 8 Variation of $\tilde{H}_z$ along the magnetic field, L.

The electron temperature is required if we are to establish the damping mechanism of the wave. In our experiment, the electron temperature was determined from the relative intensity of the spectral lines of helium with the wavelengths λ = 4921 and 4713 Å /10/. The measurements showed that the electron temperature T_e increases fairly rapidly to 30–50 eV, and subsequently remains constant despite the increase in the length of the heating pulse.

This phenomenon can be explained if we assume that the electrons lose their energy in the excitation of impurity atoms and ions with high ionization potentials.

For the measured temperatures and densities, the collision damping length according to (3) should be $l_{col} \approx 10^4$, which is greater by two orders of magnitude than the experimentally measured damping length. The collisionless damping length according to (2) is l_L = 60 cm. The measured l is 40 cm. We have thus clearly detected Čerenkov absorption of electromagnetic waves in our experiment.

BIBLIOGRAPHY

1. STEPANOV, K. N. - JETP, **38** : 265. 1960; Izvestiya vuzov. Radiofizika, **6** : 2. 1963.

2. STIX, T. H. - Phys. Rev., **106** : 1146. 1957.

3. GINZBURG, V. L. Rasprostranenie elektromagnitnykh voln v plazme (Propagation of Electromagnetic Waves in Plasma). - Moskva, Fizmatgiz. 1960.

4. RUSANOV, V. D., I. A. KOVAN, V. V. SAVICHEV, and D. A. FRANK-KAMENETSKII. - JETP, **39** : 1503. 1960.

5. HOOKE, W. M., M. A. POTHAN, P. AVIVI, and I. ADAM. - Phys. Fluids, 5: 7, 864. 1962.

6. DOLGOPOLOV, V. V., A. I. ERMAKOV, N. I. NAZAROV, K. N. STEPANOV, and V. T. TOLOK. - Nucl. Fusion, 3: 251. 1963.

7. NAZAROV, N. I., A. I. ERMAKOV, A. S. LOBKO, V. A. BONDAREV, V. T. TOLOK, and K. D. SINEL'NIKOV. - ZhTF, 32: 537. 1962.

8. KAPLANOV, M. R. and V. A. LEVIN. Avtomaticheskaya podstroika chastoty (Automatic Frequency Control). - Moskva, Gosenergoizdat. 1956.

9. NAZAROV, N. I., A. I. ERMAKOV, V. T. TOLOK, and K. D. SINEL'NIKOV. - In: "Fizika plazmy i problemy upravlyaemogo termoyadernogo sinteza", 3, p. 164. Kiev, Izdatel'stvo AN UkrSSR. 1963.

10. MARK, A. - IRE Trans., 6: 3, 33. 1959.

V. V. Dolgopolov, A. I. Ermakov, N. I. Nazarov,
K. N. Stepanov, and V. T. Tolok

ČERENKOV ABSORPTION OF "WHISTLERS" IN AN INHOMOGENEOUS PLASMA COLUMN

1. The phase velocity of the electromagnetic waves of frequency ω which is much greater than the gyrofrequency ω_i of the ions and much smaller than the gyrofrequency $|\omega_e|$ of the electrons is known to be much less than the velocity of light in a high-density plasma /1/.* The slow waves effectively interact with the plasma electrons, whose velocities along the magnetic field, V_z, are close to $\frac{\omega}{k}$, where k is the projection of the wave vector onto the direction of the magnetic field. The damping of "whistlers" in an unbounded plasma with $\frac{\omega}{k} \gg V_e$, where $V_e = \left(\frac{T_e}{m}\right)^{1/2}$ is the thermal velocity of the electrons, was investigated by Shafranov /2/ and Gershman /3/; K. N. Stepanov /4,5/ studied the phenomenon assuming an arbitrary relation between $\frac{\omega}{k}$ and V_e. Since the length of the Čerenkov damping of "whistlers" is much higher than their wavelength, they easily penetrate into a dense plasma. Čerenkov damping of "whistlers" may therefore be applied for heating the electron component of the plasma.

In the present work we investigate the absorption of waves of frequency $\omega_i \ll \omega \ll \omega_e$ propagating along a plasma cylinder and the possibility of heating of the electron component of the plasma with these waves.**

2. Let us consider the Čerenkov absorption, by plasma electrons, of the energy of the electromagnetic field generated by external azimuthal electric currents of density

$$j_{\text{col}} = j_0 \cos(kz - \omega t)\, \delta(r - R),$$

* These waves are known as "whistling atmospherics" or "whistlers"; since $\omega \ll |\omega_e|$, these waves may also be called electron Alfven waves.

** An experimental study of the excitation and absorption of "whistlers" in a plasma cylinder has been presented in /6/.

which flow through the coil enclosing the plasma cylinder. The electric and the magnetic fields of the wave are found from the equations

$$E_r = -\frac{i}{k}\cdot\frac{\partial E_z}{\partial r} + \frac{4\pi i\omega}{k^2c^2}j_r;$$
$$\frac{\partial^2 E_\varphi}{\partial r^2} + \frac{1}{r}\cdot\frac{\partial E_\varphi}{\partial r} + \left(k^2 + \frac{1}{r^2}\right)E_\varphi = -\frac{4\pi i\omega}{c^2}j_\varphi; \tag{1}$$
$$ikrj_z + \frac{\partial}{\partial r}(rj_r) = 0;$$
$$\mathbf{H} = -\frac{ic}{\omega}\operatorname{rot}\mathbf{E},$$

where

$$\mathbf{j} = e\int \mathbf{V} f d\mathbf{V}.$$

The deviation of the distribution function f from the equilibrium distribution F_0 is determined from the equation

$$i(kV_z - \omega)f + V_r\frac{\partial f}{\partial r} + \frac{V_\varphi}{r}\cdot\frac{\partial f}{\partial \varphi} + \frac{eE_0}{m}\cdot\frac{\partial f}{\partial V_r} - \omega_e\frac{\partial f}{\partial \vartheta} = -\frac{e}{m}\left(\mathbf{E} + \frac{1}{c}[\mathbf{VH}]\right)\frac{\partial F_0}{\partial \mathbf{V}}, \tag{2}$$

where E_0 is the strength of the equilibrium radial electric field resulting from charge separation;

$$F_0 = f_0 + \frac{V_\varphi}{\omega_e}\left(\frac{\partial f_0}{\partial r} - \frac{eE_0 f_0}{T_e}\right)$$
$$f_0 = \frac{n_0(r)}{[2\pi T_e(r)/m]^{3/2}}\exp\left[-\frac{mV^2}{2T_e(r)}\right].$$

Here we operate in cylindrical coordinates, where the axis z is parallel to the external magnetic field H_0:

$$r = (r,\ \varphi,\ z);\quad \mathbf{V} = (V_\perp,\ \vartheta,\ V_z);\quad V_r = V_\perp\cos(\vartheta - \varphi);$$
$$V_\varphi = V_\perp\sin(\vartheta - \varphi).$$

We assume that $8\pi n_0 T_e \ll H_0^2$, $r_L = \frac{V_e}{|\omega_e|} \ll \frac{1}{k},\ \frac{1}{k_\perp},\ a$, where $\frac{1}{k_\perp}$ is the characteristic distance over which the field E varies; a the radius of the plasma cylinder. Equation (2) can be solved by successive approximations. Setting $f = f^{(0)} + f^{(1)} + \dots$, we find

$$f^{(0)} = \frac{eV_\perp f_0}{\omega_e T_e}[E_\varphi\cos(\vartheta - \varphi) - E_r\sin(\vartheta - \varphi)] + C;$$
$$f^{(1)} = \frac{V_\perp\sin(\vartheta - \varphi)}{\omega_e}\frac{\partial C}{\partial r} + \frac{eE_0\sin(\vartheta - \varphi)}{m\omega_e}\frac{\partial C}{\partial V_\perp}, \tag{3}$$

where

$$C = \frac{ie}{kV_z - \omega}\left\{\frac{V_\perp^2 f_0}{2\omega_e T_e}\left(\frac{\partial E_\varphi}{\partial r} + \frac{E_\varphi}{r}\right) + \frac{E_\varphi}{m\omega_e}\frac{\partial f_0}{\partial r} - \frac{V_z E_z f_0}{T_e} + \frac{V_z H_r}{mc\omega_e}\left(\frac{\partial f_0}{\partial r} - \frac{eE_0 f_0}{T_e}\right)\right\}.$$

Applying (3), we find the following expression for the current density in the plasma:

$$\mathbf{j} = \mathbf{j}^{(0)} + \mathbf{j}^{(1)},$$

where

$$j_r^{(0)} = \frac{\Omega^2}{4\pi\omega_e} E_\varphi; \quad j_\varphi^{(0)} = -\frac{\Omega^2}{4\pi\omega_e} E_r;$$

$$j_\varphi^{(1)} = \frac{i}{4\pi\omega\omega_e^2} \frac{\partial}{\partial r}\left[\eta\Omega^2 V_e^2 \left(\frac{\partial E_\varphi}{\partial r} + \frac{E_\varphi}{r}\right)\right]; \tag{4}$$

$$j_z^{(0)} = \frac{i\Omega^2}{4\pi k\omega_e}(1+\eta)\left(\frac{\partial E_\varphi}{\partial r} + \frac{E_\varphi}{r}\right) + \frac{i\Omega^2 eE_0}{4\pi k\omega_e T_e}(1+\eta)E_\varphi - \frac{i\omega\Omega^2}{4\pi k^2 V_e^2}(1+\eta)E_z.$$

Here $\Omega = \left(\frac{4\pi e^2 n_0(r)}{m}\right)^{1/2}$ is the Langmuir frequency of the electron;

$$\eta = i\sqrt{\pi}\zeta w(\zeta); \quad \zeta = \frac{\omega}{\sqrt{2}kV_e}; \quad w(\zeta) = e^{-\zeta^2}\left(1 + \frac{2i}{\sqrt{\pi}}\int_0^\zeta e^{t^2}dt\right).$$

Substituting j from (4) in (1) and setting $\mathbf{E} = \mathbf{E}^{(0)} + \mathbf{E}^{(1)}$, we find

$$\frac{\partial^2 E_\varphi^{(0)}}{\partial r^2} + \frac{1}{r}\cdot\frac{\partial E_\varphi^{(0)}}{\partial r} + \left(\frac{\omega^2\Omega^4}{\omega_e^2 k^2 c^4} - k^2 - \frac{1}{r^2}\right)E_\varphi^{(0)} = 0; \tag{5}$$

$$\frac{\partial^2 E_\varphi^{(1)}}{\partial r^2} + \frac{1}{r}\cdot\frac{\partial E_\varphi^{(1)}}{\partial r} + \left(\frac{\omega^2\Omega^4}{\omega_e^2 k^2 c^4} - k^2 - \frac{1}{r^2}\right)E_\varphi^{(1)} = k^2\chi, \tag{6}$$

where

$$\chi = \frac{1}{k^2c^2\omega_e^2}\left\{\frac{\partial}{\partial r}\left[\eta\Omega^2V_e^2\left(\frac{\partial E_\varphi^{(0)}}{\partial r} + \frac{E_\varphi^{(0)}}{r}\right)\right] - \Omega^2\frac{\partial}{\partial r}\left[\frac{V_e^2}{\Omega^2(1+\eta)r}\cdot\frac{\partial}{\partial r}(r\Omega^2E_\varphi^{(0)})\right]\right\}.$$

Let $E_\varphi^{(0)} = A\psi(x)$, where $\psi(x)$ is a solution of equation (5) meeting the condition $\psi(0) = 0$ $(x \equiv kr)$. Then

$$H_z^{(0)} = -\frac{ikc}{\omega}A\left(\frac{\partial\psi}{\partial x} + \frac{\psi}{x}\right).$$

With $ka < x < kR$,

$$\psi(x) = \alpha I_1(x) + \beta K_1(x).$$

With $x > kR$,

$$E_\varphi^{(0)} = BK_1(x); \quad H_z^{(0)} = \frac{ikc}{\omega}BK_0(x).$$

From the conditions

$$E_\varphi^{(0)}(R-0) - E_\varphi^{(0)}(R+0) = 0;$$
$$H_z^{(0)}(R-0) - H_z^{(0)}(R+0) = \frac{4\pi}{c}j_0$$

we find the constants A and B:

$$A = \frac{4\pi i\omega j_0 RK_1(kR)}{ac^2}; \quad B = \frac{4\pi i\omega j_0}{ac^2}[\alpha I_1(kR) + \beta K_1(kR)].$$

The solution of equation (6) for $r \geqslant a$ has the form

$$E_\varphi^{(1)} = -\frac{D}{\alpha}K_1(x),$$

where

$$D = \int_0^{ka}\psi\chi x\,dx.$$

Hence

$$H_z^{(1)} = -\frac{ikc}{\alpha\omega} DK_0(x).$$

Applying the foregoing expressions for the fields, we can find the inflow of energy per unit length of the plasma column:

$$S = \frac{4\pi^2 \omega j_0^2 R^2 K_1^2(kR)}{c^4 \omega_r^2 \alpha^2} \int_0^{ka} \frac{dx}{x} \sqrt{\pi}\,\zeta e^{-\zeta^2} \left\{ \Omega^2 V_e^2 \left(\frac{\partial (x\psi)}{\partial x} \right)^2 + \frac{V_e^2}{\Omega^2 (1+\eta^2)} \left(\frac{\partial (x\psi\Omega^2)}{\partial x} \right)^2 \right\}. \tag{7}$$

3. If $ka \sim 1$; $R \sim a$; $\frac{\omega}{k} \sim V_e$, then

$$S \sim 2\pi a \frac{cE_\varphi H_z}{4\pi} \cdot \frac{8\pi n_0 T_e}{H_0^2},$$

where $H_z = \frac{4\pi j_0}{c}$ is the amplitude of the alternating magnetic field, $E_\varphi = \frac{4\pi j_0 \omega a}{c^2}$ the amplitude of the azimuthal electric field. The mean energy acquired by a single electron, $\frac{dw}{dt} \sim \frac{S}{\pi a^2 n_0}$, is equal in its order of magnitude to

$$\frac{dw}{dt} \sim \frac{H_z^2}{H_0^2} \omega T_e. \tag{8}$$

For example, with $H_0 \sim 10^4\, G$; $\omega \sim 10^9$ sec^{-1} $\sim 10^{-2}$ ω_e; $T_e \sim 100$ eV, and $H_z \sim 30G$, we have $\frac{dw}{dt} \sim 1$ MeV/sec.

This absorption of the wave energy is conditioned by the resonance electrons having $V_z \approx \frac{\omega}{k}$ which drift in the azimuthal direction in the constant magnetic field and in the weakly inhomogeneous and slowly varying field of the wave ($kr_L \ll 1$; $\omega \ll |\omega_e|$). The electric field E_φ of the wave performs positive work on these drift currents. Note that the resonance particles also effectively interact with the fields E_r and E_z; the interaction with the field E_z raises the energy of the particles, while the interaction with the field E_r lowers their energy. The two effects, however, are mutually cancelled. If we consider an electron as a magnetic dipole with a magnetic moment $\mu = \frac{mV_\perp^2}{2H_0} \sim \frac{T_e}{H_0}$, this dipole experiences a force $\sim \mu \frac{\partial H_z}{\partial z}$. Dipoles having longitudinal velocity in the range $\frac{\omega}{k} - \Delta V < V_z < \frac{\omega}{k} + \Delta V$, where $\Delta V \sim V_e \sqrt{\frac{H_z}{H_0}}$, are "trapped" in the potential well and effectively interact with the wave. If $V_z > \frac{\omega}{k}$, the dipole loses its energy to the wave; if $V_z < \frac{\omega}{k}$ it is accelerated by the wave field. Since in a Maxwellian distribution fast electrons are less abundant than slow electrons, there will be a net transfer of energy from the wave to the particles.

In this particular frequency range, the mechanism of collisionless damping is thus analogous to the mechanism of Landau damping of longitudinal plasma oscillations with $H_0 = 0$ (see, e.g., /7/, the quantity $\frac{\mu}{e} \frac{\partial H_z}{\partial z}$ playing the role of the longitudinal field E. A similar mechanism governs the absorption of low-frequency oscillations in "magnetic pumping" /8,9/.

In the absence of collisions, the absorption of energy by resonance particles will lead to the formation of a plateau on the equilibrium

distribution function f_0 at $V_z \approx \frac{\omega}{k}$. Formula (8) derived in the linear approximation applies to weak fields H_z only, when the energy gained by resonance particles between two successive collisions (τ being the time to collision) is much less than T_e. No plateau forms in this case. Since the number of resonance electrons in unit volume $\sim n_0 \frac{\Delta V}{V_e}$, the critical field $H_z = H_{cr}$ producing noticeable distortion of the distribution function can be estimated from the condition $\tau \frac{dw}{dt} \cdot \frac{V_e}{\Delta V} \sim T_e$. Hence

$$H_{cr} \sim H_0 (\omega\tau)^{-2/3}. \tag{9}$$

Since $\tau \sim T_e^{3/2}$, then for $\omega \sim kV_e \sim \sqrt{T_e}$ the mean energy of the particles will grow as

$$\frac{dw}{dt} = \frac{T_0}{\tau_0 (\omega_0 \tau_0)^{1/3}} \left(\frac{T_0}{T_e} \right)^{7/6},$$

where T_0, τ_0, and ω_0 are the initial values of T_e, τ, and ω. Hence it follows that $T_e \sim w$ increases with time as

$$T_e = T_0 \left(1 + \frac{t}{\tau_0 (\omega_0 \tau_0)^{1/3}} \right)^{6/13}.$$

For example, with $H_0 \sim 1\,T$, $n_0 \sim 10^{13}$ cm^{-3}, $\omega \sim 10^9$ sec^{-1},

$$\tau \frac{T_e^{3/2}}{50 n_0} \sim 10^{-6} \text{ sec}, \; H_{cr} \sim 10^{-2} \text{ T}.$$

With $T_e \sim 10$ keV,

$$\tau \sim 10^{-2} \text{sec}; \; H_{cr} \sim 10^{-5} \text{ T}.$$

Heating to $T_e \sim 10$ keV takes $t = 0.1$ sec.

The heating of the plasma can be enhanced by applying several waves with phase velocities differing by 2–3 ΔV. The maximal number of these waves is of the order of $\frac{V_e}{\Delta V} \sim \sqrt{\frac{H_0}{H_z}}$, and the critical field of each wave is given by (9). In this case, with $H \sim H_{cr}$, $\frac{dw}{dt} \sim \frac{T_e}{\tau}$ and

$$T_e = T_0 \left(1 + \frac{t}{\tau_0} \right)^{2/3}. \tag{10}$$

"Whistlers" with the phase velocity $\frac{\omega}{k} \sim V_e$ can be applied to heat up the electron component of a dense plasma ($n_0 \sim 10^{14} - 10^{15}$ cm^{-3}). The electromagnetic field of these waves easily penetrates into the plasma, whereas the high density ensures rapid thermalization of the energy acquired by the resonance particles.

4. In the foregoing we have considered forced plasma oscillations where the wave vector **k** is known, being equal to the wave vector of the excitation currents. Let us now consider the absorption of the energy of free oscillations propagating along a plasma cylinder and calculate the damping ratio.

The electric field of the wave in this case can also be determined from equations (5) and (6), where the real wave vector **k** must be replaced with a

complex quantity $k' = k + i\varkappa$. Let $\psi_i(r)$ be an eigenfunction of the equation

$$\frac{\partial^2\psi_i}{\partial r^2} + \frac{1}{r}\frac{\partial\psi_i}{\partial r} + \left(\frac{\omega^2\Omega^4}{\omega_e^2 k^2 c^4} - \frac{1}{r^2}\right)\psi_i = k_i^2\psi_i,$$

corresponding to the eigenvalue $k_i^2(k)$ (where k is a parameter). The dispersion relation specifying the wave vector as a function of frequency clearly has the form $k_i(k) = k$.* We seek the solution of equation (6) in the form $E = \Phi$, where

$$\Phi = \Sigma c_l\psi_l; \quad c_l = c_l^{(0)} + c_l^{(1)} + \dots,$$

and $c_l^{(0)} = \delta_{il}$. Substituting this expression in (6) and setting $\varkappa \ll k$, we find

$$\sum_l c_l(k_l^2 - k_i^2)\psi_l = \widehat{L}\psi_i, \tag{11}$$

where

$$\widehat{L}\psi_i = 2i\varkappa\left(\frac{\omega^2\Omega^4}{\omega_e^2 k^3 c^4} + k\right)\psi_i + \frac{1}{c^2\omega_e^2}\left\{\frac{\partial}{\partial r}\left[\eta\Omega^2 V_e^2\frac{1}{r}\cdot\frac{\partial}{\partial r}(r\psi_i)\right] - \right.$$
$$\left. - \Omega^2\frac{\partial}{\partial r}\left[\frac{V_e^2}{\Omega^2(1+\eta)r}\cdot\frac{\partial}{\partial r}(r\Omega^2\psi_i)\right]\right\}$$

Multiplying the two sides of (11) by $r\psi_i$ and integrating with respect to r, we find $\int\limits_0^\infty dr r\psi_i\widehat{L}\psi_i = 0$ (terms of second order of smallness have been omitted). Hence the damping ratio

$$\frac{\varkappa_i}{k_i} = \frac{1}{2c^2\omega_e^2\left(1+\frac{\omega^2\Omega_0^4}{\omega_e^2k^4c^4}\right)}\int\limits_0^{k_i a}\frac{dx}{x}\sqrt{\pi}\zeta e^{-\zeta^2}\left\{\Omega^2 V_e^2\left[\frac{\partial(x\psi_i)}{\partial x}\right]^2 + \right.$$
$$\left. + \frac{V_e^2}{|1+\eta|^2\Omega^2}\left[\frac{\partial(x\psi_i\Omega^2)}{\partial x}\right]^2\right\}, \tag{12}$$

where

$$\Omega_0^4 = \int\limits_0^{k_i a} x\psi_i^2\Omega^4 dx$$

If $ka \sim 1$; $R \sim a$; $\frac{\omega}{k} \lesssim V_e$, then in orders of magnitude

$$\varkappa \sim \frac{V_e\omega\Omega_0^2}{c^2\omega_e^2\left(1+\frac{\omega^2\Omega_0^4}{\omega_e^2k^4c^4}\right)}. \tag{13}$$

In the experimental conditions of /6/, $k \sim 0.5$ cm^{-1}, $\omega_e \sim 200\omega \sim 10^{10}$ sec^{-1}, $n \sim 5\cdot10^{13}$ cm^{-3}, and $V_e \sim 5\cdot10^8$ cm/sec. From (13), the damping length $l = 1/\varkappa \sim 100$ cm, which is consistent with the experimental figure $l = 40$ cm (the damping length in Coulomb collisions $l_{\text{col}} \sim 10^4$ cm).

* Note that oscillations may propagate only if in a certain region $\frac{\omega^2\Omega^4}{\omega_e^2k^4c^4} > \frac{3}{4k^2r^2}$.

BIBLIOGRAPHY

1. GINZBURG, V. L. Rasprostranenie elektromagnitnykh voln v plazme (Propagation of Electromagnetic Waves in Plasma). – Moskva, Fizmtagiz. 1960.

2. SHAFRANOV, V. D. – JETF, **34**: 1475. 1958.

3. GERSHMAN, B. N. – Izv. vuzov. Radiofizika, 1: 5-6. 1958.

4. STEPANOV, K. N. – JETP, **38**: 265. 1960.

5. STEPANOV, K. N. – Izv. vuzov. Radiofizika, **6**: 2. 1963.

6. NAZAROV, N. I., A. I. ERMAKOV, V. V. DOLGOPOLOV, K. N. STEPANOV, and V. T. TOLOK. – This volume, p. 4.

7. SHAFRANOV, V. D. Voprosy teorii plazmy (Some Aspects of Plasma Theory). – Moskva, Gosatomizdat. 1963.

8. BERGER, J. M., W. A. NEWCOMB, J. M. DAWSON, E. A. FRIEMAN, R. M. KULSRUD, and A. LENARD. – Phys. Fluids, 1: 301. 1958.

9. STEPANOV, K. N. – JETP, **45**: 1196. 1963.

M. P. Vasil'ev, L. I. Grigor'eva, V. V. Dolgopolov,
B. I. Smerdov, K. N. Stepanov, and V. V. Chechkin

EXPERIMENTAL STUDY OF THE ABSORPTION OF R-F ENERGY BY A PLASMA NEAR ION CYCLOTRON RESONANCE.

The present paper deals with the results of an experimental investigation of the absorption of r-f energy by a dense plasma near the ion cyclotron resonance. Unlike /1,2/, where the plasma was created by a powerful high-frequency generator and energy was transmitted by the so-called Stix coil, we used a pulsed hydrogen discharge with vibrating electrons as a source of plasma. The r-f power was fed into the plasma by a length of an artificial *LC*-line supplied by the higher harmonic of a self-excited generator. The computational principles for these systems are described in /3/. The *LC*-line has a lower input impedance than the Stix coil, so that power of much higher frequency can be fed into the plasma at comparatively low voltages. Furthermore, the input impedance being low, the external longitudinal r-f fields are relatively small. If the external fields are strong, the plasma electrons will rapidly escape to the discharge tube ends, and streaming instability may arise.

We measured various plasma parameters, e.g., the cross-section average electron density in the discharge tube (using a microwave interferometer), the electron temperature (from the relative intensities of singlet and triplet lines of helium, which was injected in small quantities into the tube), temperature of ions (from the Doppler broadening of the H_β line). The r-f power fed into the plasma was measured using a pulsed

transmitted power meter (PTPM); under optimal conditions it amounted to 18 kW.

We studied the dependence of the r-f power absorption in the plasma on the magnetic field strength and on plasma density in the range $(3-0.76) \cdot 10^{13}$ cm^{-3}. The results were compared with the theory of r-f energy absorption in a cold plasma near the ion cyclotron resonance /4/. The plasma density was satisfactorily recovered from the displacement of the absorption peak. The halfwidth of the resonance power absorption curve was found to agree in its order of magnitude with the approximate theory.

The plasma energy balance was also considered. When ion resonance absorption of the r-f energy was observed, almost the entire energy was transmitted to the cold plasma electrons, and the temperature of the ions could not exceed 1 eV. To achieve substantial heating of ions near the cyclotron resonance, the electron temperature must be near or higher than 10 eV.

Equipment

The block-diagram of the experimental setup with the measuring equipment is shown in Figure 1. In the following we give detailed description of some of the units.

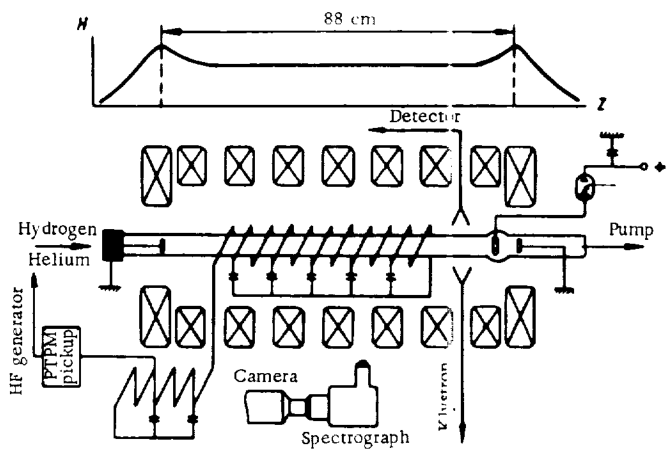

FIGURE 1. Experimental setup

Source of plasma. The plasma was created in a longitudinal magnetic field by a pulsed hydrogen discharge with vibrating electrons; hydrogen pressure $1.3-0.12$ N/m^2. Internal diameter of discharge tube 7 cm, cathode separation 88 cm, distance between ring anode and nearest cathode 6 cm. Plasma formed when a 6μF condenser was discharged through an ignitron into the anode–cathode gap. The condenser was charged to 3–5 kV. Oscillation period of discharge current 36μsec. The ignitron was killed after the second half-period. Among the advantages of this discharge

we have the comparatively high stability of the plasma parameters (from pulse to pulse), breakdown without preliminary ionization at low pressures of up to $0.0065\,N/m^2$, high degree of ionization (apparently over 50%), relatively high temperature of the plasma when conducting current ($T_e \sim 50\,eV$, $T_i \sim 5\,eV$).

Magnetic field. A quasiconstant longitudinal magnetic field H was generated by discharging a $6000\,\mu F$ condenser bank through an ignitron and a solenoid. The discharge current half-period $18\,\mu sec$. The solenoid coils gave a magnetic field which was uniform along the central part of the tube (± 1%) and increased at the ends forming mirrors with 1.4 ratio. The cathodes of the plasma source were located at points of maximum field strength, in the mirrors. The field strength was calibrated against the electron cyclotron resonance in a low-density plasma at a frequency of 10 c/s. The plasma source was turned on at the instant when the magnetic field reached its peak value. All measurements were made within $500\,\mu sec$ after plasma ignition. The field strength within this interval could be regarded as time-independent with a fair accuracy.

***LC*-line and r-f generator.** The r-f energy was fed into the plasma by an *LC*-line having the following parameters: internal helix diameter 7 cm, helix pitch 7/8 cm, cell length (distance between contacts for connecting the condensers) 7 cm, number of cells 11; $450\,\mu\mu F$ ceramic condensers were used. The ends of the helix were grounded through 10^4 pF condensers. The line was excited at $7.5 \cdot 10^6$ c/s (frequency of plasma-loaded line $7.45 \cdot 10^6$ c/s). The length of line in this case accommodated 7 half-periods (axial period λ = 23 cm.) A line segment 5 half-waves long was fitted onto the discharge tube, in the region of the uniform magnetic field. The remaining part of the line of length λ outside the solenoid was connected to the generator. The unloaded Q at the line working frequency was 200. The line impedance at voltage antinodes was 800 ohm.

The functional diagram of the self-excited generator is shown in Figure 2. The vacuum tube used is a triode GU-4A. The *LC*-circuit steps up the low sending-end impedance of the loaded line to the optimal load resistance of the generator tube (500 ohm). This LC-circuit is coupled to the line at a voltage antinode by a half-wavelength cable RK-6. The line-grid feedback is also realized by a half-wavelength cable RK-6. This resistance step-up circuit does not interfere with the rated working conditions of the generator as the line resonance frequency varies within ±7% about $7.5 \cdot 10^6$ c/s.

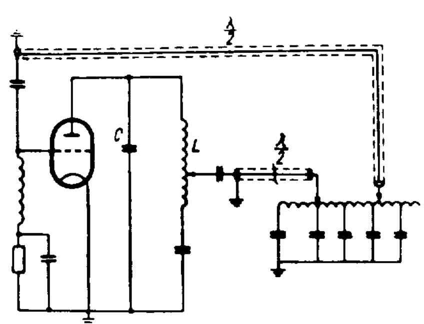

FIGURE 2. Generator circuit.

The generator was adjusted to a pulsed mode of operation by means of a keying thyratron borrowed from /5/. With no load, the envelope of the r-f line voltage gave a square pulse, whose length could be smoothly varied from 500 to $10^4\,\mu sec$. In the experiments described the length of the r-f pulse was 3 msec. The generator was turned on $300\,\mu sec$ before plasma ignition.

The maximal r-f power fed into the plasma near the ion cyclotron resonance was 18 kW with anode voltage of 5 kV.

Procedure

Plasma density. The cross-section-averaged density of the electrons in the discharge tube was measured with a microwave interferometer at a wavelength of 8.1 mm. The transmitting and the receiving horns were pointed to the plasma between the end of the helix and the anode (see Figure 1). In the presence of a r-f field, the plasma density was found to decrease exponentially with a time constant of 30 μsec in a density interval $(1.7-0.76)\cdot 10^{13}\ cm^{-3}$, which could actually be measured. We extrapolated this dependence into the region of higher densities, up to $3\cdot 10^{13}\ cm^{-3}$.

Electron temperature. The electron plasma temperature was determined from the relative intensities of the singlet and triplet helium lines (He I 4921 and He II 4713). To this end, the discharge tube was filled with helium (5% in relation to hydrogen pressure). All the optical measurements were generally made with an ISP-51 spectrograph, coupled with a long-focus camera UF-85 (f = 1300 mm); a photoelectronic attachment with a FEU-17 photomultiplier was provided at the camera outlet.

The time variation of T_e was measured by alternately setting the spectrograph to the two lines, and averaging the intensities over many pulses. Figure 3 plots the corresponding variation of electron temperature with time after plasma ignition. In the lower part of the figure we show the time curve of the discharge current. Our results for T_e support the conclusion /6/ that the electrons in discharges of this kind cool rapidly when the discharge current is turned off. In our case, $T_e < 1$ eV for $\tau > 60\,\mu$sec.

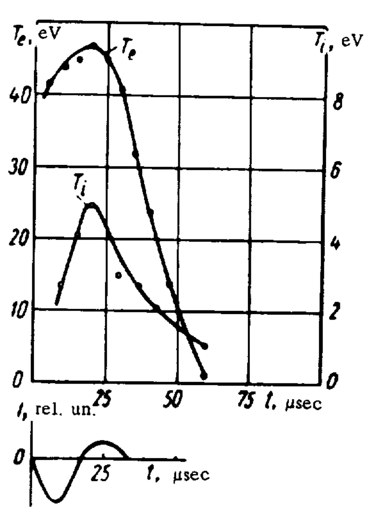

FIGURE 3. Plasma temperature vs. time after plasma ignition.

Temperature of ions. The ion plasma temperature was measured from the Doppler broadening of H_β. The line profile at various times was obtained by a variety of the scanning technique. The input slit of the optical system was narrowed down to some 20–40 μ, and the H_β was left outside the slit. The slit was then gradually broadened, and the line intensity vs. slit width was measured at constant intervals. The measured intensity is clearly proportional to the integral over the part of the line profile exposed by the slit. A whole family of these "integrated curves" taken at different times during the discharge life could be plotted. If the line profile is Gaussian, the distance $\Delta\lambda_D$ between the abscissas of the points having the ordinates 0.12 and 0.88 S_m

on the corresponding integrated curve (S_m being the peak ordinate, representing "saturation") is equal to the line half-width.

Figure 4 plots the experimental points used in calculating the temperature of the excited atoms. The figure also shows a calculated integrated curve corresponding to this temperature. The spread of the experimental points about the theoretical curve does not exceed the margin of error in our measurements. Figure 3 gives the variation of T_i with time after plasma ignition, with the r-f generator turned on, for a magnetic field of 0.56 T and pressure of 0.2 N/m^2. This dependence was obtained by treating the corresponding integrated intensity curves of H_β. An instrumental width of 0.3 Å was assumed in calculations. Unfortunately, this technique was inadequate for measuring T_i at $\tau > 60 \mu$sec, when substantial resonance absorption of r-f power was observed, since the line intensity at that time was already too low. However, an evaluation of the plasma energy balance will show that the ion temperature, even in conditions of intense r-f power absorption, cannot be much higher than 1 eV.

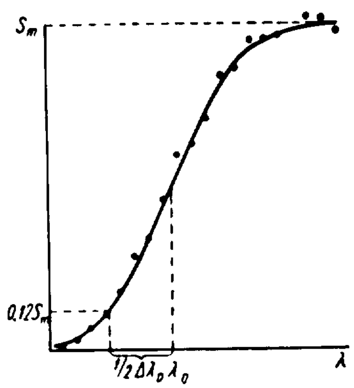

FIGURE 4. Temperature of ions determined from line intensity vs. slit width curve.

R-f power. The r-f power fed by the generator into the load was measured by a PTPM described in /7/. This device measures the pulsed active power in a load with time-variable parameters, and it is coupled to an oscilloscope displaying the waveform of the power pulse. A signal proportional to the active power was obtained by utilizing the multiplying properties of a pentode, with r-f signals proportional to the transmission line current and voltage impressed on its control and screen grids. The current and voltage probes were placed in the generator.

Figure 5 is an oscillogram of the r-f line voltage (top) and of the total r-f power fed into the line in the presence of a discharge (bottom). A signal proportional to the r-f voltage in the antinodes was picked up from the resistive divider and fed directly to the oscilloscope input. Time base 420 μsec. The time of plasma ignition can be determined from the time of appearance of a power pulse.

The power pulse can be divided into two stages in time. The first stage takes some 100 μsec, as long as plasma densities are greater than $5 \cdot 10^{13}$ cm^{-3} and the electron temperature is high. The absorption of r-f energy in this stage is not resonant: it does not depend much on variation of magnetic field strength. The nature of this nonresonance absorption is not clear yet.

The second stage of power absorption sets in roughly 100 μsec after plasma ignition, when the density has dropped to $5 \cdot 10^{13}$ cm^{-3} and the electron temperature is less than 1 eV. This is a distinct resonance absorption, varying with the magnetic field and existing only in magnetic fields somewhat higher than the field corresponding to the cyclotron resonance of a single hydrogen ion.

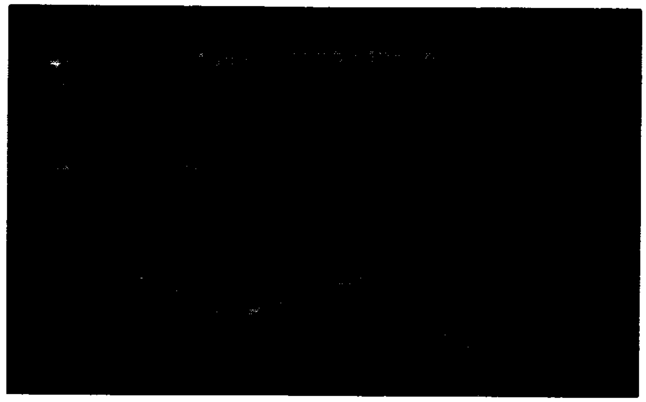

FIGURE 5. Oscillograms of r-f line voltage (top) and transmitted power (bottom).

It is this stage of r-f energy absorption by a plasma that has been investigated in the present study.

Absorption of r-f energy near ion cyclotron resonance. Comparison with theory.

Figure 6 shows a system of curves displaying the r-f power absorbed by a plasma as a function of the magnetic field strength for various plasma densities. These curves were obtained by treating the oscillograms of power pulses, like that shown in Figure 5, taken for different magnetic field strengths.

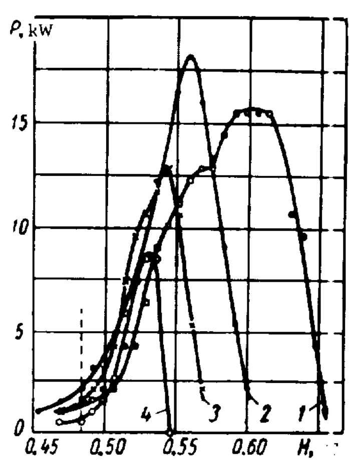

FIGURE 6. R-f power absorption in a plasma vs. magnetic field strength: 1) $n = 3 \cdot 10^{13}$; 2) $1.7 \cdot 10^{13}$; 3) $1.1 \cdot 10^{3}$; 4) $0.76 \cdot 10^{13}$ cm^{-3}.

All the curves are averages of a great many measurements. The hydrogen pressure was invariably $0.2\,\mathrm{N/m^2}$; r-f line voltage 2.3 kV. Peak power absorption (18 kW) occurs at a plasma density of $1.7\cdot10^{13}\,\mathrm{cm^{-3}}$. The dashed line in Figure 6 marks the cyclotron magnetic field H_0.

Let us compare the experimental results with the theory. In our case ($n\sim10^{13}\,\mathrm{cm^{-3}}$, $T_i\sim1\,\mathrm{eV}$, $T_e<1\,\mathrm{eV}$), the absorption of the r-f energy near the cyclotron resonance should be conditioned only by collisions of ions with other plasma components, the contribution of cyclotron damping being small.

A theoretical calculation of the absorption curve from the general formula (11) in /8/ is highly complicated and will hardly help in our case, since the exact values of T_e needed to calculate the collision frequencies of ions with electrons and neutral atoms are not known. The most reasonable approach is to compare the experimental curves with the approximate relation from /4/

$$S=\frac{\pi^2 j_0^2 R^2}{4ca}K_1^2(k_\parallel R)\left(\frac{a\omega}{c}\right)^5 n_\parallel^4 f, \tag{1}$$

where

$$f=\frac{X\gamma\omega}{(X\omega_i+\omega-\omega_i)^2+\gamma^2};\quad X=\frac{\Omega_i^2}{2k_\parallel^2c^2}; \tag{2}$$

S the r-f power absorbed in unit length of the plasma column; j_0 the current through the helix (per unit length); R the helix radius; a the radius of the plasma; $n_\parallel=\frac{k_\parallel c}{\omega}$; $k_\parallel=\frac{2\pi}{\lambda}$ the axial wave number; ω_i ion gyrofrequency; Ω_i ion plasma frequency; γ ion effective collision frequency; K_1 Macdonald function.

Relation (1) has been derived for the case of long wavelengths or small plasma radii, when $k_\parallel a\ll1$ and $k_\perp a\ll1$, $k_\perp$ being the radial wave number. In our case $k_\parallel a\simeq0.8$ and $k_\perp a\simeq1.5$, so that we may expect only order-of-magnitude agreement of the theory with the experimental results for the line half-width, the peak absorption power, and the displacement of the peak absorption relative to H_0.

As we have already observed, the exact γ is not known. We therefore make use of the fact that, in accordance with (2), the peak absorption power is proportional to $X\omega_i/\gamma$. Setting the S for peak absorption equal to the corresponding experimental quantity, and substituting the measured plasma density in the expression for X, we find γ. Thus γ can be calculated if we assume that the power is absorbed in interparticle collisions only and apply formulas (1), (2). This approximation can be evaluated by examining the fit between the half-width of the experimental curve and the theoretical half-width calculated from (1) and (2) (which is equal to $2\gamma/\omega_i$).

Another independent criterion for the applicability of this approximation is to calculate the plasma density from (2) using the experimentally measured displacement of the absorption maximum from the cyclotron magnetic field H_0. From (2) it follows that the peak absorption occurs when

$$X\omega_i+\omega-\omega_i=0. \tag{3}$$

Substituting the measured displacement $\omega-\omega_i$, we find X and hence the density. This quantity can be compared with the measured n.

In our case $R = 3.5$ cm, $j_0 = 30$ A/cm (j_0 can be calculated if the line voltage and impedance are known), $\omega = 4.68 \cdot 10^7$ sec^{-1}; a is taken equal to the internal radius of the discharge tube (3 cm).

The effective collision frequency γ, the half-width of the absorption curve, and the density for the curves in Figure 6, all calculated from (1) and (2), are compared with the experimental data from the table; the peak absorption of r-f power is also given in this table.

Density, cm^{-3}		Half-width, %		Effective collision frequency calculated from (1) and (2), sec^{-1}	Measured peak absorption, kW
Measured	Calculated from peak displacement (3)	Measured	Calculated from (1) and (2)		
$3.0 \cdot 10^{13}$	$3.03 \cdot 10^{13}$	22.6	16.3	$3.8 \cdot 10^6$	15.6
$1.7 \cdot 10^{13}$	$1.71 \cdot 10^{13}$	13.0	12.7	$2.5 \cdot 10^6$	18.0
$1.1 \cdot 10^{13}$	$1.14 \cdot 10^{13}$	9.7	11.1	$2.6 \cdot 10^6$	12.7
$0.76 \cdot 10^{13}$	$0.78 \cdot 10^{13}$	6.5	14.1	$3.3 \cdot 10^6$	8.5

We see from the table that the measured density is virtually identical with the density calculated from the displacement of the absorption peak. The half-widths, however, show satisfactory agreement with the theory for the densities of $1.7 \cdot 10^{13}$ and $1.1 \cdot 10^{13}$ cm^{-3} only. Since our case does not meet the basic requirements for which relations (1) and (2) have been derived, we can hardly expect a better agreement. Furthermore, the radius of the plasma column is a somewhat uncertain quantity, and we arbitrarily set it equal to the internal radius of the discharge tube, assuming a homogeneous plasma density across the tube. Figure 7 gives the experimental absorption curve plotted for the density of $1.7 \cdot 10^{13}$ cm^{-3} (dashed line), and the corresponding curve calculated from (1) assuming equal peak absorption (solid line).

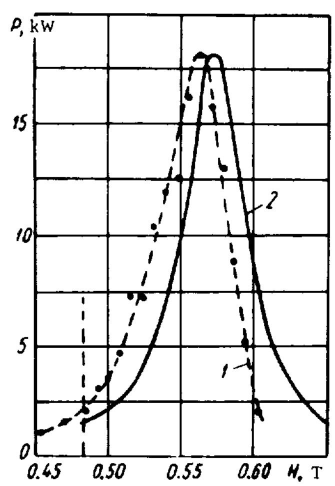

FIGURE 7. Absorption curves for plasma density of $1.7 \cdot 10^{13}$ cm^{-3}:
1) experimental; 2) theoretical.

It would be interesting to establish what collisions exactly are responsible for the absorption of r-f power. We could try to answer this question by examining the absorption curve for the density of $1.7 \cdot 10^{13}$ cm^{-3}, where the measured and the calculated half-widths are in good agreement. To estimate the contribution of collisions between ions and neutrals, it suffices to measure the peak power (or the half-width) for a constant plasma density, but various pressures, calculating γ from the measurements. Extrapolating the function $\gamma(p)$ in the direction of low pressures, we find γ_{ie} conditioned by electron-ion collisions only.

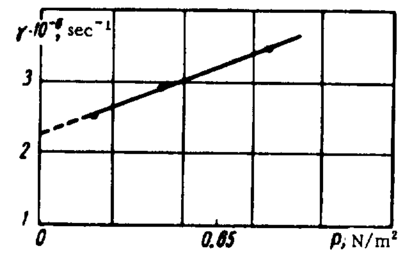

FIGURE 8. The effective collision frequency of ions vs. pressure.

Figure 8 plots the variation of the collision frequency with pressure. This graph was obtained by treating the absorption curves for the density of $1.7 \cdot 10^{13}$ cm^{-3} and pressures of 0.2, 0.47, and 0.87 N/m^2. The frequency γ was calculated from peak absorption, and it coincides to within 10% with γ determined from the half-width. Extending the experimental line to its intersection with the vertical axis ($p = 0$), we find $\gamma_{ie} = 2.25 \cdot 10^6$ sec^{-1} for the frequency of Coulomb collisions between electrons and ions. It thus seems that for the case depicted in Figure 7 the collision frequency for ions and neutrals is $0.25 \cdot 10^6$ sec^{-1}, i.e., a mere 11% of the total effective collision frequency of the ions. The effective frequency of ion–electron collisions is determined from the well-known relations /9/

$$\gamma_{ie} = \frac{m}{M}\left[\frac{5.5n}{T_e^{3/2}} \ln\left(220\frac{T_e}{n^{1/3}}\right)\right], \tag{4}$$

where m and M are the masses of the electron and the ion, respectively. The electron temperature estimated from relation (4) for this case is $1.5 \cdot 10^3$ °K.

Energy balance in a plasma

In our case, the peak r-f power fed into the plasma near the ion cyclotron resonance is 18 kW for a plasma density of $1.7 \cdot 10^{13}$ cm^{-3}. The volume occupied by the plasma is approximately 2500 cm^3. Hence, the mean power per 1 cm^3 of plasma is 7.0 J $\cdot$ cm^{-3} $\cdot$ sec^{-1}. The electron temperature, as we have shown above, is $1.5 \cdot 10^3$ °K.

The r-f energy is transmitted from the generator to the plasma ions directly, so that the temperature of the ions should be greater than T_e. The ions will therefore lose heat to the electrons. If the amount of energy lost by ions in collision with neutral atoms is neglected (in our case this simplification is justified, since as we have shown $\gamma \approx \gamma_{ie}$), we can maintain that thermal equilibrium sets in at a temperature when all the energy gained by the ions in the r-f field is transferred to the electrons.

The specific energy transferred from ions to electrons in 1 sec /10/ is

$$w_{ie} = n^2 k (T_i - T_e)\left(\frac{2\pi k T_e}{m}\right)^{1/2} \frac{m}{M}\left(\frac{e^2}{kT_e}\right) \ln\left[12\pi n\left(\frac{kT_e}{4\pi n e^2}\right)^{3/2}\right], \tag{5}$$

where k is Boltzmann's constant.

Setting the right-hand side of (5) equal to the r-f power absorbed in unit plasma volume, we can estimate the temperature of the ions. In our case ($n = 1.7 \cdot 10^{13}$ cm^{-3}, $T_e = 1.5 \cdot 10^3$ °K, $w_{ie} = 7.0$ J·cm^{-3}·sec^{-1}), this gives $T_i = 1.1$ eV.

It is much more difficult to find how the electrons expend this additional energy. In any case, judging from the rate of cooling of the plasma, the thermal losses of the electrons appear to be excessive when the discharge current is turned off. We should note that there is nevertheless a slight heating of the electrons in resonance conditions. This follows from the dependence of the H_β intensity on the magnetic field strength (see Figure 5 in /3/). This is clearly a resonance dependence, reaching a maximum in fields H corresponding to peak power absorption. However, in absolute value, this maximum amounts to no more than few fractions of a percent of the H_β intensity observed when current passes through the discharge.

To heat the ions substantially, we should increase either the generator power or the electron temperature. An estimate based on (5) shows that for plasma densities of $1.7 \cdot 10^{13}$ cm^{-3} and a moderate electron temperature of the order of 10^5 °K, the same specific power of 7.0 J·cm^{-3}·sec^{-1} would suffice to maintain the temperature of the electrons at the $3 \cdot 10^6$ °K mark. In the experiments described in /1,2/ the high electron temperature is apparently maintained by strong high-frequency longitudinal fields E_z. In our case, E_z is much weaker. An additional source of energy should therefore be applied to heat the electrons. Note that a plasma with a fairly high T_e does exist in our discharge when the current flows through, but in this stage occurs the nonresonance absorption mentioned above, whose nature is not yet clear.

The plasma electrons may be heated in a discharge tube by harnessing the phenomenon of VHF electron cyclotron resonance. The results obtained in this direction /10/ are most promising.

BIBLIOGRAPHY

1. HOOKE, W. M., F. H. TENNEY, M. H. BRENNAN, H. M. HILL, j., and T. H. STIX. – Phys. Fluids, **4**: 1131. 1961.

2. NAZAROV, N. I., A. I. ERMAKOV, A. S. LOBKO, V. A. BONDAREV, V. T. TOLOK, and K. D. SINEL'NIKOV. – ZhTF, **32**: 536. 1962.

3. BRZHECHKO, M. V., M. P. VASIL'EV, L. I. GRIGOR'EVA, V. V. DOLGOPOLOV, A. S. LOGINOV, O. S. PAVLICHENKO, B. I. SMERDOV, K. N. STEPANOV, and V. V. CHECHKIN. – In: "Fizika plazmy i problemy upravlyaemogo termoyadernogo sinteza", **3**: 109. Kiev, Izdatel'stvo AN UkrSSR. 1963.

4. VASIL'EV, M. P., L. I. GRIGOR'EVA, V. V. DOLGOPOLOV, B. I. SMERDOV, K. N. STEPANOV, and V. V. CHECHKIN. – This volume, p. 25.

5. GRUDINSKAYA, G. P., B. T. ZARUBIN, and B. I. POLYAKOV. – Radiotekhnika, **14**(4): 60. 1959.

6. PAVLICHENKO, O. S. and L. A. DUSHIN. – Optika i Spektroskopiya, **12**(5): 541. 1962.

7. YAKOVLEV, K. A., D. K. PANKRUSHINA, and YU. G. BASIN. – PTE, **4**: 89. 1961.

8. VASIL'EV, M. P., L. I. GRIGOR'EVA, V. V. DOLGOPOLOV, B. I. SMERDOV, K. N. STEPANOV, and V. V. CHECHKIN. - In: "Fizika plazmy i problemy upravlyaemogo termoyadernogo sinteza", 3 : 96. Kiev, Izdatel'stvo AN UkrSSR. 1963.

9. AL'PERT, YA. L., V. L. GINZBURG, and E. L. FEINBERG. Rasprostranenie radiovoln (Propagation of Radio Waves). - Moskva, GITTL. 1953.

10. BECKER, M. C., R. A. DANDL, H. O. EASON, jr., A. C. ENGLAND, R. J. KERR, and W. B. ARD - Nucl. Fusion. Suppl., 1 : 345. 1962.

M. P. Vasil'ev, L. I. Grigor'eva, V. V. Dolgopolov,
B. I. Smerdov, K. N. Stepanov, and V. V. Chechkin

CYCLOTRON RESONANCE IN AN INHOMOGENEOUS PLASMA COLUMN

The heating of a plasma column by a r-f field utilizing the ion cyclotron resonance has been studied in /1-3/. It has been assumed, however, that the plasma density and the temperature of the ions are constant across the plasma column. In the present paper we consider high-frequency heating of a plasma column by external currents under conditions of ion cyclotron resonance, when the plasma density and the temperature vary along the radius.

Let us consider cyclotron heating of a plasma cylinder immersed in a longitudinal magnetic field H_0 and a high-frequency field set up by the electric currents flowing in a thin coil enclosing the plasma column. The current density in the coil is assumed to have the form of a traveling wave:

$$j_\varphi^{\text{coil}} = j_0 \cos(kz - \omega t)\,\delta(r - R), \tag{1}$$

where R is the radius of the coil. The electromagnetic field in the plasma is determined from the equations

$$\operatorname{rot}\operatorname{rot}\mathbf{E} - \frac{\omega^2}{c^2}\left(\mathbf{E} + \frac{4\pi i}{\omega}\,\mathbf{j}\right) = 0, \qquad \mathbf{H} = -\frac{ic}{\omega}\operatorname{rot}\mathbf{E}. \tag{2}$$

The current density in the plasma

$$\mathbf{j} = \sum_\alpha e_\alpha \int \mathbf{v} f_\alpha d\mathbf{v},$$

where f_α is the deviation of the distribution function of particles of the species α from the equilibrium distribution

$$f_{0\alpha} = \frac{m_\alpha^{3/2} n_0(r)}{[2\pi T_\alpha(r)]^{3/2}} \exp\left[-\frac{m_\alpha v^2}{2T_\alpha(r)}\right].$$

Here $n_0(r) = 0$ for $r > a$ (a being the radius of the plasma column).

The function f_α is determined from the kinetic equation

$$i(kv_z - \omega) f_\alpha + v_r \frac{\partial f_\alpha}{\partial r} + \frac{v_\varphi}{r}\frac{\partial f_\alpha}{\partial \varphi} + \frac{e_\alpha}{m_\alpha}\mathbf{E}\frac{\partial f_{0\alpha}}{\partial \vec{v}} - \omega_\alpha \frac{\partial f}{\partial \vartheta} = 0. \tag{3}$$

where $\omega_\alpha = \frac{e_\alpha H_0}{m_\alpha c}$ is the gyrofrequency of particles of the species α; ϑ the polar angle in the velocity space.

We shall deal with a low-pressure plasma, when the magnetic pressure is much higher than the gas-kinetic pressure created by the plasma particles. In this case, the wavelength of the free plasma oscillations of frequency $\omega \sim \omega_i$ is known to be much higher than the Larmor radius of the particles with a mean thermal velocity $v_\alpha = \sqrt{\frac{T_\alpha}{m_\alpha}}$. If the wavelength of the forced oscillations, $\frac{1}{k}$, is of the same order of magnitude as the wavelength of the free oscillations (it is in this case only that waves are satisfactorily excited in a plasma), the thermal motion of the plasma particles across the magnetic field may be neglected, i.e., in equation (3) we may omit the terms proportional to v_r and v_φ. Then from (3)

$$\frac{4\pi i}{\omega} j_i = [\varepsilon_1 \delta_{ik} + (\varepsilon_3 - \varepsilon_1) h_i h_k + i\varepsilon_2 e_{ikl} h_l] E_k(\mathbf{r}); \tag{4}$$

where

$$\varepsilon_1 = i\sigma - \frac{1}{4}\frac{\Omega_i^2}{\omega_i^2}; \quad \varepsilon_2 = i\sigma - \frac{3}{4}\frac{\Omega_i^2}{\omega_i^2},$$

$$\sigma = \sqrt{\frac{\pi}{8}} \frac{\Omega_i^2 w(z_i)}{\omega_i k v_i};$$

$$\varepsilon_3 = \frac{2m_i}{m_e}\frac{\Omega_i^2}{\omega^2} z_e^2 [1 + i\sqrt{\pi} z_e w(z_e)]; \tag{5}$$

$$w(z) = e^{-z^2}\left(1 + \frac{2i}{\sqrt{\pi}} \int_0^z e^{t^2} dt\right).$$

Here $\Omega_i = \left(\frac{4\pi e^2 n_0(r)}{m_i}\right)^{1/2}$ is the Langmuir frequency of the ions; $z_e = \frac{\omega}{\sqrt{2}\, k v_e}$; $z_i = \frac{\omega - \omega_i}{\sqrt{2}\, k v_i}$.

Expressions (5) for ε_1 and ε_2 apply in the case of a "hot" plasma, when the absorption of waves is determined by the thermal motion of ions (cyclotron damping), and collisions are little effective. This case obtains when $kv_i \gg \gamma$, where γ is the effective collision frequency of ions with electrons and neutrals. In "cold" plasma ($\gamma \gg kv_i$), the absorption of waves by collision cannot be neglected. In this case

$$\varepsilon_1 = \varepsilon_2 = -\frac{\Omega_i^2}{\omega^2 - \omega_i^2 + 2i\omega\gamma};$$

$$\varepsilon_3 = -\frac{m_i \Omega_i^2}{m_e(\omega + i\nu_{ei} + i\nu_{en})\omega}, \tag{6}$$

where $\gamma = \nu_{ei}\frac{m_e}{m_i} + \nu_{in}$; ν_{in} is the collision frequency of ions with neutral particles; $\nu_{ei} = \frac{\sqrt{\pi} e^4 n_0 \Lambda}{\sqrt{m_e} T_e^{3/2}}$ the collision frequency of ions with electrons; $\Lambda = \ln\left(0.37\frac{T_e^3}{e^6 n_0}\right)$ the Coulomb logarithm; ν_{en} the collision frequency of electrons with neutrals.

Seeing that $|\varepsilon_3|$ is much greater than $|\varepsilon_1|$ and that $n_\parallel^2 = \left(\frac{kc}{\omega}\right)^2$, we find from (4)

$$E_r = \frac{i\varepsilon_2}{\varepsilon_1 - n_\parallel^2} E_\varphi; \quad E_z = \frac{in_\parallel c}{\omega\varepsilon_3}\left(E_\varphi' + \frac{E_\varphi}{r}\right);$$

$$H_r = -n_\parallel E_\varphi; \quad H_\varphi = n_\parallel E_r; \quad H_z = -\frac{ic}{\omega}\left(E_\varphi' + \frac{E_\varphi}{r}\right), \tag{7}$$

where the field $E_\varphi(r)$ is determined from the equation

$$E_\varphi'' + \frac{1}{r}E_\varphi' + \left(\frac{\omega^2}{c^2}n_\perp^2 - \frac{1}{r^2}\right)E_\varphi = 0. \tag{7'}$$

The "radial" refractive index $n_\perp(r)$ is obtained from the relation

$$n_\perp^2 = \frac{(n_\parallel^2 - \varepsilon_1)^2 - \varepsilon_2^2}{\varepsilon_1 - n_\parallel^2}. \tag{8}$$

Let us solve equation (8) for the case of a low-density plasma ($|\varepsilon_1| \ll n_\parallel^2$) and for the case of long-wave oscillations $\left(\frac{\omega}{c}|n_\perp|a \ll 1\right)$. In either case, equation (7) may be written

$$E_\varphi'' + \frac{1}{r}E_\varphi' + \left[\varkappa^2(r) - k^2 - \frac{1}{r^2}\right]E_\varphi = 0, \tag{9}$$

where $|\varkappa^2|$ is small in comparison with $k^2 + \frac{1}{r^2}$. For a low-density plasma,

$$\varkappa^2 = \frac{\omega^2}{c^2}\varepsilon_1, \tag{10}$$

for long-wave oscillations

$$\varkappa^2 = \frac{\omega^2}{c^2}n_\perp^2 + k^2. \tag{11}$$

We shall solve equation (9) by the perturbation technique. Setting

$$E_\varphi = E_\varphi^{(0)} + E_\varphi^{(1)} + \ldots, \tag{12}$$

we have

$$E_\varphi^{(0)''} + \frac{1}{r}E_\varphi^{(0)'} - \left(k^2 + \frac{1}{r^2}\right)E_\varphi^{(0)} = 0; \tag{13}$$

$$E_\varphi^{(1)''} + \frac{1}{r}E_\varphi^{(1)'} - \left(k^2 + \frac{1}{r^2}\right) E_\varphi^{(1)} = -\varkappa^2(r)E_\varphi^{(0)}; \tag{14}$$

. . . .

From (13) we find zeroth-order E_φ and H_z:
for $r < R$

$$E_\varphi^{(0)} = AI_1(kr); \quad H_z^{(0)} = -in_\parallel AI_0(kr), \tag{15}$$

for $r > R$

$$E_\varphi^{(0)} = BK_1(kr); \quad H_z^{(0)} = in_\parallel BK_0(kr), \tag{16}$$

where $I_n(x)$ is the modified Bessel function, $K_n(x)$ the Macdonald function. The constants A and B are determined from the boundary conditions

$$E_\varphi^{(0)}(R-0) = E_\varphi^{(0)}(R+0); \quad H_z^{(0)}(R-0) = H_z^{(0)}(R+0) + \frac{4\pi}{c}j_0; \tag{17}$$

$$A = \frac{4\pi i j_0 \omega R K_1(kR)}{c^2}; \quad B = A\frac{I_1(kR)}{K_1(kR)}. \tag{18}$$

Substituting $E_\varphi^{(0)}$ in equation (14) we find for $r < R$

$$\begin{aligned} E_\varphi^{(1)} &= A_1 I_1(kr) + A\left[K_1(kr)\int_0^r \varkappa^2 I_1^2(kr)\,r\,dr - I_1(kr)\int_0^r \varkappa^2 I_1(kr)K_1(kr)\,r\,dr\right]; \\ H_z^{(1)} &= in_\parallel\left\{-A_1 I_0(kr) + A\left[K_0(kr)\int_0^r \varkappa^2 I_1^2(kr)\,r\,dr + I_0(kr)\int_0^r \varkappa^2 I_1(kr)K_1(kr)\,r\,dr\right]\right\}, \end{aligned} \tag{19}$$

and for $r > R$

$$E_\varphi^{(1)} = B_1 K_1(kr);\ H_z^{(1)} = in_\parallel B_1 K_0(kr). \tag{20}$$

The constants A_1 and B_1 are determined from the condition of continuity of $E_\varphi^{(1)}$ and $H_z^{(1)}$ at the point $r = R$.

The other field components are easily obtained from (7'). To find the time-average flux of energy absorbed by unit length of the plasma column

$$S = 2\pi a \frac{c}{4\pi} \overline{E_\varphi H_z}\Big|_{r=a}, \tag{21}$$

we must have the values of $E_\varphi^{(1)}$ and $H_z^{(1)}$ at the point $r = a$. From (19)

$$E_\varphi^{(1)}(a) = AK_1(ka)\varphi(a);\ H_z^{(1)}(a) = in_\parallel AK_0(ka)\varphi(a),$$

where

$$\varphi(a) = \int_0^a \varkappa^2(r) I_1^2(kr)\, rdr. \tag{22}$$

Hence finally

$$S = \frac{4\pi^2 j_0^2 \omega R^2}{c^2} K_1^2(kR)\psi(a), \tag{23}$$

where

$$\psi(a) = \operatorname{Im}\varphi(a).$$

Let us consider expression (23) in some particular cases.

For a low-density hot plasma,

$$\psi = \frac{\omega^2}{c^2}\int_0^a \sqrt{\frac{\pi}{8}}\frac{\Omega_i^2}{\omega_i k v_i} e^{-z_i^2} I_1^2(kr)\, rdr. \tag{24}$$

In our approximation, as we see from expression (24), the profile of the absorption line is symmetrical about the frequency $\omega = \omega_i$. The absorption profile in a layer of radius r is determined by the function $e^{-z_i^2}$.

If the temperature and the density of the plasma are constant for $r < a$ (a "square"distribution of density), expression (24) takes on a simpler form:

$$\psi = \frac{\sqrt{\pi}\,\Omega_i^2}{4\sqrt{2}\,\omega k v_i}\left(\frac{\omega a}{c}\right)^2 [I_1^2(ka) - I_0(ka)\, I_2(ka)]. \tag{25}$$

For a hot plasma with long-wave oscillations, when the "radial" wavelength is much greater than the radius a of the plasma column, we find, applying expression (11) with $n_\parallel^2 \sim |\varepsilon_1|$,

$$\psi = \frac{k^4}{4}\int_0^a f(z_i)\, r^3 dr; \tag{26}$$

$$f(z) = \frac{\xi}{(\xi + u)^2 + e^{-2z^2}} e^{-z^2}, \tag{27}$$

where

$$u = \frac{2}{\sqrt{\pi}} e^{-z^2}\int_0^z e^{t^2} dt;\quad \xi = \sqrt{\frac{8}{\pi}}\frac{k^2 c^2 v_i}{\Omega_i^2 \omega_i}.$$

Since $u(z) < 0$ for $z < 0$ and $u(z) > 0$ for $z > 0$, the peak absorption occurs at a frequency $\omega < \omega_i$. The graph of the function $f(z)$, describing the profile of the absorption line in a plasma layer of radius r, is plotted in Figure 1 (1) $\xi = 0.1$; 2) $\xi = 1.0$; 3) $\xi = 0.5$; 4) $\xi = 0.3$).

For a "square" distribution, we have from (26)

$$\psi = \frac{k^4 a^4}{16} f(z_i). \tag{28}$$

In a cold ($\gamma \gg kv_i$), low-density plasma,

$$\psi = \frac{1}{2c^2} \int_0^a \frac{\Omega_i^2 \gamma \omega}{(\omega - \omega_i)^2 + \gamma^2} I_1^2(kr)\, r dr. \tag{29}$$

As in a hot plasma, the absorption is maximal at the point $\omega = \omega_i$.

If the density of the cold plasma is not small, then for long-wave oscillations with $n_{\parallel}^2 \sim |\varepsilon_1|$

$$\psi = \frac{k^4}{4} \int_0^a \frac{x \omega \gamma}{(\omega - \omega_i + x\omega_i)^2 + \gamma^2} r^3 dr, \tag{30}$$

where $x = \frac{\Omega_i^2}{2k^2c^2}$. The absorption is maximal at a frequency $\omega < \omega_i$. Expressions (23),(30) are in good agreement with the experimental results that we have obtained in /3/.

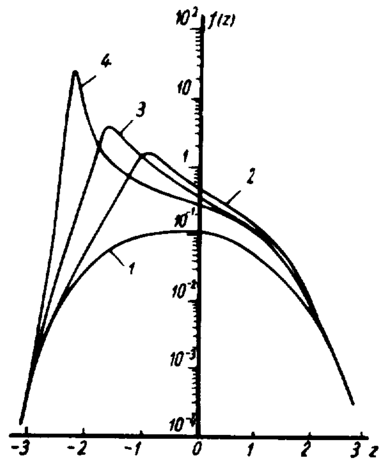

FIGURE 1.

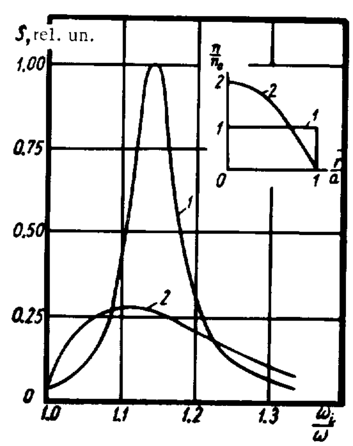

FIGURE 2.

For a "square" distribution of density, expression (30) takes the form

$$\psi = \left(\frac{ka}{2}\right)^4 \frac{x\omega\gamma}{(\omega - \omega_i + x\omega_i)^2 + \gamma^2}. \tag{31}$$

The absorption curve (31) is symmetrical about the maximum at the point $\omega = \omega_i (1 - x)$.

Deviation of the density from the "square" distribution additionally broadens the absorption curve, which loses its symmetry about the maximum. Figure 2 shows the power absorption curves (in relative units) and the corresponding density distributions: curve 1 corresponds to a square distribution, and curve 2 represents the case with a distribution $n = 2n_0\left(1 - \frac{r^2}{a^2}\right)$. In either case, the mean plasma density (over the cross section of the column) is n_0; here $\frac{\nu}{\omega} = 0.1$, $ka = 1$.

We see from Figure 2 that the absorption maximum for a square distribution is much higher than for a distribution which falls off along the radius. This is so because absorption mainly occurs in the peripheral plasma, since the field E_φ increases in this case as $\sim r$. The variation of the asymmetry of the absorption curve with $\frac{\omega_i}{\omega}$ that has been experimentally observed in /4/ is apparently attributable to the reduction of plasma density along the radius.

BIBLIOGRAPHY

1. STIX, T. H. - Phys. Fluids, 1: 308. 1958.

2. SAGDEEV, R. Z. and V. D. SHAFRANOV. - In: "Fizika plazmy i problema upravlyaemykh termoyadernykh reaktsii", 4: 430, Moskva, Izdatel'stvo AN SSSR. 1958.

3. VASIL'EV, M. P., L. I. GRIGOR'EVA, V. V. DOLGOPOLOV, B. I. SMERDOV, K. N. STEPANOV, and V. V. CHECHKIN. - This volume, p. 15.

4. VASIL'EV, M. P., L. I. GRIGOR'EVA, V. V. DOLGOPOLOV, B. I. SMERDOV, K. N. STEPANOV, and V. V. CHECHKIN. - In: "Fizika plazmy i problemy upravlyaemogo termoyadernogo sinteza", 3: 96. Kiev, Izdatel'stvo AN UkrSSR. 1963.

5. CHECHKIN, V. V., M. P. VASIL'EV, L. I. GRIGOR'EVA, and B. I. SMERDOV. - ZhTF, 31: 1033. 1961.

V. V. Dolgopolov and K. N. Stepanov

A CONTRIBUTION TO THE THEORY OF HIGH-FREQUENCY HEATING OF HOT INHOMOGENEOUS PLASMA

Collisionless absorption by a plasma of r-f electromagnetic energy whose frequency ω is much lower than the ion cyclotron frequency ω_i has been investigated in /1-3/. In /1/ an expression has been derived for the energy acquired by a particle moving along a constant magnetic field through a coil of finite length which sets up an alternating electromagnetic field. This analysis, however, fails to consider a great many effects connected with the collective interaction of particles in a plasma (quasineutrality of the plasma, inhomogeneity, possible excitation of sound waves).

The absorption of the energy of the electromagnetic field set up by external azimuthal currents flowing in an infinite homogeneous plasma has been investigated in /3/. In this case, the plasma absorbs energy only in those regions where the external currents pass. Elsewhere, the plasma loses energy. On the whole, however, net absorption is observed.

In this connection it would be interesting to investigate the absorption of r-f energy in a plasma, when the currents creating the high-frequency field flow outside the plasma. Plasma inhomogeneity must be taken into consideration in this case. In the present paper we consider the collisionless heating of a plasma column, whose density and temperature are functions of the radius, by an electromagnetic field set up by azimuthal electric currents passing outside the plasma.

The density of the external azimuthal currents

$$j_{\text{col}} = j_0 \delta(r - R) \cos(kz - \omega t).$$

The electromagnetic field in the plasma cylinder is determined from the equations

$$\text{rot rot } \mathbf{E} = i \frac{4\pi\omega}{c^2} \mathbf{j}; \quad \mathbf{H} = -i \frac{c}{\omega} \text{ rot } \mathbf{E}, \tag{1}$$

where $\mathbf{j} = \sum_\alpha e_\alpha \int \mathbf{v} f_\alpha d\mathbf{v}$; f_α is a small deviation of the distribution function of particles of the species α from the equilibrium distribution $F_{0\alpha}$.

The function $F_{0\alpha}$ is obtained from the kinetic equation, which is written in cylindrical coordinates as

$$v_\perp \cos(\vartheta - \varphi) \frac{\partial F_{0\alpha}}{\partial r} + \frac{v_\perp}{r} \sin(\vartheta - \varphi) \frac{\partial F_{0\alpha}}{\partial \varphi} + \frac{e_\alpha}{m_\alpha} E_0 \frac{\partial F_{0\alpha}}{\partial v_r} - \omega_\alpha \frac{\partial F_{0\alpha}}{\partial \vartheta} = 0, \tag{2}$$

where $\omega_\alpha = \frac{e_\alpha H_0}{m_\alpha c}$ is the gyrofrequency of particles of the species α; e_α and m_α their charge and mass; E_0 the radial electric field set up in the event of charge separation; (r, φ, z) cylindrical coordinates in the space $(\mathbf{r})$; $(v_\perp, \vartheta, v_z)$ cylindrical coordinates in the velocity space.

Assuming that the magnetic pressure in the plasma is much greater than the gas-kinetic pressure, $\frac{H_0^2}{8\pi} \gg n_0 T_\alpha$ (in this case the radial variation of H_0 can be neglected) and that the density and the temperature of the electron and the ion components of the plasma vary considerably over distances much greater than the particle Larmor radius, we solve equation (2) by successive approximations:

$$F_{0\alpha}(r, \vartheta - \varphi, v_\perp, v_z) = f_{0\alpha} + \sin(\vartheta - \varphi) \frac{v_\perp}{\omega_\alpha} \left(\frac{\partial f_{0\alpha}}{\partial r} - \frac{e_\alpha E_0}{T_\alpha} f_{0\alpha} \right), \tag{3}$$

where $f_{0\alpha}$ is independent of ϑ. We choose $f_{0\alpha}$ in the form

$$f_{0\alpha} = \left[\frac{m_\alpha}{2\pi T_\alpha(r)} \right]^{3/2} n_0(r) \, e^{-\frac{m_\alpha}{2T_\alpha(r)}(v_\perp^2 + v_z^2)}.$$

The function f_α satisfies the kinetic equation

$$i(kv_z - \omega) f_\alpha + v_\perp \cos(\vartheta - \varphi) \frac{\partial f_\alpha}{\partial r} + \frac{v_\perp}{r} \sin(\vartheta - \varphi) \frac{\partial f_\alpha}{\partial \varphi} + \frac{e_\alpha E_0}{m_\alpha} \frac{\partial f_\alpha}{\partial v_r} +$$
$$+ \frac{e_\alpha}{m_\alpha c} [\mathbf{v}\mathbf{H}_0] \frac{\partial f_\alpha}{\partial \mathbf{v}} + \frac{e_\alpha}{m_\alpha} \left(\mathbf{E} + \frac{1}{c} [\mathbf{v}\mathbf{H}] \right) \frac{\partial F_{0\alpha}}{\partial \mathbf{v}} = 0. \tag{4}$$

Assuming the pinch radius to be of the same order of magnitude as the wavelength $\left(a \sim \frac{1}{k}\right)$ and taking $\omega, kv_\alpha \ll \omega_\alpha \left(v_\alpha = \sqrt{\frac{T_\alpha}{m_\alpha}}\right)$, we find

$|E_r| \sim |E_z| \sim \frac{\omega}{\omega_i}|E_\varphi|$. Omitting terms of the order of $\left(\frac{\omega}{\omega_i}\right)^2$, $\left(\frac{kv_\alpha}{\omega_\alpha}\right)^2$, we find

$$\mathbf{E}\frac{\partial F_{0\alpha}}{\partial \mathbf{v}} = -\frac{m_\alpha}{T_\alpha}[E_r v_\perp \cos(\vartheta-\varphi) + E_\varphi v_\perp \sin(\vartheta-\varphi) + E_z v_z] f_{0\alpha} +$$

$$+\left[1-\frac{m_\alpha v_\perp^2}{T_\alpha}\sin^2(\vartheta-\varphi)\right]\left(\frac{\partial f_{0\alpha}}{\partial r} - \frac{e_\alpha E_0}{T_\alpha} f_{0\alpha}\right)\frac{E_\varphi}{\omega_\alpha};$$

$$[\mathbf{vH}]\frac{\partial F_{0\alpha}}{\partial \mathbf{v}} = \frac{v_z H_r - v_\perp \cos(\vartheta-\varphi) H_z}{\omega_\alpha}\left(\frac{\partial f_{0\alpha}}{\partial r} - \frac{e_\alpha E_0}{T_\alpha} f_{0\alpha}\right).$$

In virtue of the foregoing inequalities, we can solve equation (4) by successive approximations:

$$f_\alpha = f_\alpha^{(0)} + f_\alpha^{(1)} + f_\alpha^{(2)} + \dots . \tag{5}$$

We apply the zeroth $f_\alpha^{(0)}$ and the first $f_\alpha^{(1)}$ approximations only:

$$\omega_\alpha \frac{\partial f_\alpha^{(0)}}{\partial \vartheta} = -\frac{e_\alpha E_\varphi v_\perp \sin(\vartheta-\varphi)}{T_\alpha} f_{0\alpha};$$

$$\omega_\alpha \frac{\partial f_\alpha^{(1)}}{\partial \vartheta} = i(kv_z - \omega) f_\alpha^{(0)} + v_\perp \cos(\vartheta-\varphi)\frac{\partial f_\alpha^{(0)}}{\partial r} -$$

$$-\frac{v_\perp}{r}\sin(\vartheta-\varphi)\frac{\partial f_\alpha^{(0)}}{\partial \vartheta} + \frac{e_\alpha E_0}{m_\alpha}\cdot\frac{\partial f_\alpha^{(0)}}{\partial v_r} - \frac{e_\alpha}{T_\alpha}[E_r v_\perp \cos(\vartheta-\varphi) +$$

$$+E_z v_z] f_{0\alpha} + \frac{e_\alpha}{\omega_\alpha}\left(\frac{\partial f_{0\alpha}}{\partial r} - \frac{e_\alpha E_0}{T_\alpha} f_{0\alpha}\right)\left\{\frac{E_\varphi}{m_\alpha} - \frac{v_\perp^2}{T_\alpha}\cdot\frac{1-\cos 2(\vartheta-\varphi)}{2}E_\varphi +\right.$$

$$\left. + \frac{v_z}{m_\alpha c}H_r - \frac{v_\perp}{m_\alpha c}\cos(\vartheta-\varphi) H_z\right\}. \tag{6}$$

The integration constants entering $f_\alpha^{(n)}$ are found from the condition of ϑ-periodicity of $f_\alpha^{(n+1)}$.

For the current density $\mathbf{j} = \mathbf{j}^{(0)} + \mathbf{j}^{(1)}$ we have

$$\left.\begin{aligned}
&4\pi j_z = 4\pi j_z^{(0)} = i\frac{\Omega_i^2}{k\omega_i}\eta\left(\frac{\partial E_\varphi}{\partial r} + \frac{E_\varphi}{r}\right) + i\frac{\Omega_i^2}{k\omega_i}\frac{eE_0}{T_i}\zeta E_\varphi - i\frac{\omega\Omega_i^2}{k^2 v_i^2}\zeta E_z;\\
&4\pi j_r = 0;\\
&4\pi j_\varphi = 4\pi j_\varphi^{(1)} = i\frac{2}{\omega\omega_i^2}\left\{\frac{\partial}{\partial r}\left[\left(\frac{\partial E_\varphi}{\partial r} + \frac{E_\varphi}{r}\right)\Omega_i^2 v_i^2 \xi\right] -\right.\\
&\left.-\frac{eE_0}{2T_i}\Omega_i^2 v_i^2\left(\frac{\partial E_\varphi}{\partial r} + \frac{E_\varphi}{r}\right)\eta\right\} - \frac{i}{k\omega_i}\left[\frac{\partial}{\partial r}(\Omega_i^2 \eta E_z) - \frac{eE_0}{T_i}\Omega_i^2 E_z \zeta\right] +\\
&+\frac{i}{\omega\omega_i^2}\left[\frac{\partial}{\partial r}\left(E_\varphi \Omega_i^2 v_i^2 \frac{eE_0}{T_i}\eta\right) - \frac{e^2 E_0^2}{T_i^2}E_\varphi \Omega_i^2 v_i^2 \zeta\right],
\end{aligned}\right\} \tag{7}$$

where

$$\xi = i\sqrt{\pi}\left[z_i w(z_i) + \frac{T_e}{T_i} z_e w(z_e)\right]; \quad \eta = i\sqrt{\pi}\,[z_i w(z_i) - z_e w(z_e)],$$

$$\zeta = 1 + \frac{T_i}{T_e} + i\sqrt{\pi}\left[z_i w(z_i) + \frac{T_i}{T_e} z_e w(z_e)\right]; \quad \Omega_\alpha = \sqrt{\frac{4\pi n_0(r) e^2}{m_\alpha}};$$

$$z_\alpha = \frac{\omega}{\sqrt{2}\,kv_\alpha}; \quad w(z) = e^{-z^2}\left(1 + \frac{2i}{\sqrt{\pi}}\int_0^z e^{t^2} dt\right).$$

Since $j_r = 0$, then neglecting the displacement current we have $j_z = 0$, whence

$$E_z = \frac{kv_i^2}{\omega\omega_i}\frac{\eta}{\zeta}\left(\frac{\partial E_\varphi}{\partial r} + \frac{E_\varphi}{r}\right) + \frac{eE_0 k}{\omega\omega_i m_i}E_\varphi \tag{8}$$

For the azimuthal component of the current density we then have

$$4\pi j_\varphi = -\frac{i}{\omega\omega_i^2}\frac{\partial}{\partial r}\left[\left(\frac{\partial E_\varphi}{\partial r}+\frac{E_\varphi}{r}\right)\Omega_i^2 v_i^2\left(2\xi-\frac{\eta^2}{\zeta}\right)\right]. \qquad (9)$$

Since in the zero approximation the currents perpendicular to the magnetic field vanish, the azimuthal component of the zeroth-order electric field E_φ has the same form as in the absence of a plasma:

$$E_\varphi = i\,\frac{4\pi\omega j_0 R}{c^2} K_1(kR)\, I_1(kr), \qquad (10)$$

where $I_n(x)$ are the modified Bessel functions, $K_n(x)$ the Macdonald functions.
Applying (9) and (10), we find the following expression for the energy $S=\frac{\pi}{2}\int\limits_0^a (j_\varphi E_\varphi^* + j_\varphi^* E_\varphi)\, r dr$ absorbed in unit time by unit length of the plasma column:

$$S = -\frac{4\pi^2\omega j_0^2 k R^2 K_1^2(kR)}{c^4\omega_i^2}\int\limits_0^a dr r I_1(kr)\frac{\partial}{\partial r}[\Omega_i^2 v_i^2 I_0(kr)\,\mu], \qquad (11)$$

where

$$\mu = \mathrm{Im}\left(2\xi - \frac{\eta^2}{\zeta}\right) > 0. \qquad (12)$$

The graphs of the function (12) are given in /3/. From (11) we see that energy is absorbed only in those layers of the plasma column where the density falls off fairly rapidly along the radius:

$$\frac{\partial}{\partial r}[\Omega_i^2 v_i^2 \mu I_0(kr)] < 0.$$

Where the reverse inequality is satisfied, the plasma loses energy and cools (provided the thermal conductivity is fairly low). Assuming that at $r=a$ the density of the plasma is zero, and integrating (11) by parts, we find

$$S = \frac{4\pi^2\omega j_0^2 k^2 R^2 K_1^2(kR)}{c^4\omega_i^2}\int\limits_0^a dr r I_0^2(kr)\,\Omega_i^2 v_i^2 \mu. \qquad (13)$$

We see that there is a net absorption of energy in the plasma.
The mean energy acquired by a single particle has the order of magnitude

$$\frac{dW}{dt} \sim \frac{\widetilde{H}^2}{H_0^2}\,\omega T_\alpha, \quad ka \sim 1, \quad a \sim R, \quad v_i \sim \frac{\omega}{k}, \qquad (14)$$

where $\widetilde{H} = \frac{4\pi}{c} j_0$ is the amplitude of the alternating magnetic field. If $\widetilde{H} \sim 100$G, $H_0 \sim 10^4$ G, $\omega \sim 3\cdot 10^7$ sec^{-1}, $T_i \sim 10$ eV, then $dW/dt \sim 1$ MeV/sec. This estimate indicates that magnetic pumping may be effectively applied for the heating of a fairly hot high-density plasma ($n_0 > 10^{14}$ cm^{-3}).
The heating of the plasma can be substantially enhanced /3/ if the phase velocity of the wave $V_{\mathrm{ph}} = \frac{\omega}{k}$ is close to the velocity of sound in a collisionless nonisothermal ($T_e \gg T_i$) plasma, $V_s = \sqrt{\frac{T_e}{m_i}}$.

Applying (9), we can easily derive an expression for the energy losses with coils of different sizes. Taking for the current in the coil

$$j_{\text{col}}(z, t) = J(z)\,\delta(r - R)\cos\omega t, \tag{15}$$

we find for the influx of energy into the plasma

$$\Sigma = 2\pi \int_0^a r dr \int_{-\infty}^{\infty} dz \overline{j_\varphi E_\varphi} = \frac{8\pi^3 \omega R^2}{\omega_i^2 c^4} \int_{-\infty}^{\infty} dk \int_0^a dr r \mu \left[k \,|\, j(k) \,|\, K_1(kR)\, I_0(kr)\, \Omega_i v_i\right]^2, \tag{16}$$

where

$$j(k) = \frac{1}{2\pi} \int_{-\infty}^{\infty} J(z)\, e^{-ikz} dz.$$

For a single coil with a current density

$$J(z) = \begin{cases} j_0 \text{ for } |z| < \frac{L}{2} \\ 0 \text{ for } |z| > \frac{L}{2} \end{cases}$$

we have

$$j(k) = \frac{1}{\pi} \cdot \frac{\sin \frac{kL}{2}}{k}.$$

If $kL \sim ka \sim 1$ and $\omega L \sim v_i$, then in orders of magnitude

$$\Sigma \sim SL \sim 2\pi a \frac{c}{4\pi} E_\varphi \widetilde{H} L \frac{8\pi n_0 T_i}{H_0^2}, \tag{17}$$

where $E_\varphi \sim \frac{\omega}{kc} \widetilde{H}$ is the amplitude of the azimuthal electric field. This result is consistent (in orders of magnitude) with the results of /1/. For plasma heating by ion cyclotron resonance under identical conditions, we should have $\Sigma \sim 2\pi a \frac{c}{4\pi} E_\varphi \widetilde{H} L$. Since $\frac{H_0^2}{8\pi} \gg n_0 T_i$, the heating of the plasma by ion cyclotron resonance is more effective than its heating by Čerenkov resonance ("magnetic pumping").

For a system of N coils in "head-on" coupling

$$J(z) = \begin{cases} J_0 & 2n < \frac{z}{L} < 2n + 1 \\ -J_0 & 2n + 1 < \frac{z}{L} < 2n + 2, \end{cases}$$

where $n = 0, 1, 2, \ldots, N-1$ and L is the length of the coil. In this case

$$|j(k)|^2 = \frac{J_0^2}{\pi^2 k^2} \frac{\sin^2\left(\frac{kL}{2}\right)}{\cos^2\left(\frac{kL}{2}\right)} \sin^2 kLN.$$

If $N \gg 1$, $|j(k)|$ has a sharp maximum at $k = \frac{\pi}{L}$:

$$|j(k)|^2 = \frac{4J_0^2 LN}{\pi^5} \delta\left(k - \frac{\pi}{L}\right). \tag{18}$$

Substituting (18) in (16), we find

$$\Sigma = \frac{32\omega J_0^2 R^2 N}{\omega_i^2 c^4 L} K_1^2\left(\frac{\pi R}{L}\right)\int_0^a r dr I_0^2\left(\frac{\pi}{L} r\right)\Omega_i^2 v_i^2 \mu. \qquad (19)$$

Since a many-coil system creates an almost "monochromatic" distribution of currents in a plasma, we see that absorption sharply increases under conditions of acoustic resonance $\left(\frac{\pi}{L} V_s \approx \omega,\ T_e \gg T_i\right)$.

BIBLIOGRAPHY

1. BERGER, J. M., W. A. NEWCOMB, J. M. DAWSON, E. A. FRIEMAN, R. M. KULSRUD, and A. LENARD. – Phys. Fluids, 1: 301. 1958.

2. SHAPIRO, V. D. – In: "Fizika plazmy i problemy upravlyaemogo termoyadernogo sinteza", 1: 64. Kiev, Izdatel'stvo AN UkrSSR. 1962.

3. STEPANOV, K. N. – JETP, 45: 1196. 1963.

V. V. Dolgopolov and K. N. Stepanov

ABSORPTION OF ELECTROMAGNETIC ENERGY BY AN INHOMOGENEOUS PLASMA IN MULTIPLE ION GYRORESONANCE

The absorption of electromagnetic energy of frequency ω, which is a multiple of the cyclotron frequency of the ions, $\omega_i = \frac{eH_0}{m_i c}$ (H_0 being the external magnetic field), can be applied for effective heating of a dense plasma. In /1/ we investigated the absorption of electromagnetic waves of frequency $\omega \approx n\omega_i$ ($n = 2, 3, \ldots$) in a homogeneous plasma column. The results of /1/, however, apply only for $k_\perp a \gg 1$ ($k_\perp$ is the radial wave number, a the radius of the plasma column), when the effects connected with the presence of the transition layer, where the plasma density falls off to zero, are negligible.

In the present paper we consider the absorption of electromagnetic waves of frequency $\omega \approx 2\omega_i$ in an inhomogeneous plasma cylinder (the temperature T_i of the ions and T_e of the electrons, as well as the equilibrium density n_0 are all functions of the radius). We derive expressions for the power absorbed by the plasma in the case of forced oscillations and for the damping ratio of free oscillations propagating along the plasma column.

Let us consider the oscillations of a plasma column stimulated by azimuthal electric currents of density $j^{\mathrm{col}} = j_0 \cos(kz - \omega t)\,\delta(r - R)$ which flow through the coil accomodating the plasma cylinder. To find the current density in the plasma, we must solve the kinetic equation for a small deviation of the distribution function f from the equilibrium distribution F_0:

$$i(kv_z - \omega) f + v_\perp \cos(\vartheta - \varphi)\frac{\partial f}{\partial r} + \frac{v_\perp \sin(\vartheta - \varphi)}{r}\frac{\partial f}{\partial \varphi} + \frac{eE_0}{m_i}\frac{\partial f}{\partial v_r} -$$
$$- \omega_i \frac{\partial f}{\partial \vartheta} + \frac{e}{m_i}\left(\mathbf{E} + \frac{1}{c}[\mathbf{vH}]\right)\frac{\partial F_0}{\partial \mathbf{v}} = 0, \qquad (1)$$

where

$$F_0 = f_0 + \frac{v_\perp \sin(\vartheta - \varphi)}{\omega_i}\left(\frac{\partial f_0}{\partial r} - \frac{e_i E_0 f_0}{T_i}\right);$$

$$f_0 = n_0\left(\frac{m_i}{2\pi T_i}\right)^{3/2}\exp\left(-\frac{m_i v^2}{2T_i}\right);$$

E and **H** are the electric and the magnetic fields of the wave: E_0 is the constant radial electric field generated when the charges are separated in equilibrium; $\mathbf{r} = (r, \varphi, z)$ and $\mathbf{v} = (v_\perp, \vartheta, v_z)$.

It is assumed that the gas-kinetic pressure is much less than the magnetic pressure and that the mean Larmor radius of the ions is much less than the radius of the plasma column, a, and the wavelength of the plasma oscillations. In this case, equation (1) can be solved by successive approximations:

$$f = f^{(0)} + f^{(1)} + \ldots . \tag{2}$$

Neglecting the field E_z, we obtain for the current density

$$\mathbf{j} = \mathbf{j}^{(0)} + \mathbf{j}^{(1)}.$$

Here

$$\left.\begin{aligned}
j_r^{(0)} &= -\frac{\Omega_i^2}{6\pi i\omega_i}(E_r + 2iE_\varphi);\\
j_\varphi^{(0)} &= -\frac{\Omega_i^2}{6\pi i\omega_i}(E_\varphi - 2iE_r);\\
j_r^{(1)} &= -\frac{i}{8\sqrt{2\pi}k\omega_i^2}\cdot\frac{1}{r^2}\cdot\frac{\partial}{\partial r}\left[r^3\Omega_i^2 v_i e^{-z_i^2}\frac{\partial}{\partial r}\left(\frac{E_\varphi - iE_r}{r}\right)\right];\\
j_\varphi^{(1)} &= -\frac{1}{8\sqrt{2\pi}k\omega_i^2}\cdot\frac{1}{r^2}\cdot\frac{\partial}{\partial r}\left[r^3\Omega_i^2 v_i e^{-z_i^2}\frac{\partial}{\partial r}\left(\frac{E_\varphi - iE_r}{r}\right)\right],
\end{aligned}\right\} \tag{3}$$

where

$$\Omega_i = \left(\frac{4\pi e^2 n_0}{m_i}\right)^{1/2}; \quad z_i = \frac{\omega - 2\omega_i}{\sqrt{2}kv_i}; \quad v_i = \sqrt{\frac{T_i}{m_i}}.$$

Setting $E_\varphi = E_\varphi^{(0)} + E_\varphi^{(1)}$ and applying (3), we obtain from Maxwell's equations

$$\frac{\partial^2 E_\varphi^{(0)}}{\partial x^2} + \frac{1}{x}\cdot\frac{\partial E_\varphi^{(0)}}{\partial x} - \left[1 + \frac{1}{x^2} + \xi\frac{1-3\xi}{1+\xi}\right]E_\varphi^{(0)} = 0; \tag{4}$$

$$\frac{\partial^2 E_\varphi^{(1)}}{\partial x^2} + \frac{1}{x}\cdot\frac{\partial E_\varphi^{(1)}}{\partial x} - \left[1 + \frac{1}{x^2} + \xi\frac{1-3\xi}{1+\xi}\right]E_\varphi^{(1)} = \chi(x), \tag{5}$$

where

$$x = kr; \quad \xi = \frac{4}{3}\cdot\frac{\Omega_i^2}{k^2c^2};$$

$$\chi = i\frac{\sqrt{\pi}(1-\xi)}{\sqrt{2}\,k\omega_i c^2(1+\xi)}\cdot\frac{1}{x^2}\cdot\frac{\partial}{\partial x}\left[x^3\Omega_i^2 v_i e^{-z_i^2}\frac{\partial}{\partial x}\left(\frac{1-\xi}{1+\xi}\cdot\frac{E_\varphi^{(0)}}{x}\right)\right].$$

Let $E_\varphi^{(0)} = A\psi(x)$ for $x < kR$, where $\psi(x)$ is the solution of equation (4) satisfying the condition $\psi(0) = 0$. Clearly, for $ka < x < kR$,

$$\psi = \alpha I_1(x) + \beta K_1(x);$$

for $x > kR$

$$E_\varphi^{(0)} = BK_1(x).$$

Then

$$H_z^{(0)} = -\frac{ikc}{\omega} A\left(\frac{\partial \psi}{\partial x} + \frac{\psi}{x}\right) \quad (x < kR);$$
$$H_z^{(0)} = \frac{ikc}{\omega} BK_0(x) \quad (x > kR).$$

Applying the conditions

$$E_\varphi^{(0)}(R-0) - E_\varphi^{(0)}(R+0) = 0;$$
$$H_z^{(0)}(R-0) - H_z^{(0)}(R+0) = \frac{4\pi}{c} j_0,$$

we have

$$A = \frac{4\pi i\omega j_0 RK_1(kR)}{\alpha c^2}; \quad B = \frac{4\pi i\omega j_0 R}{\alpha c^2} [\alpha I_1(kR) + \beta K_1(kR)].$$

From (5), for $ka < x < kR$,

$$E_\varphi^{(1)} = -\frac{D}{\alpha} K_1(x); \quad H_z^{(1)} = -\frac{ikcD}{\omega\alpha} K_0(x),$$

where

$$D = \int_0^{ka} \psi(x)\chi(x)\, x dx.$$

The energy absorbed in unit time by unit length of the plasma column is

$$S = \frac{(2\pi)^{1/2} R^2 K_1^2(kR) j_0^2}{kc^4\alpha^2} \int_0^{ka} x^3 \Omega_i^2 v_i e^{-z_i^2} \left[\frac{\partial}{\partial x}\left(\frac{1-\xi}{1+\xi}\frac{\psi}{x}\right)\right]^2 dx. \tag{6}$$

If $a \sim R \sim \frac{1}{k}$, $\xi \lesssim 1$, and $|z_i| \leqslant 1$, then $\psi(x) \sim 1$ for $x < ka$, and in orders of magnitude

$$S \sim 2\pi a \frac{c}{4\pi} \widetilde{E}\widetilde{H} \left(\frac{8\pi n_0 T_i}{H_0^2}\right)^{1/2},$$

where $\widetilde{H} = \frac{4\pi j_0}{c}$ and $\widetilde{E} = \frac{4\pi j_0 \omega a}{c^2}$ are the amplitudes of the fields outside the plasma. In this case, the average energy acquired by a single plasma particle $\left(\frac{dW}{dt} \sim \frac{S}{\pi a^2 n_0}\right)$ is

$$\left(\frac{dW}{dt}\right)_{\omega=2\omega_i} \sim \frac{\widetilde{H}^2}{H_0^2} \omega T_i \left(\frac{H_0^2}{4\pi n_0 T_i}\right)^{1/2}. \tag{7}$$

When the plasma is heated by low-frequency modes ($\omega \ll \omega_i$) under conditions of Čerenkov resonance $\left(\frac{\omega}{k} \sim v_i\right)$,

$$\left(\frac{dW}{dt}\right)_{\check{C}} \sim \frac{\widetilde{H}^2}{H_0^2} \omega T_i. \tag{8}$$

For equal amplitudes of the high-frequency field $\widetilde{H}$, the ratio of the energy acquired by a particle in Čerenkov resonance to the energy acquired

in multiple cyclotron resonance is

$$\frac{\left(\frac{dW}{dt}\right)_{\check{C}}}{\left(\frac{dW}{dt}\right)_{\omega=2\omega_i}} \sim \frac{\omega_{\check{C}}}{\omega_i}\left(\frac{8\pi n_0 T_i}{H_0^2}\right)^{1/2}.$$

This ratio is much less than unity, since $\omega_{\check{C}} \ll \omega_i$ and $8\pi n_0 T_i \ll H_0^2$.

The resonance $\omega = \omega_i$ is the most effective in heating a low-density plasma. In this case,

$$\frac{dW}{dt} \sim \frac{\widetilde{H}^2}{H_0^2}\,\omega_i T_i \frac{H_0^2}{8\pi n_0 T_i}. \tag{9}$$

Equation (9) has been derived assuming $ka \sim k\delta_i \sim 1$, where $\delta_i \sim \left(\frac{v_i c^2}{\omega_i \Omega_i^2}\right)^{1/2}$ is the penetration depth of the field into the plasma for $\omega = \omega_i$.

Let us now consider the damping of free oscillations of frequency $\omega = 2\omega_i$ propagating along an inhomogeneous plasma cylinder. Solving equations (4) and (5) by the perturbation technique, like in /2/, we obtain the following expression for the damping ratio (the imaginary part of the wave vector):

$$\varkappa = \frac{\sqrt{\pi}}{2\sqrt{2}\,\omega_i c^2\left(1 + 4\int\limits_0^{ka} \frac{\xi^2}{(1+\xi)^2}\,\psi^2 x\,dx\right)} \int\limits_0^{ka} \Omega_i^2 v_i e^{-z_i^2}\left[\frac{\partial}{\partial x}\left(\frac{1-\xi}{1+\xi}\,\frac{\psi}{x}\right)\right]^2 x^3\,dx, \tag{10}$$

where $\psi(x)$ is the solution of equation (4) satisfying the conditions $\psi(0) = \psi(\infty) = 0$ and $\int\limits_0^{\infty} \psi^2 x\,dx = 1$; k is the real part of the wave vector.

BIBLIOGRAPHY

1. DOLGOPOLOV, V. V. and K. N. STEPANOV. — ZhTF, 33:1196. 1963.
2. DOLGOPOLOV, V. V., A. I. ERMAKOV, N. I. NAZAROV, K. N. STEPANOV, and V. E. TOLOK. — This volume, p. 9.

K. N. Stepanov

PROPAGATION OF ION CYCLOTRON WAVES IN A PLASMA IN THE PRESENCE OF A WEAKLY INHOMOGENEOUS MAGNETIC FIELD

The application of ion cyclotron resonance for the heating of dense plasma involves certain difficulties. A highly damped ("ordinary") wave penetrates into the plasma in conditions of ion cyclotron resonance to a depth of the order of

$$\delta_i = \left(\sqrt{\frac{2}{\pi}}\,\frac{c^2 v_i}{\Omega_i^2 \omega_i}\right)^{1/2}, \tag{1}$$

where $\Omega_i = \left(\frac{4\pi e^2 n}{m_i}\right)^{1/2}$ is the ion plasma frequency, $\omega_i = \frac{eH_0}{m_i c}$ the ion cyclotron frequency; e and m_i are the ion charge and mass; n the number density; $v_i = \left(\frac{T_i}{m_i}\right)^{1/2}$ thermal velocity, T_i being the temperature of the ion gas; H_0 is the external magnetic field. In dense plasmas, whose confinement and magnetohydrodynamic stability require high magnetic fields H_0, the frequencies Ω_i and ω_i are both large, and the penetration depth δ_i of the field may prove to be substantially less than the radius of the plasma cylinder. In this case the energy of the high-frequency field is absorbed only by ions occupying the outermost skin of the plasma cylinder having a thickness of the order of δ_i.

An electromagnetic wave of frequency $\omega \approx \omega_i$ is generally excited in a plasma by a system of coils which are paired in counterphase and which carry azimuthal alternating current /1/, or by some analogous periodic oscillatory system, e.g., an artificial LC-line /2/. The amplitude of the wave in the plasma will be large if the space period of the excitation system, l, is close to the wavelength of the free plasma oscillations, i.e., $l \sim 2\pi\delta_i$. However, the field of short coils rapidly falls off along the radius, and if the plasma is not too close to the coil, both the field in the plasma and the absorbed power are low. If $l \gg 2\pi\delta_i$, the excited wave easily penetrates into the plasma, but the absorption is weak /3/.

These difficulties are avoided in the method proposed by Stix /4/ for the cyclotron resonance heating of plasmas by means of the so-called magnetic beach geometry. Consider a plasma propagating an electromagnetic wave of frequency $\omega < \omega_i$ in the direction of a slowly decreasing magnetic field (this is what we call an ion cyclotron wave). If $\omega_i - \omega \gg kv_i$, the damping of the wave is exponentially small* and the wave vector $\mathbf{k}$ is determined from the dispersion equation

$$\mathbf{k} = \frac{\Omega_i}{c}\sqrt{\frac{\omega}{\omega_i - \omega}}. \tag{2}$$

Electromagnetic waves with a propagation constant (2) readily penetrate into the plasma and are easily excited by the coil. As the wave propagates along the plasma cylinder, the difference $\omega_i - \omega$ and, therefore, the wavelength $\lambda = 1/k$ decrease, while the cyclotron damping increases. The wave is entirely absorbed in the magnetic beach ($\omega_i - \omega \sim kv_i$), provided the transition from the excitation region to the region of high absorption is fairly smooth.**

In the present paper we investigate the propagation of an ion cyclotron wave in the transition region allowing for the space dispersion of the plasma due to the thermal motion of the ions, and, in particular, for the cyclotron wave absorption by the ions.†

* This applies only for low-density plasmas $\left(n_0 T_i \ll \frac{H_0^2}{8\pi}\right)$, to which the present discussion is limited.

** The excitation of ion cyclotron waves and their absorption in the magnetic beach have been studied experimentally in /5,6/.

† The propagation of electromagnetic waves in a plasma with a slowly varying magnetic field and a density such that the refractive index in the resonance region has a singularity of the form $|\omega_{res} - \omega|^{-1/2}$ has been studied in /7–10/ for cases when the space dispersion of the plasma can be neglected.

The integral equation

Let us consider the propagation of an electromagnetic field of frequency $\omega = \omega_i$ along a plasma cylinder of density n_0, confined in an ideally conducting enclosure which closely adjoins the plasma; the plasma is immersed in a longitudinal magnetic field $H_0(r, z)$ which slowly falls off as z increases. The electric field $\mathbf{E}(r, z)$ of the wave is determined from the equation

$$\operatorname{rot}\operatorname{rot}\mathbf{E} = \frac{4\pi i\omega}{c^2}\mathbf{j}. \tag{3}$$

The electric current density $\mathbf{j}$ can be found, following Shafranov /11/, by integrating the kinetic equation for small deviations of the ion distribution function $f(\mathbf{r}, \mathbf{v}, t)$ from the equilibrium (Maxwellian) distribution f_0 by the method of characteristics. In the kinetic equation

$$\frac{\partial f}{\partial t} + \mathbf{v}\frac{\partial f}{\partial \mathbf{r}} + \frac{e}{m_i}\mathbf{E}\frac{\partial f_0}{\partial \mathbf{v}} + \frac{e}{m_i c}[\mathbf{v}\mathbf{H}_0]\frac{\partial f}{\partial \mathbf{v}} = 0 \tag{4}$$

we change over from the variables $(\mathbf{r}, \mathbf{v}, t)$ to the Lagrange variables $(\mathbf{r}_0, \mathbf{v}_0, t)$, where $\mathbf{r} = \mathbf{r}(\mathbf{r}_0, \mathbf{v}_0, t)$ and $\mathbf{v} = \frac{d\mathbf{r}}{dt}$ are the solutions of the equations of motion

$$\frac{d^2\mathbf{r}}{dt^2} = \frac{e}{m_i c}\left[\frac{d\mathbf{r}}{dt}, \mathbf{H}_0(\mathbf{r})\right] \tag{5}$$

with the initial conditions $\mathbf{r} = \mathbf{r}_0$ and $\mathbf{v} = \mathbf{v}_0$ for $t = 0$. Equation (4) then takes the form /11/

$$\frac{\partial f(\mathbf{r}_0, \mathbf{v}_0, t)}{\partial t} = -\frac{e}{m_i}\mathbf{E}(\mathbf{r}(\mathbf{r}_0, \mathbf{v}_0, t), t)\frac{\partial f_0}{\partial \mathbf{v}(\mathbf{r}_0, \mathbf{v}_0, t)}.$$

If the field $\mathbf{E}(\mathbf{r}, t)$ is turned on when $t = -\infty$, we have

$$f(\mathbf{r}_0, \mathbf{v}_0, t) = -\frac{e}{m_i}\int_{-\infty}^{t}\mathbf{E}(\mathbf{r}(\mathbf{r}_0, \mathbf{v}_0, t'), t')\frac{\partial f_0}{\partial \mathbf{v}(\mathbf{r}_0, \mathbf{v}_0, t')}dt' \tag{6}$$

$\mathbf{E}(\mathbf{r}, t)$ and $\frac{\partial f_0(\mathbf{r}, \mathbf{v})}{\partial \mathbf{v}}$ in the integrand in equation (6) are taken at the point $(\mathbf{r}, \mathbf{v})$ occupied by a particle which has moved according to the equation of motion (5) for a time t' starting from the point $(\mathbf{r}_0, \mathbf{v}_0)$. A particle will also reach this point if it moves for a time $t - t'$ starting from the point $(\mathbf{r}, \mathbf{v})$ and retracing the trajectory in the opposite direction in a reversed magnetic field $-\mathbf{H}_0$. Hence,

$$f(\mathbf{r}, \mathbf{v}, t) = \frac{e}{m_i}\int_{-\infty}^{t}\mathbf{E}(\vec{\varrho}(t - t', \mathbf{r}, -\mathbf{v}), t')\frac{\partial f_0}{\partial \mathbf{u}(t - t', \mathbf{r}, -\mathbf{v})}dt', \tag{7}$$

where $\vec{\varrho}(t)$ and $\mathbf{u} = \frac{d\vec{\varrho}}{dt}$ are the solutions of the equations

$$\frac{d^2\vec{\varrho}}{dt^2} = -\frac{e}{m_i c}\left[\frac{d\vec{\varrho}}{dt}, \mathbf{H}_0\right] \tag{8}$$

with the initial conditions $\vec{\varrho} = \mathbf{r}$ and $\mathbf{u} = -\mathbf{v}$ at $t = 0$.

Applying equation (7), we obtain the current density

$$j_i(\mathbf{r}, t) = \frac{e^2}{m_i}\int_{-\infty}^{t}dt'\int d\mathbf{v}v_i E_k(\vec{\varrho}(t - t', \mathbf{r}, -\mathbf{v}), t')\frac{\partial f_0}{\partial u_k(t - t', \mathbf{r}, -\mathbf{v})}.$$

Hence, seeing that $\mathbf{j}, \mathbf{E} \sim e^{-i\omega t}$ and $u = v$,

$$j_l(\mathbf{r}, \omega) = -e^2 \int_0^\infty dt \int d\mathbf{v} v_l E_k(\vec{\varrho}(t, \mathbf{r}, -\mathbf{v})) e^{i\omega t} u_k(t, \mathbf{r}, -\mathbf{v}) \frac{f_0}{T_i}. \tag{9}$$

Let us now solve equations (8) for $\vec{\varrho} = (\xi, \eta, \zeta)$. If the magnetic field on the axis $H(z) = H_0(r, z)_{r=0}$ does not vary much over a distance $z \sim a$, where a is the radius of the plasma cylinder, equations (8) for the motion of a particle near the axis can be derived from the Lagrangian

$$L = \dot{\varrho}^2 - \frac{eH(\zeta)}{m_i c}(\dot{\xi}\eta - \xi\dot{\eta}). \tag{10}$$

Applying (10), we find

$$\ddot{\xi} + \frac{eH}{m_i c}\dot{\eta} + \frac{eH'}{2m_i c}\dot{\zeta}\eta = 0; \tag{11}$$

$$\ddot{\eta} - \frac{eH}{m_i c}\dot{\xi} - \frac{eH'}{2m_i c}\dot{\zeta}\xi = 0; \tag{12}$$

$$\ddot{\zeta} = \frac{eH'}{2m_i c}(\dot{\xi}\eta - \xi\dot{\eta}); \quad H' = \frac{dH}{d\zeta}. \tag{13}$$

Setting $u = \xi + i\eta$, we write equations (11) and (12) in the form

$$\ddot{u} - i\omega_i\dot{u} - \frac{i}{2}\dot{\omega}_i u = 0; \quad \omega_i = \frac{eH}{m_i c}.$$

Hence, for $w = u \exp\left(-\frac{i}{2}\int_{t_0}^{t} \omega_i dt\right)$,

$$\ddot{w} + \frac{1}{4}\omega_i^2 w = 0. \tag{14}$$

We assume that the magnetic field H does not vary much over the distance corresponding to the axial displacement of the guiding center in the time it takes the particle to complete one Larmor revolution, i.e.,

$$\left|\frac{\dot{\omega}_i}{\omega_i^2}\right| \sim \left|\frac{r_i}{H}\frac{dH}{dz}\right| \ll 1,$$

where $r_i \sim \frac{v_i}{\omega_i}$ is of the order of magnitude of the ion Larmor radius. Equation (14) then may be solved in the WKB approximation:

$$w = \sqrt{\frac{\omega_i(t_0)}{\omega_i(t)}}\left[Ae^{\frac{i}{2}\psi} + Be^{-\frac{i}{2}\psi}\right], \quad \psi = \int_{t_0}^{t} \omega_i dt. \tag{15}$$

Hence, applying the initial conditions, we have

$$\begin{aligned} \xi(t, \mathbf{r}, -\mathbf{v}) &= \sqrt{\frac{\omega_i(z)}{\omega_i(\zeta)}}\left[x + \frac{v_y}{\omega_i(z)}(1 - \cos\psi) - \frac{v_x}{\omega_i(z)}\sin\psi\right]; \\ \eta(t, \mathbf{r}, -\mathbf{v}) &= \sqrt{\frac{\omega_i(z)}{\omega_i(\zeta)}}\left[y - \frac{v_x}{\omega_i(z)}(1 - \cos\psi) - \frac{v_y}{\omega_i(z)}\sin\psi\right]. \end{aligned} \tag{16}$$

Expressions (16) for ξ and η may also be written using polar coordinates in the velocity space, $\mathbf{v} = (v_\perp, \varphi, v_\parallel)$:

$$\xi = \sqrt{\frac{\omega_i(z)}{\omega_i(\zeta)}}\left[x + \frac{v_\perp \sin\varphi}{\omega_i(z)} - \frac{v_\perp \sin(\varphi+\psi)}{\omega_i(z)}\right];$$

$$\eta = \sqrt{\frac{\omega_i(z)}{\omega_i(\zeta)}}\left[y - \frac{v_\perp \cos\varphi}{\omega_i(z)} + \frac{v_\perp \cos(\varphi+\psi)}{\omega_i(z)}\right]. \tag{17}$$

From (17) follows the conservation of the adiabatic invariant

$$\frac{\xi^2+\eta^2}{H(\zeta)} = \frac{v_\perp^2}{H(z)} = \text{const}. \tag{18}$$

Applying (18) and the conservation-of-energy equation $\dot{\vec{\varrho}}^2 = v^2$, we find

$$\dot{\zeta} = \mp\sqrt{v^2 - v_\perp^2\frac{H(\zeta)}{H(z)}}; \tag{19}$$

$$t = \mp\int\limits_z^\zeta \frac{d\zeta}{\sqrt{v^2 - v_\perp^2\frac{H(\zeta)}{H(z)}}}. \tag{20}$$

Equation (20) gives an implicit relation between ζ and t and the initial values z, $v_\parallel$, $v_\perp$.

Applying (20), we may write the phase ψ in the form

$$\psi = \mp\int\limits_z^\zeta \frac{\omega_i(\zeta)}{\sqrt{v^2 - v_\perp^2\frac{H(\zeta)}{H(z)}}}\,d\zeta \tag{21}$$

The current density j can be found from expressions (17) and (20) for $\vec{\varrho}$. In a low-density plasma $\left(n_0T_i \ll \frac{H_0^2}{8\pi}\right)$, the wavelength at right angles to H_0 is much greater than the Larmor radius of thermal ions, so that we may neglect the space dispersion in this direction, setting in (9)

$$\mathbf{E}(\vec{\varrho}(t, \mathbf{r}, -\mathbf{v})) = \mathbf{E}(r, \zeta(t, z, -\mathbf{v})); \quad f_0(\vec{\varrho}, v) = f_0(r, v).$$

Since in the region of low frequencies $\omega \approx \omega_i$ we may take $E_z \approx 0$, it follows from equation (9)

$$j_r = \hat{\sigma}(E_r + iE_\theta); \; j_\theta = \hat{\sigma}(E_\theta - iE_r) \tag{22}$$

Here

$$\hat{\sigma}f(z) = \frac{\Omega_i^2}{2^4\pi\sqrt{2\pi}v_i^5}\int\limits_0^\infty dt\int\limits_0^\infty v_\perp^3 dv_\perp \int\limits_{-\infty}^\infty dv_\parallel f(\zeta) \times$$

$$\times\sqrt{\frac{H(\zeta)}{H(z)}}\,e^{-\frac{v^2}{2v_i^2}+i\omega t-i\int\limits_0^t \omega_i(\zeta(t))dt}, \tag{23}$$

where $\zeta(t) = \zeta(t, z, v_\parallel, v_\perp)$ is defined by (20).

Maxwell's equations have the form

$$\frac{\partial^2 E_r}{\partial z^2} = -\frac{4\pi i\omega}{c^2} \hat{\sigma}(E_r + iE_\vartheta); \tag{24}$$

$$\frac{\partial^2 E_\vartheta}{\partial z^2} + \frac{\partial}{\partial r}\left[\frac{1}{r}\frac{\partial (rE_\vartheta)}{\partial r}\right] = -\frac{4\pi i\omega}{c^2} \hat{\sigma}(E_\vartheta - iE_r). \tag{25}$$

The magnetic field of the wave is found from the equation

$$\mathbf{H} = -\frac{ic}{\omega} \operatorname{rot} \mathbf{E}$$

The set of integro-differential equations (23)-(25) defines the behavior of an ion cyclotron wave propagating along a plasma cylinder immersed in a weakly inhomogeneous magnetic field $\left(\frac{r_i}{H}\left|\frac{dH}{dz}\right| \ll 1\right)$.

If the density and the temperature of the ions are independent of r (homogeneous plasma), E_r and E_ϑ are proportional to Bessel's function $I_1(k_\perp r)$, where $k_\perp = \frac{\alpha_n}{a}$, α_n being the zero of the function I_1. Equation (25) then takes the form

$$\frac{\partial^2 E_\vartheta}{\partial z^2} - k_\perp^2 E_\vartheta = -\frac{4\pi i\omega}{c^2} \hat{\sigma}(E_\vartheta - iE_r). \tag{26}$$

Equations (23)–(25) should be considered in conjunction with the boundary condition $E_\vartheta = E_\vartheta^0(e^{ik_\parallel z} + ae^{-ik_\parallel z})$ for $z \to -\infty$, and $E_\vartheta \to 0$, $E_r \to 0$ for $z \to \infty$, where $k_\parallel$ is the propagation constant in the case of no space dispersion (we neglect the effects of space dispersion of the plasma to the left from the transition region, in particular, the exponentially small cyclotron damping).

The geometrical-optics approximation

Let us first consider "longitudinal" propagation, when $k_\perp \ll k_\parallel(z)$, $\frac{1}{k_\parallel}$ being a characteristic length along the z axis over which the field $\mathbf{E}$ changes. Neglecting the second term in the left-hand side of equation (25), we find $E_r = iE_\vartheta$, where E_ϑ is given by

$$\frac{\partial^2 E_\vartheta}{\partial z^2} = -\frac{8\pi i\omega}{c^2} \hat{\sigma} E_\vartheta. \tag{27}$$

Setting

$$E_\vartheta = Ae^{i\int_{z_0}^{z} k(z')dz'}$$

we write (27) in the form

$$k^2 - i\frac{dk}{dz} = \frac{i\Omega_i^2\omega}{(2\pi)^{1/2}c^2v_i^5}\int_0^\infty dt\int_0^\infty v_\perp^3 dv_\perp \int_{-\infty}^{\infty} dv_\parallel \sqrt{\frac{H(\zeta)}{H(z)}}\, e^{-\frac{v^2}{2v_i^2}+i\Phi}. \tag{28}$$

where

$$\Phi = \omega t - \int_0^t \omega_i(\zeta(t'))\,dt' + \int_z^\zeta k(z')\,dz'$$

If H is independent of z, then $\zeta = z - v_{\parallel} t$. In his case, equation (28) yields a dispersion equation for longitudinal propagation*

$$k^2 = \frac{\omega^2}{c^2} \varepsilon(\omega, k), \tag{29}$$

where

$$\begin{gathered} \varepsilon(\omega, k) = i \sqrt{\frac{\pi}{2}} \frac{\Omega_i^2}{\omega k v_i} w(x); \\ w(x) = e^{-x^2}\left(1 + \frac{2i}{\sqrt{\pi}} \int_0^x e^{t^2} dt\right); \\ x = \frac{\omega - \omega_i}{\sqrt{2} k v_i}. \end{gathered} \tag{30}$$

For $|x| \gg 1$, equation (29) reduces to dispersion equation (2). If $|x| \sim 1$, then from (29) $k\delta_i \sim 1$ in orders of magnitude.

For a weakly inhomogeneous field $H(z)$, we have from (20)

$$t = -\frac{1}{v_{\parallel}}\left[\zeta - z + \frac{v_{\perp}^2 H'}{4 v_{\parallel}^2 H}(\zeta - z)^2\right]. \tag{31}$$

Hence

$$\zeta = z - v_{\parallel} t - \frac{v_{\perp}^2 H'}{4H} t^2.$$

The expansion (31) applies if $\left|\frac{v_{\perp}^2 H'}{4 v_{\parallel}^2 H}(\zeta - z)\right| \ll 1$. Since in the integral (28) $v_{\perp} \sim v_{\parallel} \sim v_i$ and $|\zeta - z| \sim \lambda = \frac{1}{k}$ are real, (31) holds true if

$$\frac{\lambda}{H} \cdot \frac{dH}{dz} \ll 1, \tag{32}$$

i.e., the variation of the magnetic field over a distance of the order of magnitude of the wavelength is small in comparison with the magnetic field. Condition (32) is met if the geometrical-optics approximation applies, i.e., if $\left|\frac{d\lambda}{dz}\right| \ll 1$; in conjunction with equation (2), for $\omega_i - \omega \sim k v_i$, this condition takes the form

$$\frac{\delta_i}{H}\left|\frac{dH}{dz}\right| \ll \left(\frac{8\pi n_0 T_i}{H_0^2}\right)^{1/4} \ll . \tag{33}$$

Applying (32) and (33), we have

$$\begin{gathered} \sqrt{\frac{H(\zeta)}{H(z)}} \approx 1 - \frac{H'}{2H} v_{\parallel} t; \\ e^{i\Phi} \approx e^{i\Phi_0}\left(1 - \frac{i k v_{\perp}^2 H'}{4H} t^2 + \frac{i}{2} k' v_{\parallel}^2 t^2 + \frac{i}{2} \omega_i' v_{\parallel} t^2\right), \end{gathered}$$

where

$$\Phi_0 = |\omega - \omega_i(z) - k(z) v_{\parallel}| t.$$

Equation (28) then takes the form

$$\begin{aligned} k^2 - ik' = i \sqrt{\frac{\pi}{2}} \cdot \frac{\Omega_i^2 \omega}{c^2 k v_i} \Bigg\{ & w - \frac{ik'}{k^2}\left(w + 2x \frac{dw}{dx} + \frac{x^2}{2} \cdot \frac{d^2 w}{dx^2}\right) - \\ & - \frac{i\omega_i}{\sqrt{2} k^2 v_i}\left(\frac{dw}{dx} + \frac{1}{2} x \frac{d^2 w}{dx^2}\right) + \frac{i\omega_i'}{2k\omega_i}\left(w + x\frac{dw}{dx} + 2\frac{d^2 w}{dx^2}\right)\Bigg\}. \end{aligned} \tag{34}$$

*This equation was originally derived by Gershman /14/.

where

$$w = w(x); \quad x = \frac{\omega - \omega_i}{\sqrt{2}k_{\parallel}(z)v_i}.$$

Since $kv_i \ll \omega_i$, the last two terms in braces in equation (34) are small in comparison with the first and the third terms (this implies that the variation of the longitudinal velocity of a particle moving in an inhomogeneous magnetic field is negligible, so that we may set $\zeta = z - v_{\parallel}t$). Omitting these terms and taking $k = k_{\parallel} + ik_1$, where $|k_1| \ll |k_{\parallel}|$, we have

$$k_{\parallel}^2 = \frac{\omega^2}{c^2}\varepsilon(\omega, k_{\parallel});$$

$$k_1 = -\frac{i}{2}\frac{\left(k_{\parallel} - \frac{1}{2}\cdot\frac{\omega^2}{c^2}\cdot\frac{d\varepsilon(\omega, k_{\parallel})}{dk_{\parallel}}\right)'}{k_{\parallel} - \frac{1}{2}\cdot\frac{\omega^2}{c^2}\cdot\frac{d\varepsilon(\omega, k_{\parallel})}{dk_{\parallel}}}. \tag{35}$$

Hence

$$E_{\vartheta}(z) = E_{\vartheta}^0\sqrt{\frac{k(z_0)\left[3 + \frac{x_0 d\ln w(x_0)}{dx_0}\right]}{k(z)\left[3 + \frac{x\,d\ln w(x)}{dx}\right]}}\, e^{i\int\limits_{z_0}^{z} k_{\parallel}(z')dz'}, \tag{36}$$

where $x_0 = \frac{\omega - \omega_i(z_0)}{\sqrt{2}k_{\parallel}(z_0)v_i}$. For $|x| \gg 1$, formula (36) gives the conventional result of geometrical optics.

Substituting the variable $\eta = k_{\parallel}\delta_i$, we write the dispersion equation (30) as

$$\eta^3 = iw\left(-\frac{\Delta}{\eta}\right), \tag{37}$$

where

$$\Delta = \left(\frac{\omega_i}{\omega} - 1\right)\left(\frac{H_0^2}{\sqrt{\pi}8\pi n_0 T_i}\right)^{1/3}$$

Setting $\eta = \eta' + i\eta''$ and seeing that for $\Delta \gg 1$ the damping is comparatively small ($\eta'' \lesssim 0.1\eta'$), we find

$$\eta'^3 = v\left(\frac{\Delta}{\eta'}\right);$$

$$\eta'' = \eta' e^{-\left(\frac{\Delta}{\eta'}\right)^2}\left\{3v\left(\frac{\Delta}{\eta'}\right) + \frac{2\Delta}{\eta'}\left[\frac{1}{\sqrt{\pi}} - \frac{\Delta}{\eta'}\,v\left(\frac{\Delta}{\eta'}\right)\right]\right\}^{-1},$$

where

$$v(x) = \frac{2}{\sqrt{\pi}}e^{-x^2}\int\limits_0^x e^{t^2}dt.$$

The figure plots the functions $y = \eta'(\Delta)$ (curve I), $y = 10\frac{\eta''(\Delta)}{\eta'(\Delta)}$ (curve II), and $y = 10\eta''(\Delta)$ (curve III). We see from the figure that the damping η'' rapidly falls off with increasing Δ: already for $\Delta = 2$ $\frac{\eta''}{\eta'} = 0.033$, and for $\Delta = 2.5$ $\frac{\eta''}{\eta'} = 0.0045$. For $\Delta = 1$, the damping is considerable: $\frac{\eta''}{\eta'} = 0.14$. If $\Delta = 0$, then $\eta' = \frac{\sqrt{3}}{2}$; $\eta'' = \frac{1}{2}$. Note, however, that since in this approximation the transition region, in accordance with condition (33), should

accommodate a large number of waves, the waves are actually damped in the region $\Delta \geqslant 1$, so that there is no need to consider the zone of high damping ($\Delta < 1$, $\eta'' \sim \eta'$).

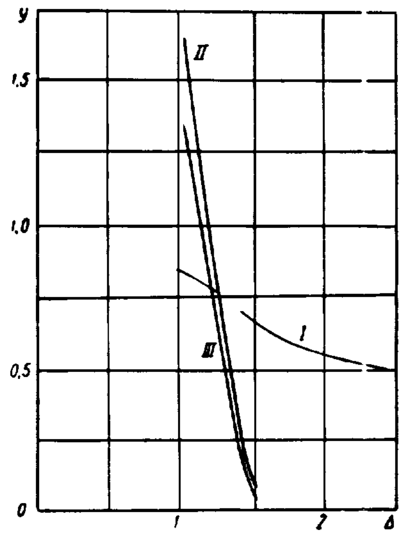

Let us consider the case of "oblique" propagation ($k_\perp \neq 0$). First note that in the geometrical-optics approximation, when inequality (33) is satisfied, the variation of the longitudinal velocity of a particle moving along the z axis may be neglected. Equation (23) then takes the form

$$\hat{\sigma} f(z) = \frac{\Omega_i^2}{4(2\pi)^{3/2} v_i} \int_0^\infty dt \int_{-\infty}^{\infty} dv_\parallel \, e^{-\frac{v_\parallel^2}{2v_i^2} + i\left[\omega t - \int_0^t \omega_i(\zeta(t'))\,dt'\right]} f(\zeta), \tag{38}$$

where $\zeta = z - v_\parallel t$. In a homogeneous plasma, the solution of equations (24)–(26) may be written in the form

$$E_{r,\vartheta} = A_{r,\vartheta} e^{ik_\parallel z}.$$

Then, from (24) and (26) we have

$$\left(-k_\parallel^2 + \frac{1}{2}\frac{\omega^2}{c^2}\varepsilon(\omega, k_\parallel)\right) A_r + \frac{i\omega^2}{2c^2}\varepsilon(\omega, k_\parallel) A_\vartheta = 0;$$

$$-\frac{i\omega^2}{2c^2}\varepsilon(\omega, k_\parallel) A_r + \left(-k_\parallel^2 - k_\perp^2 + \frac{1}{2}\frac{\omega^2}{c^2}\varepsilon(\omega, k_\parallel)\right) A_\vartheta = 0.$$

Setting the determinant of this system equal to zero, we obtain a dispersion equation for the ion cyclotron waves in the case of "oblique" propagation /12,13/:

$$k_\parallel^4 - \left(\varepsilon(\omega, k_\parallel)\frac{\omega^2}{c^2} - k_\perp^2\right) k_\parallel^2 - \frac{1}{2}\frac{\omega^2}{c^2}\varepsilon(\omega, k_\parallel) k_\perp^2 = 0. \tag{39}$$

If $|x| = \left|\frac{\omega - \omega_i}{\sqrt{2}k_\| v_i}\right| \gg 1$, then from (39)

$$k_\|^2 = \frac{1}{2}\left\{\varepsilon(\omega)\frac{\omega^2}{c^2} - k_\perp^2 + \sqrt{\left[\varepsilon(\omega)\frac{\omega^2}{c^2} - k_\perp^2\right]^2 + 2\varepsilon(\omega)\left(\frac{\omega^2}{c^2}\right)k_\perp^2}\right\},$$

where

$$\varepsilon(\omega) = \frac{\Omega_i^2}{\omega(\omega_i - \omega)}.$$

For a weakly inhomogeneous magnetic field, we seek a solution of (24)–(26) in the form

$$E_{r,\vartheta} = A_{r,\vartheta}(z)\, e^{i\int_{z_0}^{z} k_\|(z')\,dz'} \tag{40}$$

where $k_\|(z)$ is the wave vector determined from the dispersion equation (39), where $\omega_i = \omega_i(z)$; $A_{r,\vartheta}(z)$ is the slowly varying amplitude. Neglecting $A''_{r,\vartheta}$ in comparison with $k'A_{r,\vartheta}$ in equations (24) and (26) and applying inequalities (33), we find

$$k_\|^2 A_r - ik'_\| A_r - 2ik_\| A'_r = \frac{\omega^2}{2c^2}\left\{\varepsilon(\omega, k_\|)(A_r + iA_\vartheta) - \right.$$

$$\left. - \frac{i}{2}\left(\frac{d\varepsilon(\omega, k_\|)}{dk_\|}\right)'(A_r + iA_\vartheta) - i\frac{d\varepsilon(\omega, k_\|)}{dk_\|}(A'_r + iA'_\vartheta)\right\}; \tag{41}$$

$$(k_\|^2 + k_\perp^2)A_\vartheta - ik'_\| A_\vartheta - 2ik_\| A'_\vartheta = \frac{\omega^2}{2c^2}\left\{\varepsilon(\omega, k_\|)(A_\vartheta - iA_r) - \right.$$

$$\left. - \frac{i}{2}\left(\frac{d\varepsilon(\omega, k_\|)}{dk_\|}\right)'(A_\vartheta - iA_r) - i\frac{d\varepsilon(\omega, k_\|)}{dk_\|}(A'_\vartheta - iA'_r)\right\}. \tag{42}$$

Setting

$$A_r = \frac{2i}{\varepsilon}\left[(k_\|^2 + k_\perp^2)\frac{c^2}{\omega^2} - \frac{\varepsilon}{2}\right]A_\vartheta + \delta A_r,$$

where $|\delta A_r| \ll |A_r|$, we have from (42)

$$\delta A_r = \frac{2c^2 k'_\|}{\omega^2\varepsilon}A_\vartheta + \frac{4c^2 k_\|}{\omega^2\varepsilon}A'_\vartheta - \frac{c^2}{\omega^2\varepsilon^2}\left(\frac{d\varepsilon}{dk_\|}\right)'(k_\|^2 + k_\perp^2)A_\vartheta +$$

$$+ \frac{2c^2}{\omega^2\varepsilon^2}\frac{d\varepsilon}{dk_\|}[\varepsilon'(k_\|^2 + k_\perp^2) - 2\varepsilon k_\| k'_\|]A_\vartheta - \frac{2c^2}{\omega^2\varepsilon^2}\frac{d\varepsilon}{dk_\|}(k_\|^2 + k_\perp^2)A'_\vartheta.$$

Substituting this expression for A_r in (41), we find

$$\frac{A'_\vartheta}{A_\vartheta} = -\frac{q_1}{2q_2},$$

where

$$q_1 = \frac{k_\|^2 + k_\perp^2}{\varepsilon(\omega, k_\|)}\left(\frac{d\varepsilon(\omega, k_\|)}{dk_\|}\right)' + 2\frac{d\varepsilon(\omega, k_\|)}{dk_\|}\left(\frac{k_\|^2 + k_\perp^2}{\varepsilon(\omega, k_\|)}\right)' +$$

$$+ \frac{2}{k_\|^2\varepsilon(\omega, k_\|)}[2k_\|\varepsilon'(\omega, k_\|)(k_\|^2 + k_\perp^2) - \varepsilon(\omega, k_\|)k'_\|(6k_\|^2 +$$

$$+ k_\perp^2 - \varepsilon(\omega, k_\|))];$$

$$q_2 = \frac{k_\|^2 + k_\perp^2}{\varepsilon(\omega, k_\|)}\frac{d\varepsilon(\omega, k_\|)}{dk_\|} - \frac{2(k_\perp^2 + 2k_\|^2 - \varepsilon(\omega, k_\|))}{k_\|}.$$

Hence, finally

$$E_\vartheta = E_\vartheta^0 e^{-\frac{1}{2}\int\limits_{z_0}^{z} \frac{q_1(z')}{q_r(z')}\,dz'} e^{\int\limits_{z_0}^{z} k_\parallel(z')\,dz'}; \tag{43}$$

$$E_r = iE_\vartheta\left[\frac{2(k_\parallel^2 + k_\perp^2)c^2}{\omega^2\varepsilon(\omega, k_\parallel)} - 1\right]. \tag{44}$$

For $k_\perp = 0$, formula (43) goes into formula (36).

Expressions (39),(43),(44) enable us to find the wavelength, the damping coefficient, and the phase and the amplitude of the fields as a function of z in the case of "oblique" propagation.

BIBLIOGRAPHY

1. STIX, T.H. – Phys. Fluids, **1**:308. 1958.

2. BRZHECHKO, M.V., M.P. VASIL'EV, L.I. GRIGOR'EVA, V.V. DOLGOPOLOV, A.S. LOGINOV, O.S. PAVLICHENKO, B.I. SMERDOV, K.N. STEPANOV, and V.V. CHECHKIN. – In: "Fizika plazmy i problemy upravlyaemogo termoyadernogo sinteza", **3**:109. Kiev, Izdatel'stvo AN UkrSSR. 1963.

3. VASIL'EV, M.P., L.I. GRIGOR'EVA, V.V. DOLGOPOLOV, B.I. SMERDOV, K.N. STEPANOV, and V.V. CHECHKIN. – In: "Fizika plazmy i problemy upravlyaemogo termoyadernogo sinteza", **3**:96. 1963.

4. STIX, T.H. – Phys. Fluids, **3**:19. 1960.

5. HOOK, W.H., F.H. TENNEY, M.H. BRENNAN, H.M. HILL, jr., and T.H. STIX. – Phys. Fluids, **4**:1131. 1961.

6. NAZAROV, N.I., A.I. ERMAKOV, A.S. LOBKO, V.A. BONDAREV, V.T. TOLOK, and K.D. SINEL'NIKOV. – ZhTF, **32**:536. 1962.

7. DENISOV, N.G. – JETP, **31**:609. 1956.

8. DENISOV, N.G. – Radiotekhnika i Elektronika, **1**:732. 1956; **4**:388. 1959.

9. MAKAROV, G.I. – In: "Problemy difraktsii i rasprostraneniya radiovoln", **1**:5,63. Leningrad, Izdatel'stvo Leningradskogo Universiteta. 1962.

10. MAKAROV, G.I. – In: "Problemy difraktsii i rasprostraneniya radiovoln", **2**:39,62. Leningrad, Izdatel'stvo Leningradskogo Universiteta. 1962.

11. SHAFRANOV, V.D. – In: "Fizika plazmy i problema upravlyaemykh termoyadernykh reaktsii", **4**:416. Moskva, Izdatel'stvo AN SSSR. 1958.

12. SHAFRANOV, V.D. – In: "Fizika plazmy i problema upravlyaemykh termoyadernykh reaktsii", **4**:426. Moskva, Izdatel'stvo AN SSSR. 1958.

13. SAGDEEV, R.Z. and V.D. SHAFRANOV. – In: "Fizika plazmy i problemy upravlyaemykh termoyadernykh reaktsii", **4**:430. Moskva, Izdatel'stvo AN SSSR. 1958.

14. GERSHMAN, B.N. – JETP, **24**:453. 1953.

I. A. Akhiezer and Yu. L. Bolotin

A CONTRIBUTION TO THE THEORY OF INTERACTION OF PARTICLES AND WAVES WITH A NONEQUILIBRIUM PLASMA

Anomalously large, so-called critical, fluctuations are possible in a nonequilibrium plasma which is close to instability /1,2/ (see also the review in /5/). The onset of critical fluctuations is reflected in the anomalously high cross sections for the scattering of light in these plasmas /1/, and also in the anomalously high coefficients of scattering of longitudinal waves and in their conversion into transverse modes /3/.

In the present paper we investigate the interaction of charged particles with nonequilibrium plasmas. If a plasma is close to instability, the cross section for the scattering of particles by the collective plasma oscillations and the loss of particle energy via Čerenkov radiation may be anomalously high.* We also investigate the conversion of the transverse electromagnetic waves into longitudinal waves in interactions with critical fluctuations. The problem is also considered of the angular distribution of the scattered radiation in the interaction of plasma oscillations with critical fluctuations, and it is shown that under certain conditions the scattered intensity may be exceptionally high.

Scattering of particles in a plasma in the presence of ordered electron motion

Let us first consider the scattering of charged particles in a non-equilibrium plasma. The probability that a particle passes from a state with momentum $\mathbf{p}$ to a state with momentum $\mathbf{p}'$ is related with charge density fluctuations by the well-known expression

$$dW = \left(\frac{4\pi e z}{\hbar q^2}\right)^2 <\varrho^2>_{\mathbf{q}\omega} \frac{d\mathbf{p}'}{(2\pi\hbar)^3}\,, \tag{1}$$

where $<\varrho^2>$ is the correlation function of charge density; $\hbar\mathbf{q} = \mathbf{p}' - \mathbf{p}$ and $\hbar\omega = \frac{(p'^2 - p^2)}{2\mu}$ are the variations in the momentum and the energy of the particles; ez the charge; μ the mass of the particle. If the plasma consists of hot electrons moving relative to cold ions, then in the frequency range $q\left(\frac{T_i}{M}\right)^{1/2} \ll \omega \ll q\left(\frac{T}{m}\right)^{1/2}$, the charge-density correlator /1/

$$<\varrho^2>_{\mathbf{q}\omega} = \frac{1}{2}\left(\frac{Tq^2}{\Omega}\right)^2 \frac{(qs)^3}{m\,|\,\omega - \mathbf{q}\mathbf{u}\,|}\,\delta(\omega^2 \; q^2 s^2), \tag{2}$$

where T, T_i are the temperatures, and m, M the masses of the electrons and the ions, respectively; $\mathbf{u}$ is the mean streaming velocity of the electrons; $\Omega = \left(\frac{4\pi e^2 n}{m}\right)^{1/2}$ is the plasma frequency; $s = \left(\frac{T}{M}\right)^{1/2}$ the velocity of nonisothermal sound.

* The interaction of particles with a plasma where a nonequilibrium wave distribution has been created by an external source is investigated by Tsytovich /6/.

Substituting (2) in (1), we find the cross section for the scattering of a particle by the nonisothermal sound oscillations, per one plasma electron:

$$d\sigma = \left(\frac{2\pi ezT}{\Omega}\right)^2 \frac{s\sqrt{(\Delta p)^2 + p^2\vartheta^2}}{\hbar m v\,|v\Delta p - (\mathbf{p}' - \mathbf{p})\mathbf{u}|} \cdot \times$$
$$\times \left\{\delta\left(v\Delta p - s\sqrt{(\Delta p)^2 + p^2\vartheta^2}\right) + \delta\left(v\Delta p + s\sqrt{(\Delta p)^2 + p^2\vartheta^2}\right)\right\} \frac{d\mathbf{p}'}{n(2\pi\hbar)^3}, \qquad (3)$$

where $\Delta p = p' - p$ and ϑ is the scattering angle (the angle between the vectors $\mathbf{p}'$ and $\mathbf{p}$). Formula (3) applies when the scattering angle and the exchanged energy are fairly small, $\Delta \mathbf{p}\, a \ll \hbar$, $pa\vartheta \ll \hbar$ (a being the Debye length in the plasma): it is only under these conditions that the sound oscillations are weakly damped.

Integrating in (3) with respect to the magnitude of the vector $\mathbf{p}'$, we obtain the cross section for the particles scattered in a unit solid angle:

$$\frac{d\sigma}{do} = \left(\frac{ezT}{\hbar^2\Omega}\right)^2 \frac{\mu^2}{\pi mn} \cdot \frac{(\theta' - \theta)^2 + \varphi^2 \sin\theta}{(\theta' - \theta)^2\left(1 - \frac{u^2}{s^2}\sin^2\theta\right) + \varphi^2\sin^2\theta}, \qquad (4)$$

where θ, θ' are the angles between the vectors $\mathbf{p}$, $\mathbf{p}'$ and the direction $\mathbf{u}$; φ is the angle between the planes $(\mathbf{p}, \mathbf{u})$ and $(\mathbf{p}', \mathbf{u})$; $\theta' \approx \theta$ and $\varphi \ll 1$ (to avoid ambiguity, we take $v \gg s$). It is easily seen that if $\frac{u}{s} \approx 1$ and the particle moves almost at right angles to the direction u, $\frac{d\sigma}{do}$ may be anomalously large.

The quantity $\frac{d\sigma}{do}$ may become infinite only in the linear theory, where formula (2) for charge density fluctuations actually belongs. In reality, however, nonlinear effects result in a saturation of the critical fluctuations, and the scattering cross section remains finite. Nonlinear effects also impose rigid restrictions on the anomalous growth of the Čerenkov radiation intensity, the energy losses, the scattering coefficients, and wave conversion. In the present paper we operate within the framework of the linear theory, and the calculation of these growth restrictions is beyond the scope of our study.

Applying relations (1) and (2), we can find the energy expended by a particle in unit time in the excitation of sound oscillations:

$$dQ = \left(\frac{ezT}{\Omega}\right)^2 \frac{(qs)^2}{m} \left\{\frac{\delta\left(\mathbf{q}\mathbf{v} + qs + \frac{\hbar q^2}{2\mu}\right)}{qs + \mathbf{q}\mathbf{u}} - \frac{\delta\left(\mathbf{q}\mathbf{v} - qs - \frac{\hbar q^2}{2\mu}\right)}{qs - \mathbf{q}\mathbf{u}}\right\} \frac{d\mathbf{q}}{2\pi\hbar}. \qquad (5)$$

The first term in this expression describes forced emission, and the second—absorption of oscillations by a particle. (Since we are dealing with plasmas close to instability, when the sound modes are particularly abundant, we obviously need not introduce in (5) the additional term representing spontaneous emission, as it does not depend on the density of the modes.)

Integrating in (5) with respect to the angular variables, we find the intensity of Čerenkov radiation in a frequency interval specified. In the simplest case, with $\mathbf{u} \parallel \mathbf{v}$,

$$\frac{dQ}{d\omega} = \left(\frac{ezT\omega}{\Omega s^2}\right)^2 \frac{\omega u}{m\mu\,(v - u)^2}. \qquad (6)$$

This formula applies if $u \leqslant s$. In this case, the sound oscillations are stable yet, and the correlator may be taken in the form (2); furthermore,

in deriving the formula we have assumed $v - s \gtrsim \frac{\hbar}{\mu a}$.

Integrating (6) with respect to frequency, we find the energy expended by a particle in the excitation of sound modes:

$$Q = \left(\frac{ezT}{2\Omega\tilde{a}^2}\right)^2 \frac{u}{m\mu (v-u)^2}, \tag{7}$$

where $\tilde{a}$ is a quantity of the order of several Debye lengths. If the velocity of a particle v, the velocity of sound s, and the streaming velocity of the electrons u are all close to one another, Q is very large, possibly greater than the energy lost by particles in binary collisions.

In general, when the angle Θ_0 between the direction in which the particle moves and the direction of $\mathbf{u}$ is other than zero, anomalously large intensity of Čerenkov radiation is observed for $v \cos\Theta_0 \approx u \approx s$. Then

$$\frac{dQ}{d\omega} = \left(\frac{ezT\omega}{\Omega s^2}\right)^2 \frac{\omega s}{m\mu (v\cos\Theta_0 - u)^2} \tag{8}$$

Hence the energy lost by a particle in the excitation of sound oscillations is

$$Q = \left(\frac{ezT}{2\Omega\tilde{a}^2}\right)^2 \frac{s}{m\mu (v\cos\Theta_0 - u)^2} \tag{9}$$

For $(v\cos\Theta_0 - u)^2 < \frac{1}{4} uv \frac{m}{\mu}\left(\frac{a}{\tilde{a}}\right)^4$, $Q > Q_0$, where $Q_0 = \frac{(ez\Omega)^2}{v}$ is a characteristic energy loss in binary collisions (neglecting the Coulomb logarithm).

Note that formulas (6)–(9), as well as (15)–(17) do not apply for very small values of $\mathbf{vu} - u^2$, when the critical fluctuations, responsible for the loss of energy by the particles, become so large that they must be described in terms of a nonlinear theory.

In conclusion of this section, we give an expression for the angular distribution of Čerenkov radiation:

$$\frac{dQ}{do} = \frac{s}{6\pi\hbar m v \tilde{a}}\left(\frac{ezT}{\Omega\tilde{a}}\right)^2 \left\{\frac{\delta\left(\cos\chi + \frac{s}{v}\right)}{1 + \frac{u}{s}\cos\Theta} - \frac{\delta\left(\cos\chi - \frac{s}{v}\right)}{1 - \frac{u}{s}\cos\Theta}\right\}, \tag{10}$$

where Θ the angle between the vectors $\mathbf{q}$ and $\mathbf{u}$; χ the angle between $\mathbf{q}$ and $\mathbf{v}$. Formula (10) applies when $|\cos\Theta| < \frac{s}{u}$ since in this case the sound modes being considered do not grow. It is easily seen that if $|\cos\Theta| \to \frac{s}{u}$, the coefficient of one of the δ - functions in (10) increases indefinitely.

Interaction of a particle with a plasma in the presence of a beam

Let us now consider the scattering of charged particles in a plasma carrying a compensated beam of charged particles. The beam velocity u is assumed to be greater than the thermal velocity of the plasma electrons; the beam temperature T_1 is taken as moderately high, so that the plasma oscillations are mainly damped while interacting with the electrons of the

beam. Under these conditions, the charge density correlator in the high-frequency region $\left(\omega \gg q\sqrt{\frac{T}{m}}\right)$ has the form /2/

$$<\rho^2>_{q\omega} = \frac{1}{2}\frac{T_1 q^2 \Omega^2}{|\omega - \mathbf{qu}|}\,\delta(\omega^2 - \Omega^2). \tag{11}$$

The presence of a hot beam invariably leads to a growth of fairly short-wave plasma oscillations, having $|\mathbf{qu}| > \Omega$. Neglecting the nonlinear effects of interaction between fluctuations, we may apply formula (11) in the region of wave vectors where plasma oscillations do not grow yet.

Substituting (11) in (1), we find the cross section for the scattering of a fast particle $\left(v \gg \sqrt{\frac{T}{m}}\right)$ by plasma oscillations per one plasma electron:

$$d\sigma = \frac{(ez)^2}{2\pi\hbar v n}\,\frac{T_1\Omega}{(\Delta p)^2 + p^2\vartheta^2}\left\{\frac{\delta(v\Delta p - \hbar\Omega)}{\hbar\Omega - (\mathbf{p}' - \mathbf{p})\mathbf{u}} + \frac{\delta(v\Delta p + \hbar\Omega)}{\hbar\Omega + (\mathbf{p}' - \mathbf{p})\mathbf{u}}\right\} d\mathbf{p}'. \tag{12}$$

For this formula to apply, Δp and ϑ must be subject to the same restrictions as in formula (3).

Integrating in (12) with respect to the magnitude of the vector $\mathbf{p}'$, we find the cross section for the scattering of particles in unit solid angle:

$$\frac{d\sigma}{do} = \left(\frac{ez}{\hbar v\vartheta}\right)^2 \frac{T_1}{2\pi n}\left\{\left|1 - \frac{u}{v}\cos\Theta' - \frac{pu}{\hbar\Omega}(\cos\Theta' - \cos\Theta)\right|^{-1} + \right.$$
$$\left. + \left|1 - \frac{u}{v}\cos\Theta' + \frac{pu}{\hbar\Omega}(\cos\Theta' - \cos\Theta)\right|^{-1}\right\} \tag{13}$$

(to avoid ambiguity, we take $\vartheta \gg \frac{\hbar\Omega}{pv}$). It is easily seen that for a given Θ, close to Θ, $\frac{d\sigma}{do}$ becomes anomalously large.

Applying (1) and (11), we can find the energy expended by a particle in unit time in the excitation of plasma oscillations:

$$dQ = \left(\frac{ez\Omega}{q}\right)^2 T_1 \left\{\frac{\delta\left(\mathbf{qv} + \Omega + \frac{\hbar q^2}{2\mu}\right)}{\Omega + \mathbf{qu}} - \frac{\delta\left(\mathbf{qv} - \Omega + \frac{\hbar q^2}{2\mu}\right)}{\Omega - \mathbf{qu}}\right\}\frac{d\mathbf{q}}{2\pi\hbar} \tag{14}$$

This formula correctly allows for the interaction of a particle with non-growing oscillations, i.e., modes whose wave vectors satisfy the inequality $|\mathbf{qu}| < \Omega$.

Integrating (14) with respect to angular variables, we obtain the intensity of Čerenkov radiation in a given range of wave numbers q. In the simplest case of $\mathbf{u} \parallel \mathbf{v}$,

$$\frac{dQ}{dq} = \frac{(ez)^2 T_1 q u}{\mu (v - u)^2} \tag{15}$$

(in deriving this formula, we have assumed $v - u \gtrsim \hbar u(\mu\Omega a^2)^{-1}$).

Integrating (15) with respect to q, we find the energy lost by a particle in the excitation of plasma oscillations:

$$Q = \left(\frac{ez}{\tilde{a}}\right)^2 \frac{T_1 u}{2\mu(v - u)^2}. \tag{16}$$

If the velocity of a particle v is close to the velocity of the beam u, Q is very large, possibly higher than energy losses in binary collisions, as well as the losses in the excitation of plasma oscillations in the absence of a beam. For this to apply, the inequality $(v-u)^2 < u^2 \frac{m}{\mu} \frac{T_1}{T} \left(\frac{u}{2a}\right)^2$ must be satisfied.

If the angle Θ_0 between $\mathbf{u}$ and $\mathbf{v}$ is not zero and $q \approx \frac{\Omega}{u}$, we have

$$\frac{dQ}{dq} = \frac{(ez)^2 T_1 q u}{\mu (v \cos\Theta_0 - u)^2}. \tag{17}$$

The expression for the energy Q lost by a particle in the excitation of plasma oscillations in this case $\Theta_0 \sim 1$, unlike formulas (9) and (16), contains no "anomalous" denominator $(\mathbf{uv} - u^2)^2$. The energy losses Q in this case are proportional to the logarithm of a large parameter characterizing the amplitude "cutoff" of the critical fluctuations due to nonlinear effects, and they are therefore large.

The difference in the structure of the expressions for energy losses with $\Theta_0 \sim 1$ and $\Theta_0 \ll 1$ is attributable to the intense interaction of the particles with oscillations whose wave vectors satisfy the relation $\mathbf{qv} \approx \Omega$, while the amplitudes of the waves having $\mathbf{qu} \approx \Omega$ are anomalously large. Therefore, it is only with $u \approx v$ and $\Theta_0 \ll 1$ that all the waves with which the particle interacts have anomalously large amplitudes, regardless of their actual wave vectors.

In conclusion, we give an expression for the angular distribution of the plasma oscillations emitted by a particle:

$$\frac{dQ}{do} = \frac{(ez)^2 \Omega T_1}{2\pi h} \cdot \frac{-1}{v\cos\chi - u\cos\Theta}, \tag{18}$$

where Θ is the angle between $\mathbf{q}$ and $\mathbf{u}$; χ the angle between $\mathbf{q}$ and $\mathbf{v}$. Formula (18) applies when $(v\cos\chi - u\cos\Theta)\cos\chi > 0$, since in this case plasma oscillations do not grow. It is easily seen that with $\left|\cos\chi - \frac{u}{v}\cos\Theta\right| \ll 1$, $\frac{dQ}{do}$ is anomalously large.

Conversion of a transverse wave into a longitudinal wave in a plasma with net electron drift

Let us consider the transformation of a transverse wave into a longitudinal one by fluctuations in a nonequilibrium plasma. The coefficient of conversion $U = \frac{\dot{\mathcal{E}}}{VE_0^2}$ (where $\dot{\mathcal{E}}$ is the change of energy of the secondary wave in unit time, E_0 the amplitude of the incident wave, V the volume of the system) is related with the charge density correlator by the expression (see, e.g., /4/)

$$U = \int dU;$$
$$dU = \frac{\pi e^2 \Omega^2}{(2Tq^2)^2} \langle \varrho^2 \rangle_{q,\Delta\omega} \sin^2\vartheta \frac{dk'}{(2\pi)^3}, \tag{19}$$

where $\Delta\omega = \omega' - \omega \, (|\Delta\omega| \sim qs)$; $\mathbf{q} = \mathbf{k} - \mathbf{k}'$; ω, $\mathbf{k}$ and ω', $\mathbf{k}'$ are the frequencies and the wave vectors of the incident and the secondary waves; ϑ the angle

between the vectors $\mathbf{k}$ and $\mathbf{k}'$. Substituting (2), we find

$$dU = \frac{\pi e^2}{4m} \frac{(qs)^2}{|\Delta\omega - \mathbf{qu}|} \sin^2\vartheta\,\delta(\Delta\omega^2 - q^2 s^2) \frac{d\mathbf{k}'}{(2\pi)^3}. \tag{20}$$

Seeing that the dispersion relation for oscillations in a plasma with drifting electrons is $\omega' = \Omega + \mathbf{k}'\mathbf{u}$ and setting $k' \gg k$, we write expression (20) as

$$dU = \frac{\pi e^2 k' s \cdot \sin^2\vartheta}{4m\left|\mathbf{ku} - \frac{c^2k^2}{2\Omega}\right|} \left\{\delta\left(\mathbf{k}'\mathbf{u} - k's - \frac{c^2k^2}{2\Omega} + ks\cos\vartheta\right) + \right.$$
$$\left. + \delta\left(\mathbf{k}'\mathbf{u} + k's - \frac{c^2k^2}{2\Omega} + ks\cos\vartheta\right)\right\} \frac{dk'}{(2\pi)^3}. \tag{21}$$

Integrating this expression with respect to the magnitude of the vector $\mathbf{k}'$, we find the conversion ratio per unit solid angle:

$$\frac{dU}{do} = \frac{e^2k^3\sin^2\Theta}{32\pi^2 m}\left|\mathbf{ku} - \frac{c^2k^2}{2\Omega}\right|^{-1} \{g(\Theta, \Theta', \varphi) + g(\Theta, \pi - \Theta', \varphi)\}, \tag{22}$$

where Θ (Θ') is the angle between $\mathbf{k}$ ($\mathbf{k}'$) and $\mathbf{u}$; φ the angle between the planes $(\mathbf{k}, \mathbf{u})$ and $(\mathbf{k}', \mathbf{u})$;

$$g(\Theta, \Theta', \varphi) = \left(\frac{\left|\mathbf{ku} - \frac{c^2k^2}{2\Omega}\right|}{ks} + \sin\Theta \cdot \cos\varphi\ \ \Theta'\right)^3 \left(\frac{s-u}{s} + \frac{1}{2}\Theta'^2\right)^{-1}$$

(we take $\sin\Theta' \ll 1$, since otherwise $\frac{dU}{do}$ will not be anomalously large). It is easily seen that for $\cos\Theta \to \frac{c^2k}{2\Omega u}$, the coefficients in (21) and (22) increase indefinitely.

Singularities in the angular distribution of the scattered radiation

The coefficient of scattering of plasma oscillations by sound waves in a plasma with drifting electrons has the form (the attenuation of sound is neglected) /3/

$$dU = \frac{\pi e^2\cos^2\vartheta\,(qs)^2}{3m\Omega a^2\,|k'^2 - k^2|}\,\delta(\Delta\omega^2 - q^2s^2)\,\frac{d\mathbf{k}'}{(2\pi)^3}, \tag{23}$$

where $\Delta\omega = \mathbf{qu} + \frac{3}{2}\Omega a^2(k'^2 - k^2)$. Integrating (23) with respect to the magnitude of the vector $\mathbf{k}'$, we find the angular distribution of the scattered plasma oscillations. We are interested in the scattering of radiation at the angles $\Theta' \approx \pi - \Theta$, $\varphi \ll 1$ (φ is the angle between the planes $(\mathbf{k}', \mathbf{u})$ and $(\mathbf{k}, \mathbf{u})$), when the effects related with the drift of the electrons are particularly pronounced. In this case, with $u \approx s$,

$$\frac{dU}{do} = \frac{e^2k^2\cos^2 2\Theta}{32\pi^2 ms\,|f_1 f_2\cos\Theta|}, \tag{24}$$

where

$$f_1(\Theta, \Theta', \varphi) = 1 - \frac{u}{s}\left(1 - \frac{\pi - \Theta - \Theta'}{2}\,\mathrm{tg}\,\Theta - \frac{\varphi^2}{8}\,\mathrm{tg}^2\,\Theta\right);$$
$$f_2(\Theta, \varphi) = 1 - \frac{u}{s}\left(1 - \frac{\varphi^2}{8}\,\mathrm{tg}^2\,\Theta\right) \quad \left(\Theta \neq \frac{\pi}{2}\right). \tag{25}$$

Besides the singularity at $f_2 \to 0$, due to critical fluctuations, expression (24) has yet another singularity at $f_1 \to 0$. The latter is attributable to us having neglected the damping of the sound waves.

To introduce the attenuation of sound, the δ- function in (23) must be replaced with the expression

$$\frac{\gamma}{2\pi qs}\{[(\Delta\omega - qs)^2 + \gamma^2]^{-1} + [(\Delta\omega + qs)^2 + \gamma^2]^{-1}\},$$

where γ is the decrement of damping,

$$\gamma = g(\Delta\omega - \mathbf{qu}), \quad g = \frac{1}{2}\sqrt{\frac{\pi m}{2M}}. \tag{26}$$

This substitution gives an expression for the scattering coefficient which should replace formula (24) for $f_1 \to 0$:

$$\frac{dU}{do} = \frac{e^2k^2\cos^2 2\Theta}{32\pi^2 ms\sqrt{g}\,|f_2|^{3/2}\sin\Theta}. \tag{27}$$

This expression is proportional to the large quantity $g^{-1/2}$, and also carries a factor $|f_2|^{-3/2}$. Near the angles meeting the condition $f_1 = 0$, the scattering coefficient $\frac{dU}{do}$ approaches infinity as $f_2 \to 0$ much more rapidly than with $f_1 \neq 0$.

Interacting with fluctuations, the plasma wave is not only scattered (i.e., converted into a plasma wave with a different wave vector), but also transformed into a transverse wave. The coefficient of conversion of longitudinal plasma waves changing over into transverse waves in a plasma with drifting electrons (neglecting the attenuation of sound) is /3/

$$dU = \frac{\pi e^2(qs)^2\sin^2\vartheta}{2m\,|\Delta\omega - \mathbf{qu}|}\,\delta(\Delta\omega^2 - q^2s^2)\,\frac{dk'}{(2\pi)^3}, \tag{28}$$

where $\Delta\omega = \frac{c^2k'^2}{2\Omega} - \mathbf{ku}$. Integrating this expression with respect to the magnitude of the vector $\mathbf{k}'$, we find the angular distribution of the transverse waves generated by this process.

Without giving the general expression for $\frac{dU}{do}$, we only observe that besides the singularity arising when $|\Delta\omega - \mathbf{qu}|$ vanishes (this is due to critical fluctuations), $\frac{dU}{do}$ is also infinite when $\frac{\partial}{\partial k'}(\Delta\omega^2 - q^2s^2) = 0$, i.e.,

$$\cos\vartheta = \frac{c}{s}\left[\frac{2k}{\Omega}(s - u\cos\Theta)\right]^{1/2} \tag{29}$$

(assuming $k' \ll k$). The second singularity arose since we neglected the damping of sound waves.

Introducing the attenuation of sound near the scattering angles defined by condition (29), we find

$$\frac{dU}{do} = \frac{e^2\Omega k}{(2\pi)^2 mc^2\sqrt{g}} \cdot \frac{\sin^2\Theta'}{\cos\Theta'} \tag{30}$$

($\cos\Theta' \neq 0$). Since $g \ll 1$, expression (30) is anomalously large. Note that condition (29) imposes very rigid restrictions on the drift velocity of the electrons, $|s - u\cos\Theta| \sim \left(\frac{s^2}{c}\right)\frac{\Omega}{k}$.

BIBLIOGRAPHY

1. ICHIMARU, S., D. PINES, and N. ROSTOKER. — Phys. Rev. Lett., 8: 231. 1962.

2. BOGDANKEVICH, L. S., A. A. RUKHADZE, and V. P. SILIN. — Izv vuzov. Radiofizika, 5: 1093. 1962.

3. AKHIEZER, I. A., I. A. DANELIYA, and N. L. TSINTSADZE. — JETP, 46: 300. 1964; this volume, p. 428.

4. BASS, F. G. and A. YA. BLANK. — JETP, 43: 1478. 1962.

5. ICHIMARU, S. — Ann. Phys., 20: 78. 1962.

6. TSYTOVICH, V. N. — JETP, 42: 809. 1962; 44: 946. 1963; DAN SSSR, 142: 319. 1962.

S. S. Kalmykova and V. I. Kurilko

EXCITATION OF A PLASMA WAVEGUIDE BY A COAXIAL WAVEGUIDE

Consider a semi-infinite cylindrical plasma-filled waveguide ($z > 0$; $r \leqslant a$), used as an extension of the central core of a coaxial cable ($z < 0$; $a \leqslant r \leqslant b$) and terminating with an ideally conducting diaphragm ($z = 0$, $0 \leqslant r \leqslant a$). A TEM wave propagates from the coaxial cable ($z < 0$). Let us estimate the efficiency of excitation of the plasma waveguide by the coaxial waveguide.

We substitute an anisotropic dielectric for the plasma waveguide and seek a solution for the scattered waves as a superposition of plane waves, each satisfying Maxwell's equations. For example, the field H_φ is taken in the form

$$
\begin{gathered}
H_\varphi(r, z) = \int\limits_{-\infty}^{+\infty} H(t)\,[J_1(vr)\,K_0(vb) + I_0(vb)\,K_1(vr)]\exp(itz)\,dt \\
(a \leqslant r \leqslant b), \; (-\infty < z < +\infty); \\
H_\varphi(r, z) + \int\limits_{-\infty}^{+\infty} h(t)\,J_1(\beta r)\exp(itz)\,dt \\
(0 \leqslant r \leqslant a), \quad (z \geqslant 0),
\end{gathered}
\tag{1}
$$

where

$$
v = (t^2 - k^2)^{1/2}; \quad \beta = \left| \frac{\varepsilon_\parallel}{\varepsilon_\perp}(\varepsilon_\perp k^2 - t^2) \right|^{1/2}; \quad k = \frac{\omega}{c};
$$

$H(t)$ and $h(t)$ are unknown functions which are to be determined from the boundary conditions on the surface $r = a$:

$$
z < 0 \quad E_z(r = a + 0) = 0; \tag{2}
$$

$$
\begin{aligned}
z > 0 \quad & H_\varphi^t(r = a + 0) = H_\varphi(r = a - 0); \\
& E_z(r = a + 0) = E_z(r = a - 0);
\end{aligned}
\tag{2a}
$$

$$
z = 0 \quad E_r(r \leqslant a) = 0. \tag{2b}
$$

In (2a) the superscript t denotes the total field, i.e., the resultant of the incident and the scattered waves.

Applying Rapoport's lemma /1/, we find from the boundary conditions (2)–(2b)

$$\chi^{+}(t) = [Z_g(t) - Z_b(t)]\,\varphi^{-}(t) + Z_g(t)\,\varphi^{+}(t) + \frac{1}{2\pi i a}\,\frac{1}{t-k};\qquad (3)$$
$$\varphi^{-}(t) = \varphi^{+}(t),$$

where the superscripts + and − indicate that the corresponding functions are analytical in the upper and the lower t half-planes, respectively, and the functions $Z_{b,g}$ are defined by

$$Z_b(t) = \frac{k}{v}\,\frac{\Delta_1(t)}{\Delta_0(t)};\quad Z_g(t) = \frac{k\varepsilon_{\parallel}}{\beta}\,\frac{J_1(\beta a)}{J_0(\beta a)};$$
$$\Delta_0(t) = I_0(va)\,k_0(vb) - I_0(vb)\,K_0(va);$$
$$\Delta_1(t) = I_1(va)\,K_0(vb) + I_0(vb)\,K_1(va).$$

Applying solution (3), we find the unknown functions

$$H(t) = \frac{k}{v}\,\frac{\varphi^{-}(t)}{\Delta_0(t)};\quad h(t) = \frac{k\varepsilon_{\parallel}}{\beta J_0(\beta a)}\,[\varphi^{+}(t) + \varphi^{-}(t)].\qquad (4)$$

Relation (3) is equivalent to a system of two boundary conditions for two piecewise-holomorphic functions. Since $\varphi^{-}(t) \equiv \varphi^{+}(-t)$, this system, according to /3/, can be reduced to a single integral equation with a Cauchy-type kernel:

$$\hat{I}\,[Z_b\varphi] - (2Z_g - Z_b)\,\hat{I}\,[\varphi] = \frac{k}{\pi i a}\cdot\frac{1}{t^2 - k^2},\qquad (5)$$

where $\varphi(t) = \varphi^{+}(t) - \varphi^{-}(t)$, and the operator $\hat{I}$ stands for the integral in the sense of its main value,

$$\hat{I}f \equiv \frac{1}{\pi i}\int_{-\infty}^{+\infty}\frac{dt'}{t'-t}\,f(t').$$

Since $\operatorname{Im} k > 0$ (we seek a time-dependence of the form $\exp(-i\omega t)$), the coefficient preceding the singular part of equation (5) does not vanish on the integration contour. This implies that the homogeneous equation corresponding to (5) has a unique solution $\varphi_0 \equiv 0$. Hence, equation (5) is equivalent to a single Fredholm equation /4/

$$\varphi(u) = \frac{k}{a(\pi i)^2}\int_{-\infty}^{+\infty}\frac{dt}{t-u}\cdot\frac{v^{-2}}{Z(t)} - \frac{1}{2(\pi i)^2}\int_{-\infty}^{+\infty}\frac{dt'}{Z(t')(t'-u)}\int_{-\infty}^{+\infty}\frac{Z_b(t) - Z_b(t')}{t-t'}\,\varphi(t)\,dt,\qquad (6)$$

where

$$Z(t) = Z_g(t) - Z_b(t).$$

Formulas (1)–(6) can be applied to a plasma waveguide immersed in a magnetic field H_0 in three limiting cases:

1) $H_0 = 0$. In this case $\varepsilon_{\parallel} = \varepsilon_{\perp} = 1 - \frac{\omega_0^2}{\omega}$;

2) $H_0 \to \infty\left(\omega_H = \frac{eH_0}{mc} \gg \omega_0, \omega\right)$. In this case $\varepsilon_{\perp} = 1$; $\varepsilon_{\parallel} = 1 - \frac{\omega_0^2}{\omega^2}$;

3) $\omega \ll \frac{eH_0}{Mc} = \Omega_H$ (a magnetohydrodynamic waveguide, M being the mass of the ion). In this case $\varepsilon_{\parallel} = 1 - \frac{\omega_0^2}{\omega}$; $\varepsilon_{\perp} = 1 + \frac{\omega_0^2}{\omega_H \Omega_H}$.

In the first case, the waveguide propagates one slow wave only, and the efficiency of its excitation may therefore be characterized by the reflection coefficient of the coaxial wave. Solving equation (6) by iteration for high plasma line density $\left(\lambda \gg b > a \gg \delta = \frac{c}{\omega_0}\right)$, we obtain an expression for the reflection coefficient (see also /5,6/)

$$R = q\frac{\delta}{a}\left\{1 - 3q\frac{\delta}{a}\right\};$$
$$q = \left|4 \ln \frac{b}{a}\right|^{-1} \tag{7}$$

Since equation (6) is exact, we can find with its aid the error arising when an impedance is substituted for the plasma rod /5,6/. The applicability of the impedance approximation has been established assuming that all the characteristic dimensions in the medium are large in comparison with the skin layer thickness /7/. In our problem, however, one of the parameters — the dimension of the transition region from the plasma waveguide to the coaxial cable — is small in comparison with the skin layer thickness. An analysis of the asymptotic behavior of $\varphi(t)$ as $t \to \infty$ /8/ shows that the correction factor to be introduced into the reflection coefficient (7) in this case is of the order of magnitude of $\frac{\delta^3}{\lambda^3} \ln \frac{\lambda}{\delta}$.

Formula (7) gives the reflection coefficient as a power series in the parameters $\frac{\delta}{a}$ and $\frac{a}{\lambda}$. Setting $\delta \simeq a$, we may prove that even in this case only an insignificant portion of the power (less than 10%) is reflected from the junction between the plasma and the coaxial waveguides.

In the second case, in the presence of a high magnetic field $\omega_H \gg \omega, \omega_0$, the plasma waveguide propagates, not one, but infinitely many slow waves. The wave numbers of these waves are determined by the dispersion equation

$$\frac{\lambda_n J_1(\lambda_n)}{J_0(\lambda_n)} = 4q; \quad \lambda_n^2 = \varepsilon_{\parallel}(k^2 - \gamma_n^2)a^2. \tag{8}$$

Solving (6) by successive approximations (for $\lambda \gg b > a \gg \delta$), we find the excitation coefficient of these waves in the zeroth approximation

$$T_n = 8q\left(1 + 4q\frac{\delta}{a}\right)\frac{1}{\lambda_n^2}. \tag{9}$$

The reflection coefficient of the coaxial wave in this case

$$R_\infty \approx 4q\frac{\delta}{n}\left(1 + q\frac{\delta}{a}\right) \tag{10}$$

In the case of a magnetohydrodynamic waveguide, with $\lambda \gg b > a \gg \delta$, $\varepsilon_\perp \gg 1$, only one slow wave has a phase velocity of the order of c. The other waves, as it follows from the dispersion equation (8), have small phase velocities (slowing of the order of $\left[\varepsilon_\perp\left(1 + \lambda_n^2 \frac{\delta^2}{a^2}\right)^{1/2}\right]$), and their amplitudes are therefore

not large. Neglecting the contribution of these waves, we obtain for the reflection ratio

$$R_H = \frac{q|q|}{k^2 a |\varepsilon_\parallel|}; \quad g^2 = \frac{\varepsilon_\parallel}{\varepsilon_\perp}(\varepsilon_\perp k^2 - \gamma^2), \tag{11}$$

where $\gamma \simeq k$ is the wave vector of the principal mode of the plasma waveguide.

In a weak magnetic field ($\varepsilon_\perp \gg 1$), expression (11) coincides with the first term of equation (7). In strong magnetic fields, when $\varepsilon_\perp - 1 \sim 1$, we cannot neglect the slow waves excited in a magnetohydrodynamic waveguide, whose fields oscillate inside a plasma rod. The corresponding reflection ratio

$$R = R_H - \frac{n_\perp}{(n_\perp^2 - 1)(n_\perp + 1)} \cdot \frac{\delta^4}{a^4} \sum_{\lambda_n < \frac{a}{\delta}} \lambda_n^2, \tag{12}$$

where

$$n_\perp^2 = \varepsilon_\perp; \quad J_1(\lambda_n) = 0.$$

The second term has the order of magnitude of $\frac{n_\perp}{(n_\perp + 1)(n_\perp^2 - 1)} \cdot \frac{\delta}{a}$, so that equation (12) reduces to equation (11) with $n_\perp \gg 1$.

Thus, with high plasma line density in the plasma-filled waveguide ($n_0 a^2 \gg 10^{12}$), its excitation by a coaxial waveguide is effective on low frequencies both with and without a magnetic field.

BIBLIOGRAPHY

1. RAPOPORT, I. M. – DAN SSSR, 59: 1403. 1948.
2. NOBLE, B. The Wiener–Hopf Method. – [Russian translation. 1962.]
3. MUSKHELISHVILI, N. I. Singulyarnye integral'nye uravneniya (Singular Integral Equations). – Moskva, Fizmatgiz. 1962.
4. VEKUA, I. N. – Soobshcheniya AN GruzSSR, 2: 697. 1941.
5. MILLER, M. A. and V. I. TALANOV. – Izv. vuzov. Radiofizika, 4: 795. 1961.
6. KALMYKOVA, S. S. – ZhTF, 31: 1375. 1961.
7. LEONTOVICH, M. A. – In: "Issledovaniya po rasprostraneniyu radiovoln", 2: 5. Moskva–Leningrad, Izdatel'stvo AN SSSR. 1948.
8. VERTGEIM, B. A. – In: "Issledovaniya po sovremennym problemam teorii funktsii kompleksnogo peremennogo", p. 450. Moskva, Fizmatgiz. 1961.

A. N. Kondratenko

A CONTRIBUTION TO THE NONLINEAR THEORY OF A PLASMA WAVEGUIDE IN A HIGH MAGNETIC FIELD

The linear theory of a plasma-filled waveguide has been studied in fairly great detail /1–4/. However, only the nonlinear solution can settle the various important problems connected with the arisal of the higher harmonics, the dependence of the wave phase velocity on the field amplitude, etc. The nonlinear theory of a plasma waveguide in the absence of a magnetic field has been considered in the approximation of small nonlinearity in /5,6/. We shall discuss here the propagation of an electromagnetic wave in a plasma-filled cylindrical waveguide immersed in an infinitely strong magnetic field ($\omega_H^2 \gg \Omega_0^2, \omega^2$) pointing along the waveguide axis (the z axis). *

The kinetic approach appears to be the most consistent. However, nonlinear kinetic analysis constitutes a highly complicated problem. If the phase velocity of the wave is much higher than the electron mean thermal velocity, the hydrodynamic techniques apply. The thermal motion is introduced by considering a pressure gradient in the equations of motion.

The starting set of equations comprises Maxwell's equations

$$\operatorname{rot} \mathbf{E} = -\frac{1}{c}\frac{\partial \mathbf{H}}{\partial t}; \tag{1}$$

$$\operatorname{rot} \mathbf{H} = \frac{1}{c}\frac{\partial \mathbf{E}}{\partial t} - \frac{4\pi e}{c} n\mathbf{v}, \tag{2}$$

the equation of motion of the plasma electrons

$$\frac{\partial \mathbf{v}}{\partial t} + (\mathbf{v}\nabla)\,\mathbf{v} = -\frac{e}{m}\mathbf{E} - \frac{1}{mn}\nabla p - \frac{e}{mc}[\mathbf{v}, \mathbf{H}] \tag{3}$$

and the equation of continuity

$$\frac{\partial n}{\partial t} + \operatorname{div} n\mathbf{v} = 0, \tag{4}$$

where n and p are, respectively, the number density and the pressure of the plasma electrons. The motion of ions, having a density n_0, is neglected.

In an infinitely strong magnetic field, the velocity component along the magnetic field, v_z, is the only one that does not vanish.

The time and position dependence of all the quantities is sought in the form /5/ $\sum_i R_i(r)\,\varphi_i(\xi)$, where $\xi = t - \frac{z}{c\beta}$; $\beta = \frac{V_{ph}}{c}$; V_{ph} wave phase velocity. Since in an infinitely strong magnetic field the E and H waves are separated, we can apply equations (1)–(4) setting $p = \alpha n^\gamma$ (γ the adiabatic index, α a constant) to obtain nonlinear equations for the E-wave in the nonrelativistic approximation:

$$H_\varphi = \beta E_r; \tag{5}$$

$$E_r = -\frac{c\beta k_\perp}{1-\beta^2}\cdot\frac{\partial}{\partial x}\int E_z d\xi, \quad x = k_\perp r; \tag{6}$$

* It is shown in /7/ that an electromagnetic wave propagating in such a waveguide is unstable with respect to "decay" into two similar waves with different frequencies and phase velocities. The analysis that follows therefore applies to times accommodating a few hundreds of wave periods, the life of the original wave to its "decay".

$$E_z = -\frac{mc\beta}{e}\frac{\partial w}{\partial \xi}, \quad w = u - \frac{u^2}{2} + \frac{\delta}{1-\gamma}(1-u)^{1-\gamma}; \tag{7}$$

$$\frac{c^2\beta^2 k_\perp^2}{1-\beta^2}\cdot\frac{1}{x}\cdot\frac{\partial}{\partial x}x\frac{dw}{dx} + \frac{\partial^2 w}{\partial \xi^2} + \Omega_0^2\frac{u}{1-u} = 0, \tag{8}$$

where

$$u = \frac{v_z}{V_{\text{ph}}}; \quad \delta = \frac{\gamma p_0}{mn_0 V_{\text{ph}}^2}; \quad \Omega_0^2 = \frac{4\pi e^2 n_0}{m}.$$

The boundary conditions for equations (5)–(8) postulate continuity of the tangential components of the vectors $\mathbf{E} + \frac{1}{c}[\mathbf{v}, \mathbf{H}]$ and $\mathbf{H} - \frac{1}{c}[\mathbf{v}, \mathbf{E}]$ at the plasma-vacuum interface /8/. Denoting by $\{A\}$ the discontinuity of the quantity A across the interface, we find that the field E_z is continuous, while for the discontinuity of the field H_φ we obtain $\{H_\varphi\} = \frac{v_z}{c}\{E_r\}$. The term in the right-hand side of the last equation is contributed by the surface current $j_\sim^n = -en_\sim^n v_{z\sim}^n$. The current $j_\sim^n$ is of second order of smallness relative to the field, and it therefore does not enter the linear theory. In the nonlinear theory, $j_\sim^n$ in general is other than zero. However, in our case, in virtue of relation (5) and $v_z \neq V_{\text{ph}}$, the fields H_φ and E_r are also continuous at the plasma–vacuum interface.

Thus at the waveguide boundary

$$\{E_z\} = \{E_r\} = \{H_\varphi\} = 0. \tag{9}$$

Equations (5)–(8) cannot be solved for an arbitrary nonlinearity. We shall therefore consider the particular case of small nonlinearity, when $u \ll 1$.

Starting with equation (6), we find the field E_r, and from (7) and (8), the electron velocity u and the field E_z. Apart from u^3, we find

$$\frac{\partial u}{\partial \xi} = -\frac{eE_z}{mc\beta(1-\delta)} + \frac{1+\gamma\delta}{1-\delta}\frac{\partial}{\partial \xi}\cdot\frac{u^2}{2} + \frac{\gamma\delta(1+\gamma)}{2(1-\delta)}u^2\frac{\partial u}{\partial \xi}; \tag{10}$$

$$\frac{c^2\beta^2 k_\perp^2}{1-\beta^2}\cdot\frac{1}{x}\frac{\partial}{\partial x}\cdot\frac{\partial E_z}{\partial x} + \frac{\partial^2 E_z}{\partial \xi^2} + \Omega^2 E_z =$$

$$= \frac{mc\beta\Omega^2}{2e}\left[(3+\gamma\delta-2\delta)\frac{\partial u^2}{\partial \xi} + [\gamma\delta(1+\gamma) + 6(1-\gamma)]u^2\frac{\partial u}{\partial \xi}\right], \tag{11}$$

where

$$\Omega^2 = \frac{\Omega_0^2}{1-\delta}.$$

Equations (10) and (11) can be solved by expansion of the partial differential equations in terms of a small parameter /6/. If the first-order radial functions fall at infinity, this method can be applied for any a (a being the waveguide radius).

Solving equations (6), (10), and (11) in the first, linear approximation, we find the fields and the electron velocity in the plasma:

$$E_z = E_0 J_0(x)\cos\psi; \tag{12}$$

$$E_r = -\frac{\omega\varepsilon_3}{c\beta k_\perp}E_0 J_1(x)\sin\psi; \tag{13}$$

$$u = -\varepsilon J_0(x)\sin\psi, \tag{14}$$

where

$$\varepsilon = \frac{eE_0}{mc\beta\omega(1-\delta)}; \quad \varepsilon_3 = 1 - \frac{\Omega^2}{\omega^2}; \quad \psi = \omega\xi;$$

$$k_\perp^2 = -\varepsilon_3 \frac{\omega^2}{c^2\beta^2}(1-\beta^2); \tag{15}$$

J_1 and J_0 are Bessel's functions of first and zeroth order, respectively.

In the vacuum ($n_0 = 0$), the solution of equations (6) and (11) approaching zero as $r \to \infty$ has the form

$$E_z = E_{01} K_0(\varkappa r)\cos\psi; \tag{16}$$

$$E_r = \frac{\omega}{\varkappa c\beta} E_{01} K_1(\varkappa r)\sin\psi, \tag{17}$$

where K_1 and K_0 are Macdonald functions;

$$\varkappa^2 = \frac{\omega^2}{c^2\beta^2}(1-\beta^2). \tag{18}$$

Since the fields at the plasma–vacuum interface are continuous, we obtain the following equation for the waves propagating in the waveguide /4/:

$$-\varepsilon_3 \frac{\varkappa}{k_\perp} \cdot \frac{J_1(k_\perp a)}{J_0(k_\perp a)} = \frac{K_1(\varkappa a)}{K_0(\varkappa a)}. \tag{19}$$

Since K_1 and K_0 oscillate, in general there is an infinity of waves of different phase velocities β corresponding to a given frequency ω. We shall consider the case when there is but one wave propagating in the waveguide, whose phase velocity is such that $k_\perp^2 a^2 \ll 1$. *

To find an equation of second order for the field E_z, we substitute the linear solution in the right-hand side of (11). Seeking a second-order field E_z in the form $E^{(2)} = E_0 R_2(x) \sin 2\psi$, we obtain an equation for the function R_2:

$$\frac{1}{x} \cdot \frac{\partial}{\partial x} x \frac{\partial R_2}{\partial x} + q^2 R_2 = f_0 J_0^2(x), \tag{20}$$

where

$$q^2 = \frac{\Omega^2 - 4\omega^2}{-\omega^2\varepsilon_3}; \quad f_0 = -\varepsilon \frac{\Omega^2}{2\omega^2\varepsilon_3} \frac{3-\delta(2-\gamma)}{1-\delta}$$

For $x^2 \ll 1$, we have (to terms of the order of x^2, inclusive)

$$E_z^{(2)} = E_0\left[C\left(1 - \frac{q^2x^2}{4}\right) + f_0 \frac{x^2}{4}\right]\sin 2\psi; \tag{21}$$

$$E_r^{(2)} = -\frac{\omega\varepsilon_3}{2c\beta k_\perp} E_0 (f_0 - q^2 C)\frac{x}{2}\cos 2\psi, \tag{22}$$

where C is a constant.

The field in the vacuum, falling off to zero as $r \to \infty$, now has the form

$$E_z^{(2)} = E_{02} K_0(2\varkappa r)\sin 2\psi; \tag{23}$$

$$E_r^{(2)} = -\frac{\omega}{c\beta\varkappa} E_{02} K_1(2\varkappa r)\cos 2\psi. \tag{24}$$

* This inequality is not obligatory: it has been introduced solely for the purpose of computing indefinite integrals of products of three cylindrical functions.

Seeing that the field is continuous at the plasma–vacuum interface, we can determine the unknown constants C and E_{02}:

$$C = \frac{f_0}{n}; \quad E_{02} = \frac{E_0 C}{K_0(2\varkappa a)}; \quad n = q^2 - \frac{K_0(\varkappa a)}{K_0(2\varkappa a)}. \tag{25}$$

The second-order electron velocity (14) is

$$u^2 = \frac{\varepsilon}{2}\left(C - \frac{\varepsilon}{2} \cdot \frac{1+\delta\gamma}{1-\delta}\right)\cos 2\psi. \tag{26}$$

For

$$k_\perp^2 a^2 \ll 1; \quad \Omega^2 \gg \omega^2; \quad \delta \ll \frac{3}{2-\gamma} \tag{27}$$

all the relations are much simpler:

$$E_z^{(2)} = E_0 C \sin 2\psi, \quad C = \frac{3\varepsilon}{2(1-\delta)} \frac{\gamma_1 + \ln \varkappa a}{\ln 2}; \tag{28}$$

$$E_r^{(2)} = \frac{\omega\varepsilon_3}{2c\beta k_\perp} E_0 C \frac{x}{2} \cos 2\psi; \tag{29}$$

$$u^{(2)} = \frac{\varepsilon}{2} C \cos 2\psi, \tag{30}$$

where $\gamma_1 = 0.577\ \ldots$ is Euler's constant.

Substituting the first and the second-order fields E, in the right-hand side of (11), we obtain on third approximation (for $x^2 \ll 1$)

$$\frac{1}{x} \cdot \frac{\partial}{\partial x} x \frac{\partial E_z^{(3)}}{\partial x} + \frac{1-\beta^2}{c^2\beta^2 k_\perp^2}\left(\frac{\partial^2 E_z^{(3)}}{\partial \xi^2} + \Omega^2 E_z^{(3)}\right) = f_{03}\cos\psi + A_3 \cos 3\psi, \tag{31}$$

where A_3 is a certain coefficient specifying the third harmonic;

$$f_{03} = \frac{-\varepsilon^2}{8(1-\delta)} \cdot \frac{\Omega^2}{\varepsilon^2\omega^2}\left[(3+\gamma\delta-2\delta)\left(\frac{2C}{\varepsilon} - \frac{1+\gamma\delta}{1-\delta}\right) - [\gamma\delta(1+\gamma) + 6(1-\delta)\right].$$

The left-hand side of (31) is an equation for the first-order field E_z. The first harmonic entering the right-hand side of this equation does not lead to secular variation, the left-hand side being a partial differential equation; it only alters the first-order radial function. This, in turn, changes the phase velocity of the wave.

We seek a solution of equation (31) in the form

$$E_z^{(3)} = E_0 R_3(x)\cos\psi.$$

For $R_3(x)$ we have

$$\frac{1}{x} \cdot \frac{\partial}{\partial x} x \frac{\partial R_3}{\partial x} + R_3 = f_{03}. \tag{32}$$

Its solution, to within x^2 inclusive, is

$$R_3(x) = C_3\left(1 - \frac{x^2}{4}\right) - f_{03}\frac{x^2}{4}. \tag{33}$$

To find the constant C_3, we apply the boundary condition at the waveguide axis:

$$E_z(0, \xi) = E_0 \cos\omega\xi. \tag{34}$$

In virtue of (34), $C_3 = 1$, and for the first field harmonics in a plasma we have on third approximation

$$E_z = E_0\left[1-(1-f_{03})\frac{x^2}{4}\right]\cos\psi; \tag{35}$$

$$E_r = -\frac{\omega\varepsilon_3}{c\beta k_\perp}E_0(1-f_{03})\frac{x}{2}\sin\psi. \tag{36}$$

Applying (27),

$$f_{03} = \frac{9e^2}{8(1-\delta)^2}\cdot\frac{\gamma_1+\ln \varkappa a}{\ln 2}. \tag{37}$$

Seeing that the fields are continuous at the plasma–vacuum interface and applying the new expressions (35) and (36) for the first field harmonics in the plasma, we obtain a nonlinear dispersion equation

$$\beta^2 = \frac{\Omega_0^2 a^2}{2c^2(1-\delta)}(1-f_{03})\ln\frac{c\beta}{\omega a}. \tag{38}$$

Since $\varkappa a \ll 1$, we have $f_{03} < 0$ and the wave phase velocity increases with the wave field amplitude.

Setting $\beta^2 = \beta_0^2(1-f_{03})$, we obtain from (15) for $\beta^2 \ll 1$

$$k_\perp^2 = \frac{k_\perp^2}{1-f_{03}}; \quad k_{10}^2 = -\frac{\varepsilon_3\omega^2}{c^2\beta_0^2}. \tag{39}$$

Applying (39), we find from (35) and (36) that the nonlinear coupling does not affect the field E_z and enhances the field E_r (and consequently also H_φ).

BIBLIOGRAPHY

1. SHUMAN, W. O. – Zs Phys., **128**: 629. 1950.
2. FAINBERG, Ya. B. – CERN Symp., **1**: 84. 1956.
3. PYATIGORSKII, L. M. – Uchenye Zapiski Khar'kovskogo Universiteta, **49**: 38. 1953.
4. FAINBERG, Ya. B. and M. F. GORBATENKO. – ZhTF, **29**: 549. 1959.
5. FAINBERG, Ya. B. – Atomnaya Energiya, **6**: 447. 1959.
6. KONDRATENKO, A. N. – ZhTF, **34**: 154. 1964.
7. KONDRATENKO, A. N. – This volume, p. 173.
8. LANDAU, L. D. and E. M. LIFSHITZ. Elektrodinamika sploshnykh sred (Electrodynamics of Continuous Media). – Moskva, Fizmatgiz. 1959.

V. D. Shapiro

NONLINEAR OSCILLATIONS IN AN INHOMOGENEOUS PLASMA IN THE PRESENCE OF A MAGNETIC FIELD

Nonlinear electron plasma oscillations in a "cold" plasma have been investigated in detail in /1-5/. However, it has been invariably assumed that in the absence of oscillations the plasma is homogeneous. We consider the case of plasma oscillations set against an inhomogeneous "background".

We assume that there are no thermal motions in the plasma, and that a uniform magnetic field H_0 is impressed, lying in the YZ plane and making an angle ϑ with the Z axis, which points in the direction of oscillation. The starting set of equations in this case has the form

$$\left.\begin{aligned} &\frac{\partial v_x}{\partial t} + v_z\frac{\partial v_x}{\partial z} = -\omega_H(v_y\cos\vartheta - v_z\sin\vartheta)\\ &\frac{\partial v_y}{\partial t} + v_z\frac{\partial v_y}{\partial z} = \omega_H v_x\cos\vartheta\\ &\frac{\partial v_z}{\partial t} + v_z\frac{\partial v_z}{\partial z} = -\frac{e}{m}E - \omega_H v_x\sin\vartheta\\ &\frac{\partial N}{\partial t} + \frac{\partial}{\partial z}(Nv_z) = 0\\ &\frac{\partial E}{\partial z} = -4\pi e(N - N_1), \end{aligned}\right\} \tag{1}$$

$$\left|\omega_H = \frac{eH_0}{mc}\right|.$$

Let us consider the case when in steady state the electron velocities are all zero and there is no electric field, i.e.,

$$N_{0e}(z) = N_{0i}(z) \equiv N_0(z).$$

It has been shown in /4/ that (1) are easily solved by substituting $\{t, x, y, z\}$ for the original variables $\{t, x, y, \psi\}$, $\psi(t, z)$ being defined by the equations

$$\frac{\partial\psi}{\partial z} = \frac{N}{N_0'};\quad \frac{\partial\psi}{\partial t} = -\frac{Nv_z}{N_0'} \tag{2}$$

(N_0' the maximal steady-state density). From (2) it follows that the equation of continuity is satisfied automatically. Integrating Poisson's equation, we find

$$E = -4\pi e\left(\psi N_0' - \int_0^z N_0 dz\right) + g(t). \tag{3}$$

Without oscillations $\psi = \frac{1}{N_0'}\int_0^z N_0 dz$ and $E = 0$, and in our case we must set $g(t) = 0$, which corresponds to a zero external electric field. From (2) it furthermore follows that $\frac{d\psi}{dt} = \frac{\partial\psi}{\partial t} + v_z\frac{\partial\psi}{\partial z} = 0$.

Therefore

$$\frac{d\mathbf{v}}{dt} = \frac{\partial\mathbf{v}}{\partial t} + v_z\frac{\partial\mathbf{v}}{\partial z} = \frac{\partial\mathbf{v}}{\partial t_\psi} + \frac{\partial\mathbf{v}}{\partial\psi}\,\frac{d\psi}{dt} = \frac{\partial\mathbf{v}}{\partial t_\psi} = \frac{\partial^2\mathbf{r}}{\partial t_\psi^2}. \tag{4}$$

Substituting (3) and (4) in the equation of motion, we find in the variables t, ψ

$$\frac{\partial^2 z}{\partial t^2} + \frac{4\pi e^2}{m}\int_0^z N_0 dz = \frac{4\pi e^2 N_0}{m}\psi - \omega_H \sin\vartheta v_x;$$

$$v_y = \omega_H x \cos\vartheta - \omega_H x_0 \cos\vartheta;$$

$$v_x = -\omega_H (y\cos\vartheta - z\sin\vartheta) + \omega_H (y_0\cos\vartheta - z_0(\psi)\sin\vartheta). \qquad (5)$$

In the last two equations, the integration constants are chosen from the following condition: $v_x = v_y = 0$ and $r = r_0(\psi)$ in the absence of oscillations. Eliminating v_x from (5), we obtain a final set of equations in $z(t, \psi)$ and $y(t, \psi)$:

$$\left.\begin{aligned}
&\frac{\partial^2 z}{\partial t^2} + \frac{4\pi e^2}{m}\int_0^z N_0 dz + \omega_H^2(\sin^2\vartheta z - \sin\vartheta\cos\vartheta\, y) = \\
&= \frac{4\pi e^2 N_0}{m}\psi + \omega_H^2(\sin^2\vartheta z_0(\psi) - \sin\vartheta\cos\vartheta\, y_0) \\
&\frac{\partial^2 y}{\partial t^2} + \omega_H^2(\cos^2\vartheta y - \sin\vartheta\cos\vartheta z) = \\
&= \omega_H^2(\cos^2\vartheta y_0 - \sin\vartheta\cos\vartheta z_0(\psi)).
\end{aligned}\right\} \qquad (6)$$

In a homogeneous plasma ($N_0 = \text{const}$), substituting $z = z_0 + \delta z$; $y = y_0 + \delta y$; $z_0 = \psi$ in (6), we find that the frequency of the nonlinear plasma oscillations in the presence of a magnetic field is identical to the frequency of the linear oscillations. This result was originally obtained by K. N. Stepanov /5/.

With $N_0 \neq \text{const}$, the system (6) is highly complex. We investigated this system only for cases when it separated into two independent equations, i.e., for $\vartheta = 0$, $\vartheta = \frac{\pi}{2}$.

1. $\vartheta = 0$. Substituting $z = z_0 + \delta z$, where z_0 is determined from $\int_0^z N_0 dz = N_0'\psi$, we find for $\delta z(t, \psi)$

$$\frac{\partial^2 \delta z}{\partial t^2} + \frac{4\pi e^2}{m}\int_{z_0}^{z_0+\delta z} N_0(z')\,dz' = 0. \qquad (7)$$

From (7), the energy integral

$$\frac{1}{2}\left(\frac{\partial \delta z}{\partial t}\right)^2 - \frac{4\pi e^2}{m}\int_{\delta z}^{a} du \int_0^u N_0(z_0 + u')\,du' = 0, \qquad (8)$$

where a is the oscillation amplitude; the integration limits have been chosen from the condition $\delta z = a$; the velocity $\frac{\partial \delta z}{\partial t} = 0$ ($\delta z = a$ the point of reversal). Taking $\frac{\partial \delta z}{\partial t}$ from the energy integral and integrating the resulting equation with respect to time, we find

$$t = \int_{\delta z_0}^{\delta z} \frac{du}{\left[\frac{8\pi e^2}{m}\int_u^a du' \int_0^{u'} N_0(z_0 + u'')\,du''\right]^{1/2}}. \qquad (9)$$

This relation gives $\delta z\,(t,\psi)$. Applying

$$N = \frac{N_0'}{\frac{\partial z_0}{\partial\psi} + \frac{\partial \delta z}{\partial\psi}}; \quad v_z = \frac{\partial \delta z}{\partial t}; \quad E = -4\pi e \int\limits_{z_0}^{z_0+\delta z} N_0(z)\,dz, \tag{10}$$

we can also find the density, the particle velocity, and the field in the plasma in terms of the variables t and ψ.

To return to the original variables t and z, we should substitute $N\,(t,\psi)$ and $v_z\,(t,\psi)$ from (10) in equation (2) and solve it for $\psi\,(t,z)$. By way of an example, we shall determine the frequency of the nonlinear oscillations. From (9) we find for the period of oscillation

$$T = 4\int\limits_0^a \frac{du}{\left[\frac{8\pi e^2}{m}\int\limits_u^a du' \int\limits_0^{u'} N_0(z_0+u'')\,du''\right]^{1/2}}. \tag{11}$$

Let the plasma density vary as $N_0(z) = N_0'\left(1 - \frac{z^2}{l^2}\right)$; $|z| \leqslant l$. Substituting $N_0\,(z)$ in (11), we calculate $T\,(a, z_0)$; $z = z_0$ is the plane where the oscillations with $a \to \infty$ are localized. For simplicity, we shall henceforth limit the discussion to the case $z_0 = 0$. Then from (11)

$$T = \frac{4}{\omega_L(0)}\,\frac{1}{\sqrt{1-\frac{a^2}{6l^2}}}\,K\left(\frac{a}{\sqrt{6l^2-a^2}}\right), \tag{12}$$

where K is a complete elliptical integral of the 1st kind. With $a \ll l$, $\omega = \omega_L(0) = \sqrt{\frac{4\pi e^2 N_0'}{m}}$; with $a \sim l$, the amplitude dependence of frequency can no longer be neglected. The frequency falls off from $\omega_L(0)$ for $a \ll l$ to $\frac{5}{6}\omega_L(0)$ for $a = l$.

2. $\vartheta = \pi/2$. As in the derivation of (11), we can obtain from (6) a formula for the period of oscillation:

$$T = 4\int\limits_0^a \frac{du}{\left[\omega_H^2(a^2-u^2) + \frac{8\pi e^2}{m}\int\limits_u^a du' \int\limits_0^{u'} N_0(z_0+u'')\,du''\right]^{1/2}}. \tag{13}$$

Substituting $N_0(z) = N_0'\left(1 - \frac{z^2}{l^2}\right)$ and setting as before $z_0 = 0$, we find

$$T = \frac{4}{(\omega_L^2(0)+\omega_H^2)}\,\frac{1}{\sqrt{1-\frac{a^2}{6l^2}\frac{\omega_L^2(0)}{\omega_L^2(0)+\omega_H^2}}}\,K \times$$

$$\times\left(\frac{a\frac{\omega_L(0)}{\sqrt{\omega_L^2(0)+\omega_H^2}}}{\sqrt{6l^2 - a^2\frac{\omega_L^2(0)}{\omega_L^2(0)+\omega_H^2}}}\right). \tag{14}$$

BIBLIOGRAPHY

1. POLOVIN, R. V. - JETP, **31**: 354. 1956.

2. STURROCK, P. A. - Proc. Roy. Soc., **242A**: 277. 1957.

3. DAWSON, I. - Phys. Rev., **113**: 383. 1959.

4. KALMAN, G. - Ann. Phys., **10**: 1. 1960.

5. STEPANOV, K. N. - ZhTF, **33**: 246. 1963.

V. D. Shapiro

A CONTRIBUTION TO THE NONLINEAR THEORY OF CHARGE-DENSITY WAVES IN BEAMS WITH VARIABLE PARAMETERS

Parametric excitation of charge-density waves is possible in beams of variable density and velocity. In the linear theory /1–3/, the wave amplitude exponentially increases along the beam for certain relations (characteristic of parametric resonance) between the velocity or the density modulation wavelength L of the beam and the plasma wavelength $\lambda_p = 2\pi \frac{v_0'}{\omega_0'}$,

$$2L = n\lambda_p, \quad n = 1, 2 \ldots.$$

Parametric resonance is widely applied in radio engineering in the amplification of microwaves, but the theory of this phenomenon is practically limited to the linear amplitude approximation. The linear theory, as usual, is adequate for establishing the onset of instability and the growth rates in the initial stage, but it is insufficient for examining the behavior of the solution for large amplitudes or finding the maximal oscillation amplitudes. In the present work we consider the nonlinear theory of parametric excitation for the simplest case of an infinitely broad beam of low percentage modulation which is homogeneous over its cross section. Unlike /4/, our analysis is not restricted by the requirement of small nonlinearity and time-independence of amplitude and phase.

The starting set of equations is

$$\left.\begin{aligned} &\frac{\partial V}{\partial t} + V\frac{\partial V}{\partial z} = -\frac{e}{m}E \\ &\frac{\partial N}{\partial t} + \frac{\partial}{\partial z}(NV) = 0 \\ &\frac{\partial E}{\partial z} = -4\pi e(N - N_+), \end{aligned}\right\} \tag{1}$$

where N, V are the number density and the velocity of the electron beam, N_+ the density of the background ions. In the steady state, N and V are given by the relations

$$N_0 = N_0'(1 + \varepsilon\cos kz); \quad V_0 = \frac{V_0'}{1 + \varepsilon\cos kz}; \quad \varepsilon \ll 1 \tag{2}$$

(to avoid ambiguity, we shall take $\varepsilon > 0$). The particle flux NV in the steady state is conserved along the beam $\left(\frac{\partial}{\partial z}(NV) = 0\right)$, and the velocity variations in the electron beam set up a steady-state electric field

$$E_0(z) = -4\pi e\left(\int_0^z N_0 dz' - \int_0^z N_+ dz'\right) = -\frac{m}{2e} \cdot \frac{\partial}{\partial z} V_0^2. \tag{3}$$

Let us consider a boundary-value problem. Time-dependent perturbations are imposed on the steady-state velocity and flux of the streaming particles at $z = 0$:

$$j(z=0) = N_0'\left(V_0' - \frac{dg}{dt}\right); \quad V(z=0) = \frac{V_0'}{1+\varepsilon} + \omega_0' s(t),$$
$$\omega_0'^2 = \frac{4\pi e^2 N_0'}{m}. \tag{4}$$

These perturbations set up charge density fluctuations in the beam. Our problem is to establish how these fluctuations propagate along the beam, without assuming small amplitudes or linearizing the starting equations.*

The analysis of nonlinear oscillations in a variable-parameter beam is conveniently carried out by substitution of independent variables: t and ψ are substituted for the ordinary variables t and z, where $\psi(t, z)$ is determined from

$$\frac{\partial\psi}{\partial z} = \frac{N}{N_0'}; \quad \frac{\partial\psi}{\partial t} = -\frac{NV}{N_0'}. \tag{5}$$

Here $\psi(t, z)$ is a stream function which is conserved along the particle trajectory:

$$\frac{d\psi}{dt} = \frac{\partial\psi}{\partial t} + V\frac{\partial\psi}{\partial z} = 0.$$

$\psi(t, z)$ was successfully introduced as an independent variable in the solution of some problems in gas dynamics /5/. Kalman /6/ was the first to apply this transformation to the problem of nonlinear plasma oscillations in a one-component plasma.

If relations (5) are satisfied, the equation of continuity applies automatically, and Poisson's equation is readily integrated to yield a relation for the electric field:

$$E = -4\pi e\left(N_0'\psi - \int_0^z N_+ dz\right) + G(t).$$

To find $G(t)$, we make use of the fact that in the steady state, with no fluctuations,

$$E = E_0(z) = -4\pi e\left[\int_0^z (N_0 - N_+)\, dz'\right]; \quad \psi = \frac{1}{N_0'}\int_0^z N_0 dz - V_0' t.$$

* The case in hand can be realized experimentally in the following way. An electron beam is injected into a space where an electric field (3) is set up by modulating grids; a high-frequency voltage is impressed on the beam at the input, and the nonlinear oscillations of the beam particles are investigated.

Therefore, limiting the discussion to a case of zero external electric field, we find for $E(t, \psi)$

$$E = -4\pi e N_0' \left(\psi - \frac{1}{N_0'} \int_0^z N_0 dz + V_0' t \right) + E_0. \tag{6}$$

Since $\frac{d\psi}{dt} = 0$,

$$\frac{dV}{dt} = \frac{\partial V}{\partial t} + V \frac{\partial V}{\partial z} = \left(\frac{\partial V}{\partial t}\right)_\psi + \frac{\partial V}{\partial \psi} \cdot \frac{d\psi}{dt} = \left(\frac{\partial V}{\partial t}\right)_\psi = \left(\frac{\partial^2 z}{\partial t^2}\right)_\psi.$$

Substituting in the equation of motion $E_0(t, \psi)$ from (6) and N_0 from (2), we find an equation for $z(t, \psi)$, viz., the displacement of the beam electrons:

$$\frac{\partial^2 z}{\partial t^2} + \omega_0'^2 \left(z + \frac{\varepsilon}{k} \sin kz \right) = \omega_0'^2 (\psi + V_0' t) - \frac{e}{m} E_0. \tag{7}$$

We write $z(t, \psi)$ as $z = z_0(t, \psi) + \delta z(t, \psi)$, where the steady-state displacement $z_0(t, \psi)$ is defined by

$$z_0 + \frac{\varepsilon}{k} \sin kz_0 = \psi + V_0' t. \tag{8}$$

ε being small, we approximately have for z_0

$$z_0 \sim \psi + V_0' t - \frac{\varepsilon}{k} \sin k (\psi + V_0' t) \tag{8'}$$

Applying (3) and (8), we can easily show that $z_0(t, \psi)$ also satisfies the equation

$$\frac{\partial^2 z_0}{\partial t^2} = -\frac{e}{m} E_0.$$

Equation (7) is conveniently written using the variables ζ, ψ, where $\zeta = \psi + V_0' t$. Substituting $z_0(t, \psi)$ from (8') and retaining only terms linear in ε, we obtain the following expression for the perturbation displacement $\delta z(t, \psi)$:

$$\frac{\partial^2 \delta z}{\partial \zeta^2} + \frac{\omega_0'^2}{V_0'^2} \delta z = \varepsilon \frac{\omega_0'^2}{k V_0'^2} [\sin k\zeta - \sin k(\zeta + \delta z)]. \tag{9}$$

Linearizing with respect to δz, we reduce (9) to a Mathieu equation with instability zones

$$k \frac{n}{2} \simeq \frac{\omega_0'}{V_0'}; \; n = 1, 2 \ldots.$$

In the ε-linear approximation, instability is possible only with $n = 1$. Having determined $\delta z(t, \psi)$ from (9), we can find the density and the velocity of the electrons from the relations

$$V = V_0 + \frac{\partial \delta z}{\partial t}; \quad N = \frac{N_0'}{\frac{\partial z_0}{\partial \psi} + \frac{\partial \delta z}{\partial \psi}}. \tag{10}$$

For arbitrary δz, (9) is an oscillator equation with a nonlinear term proportional to a small parameter ε and dependent on the variable ζ.

Equations of this type are solved in /7/. For simplicity, we restrict the analysis to the 1st unstable zone, setting $\frac{k}{2} \simeq \frac{\omega_0'}{V_0'}$.* In this case, in accordance with the results of /7/, the solution of equation (9) has the form

$$\delta z = a(\zeta,\ \psi)\cos\left[\frac{k\zeta}{2} + \vartheta(\zeta,\ \psi)\right] + u_1(\zeta,\ a,\ \vartheta). \tag{11}$$

Here u_1 is a ζ-oscillating function proportional to a small parameter ε. The explicit form of u_1 is of no significance in what follows, since for small ε, the term u_1 introduces but a small distortion in the fundamental harmonic term whose amplitude and phase vary slowly with ζ. The ζ-variation of the amplitude a and the phase ϑ is found from the equations

$$\frac{\partial a}{\partial \zeta} = -\frac{\varepsilon}{8\pi^2}\sum_\sigma e^{2i\sigma\vartheta}\int_0^{2\pi} dk\zeta e^{i\sigma k\zeta} \times \int_0^{2\pi} d\psi \sin\psi e^{-2i\sigma\psi}[\sin k\zeta - \sin k(\zeta + a\cos\psi)];$$

$$\frac{\partial \vartheta}{\partial \zeta} = \frac{\omega_0'}{V_0'} - \frac{k}{2} - \frac{\varepsilon}{8\pi^2}\sum_\sigma e^{2i\sigma\vartheta}\int_0^{2\pi} d(k\zeta)\, e^{i\sigma k\zeta} \times$$
$$\times \int_0^{2\pi} d\psi \cos\psi e^{-2i\sigma\psi}[\sin k\zeta - \sin k(\zeta + a\cos\psi)]. \tag{12}$$

Applying the expansion

$$e^{ika\cos\psi} = \sum_n e^{in\left(\psi + \frac{\pi}{2}\right)} J_n(ka)$$

and taking the integrals in (12), we find a set of equations in $a(\zeta,\ \psi)$, $\vartheta(\zeta,\ \psi)$:

$$\left.\begin{aligned} \frac{\partial a}{\partial \zeta} &= \frac{\varepsilon \sin 2\vartheta}{4}(J_1(ka) + J_3(ka)) \\ \frac{\partial \vartheta}{\partial \zeta} &= \frac{\omega_0'}{V_0'} - \frac{k}{2} + \frac{\varepsilon\cos 2\vartheta}{4a} J_1(ka) - J_3(ka), \end{aligned}\right\} \tag{13}$$

where $a(0, \psi)$, $\vartheta(0, \psi)$ are determined from boundary conditions (4). For $z = 0$, we have from equations (4)

$$\psi = -V_0't + g(t). \tag{14}$$

Since the oscillation amplitude is small for $z = 0$, we approximately have $t \simeq -\frac{\psi|_{z=0}}{V_0'}$, i.e., for $z = 0$, $\zeta = 0$. Substituting ψ from (14) in (6) and replacing t with $-\frac{\psi}{V_0'}$, we find for $z = 0$

$$E = E_0 - 4\pi e N_0' g\left(-\frac{\psi}{V_0'}\right). \tag{15}$$

* For a nonlinear oscillator (9), the condition of parametric resonance has the form $\frac{nk}{m} \simeq \frac{\omega_0'}{V_0'}$ (m and n integers). However, resonances with $n \neq 1$ are permitted only in the ε-nonlinear approximation, and with $m \neq 2$ only in the amplitude-nonlinear approximation.

From equations (4) we similarly have for V at $z = 0$

$$V = \frac{V_0}{1+\varepsilon} + \omega_0 s\left(-\frac{\psi}{V_0'}\right). \tag{15'}$$

On the other hand, applying solution (11) and neglecting the small terms proportional to ε, we find for $\zeta = 0$

$$E = E_0 + 4\pi e N_0' \delta z = E_0 + 4\pi e N_0' a(0, \psi)\cos[\vartheta(0, \psi)];$$

$$V = V_0 + \frac{\partial \delta z}{\partial t} = \frac{V_0'}{1+\varepsilon} - \omega_0' a(0, \psi)\sin[\vartheta(0, \psi)]. \tag{15''}$$

Comparing (15) and (15') with (15''), we find

$$a^2(0, \psi) = s^2\left(-\frac{\psi}{V_0'}\right) + g^2\left(-\frac{\psi}{V_0'}\right);$$

$$\vartheta(0, \psi) = \operatorname{arc\,tg}\left[\frac{s\left(-\frac{\psi}{V_0'}\right)}{g\left(-\frac{\psi}{V_0'}\right)}\right] \tag{16}$$

The problem thus reduces to the solution of a system of ordinary differential equations of first order (13) with boundary conditions (16).

For $ka \ll 1$, equations (13) are simplified:

$$\frac{\partial a}{\partial \zeta} = \frac{\varepsilon}{8}\sin 2\vartheta ka$$

$$\frac{\partial \vartheta}{\partial \zeta} = \frac{\omega_0'}{V_0'} - \frac{k}{2} + \frac{\varepsilon k}{8}\cos 2\vartheta. \tag{17}$$

The solution of (17) has the form

$$a = \left|g\left(-\frac{\psi}{V_0'}\right)\right|\sqrt{\operatorname{ch}^2\lambda\zeta + \frac{1}{\lambda^2}\left(\frac{\varepsilon k}{8} + \frac{\omega_0'}{V_0'} - \frac{k}{2}\right)^2 \operatorname{sh}^2\lambda\zeta};$$

$$\vartheta = \operatorname{arc\,tg}\left[\frac{\frac{\varepsilon k}{8} + \frac{\omega_0'}{V_0'} - \frac{k}{2}}{\lambda}\operatorname{th}\lambda\zeta\right] \tag{18}$$

Here for simplicity we set $s = 0$ and write

$$\lambda = \sqrt{\frac{\varepsilon^2}{64}k^2 - \left(\frac{\omega_0'}{V_0'} - \frac{k}{2}\right)^2}$$

Instability thus sets in for

$$\left|\frac{\omega_0'}{V_0'} - \frac{k}{2}\right| \leqslant \frac{\varepsilon k}{8} \tag{18'}$$

In case of instability the phase approaches a constant value

$$\vartheta_m = \operatorname{arc\,tg}\frac{\left|\frac{\varepsilon k}{8} + \frac{\omega_0'}{V_0'} - \frac{k}{2}\right|}{\lambda}.$$

and the amplitude, in the framework of the linear theory, increases indefinitely. However, for $ka \sim 1$ the nonlinear effects cannot be neglected, and the solution must be obtained for the exact system (13).

Seeing that

$$ka\,[J_1(ka) + J_3(ka)] = 4J_2(ka); \quad J_1(ka) - J_3(ka) = \frac{2}{k}\cdot\frac{dJ_2(ka)}{da},$$

we write (13) as

$$\frac{da}{d\zeta} = 3\varepsilon\,\frac{J_2(ka)}{ka}\sin 2\vartheta;$$
$$\frac{d\vartheta}{d\zeta} = \frac{\omega_0'}{V_0'} - \frac{k}{2} + \frac{3\varepsilon}{2ka}\,\frac{dJ_2(ka)}{da}\cos 2\vartheta. \qquad (19)$$

Setting for convenience

$$\frac{3\varepsilon k\zeta}{2} = \tau; \quad ka = x; \quad \frac{\omega_0'}{V_0'} - \frac{k}{2} = \frac{3\varepsilon k}{8}\Delta,$$

we obtain for (19)

$$\frac{dx}{d\tau} = \frac{2J_2(x)}{x}\sin 2\vartheta;$$
$$\frac{d\vartheta}{d\tau} - \frac{\Delta}{4} = \frac{1}{x}\,\frac{dJ_2(x)}{dx}\cos 2\vartheta \qquad (20)$$

or

$$\frac{x\,dx}{d\tau} = -\frac{\partial H}{\partial\vartheta};$$
$$x\left(\frac{d\vartheta}{d\tau} - \frac{\Delta}{4}\right) = \frac{\partial H}{\partial x}, \qquad (21)$$

where

$$H(x,\ \vartheta) = J_2(x)\cos 2\vartheta.$$

Multiplying the first equation in (21) by $-\frac{d\vartheta}{d\tau}$ and the second by $\frac{dx}{d\tau}$ and adding them up, we find

$$\frac{d}{d\tau}\left[H(x,\ \vartheta) + \frac{\Delta}{8}x^2\right] = 0,$$

i.e., equations (21) have an integral

$$H(x,\ \vartheta) + \frac{\Delta}{8}x^2 = \text{const} = J_2(x_0)\cos 2\vartheta_0 + \frac{\Delta}{8}x_0^2, \qquad (22)$$

where $x_0 = ka_0$, a_0, ϑ_0 are the amplitude and the phase for $\zeta = 0$, as defined by (16).

Solving (22) for $\sin 2\vartheta$, we substitute the result in the first equation in (21) and integrate with respect to τ*:

$$\tau = \int_{x_0^2}^{x^2} \frac{dx^2}{\sqrt{\Phi(x^2,\ x_0^2,\ \xi_0)}}, \qquad (23)$$
$$\Phi = 16J_2^2(x) - \left[\frac{\Delta}{2}(x^2 - x_0^2) - 4J_2(x_0)\,\xi_0\right]^2; \quad \xi_0 = \cos 2\vartheta_0$$

The x defined by equation (23) is a periodic function of τ, varying between x_{min} and x_{max}, where x_{min}, x_{max} are the two smallest positive roots of the equation

$$\Phi(x^2,\ x_0^2,\ \xi_0) = 0.$$

* The author is grateful to V. K. Yulpatov, who suggested this method of solution of (13) for arbitrary k, a.

It is easily seen that $x_{\min}<x_0$; in the instability zone, i.e., for $|\Delta|<1$, $x_{\max}$ is much greater than x_0, and it therefore can be determined with higher precision by solving the equation

$$8J_2(x_{\max}) = |\Delta| x_{\max}^2 .^{*} \tag{24}$$

The period of the function $x(\tau)$ is also easily found from (23):

$$\tau_0 = 2 \int\limits_{x^2_{\min}}^{x^2_{\max}} \frac{dx^2}{\sqrt{\Phi(x^2, x_0^2, \xi_0)}} .$$

Near the boundaries of the instability zone, where $\Delta = \pm(1-\delta)$; $\delta \ll 1$, the amplitude is small for any ξ, and $J_2(x)$ in (23) can be expanded in powers of x, retaining the two leading terms only: $J_2(x) = \frac{1}{8}\left(x^2 - \frac{x^4}{12}\right)$. Seeing that $x \ll 1$; $x_0 \ll 1$; $\delta \ll 1$ and retaining the leading terms only, we obtain for (23)

$$\frac{\tau}{2\sqrt{6}} = \int\limits_{\eta_0}^{\eta} \frac{d\eta}{\sqrt{12\delta\eta^2 - \eta^3 + 12\eta\eta_0\gamma - 6\eta_0^2\gamma^2}};$$

$$\eta = x^2; \quad \eta_0 = x_0^2; \quad \gamma = 1 - \delta \pm \xi_0. \tag{25}$$

It is assumed that $\gamma \neq 0$.

Equation (25) can also be written as

$$\frac{\tau}{2\sqrt{6}} = \int\limits_{\eta_0}^{\eta} \frac{d\eta}{\sqrt{(\eta_3 - \eta)(\eta - \eta_2)(\eta - \eta_1)}} . \tag{25'}$$

The roots η_i can be easily found seeing that $\eta_0 \ll \delta$:

$$\eta_1 = -\frac{\eta_0}{\delta}\gamma; \quad \eta_2 = \frac{\eta_0\gamma}{2}; \quad \eta_3 = 12\delta + \frac{\eta_0\gamma}{\delta}. \tag{26}$$

The integral in the right-hand side of (25') has been calculated in /8/. Three different cases are considered depending on γ.

1. $\gamma > 0$. Then $\eta_1 < 0$, $0 < \eta_2 < \eta_0$. From (25') we have

$$F\left[\arcsin\sqrt{\frac{\eta_3-\eta_1}{\eta_3-\eta_2}\cdot\frac{\eta-\eta_2}{\eta-\eta_1}};\ \sqrt{\frac{\eta_3-\eta_2}{\eta_3-\eta_1}}\right] - F\left[\arcsin\sqrt{\frac{\eta_3-\eta_1}{\eta_3-\eta_2}\cdot\frac{\eta_0-\eta_2}{\eta_0-\eta_1}};\ \sqrt{\frac{\eta_3-\eta_2}{\eta_3-\eta_1}}\right] = \frac{\tau}{4\sqrt{6}}\sqrt{\eta_3-\eta_1}, \tag{27}$$

where F is an elliptic integral of the 1st kind. From (27) we have for η

$$\eta = \frac{\eta_2 - \eta_1 \frac{\eta_3-\eta_2}{\eta_3-\eta_1}\,\mathrm{sn}^2\left[w,\ \sqrt{\frac{\eta_3-\eta_2}{\eta_3-\eta_1}}\right]}{1 - \frac{\eta_3-\eta_2}{\eta_3-\eta_1}\,\mathrm{sn}^2\left[w,\ \sqrt{\frac{\eta_3-\eta_2}{\eta_3-\eta_1}}\right]}, \tag{28}$$

* For fairly large amplitudes, $ka \sim 1$, trajectories may intersect resulting in a multistream motion. The boundaries of multistream motion are determined by setting the derivative $\left(\frac{\partial z}{\partial\psi}\right)_{t=\mathrm{const}}$ equal to zero; this is equivalent to a zero distance between two trajectories with different ψ. Applying (8'), (11), and (13) and neglecting small corrections $\sim x_0, \varepsilon$, we find the boundaries of multistream motion $\zeta_b(\psi)$ from the equation

$$ka(\zeta_b, \psi)\sin\left[\frac{k}{2}\zeta_b + \vartheta(\zeta_b, \psi)\right] = 2.$$

where $\operatorname{sn}\left[w, \sqrt{\frac{\eta_3-\eta_2}{\eta_3-\eta_1}}\right]$ is the elliptic sine;

$$w = \frac{\varepsilon k \zeta}{8}\sqrt{\frac{3(\eta_3-\eta_1)}{2}} + F\left(\arcsin\sqrt{\frac{\eta_3-\eta_1}{\eta_3-\eta_2}\cdot\frac{\eta_0-\eta_2}{\eta_0-\eta_1}};\ \sqrt{\frac{\eta_3-\eta_2}{\eta_3-\eta_1}}\right). \tag{29}$$

The last term in (29) is negligible for fairly large ζ, when $\eta \gg \eta_0$.

Applying the well-known properties of the elliptic sine (see, e.g., /9/), we can find the period of the function $a(\zeta)$:

$$\zeta_0 = \frac{16}{\varepsilon k}\sqrt{\frac{2}{3(\eta_3-\eta_1)}}\,K\left(\sqrt{\frac{\eta_3-\eta_2}{\eta_3-\eta_1}}\right), \tag{30}$$

where K is a complete elliptic integral of the 1st kind. Over a single period, a first increases from a_0 to $a_{\max} = \frac{1}{k}\sqrt{\eta_3}$ at $\zeta = \frac{\zeta_0}{2}$, and then decreases to $a_{\min} = \frac{1}{k}\sqrt{\eta_2}$, again increasing to a_0.

2. $-\delta \leqslant \gamma < 0$. Then $\eta_2 < 0$, $0 < \eta_1 \leqslant \eta_0$. In this case, η_1 and η_2 should be interchanged in both (28) and (29). The maximal and the minimal amplitudes are $a_{\max} = \frac{1}{k}\sqrt{\eta_3}$, $a_{\min} = \frac{1}{k}\sqrt{\eta_1}$.

3. $\gamma = 0$. Formula (25) does not apply, since more terms must be retained in the expansion of $J_2(x_0)$ in powers of x_0. In this case, we obtain for (25)

$$\frac{\tau}{2\sqrt{6}} = \int_{\eta_0}^{\eta}\frac{d\eta}{\sqrt{12\delta\eta^2 - \eta^3 + \eta\eta_0^2}}. \tag{31}$$

Equation (31) may be reduced to the form of (25) by setting

$$\eta_1 = -\frac{\eta_0^2}{12\delta};\quad \eta_2 = 0;\quad \eta_3 = 12\delta + \frac{\eta_0^2}{12\delta}. \tag{31'}$$

Then, for (27) we have

$$\frac{\tau}{4}\sqrt{\frac{\eta_3-\eta_1}{6}} = F\left[\arcsin\sqrt{\frac{\eta_3-\eta_1}{\eta_3}\cdot\frac{\eta}{\eta-\eta_1}};\ \sqrt{\frac{\eta_3}{\eta_3-\eta_1}}\right] - F\left[\arcsin\sqrt{\frac{\eta_3-\eta_1}{\eta_3}\cdot\frac{\eta_0}{\eta_0-\eta_1}};\ \sqrt{\frac{\eta_3}{\eta_3-\eta_1}}\right].$$

Then for η

$$\eta = \frac{-\eta_1\eta_3\operatorname{sn}^2\left[\bar{w}, \sqrt{\frac{\eta_3}{\eta_3-\eta_1}}\right]}{\eta_3\left\{1-\operatorname{sn}^2\left[\bar{w}, \sqrt{\frac{\eta_3}{\eta_3-\eta_1}}\right]\right\}-\eta_1}, \tag{32}$$

where

$$\bar{w} = \frac{\varepsilon k \zeta}{8}\sqrt{\frac{3(\eta_3-\eta_1)}{2}} + F\left\{\arcsin\sqrt{\frac{\eta_3-\eta_1}{\eta}\cdot\frac{\eta_0}{\eta_0-\eta_1}};\ \sqrt{\frac{\eta_3}{\eta_3-\eta_1}}\right\}; \tag{32'}$$

$$a_{\max} = \frac{1}{k}\sqrt{\eta_3};\quad a_{\min} = 0;\quad \zeta_0 = \frac{16}{\varepsilon k}\sqrt{\frac{2}{3(\eta_3-\eta_1)}}\cdot K\left(\frac{\eta_3}{\eta_3-\eta_1}\right).$$

The original variables t and z can be recovered in the case of small oscillations by applying the formulas

$$\zeta = z;\quad \psi = z - V_0 t.$$

In terms of the original variables t and z, $\eta = k^2a^2$ is thus determined by formulas (28) and (32), where w is found, either from (29) or from (32') by substituting z for ζ, and η_t is obtained from (26) and (31'). In (25) and (31'), ξ_0 and η_0 are expressed with the aid of (16) in terms of s and g entering the boundary conditions (4):

$$\xi_0 = \frac{g^2\left(t - \frac{z}{V_0'}\right) - s^2\left(t - \frac{z}{V_0'}\right)}{g^2\left(t - \frac{z}{V_0'}\right) + s^2\left(t - \frac{z}{V_0'}\right)};$$
$$\eta_0 = k^2\left[g^2\left(t - \frac{z}{V_0'}\right) + s^2\left(t - \frac{z}{V_0'}\right)\right]. \tag{33}$$

The variation of the phase ϑ with ζ is found from (22) by substituting $\eta = x^2$ from (28), (32).

Let us dwell on some peculiar properties of our solution. In the case of fairly large amplitudes, $a \sim a_{\max} \gg a_0$, the amplitude and the phase of the solution are virtually independent of their values at $\zeta = 0$; a_0 and ϑ_0 are thus independent on ψ. In Eulerian coordinates this corresponds to time-independent amplitude and phase $\frac{\partial a}{\partial t} = 0$, $\frac{\partial \vartheta}{\partial t} = 0$ in those z-regions where $a \sim a_{\max}$.

The electric field of the oscillations is defined by (15''), with δz substituted from (11). This gives

$$E = 2\pi e N_0' \frac{V_0'}{\omega_0} ka \cdot \cos\left[\frac{k}{2}\zeta + \vartheta\right]. \tag{34}$$

Hence for the potential energy density averaged over the period of fast oscillations

$$\frac{\langle E^2\rangle}{8\pi} = \frac{x^2}{16} N_0' m V_0'^2; \; x = ka. \tag{35}$$

If the trajectories do not intersect, as assumed in this paper, $x \leqslant 2$ and the maximal potential energy density of the oscillations $\frac{\langle E^2\rangle}{8\pi}$ does not exceed half the energy density of the original beam.

The velocity and the number density of the beam are determined from (10). For $a \sim a_{\max}$, omitting small terms $\sim x_0$, ε, we find

$$V = V_0'\left\{1 - \frac{ka}{2}\sin\left[\frac{k}{2}\zeta + \vartheta\right]\right\};$$
$$N = N_0' \frac{1}{1 - \frac{ka}{2}\sin\left[\frac{k}{2}\zeta + \vartheta\right]}. \tag{36}$$

A characteristic feature of our solution is that the oscillation amplitudes may be fairly high ($ka \sim 1$) in the instability zone even for a small percentage modulation, $\varepsilon \ll 1$. Then, according to (35) and 36), the oscillations will substantially alter the state of the beam.

In conclusion we should dwell on the advantages connected with the introduction of the stream function ψ as an independent variable in the analysis of parametric resonance in beams. In this case, the fundamental equation – the equation of the nonlinear oscillator (9) – contains derivatives with respect to ζ only; ψ enters the solution via the boundary conditions. Equation (9) could thus be solved by applying the well-known techniques of

the nonlinear theory of oscillations, developed by van der Pol, N. M. Krylov, N. N. Bogolyubov. On the other hand, when the problem is treated in the variables t and z (as, e.g., in /4/), the oscillator equation (9) is replaced with a nonlinear partial differential equation. Since no accepted methods are available for the solution of these equations, additional simplifying assumptions have been imposed in /4/. Furthermore, the starting nonlinear equation in the variables t and z is complicated to such an extent that it is solved in /4/ assuming a small ε and a small amplitude ($ka \ll 1$). The condition of small amplitudes is not observed at a distance from the boundary of the instability zone ($\delta \sim 1$).

BIBLIOGRAPHY

1. RYDBECK, O. E. H. and B. AGDUR. — L'onde Electr., **34**: 499. 1954.
2. PETER, R. W., S. BLOOM, and J. A. RUETZ. — RCA Rev., **15**: 113. 1954.
3. BLIOKH, P. V. and Ya. B. FAINBERG. — ZhTF, **26**: 530. 1956.
4. BLIOKH, P. V. Candidate thesis, Khar'kov State University. 1958.
5. COURANT, R. and K. O. FRIEDRICHS. — Supersonic Flow and Shock Waves. New York. 1948.
6. KALMAN, G. — Ann. Phys., **10**: 1. 1960.
7. BOGOLYUBOV, N. N. and Yu. A. MITROPOL'SKII. Asimptoticheskie metody v teorii nelineinykh kolebanii (Asymptotic Techniques in the Theory of Nonlinear Oscillations). — Moskva, Fizmatgiz. 1958.
8. GRADSHTEIN, I. S. and I. M. RYZHIK. Tablitsy integralov, summ, ryadov, proizvedenii (Tables of Integrals, Sums, Series, and Products). — Moskva, Fizmatgiz. 1962.
9. ERDELYI et al. Higher Transcendental Functions. V. II. New York. 1953.

V. L. Sizonenko and K. N. Stepanov

THE EFFECT OF ELECTRON THERMAL MOTION ON NONLINEAR PLASMA OSCILLATIONS

The frequency of one-dimensional longitudinal plasma oscillations is amplitude-independent /1,2/. This result, however, does not apply if we take into consideration the relativistic effects /2,3/, the relation among longitudinal and transverse oscillations /3/, and the motion of ions /4/. In the present paper we investigate the effect the thermal motion of plasma electrons has on the propagation of plane longitudinal plasma oscillations.

The starting set of equations is

$$\frac{\partial n}{\partial t} + \frac{\partial (nv)}{\partial x} = 0; \tag{1}$$

$$mn\left(\frac{\partial v}{\partial t} + v\frac{\partial v}{\partial x}\right) = -neE - \frac{\partial \sigma}{\partial x}; \tag{2}$$

$$\left(\frac{\partial}{\partial t} + v\frac{\partial}{\partial x}\right)\frac{\sigma}{n^3} = 0; \tag{3}$$

$$\frac{\partial E}{\partial x} = -4\pi e\,(n - n_0). \tag{4}$$

where $-e$ and m are the electron charge and mass; n and v the density and the velocity of the electron fluid; $\sigma = nT$ the pressure; E the electric field strength; n_0 the number density of the ions, assumed to be at rest. Plasma oscillations are regarded as being adiabatic with one degree of freedom (an adiabatic index of three). This can be shown to apply if the phase velocity is much higher than the electron thermal speed /5/. We shall in fact restrict the analysis to this case.

All the variable quantities are taken to be functions of a single variable, $\xi = x + Vt$, where V is the phase velocity of the wave. Then in the wave's own frame, we have from (1)

$$nv = n_0 V. \tag{5}$$

From (3)

$$\sigma = \sigma_0\left(\frac{n}{n_0}\right)^3, \tag{6}$$

where $\sigma_0 \equiv mn_0 v_t^2 =$ const is the equilibrium pressure, v_t being a certain mean thermal velocity (for a Maxwellian distribution, $v_t^2 = \frac{T_e}{m}$). Since from (5) and (6)

$$\frac{\partial\sigma}{\partial\xi} = \frac{3n^2\sigma_0}{n_0^3}\cdot\frac{\partial n}{\partial\xi} = -\frac{3\sigma_0 n^2 V}{n_0^2 v^2}\cdot\frac{\partial v}{\partial\xi},$$

equations (2) and (4) yield

$$v\frac{\partial v}{\partial\xi}\left(1 - \frac{3\sigma_0 V^2}{mn_0 v^4}\right) = -\frac{e}{m}E; \quad \frac{\partial E}{\partial\xi} = -4\pi e n_0\left(\frac{V}{v} - 1\right).$$

Setting

$$u = \frac{v}{V};\ E = \sqrt{4\pi n_0 m V^2}\cdot\varepsilon;$$

$$u_t = \frac{\sqrt{3}\,v_t}{V}; \quad \xi = \sqrt{\frac{mV^2}{4\pi n_0 e^2}}\cdot\zeta \tag{7}$$

we write these equations as

$$u\left(1 - \frac{u_t^2}{u^4}\right)u' = -\varepsilon; \tag{8}$$

$$\varepsilon' = \frac{u-1}{u}, \tag{9}$$

where prime denotes differentiation by ζ. Hence

$$(u-1)\left(1 - \frac{u_t^2}{u^4}\right)du + \varepsilon d\varepsilon = 0.$$

Integrating,

$$\varepsilon^2 + u^2 - 2u + \frac{u_t^2}{u^2} - \frac{2}{3}\frac{u_t^2}{u^3} = \text{const}.$$

Applying (8), we obtain for u

$$u^2\left(1-\frac{u_t^2}{u^4}\right)u'^2+(u-1)^2\left[1-\frac{u_t^2(2+u)}{3u^3}\right]=C^2, \tag{10}$$

where C is a constant. Hence

$$\zeta=\pm\int\frac{u\left(1-\frac{u_t^2}{u^4}\right)du}{\sqrt{C^2-(u-1)^2\left[1-\frac{u_t^2(2+u)}{3u^3}\right]}}. \tag{11}$$

Plasma oscillations correspond to periodic solutions

$$\varepsilon(\zeta+l)=\varepsilon(\zeta);\quad u(\zeta+l)=u(\zeta). \tag{12}$$

We define a parameter ϑ by the relation

$$u=1+C\cos\vartheta. \tag{13}$$

Then $\zeta=\zeta(\vartheta)$; $\varepsilon=\varepsilon(\vartheta)$.

For nonlinear oscillations $v\sim V$, $u\sim 1$. Since $v_t\ll V$, we have $u_t\ll 1$. The quantity $\zeta(\vartheta)$ defined by (11) can therefore be expanded in powers of u_t^2:

$$\zeta=\pm\int\frac{udu}{\sqrt{C^2-(u-1)^2}}\mp u_t^2\int\left\{\frac{1}{u^3\sqrt{C^2-(u-1)^2}}+\right.$$
$$\left.+\frac{(2+u)(u-1)^2}{6u^2\left[C^2-(u-1)^2\right]^{3/2}}\right\}du.$$

Applying (13), we find

$$\zeta(\vartheta)=\mp(\vartheta+C\sin\vartheta)\mp u_t^2\left[I_1(\vartheta)+\frac{1}{6}I_2(\vartheta)\right], \tag{14}$$

where

$$I_1(\vartheta)=-\frac{1}{2C}\frac{\partial}{\partial C}\left\{C^2\frac{\partial}{\partial C}\left[\frac{2C}{\sqrt{1-C^2}}\operatorname{arc\,tg}\left(\sqrt{\frac{1-C}{1+C}}\operatorname{tg}\frac{\vartheta}{2}\right)\right]\right\};$$
$$I_2(\vartheta)=\frac{\partial}{\partial C}\left\{2C\frac{\partial}{\partial C}\left[\frac{2C}{\sqrt{1-C^2}}\operatorname{arc\,tg}\left(\sqrt{\frac{1-C}{1+C}}\operatorname{tg}\frac{\vartheta}{2}\right)\right]-\right.$$
$$\left.-\frac{2C}{\sqrt{1-C^2}}\operatorname{arc\,tg}\left(\sqrt{\frac{1-C}{1+C}}\operatorname{tg}\frac{\vartheta}{2}\right)\right\}.$$

The electric field is given by

$$\varepsilon=C\sin\vartheta\sqrt{1+u_t^2\operatorname{ctg}^2\vartheta\,\frac{(3+C\cos\vartheta)}{3(1+C\cos\vartheta)^3}}. \tag{15}$$

For the spatial "period" of oscillation, we have from (14)

$$l=|\zeta(\vartheta+2\pi)-\zeta(\vartheta)|=2\pi\left|1-\frac{u_t^2}{2(1-C^2)^{5/2}}\right|. \tag{16}$$

The frequency $\omega=\frac{2\pi V\omega_p}{Vl}$ of the nonlinear oscillations

$$\omega=\omega_p\left[1+\frac{3v_t^2}{2V^2(1-C^2)^{5/2}}\right]=\omega_p\left[1+\frac{3<T>}{2mV^2(1-C^2)^2}\right], \tag{17}$$

where $\langle T \rangle$ is the temperature averaged over the oscillation period.

In the case of linear oscillations ($C \to 0$), formula (17) gives a result which also follows from the kinetic theory for $v_t \ll V$ /6, 7/. The nonlinear frequency (17) varies with amplitude as $\sim 1/(1-C^2)^2$.

BIBLIOGRAPHY

1. AKHIEZER, A.I. and G. Ya. LYUBARSKII. — DAN SSSR, **80**: 193. 1951.
2. POLOVIN, R. V. — JETP, **31**: 354. 1956.
3. AKHIEZER, A.I. and R. V. POLOVIN. — JETP, **30**: 915. 1956.
4. RUSSEL, V. — Phys. Fluids, **4**: 1524. 1961.
5. KITSENKO, A.B. and K.N. STEPANOV. — In: "Fizika plazmy i problemy upravlyaemogo yadernogo sinteza". **3**: 3. Kiev, Izdatel'stvo AN UkrSSR. 1963.
6. VLASOV, A. A. — JETP, **8**: 291. 1938.
7. LANDAU, L. D. — JETP, **16**: 574. 1946.

V. F. Aleksin

PENETRATION OF A LONGITUDINAL ELECTRIC FIELD INTO A BOUNDED PLASMA

Landau /1/ considered the penetration of a monochromatic longitudinal field into an electron plasma occupying a half-space. The penetration of an electric field into a bounded plasma is also of some interest.

In the present paper, proceeding from the kinetic theory, we investigate the distribution of the electric field in a plane-parallel layer of electron–ion plasma immersed in an external monochromatic electric field directed at right angles to the walls. An expression is also derived for the energy lost by the electric field in the plasma. It is shown that for certain values of the plasma parameters and a certain frequency of the external field the plasma will resonate, maximizing the energy losses. It is assumed that the particles are specularly scattered at the plasma boundary, and that the strength of the alternating electric field remains fairly low. The second assumption justifies the application of the linear approximation.

Consider a system of coordinates with the x axis perpendicular to the plasma boundaries, which lie in the planes $x = 0$ and $x = a$ (a being the thickness of the plasma layer). In an external electric field parallel to the x axis, the velocity distribution function of the particles and the field in the plasma depend on the coordinate x only. Furthermore, the velocity components perpendicular to the x axis are of no significance in the distribution function, and we shall henceforth operate with distribution functions

integrated over these components. In a monochromatic field $E(x, t) = E(x)e^{-i\omega t}$ the distribution function of particles of the species α can be written as a sum $f_{0\alpha}(v) + f_\alpha(v, x)e^{-i\omega t}$, where v is the velocity component along the x axis, ω the frequency of the external field, $f_{0\alpha}(v)$ the equilibrium distribution function (henceforth $\alpha = e$ denotes electrons, $\alpha = i$ ions).

The function $f_\alpha = f_\alpha(v, x)$ is determined from the kinetic equation

$$-i\omega_\alpha f_\alpha + v\frac{\partial f_\alpha}{\partial x} + \frac{e_\alpha}{m_\alpha}E(x)\frac{df_{0\alpha}}{dv} = 0 \quad (0 < x < a), \tag{1}$$

where $\omega_\alpha = \omega + i\nu_\alpha$; e_α, m_α, and ν_α are the charge, the mass, and the effective collision frequency of particles of the species α. If the distribution function f_α satisfies the conditions of specular reflection of particles from the walls, $f_\alpha(v, 0) = f_\alpha(-v, 0)$, $f_\alpha(v, a) = f_\alpha(-v, a)$, we have from equation (1)

$$f_\alpha(v, x) = e^{i\frac{\omega_\alpha}{v}x}\frac{e_\alpha}{m_\alpha v}\int_0^a E(\xi)\frac{df_{0\alpha}}{dv}\left[\frac{\sin\frac{\omega_\alpha}{v}(a-\xi)}{\sin\frac{\omega_\alpha}{v}a} - \Theta(x-\xi)e^{-i\frac{\omega_\alpha}{v}\xi}\right]d\xi, \tag{2}$$

where $\Theta(x) = 1$ if $x > 0$, and $\Theta(x) = 0$ if $x < 0$.

As the second equation, we take the equation of continuity for the current density $j = j(x)$, which yields

$$j = \frac{i\omega}{4\pi}(E - E_0), \tag{3}$$

where E_0 is the amplitude of the external field at the plasma boundaries, and

$$j = \sum_{\alpha=e,\,i} e_\alpha\int_0^a vf_\alpha(v, x)\,dv. \tag{4}$$

Substituting f_α from (2) in (4), we have

$$j = \frac{i\omega}{4\pi}\int_0^a K(x, \xi)E(\xi)\,d\xi, \tag{5}$$

where the kernel $K(x, \xi)$, symmetrical under the interchange of x and ξ, has the form

$$K(x, \xi) = \sum_{\alpha=e,\,i}\frac{8\pi e_\alpha^2}{m_\alpha\omega}\int_0^\infty H_\alpha(v; x, \xi)\frac{df_{0\alpha}}{dv}\,dv;$$

$$H(v; x, \xi) = \begin{cases} \dfrac{\sin\frac{\omega_\alpha}{v}(a-x)\sin\frac{\omega_\alpha}{v}\xi}{\sin\frac{\omega_\alpha}{v}a} & \text{for } x > \xi, \\[2ex] \dfrac{\sin\frac{\omega_\alpha}{v}(a-\xi)\sin\frac{\omega_\alpha}{v}x}{\sin\frac{\omega_\alpha}{v}a} & \text{for } x < \xi. \end{cases} \tag{6}$$

Substituting (5) in (3), we obtain an inhomogeneous Fredholm integral equation for the electric field in the plasma:

$$E(x) = E_0 + \int_0^a E(\xi)K(x, \xi)\,d\xi. \tag{7}$$

The function $E = E(x)$ is equal to E_0 at the boundaries $x = 0$ and $x = a$, and we may therefore conveniently pass to a function $E_1 = E - E_0$ with zero boundary conditions $E_1(0) = E_1(a) = 0$. The integral equation in E_1 has the form

$$E_1(x) - \int_0^a K(x, \xi) E_1(\xi)\, d\xi = E_0 \int_0^a K(x, \xi)\, d\xi. \tag{8}$$

The solution of equation (8) satisfying the zero boundary conditions is sought as an expansion in terms of functions which constitute a complete system in the interval $(0,a)$. The functions $\sin\frac{\pi n}{a} x$, where $n = 1, 2, \ldots,$ meet this requirement. The kernel $K(x, \xi)$ of the integral equation is representable as

$$K(x, \xi) = \sum_{n=1}^{\infty} K_n \sin\frac{\pi n}{a} x \cdot \sin\frac{\pi n}{a} \xi, \tag{9}$$

where the expansion coefficients are

$$K_n = - \sum_{\alpha = e, i} \frac{4\pi e_\alpha^2}{m_\alpha \omega} \int_{-\infty}^{\infty} \frac{v \frac{df_{0\alpha}}{dv}}{\omega_\alpha - k_n v}\, dv, \quad k_n = \frac{\pi n}{a}. \tag{10}$$

Setting

$$E_1(x) = \sum_{n=1}^{\infty} a_n \sin\frac{\pi n}{a} x,$$

we find from (9)

$$a_{2n} = 0; \quad a_{2n+1} = \frac{4}{\pi(2n+1)} \quad \frac{K_{2n+1}}{1 - K_{2n+1}} \quad (n = 0, 1, 2 \ldots). \tag{11}$$

Hence, the electric field in the plasma is

$$E(x) = E_0 \left(1 + \frac{4}{\pi} \sum_{n=0}^{\infty} \frac{K_{2n+1}}{1 - K_{2n+1}} \cdot \frac{\sin\frac{2n+1}{a}\pi x}{2n+1} \right). \tag{12}$$

For an electron plasma, expression (12) was derived by an alternative technique in a recently published work /2/.

Seeing that

$$\sum_{n=0}^{\infty} \frac{\sin\frac{2n+1}{a}\pi x}{2n+1} = \frac{\pi}{4} \quad (0 < x < a)$$

expression (12) is easily written as

$$E(x) = \frac{E_0}{\varepsilon} \left(1 + \frac{4}{\pi} \sum_{n=0}^{\infty} \frac{K_{2n+1} - K_0}{1 - K_{2n+1}} \cdot \frac{\sin\frac{2n+1}{a}\pi x}{2n+1} \right), \tag{13}$$

where $\varepsilon = 1 - K_0$ is the permittivity of the plasma in the absence of space dispersion. For a Maxwellian equilibrium distribution function

$$f_{0\alpha}(v) = n_\alpha \sqrt{\frac{m_\alpha}{2\pi T_\alpha}}\, e^{-\frac{m_\alpha v^2}{2T_\alpha}}$$

(n_a and T_a being the equilibrium density and temperature of the particles),

$$K_0 = -\sum_{\alpha=e,\,i} \frac{\Omega_\alpha^2}{\omega\omega_\alpha},$$

where $\Omega_\alpha = \sqrt{\frac{4\pi e_\alpha^2 n_\alpha}{m_\alpha}}$ is the plasma frequency of particles of the species α.

With $a \to \infty$ and finite x, expression (13) reduces to an expression for the electric field strength in a semi-infinite plasma/1/.

The mean quantity of electric energy absorbed by the plasma in unit time per unit surface area is given by

$$Q = \frac{1}{4}\int_0^a (Ej^* + E^*j)\,dx. \tag{14}$$

Applying expression (13) for the field E and formula (3), we find on integration with respect to x

$$Q = -\frac{a\omega}{8\pi}|E_0|^2 \operatorname{Im}\frac{1}{\varepsilon}\left\{1 + \frac{8}{\pi^2}\sum_{n=0}^{\infty}\frac{K_{2n+1} - K_0}{(1 - K_{2n+1})(2n+1)^2}\right\}. \tag{15}$$

The first term in (15) describes the absorption of energy in unit time in a medium without space dispersion.

Expressions (13) and (15) are conveniently represented in terms of line integrals:

$$E(x) = \frac{E_0}{\varepsilon}\left(1 + \frac{i}{\pi}\int_{-\infty}^{\infty}\frac{K_0 - K_-}{1 - K_-}\cdot\frac{\cos k\left(\frac{a}{2} - x\right)}{\cos k\frac{a}{2}}\cdot\frac{dk}{k} + \right.$$

$$\left. + \frac{i\varepsilon}{\pi}\int_0^{\infty}\frac{K_- - K_+}{(1 - K_-)(1 - K_+)}\cdot\frac{\cos k\left(\frac{a}{2} - x\right)}{\cos k\frac{a}{2}}\cdot\frac{dk}{k}\right); \tag{16}$$

$$Q = -\frac{a\omega}{8\pi}|E_0|^2 \operatorname{Im}\frac{1}{\varepsilon}\left\{1 + \frac{2i}{\pi a}\int_{-\infty}^{\infty}\frac{K_0 - K_-}{1 - K_-}\operatorname{tg} k\frac{a}{2}\frac{dk}{k^2} + \right.$$

$$\left. + \frac{2i\varepsilon}{\pi a}\int_0^{\infty}\frac{K_- - K_+}{(1 - K_-)(1 - K_+)}\operatorname{tg} k\frac{a}{2}\cdot\frac{dk}{k^2}\right\}. \tag{17}$$

where the integration contours follow the real axis lifting to clear the zeros of the function $\cos k\frac{a}{2}$. For a Maxwellian equilibrium distribution function,

$$K_\pm(k) = -\sum_{\alpha=e,\,i}\frac{2\Omega_\alpha^2}{\omega\omega_\alpha}z_\alpha^2(1 + i\sqrt{\pi}z_\alpha w_\pm(z_\alpha)),$$

where

$$w_\pm(z) = e^{-z^2}\left(\pm 1 + \frac{2i}{\sqrt{\pi}}\int_0^z e^{t^2}dt\right); \quad z_\alpha = \frac{\omega_\alpha}{\sqrt{2}kv_\alpha}, \tag{18}$$

$v_\alpha = \sqrt{\frac{T_\alpha}{m_\alpha}}$ the thermal velocity of particles of the species α.

The function $K_-(k)$ displays no singularities in the upper half-plane of the complex variable k, and the first integrals in (16) and (17) therefore

reduce to residues at the poles in the upper half-plane. The second integral in (16) is conveniently reduced to the integral along the line of fastest descent l in the first quadrant of the complex plane k and the sum of the residues of the integrand at the poles between the contour l and the real axis. This approach gives an asymptotic expression for the electric field in the plasma far from the walls for $x \gg \frac{v_a}{\omega}$ and $a - x \gg \frac{v_a}{\omega}$. The integration contour in the expression for Q can be transformed, with the aid of the residues, into a line l' following the ray with $\arg k = \pi/4$. The integral along the line l' is easily evaluated for some particular cases.

Taking the integral along the line l for $x \gg \frac{v_a}{\omega}$ and $a - x \gg \frac{v_a}{\omega}$, we obtain by the saddle-point method

$$I_l = \frac{i}{\pi} \int\limits_l \frac{K_- - K_+}{(1 - K_-)(1 - K_+)} \cdot \frac{\cos k\left(\frac{a}{2} - x\right)}{\cos k \frac{a}{2}} \frac{dk}{k} =$$

$$= \sum_{\alpha = e,\, i} \frac{4\sqrt{3}\Omega_\alpha^2}{\omega^2 \varepsilon'^2} \left(\xi_\alpha e^{-\xi_\alpha} + \eta_\alpha e^{-\eta_\alpha}\right), \qquad (19)$$

where

$$\varepsilon' = 1 - \frac{\Omega_e^2}{\omega^2}; \quad \xi_\alpha = \frac{3}{2}\left(\frac{x\omega}{v_\alpha}\right)^{2/3} e^{-i\frac{\pi}{3}}; \quad \eta_\alpha = \frac{3}{2}\left(\frac{(a - x)\,\omega}{v_\alpha}\right)^{2/3} e^{-i\frac{\pi}{3}}$$

In (19) we neglected the interparticle collisions, which, the ratio $\frac{\nu_a}{\omega}$ being small, are insignificant.

The integral along the line l decreases as $\exp x^{2/3}$ or $\exp (a - x)^{2/3}$ with the increase of x or $(x - a)$, while the sum of the residues falls off as $e^{-\gamma x}$ or $e^{-\gamma(a-x)}$ (γ being the imaginary part of the poles of the integrands).

If the poles of the integrands are far from the real axis, the integral I_l dominates the expression for E at large distances from the walls. Thus,

$$E(x) = \frac{E_0}{\varepsilon}\left[1 + \sum_{\alpha = e,\, i} \frac{4\sqrt{3}\Omega_\alpha^2}{\omega^2 \varepsilon'} \left(\xi_\alpha e^{-\xi_\alpha} + \eta_\alpha e^{-\eta_\alpha}\right)\right]. \qquad (20)$$

This behavior of the field $E(x)$ at large distances from the walls is conditioned by the displacement of the charged particles whose velocities are much greater than the average thermal speed v_α. Expression (20), however, has been derived in the nonrelativistic approximation, and it therefore applies if x or $a - x$ are not excessively large $\left(x \ll \frac{c}{\omega},\ a - x \ll \frac{c}{\omega}\right)$.

Of independent interest is the case of a small damping ratio γ, e.g., near a resonance point, where the frequency ω is close to the plasma frequency. The resonance electric field and the resonance energy losses are mainly determined by the contribution of the residues at the poles of the integrands in (16) and (17).

For a resonance at the plasma frequency Ω_e, the electric field E and the losses Q are given by

$$E(x) = \frac{E_0}{\varepsilon}\left(1 - \frac{\cos k\left(\frac{a}{2} - x\right)}{\cos k \frac{a}{2}}\right); \qquad (21)$$

$$Q = -\frac{a\omega}{8\pi}\,|E_0|^2\,\mathrm{Im}\,\frac{1}{\varepsilon}\left(1 - \frac{\operatorname{tg} k\frac{a}{2}}{k\frac{a}{2}}\right), \tag{22}$$

where

$$\begin{gathered} k = \varkappa + i\gamma; \\ \varkappa = \frac{1}{\sqrt{6}d_e}\left(\sqrt{\varepsilon'^2 + \frac{\nu_e^2}{\omega^2}} + \varepsilon'\right)^{1/2}; \\ \gamma = \frac{1}{\sqrt{6}d_e}\left(\sqrt{\varepsilon'^2 + \frac{\nu_e^2}{\omega^2}} - \varepsilon'\right)^{1/2} + \Theta(\varepsilon')\,\frac{3}{2}\sqrt{\frac{\pi}{2}}\cdot\frac{1}{\varepsilon'}\,e^{-\frac{3}{2\varepsilon'}}; \end{gathered} \tag{23}$$

d_e the electron Debye length $\left(d_e = \frac{v_e}{\Omega_e}\right)$. For $x = 0$ and $x = a$, we see from (21) that $E = 0$, rather than $E = E_0$. This is so because in calculating E we neglected terms of the order of ε. For $\omega \approx \Omega_e$ the integral along the line l in (17) is of the order of $\frac{\varepsilon d_e}{a}$, and it may therefore be neglected in the calculation of electric energy losses.

From (22) it follows that for $\omega \gtrsim \Omega_e$ the energy losses Q in a bounded plasma are maximal at the points $\varkappa = \frac{2n+1}{a}\pi$ $(n = 0, 1, 2, \ldots)$, corresponding to a spatial resonance. If $\nu_e = 0$, the resonance losses Q at the maximum points $\left(\varkappa = \frac{2n+1}{a}\pi\right)$ for $\omega \gtrsim \Omega_e$ and $\gamma a \ll 1$ are given by

$$Q_m = \frac{1}{12}\left(\frac{2}{\pi}\right)^{3/2}\frac{\omega d_e}{\varepsilon'}\,e^{\frac{3}{2\varepsilon'}}. \tag{24}$$

For $\omega < \Omega_e$ and $\nu_e = 0$, the energy losses are zero.

A plasma whose electron temperature is much higher than the temperature of the ions $(T_e \gg T_i)$ may propagate, not only weakly damped waves of frequency $\omega \approx \Omega_e$, but also weakly damped sound waves of frequency $\omega \ll \Omega_i$ and waves of frequency ω close to the ion plasma frequency Ω_i /3/. The longitudinal electric field may freely penetrate into the plasma also in the neighborhood of these frequencies.

If the frequency ω is close to Ω_i, then for $T_e \gg T_i$, among the infinity of roots of the equations $K_+(k) = 1$ and $K_-(k) = 1$ there are roots $k_1 = \varkappa_1 + i\gamma_1$ and $k_2 = \varkappa_2 + i\gamma_2$, respectively, lying in the upper half-plane $(\gamma_{1,2} > 0)$ near the real axis. The real and the imaginary parts of these roots are

$$\begin{gathered} \varkappa_1 = \frac{1}{\sqrt{6}d_i}\left(1 - \frac{\Omega_i^2}{\omega^2} + \zeta\right)^{1/2}; \\ \gamma_1 = \frac{\varkappa_1}{2\zeta}\left\{\frac{\nu_i}{\Omega_i} + \frac{\nu_e}{\Omega_i}\,\frac{T_e}{\varkappa_1^2 d_i^2 T_i} + \sqrt{\frac{\pi}{2}}\left(\frac{m_e}{m_i}\right)^{1/2}\left(\frac{T_i}{T_e}\right)^{3/2}\frac{1}{\varkappa_1^3 d_i^3} + \right. \\ \left. + \sqrt{\frac{\pi}{2}}\,\frac{1}{\varkappa_1^3 d_i^3}\,e^{-\frac{1}{2\varkappa_1^2 d_i^2}}\right\}; \\ \varkappa_2 = \frac{1}{\sqrt{6}d_i}\,\frac{\nu_i}{2\Omega_i\zeta}\left(\zeta - 1 + \frac{\Omega_i^2}{\omega^2}\right)^{1/2}; \\ \gamma_2 = \frac{1}{\sqrt{6}d_i}\left(\zeta - 1 + \frac{\Omega_i^2}{\omega^2}\right)^{1/2}, \end{gathered} \tag{25}$$

where
$$\zeta=\sqrt{\left(1-\frac{\Omega_i^2}{\omega^2}\right)^2+12\frac{T_i}{T_e}};\quad d_i=\frac{v_i}{\Omega_i}.$$

Taking the corresponding residues, we find

$$E(x)=\frac{E_0}{\varepsilon}\left(1+A_1\frac{\cos k_1\left(\frac{a}{2}-x\right)}{\cos k_1\frac{a}{2}}+A_2\frac{\cos k_2\left(\frac{a}{2}-x\right)}{\cos k_2\frac{a}{2}}\right);\tag{26}$$

$$Q=-\frac{a\omega}{8\pi}|E_0|^2\,\mathrm{Im}\,\frac{1}{\varepsilon}\left(1+A_1\frac{\mathrm{tg}\,k_1\frac{a}{2}}{k_1\frac{a}{2}}+A_2\frac{\mathrm{tg}\,k_2\frac{a}{2}}{k_2\frac{a}{2}}\right),\tag{27}$$

where
$$A_1=-\frac{\varepsilon}{\zeta}\left\{1-\frac{i}{\zeta^2}\left[\frac{\nu_i}{\Omega_i}\left(1-\frac{\Omega_i^2}{\omega^2}\right)+6\frac{\nu_e}{\Omega_i}\frac{T_i}{T_e}+\right.\right.$$
$$+\sqrt{\frac{\pi}{2}}\left(\frac{m_e}{m_i}\right)^{1/2}\left(\frac{T_i}{T_e}\right)^{3/2}\frac{1}{\varkappa_1^3d_i^3}\left(1-\frac{\Omega_i^2}{\omega^2}+\frac{3}{2}\zeta\right)-$$
$$\left.\left.-\sqrt{\frac{\pi}{8}}\frac{1}{\varkappa_1^5d_i^5}e^{-\frac{1}{2\varkappa_1^2d_i^2}}\right]\right\};$$
$$A_2=\frac{\varepsilon}{\zeta}\left[1-i\frac{\nu_i}{\Omega_i\zeta^2}\left(1-\frac{\Omega_i^2}{\omega^2}\right)\right].$$

For $x=0$ and $x=a$ we see from (26) that the field E is different from E_0. This difference, as in the case of the Ω_e resonance, is attributable to the omission of the line integral and the simplifications adopted in the calculation of the poles of the integrands. In particular, in the derivation of (26) and (27) we neglected all quantities of the order of $\frac{T_i}{T_e}$; $\frac{m_e}{m_i}$; $\left(1-\frac{\Omega_i^2}{\omega^2}\right)$.

For points located at distances greater than $l\sim d_i\left(\frac{T_e}{T_i}\right)^{1/4}$ from the wall, the last term in (26) may be neglected in comparison with the second term and the line integral (19).

When deriving (26), we neglected the line integral, which is permitted only for $x\lesssim\frac{1}{\gamma_1}$, $a-x\lesssim\frac{1}{\gamma_2}$. Elsewhere, the integral I_e cannot be neglected. The electric field in this case is determined from (20). In (27) we only considered the contribution of the residues and dropped the term connected with integration along the line l', having the order of $\omega d_i\,|E_0|^2\max\left(1,\sqrt{\frac{m_eT_e}{m_iT_i}}\right)$. Expression (27) for the electric energy losses in a plasma therefore applies to cases when this term is indeed negligible. It furthermore appears that the imaginary parts of the coefficients A_1 and A_2 are invariably negligible. Let us consider some examples.

If $\nu_{e,i}=0$, and the inequalities $\left|\left(1-\frac{\Omega_i^2}{\omega^2}\right)\right|\ll\sqrt{\frac{T_e}{T_i}}$; $\left(\frac{m_eT_i}{m_iT_e}\right)^{1/2}\ll\frac{d_i}{a}\ll\left(\frac{T_i}{T_e}\right)^{1/4}$ are satisfied, the energy losses Q are given by

$$Q=\frac{a\omega}{32\pi}\sqrt{\frac{\pi}{2}}\,|E_0|^2\left(\frac{m_e}{m_i}\right)^{1/2}\left(\frac{T_e}{3T_i}\right)^{1/4}\frac{1}{\cos\varkappa_1a+1+\frac{\gamma_1^2a^2}{2}},\tag{28}$$

where

$$\varkappa_1 = \frac{1}{d_i}\left(\frac{T_i}{3T_e}\right)^{1/4}, \ \gamma_1 = \frac{1}{4d_i}\sqrt{\frac{\pi}{2}}\left(\frac{m_e}{m_i}\right)^{1/2}\left(\frac{T_i}{T_e}\right)^{1/8}.$$

The line integral can be neglected when $\frac{d_i}{a} \ll \left(\frac{T_i}{T_e}\right)^{1/4}$. From (28) it follows that in the low-frequency region, as well as for $\omega \approx \Omega_e$, resonance may occur at $\varkappa_1 = \frac{2n+1}{a}\pi$. In case of resonance,

$$Q_p = \frac{6\omega}{\pi^2 a}\sqrt{\frac{\pi}{2}}\,|E_0|^2 d_i^2 \left(\frac{m_i}{m_e}\right)^{1/2}\left(\frac{T_e}{3T_i}\right)^{5/4}. \tag{29}$$

If $\nu_{e,i} = 0$, $\left|1 - \frac{\Omega_i^2}{\omega^2}\right| \ll \sqrt{\frac{T_i}{T_e}}$ and $\frac{d_i}{a} \ll \frac{v_i}{v_e}$, the losses

$$Q = \frac{d_i\omega}{24\pi}\,|E_0|^2 \left(\frac{3T_e}{T_i}\right)^{3/4}. \tag{30}$$

The line integral is clearly negligible in this case also.

Let us consider the region of acoustic frequencies $\omega \ll \Omega_i$.

If $T_e \gg T_i$, the equation $K_+(k) = 1$ has a root lying near the real axis. Neglecting interparticle collisions, we can easily find an expression for this root:

$$k = \omega\sqrt{\frac{m_i}{T_e}}\left[1 + i\sqrt{\frac{\pi}{8}}\left(\sqrt{\frac{m_e}{m_i}} + \left(\frac{T_e}{T_i}\right)^{3/2} e^{-\frac{T_e}{2T_i}}\right)\right]. \tag{31}$$

The root of the equation $K_-(k) = 1$ is located on the imaginary axis, $k = k_2 = i\,\frac{\Omega_i}{\sqrt{3}\,d_i\omega}$; it is not far from the real axis, and the residue at this root in the expression for E is therefore negligible for $x \gg \frac{1}{|k_2|}$, $a - x \gg \frac{1}{|k_2|}$. The purely imaginary root obviously has no influence on the expression for Q, either.

Taking the residue at the pole (31), we obtain

$$E = -E_0\frac{\omega^2}{\Omega_e^2}\left(1 + A\frac{m_i}{m_e}\cdot\frac{\cos k\left(\frac{a}{2} - x\right)}{\cos k\frac{a}{2}}\right); \tag{32}$$

$$Q = \frac{a\omega^3}{8\pi\Omega_i^2}\,|E_0|^2\,\mathrm{Im}\,A\,\frac{\mathrm{tg}\,k\frac{a}{2}}{k\frac{a}{2}}, \tag{33}$$

where

$$A = 1 - i\sqrt{\frac{\pi}{2}}\left(\frac{3}{2}\sqrt{\frac{m_e}{m_i}} + \left(\frac{T_e}{T_i}\right)^{3/2} e^{-\frac{T_e}{2T_i}}\right).$$

Note that in (32),(33) the imaginary part of the coefficient A can be neglected. In calculation of losses, the imaginary part of A is substantial only for small a ($|k|a \ll 1$). But in this case the line integral

$$\mathscr{P} \sim |E_0|^2\frac{\omega^2}{\Omega_i^2}\max\left(v_i,\ v_e\frac{m_e}{m_i}\right)$$

cannot be neglected either.

Expression (32) applies only near the walls in a layer whose thickness l is of the order of $\frac{v_e}{\omega}$. Outside this layer, the integral along the line l must be taken into consideration. For $x = 0$ and $x = a$, $E \neq E_0$; this difference, as previously, is attributable to the approximate calculation of the poles of the integrands and to the omission of the residue at k_2, whose influence is felt for $x < \frac{1}{|k_2|}$ and $(a - x) < \frac{1}{|k_2|}$.

Let us consider some particular cases.

If $a \gg \frac{v_e}{\omega}\sqrt{\frac{T_i}{T_e}}$; $a \ll \frac{v_e}{\omega}$, then

$$Q = \frac{a\omega^3}{8\pi\Omega_i^2}\sqrt{\frac{\pi}{2}}\left(\sqrt{\frac{m_e}{m_i}} + \left(\frac{T_e}{T_i}\right)^{3/2} e^{-\frac{T_e}{2T_i}}\right)\frac{1}{\cos\varkappa a + 1 + \frac{\gamma^2 a^2}{2}}, \tag{34}$$

where

$$\varkappa = \omega\sqrt{\frac{m_i}{T_e}}; \quad \gamma = \varkappa\sqrt{\frac{\pi}{8}}\left(\sqrt{\frac{m_e}{m_i}} + \left(\frac{T_e}{T_i}\right)^{3/2} e^{-\frac{T_e}{2T_i}}\right).$$

At resonance points $\varkappa = \frac{2n+1}{a}\pi$,

$$Q = \frac{1}{\pi}\sqrt{\frac{2}{\pi}}|E_0|^2\frac{\omega T_e}{a\Omega_i^2 m_i}\left[\sqrt{\frac{m_e}{m_i}} + \left(\frac{T_e}{T_i}\right)^{3/2} e^{-\frac{T_e}{2T_i}}\right]^{-1} \tag{35}$$

If the layer thickness $a \gg \frac{V_e}{\omega}$, then

$$Q = \frac{\omega^2}{4\pi v_i^2}\sqrt{\frac{T_e}{m_i}}|E_0|^2. \tag{36}$$

BIBLIOGRAPHY

1. LANDAU, L. D. – JETP, 16: 574. 1946.

2. WEISSGLAS, P. – Plasma Phys., J. Nucl. Energy, Part C, 4: 329 1962.

3. GORDEEV, G. V. – JETP, 27: 18. 1954.

V. F. Aleksin and K. N. Stepanov

EXCITATION OF ELECTROMAGNETIC WAVES IN A PLASMA BY EXTERNAL CURRENTS

Excitation of electromagnetic waves in a plasma by external electric currents is of interest in connection with problems of high-frequency plasma heating and plasma diagnostics, and also in the study of the passage of charged particles through plasma.

The excitation of magnetohydrodynamic waves in a plasma by external currents was investigated in /1/ in the hydromagnetic approximation (see also /2/). Wave excitation on the basis of the two-fluid plasma theory, neglecting the thermal motion of electrons and ions, was dealt with in /3–7, 13/. The foregoing papers studied in detail the various means for the excitation of waves in a plasma by external currents (surface current perpendicular to the external magnetic field /1–3,6,7/, ring current flowing in a perpendicular plane /3/, modulated line current /7/, etc.).

In the present paper we investigate the excitation of electromagnetic waves in an unbounded magnetoactive plasma by external currents utilizing the kinetic-theoretical approach. General expressions are derived for the fields set up by these currents in the plasma, and an expression for energy losses. The excitation of waves by azimuthal and axial currents modulated in the direction of the external magnetic field is treated in detail. In particular, the case of electron and ion cyclotron resonance and of "hybrid" resonances near which the thermal motion of the plasma electrons and ions cannot be neglected is considered.

Electromagnetic fields and energy losses

The electric $\mathbf{E}$ and the magnetic $\mathbf{H}$ fields set up in a plasma by external electric currents of density $\mathbf{j}(\mathbf{r}, t)$ are determined from Maxwell's equations, which have the following form for the Fourier-components $\mathbf{E}(\mathbf{k}, \omega)$ and $\mathbf{H}(\mathbf{k}, \omega)$:

$$T_{ik}E_k = -\frac{4\pi i}{\omega} j_i; \quad \mathbf{H} = n[\vec{\varkappa}\mathbf{E}], \tag{1}$$

where

$$\mathbf{n} = \frac{\mathbf{k}c}{\omega}; \quad \vec{\varkappa} = \frac{\mathbf{k}}{k};$$
$$T_{ik} = n^2(\varkappa_i\varkappa_k - \delta_{ik}) + \varepsilon_{ik}. \tag{2}$$

The Fourier-components are defined as

$$\varphi(\mathbf{r}, t) = \iint \varphi(\mathbf{k}, \omega) e^{i(\mathbf{kr}-\omega t)} d\mathbf{k} d\omega. \tag{3}$$

The permittivity tensor ε_{ik} of a plasma in the presence of an external magnetic field $\mathbf{H}_0$ is given by /8/

$$\varepsilon_{ik} = a\delta_{ik} + b\varkappa_i\varkappa_k + ch_ih_k + d\varepsilon_{ikl}h_l +$$
$$+ e(\varkappa_i[\vec{\varkappa}\mathbf{h}]_k - \varkappa_k[\vec{\varkappa}\mathbf{h}]_i) + f[\vec{\varkappa}\mathbf{h}]_i[\vec{\varkappa}\mathbf{h}]_k, \tag{4}$$

where $\mathbf{h}$ is the unit vector along the external magnetic field. The coefficients $a, b, c, \ldots$ are functions of $k_{\parallel} = (\mathbf{k}\,\mathbf{h})$ and $k_{\perp} = \sqrt{k^2 - k_{\parallel}^2}$. The expressions for the coefficients $a, b, c, \ldots$ in the case of a Maxwellian velocity distribution of the plasma particles are given in /8/.

From (4)

$$E_i = -\frac{4\pi i}{\omega D} u_{ik} j_k. \tag{5}$$

Here

$$D = det\,(T_{ik}); \tag{6}$$

$$\begin{gathered} u_{ik} = u_1\delta_{ik} + u_2\varkappa_i\varkappa_k + u_3h_ih_k + u_4e_{ikl}h_l + u_5(\varkappa_i[\vec{\varkappa\mathbf{h}}]_k - \varkappa_k[\vec{\varkappa\mathbf{h}}]_i) + \\ + u_6[\vec{\varkappa\mathbf{h}}]_i[\vec{\varkappa\mathbf{h}}]_k + u_7(\varkappa_ih_k + \varkappa_kh_i) + u_8(h_i[\vec{\varkappa\mathbf{h}}]_k - h_k[\vec{\varkappa\mathbf{h}}]_i), \end{gathered} \tag{7}$$

where

$$\begin{gathered} u_1 = (a - n^2)(a + b + c) + \varkappa_{\perp}^2[f(a + b + c) + c(b + n^2) - 2de - e^2]; \\ u_2 = (n^2 - a - c)(b + n^2) + 2de - \varkappa_{\perp}^2(e^2 + bf + n^2f); \\ u_3 = d^2 - (a + b)c - \varkappa_{\perp}^2 cf; \\ u_4 = -d(a + b + c + \varkappa_{\perp}^2 f); \\ u_5 = -d(n^2 + b + f) - e(a + c - n^2); \\ u_6 = e(2d - e) - f(a + b + c); \\ u_7 = \varkappa_{\parallel}(bc + n^2c - de); \\ u_8 = \varkappa_{\parallel}(ec + fd); \\ \varkappa_{\parallel} = \frac{k_{\parallel}}{k}; \quad \varkappa_{\perp} = \frac{k_{\perp}}{k} = \sqrt{1 - \varkappa_{\parallel}^2}. \end{gathered}$$

Substituting (5) in (3), we obtain for the electric field strength

$$E_i(\mathbf{r},\ t) = \iint G_{ik}(\mathbf{r} - \mathbf{r}',\ t - t')\, j_k(\mathbf{r}',\ t')\, d\mathbf{r}'dt', \tag{8}$$

where Green's function $G_{ik}(\mathbf{r},\ t)$ is defined by

$$G_{ik}(\mathbf{r},\ t) = -\frac{i}{4\pi^3}\iint \frac{u_{ik}}{\omega D} e^{i(\mathbf{kr} - \omega t)}\, d\mathbf{k}d\omega. \tag{9}$$

Seeing that $D, u_1, u_2, \ldots$ are functions of $k_{\perp}, k_{\parallel}$, and ω only, we conveniently introduce a cylindrical system of coordinates $\mathbf{r} = (r_{\perp}, \varphi, z)$ and expand the current density $\mathbf{j}(\mathbf{r}, t)$ into a series

$$\mathbf{j}(\mathbf{r},\ t) = \sum_{n=-\infty}^{\infty} \mathbf{j}^{(n)} e^{in\varphi}. \tag{10}$$

Expression (8) in this case takes the form

$$\mathbf{E}(\mathbf{r},\ t) = -\frac{i}{\pi}\sum_{n=-\infty}^{\infty}\int \frac{J_n(k_{\perp}r_{\perp}')}{\omega D}\mathbf{q}^{(n)} e^{ik_{\parallel}(z - z') - i\omega(t - t') + in\varphi} k_{\perp}\, dk_{\perp}dk_{\parallel}r_{\perp}'dr_{\perp}'dz'dt'd\omega, \tag{11}$$

where $J_n(x)$ is Bessel's function;

$$q_i^{(n)} = a_{ik}^{(n)} j_k^{(n)}; \tag{12}$$

$$
\begin{aligned}
a_{ik}^{(n)} = a_1^{(n)}\delta_{ik} + a_2^{(n)}\frac{r_i r_k}{r_\perp^2} + a_3^{(n)} h_i h_k + \\
+ a_4^{(n)} e_{ikc} h_c + a_5^{(n)} \frac{[\mathbf{rh}]_i [\mathbf{rh}]_k}{r_\perp^2} + \\
+ a_6^{(n)} \frac{r_i h_k + r_k h_i}{r_\perp} + a_7^{(n)} \frac{h_i [\mathbf{rh}]_k - h_k [\mathbf{rh}]_i}{r_\perp} + \\
+ a_8^{(n)} \frac{r_i [\mathbf{rh}]_k - r_k [\mathbf{rh}]_i}{r_\perp^2} + a_9^{(n)} \frac{h_k r_i - h_i r_k}{r_\perp} + \\
+ a_{10}^{(n)} \frac{r_i [\mathbf{rh}]_k + r_k [\mathbf{rh}]_i}{r_\perp^2} + a_{11}^{(n)} \frac{h_i [\mathbf{rh}]_k + h_k [\mathbf{rh}]_i}{r_\perp}.
\end{aligned}
\tag{13}
$$

The coefficients $a_i^{(n)}$ $(i = 1, 2, \ldots, 11)$ are given by

$$
\begin{aligned}
a_1^{(n)} &= u_1 J_n (k_\perp r_\perp); \\
a_2^{(n)} &= \frac{\varkappa_\perp^2}{2}\left[(u_2 + u_6) J_n + \frac{1}{2}(u_6 - u_2)(J_{n+2} + J_{n-2})\right]; \\
a_3^{(n)} &= \left[u_3 + u_2\varkappa_\parallel^2 + 2u_7\varkappa_\parallel + \frac{\varkappa_\perp^2 z^2}{2r_\perp^2}(u_6 + u_2)\right] J_n + \\
&+ \frac{\varkappa_\perp^2 z^2}{4r_\perp^2}(u_6 - u_2)(J_{n+2} + J_{n-2}) - i\varkappa_\perp (u_2\varkappa_\parallel + u_7)\frac{z}{r_\perp}(J_{n+1} - J_{n-1}); \\
a_4^{(n)} &= u_4 J_n; \\
a_5^{(n)} &= \frac{\varkappa_\perp^2}{2}\left[(u_6 + u_2) J_n - \frac{1}{2}(u_6 - u_2)(J_{n+2} + J_{n-2})\right]; \\
a_6^{(n)} &= -\frac{\varkappa_\perp z}{2r_\perp}\left[(u_6 + u_2) J_n + \frac{1}{2}(u_6 - u_2)(J_{n+2} + J_{n-2})\right] + \\
&+ \frac{i\varkappa_\perp}{2}(u_2\varkappa_\parallel + u_7)(J_{n+1} - J_{n-1}); \\
a_7^{(n)} &= -\frac{\varkappa_\perp^2 z}{r_\perp} u_5 J_n + \frac{i\varkappa_\perp}{2}(u_5\varkappa_\parallel + u_8)(J_{n+1} - J_{n-1}); \\
a_8^{(n)} &= \varkappa_\perp^2 u_5 J_n; \\
a_9^{(n)} &= \frac{-1}{2}\varkappa_\perp (u_5\varkappa_\parallel + u_8)(J_{n+1} + J_{n-1}); \\
a_{10}^{(n)} &= -\frac{i}{4}\varkappa_\perp^2 (u_6 - u_2)(J_{n+2} - J_{n-2}); \\
a_{11}^{(n)} &= \frac{i\varkappa_\perp^2 z}{2r_\perp}(u_6 - u_2)(J_{n+2} - J_{n-2}) + \frac{\varkappa_\perp}{2}(u_2\varkappa_\parallel + u_7)(J_{n+1} + J_{n-1}); \\
J_n &\equiv J_n (k_\perp r_\perp).
\end{aligned}
\tag{14}
$$

Applying Maxwell's equations, we can easily obtain for $\mathbf{H}(\mathbf{r}, t)$ expressions analogous to (8) and (11).

Energy losses per unit time are

$$
Q = -\int \mathbf{jE} d\mathbf{r} = 8\pi^2 i \int \frac{u_{ik}(\mathbf{k}, \omega)}{\omega D(\mathbf{k}, \omega)} j_i(-\mathbf{k}, \omega) j_k(\mathbf{k}, \omega) e^{i(\omega + \omega')t} d\mathbf{k} d\omega d\omega . \tag{15}
$$

In the following we shall apply the expressions for the fields $\mathbf{E}$ and $\mathbf{H}$ and the energy losses Q in the case of azimuthal and axial currents modulated in the direction of the magnetic field with a frequency ω and a wave vector $k_\parallel$.

Wave excitation by modulated azimuthal currents

Electric field and energy losses. Let us consider the waves excited in a plasma by modulated azimuthal currents flowing over a cylindrical surface

of radius a,

$$\mathbf{j}(\mathbf{r}, t) = j_0 \cos(k_\parallel z - \omega t)\,\delta(r_\perp - a)\frac{[\mathbf{hr}]}{r_\perp}. \tag{16}$$

This current can be created by injecting a modulated electron beam into the plasma at right angles to the magnetic field /5/.

In virtue of the problem's symmetry, we may set $\varphi = 0$ in (11). In the sum (10) only the term with $n = 1$ remains. From (11) we have

$$\mathbf{E}(\mathbf{r}, t) = \frac{4\pi j_0 a\omega}{c^2} \operatorname{Im}\left\{e^{i(k_\parallel z - \omega t)} \int_0^\infty \frac{J_1(k_\perp a)}{D} \mathbf{q}(n_\perp) n_\perp dn_\perp\right\}, \tag{17}$$

where

$$\mathbf{q}(n_\perp) = (u_1 + \varkappa_\perp u_6) J_1(n_\perp \varrho) \frac{[\mathbf{hr}]}{r_\perp} + (u_4 - u_5 \varkappa_\perp) J_1(n_\perp \varrho) \frac{\mathbf{r}_\perp}{r_\perp} - \\ - i\varkappa_\perp (u_6 \varkappa_\parallel + u_8) J_0(n_\perp \varrho)\,\mathbf{h}.$$

Here

$$n_\parallel = \frac{k_\parallel c}{\omega}; \quad n_\perp = \frac{k_\perp c}{\omega}; \quad \varrho = \frac{r_\perp \omega}{c}; \quad \alpha = \frac{a\omega}{c}.$$

The energy losses per unit time and unit length of the cylinder are

$$Q = -\frac{4\pi^2 j_0^2 a^2 \omega}{c^2} \operatorname{Im} \int_0^\infty \frac{1}{D}(u_1 + \varkappa_\perp^2 u_6) J_1^2(n_\perp \alpha) n_\perp dn_\perp. \tag{18}$$

Hydrodynamic approximation. The integrals in (17) and (18) are taken in the limiting case of a "cold" plasma, when the thermal motion of electrons and ions can be assumed to have no influence on the radiation and propagation of electro-magnetic waves.

For a "cold" plasma, the permittivity tensor

$$\varepsilon_{ik} = \varepsilon_1 \delta_{ik} + (\varepsilon_3 - \varepsilon_1) h_i h_k + i\varepsilon_2 e_{ike} h_e, \tag{19}$$

where ε_1, ε_2 and ε_3 are independent on $\mathbf{k}$. In case of high-frequency (electron) oscillations

$$\varepsilon_1 = 1 - \frac{\Omega^2(\omega + i\nu)}{\omega(\omega^2 - \omega_H^2 + 2i\omega\nu)};$$

$$\varepsilon_2 = \frac{\Omega^2 \omega_H}{\omega(\omega^2 - \omega_H^2 + 2i\omega\nu)}; \qquad \varepsilon_3 = 1 - \frac{\Omega^2}{\omega(\omega + i\nu)}, \tag{20}$$

where $\Omega = \Omega_e = \left(\frac{4\pi e^2 n_0}{m}\right)^{1/2}$ is the electron plasma frequency, $\omega_H = -\omega_e = \frac{eH_0}{mc}$ the electron gyrofrequency, n_0 the electron number density, $\nu = \frac{\sqrt{8\pi} e^4 n_0 \Lambda}{\sqrt{mT^3}}$ the effective collision frequency of electrons and ions. In the low-frequency region, the motion of ions cannot be neglected. Neglecting the interparticle collisions, we have for the permittivity

$$\varepsilon_1 = 1 - \sum_{\alpha = e, i} \frac{\Omega_\alpha^2}{\omega^2 - \omega_\alpha^2}; \quad \varepsilon_2 = -\sum_{\alpha = e, i} \frac{\Omega_\alpha^2 \omega_\alpha}{\omega(\omega^2 - \omega_\alpha^2)};$$

$$\varepsilon_3 = 1 - \sum_{\alpha = e, i} \frac{\Omega_\alpha^2}{\omega^2}, \tag{21}$$

where Ω_α is the plasma frequency of particles of the species α; ω_α their gyrofrequency (the sign of ω_α is the sign of the charge of the particle α).

Applying (6), (7), and (19), we find

$$
\begin{gathered}
u_1 + \varkappa_\perp^2 u_6 = (\varepsilon_1 - n_\parallel^2)\,\varepsilon_3 - \varepsilon_1 n_\perp^2; \\
u_4 - u_5 \varkappa_\perp^2 = i\varepsilon_2 (n_\perp^2 - \varepsilon_3); \\
\varkappa_\perp (u_5 \varkappa_\parallel + u_8) = - i\varepsilon_2 n_\parallel n_\perp; \\
D = \varepsilon_1 n_\perp^4 + [(\varepsilon_1 + \varepsilon_3)\, n_\parallel^2 - \varepsilon_1^2 + \varepsilon_2^2 - \varepsilon_1\varepsilon_3]\, n_\perp^2 + \varepsilon_3 n_\parallel^4 - 2\varepsilon_1\varepsilon_3 n_\parallel^2 + \\
+ \varepsilon_3 (\varepsilon_1^2 - \varepsilon_2^2).
\end{gathered}
\tag{22}
$$

The equation $D = 0$ gives the "transverse" refractive index $n_\perp$ as a function of ε_1, ε_2, ε_3, and the "longitudinal" refractive index $n_\parallel$:

$$
\begin{gathered}
n_j^2 = \frac{1}{2\varepsilon_1}\Big\{(\varepsilon_1 + \varepsilon_3)(\varepsilon_1 - n_\parallel^2) - \varepsilon_2^2 \pm \\
\pm \sqrt{[(\varepsilon_1 + \varepsilon_3)(\varepsilon_1 - n_\parallel^2) - \varepsilon_2^2]^2 - 4\varepsilon_1\varepsilon_3\,[(n_\parallel^2 - \varepsilon_1)^2 - \varepsilon_2^2]}\Big\}.
\end{gathered}
\tag{23}
$$

If interparticle collisions are neglected, propagation and also radiation of waves is permitted only for those ε_1, ε_2, ε_3 and $n_\parallel$ when n_j^2 is a positive real number. The number of waves propagating in the high-frequency region, where the motion of ions can be neglected, is given in the third column of the table for different combinations of the parameters $v = \frac{\Omega^2}{\omega^2}$, $u = \frac{\omega_H^2}{\omega^2}$ and $n_\parallel$. The first column lists the different regions of variation of u and v, as indicated in Figures 1 and 2. The second column defines the range of $n_\parallel$. The parameters $n_\pm$ and $\tilde{n}_\pm$ are given by the expressions

$$
n_\pm^2 = \varepsilon_1 \pm \varepsilon_2 = 1 - \frac{v}{1 \pm \sqrt{u}}; \quad \tilde{n}_\pm = \frac{1}{\sqrt{u}}(\sqrt{u + v - 1} \pm \sqrt{v - 1}).
$$

Region number	Range of $n_\parallel$	Number of waves	Region number	Range of $n_\parallel$	Number of waves
I	$0 < n_\parallel < n_-$ $n_- < n_\parallel < n_+$ $n_\parallel > n_+$	2 1 0	VII	$n_\parallel < n_+$ or $n_\parallel > n_-$ $\tilde{n}_+ < n_\parallel < n_-$ $n_+ < n_\parallel < \tilde{n}_+$	1 2 0
II	$n_\parallel < n_+$ $n_\parallel > n_+$	1 0	VIII	$n_\parallel < n_+$ or $n_\parallel > n_-$ $n_+ < n_\parallel < n_-$	1 0
III	$n_\parallel < n_+$ $n_\parallel > n_+$	2 1	IX	$n_\parallel < n_+$ or $n_\parallel > n_-$ $n_+ < n_\parallel < \tilde{n}_-$ $\tilde{n}_- < n_\parallel < n_-$	1 2 0
IV	$n_\parallel < n_+$ $n_\parallel > n_+$	1 0			
V	$0 < n_\parallel < \infty$	0	X	$n_\parallel < n_+$ $n_\parallel > n_+$	1 0
VI	$n_\parallel < n_+$ $n_+ < n_\parallel < n_-$ $n_\parallel > n_-$	2 1 0	XI	$n_\parallel < n_+$ $n_+ < n_\parallel < \tilde{n}_-$ $n_\parallel > \tilde{n}_-$	1 2 0

Choosing n_j so that $\mathrm{Im}\, n_j > 0$, we obtain for the electric field

$$\mathbf{E} = \sum_{j=1,2} \mathbf{E}^{(j)}, \tag{24}$$

where $\mathbf{E}^{(j)}$ is the electric field of the j-th normal mode:

$$\mathbf{E}^{(j)} = (-1)^j \frac{2\pi^2 j_0 a\omega}{c^2} \mathrm{Re} \frac{1}{\varepsilon_1 (n_1^2 - n_2^2)} \left\{ \varepsilon_1\varepsilon_3 - n_\parallel^2 \varepsilon_3 - n_j^2 \varepsilon_1) \frac{[\mathbf{h r}]}{r_\perp} f_1(\varrho) + \right.$$
$$\left. + i\varepsilon_2 (n_j^2 - \varepsilon_3) \frac{\mathbf{r}_\perp}{r_\perp} f_1(\varrho) + \varepsilon_2 n_\parallel n_j \mathbf{h} f_0(\varrho) \right\} e^{i(k_\parallel z - \omega t)}. \tag{24'}$$

Here the functions $f_{0,1}$ are defined by

$$f_k(\varrho) = \begin{cases} J_1(n_j a) H_k^{(1)}(n_j \varrho) & \text{for } \varrho > a, \\ J_k(n_j \varrho) H_1^{(1)}(n_j a) & \text{for } \varrho < a, \end{cases} \tag{25}$$

where $H_n^{(1)}(x)$ is Hankel's function of the first kind.

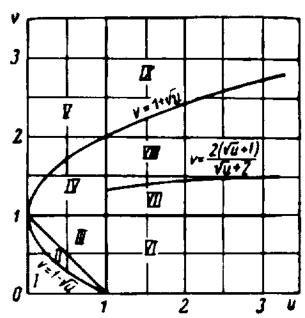

FIGURE 1.

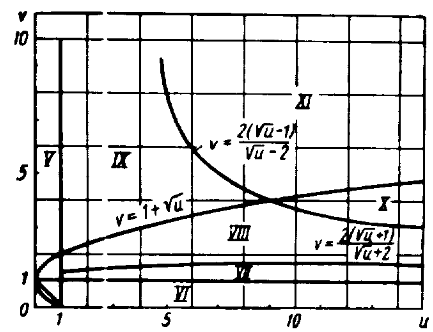

FIGURE 2.

The energy expended in the radiation of the j-th mode in unit time per unit current length is

$$Q^{(j)} = \frac{2\pi^3 j_0^2 a^2 \omega (-1)^j}{c^2} \mathrm{Re} \frac{\varepsilon_3(\varepsilon_1 - n_\parallel^2) - \varepsilon_1 n}{\varepsilon_1 (n_1^2 - n_2^2)} J_1(n_j a) H_1^{(1)}(n_j a) \tag{26}$$

Hence it follows that if waves cannot propagate ($n_j^2 < 0$ or n_j^2 is a complex number), then in the absence of interparticle collisions $Q^{(j)} = 0$, whereas if $n_j^2 > 0$, expression (26) in the absence of interparticle collisions takes the form

$$Q^{(j)} = \frac{2\pi^3 j_0^2 a^2 \omega (-1)^j}{c^2} \cdot \frac{\varepsilon_3(\varepsilon_1 - n_\parallel^2) - \varepsilon_1 n_j^2}{\varepsilon_1 (n_1^2 - n_2^2} J_1^2(n_j a) \tag{26'}$$

Electron cyclotron resonance. When the frequency ω approaches the electron gyrofrequency, the cyclotron damping of the waves in the plasma is enhanced. The skew-Hermitian part of the tensor ε_{ik} conditioned by

cyclotron absorption becomes of the same order of magnitude as the Hermitian part when $z_1 = \frac{\omega - \omega_H}{\sqrt{2}k_\parallel v_e} \lesssim 1$, where $v_e = \sqrt{\frac{T_e}{m}}$ is the electron thermal velocity, providing the plasma is fairly dense $\left(\frac{\Omega^2}{\omega_H k_\parallel v_e} \gtrsim 1\right)$. However, for $n_\parallel \lesssim 1$, cyclotron absorption hardly influences the propagation of electromagnetic waves in a dense plasma $\left(\frac{\Omega^2}{\omega_H k_\parallel v_e} \gg 1\right)$, even with $|z_1| \lesssim 1$ /9/. The radiation intensity is determined, as before, by formula (26), setting $\omega = \omega_H$.

If now $n_\parallel \gg 1$, one of the radiated waves is strongly absorbed:

$$n_\perp^2 = 2\left(1 - \frac{\Omega^2}{\omega_H^2}\right)\left[1 + i\frac{(k_\parallel \delta_e)^3}{2w(z_1)}\right], \tag{27}$$

where $\delta = \left(\sqrt{\frac{8}{\pi}} \cdot \frac{c^2 v_e}{\Omega^2 \omega_H}\right)^{1/3}$ is the depth of the anomalous skin effect; $w(z) = e^{-z^2}\left(1 + \frac{2i}{\sqrt{\pi}}\int_0^z e^{t^2} dt\right)$ a complex probability integral. Applying (27), we obtain for the energy expended in the radiation of the highly damped wave

$$Q = \frac{2\pi^3 j_0^2 a^2 \omega \varepsilon_3}{c^3 n_\parallel^2} \operatorname{Im} J_1(n_\perp a) H_1^{(1)}(n_\perp a), \tag{28}$$

where $\operatorname{Im} n_\perp > 0$.

If $\Omega < \omega_H$ and $|z_1| \lesssim 1$, the energy is absorbed over a distance l of the order of $l \sim \frac{c}{\omega_H}(k_\parallel \delta_e)^{1/2}$ for $k_\parallel \delta_e \gtrsim 1$ and $l \sim \frac{c}{\omega_H}(k_\parallel \delta_e)^3$ for $k_\parallel \delta_e \lesssim 1$. If now $\Omega > \omega_H$ and $|z_1| \lesssim 1$, the penetration depth $l \sim \frac{c}{\Omega}$ for $k_\parallel \delta_e \lesssim 1$ and $l \sim \frac{c}{\Omega}(k_\parallel \delta_e)^{3/2}$ for $k_\parallel \delta_e \gtrsim 1$.

Ion cyclotron resonance. For $\omega \to \omega_i$, we obtain from (26) for a dense plasma with $|\varepsilon_3| \gg |\varepsilon_1| \approx |\varepsilon_2|$,

$$Q = \frac{2\pi^3 j_0^2 a^2 \omega}{c^2} J_1^2(n_\perp a), \tag{29}$$

where

$$n_\perp^2 = \frac{(\varepsilon_1 - n_\parallel^2)^2 - \varepsilon_2^2}{\varepsilon_1 - n_\parallel^2} > 0. \tag{30}$$

This result has been previously derived in /5/.

Expression (29) applies only in the case of a "cold" plasma, where the cyclotron damping due to the ion thermal motion is small, for $|z_i| \gg 1$, where $z_i = \frac{\omega - \omega_i}{\sqrt{2}k_\parallel v_i}$; $v_i = \sqrt{\frac{T_i}{m_i}}$ being the ion mean thermal velocity. If this inequality is not satisfied, but $H_0^2 \gg 8\pi n_0 T_i$, the permittivity tensor ε_{ik} retains its previous form (19), where

$$\begin{gathered}\varepsilon_1 = i\sqrt{\frac{\pi}{8}} \cdot \frac{\Omega_i^2 w(z_i)}{\omega_i k_\parallel v_i} - \frac{\Omega_i^2}{4\omega_i^2}; \quad \varepsilon_2 = i\sqrt{\frac{\pi}{8}} \cdot \frac{\Omega_i^2 w(z_i)}{\omega_i k_\parallel v_i} - \frac{3}{4}\frac{\Omega_i^2}{\omega_i^2}; \\ \varepsilon_3 = \frac{2m_i \Omega_i^2}{m_e \omega_i^2} z_0^2 (1 + i\sqrt{\pi} z_0 w(z_0)), \quad z_0 = \frac{\omega}{\sqrt{2}k_\parallel v_e}.\end{gathered} \tag{31}$$

Seeing that in a dense plasma $|\varepsilon_3| \gg |\varepsilon_1| = |\varepsilon_2|$, we obtain for the electric field with $\omega \approx \omega_i$

$$\mathbf{E} = \frac{2\pi^2 j_0 a\omega}{c^2} \operatorname{Re} e^{i(k_\parallel z - \omega t)} \left(-\frac{[\mathbf{hr}]}{r_\perp} + \frac{i\varepsilon_1}{\varepsilon_1 - n^2} \cdot \frac{\mathbf{r}_\perp}{r_\perp} \right) f_1(\varrho), \tag{32}$$

where $f_1(\varrho)$ is defined by (25). The index n_j entering (25) is found in this case from (30), where ε_1 and ε_2 are substituted from (31).

The energy losses for $\omega \approx \omega_i$

$$Q = \frac{2\pi^3 j_0^2 a^2 \omega}{c^2} \operatorname{Re} J_1(n_\perp a) H_1^{(1)}(n_\perp a). \tag{33}$$

For $|z_i| \gg 1$, this formula reduces to (29).

Let us consider the "transverse" refractive index (30) for $|z_i| \lesssim 1$ in some particular cases. If $n_\parallel^2 \sim |\varepsilon_1|$, then $|n_\perp^2| = n_\parallel^2 \dfrac{n_\parallel^2 - 2\varepsilon_1}{\varepsilon_1 - n_\parallel^2} \sim n_\parallel^2$ and the electromagnetic field penetrates into the plasma to a distance of the order of $\delta_i = \left(\sqrt{\dfrac{8}{\pi}} \cdot \dfrac{c^2 v_i}{\Omega_i^2 \omega_i} \right)^{1/2}$. For $n_\parallel^2 \gg |\varepsilon_1| (k_\parallel \delta_i \gg 1)$, the presence of a plasma hardly influences the field distribution in the region $r \ll \dfrac{c}{\omega_i}$, since $n_\perp^2 = -n_\parallel^2 \left(1 - \dfrac{\varepsilon_1}{n_\parallel^2} \right) \approx -n_\parallel^2$. If now $n_\parallel^2 \ll |\varepsilon_1|$, then $n_\perp^2 = \dfrac{\Omega_i^2}{\omega_i^2} - 2n_\parallel^2$. For $\dfrac{\Omega_i^2}{\omega_i^2} > 2n_\parallel^2$ a weakly damped wave is excited in plasma, circularly polarized in a sense opposite to the sense of rotation of the ions.

Wave excitation by axial currents

Electric field and energy losses. Let us consider the excitation of waves in a plasma by a cylindrical current flowing along the magnetic field with a density

$$\mathbf{j} = \frac{j_0}{\pi a^2} \cos(k_\parallel z - \omega t) \mathbf{h} \tag{34}$$

for $r \leq a$ and $j = 0$ for $r > a$ (j_0 being the total current strength). For $a \to 0$, we have a linear current

$$\mathbf{j} = j_0 \cos(k_\perp z - \omega t) \delta(r_\perp) \frac{1}{2\pi r_\perp}.$$

The excitation of waves by the current (34) is relevant to the problem of interaction of a modulated beam of electrons (or ions) traversing a plasma in the direction of the magnetic field.

Applying (34), we obtain from (11)

$$\mathbf{E}(\mathbf{r}, t) = \frac{4 j_0 a}{\omega a^2} \operatorname{Im} e^{i(k_\parallel z - \omega t)} \left(U_\varphi \frac{[\mathbf{hr}]}{r_\perp} + U_\perp \frac{\mathbf{r}_\perp}{r_\perp} + U_\parallel \mathbf{h} \right), \tag{35}$$

where

$$U_\varphi = \int_0^\infty \frac{J_1(n_\perp a) J_1(n_\perp \varrho)}{D} i\varkappa_\perp (u_5 \varkappa_\parallel + u_6) \, dn_\perp;$$

$$U_\perp = \int_0^\infty \frac{J_1(n_\perp a) J_1(n_\perp \varrho)}{D} i\varkappa_\perp (u_2 \varkappa_\parallel + u_7) \, dn_\perp;$$

$$U_\parallel = \int_0^\infty \frac{J_1(n_\perp a) J_0(n_\perp \varrho)}{D} (u_1 + u_3 + u_2 \varkappa_\parallel^2 + 2u_7 \varkappa_\parallel) \, dn_\perp.$$

Energy losses per unit current length in unit time

$$Q = -\frac{4j_0^2}{\omega a^2}\,\mathrm{Im}\int\limits_0^{\infty}\frac{J_1^2(n_\perp a)}{n_\perp D}\,(u_1 + u_3 + u_2\varkappa_\parallel^2 + 2u_7\varkappa_\parallel)\,dn_\perp. \tag{36}$$

Hydrodynamic approximation. Applying (19), we obtain on hydrodynamic approximation

$$U_\alpha = \sum_{j=1,2} U_\alpha^{(j)}.$$

$U_\alpha^{(j)}$ are given by

$$U_\perp = \frac{\pi(-1)^{j-1} n_\parallel(\varepsilon_1 - n_\parallel^2 - n_j^2)}{2\varepsilon_1(n_1^2 - n_2^2)}\left[f_1(\varrho) - \frac{2\varepsilon(\alpha-\varrho)}{i\pi\alpha n_j}\right];$$

$$U_\varphi = \frac{\pi i(-1)^{j-1}\varepsilon_2 n_\parallel n_j}{2\varepsilon_1(n_1^2 - n_2^2)}\,f_1(\varrho); \tag{37}$$

$$U_\parallel = \frac{\pi i(-1)^{j-1}\left[(n_\parallel^2 - \varepsilon_1)n_j^2 + (n_\parallel^2 - \varepsilon_1)^2 - \varepsilon_2^2\right]}{2\varepsilon_1(n_1^2 - n_2^2)\,n_j}\left[f_0(\varrho) - \frac{2\varepsilon(\alpha-\varrho)}{i\pi\alpha n_j}\right],$$

where $\varepsilon(x) = 0$ for $x < 0$ and $\varepsilon(x) = 1$ for $x > 0$.

The radiation intensity (26)

$$Q = \sum_{j=1,2} Q^{(j)},$$

where

$$Q^{(j)} = \frac{2\pi j_0^2\omega}{c^2a^2}\,\mathrm{Re}\,\frac{(-1)^j\left[(n_\parallel^2 - \varepsilon_1)n_j^2 + (n_\parallel^2 - \varepsilon_1)^2 - \varepsilon_2^2\right]}{\varepsilon_1(n_1^2 - n_2^2)\,n_j^2}\left[J_1(an_j)\,H_1^{(1)}(an_j) - \right.$$
$$\left. - \frac{2}{\pi i}\right]. \tag{38}$$

The "transverse" refractive indices n_j entering (37) and (38) are determined from (23).

If the propagating waves ($n_j^2 > 0$) are not damped,

$$Q^{(j)} = \frac{\pi j_0^2\omega}{2c^2}\cdot\frac{(-1)^j\left[(n_\parallel^2 - \varepsilon_1)n_j^2 + (n_\parallel^2 - \varepsilon_1)^2 - \varepsilon_2^2\right]}{\varepsilon_1(n_1^2 - n_2^2)}\cdot\frac{4J_1^2(an_j)}{a^2n_j^2}. \tag{39}$$

If now $n_j^2 < 0$ or n_j^2 is a complex number, then $Q^{(j)} = 0$ in the absence of dissipation.

In the particular case $an_j \ll 1$, formula (39) gives the energy losses of a linear current.

High-frequency "hybrid" resonance. The radiation intensity of a linear current sharply increases if the radiation frequency approaches the "hybrid" frequency $\omega_1 = \sqrt{\Omega^2 + \omega_H^2}$ (ω_1 the frequency of plasma oscillations propagating at right angles to the magnetic field). Since in this case $\varepsilon_1 \to 0$, one of the refractive indices (19) ($j = 2$, extraordinary wave) has a singularity

$$n_2^2 = -\frac{(1 + n_\parallel^2)\,uv}{1 - u - v} \to \infty \tag{40}$$

(the ordinary wave, $j = 1$, has no singularities at $\omega = \omega_1$). Expression (39) in this case is simplified:

$$Q = \frac{\pi j_0^2\omega n_\parallel^2 v}{2c^2(u + v - 1)}\cdot\frac{4J_1^2(an_2)}{a^2n_2^2}. \tag{41}$$

Expression (41) was derived for the case of a linear current by A.N. Kondratenko /7/. From (41) we see that as $\omega \to \omega_1$ the radiation intensity of the linear current increases as $(\omega_1 - \omega)^{-1}$. However, when n_2 becomes excessively large ($an_2 \gg 1$), the losses approach zero as $\sqrt{\omega_1 - \omega}$.

Collisions and thermal motion of the plasma electrons restrict the value of n_2 at $\omega = \omega_1$. Introducing interparticle collisions, we obtain at $\omega \approx \omega_1$

$$Q = \frac{2\pi j_0^2 \omega n_\parallel^2}{c^2 a^2 (1 + n_\parallel^2)} \mathrm{Re}\,[J_1(an_2) H_1^{(1)}(an_2)], \tag{42}$$

where

$$n_2^2 = -\frac{(1 + n_\parallel^2) u}{\varepsilon_1}; \quad \varepsilon_1 = 1 - \frac{v}{1 - u} + i \frac{\nu}{\omega} \cdot \frac{1 + u}{1 - u}.$$

Let us consider the effect of the electron thermal motion on the radiation of waves at $\omega \approx \omega_1$. When the electron thermal motion is taken into consideration, the refractive indices of the extraordinary wave remain finite at $\omega = \omega_1$ and furthermore a third normal mode arises (a plasma wave). Setting $\beta^2 n_\perp^2 \ll 1$; $\beta^2 n_\parallel^2 \ll 1$; $\beta^2 n_\parallel^2 \ll |1 - 4u|$; $\beta^2 n_\parallel^2 \ll |1 - u|$, where $\beta = \frac{v_T}{c}$ is the ratio of the electron thermal velocity to the velocity of light, we find

$$n_j^2 = \frac{2uv(1 + n_\parallel^2)}{\sqrt{\varkappa}} \varphi_\pm(x), \tag{43}$$

where

$$\varphi_\pm(x) = \Delta(x \pm \sqrt{x^2 + \Delta}); \quad \Delta = \mathrm{sgn}(1 - 4u);$$
$$x = \frac{1 - u - v}{\sqrt{\varkappa}}; \quad \varkappa = \frac{12\beta^2 v^2 u (1 + n_\parallel^2)}{|1 - 4u|}. \tag{44}$$

The function $\varphi_\pm(x)$ is plotted in Figure 3 (for $\Delta = -1$) and Figure 4 ($\Delta = 1$). We see that for $\Delta = 1$ a single mode propagates (extraordinary wave), while for $\Delta = -1$ there are the plasma wave and the extraordinary wave. For $x \gg 1$, one of the refractive indices (42) reduces to (40), while for the second we have /10/

$$n^2 = \frac{(1 - 4u)(1 - u - v)}{3\beta^2 v}. \tag{45}$$

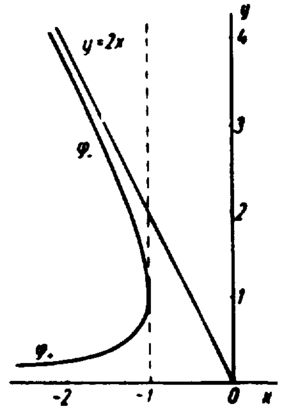

FIGURE 3.

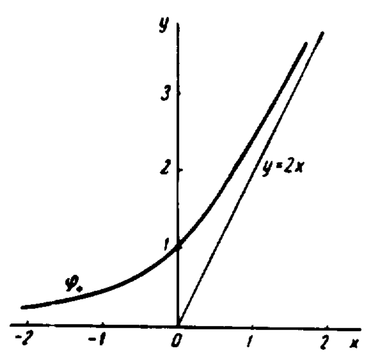

FIGURE 4.

Applying (42), we obtain expression (35) for the electric field of the extraordinary and the plasma waves with $U_\alpha = U_\alpha^{(j)}$, where

$$U_\perp^{(j)} = \frac{\pi(-1)^{j-1}(1-4u)\, n_\parallel n_j^2}{6\beta^2 (n_1^2 - n_2^2)} \left[f_1(\varrho) - \frac{2\varepsilon(\alpha-\varrho)}{i\pi a n_j} \right];$$

$$U_\varphi^{(j)} = -\frac{i\pi(-1)^{j-1}(1-4u)\,\varepsilon_2 n_\parallel n_j}{6\beta^2 (n_1^2 - n_2^2)} f_1(\varrho);$$

$$U_\parallel^{(j)} = \frac{i\pi(-1)^{j}(1-4u)\, n_\parallel^2}{6\beta^2 (n_1^2 - n_2^2)\, n_j} \left[f_0(\varrho) - \frac{2\varepsilon(\alpha-\varrho)}{i\pi a n_j} \right].$$

The radiation intensity for propagating waves ($n_j^2 > 0$) is given by

$$Q^{(j)} = \frac{\pi j_0^2 \omega n_\parallel^2}{2c^2} \cdot \frac{(1-4u)(-1)^{j-1}}{3\beta^2 (n_1^2 - n_2^2)} \cdot \frac{4J_1^2(a n_j)}{a^2 n_j^2}. \tag{46}$$

As it follows from (43), for $\beta \gtrsim |1-u-v|$, $n \sim \frac{1}{\sqrt{\beta}}$, and for the linear current ($a < \sqrt{\beta}$) the losses are of the order of $Q \sim \frac{Q_0}{\beta}$, where Q_0 denotes the losses at the frequency $\sim \omega_1$ in the absence of resonance.

Waves with a very large refractive index (45) are weakly radiated, provided that the current scale a is not too small, since $J_1^2(a n_j) \to 0$ as $a n_j \to \infty$.

Note that for $\Delta = -1$ the intensity of radiation of extraordinary and plasma waves tends to infinity as $\frac{1}{\sqrt{x^2-1}}$ for $x \to 1$ (at the point $x = 1$ the phase velocities of these waves are equal). In this region, the dissipation of wave energy in collisions cannot be neglected. Introducing collisons, we obtain for (46)

$$Q^{(j)} = \frac{2\pi j_0^2 \omega n_\parallel^2 (1-4u)(-1)^j}{3c^2 a^2 \beta^2} \operatorname{Re} \frac{J_1(a n_j) H_1^{(1)}(a n_j) - \frac{2}{\pi i}}{n_j^2 (n_1^2 - n_2^2)}. \tag{47}$$

Here n_j are determined from (43), where we set

$$x = \frac{1 - u - v + i\frac{\nu}{\omega}(1+u)}{\sqrt{\varkappa}}.$$

Excitation of longitudinal plasma oscillations in conditions of multiple cyclotron resonance. If the "hybrid" frequency $\omega_1 = \sqrt{\Omega^2 + \omega_H^2}$ is close to $2\omega_H$, then in conditions of double resonance, $\omega \approx \omega_1 \approx 2\omega_H$, intense cyclotron damping of the extraordinary wave is observed, and furthermore the plasma wave is also highly damped /10/ (the refractive index of the ordinary wave has no singularities at $\omega \approx \omega_1 \approx 2\omega_H$). The refractive indices of the highly damped waves, cyclotron damping included, have the form

$$n_j^2 = \frac{4(u+v-1) \pm \sqrt{16(u+v-1)^2 - 9i\xi(1+n_\parallel^2)}}{6i\xi}, \tag{48}$$

where

$$\xi = \sqrt{\frac{\pi}{8}} \cdot \frac{\Omega^2 \beta}{\omega_H^2 n_\parallel} w(z_2); \quad z_2 = \frac{\omega - 2\omega_H}{\sqrt{2} k_\parallel v_e}. \tag{48'}$$

We see from (48) and (48') that for $|z_2| \lesssim 1$ and $|u+v-1| \lesssim \sqrt{\beta}$, $\mathrm{Re}\, n_j \sim \mathrm{Im}\, n_j \sim \frac{1}{\sqrt[4]{\beta}}$. For $|z_2| \gg 1$, cyclotron damping is exponentially small. Formula (48) then reduces to (43).

The intensity of radiation per unit current length in unit time, making use of (48), is

$$Q^{(j)} = \frac{2\pi j_0^2 n_\parallel^2}{a^2 \omega} (-1)^j \,\mathrm{Re}\, \frac{J_1(an_j) H_1^{(1)}(an_j) - \frac{2}{\pi i}}{i\xi n_j^2 (n_1^2 - n_2^2)} \tag{49}$$

For $|z_2| \gg 1$, formula (49) reduces to (46).

Excitation of longitudinal plasma oscillations. Let us consider the radiation of electromagnetic waves for $n_\parallel \gg 1$. In this case, the refractive index $n_\perp$ is also large:

$$n_j^2 = -\frac{\varepsilon_3}{\varepsilon_1} n_\parallel^2.$$

This equality implies that the frequency ω is close to one of the natural frequencies of the longitudinal plasma oscillations in a magnetic field, ω_+ or ω_-, where

$$\omega_\pm^2 = \frac{1}{2}(\Omega^2 + \omega_H^2) \pm \frac{1}{2}\sqrt{(\Omega^2 + \omega_H^2)^2 - 4\Omega^2\omega_H^2 \cos^2\vartheta};$$

$$\mathrm{tg}^2\,\vartheta = \frac{n_j^2}{n_\parallel^2}.$$

Radiation is clearly permitted ($n_j^2 > 0$) if $u > 1$, $v > 1$ (regions VII–XI in Figure 2, the $j = 1$ mode), or if $u < 1$, $v < 1$, and $u + v > 1$ (region III in Figure 1, the $j = 2$ mode). The intensity of radiation

$$Q^{(j)} = \frac{2\pi j_0^2 \omega}{c^2 a^2 |\varepsilon_3|} J_1^2(an_j). \tag{50}$$

In the case of a linear current, the losses are proportional to $n_\parallel^2$.

Low-frequency hybrid resonance. Let us investigate the radiation of waves near the low-frequency hybrid resonance. The refractive index (23) is infinite for $\varepsilon_1 = 0$. The equation $\varepsilon_1 = 0$ is solvable not only in the high-frequency region ($\omega = \omega_1$), but in the low-frequency region as well ($\omega = \omega_2$) /11/. Here

$$\omega_2^2 = \omega_i^2 + \frac{\Omega_i^2}{1 + w}, \tag{51}$$

where $w = \frac{\Omega_i^2}{\omega_i^2}$. If $\omega \to \omega_2$, then for $n_\parallel^2 \gg |\varepsilon_1|$ the refractive index of the ordinary wave is

$$n_\perp^2 = -\frac{\varepsilon_2^2 + \varepsilon_3 n_\parallel^2}{\varepsilon_1} \tag{52}$$

(the refractive index of the extraordinary wave displays no singularities at $\omega = \omega_2$). The radiation intensity of a wave with a refractive index (52) is given by (41).

Expression (52) applies only for frequencies ω which are not too close to ω_2, when the thermal motion of the plasma electrons and ions can be neglected. If the thermal motion is taken into consideration, the refractive index of the plasma remains finite at $\omega = \omega_2$ and a third normal mode arises

(the plasma wave). Setting $\beta_i n_\parallel \ll 1$; $\beta_i^2 n_\perp^2 \frac{\omega^2}{\omega_i^2} \ll 1$; $\beta_e n_\parallel \ll 1$, where $\beta_i = \sqrt{\frac{T_i}{m_i c^2}}$,

we obtain for $T_i \gg T_e$ the following expression for the refractive indices of the ordinary and the plasma waves:

$$n_j^2 = \sqrt{\frac{4\,|n_\parallel^2 \varepsilon_3 + \varepsilon_2^2|\,\omega^2}{3\beta_i^2 \Omega_i^2 |\xi|}}\,\varphi_j(x)\,\mathrm{sgn}\,\xi, \tag{53}$$

where φ_j is defined by (44) with $\Delta = \mathrm{sgn}\,\xi\,(n_\parallel^2 \varepsilon_3 + \varepsilon_2^2)$,

$$x = \frac{(1+w)(\omega^2 - \omega_2^2)\,\omega_i}{(\omega^2 - \omega_i^2)\sqrt{12\beta_i^2 \Omega_i^2 |\xi|\,|n_\parallel^2 \varepsilon_3 + \varepsilon_2^2|}}; \tag{54}$$

$$\xi = \frac{\omega^4}{(\omega^2 - \omega_i^2)(\omega^2 - 4\omega_i^2)}. \tag{55}$$

We see from (55) that for $T_e \sim T_i$ the electron thermal motion is significant only when $\omega_2 \sim \sqrt{\omega_i |\omega_e|}$. This is observed in a dense plasma, with $w \gtrsim 1$.

The intensity of radiation of the ordinary and the plasma waves at $\omega \approx \omega_2$ is given by

$$Q^{(j)} = \frac{2\pi j_0^2 n_\parallel^2 \omega_i^2 (-1)^{j-1}}{3c^2 \beta_i^2 \Omega_i^2 \xi (n_1^2 - n_2^2)} \cdot \frac{J_1^2(\alpha n_j)}{\alpha^2 n_j^2}. \tag{56}$$

It follows from (56) that the resonance energy losses ($\omega \to \omega_2$) are higher for a linear current.

BIBLIOGRAPHY

1. AKHIEZER, A. I. and A. G. SITENKO. – JETP, **35**: 116. 1958.

2. TSINTSADZE, N. L. and A. D. PATARAYA. – ZhTF, **30**: 1178. 1960.

3. SITENKO, A. G. and Yu. A. KIROCHKIN. – ZhTF, **29**: 801. 1959.

4. KIPPENHAHN, R. and H. VRIES. – Zs. Naturforsch. **15a**: 506. 1960.

5. GLAZOV, O. A., L. V. DUBOVOI, and B. N. RUTKEVICH. – ZhTF, **31**: 84. 1961.

6. KONDRATENKO, A. N. – UFZh, **7**: 371. 1962.

7. KONDRATENKO, A. N. – In: "Fizika plazmy i problemy upravlyaemogo termoyadernogo sinteza", **2**: 186. Kiev, Izdatel'stvo AN UkrSSR. 1962.

8. PAKHOMOV, V. I., V. F. ALEKSIN, and K. N. STEPANOV. – ZhTF, **31**: 1170. 1961.

9. SITENKO, A. G. and K. N. STEPANOV. – JETP, **31**: 642. 1956.

10. GERSHMAN, B. N. – JETP, **24**: 659. 1953.

11. KORPER, K. – Zs. Naturforsch. **12a**: 815. 1957.

12. CANOBBIO, E. – Nucl. Fusion, **1**: 172. 1961.

13. [Not given.]

S. S. Kalmykova and V. I. Kurilko

DIFFRACTION OF A SURFACE WAVE ON AN IDEALLY CONDUCTING WEDGE

Consider the quarter-space $x>0$, $z>0$ filled with an anisotropic dielectric ($\varepsilon_x = \varepsilon_\perp$, $\varepsilon_z = \varepsilon_\parallel$) and having a common boundary with an ideally conducting rectangular wedge ($x>0$, $z<0$). A surface wave propagates along the surface of the dielectric travelling from $z>0$; the wave field in the plane $x=0$ varies as $\exp[-i(\omega\tau+\gamma z)]$ and the wave vector γ is determined by the dispersion equation

$$-\varepsilon_\parallel v = \beta; \qquad (1)$$
$$v(t) = (t^2 - k^2)^{1/2}; \quad \beta(t) = \left[\frac{\varepsilon_\parallel}{\varepsilon_\perp}(t^2 - k^2\varepsilon_\perp)\right]^{1/2},$$

where $\varepsilon_\parallel < 0$; $\varepsilon_\perp > 1$; $k^2 < \gamma^2 < k^2\varepsilon_\perp$; $k = \frac{\omega}{c}$.

We shall determine the field scattered by the wedge and, in particular, the amplitude of the reflected surface wave. The scattered fields are sought as superpositions of plane waves, each satisfying Maxwell's equations /1/. For example, we seek the field H_y in the form

$$H_y = \begin{cases} \int\limits_{-\infty}^{+\infty} dt h(t) \exp[itz + v(t)x], & x<0, \ -\infty < z < \infty; \\ \int\limits_{-\infty}^{+\infty} dt H(t) \exp[itz - \beta(t)x], & x>0, \ 0 \le z < \infty, \end{cases} \qquad (2)$$

where $h(t)$ and $H(t)$ are unknown functions to be found from the boundary conditions. By way of boundary conditions we assume that the tangential components of the scattered fields are all equal at the surface of the dielectric and that the tangential components of the total fields vanish at the surface of the ideally conducting wedge:

$$\left.\begin{array}{l} H_y(x>0) = H_y(x<0) \\ E_z(x>0) = E_z(x<0) \end{array}\right\} x=0, \quad z>0;$$
$$E_z + \frac{g}{ik\varepsilon_\parallel}\exp(i\gamma z) = 0, \quad x=0, \quad z<0; \qquad (3)$$
$$E_x + \frac{\gamma}{k\varepsilon_\perp}\exp(-gx) = 0, \quad x>0, \quad z=0, \quad g=\beta(\gamma).$$

Applying Rapoport's lemma /2/, we find from boundary conditions (3) the following relations for the unknown functions $h(t)$ and $H(t)$:

$$H(t) - h(t) = \varphi^+(t);$$
$$Z_+(t)H(t) + Z_-(t)h(t) = \psi^+(t);$$
$$Z_-(t)h(t) - \frac{Z_0}{2\pi i(t+\gamma)} = \zeta^-(t); \qquad (4)$$
$$H(t) - H(-t) = \delta(t-\gamma) - \delta(t+\gamma);$$
$$Z_+(t) = \frac{\beta(t)}{k\varepsilon_\parallel}; \quad Z_-(t) = \frac{v(t)}{k}; \quad Z_0 \equiv Z_-(\gamma),$$

where the superscripts + and - imply that the corresponding functions are analytical respectively in the upper and the lower half-planes of the complex variable t.

Eliminating $h(t)$ and $H(t)$ from (4), we obtain an equation for the function $\zeta_\perp(t) = \zeta^+(t) - \zeta^-(t) - \frac{1}{\pi i}\frac{t}{t^2-\gamma^2}$, where $\zeta^+(t) = \zeta^-(-t)$:

$$\frac{\Delta(t)}{v\beta}\cdot\frac{1}{\pi i}\int\limits_{-\infty}^{+\infty}\frac{\zeta_\perp(t')\,dt'}{t'-t} + \frac{1}{2\pi i}\int\limits_{-\infty}^{+\infty}\left[\frac{1}{v(t')}-\frac{1}{v(t)}\right]\frac{\zeta_\perp(t')\,dt'}{t'-t} =$$
$$= \frac{1}{\pi i}\cdot\frac{Z_0\gamma}{t^2-\gamma^2}\cdot\frac{\Delta(t)}{v\beta} + \frac{1}{\pi i}\cdot\frac{1}{\beta(\beta+g)}, \tag{5}$$

where

$$\Delta(t) = \varepsilon_\parallel v(t) + \beta(t).$$

Since $\operatorname{Im} k > 0$, the coefficient of the singular part in (5) does not vanish on the integration contour. Therefore, the homogeneous equation corresponding to equation (5) does not have any trivial solutions, and it is thus equivalent to a single Fredholm equation /3,4/

$$\zeta_\perp(t) = -\frac{Z_0}{\pi i}\cdot\frac{\gamma t}{t^2-\gamma^2} + \frac{1}{\pi i}\cdot\int\limits_{-\infty}^{+\infty}\frac{v(t')\,[\beta(t')+g]^{-1}dt'}{\Delta(t')(t'-t)} +$$
$$+ \frac{1}{\pi i}\cdot\int\limits_{-\infty}^{+\infty}\frac{v(t')\,\beta(t')\,dt'}{2\pi i\Delta(t')(t'-t)}\cdot\int\limits_{-\infty}^{+\infty}\left[\frac{1}{v(t'')}-\frac{1}{v(t')}\right]\frac{\zeta_\perp(t'')\,dt''}{t''-t'}. \tag{6}$$

For $|\varepsilon_\parallel| \gg 1$ the kernel in equation (6) contains a small parameter and is therefore solved by the iterative technique. In the zeroth approximation, $\zeta_1^0 = -\frac{Z_0}{\pi i}\cdot\frac{t}{t^2-\gamma^2}$, and the reflection coefficient, according to (3), is zero. On first approximation we have for the reflection coefficient

$$R^a(\pi/2) = \frac{1}{2}Z_0^2\,[1 + 0(Z_0)]. \tag{7}$$

For $|\varepsilon_\parallel| \simeq Z_0^{-2} \gg 1$ the iterative technique gives ζ_1 as an expansion in terms of the parameter $\frac{\delta}{\lambda} \simeq Z_0$ for small t only $(t < kZ_0^{-1})$. For large t, (6) can be solved applying the results of /5/. Equating the terms of equal negative order in (6) as $t \to \infty$, we find

$$\zeta_1^0(t \to \infty) = \frac{\text{const}}{(t/k)^{1-\alpha}}; \tag{8}$$
$$\alpha = \frac{1-i}{\pi}\,(\varepsilon_\perp|\varepsilon_\parallel|)^{-1/4};\quad t \gg k\exp[2\pi(\varepsilon_\perp|\varepsilon_\parallel|)^{1/4}].$$

The corresponding correction to (7) is thus exponentially small.

For a wedge with an angle $\vartheta = 0$ (an ideally conducting half-plane $z<0$ on top of an anisotropic half-space $x>0$), the analogous reflection coefficient is

$$R^a(0) = R^a\left(\frac{\pi}{2}\right)\left(\frac{n_\perp-\gamma}{n_\perp+\gamma}\right)^{1/4}[1 + 0(Z_0)];\quad n_\perp^2 = \varepsilon_\perp k^2. \tag{9}$$

The case of an isotropic dielectric $(\varepsilon_\perp = \varepsilon_\parallel = \varepsilon < 0)$ is treated analogously. In this case, the reflection coefficients for $\vartheta = \pi/2$ and $\vartheta = 0$ differ only in

the first approximation in Z_0:

$$R^{\perp}(\pi/2) = \frac{1}{2} Z_0^2 \left[1 - i \frac{Z_0}{\pi} + 0(Z_0^2) \right], \quad Z_0 = \frac{1}{\sqrt{|\varepsilon|}}; \tag{10}$$

$$R^{\perp}(0) = \frac{1}{2} Z_0^2 \left[1 + iZ_0 \frac{\pi - 1}{\pi} + 0(Z_0^2) \right]. \tag{11}$$

It would be interesting to compare expressions (7), (9), and (10) with the results obtained when Leontovich's boundary conditions are applied at the dielectric surface /1/. The corresponding results coincide to within terms of the order of Z_0^2 with equations (7) and (10), respectively.

Thus despite the presence of a parameter which is small in comparison with the skin layer depth δ (the thickness of the transition layer between the dielectric and the wedge) /1/, Leontovich's boundary conditions lead to a correct expression for the coefficient of reflection from a rectangular ideally conducting wedge. These results will apparently apply for a wedge with an angle $\vartheta \sim 1$ also.

Our results may be applied to a plasma in the following cases:

1. In the presence of a constant magnetic field $H_z = H_0$, in the low-frequency region $\omega \ll \Omega_H = \frac{eH_0}{Mc}$ (M being the mass of the ion). Then $\varepsilon_{\perp} = 1 + \frac{\omega_0^2}{\omega_H \Omega_H}$; $\varepsilon_{\parallel} = 1 - \frac{\omega_0^2}{\omega^2} \left(\omega_0^2 = \frac{u\pi e^2 n_0}{m} \right.$; n_0 plasma density; m electron mass; $\left. \omega_H = \frac{M}{m} \cdot \Omega_H \right)$.

2. In the absence of a magnetic field. Then $\varepsilon_{\parallel} = \varepsilon_{\perp} = 1 - \frac{\omega_0^2}{\omega^2}$.

BIBLIOGRAPHY

1. LEONTOVICH, M. A., V. A. FOK, G. A. GRINBERG, and E. L. FEINBERG. — In: "Issledovaniya po rasprostraneniyu radiovoln", 2(5): 69. Moskva, Izdatel'stvo AN SSSR. 1948.

2. RAPOPORT, I. M. — DAN SSSR, 59: 1403. 1948.

3. MUSKHELISHVILI, N. A. Singulyarnye integral'nye uravneniya (Singular Integral Equations). — Moskva, Fizmatgiz. 1962.

4. VEKUA, I. N. — Soobshcheniya AN GruzSSR, 12: 697. 1941.

5. VERTGEIM, B. A. — In: "Issledovaniya po sovremennym problemam teorii funktsii kompleksnogo peremennogo", p. 450. Moskva, Fizmatgiz. 1961.

V. B. Krasovitskii and V. I. Kurilko

THE EFFECT OF RADIATION ON RESONANCE ACCELERATION OF PARTICLES

The motion of a particle in the field of a plane wave in the presence of a constant and homogeneous magnetic field has been considered in the linear /1/ and the nonlinear /2/ approximations. It has been established that in

the presence of a constant magnetic field H the force $f_H = \left(\mathbf{v} \cdot \widetilde{\mathbf{H}}, \frac{\mathbf{H}}{H}\right)$ may reach fairly high values, while in the absence of a magnetic field this force is small (of the order of $\frac{e^2}{m_0 c^2 \lambda}$, where λ is the wavelength). A particle moving along a constant and homogeneous magnetic field may thus be accelerated by the field of a plane wave, although its electric component in this direction is zero. This acceleration is a further extension of the mechanism of field-quadratic forces proposed by V. I. Veksler /3/.

However, the authors of /1,2/ neglected one important point (which follows directly from equations (5) in /2/), namely the self-resonance occuring in the absence of radiation. It is the self-resonance, discovered and investigated in /4,5/, that makes this acceleration mechanism particularly effective.

Let us consider the effect of radiation on the self-resonance acceleration of particles. The equations of motion

$$\frac{da}{ds} = \frac{\varepsilon}{2\Omega} \cos \vartheta - \gamma a \left(1 + \frac{1}{2} a^2\right); \tag{1}$$

$$b \frac{d\vartheta}{ds} = \frac{1}{2} (1 - b^2) - \frac{\varepsilon}{2\Omega a} \sin \vartheta; \tag{2}$$

$$\frac{db}{ds} = - \frac{\gamma}{2} ab (1 + b^2) \tag{3}$$

(all symbols as in /2/).

Setting $\gamma = 0$ in (1)-(3), we obtain a set of equations whose solutions for $b = b_0 = 1$ and $a_0 = \vartheta_0 = 0$ are

$$a_1 = \frac{\varepsilon s}{2\Omega}; \quad \vartheta_1 = 0. \tag{4}$$

Let us investigate the effect of radiation on the motion of a particle ($\gamma \neq 0$). Integrating (3), we obtain for $b_0 = 1$

$$b = [2 \exp (\gamma \int a^2 ds) - 1]^{-\frac{1}{2}}. \tag{5}$$

For $a^3 \ll \frac{\varepsilon}{2\Omega\gamma}$, from equations (1) and (2), applying (3), we can obtain an equation for a:

$$a''' + a''^2 a' \left[\frac{\varepsilon^2}{4\Omega^2} - a'^2\right]^{-\frac{3}{2}} - \frac{a'}{a^2} \left[\frac{\varepsilon^2}{4\Omega^2} - a'^2\right]^{\frac{1}{2}} - \\ - \frac{a'a''}{a} \left[\frac{\varepsilon^2}{4\Omega^2} - a'^2\right]^{-\frac{1}{2}} = \gamma a^2, \tag{6}$$

where prime denotes differentiation by s.

We seek a solution of equation (6) in the form

$$a = \frac{\varepsilon s}{2\Omega} - \sigma (s); \quad \frac{\varepsilon s}{2\Omega} \gg \sigma (s).$$

For $\sigma' (s)$ we have

$$\sigma' (s) = \frac{\gamma^2 \varepsilon^5}{120^2 \Omega^5} s^8. \tag{7}$$

Substituting (7) in (2), we obtain an expression for the phase of the particle velocity relative to the wave field:

$$\vartheta = \arc\cos\left(1 - \frac{\gamma^2 \varepsilon^4}{2 \cdot 60^2 \Omega^4}\right). \tag{8}$$

We see from (8) that ϑ increases with s, and the field-particle resonance may be broken. The resonance is sustained if $\vartheta \ll 1$, i.e., $s \ll \left(\frac{60}{\gamma \varepsilon^2}\right)^{\frac{1}{4}}$; in this case the condition $a^s \ll \frac{\varepsilon}{2\Omega\gamma}$ is automatically satisfied.

The principal effect of radiation thus reduces to the displacement of the phase of the particle velocity relative to the field, breaking the synchronism. This sets a limit to the maximal attainable energy. Finding s_{max} from the condition $\vartheta = 1$ and applying the expression for energy derived in /5/, we write

$$W_{max} \simeq \frac{\varepsilon^2}{8\Omega} m_0 c^2 s^2_{max} \simeq \frac{\varepsilon}{\sqrt{\gamma}} m_0 c^2. \tag{9}$$

It is remarkable that W_{max} does not depend on Ω, i.e., on the energy from which the acceleration begins. For $\varepsilon = \frac{E}{H} \simeq 10^{-2}$ and $H \simeq 2.5 \cdot 10^7$ A/m, we have $\gamma = 2.5 \cdot 10^{-11}$. In this case, $W_{max} \simeq 2 \cdot 10^3 m_0 c^2$. For a plasmoid of N coherent particles

$$W^N_{max} = \frac{W_{max}}{\sqrt{N}}.$$

BIBLIOGRAPHY

1. OLLENDORF. – Bull. Res. Council. Israel, 3: 348. 1954.

2. FAINBERG, Ya.B. and V.I. KURILKO. – ZhTF, 29: 939. 1959.

3. VEKSLER, V.I. – Atomnaya Energiya, 2(5): 427. 1957.

4. DAVYDOVSKII, V.Ya. – JETP, 43: 886. 1962.

5. KOLOMENSKII, A.A. and A.N. LEBEDEV. – DAN SSSR, 145: 1259. 1962; JETP, 44: 261. 1963.

Section Two

PLASMA — BEAM INTERACTION

A. K. Berezin, G. P. Berezina, L. I. Bolotin,
Yu. M. Lyapkalo, and Ya. B. Fainberg

INTERACTION OF MODULATED HIGH-CURRENT PULSED ELECTRON BEAMS WITH A PLASMA IN A LONGITUDINAL MAGNETIC FIELD

It has been shown theoretically /1—3/ and experimentally /4, 5/ that one of the reasons for the effective interaction of an initially unmodulated electron beam with a plasma is self-modulation leading to a coherent plasma—beam interaction. However, since the depth of modulation is determined by the field of the growing oscillations, and the field strength depends significantly on the initial perturbation amplitude, which in the case of initially unmodulated beams is conditioned by the comparatively small field fluctuations, self-modulation becomes considerable mostly toward the end of the interaction, when exponential growth raises the field strength to a substantial level.

The interaction of an electron beam with a plasma can be made much more effective if the beam has been initially modulated by a high-frequency field /3, 6—12/. This is due to the following reasons: the amplitude of the initial field strengths is much higher than the amplitude of normal field fluctuations; the external high-frequency field may produce a certain grouping or bunching of particles in the beam, thus enhancing the coherence properties. If the modulation is very deep, the plasma—beam system will eventually settle to a state with oscillations which grow neither in time nor in space.

The interaction of modulated beams of charged particles with a plasma can be applied as a means of plasma heating, particle trapping, amplification and generation of high-frequency oscillations /3/, and also as a tool in the development of new techniques of charged particle acceleration.

The exponential growth of instability is attributable to the fields resulting from instability, which enhance the grouping of the particles and this in turn amplifies the field. Deep modulation at a given frequency corresponds to a state of limiting grouping, so that further increase of field strength does not affect the beam, and the fields do not grow. Preliminary modulation at a certain frequency destroys the grouping of particles at all other frequencies and thus cuts off a whole spectrum of instabilities. The excitation of plasma oscillations, however, must not satisfy the coherence conditions $a < \lambda_{\mathrm{pl}}$, where a is the length of the bunch of particles. To this end it suffices to take the modulation wavelength λ_m equal to $a/2$. Although modulation eliminates the ordinary instabilities, it may lead to instabilities connected with parametric resonances. But since the width of the parametric resonances is small, the inhomogeneities and the interparticle collisions occurring in real plasmas will damp these instabilities.

The interaction of a modulated beam with a plasma depends on the method of modulation. For example, with klystron modulation the bunching of particles is conditioned by the difference in their velocities. The klystron technique in some cases will therefore attenuate or even suppress the growth of the instability owing to the large spread of velocities in the beam.

In our experiments the initial modulation was produced using a short helix ($L_h < L_{in}$, where L_h is the length of the helix, L_{in} the length of the plasma interaction space). In this case, klystron or phase grouping could be imposed depending on the length of the helix. Since no complete theoretical solution is available for the interaction of an electron beam modulated in this way with a plasma, we shall give some tentative estimates suggesting how the interaction can be made more effective by means of initial modulation.

In the interaction of an unbounded plasma with a modulated electron beam where the current density j varies as

$$j = \delta j_0 \exp\{i(\omega t - k_3 z)\},$$

the maximal strength of the electric field generated in the system is

$$E_z^0 = \frac{2\pi\delta j_0}{\nu},$$

where δ is the modulation depth of the electron beam, ν the collision frequency /8/. This relation has been derived for a case when the temperatures of the beam and the plasma are neglected and the beam current is assumed constant. This means that the reaction of the field is neglected when considering the behavior of the beam. For a current density $j_0 = 5\ \mathrm{A/cm^2}$, modulation depth $\delta \sim 0.1$, and collision frequency $\nu = 10^8\ \mathrm{sec^{-1}}$, we have

$$E_z^0 \sim 30\ \mathrm{kV/cm}.$$

The interaction of a plasma with an electron beam modulated by a pair of grids has been considered in /7/. It follows from this paper that the field strength in the plasma—beam system is related with the modulating voltage by the expression

$$E = V_0 \frac{\omega_0^2 e^{\gamma_{am} z}}{8\pi v_0 \left(1 - \frac{\omega_0^2}{\omega^2}\right)\omega}$$

on the assumption $\left(1 - \frac{\omega_0^2}{\omega^2}\right) \approx \frac{\gamma}{\omega_0}$ and $\gamma \approx \left(\frac{n_1}{n_0}\right)^{1/3}\omega_0$, where V_0 is the modulating voltage, ω_0 plasma frequency, ω modulation frequency, v_0 velocity of the beam, γ_{am} amplification ratio, γ growth increment, n_1 beam density, n_0 plasma density. For a current of 5 A, modulation voltage amplitude of 100 V, and interaction length of 32 cm, this formula gives 6 kV/cm for the field strength at the end of the system. These numbers should be treated as tentative estimates only, since in our case the modulation is produced by a short helix.

In the present paper we consider the results of experimental studies of the interaction of modulated high-current pulsed electron beams with a plasma in a longitudinal magnetic field. It is shown that under certain conditions, the initial modulation intensifies the plasma—beam interaction to a considerable extent. The field of the longitudinal waves excited in the beam and in the plasma is substantially smaller (approximately 1/7) than the field generated in the absence of modulation. The experimental results are interpreted.

Equipment

A block-diagram of the experimental equipment is shown in Figure 1. A previously described electron gun /15/ was used as a source of electrons. An electron beam 10—11 mm in diameter carrying a current of up to 5 A, 50 c/s passed through a modulating helical coupler, a plasma chamber, and a demodulating helical coupler and hit the collector. High-frequency oscillations of known frequency and constant power were fed from a special generator through a coaxial cable to the modulation helix, where the electron beam entering the plasma chamber acquired its initial modulation. The helical coupler was also used to set up a pressure gradient from $1.33 \cdot 10^{-3}$ to $2.66 \cdot 10^{-1}$ N/m^2 between the electron gun enclosure and the plasma chamber. The modulating helical coupler is a system comprising two helixes wound in opposite directions (the radius of the inner helix ~ 0.6 cm, the radius of the outer helix ~ 1.2 cm). One of the helixes was inserted in a glass tube with i.d. of 13 mm, and the other, shorter helix was fitted from the outside. The helix parameters were chosen so that the phase velocity of a wave traveling through the helix was approximately equal to the velocity of the electron beam and, hence, to the phase velocity of a wave propagating in the plasma. The glass tube was coupled to vacuum at either end.

The external helix was connected to a coaxial cable with an impedance of 75 ohm. The inner helix was dc-coupled to a "grounded" electrode. The ends of the glass tube were coated with Aquadag. The electrons impinging on the end surfaces of the glass tube and on the helix thus escaped to ground. The length of the helical coupler was some 12 cm. The voltage standing wave ratio (VSWR) at the input of this coupler did not exceed 2.0 in the range of 650—5000 Mc/s. The beam was initially modulated at frequencies of 835 and 900 Mc/s, with VSWR ≤ 1.4. The standard measurements were made without the electron beam. The VSWR, however, hardly changes when an electron beam passes through the helix.

Passing through the plasma chamber, the electron beam ionized the residual gas (air), created a plasma, and interacted with it. The density of the plasma was measured by a technique based on the properties of plasma waveguides /13/. For the optimal case of interaction at a pressure of $2.66 \cdot 10^{-2}$ N/m^2, the density is $2 \cdot 10^{10}$ cm^{-3} without initial modulation (5 A, 21 keV electron beam, magnetic field strength $1.03 \cdot 10^5$ A/m). The density of the plasma created by a beam initially modulated at a frequency of some 835 Mc/s with a power of 600 W was found to be $2.5 \cdot 10^{10}$ cm^{-3}.

Having passed through the plasma chamber, the beam entered a demodulation helix and then hit the collector. In this helix the beam gave

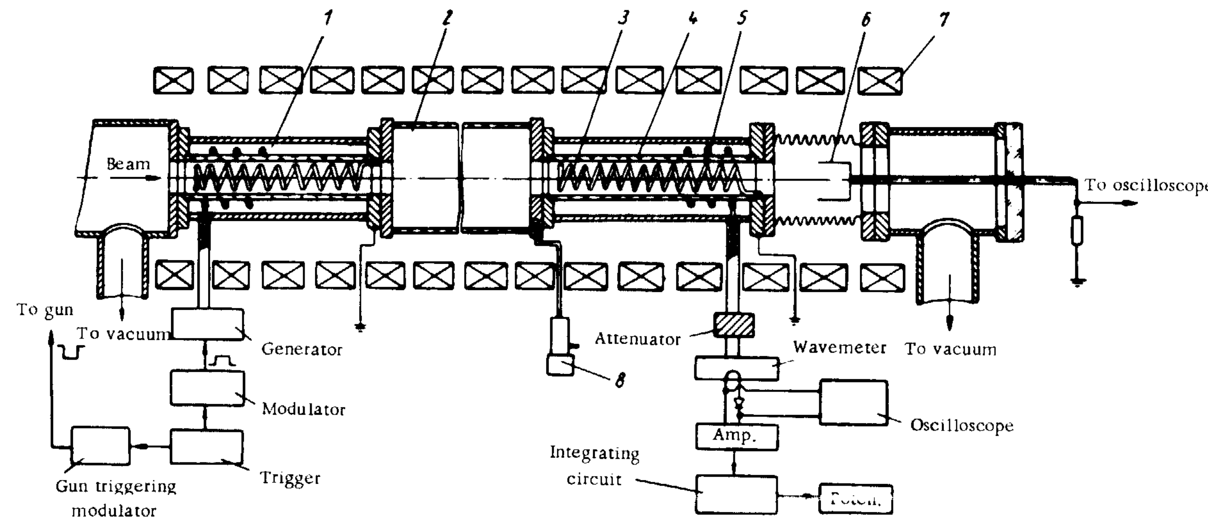

FIGURE 1. Block-diagram of the system for studying the interaction of modulated electron beams with a plasma in a longitudinal magnetical field:

1) first helical coupler; 2) plasma chamber; 3) inner helix of the second helical coupler; 4) glass tube; 5) external helix; 6) current collector; 7) solenoid setting up a longitudinal magnetic field; 8) capillary leak.

off its r-f power. The design and the specifications of the demodulation coupler are entirely analogous to those of the modulation helix, with the exception of some technical details. The length of the second coupler 15 cm. The axial clearance in the second helical coupler was 15 mm, and not 10.5 mm as in the first coupler, to allow for the radial spread of the beam in the system. This system transmitted to the collector 75—80% of the total current of the beam interacting with the plasma.

The high-frequency oscillations induced in the demodulation helix were transmitted to a resonance wavemeter, passing through a coaxial line with a 75 ohm impedance and through locked attenuators. From the crystal

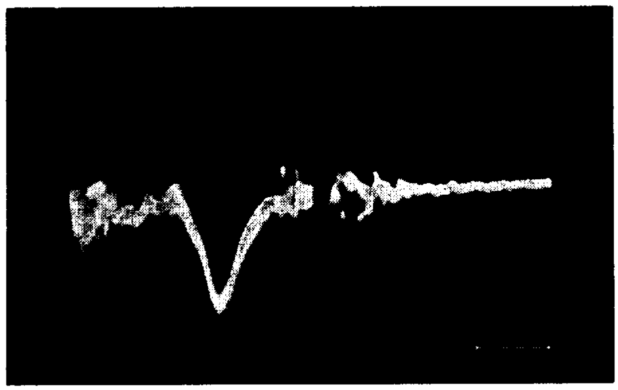

FIGURE 2. Oscillogram showing the variation of r-f power in time (at the output of the plasma – beam system): beam current 5 A, energy 21 keV, longitudinal magnetic field $1.03 \cdot 10^5$ A/m, modulation frequency 835 Mc/s; scale 1 μsec.

detector at the wavemeter output, the signal was fed to the vertical input of an oscilloscope. A specimen oscillogram for a 5 A current taken at a frequency of 835 Mc/s is shown in Figure 2.

The peak r-f power was determined as in the preceding experiments, using locked attenuators and a calibrated wavemeter with a passband half-width of 1.5 Mc/s. The wavemeter with a crystal detector was initially calibrated by means of a standard generator. An oscilloscope and a wide-band amplifier were connected in parallel at the wavemeter output; the amplifier was coupled through a cathode follower into an integrating circuit and an electronic potentiometer EPP-09.

When the frequency of the resonance wavemeter was varied, the potentiometer recorded the frequency spectra of the oscillations excited in the electron beam (frequency-amplitude plots).

Results of measurements

The frequency spectra were recorded for oscillations resulting from the interaction of a plasma with initially modulated and unmodulated electron

beams carrying currents of 5, 3.8, and 2.3 A. The current reaching the collector was 4, 3 and 2 A, respectively. The energy of the beam was 21 keV, strength of longitudinal magnetic field some $1.03 \cdot 10^5$ A/m. The

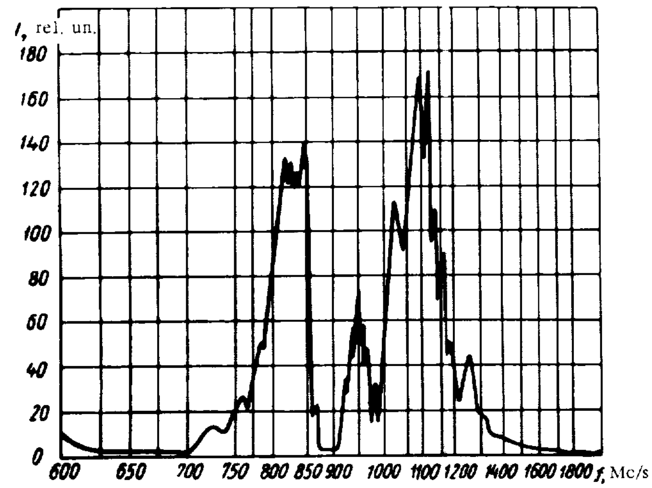

FIGURE 3. Spectrum of oscillations in an initially unmodulated electron beam:
beam current 5 A, beam energy 21 keV, strength of longitudinal magnetic field $1.05 \cdot 10^5$ A/m, pressure $2.66 \cdot 10^{-2}$ N/m^2.

intensity of the oscillations was the highest for air pressure of $\sim 2.66 \cdot 10^{-2}$ N/m^2 in the plasma chamber. The spectrum of the oscillations in an initially unmodulated electron beam of 5 A current at the end of the interaction path is shown in Figure 3.

We see from the graph that peak power is registered at frequencies of 800—840 and 1000—1150 Mc/s. No oscillations with frequencies $\sim$ 900 Mc/s occur in the spectrum. The maximal specific power of the oscillations for 5 A current is 120—150 W. The specific power for 3.8 and 2.3 A currents is 70 and 19 W, respectively. The beam was modulated at frequencies of 835 and 900 Mc/s. The generator operated in the 700—950 Mc/s frequency range, with a power output of 1—16 W in the continuous mode of operation and 3—600 W in the pulsed mode (pulse length 10 μsec).

In the pulsed mode of operation, the generator was actuated by a special triggering circuit synchronized with the pulsed line feeding the electron gun. Initial modulation at a frequency of 900 Mc/s gave a spectrum which contained the oscillations of an unmodulated beam (800—840 and 1000—1150 Mc/s), as well as oscillations with a frequency of 900 Mc/s and a specific power equal to 1/2—1/2.5 of the initial modulation power. For example, with 600 W modulation power, the modulation-frequency oscillations (900 Mc/s) registered at the output had a power of 300 W. The frequency spectrum of oscillations in a beam with a 5 A current modulated at a frequency of 900 Mc/s is shown in Figure 4.

For initial modulation at 835 Mc/s, the plasma—beam system acts as an amplifier: amplified signals of considerable intensity are registered

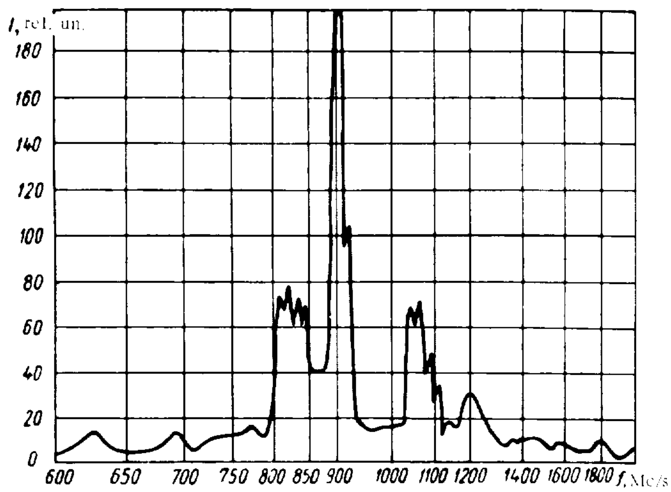

FIGURE 4. Spectrum of oscillations in an electron beam modulated at 900 Mc/s (other parameters as in Figure 3).

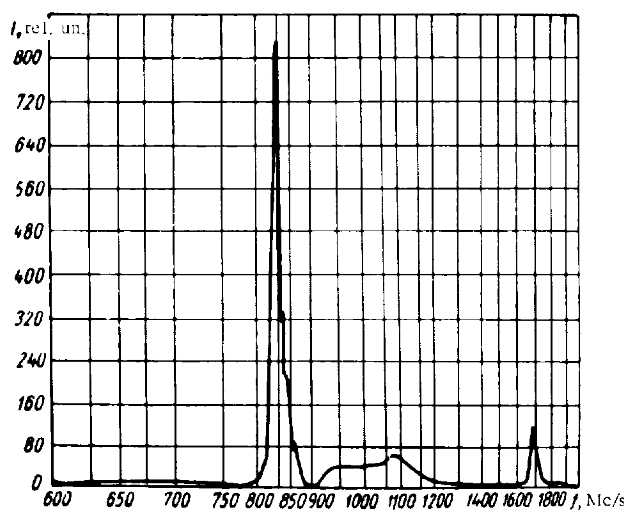

FIGURE 5. Spectrum of oscillations in an electron beam modulated at 835 Mc/s (other parameters as in Figure 3).

at its output (with a pass halfwidth of 8 — 10 Mc/s). The frequency spectrum of oscillations in a beam with a 5 A current modulated at 835 Mc/s is shown in Figure 5.

Comparing the spectra of modulated and initially unmodulated beams (Figures 3 and 5), we see that modulation suppresses oscillations in a broad frequency band. The power of the oscillations generated at the

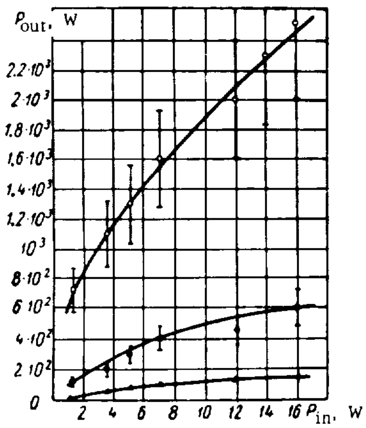

FIGURE 6. Power of high-frequency oscillations at the output of the plasma — beam system as a function of modulation power for various currents: ○ 5 A, ● 3.8 A, △ 2.3 A; modulation frequency 835 Mc/s.

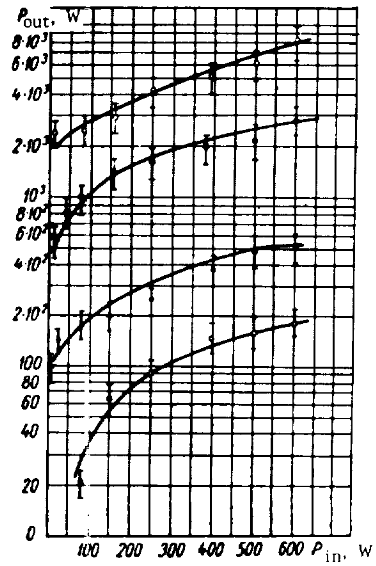

FIGURE 7. Power of high frequency oscillations at the output of the plasma — beam system as a function of modulation power for various currents: ○ 5 A, ● 3.8 A, △ 2.3 A; modulation frequency 835 Mc/s; □ the second harmonic (1670 Mc/s) for 5 A current.

modulation frequency 835 Mc/s, however, is considerably amplified (from 120 — 150 W in unmodulated beams to 8 kW for modulation with 600 W power).

Figures 6 and 7 give the peak output power of the amplified oscillations as a function of the initial modulation power (1 to 600 W) at a frequency of 835 Mc/s for currents of 5, 3.8, and 2.3 A. Identical results were obtained for continuous and pulsed operation of the generator, and all the experimental points closely fit the corresponding curves. Hence it follows that the running mode of the generator does not influence the results.

We see from the graphs (Figures 6 and 7) that the amplification of the plasma — beam system increases with the current of the beam. By amplification in this case we mean the ratio of the r-f power at the output to the power of the modulating signal. The amplification for a system length of 40 cm is equal to 12, 19, and 26 db for currents of 2.3, 3.8, and 5 A, respectively. The amplification of the plasma — beam system falls off with increasing modulation power. It decreases from 26 db for 5 A current with modulation signals of a few watt to 11 db with 600 W modulation

(for the same interaction length). For a 2.3 A current, the amplification is 12 db for low-power modulation (a few watt), reaching saturation at 500—600 W input.

The electric fields in the beam resulting from its interaction with the plasma were determined at the end of the interaction path. Since the phase velocity of the wave is approximately equal to the velocity of the beam and, hence, to the phase velocity of the wave propagating in the demodulation helix, and since there is no dispersion in the frequency range being considered, we can find the r-f electric field in the beam from the relation

$$E = 300\sqrt{\frac{4\pi P}{v}},$$

where P is the flux of r-f energy transported by the electron beam, erg/cm^2; E the electric field strength, V/cm; v the phase velocity of the wave in the beam, cm/sec.

Our measurements show that the electric field of the longitudinal charge—density wave at the end of the interaction path is approximately equal to 0.45 kV/cm for an initially unmodulated electron beam and 3.2 kV/cm for a modulated beam (600 W modulation power, 5 A current). Initial modulation of the electron beam thus enhanced the electric field of the longitudinal charge—density wave approximately by a factor of 7.

We see from the graph in Figure 5 that for initial modulation at 835 Mc/s, overtones of the modulation frequency, as well as the fundamental harmonic, are observed; none of these overtones appear in the frequency spectra of the modulating generator and the initially unmodulated beam. Figure 5 shows the plot of the second harmonic (1670 Mc/s). The power of this overtone increases with the modulation power. For 600 W modulation power, the power of the second harmonic at the end of the interaction path is 180 W.

Six harmonics (including the fundamental frequency) were recorded in our experiments. The table lists the power of the first six harmonics for

No. of harmonic	Frequency, Mc/s	Peak power, W
1	835	$8\cdot10^3$
2	1670	180
3	2505	7
4	3340	0.2
5	4175	10^{-3}
6	5010	10^{-4}

a beam with 5 A current and 600 W modulation power. We see from the table that the amplitudes decrease from one harmonic to the next higher one.

The axial distribution of the E_z-component of the r-f field in the plasma was measured. The block-diagram of the equipment is shown in Figure 8. Reflection at the ends of the plasma chamber was avoided by providing a graphite cone which acted as an adiabatic absorbing load for waves propagating in the plasma. This cone also served as a current collector. A coaxial cable with a half-wavelength dipole was moved along the axis, measuring the E_z-component of the r-f field.

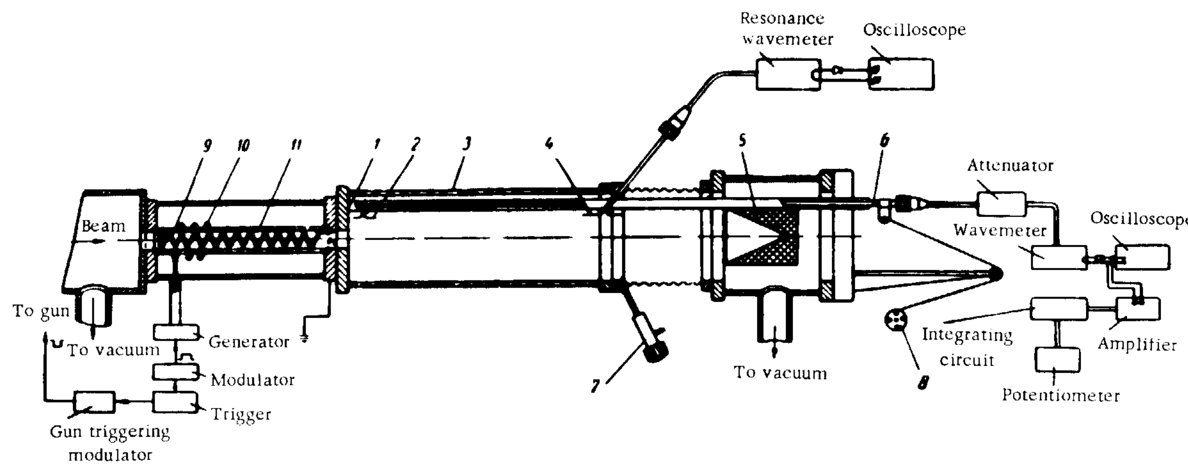

FIGURE 8. Block-diagram of the system for measuring the axial distribution of the E_z-component of the r-f field:
1) guide; 2) half-wavelength dipole; 3) plasma chamber; 4) receiving antenna (fixed); 5) adiabatic load (current collector); 6) coaxial cable; 7) capillary leak; 8) motor DR-09; 9) inner helix; 10) external helix; 11) glass tube.

The graphs of the axial distribution of the E_z-component of the r-f field for various modulation powers (50, 80, 350 W) and constant beam current (5 A) are given in Figure 9.

The axial distribution of the E_z-component of the r-f field for various beam currents (2.3, 3.8, and 5 A) and constant modulation power (600 W) is shown in Figure 10.

From these graphs we can calculate the amplification ratio for various beam currents and modulation powers. For 50 W modulation power, the

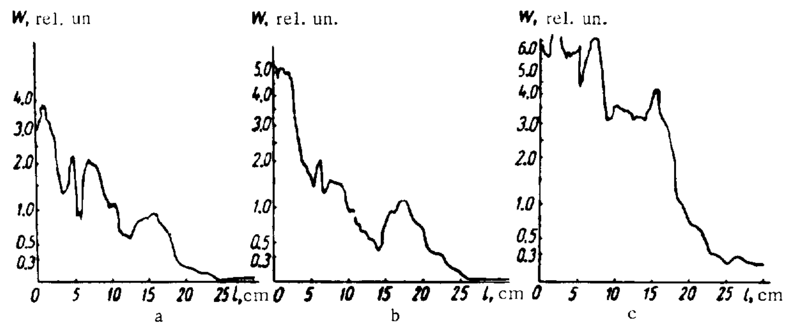

FIGURE 9. Axial distribution of the E_z-component of the r-f field in a plasma for various modulation powers and constant beam current (5 A): modulation frequency 835 Mc/s; a) 50 W; b) 80 W; c) 350 W.

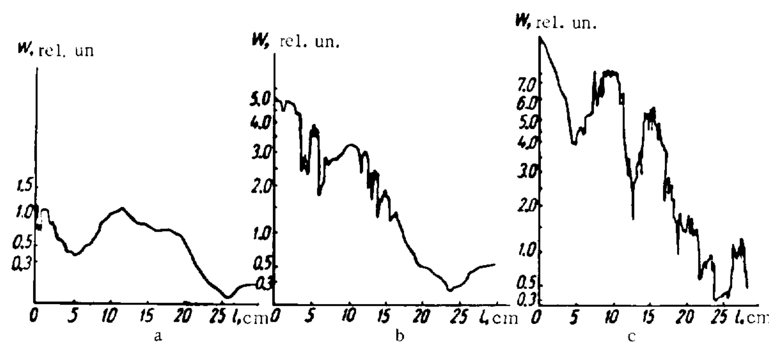

FIGURE 10. Axial distribution of the E_z-component of the r-f field in a plasma for various beam currents and constant modulation power (600 W): modulation frequency 835 Mc/s; a) 2.3 A; b) 3.8 A; c) 5 A.

amplification ratio is 0.08 cm^{-1}, and for 600 W modulation power it is 0.13 cm^{-1} (5 A current). For 600 W modulation power and currents of 5, 3.8, and 2.3 A, the amplification ratio is 0.13, 0.9, and 0.06 cm^{-1}, respectively.

The amplification ratio thus sharply increases with beam current and r-f modulation power.

It follows from our experiments that the interaction of a modulated electron beam with a plasma is more effective than the interaction of an

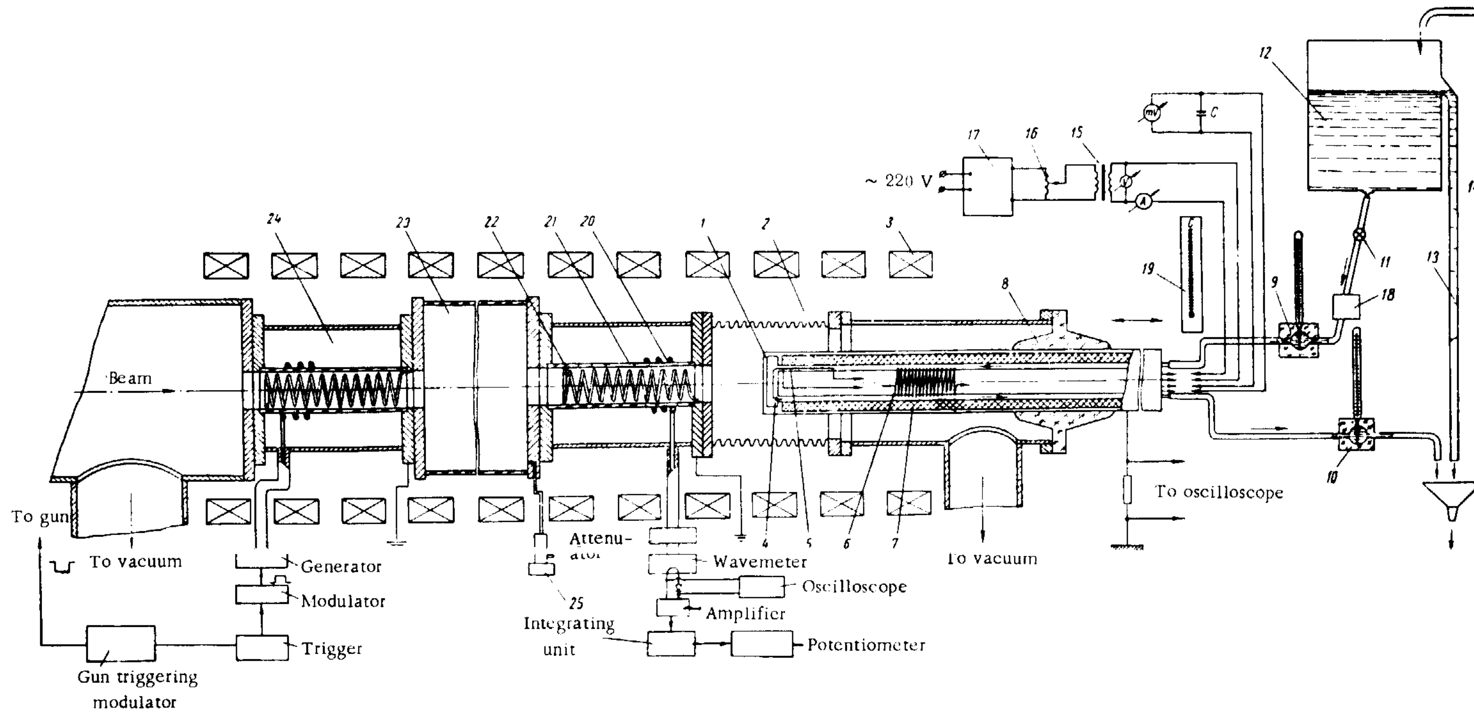

FIGURE 11. Block-diagram of the system for measuring the excess energy losses of a modulated beam:
1) calorimeter; 2) bellows; 3) solenoid; 4) water-cooled calorimeter chamber; 5) calibrating element; 6) thermopile; 7) thermal insulation; 8) plexiglas insulator; 9) thermometer measuring the temperature of the water entering the calorimeter; 10) thermometer measuring the temperature of the water leaving the calorimeter; 11) stopcock regulating the flow of water; 12) water tank; 13) overflow pipe; 14) water supply; 15) 220/20 V transformer; 16) variac; 17) electronic stabilizer; 18) device for removing air bubbles from the water; 19) thermometer measuring the ambient temperature; 20) external helix; 21) glass tube; 22) inner helix; 23) plasma chamber; 24) modulating helical coupler; 25) capillary leak.

initially unmodulated beam. In other words, a modulated electron beam passing through a plasma gives off a higher proportion of its energy than an initially unmodulated beam does.

To confirm this conclusion, a high-sensitivity calorimeter was applied to measure the mean energy of a 5 A, 21 keV electron beam passing through the demodulation helix; measurements were made for initially unmodulated beams and beams modulated at 835 Mc/s with a power of 600 W.

The block-diagram of the equipment is shown in Figure 11. The mean energy of the electron beam was measured with a calorimeter to within $\pm 1 - 1.5\%$. The calorimeter was provided at the end of the interaction path. The variation of the energy of a modulated beam was determined from these measurements. The energy loss of a modulated electron beam was $7 \pm 3\%$ higher than the energy loss of an initially unmodulated beam under identical conditions (beam current 5 A, energy 21 keV, longitudinal magnetic field $1.03 \cdot 10^{-5}$ A/m). Calorimetric measurements thus confirm the results of previous measurements.

Conclusions

The experiments show that initial modulation of an electron beam (beam current 5 A, energy 21 keV, modulation power 600 W) raises the energy losses in plasma—beam interactions by $7 \pm 3\%$ in comparison with the losses registered for an initially unmodulated beam under identical conditions. The specific power of the oscillations excited in a modulated electron beam is substantially higher (approximately by a factor of 60) than the high-frequency power in an unmodulated beam; the power of the oscillations at ~ 835 Mc/s is as high as 8 kW at the system output. Excitation of oscillations at 835 Mc/s is accompanied by a suppression of oscillations near 1100 Mc/s. The halfwidth of the frequency spectrum of the oscillations is substantially smaller (1/5—1/7), and the electric field of the oscillations set up in the modulated beam is substantially higher (by a factor of 7) than without modulation, reaching a strength of 3.2 kV/cm at the end of the interaction path.

BIBLIOGRAPHY

1. AKHIEZER, A. I. and Ya. B. FAINBERG. – DAN SSSR, **69**: 555. 1949.

2. AKHIEZER, A. I. and Ya. B. FAINBERG. – JETP, **21**: 1262. 1951.

3. FAINBERG, Ya. B. Atomnaya Energiya, **11**: 313. 1961.

4. KHARCHENKO, I. F., Ya. B. FAINBERG, R. M. NIKOLAEV, E. A. KORNILOV, E. I. LUTSENKO, and N. S. PEDENKO. – JETP, **38**: 685. 1960.

5. KHARCHENKO, I. F., Ya. B. FAINBERG, R. M. NIKOLAEV, E. A. KORNILOV, E. I. LUTSENKO, and N. S. PEDENKO. – In: "Fizika plazmy i problemy upravlyaemogo termoyadernogo sinteza", Vol. 2, p. 118. Kiev, Izdatel'stvo AN UkrSSR. 1963.

6. FAINBERG, Ya. B. – In: "Fizika plazmy i problemy upravlyaemo,o termoyadernogo sinteza", Vol. 1, p. 20. Kiev, Izdatel'stvo AN UkrSSR. 1962.

7. FAINBERG, Ya. B. and N. A. KHIZHNYAK. – In: "Fizika plazmy i problemy upravlyaemogo termoyadernogo sinteza", Vol. 1, p. 71. Kiev, Izdatel'stvo AN UkrSSR. 1962.

8. KONDRATENKO, A. N. – UFZh, 7: 371. 1962; In: "Fizika plazmy i problemy upravlyaemogo termoyadernogo sinteza", Vol. 3, p. 91. Kiev, Izdatel'stvo AN UkrSSR. 2963.

9. GLAZOV, O. A., L. V. DUBOVOI, and B. N. RUTKEVICH. – In: ". izika plazmy i problemy upravlyaemogo termoyadernogo sinteza", Vol. 2, p. 180. K.ev, Izdatel'stvo AN UkrSSR. 1963.

10. BOYD, G., L. FIELD, and R. GOULD. – Phys. Rev., **109**: 1393. 1958.

11. BOGDANOV, E. V., V. Ya. KISLOV, and Z. S. CHERNOV. – Radiotekhnika i Elektronika, **5**: 229. 1960.

12. KISLOV, V. Ya. and E. V. BOGDANOV. – Radiotekhnika i Elektronika, **5**: 229. 1960.

13. BEREZIN, A. K., G. P. BEREZINA, L. I. BOLOTIN, Yu. M. LYAPKALO, and Ya. B. FAINBERG. – In: "Fizika plazmy i problemy upravlyaemogo termoyaderi ogo sinteza", Vol. 3, p. 125. Kiev, Izdatel'stvo AN UkrSSR. 1963.

14. FAINBERG, Ya. B., V. I. KURILKO, and V. D. SHAPIRO. – ZhTF, 31: 633. 1961.

15. BEREZIN, A. K., V. G. STUPAK, G. P. BEREZINA, L. I. BOLOTIN, Yu. M. LYAPKALO, D. P. SOLOPIKHIN, and V. P. BONDARENKO. – PTE, **2**: 136. 1962.

E. A. Sukhomlin, V. A. Suprunenko, and N. I. Reva

SOME PROPERTIES OF A POWERFUL PULSED ELECTRON BEAM EMERGING FROM A PLASMA SOURCE

Powerful pulsed beams of "runaway" electrons were obtained in experiments with a plasma in strong electric fields, and these beams were allowed to emerge into a space free from electric forces.

The plasma was generated in a cylindrical alundum tube by a linear pinch discharge stabilized by a magnetic field. A condenser bank of 15 μF capacity and 30 kV discharge voltage was discharged through the electrodes of the tube. The discharge current reached 100 kA, with a period of 9 μsec, pressure from 13.3 to 0.133 N/m^2. Hydrogen was used as the working gas. A powerful pulsed beam of electrons passed through an 8 mm hole in the electrode (the source anode). The beam was transmitted through a dielectric channel to a distance of 10 cm from the electrode. The channel comprised a quartz tube with an i. d. of 8 mm. The residual gas pressure in the channel was 0.399 N/m^2. The beam fell on a current detector in the form of a Faraday cylinder with a carbon insert (to reduce secondary emission). The beam current was measured with a high-sensitivity Rogowsky loop provided on the current detector. The current detector was also equipped with a mechanism for its displacement in the vacuum: the position of the current detector relative to the electrode (the source anode) could thus be varied.

Preliminary experiments showed that the beam did not pass through a metallic channel, but was easily transmitted in the quartz tube. In the absence of an external magnetic field, the beam would not pass through the dielectric tube either. However, a comparatively low external magnetic field (0.1 T) sufficed to transport the beam to the current detector, which registered the stream of charged particles. Measurements of the current of fast electrons showed that the beam did not change over distances of up to 10 cm, abruptly stopping at the 10 cm mark.

Figure 1 shows the results of these measurements. The ratio H/H_0 characterizes the decrease of the external magnetic field, which does not vary much in the region up to 12 cm from the electrodes. It is therefore hardly possible to explain the current cutoff by this variation of the magnetic field.

The passage of the beam through the quartz tube can be visualized as follows. Emerging from the hole in the electrode, a dense beam (current

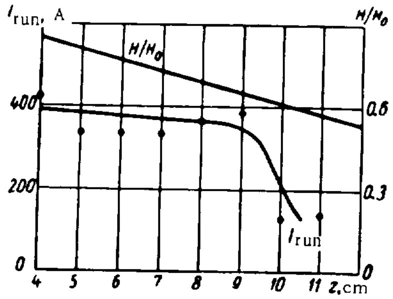

FIGURE 1. The current of fast electrons vs. distance from the electrode.

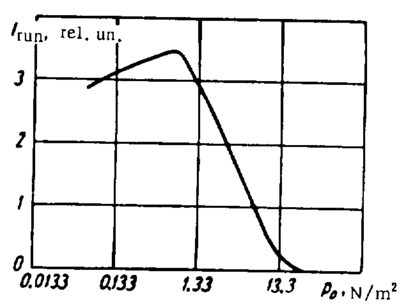

FIGURE 2. Electron current vs. initial pressure.

density $6 \cdot 10^6$ A/m²) of fast electrons ionizes the residual gas and creates a plasma which compensates the space charge. This permits the passage of the dense beam through the channel. However, instabilities set in, breaking up the beam. These instabilities have been described in several papers /1, 2/, and they may be responsible for the abrupt cutoff after the beam has covered a certain distance virtually without damping.

In this experiment we made a rough estimate of the energy of the electrons in the beam. The maximum energy registered with foils and a photographic plate was $1.6 \cdot 10^{-15}$ J.

We determined the optimal régime of discharge, corresponding to the peak current of "runaway" electrons. The peak current was attained for an initial pressure $p_0 = 0.399$ N/m² (Figure 2). The corresponding magnetic field was 0.5 T, and the interelectrode voltage 12 kV.

BIBLIOGRAPHY

1. BEREZIN, A.K., V.G. STUPAK, A.I. BOLOTIN, and G.P. BEREZINA. — ZhTF, 32: 600. 1962.
2. KHARCHENKO, I.F., Ya.B. FAINBERG, R.M. NIKOLAEV, E.A. KORNILOV, E.I. LUTSENKO, and N.S. PEDENKO. — ZhTF, 31: 761. 1961.

E. A. Kornilov, O. F. Kovpik, Ya. B. Fainberg, and
I. F. Kharchenko

CHARACTERISTICS OF A PLASMA GENERATED BY AN ELECTRON BEAM WITH THE ONSET OF INSTABILITY

The ionization of a gas by a beam of electrons is generally little effective. The density of the plasma generated by this ionization cannot be much higher than the beam density /1, 2/. However, with the onset of instability in an electron beam passing through a plasma, the plasma density under certain conditions may exceed the beam density by several orders of magnitude. The plasma is simultaneously heated /3–6/.

The onset of instability is accompanied by the excitation of high-frequency oscillations in the beam and in the plasma, and the observed increase in plasma density may be attributed to the enhanced ionization by plasma electrons accelerated in these high-frequency fields. No detailed analysis has been made of the actual mechanism of generation of a dense plasma by this enhanced ionization.

The aim of this paper is to study the mechanism of plasma generation with the onset of instability and to measure the parameters of this plasma. A schematic diagram of the experimental facility used is given in Figure 1.

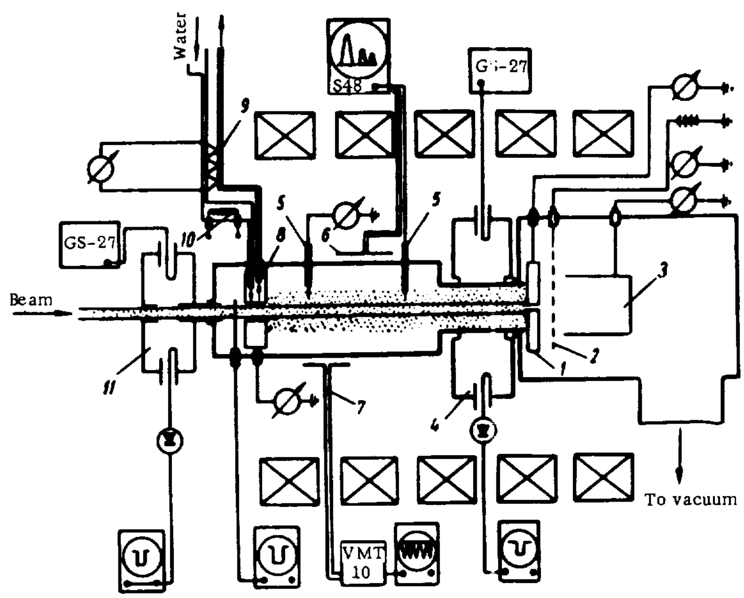

FIGURE 1. Schematic diagram of the machine.

An electron beam with an energy of 2–5 keV was fed at a rate of 10–50 mA into a glass envelope 10 cm in diameter and 40 cm long. The pressure in the envelope could be maintained between $1.3 \cdot 10^{-6}$ and $1.3 \cdot 10^{-3}\,N/m^2$. The length of the envelope, i.e., of the system, could be varied. The envelope was immersed in a magnetic field of 0–160 A/m. A particle

energy analyzer with a stopping field was provided at the outlet of the system. The analyzer comprises a collector diaphragm 1 with a hole 0.06 cm in diameter, 0.6 cm long (the collector potential could be varied), an analyzing grid 2 (mesh size 0.012 × 0.012 cm), and a Faraday cylinder 3.

The energy of the plasma particles was determined with a calorimeter 8. The temperature of the calorimeter was measured with a thermopile 9. The calorimeter was calibrated with the heating element 10. Plasma diagnostics was performed with Langmuir probes (single and double) 5 set at right angles to the magnetic field, a resonator 4 tuned to 3000 Mc/s, and a r-f interferometer (not shown) with a natural frequency of 10,000 Mc/s. The oscillations resulting from instability were registered with frequency analyzers and resonance wavemeters. R-f oscillations were picked up by a dipole antenna 7 mounted outside the envelope. Low-frequency oscillations were registered by the probes 5 and the antenna 6. The beam could be modulated using the resonator 11.

Figure 2 shows the plasma density in hydrogen as a function of gas pressure in the region of interaction. The plasma density was measured by the method of resonator mistuning, correcting for the change in formfactor. The current in the electron beam was 20 mA, the energy 4.5 keV. The density of electrons in the beam was 10^8 el/cm^3. The density curve is plotted for a magnetic field of $64 \cdot 10^3$ A/m.

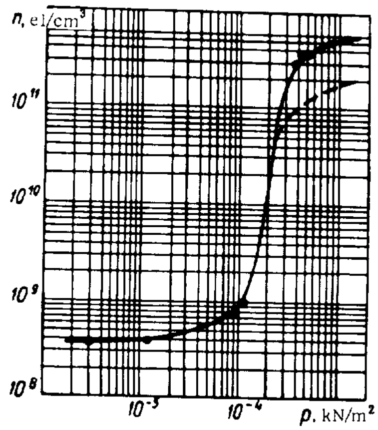

FIGURE 2. Plasma density vs. pressure in hydrogen.

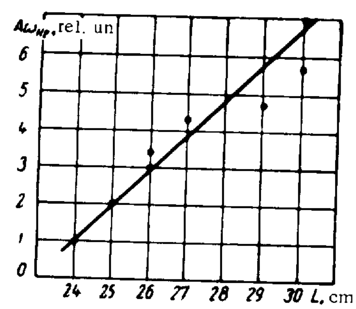

FIGURE 3. The amplitude of electron cyclotron oscillations as a function of system length.

The plasma density in the pressure range $10^{-5} - 10^{-6}$ kN/m^2 is approximately equal to the density of the beam; it sharply increases at a pressure of $2.7 \cdot 10^{-4}$ kN/m^2 reaching values of $5 \cdot 10^{11}$ el/cm^3. The plasma density does not remain constant in this peak region, varying by as much as 50% in time. The limits of plasma density are indicated in Figure 2 by the solid and the dashed curves. The frequency of density fluctuations depends on the particular gas employed. In argon, the fluctuation frequency is in the range of 10 – 300 kc/s, and in hydrogen, 10 – 1000 kc/s.

The growth of plasma density in argon and in air is observed for pressures of the order of 10^{-5} kN/m^2. The density of the plasma in these

gases also reaches values of the order of 10^{11} el. cm^3. The increase of plasma density is accompanied by an abrupt rise in glow intensity and a broadening of the plasma column. In argon and in air, the diameter of the column reaches 10 cm, and in hydrogen, 2 cm, for beams 0.3—0.5 cm in diameter.

The spectra and the intensity of the oscillations are measured as a function of pressure to establish their role in plasma generation. It has been found that at low pressures, of the order of 10^{-6} kN/m^2, low-intensity oscillations with frequencies of some 1—3 Mc/s (argon) are excited in the plasma. These frequencies correspond to the ion plasma frequency. The frequency of these modes increases linearly with the beam current, pressure, or magnetic field. The amplitude of the oscillations decreases with the increase of pressure or magnetic field. These oscillations vanish entirely near the critical pressure, corresponding to the sharp rise in density. It thus seems that these oscillations are not of a decisive significance in the process of plasma generation. Analogous oscillations arising under similar conditions have also been described in /7/.

Near the critical pressure, high-frequency oscillations of electron cyclotron frequency ω_{He} are the only ones observed. These oscillations vanish when the plasma density increases abruptly: they are converted into modes with $\omega \sim \sqrt{\omega_p^2 + \omega_{He}^2} \sim \omega_p$.

Figure 3 gives the amplitude of the electron cyclotron oscillations as a function of system length. Measurements were made with a dipole antenna inserted in the envolope at a distance of 20 cm from beam inlet. System length was varied by moving the collector. We see from the graph that the amplitude of these oscillations increases linearly with system length. The power of the oscillations is no less than 12—26 mW.

The excitation of electron cyclotron oscillations by an electron beam passing through a plasma is considered theoretically in /8/. If $\omega_p \ll \omega_{He}$, electron cyclotron instability may set in due to plasma—beam interaction conditioned by the Čerenkov effect or the anomalous Doppler effect in the region of anomalous wave dispersion of the plasma waveguide (the back wave). The respective frequency increments of the two effects are

$$\operatorname{Im}\omega = \frac{\sqrt{3}}{2^{4/3}}\left[\frac{a_2\omega_p^2\omega_{He}\omega_b^2}{V_0^2\lambda_p^2}\right]^{1/3};$$

$$\operatorname{Im}\omega = \frac{\omega_p\omega_b}{2\omega_{He}},$$

where ω_p is the electron plasma frequency, ω_b the plasma frequency of the beam, ω_{He} the electron cyclotron frequency, a the radius of the plasma, V_0 the velocity of the beam, λ_p the root of Bessel's function. The two increments have the same order of magnitude under our conditions. The numerical values of the increments are such that, for an interaction length of 30 cm, the r-f fields resulting from instability may easily grow to a level sufficient for the breakdown of the residual gas.

When the density rises abruptly, the ω_{He} modes vanish. Much stronger oscillations with a frequency $\omega_p \lesssim \omega < (\omega_p^2 + \omega_{He}^2)^{1/2}$ grow in this region /3/. In this case $\omega_p > \omega_{He}$ and the onset of instability is connected with the Čerenkov effect in the region of anomalous wave dispersion of the plasma waveguide.

The curve plotting the intensity of these oscillations as a function of pressure is shown in Figure 4.

The process of plasma generation can thus be described as follows. Electron cyclotron instability sets in when a beam of electrons passes, in the presence of a longitudinal magnetic field, through the plasma generated

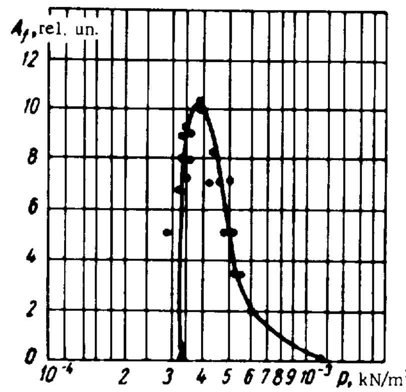

FIGURE 4. The amplitude of high-frequency oscillations as a function of pressure in hydrogen.

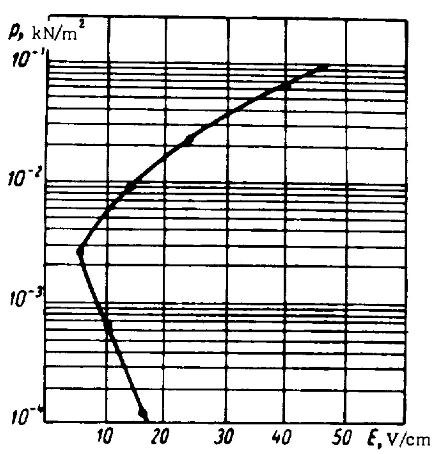

FIGURE 5. Critical pressure as a function of the electric field in hydrogen.

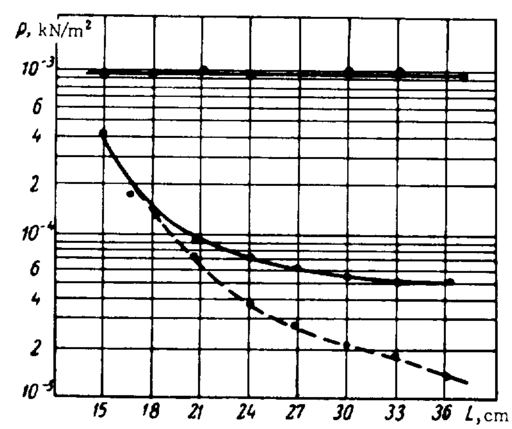

FIGURE 6. Critical pressure as a function of system length in argon.

by the ionization of the gas with the electrons of the beam. At a certain pressure, breakdown of the gas occurs at the electron cyclotron frequency. The critical pressure apparently specifies the conditions under which the plasma electrons, moving between successive collisions in the r-f field of the wave, acquire energy sufficient for the ionization of the gas.

The existence of a critical pressure has been established in experiments with the breakdown of gases in conditions of electron cyclotron resonance /9—11/. Figure 5 plots the critical pressure in hydrogen as a function of

the r-f electric field. The curve is based on experimental data from /9, 10/. For a constant electric field, there is a range of pressures where breakdown is observed in conditions of electron cyclotron resonance at a frequency of 3000 Mc/s. The power of the high-frequency oscillations leading to breakdown is no more than few tenths of a milliwatt.

The minimal field strength when breakdown may occur is 5 V/cm at a pressure of $2.6 \cdot 10^{-3}$ kN/m^2. The range of pressures where breakdown occurs broadens as the strength of the r-f field increases. The field strength in our case can be regulated by varying the length of the system (see Figure 3). Therefore, plotting the breakdown pressure as a function of the interaction length, we obtain the variation of the range of critical pressures with the r-f field. These curves are shown in Figure 6 for argon and Figure 7 for hydrogen. In Figure 6, the dashed line marks the

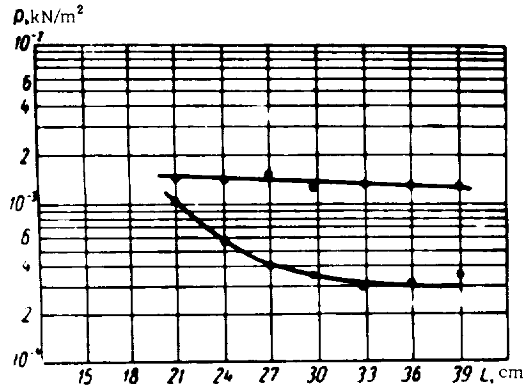

FIGURE 7. Critical pressure as a function of system length in hydrogen.

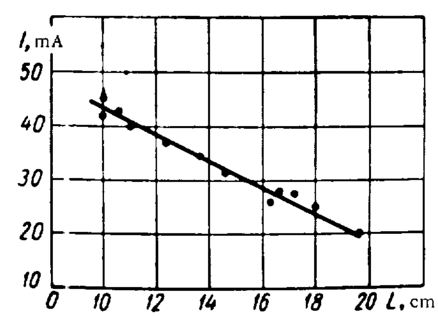

FIGURE 8. Critical length as a function of the electron beam current.

constriction of the discharge when passing from high to low pressures. We see from the graphs that a certain minimal length exists when breakdown is just possible. This length sets the minimal field strength for which breakdown may occur at any given frequency. The critical length in hydrogen is greater than that in argon. The range of critical pressures is narrower in hydrogen. These features are attributable to the higher ionization cross section of argon.

Figure 8 plots the critical length as a function of the beam current for constant pressure and magnetic field. This length decreases with the increase of current. This variation of critical length is attributable to the growth of the high-frequency oscillations with the increase of beam current /12, 13/.

As we have previously observed, the plasma density reaches values of 10^{11} el/cm^3 on breakdown, and the frequency of the oscillations is close to ω_p. After that, the plasma density is sustained by these oscillations. Periodic variation of plasma density in time in this region is attributable to a change in the efficiency of the interaction due to the Čerenkov effect in the region of anomalous wave dispersion.

Measurements of the energy of a beam emerging from the plasma show that the beam is stopped when the plasma density rises abruptly. The r-f power radiated at that time from the plasma accounts for no more than a few percent of the total beam power. The kinetic energy of the beam is thus largely expended in the creation and the heating of the plasma. In our case, with a beam of 80 W, a plasma with 10% ionization has been created in argon, and with 1% ionization in hydrogen.

Measurements of ion energies during plasma generation, made with an energy analyzer with a stopping field and a calorimeter, gave values of 40–200 eV for the energy of the ions. It is not clear at present how the ions are accelerated in this plasma.

We have established experimentally that the acceleration of the plasma electrons in the field of the high-frequency oscillations which are excited in a plasma with the onset of instability and the ionization of the residual gas by these electrons suggest the harnessing of the kinetic energy of electron beams for the creation of dense plasmas.

BIBLIOGRAPHY

1. FIELD, L. M., K. SPANGENBERG, and R. HELM. – Electr. Comm. **24**(1): 108. 1947.
2. HINES, M. E., G. W. HOFFMAN, and A. SALOOM. – J. Appl. Phys., **26**(9): 1157. 1955.
3. KHARCHENKO, I. F., Ya. B. FAINBERG, E. A. KORNILOV, R. M. NIKOLAEV, E. I. LUTSENKO, and N. S. PADENKO. Plasma Physics Conference Paper, Salzburg. 1962.
4. SMULLIN, L. D., and W. D. GETTY. – Phys. Rev. Lett., **9**: 13. 1962.
5. HEDVAL, P. – J. Appl. Phys., **33**(8): 2426. 1962.
6. KHARCHENKO, I. F. Ya. B. FAINBERG, E. A. KORNILOV, N. S. PEDENKO, E. I. LUTSENKO, and R. M. NIKOLAEV. – ZhTF, **31**(7): 761. 1961.
7. FEDORCHENKO, V. D., V. I. MURATOV, and B. N. RUTKEVICH. – ZhTF, **32**(8): 958. 1962.
8. GORBATENKO, M. F. – ZhTF, **32**: 1070. 1963.
9. BROWN, S. Elementary Processes in the Plasma of a Gas Discharge. – [Russian translation. 1961.]
10. DRUMMOND, J. E., ed. Plasma Physics. McGraw-Hill Book Co. Inc. 1961.
11. KELLY, D. C., H. MARGENAW, and S. C. BRAWN. – Phys. Rev., **108**: 1367. 1957.
12. AKHIEZER, A. I. and Ya. B. FAINBERG. – DAN SSSR, **69**: 559. 1949; JETP, **21**: 1262. 1951.
13. BOYD, G. D., R. W. GOULD, and L. M. FIELD. – Proc. IRE, **49**(12): 204. 1961.

V. D. Fedorchenko, V. I. Muratov, and B. N. Rutkevich

AZIMUTHAL R-F FIELDS IN PLASMA—BEAM INTERACTIONS

When an electron beam interacts with the plasma created by the same beam in a magnetic field of $2 \cdot 10^5$ A/m, oscillations with a frequency of some 50 Mc/s arise, propagating with a phase velocity of some $7 \cdot 10^6$ m/sec /1, 2/. Measurements carried out with probes and probing beams show that the electric field of the wave has a longitudinal component with an amplitude ~ 500 V/m, which plays an important part in the process of compensation and "overcompensation" of the space charge. The wave field E_z accelerates and removes from the channel those electrons which are formed in the ionization of the residual gases.

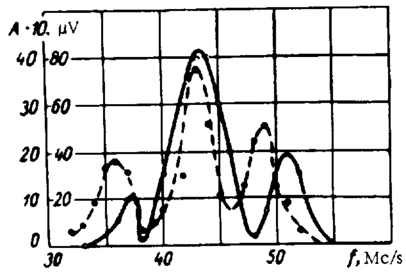

FIGURE 1. The spectra of the longitudinal and the azimuthal components of the r-f field: energy of electron beam U_n = 250 V, beam current I_n = 40 mA, pressure p = $266 \cdot 10^{-5}$ N/m², magnetic field H = $1.4 \cdot 10^5$ A/m, o E_φ-component, ● E_z-component.

Besides the longitudinal field, the beam also sustains transverse fields E_r and E_φ. The present paper describes some experiments concerned with the properties of the azimuthal fields E_φ.

The measurements were made with a moving screened loop set coaxially with the beam. The loop voltage was measured with a tube voltmeter VLU-2, the frequency with a spectrum analyzer ASSh-2 and a circuit-noise meter IP-26

The fields E_φ and E_z are correlated. They appear simultaneously when a certain pressure is established in the system. They have the same frequency. The frequencies of the fields E_φ and E_z vary with pressure,

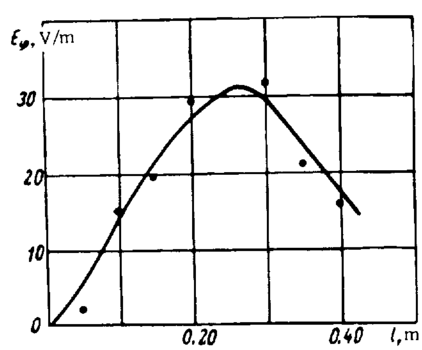

FIGURE 2. Axial distribution of the azimuthal field:
U_n = 250 V, I_n = 40 mA, p = $200 \cdot 10^{-5}$ N/m², H = $1.28 \cdot 10^5$ A/m, l distance between the measuring loop and the electron gun.

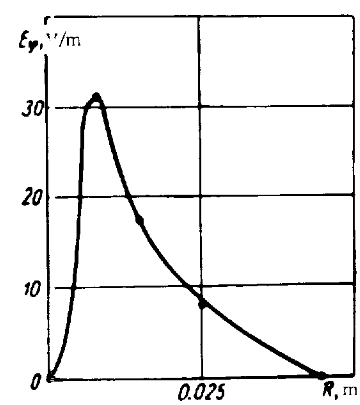

FIGURE 3. Radial distribution of the azimuthal field:
U_n = 250 V, I_n = 40 mA, p = $200 \cdot 10^{-5}$ N/m², H = $1.28 \cdot 10^5$ A/m, l = 0.25 m.

remaining equal to each other. We see from Figure 1 that the spectra of the E_φ and E_z fields obtained with a circuit-noise meter are virtually identical. All this suggests that the fields E_φ and E_z are the two components of a single wave propagating along the axis of the beam.

The amplitude of the azimuthal field reaches 50 V/m, which is approximately 1/10-th of the amplitude of the longitudinal r-f component E_z.

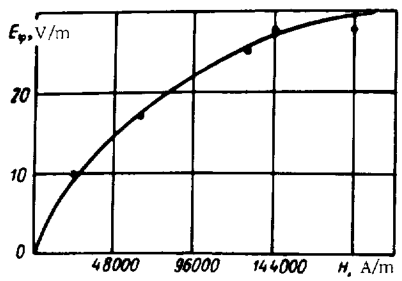

FIGURE 4. Azimuthal field E_φ as a function of the magnetic field H:
$U_n = 250$ V, $I_n = 40$ mA, $p = 200\cdot10^{-5}$ N/m^2, $l = 0.25$ m.

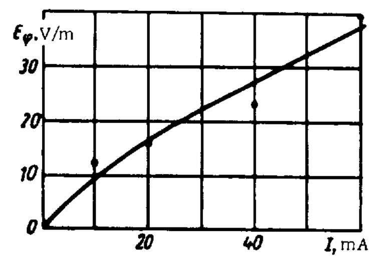

FIGURE 5. E_φ as a function of the current in the electron beam:
$U_n = 250$ V, $p = 200\cdot10^{-5}$ N/m^2, $H = 1.4\cdot10^5$ A/m, $l = 0.25$ m.

The amplitude is maximal at the center, falling off toward the ends of the vacuum envelope, limited from either side by the anode of the electron gun and the collector. Longitudinal and radial distributions are shown in Figures 2* and 3.

The amplitude of the oscillations increases with the magnetic field and the beam current (Figures 4 and 5). The amplitude, like frequency, is a function of pressure. It is maximal for pressures near $2\cdot10^{-3}$ N/m^2 (Figure 6).

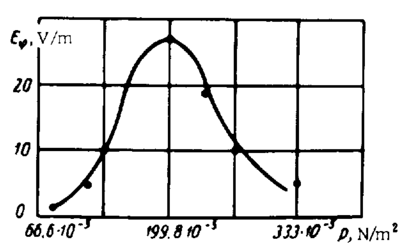

FIGURE 6. E_φ as a function of pressure in the vacuum chamber:
$U_n = 250$ V, $I_n = 40$ mA, $H = 1.4\cdot10^5$ A/m, $l = 0.25$ m.

The appearance of an azimuthal, as well as a longitudinal, component in a bounded plasma in the presence of a magnetic field is quite natural. Indeed, in a bounded plasma the space charge-density wave generates a longitudinal E_z and a transverse E_r field. For frequencies much less than the electron cyclotron frequency $\frac{e}{m}B$, the field E_r may lead to an azimuthal drift of the electrons, manifested in an azimuthal current I_φ. The latter results in a periodic variation of magnetic flux density, which induces an e.m.f. in the measuring loop. Taking the azimuthal field equal to 50 V/m and an oscillation frequency of 50 Mc/s, we can estimate the modulating magnetic field and the corresponding current, $I_\varphi \approx 20$ A/m.

* The effective field $E_\varphi = \frac{E_{\varphi,\mathrm{ampl}}}{1.4}$.

Note that in crossed fields E_φ and B_z the plasma particles should drift in radial direction. This drift could apparently be held responsible for the fast radial motion of particles forming in the ionization of residual gases. For beam diameters of ≈ 2 cm, these particles virtually fill the entire section of the chamber, which has a diameter of 9 cm, and set up longitudinal currents of some 1 mA.

It is obvious, however, that the r-f field E_φ that we have measured cannot produce radial drift of particles. In our experiment, when the frequency of the oscillations is much less than the electron cyclotron frequency (by two orders of magnitude), the motion of the electrons is adiabatic; the electrons therefore move together with the magnetic lines of force, which vibrate in the radial direction. The field E_φ detected with a rigid measuring loop does not affect the electrons which are "stuck" to the magnetic lines of force. Preliminary experiments indicate that the radial drift of particles is connected with low-frequency plasma oscillations (100 kc/s). These oscillations are not axially symmetric, and they set up transverse electric fields in which the particles drift in the radial direction.

BIBLIOGRAPHY

1. FEDORCHENKO, V. D., V. I. MURATOV, and B. N. RUTKEVICH. – In: "Fizika plazmy i problemy upravlyaemogo termoyadernogo sinteza", Vol. 3, p. 36. Kiev. Izdatel'stvo AN UkrSSR. 1963.

2. FEDORCHENKO, V. D., V. I. MURATOV, and B. N. RUTKEVICH. – In: "Fizika plazmy i problemy upravlyaemogo termoyadernogo sinteza", Vol. 3, p. 44. Kiev. Izdatel'stvo AN UkrSSR. 1963.

R. V. Mitin

THE ELECTRIC FIELD IN THE COLUMN OF A HIGH-PRESSURE LONG ARC

One of the aims of our experiments with high-pressure long arcs described in /1–3/ was to study, and if possible to explain, the influence of the gas pressure p and the current I on the electric field E in the arc. In /1/, the equations of the energy balance and Ohm's law in the discharge column were applied to explain the experimentally observed dependence $E(I, p)$. The limiting cases of high currents and pressures (radiation predominating) and of low currents and pressures (heat conduction predominating) were approximately considered, and simple formulas were derived qualitatively explaining the results of the experiments.

In the present paper we shall consider a general case, when both heat conduction and radiation must be introduced in the energy balance; the theoretical results will be compared with the experimental data /1/ (helium arc) and /2, 3/ (argon arc).

We write the equation of energy balance and Ohm's law using the symbols of /1/:*

$$IE = W_t + W_r = 2B\frac{T^{3/2}}{\sqrt{M}\,Q_a \ln\frac{R}{r}} + Cr^2pe^{-\frac{eV_i}{kT}}; \tag{1}$$

$$\frac{I}{E} = A\frac{r^2T^{3/4}}{Q_e\sqrt{p}}\,e^{-\frac{eV_i}{2kT}}. \tag{2}$$

As in /1/ it is assumed that the electric current flows in a channel of radius r, where the number density of the particles and the temperature are constant; the heat is transferred by conduction, a process governed by the temperature gradient in the gas surrounding the arc, and by recombination radiation** from the arc channel; the arc plasma is weakly ionized and transparent to radiation.

Eliminating the temperature from equation (1) and (2), we have

$$E^3 - aE^2 - b = 0, \tag{3}$$

where

$$a = \frac{2BT^{3/2}}{\sqrt{M}\,Q_a \ln\frac{R}{r}}\cdot\frac{1}{I}; \tag{4}$$

* The numerical values of the constants A and C given in /1/ apply for hydrogen-like atoms only. In the general case A must be replaced with $\left(\frac{g_i g_e}{g_a}\right)^{1/2}A$ (g_i, g_e, g_a being the statistical weights of the ion, the electron, and the atom). The constant C is a fairly complex function of the atomic species and it cannot be written in a simple form (see, e.g., /5/).

** The significance of the line emission of excited atoms will be considered in the following.

$$b = \frac{C}{A^2} \cdot \frac{Q_e^2}{T^{3/2} \cdot r^2} p^2 I. \tag{5}$$

We neglected the dependence of the coefficients a and b on T in comparison with the much steeper T-variation of the exponential terms.

It is easily shown that equation (3) has two imaginary roots and one real root (Cardan's formula), which is the relevant solution of our problem. This root has the form

$$E = \frac{a}{3} + \sqrt[3]{\frac{a^3}{27} + \frac{b}{2} + \sqrt{\frac{a^3 b}{27} + \frac{b^2}{4}}} + \sqrt[3]{\frac{a^3}{27} + \frac{b}{2} - \sqrt{\frac{a^3 b}{27} + \frac{b^2}{4}}}. \tag{6}$$

Expression (6) relating E, I, p, T, r will now be compared with the experimental function $E(I)$ obtained in /1—3/ for helium and argon arcs. The following simplifying assumptions are introduced: first, T is taken to be independent on I and p in (6); this approximation applies when p and I do not change much, since from (1) and (2) p and I are logarithmic functions of the temperature; second, we shall assume that in the region of small p and I, the field E does not depend on r, since b in this case is small, and a is a logarithmic function of r; in the region of large p and I, we may apparently take r = const, since according to /2/ the diameter of the argon discharge column remains fairly constant for $p > 1.5 \cdot 10^6\,\mathrm{N/m^2}$, $I > 20\,\mathrm{A}$. Hence,

$$a = \frac{a_1}{I}; \quad b = b_1^3 p^2 I,$$

where a_1 and b_1 are independent of I and p.

The only quantities entering formula (6) are now E, I, p, and it can therefore be compared with the dependence $E(I, p)$ found experimentally. To this end the coefficients a_1 and b_1 are needed these two may be calculated from formulas (4) and (5), but unfortunately many of the relevant quantities $A, B, C, T_0, Q_a, Q_e, r$ entering these expressions are unknown. We shall therefore determine a_1 and b_1 from experimental data.

We write the asymptotic expressions of (6) in the limiting cases of small p, I ($W_e \gg W_r$) and large p, I ($W_e \ll W_r$):

$$E = \frac{a_1}{I}; \tag{7}$$

$$E = b_1 I^{1/3} p^{2/3}. \tag{8}$$

Formulas (7) and (8) naturally coincide with expressions (14) and (15) of /1/, which have been obtained by solving equations (1) and (2) in the two limiting cases specified.

From (7) and (8) we see that the constants a_1 and b_1 can be easily found by extrapolating the experimental dependence $E(p, I)$ in the region of small and large p, I, respectively.

Experimental data for the dependence $E(p)$ at a constant arc current $I = 100\,\mathrm{A}$, borrowed from /1, 3/, are plotted in Figure 1 in logarithmic scale. The curves follow formula (6), and the constants a_1 and b_1 are

determined by extrapolating the experimental data in the region of low and high pressures. For helium this technique gives $E_{p\to 0} = 7$ V/cm, $E_{p>3.0\cdot 10^6\ \mathrm{N/m^2}} = 1.16\cdot 10^{-3} p^{1/3}$. Hence, from (7) and (8), $(a_1)_{He} = 700$, $(b_1)_{He} = 2.5\cdot 10^{-4}$. For argon, $E_{p\to 0} = 1.2$ V/cm, $E_{p>3.0\cdot 10^6\ \mathrm{N/m^2}} \simeq 3.1\cdot 10^{-4} p^{1/3}$, whence $(a_1)_A = 120$, $(b_1)_A = 6.7\cdot 10^{-5}$.

Figure 1 reveals satisfactory agreement of theoretical and experimental data in the range of intermediate pressures. The E in argon increases somewhat faster than $p^{1/3}$ ($\sim p^{1/4}$), which is possibly attributable to the variation of the radius of the arc channel with increasing pressure that we have neglected.

Applying the numerical values of a_1 and b_1, we make use of (6) to plot the E (I) characteristics for constant pressure and compare them with experimental data (Figure 2). We see that again the experiment fits the calculations, although the constants a_1 and b_1 have been determined independently from the data in Figure 1.

The following practical conclusions can be further drawn from the curves shown in Figures 1, 2: a) with a constant current $I = 100$ A, radiation becomes of any significance in the total energy balance of the arc column

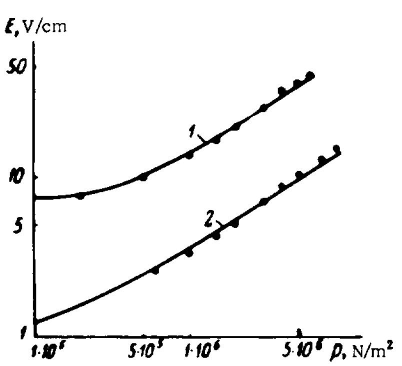

FIGURE 1. The electric field in the column of an arc as a function of pressure for $I = 100$ A. The curves E (p) for He (curve 1) and A (curve 2) have been calculated from (6).

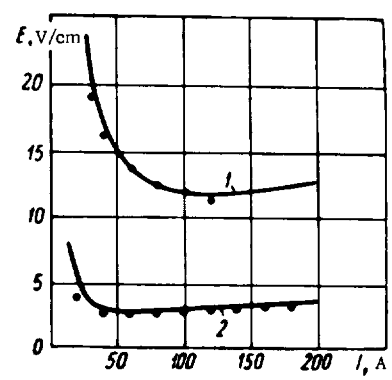

FIGURE 2. The electric field in the column as a function of current for $p = 7\cdot 10^5$ N/m^2. The curves E (I) for He (curve 1) and A (curve 2) have been calculated from (6).

only at pressures higher than $2.5-3.0\cdot 10^6$ N/m^2 for helium and higher than $\sim 10\cdot 10^6$ N/m^2 for argon; b) with a constant pressure $p = 7\cdot 10^5$ N/m^2, radiation is insignificant up to currents of $I = 120$ A for the arc in helium, while for the argon arc radiation is substantial for currents higher than 40—50 A. The conclusions pertaining to argon have been experimentally confirmed in /3/, where direct radiation measurements are used to show that in the interval of currents 30—150 A (for $p = 2\cdot 10^6$ N/m^2) and in the interval of pressures $0.7-6\cdot 10^6$ N/m^2 (for $I = 100$ A) the entire energy fed into the column of a long arc in argon is dissipated by radiation. Measurements of radiation from the column of a long arc in helium are under way now.

Let us try to correlate the empirical constants a_1 and b_1 with accepted theoretical notions. According to (4) and (5),

$$\frac{(a_1)_{He}}{(a_1)_A} \simeq \left(\frac{T_{He}}{T_A}\right)^{3/4} \left(\frac{M_A}{M_{He}}\right)^{1/2} \frac{Q_a(A)}{Q_a(He)} \tag{9}$$

where M is the atomic mass, Q_a the effective cross section for interatomic interactions. Taking $\frac{T_{He}}{T_A} \simeq \frac{V_i(He)}{V_i(A)}$ and applying the tabulated values of the gas-kinetic diameters of argon and helium atoms, we find from (9)

$$\frac{a_1(He)}{a_1(A)} \simeq 12,$$

while the experimental ratio is ~ 6. The agreement is apparently satisfactory, since it must be remembered that in the region of arc temperatures the effective atomic diameters may substantially differ from the gas-kinetic values, which are determined in the range of standard temperatures.

For the ratio of the constants b_1 we analogously have

$$\frac{(b_1)_{He}}{(b_1)_A} \simeq \left(\frac{C_{He}}{C_A}\right)^{1/3} \left(\frac{r_A}{r_{He}}\right)^{2/3} \left(\frac{T_A}{T_{He}}\right)^{1/2} \left(\frac{Q_e(He)}{Q_e(A)}\right)^{2/3}, \tag{10}$$

where Q_e are the effective cross sections for the interaction of electrons with atoms.

The cross sections $Q_e(A)$ and $Q_e(He)$ in the region of arc temperatures were determined experimentally in /4/. From these data, we find

$$\frac{(b_1)_{He}}{(b_1)_A} \simeq 2\left(\frac{r_A}{r_{He}}\right)^{2/3},$$

while the experimental ratio is close to 4.

The orders of magnitude of the ratios are thus again in agreement since it is unlikely that the arc radii in helium and in argon should differ considerably.

Let us consider in greater detail the radiation from the arc plasma. In the equation of energy balance in the arc column we introduced recombination radiation of the plasma, neglecting the line emission of the excited atoms, which in general may be fairly substantial even in weakly ionized plasmas. The line emission intensity W^* is known to be proportional to $\frac{p}{T}\sum_a e^{-\frac{eV_a^*}{kT}}$, where V_a^* are the atomic excitation potentials. Since for helium and argon all the excited levels cluster near the continuum boundary ($V_i(He) = 24.5$ eV, $V_1^*(He) = 20.5$ eV, $V_i(A) = 15.7$ eV, $V_1^*(A) = 13$ eV), a certain effective level V^* can be approximately substituted for the different levels of the excited atoms. We may then write $W^* \sim \frac{p}{T} e^{-\frac{eV^*}{kT}}$. Equations (1) and (2) are now solved assuming line emission and heat conduction only. Equation (3) takes the form

$$E^{2\frac{V^*}{V_i}+1} - \frac{a_1}{I} E^{2\frac{V^*}{V_i}} - \mathrm{const}\, p^{\frac{V^*}{V_i}+1} I^{\frac{2V^*}{V_i}-1} = 0. \tag{11}$$

This equation is difficult to solve in the general case, but the limiting cases are easily found:

$$E = \frac{a_1}{I} \text{ for } W^* \ll W_i,$$

which is clearly identical with (7), and

$$E \sim I^{\frac{2\frac{V^*}{V_i} - 1}{2\frac{V^*}{V_i} + 1}} p^{\frac{\frac{V^*}{V_i} + 1}{2\frac{V^*}{V_i} + 1}} \text{ for } W^* \gg W_i. \tag{12}$$

Taking $\frac{V^*}{V_i}$ equal to, say, 0.85 (the effective level is close to the first excited level in both A and He), we obtain for (12)

$$E \sim I^{1/3.9} p^{2/2.9} \tag{13}$$

The difference between (8) and (13) is insignificant, and we may therefore conclude that a general solution of equation (11) will yield a dependence $E(I, p)$ close to that corresponding to formula (6).

We have thus established that introduction of line emission will not distort the results based on recombination radiation only.

BIBLIOGRAPHY

1. BOROVIK, E. S., R. V. MITIN, and Yu. R. KNYAZEV. – ZhTF, 31 : 1329. 1961.
2. MITIN, R. V., Yu. R. KNYAZEV, and V. I. PETRENKO. – ZhTF, 34 : 340. 1964.
3. KNYAZEV, Yu. R., R. V. MITIN, E. S. BOROVIK, and V. I. PETRENKO. – ZhTF, 34 : 1224. 1964.
4. DRAWIN, H. W. – Zs. Phys. 146 : 295. 1956.
5. BIBERMAN, L. M., G. E. NORMAN, and K. N. UL'YANOV. – AZh, 39 : 107. 1962.

Yu. R. Knyazev, R. V. Mitin, V. I. Petrenko, and E. S. Borovik

THE RADIATION OF A HIGH-PRESSURE ARGON ARC

In previously published papers /1, 2/ we described a setup permitting generation of long high-pressure arcs (arc length up to 8 cm, argon or helium pressure up to 9 MN/m^2). The long arc is stabilized by rotating a system of screens rigidly connected with the rotor of an electric motor, which is also kept in the high-pressure chamber. This method of arc stabilization has two shortcomings. First, it interferes with optical measurements of the arc (the "stroboscopic" method of radiation measurements described in /2/ is inconvenient for absolute measurements

since the size and the shape of the holes in the incandescent screens cannot be maintained constant). Second, the possibility of investigating the behavior of a long high-pressure arc in a magnetic field is *a priori* excluded (when a magnetic field is turned on, the electric motor stops and the arc parameters change radically).

In the present paper we describe two new stabilization techniques. One of these techniques is adapted to absolute radiation measurements of an arc up to 8 cm long in the pressure range $0.2-10\,\mathrm{MN/m^2}$, the other makes it possible to increase the arc length up to 25 cm in the pressure range $1-2.5\,\mathrm{MN/m^2}$, simultaneously impressing an external magnetic field on the arc.

Equipment and procedure

As in our previous papers /1, 2/, the long argon arc was stabilized by rapid rotation of the gas.

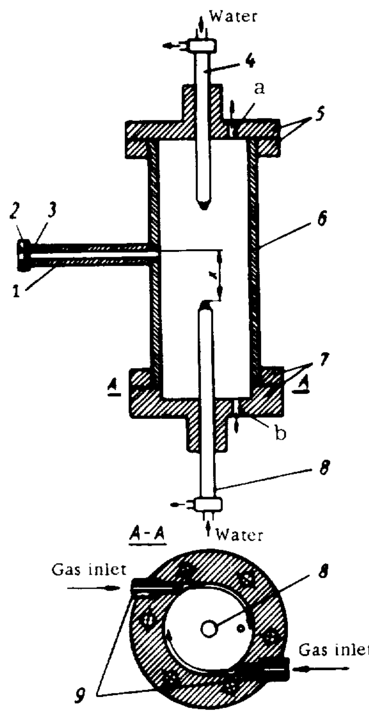

FIGURE 1. Schematic diagram of the setup:
1) tube; 2) nut; 3) quartz window; 4) upper electrode; 5, 7) top and bottom flanges; 6) chamber; 8) lower electrode; 9) nozzles; a) top outlet; b) bottom outlet; x is the distance from the upper edge of the window to the lower electrode.

The first method utilized the equipment described in /1, 2/; the gas is rotated by an electric motor mounted in the high-pressure chamber, but the rotation is transmitted from the rotor to the gas by means of an impeller mounted on the shaft (and not by a system of screens). The rotor with the impeller is a mere 1.5 cm longer than the stator; the remaining part of the chamber is thus occupied by the rotating gas, which experiences a stopping force at the walls. This transmission ensures that the gas rotates approximately at half the angular velocity of the rotor. (The angular velocity of the gas was measured by a light-weight vane provided in the chamber which interrupted a beam of light directed along the axis; viewing ports were substituted for the electrodes). However, the reduction in the velocity of rotation of the gas had no detrimental effects on the stability of the long arc if the angular velocity of the rotor was sufficiently high. This stabilization technique thus gives satisfactory results only if the motor is fed by high-frequency current (200 c/s), so that the rotor rotates at a rate of 600—800 rad/sec.

In the second method of stabilization, the gas is rotated by a continuous stream of argon blown tangentially into the discharge chamber. The corresponding setup is shown in Figure 1. The ignition chamber and the electrodes are the same as in /1, 2/, with the difference that quartz screens are provided

to protect the electrodes and two conically converging nozzles are fitted in the bottom flange through which argon is admitted. The gas leaves the chamber through the top or the bottom (outlets a and b, respectively). Argon was pumped by a compressor at a rate of 2.78 mm^3/sec (maximum gas pressure up to 6 MN/m^2). From the compressor the argon at a pressure of 4 — 6 MN/m^2 was passed through an oil separator* and fed into the inlet nozzles. The spent gas ejected from the chamber is cooled with running water and fed back to the compressor through a high-precision valve (regulating the flow rate and the pressure in the chamber) and a flow meter; a certain quantity of argon is thus continuously recirculated through the chamber.

The angular velocity of the gas in the chamber was measured as before; it was found to vary as follows with the argon flow rate Q (m^3/sec) and pressure p (N/m^2) in the chamber:

$$f(\text{rad/sec}) = a\frac{Q}{p}. \tag{1}$$

The constant a is a function of the nozzle diameter; for nozzles with a diameter of 1.6 mm, 0.9 mm, 0.55 mm, and 0.3 mm it is respectively equal to $6.3 \cdot 10^{10}$, $9.6 \cdot 10^{10}$, $1.4 \cdot 10^{11}$, and $1.7 \cdot 10^{11}$. All the experiments with a long argon arc were made using nozzles 0.3 mm in diameter and a flow rate of 2.22 mm^3/sec; the gas in the chamber thus rotated at a rate of 200 — 500 rad/sec. Argon arcs up to 25 cm long were generated on this setup at pressures of 1 — 2 MN/m^2 and currents of 30 — 150 A. The arc is ignited by touching the electrodes and it is stretched to size by moving the lower electrode (cathode).

The stability and the electric parameters of the long arc are the same irrespective of whether the spent gas is ejected through outlet a or b; however, when the gas leaves through the bottom outlet, it carries away approximately half the amount of heat removed by the gas through the top vent.

The arc is fairly stable up to the maximum length (25 cm), but a slight (~ 5 — 6%) fluctuation of arc voltage and current is observed; the arc as seen through the viewing ports presents a column slightly oscillating about the axis, which appears to be constricted and brighter near the electrodes. The diameter of the luminous channel increases with arc current and gas pressure in the chamber; the numerical values of the diameter are virtually identical with the data of /2/ for an arc stabilized with rotating screens. If necessary, the arc may be reversed (setting the anode as the bottom electrode); the electric parameters of the arc hardly change, but the stability is poor, especially for long arcs. Grounding any of the electrodes did not affect the electric parameters and the stability of the arc.

Experimental results

Figure 2 shows how effective the various stabilization techniques are: it plots the arc voltage U against the arc length l for various methods of stabilization (for all curves, $p = 2.2\ MN/m^2$, $I = 100\ A$).

* It is highly important to purify the argon from all traces of oil, which may sharply distort the arc characteristics. In our experiments, an oil filter was used with several layers of silica gel and felt.

Curve 1 corresponds to an arc burning in a stationary gas; the chamber walls are cold (not screened). The arc is thus stabilized by the natural convective currents. We see that the arc is highly unstable in this case, breaking when an attempt is made to stretch it beyond ~ 4 cm.

Curve 2 represents the same case, but the convection has been killed by rotating the gas around the arc with the aid of nozzles (see Figure 1).

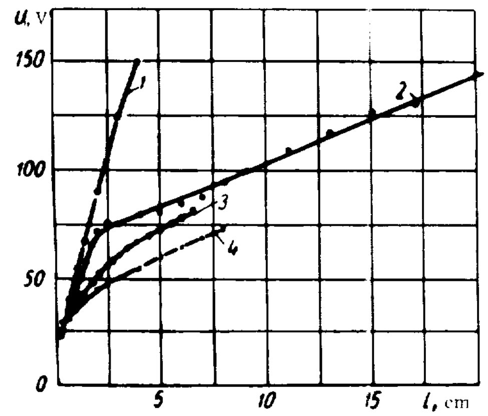

FIGURE 2. Total arc voltage vs. interelectrode gap for various stabilization techniques ($p = 2.2$ MN/m^2, $I = 100$ A).

The arc is very stable, and its length is limited by the size of the ignition chamber. We see from the figure that the voltage and the voltage gradient across the arc drop sharply, and a long uniform arc column with a constant voltage gradient is easily formed.

Curve 3 corresponds to stabilization of a cold gas by rotation with an impeller. The arc is stable, but much shorter, since a large part of the chamber is occupied by the motor with the impeller.

Finally, curve 4 shows the behavior of an arc stabilized by rotating hot screens. If the screens are at rest, convection takes over, but not to so high a degree as in the case of cold walls. The points corresponding to tests with stationary screens accidentally fell on curve 3, as we see from the figure. The arc in this case becomes unstable: for lengths greater than ~ 4 cm, it either breaks or switches to the stationary screens.

We see from Figure 2 (curves 2, 3, 4) that the various stabilization techniques are represented by somewhat different curves, but a common feature of them all is the formation of a steady arc column with a constant voltage gradient along the arc, which is longer than 2—3 cm. Figure 3 plots the arc voltage against the pressure of argon in the chamber, for different arc lengths and different stabilization techniques (curves 1, 3— stabilization with nozzles, $U(p)$ for $l = 11$ and 4 cm, respectively; curves 2, 4— stabilization with an impeller, $U(p)$ for $l = 6.5$ and 3.5 cm, respectively). From these curves we calculated the electric field E in the arc column (curve 5 for stabilization with an impeller, curve 6 with nozzles). For purposes of comparison, the figure also gives the dependence

$E(p)$ for stabilization by rotating screens (the crosses on curve 5, which are borrowed from /2/). We see that screen and impeller stabilizations give identical values of E, although the total arc voltage may be somewhat different with the two techniques (see Figure 2). For nozzle stabilization, E are less by $\sim 20\%$ (curve 6).

An examination of the current-voltage characteristics of the arc showed that, irrespective of the stabilization technique, the total arc voltage U, and the voltage field E in the arc column vary but slightly in the current range of from 40 to 120 A; when the current is lowered below $\sim 30-20$ A, U and E increase rapidly, and when the current is raised to $150-200$ A, U and E grow comparatively slowly.*

The radiation of the high-pressure arc was measured with a thermopile extracted from a radiation pyrometer. The sensitivity of the thermopile was determined in calorimetric tests, by heating some water in a thermostat

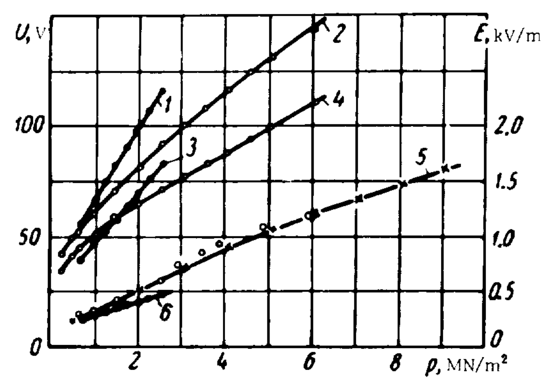

FIGURE 3. Arc voltage and the electric field in the column vs. pressure at I = 100 A.

with sun rays; the intensity of the solar radiation was registered by the thermopile. The corresponding thermopile sensitivity was $500 \pm 50\,\mathrm{kW/m^2V}$. The wavelengths picked up by the thermopile were determined in our tests by the transmission of the quartz window of the chamber (from 0.19 to 2.5 μ).

The distribution of radiation along the column of a long arc in argon is shown in Figure 4, which plots the intensity of radiation reaching the thermopile against x (see Figure 1). As the arc length is gradually increased by moving the bottom electrode (a cathode in our case), different sections of the arc column adjoining the moving electrode pass against the viewing port. Curve 1 corresponds to arc stabilization by rotating screens, curve 2 stabilization by an impeller, and curve 3 nozzle stabilization.

In plotting curve 1, we took into consideration the time-average attenuation of the light passing through the holes in rotating screens (attenuation ratio $\sim \frac{nS}{\pi Dd} \simeq \frac{1}{20}$, where S the area and d the diameter of the holes, n their number, D the diameter of the screens), and also the

* A discussion of this behavior of $E(I)$, as well as of $E(p)$, and comparison with analogous functions for a helium arc /1/ will be found in /3/.

attenuation of light passing through the water filter, which was interposed to filter off the fairly strong infrared radiation of the hot screens. A cell with quartz windows filled with distilled water served as the water filter.

Curve 4 shows that near the peak* the radiation curves follow different paths, but they approach a common limit at distances of 1.5—2 cm from the cathode; this common limit corresponds to the radiation from the uniform positive column of the arc. Similar tests made near the anode give an analogous pattern for radiation distribution, but the peak radiation of all the curves is reduced approximately by one half.

As with the dependence of the total arc voltage on arc length (see Figure 2), we come to the conclusion that a uniform column of constant voltage gradient and constant radiation intensity per unit length is formed in a long arc at a distance of 1.5—2 cm from the electrodes.

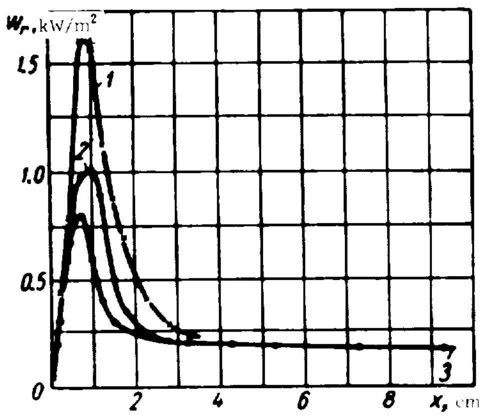

FIGURE 4. The intensity of the radiation reaching the thermopile vs. x (p = 1 MN/m², I = 100 A).

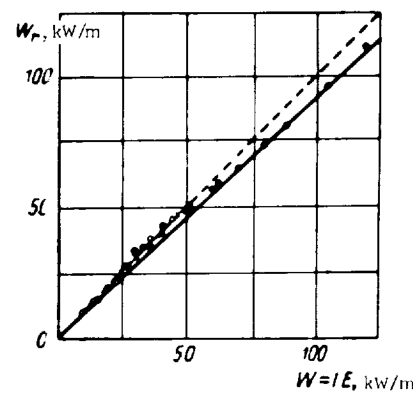

FIGURE 5. Power radiated per unit column length as a function of the electrical power: dots (•) correspond to arc stabilization with an impeller; circles (O) and crosses (x) to nozzle stabilization (circles for p = 1 MN/m², I = 30 – 150 A, crosses for p = 0.5 – 2.5 MN/m², I = 100 A).

The radiation of the uniform column was studied as a function of argon pressure and current intensity on machines provided with nozzle stabilization (I = 30 — 150 A, p = 1.0—2.6 MN/m²) and impellers (I = 30 — 150 A, p = 0.5—7.5 MN/m²).

It is easily seen that the power radiated per unit column length, W_r, is related with the readings ε of the thermopile by the formula

$$W_r\,[\mathrm{kW/m}] = \frac{4\pi L\left(L - \frac{D}{2}\right)}{\gamma d_1}\, q\varepsilon, \tag{2}$$

where q is the thermopile sensitivity, D the internal diameter of the chamber (0.084 m), d_1 the diameter of the port in the chamber wall

* Note that the maxima of curves 1, 2, and 3 correspond to radiation from the bright sections of the arc near the electrodes, and not from the surface of the electrodes, as might appear at a first glance.

(~ 0.01 m), L the distance from the thermopile to the arc axis (~ 0.30 m), γ the coefficient of attenuation of light passing through the quartz window (~ 0.93).

Since each pair of values p and I corresponds to a certain power fed per unit column length, $W = IE$, we can easily investigate the dependence of W_r calculated from (2) on the product IE. We plotted the results for various values of the arc current and gas pressure in the chamber (Figure 5). The power $W = IE$ was calculated from the data of Figure 3 (curve 5 for the impeller, curve 6 for the nozzles). We see from Figure 5 that the data obtained in two different machines with two different stabilization techniques lie on a curve which is very close to the straight line with a slope of $\pi/4$ rad (the dashed line) in a wide range of arc currents (30 – 150 A) and argon pressures (0.7 – 6.0 MN/m^2). It thus seems that the entire electrical energy fed into the uniform column of the long arc is carried away by radiation. We suggested that this was so in previous papers /1, 2/, but then only indirect proof was available. In the present study we obtained an experimental proof of this for the case of a long arc in argon.

According to the best of our knowledge, absolute radiation measurements of arcs (analogous to our measurements) have been published in two references only /4, 5/. Elenbaas /4/ studied a high-pressure mercury arc (up to 2.45 MN/m^3); thermopile measurements showed that in the interval of $W = IE$ from 2.0 to 7.5 kW/m the power radiated per unit column length W_r followed the relation $W_r = 0.72\ (W - 1.0)$, i.e., at variance with our experiments, only 70% of the power are lost by radiation, which is apparently attributable to the lower power of Elenbaas' arc than in our tests. In /5/ an arc in argon was investigated at atmospheric pressure; the formula $W_r = 0.52\ (W = 9.5)$ kW/m was obtained by an analogous technique for $W > 15.0$ kW/m. The lack of agreement with our results is attributable to the low argon pressure in /5/, so that heat conduction successfully competes with radiation (see 1, 3/).

l, cm	IU, kW	W_a, kW	W_c, kW	W_{gas}, kW	W_w, kW	$\int W_r\,dl$, kW
1	4	1.2	0.5	0.2	2.1	—
3	5.9	1.7	0.7	0.3	3.2	3.0
5	6.5	1.3	1.0	0.5	3.7	3.9
8	7.6	1.4	0.9	0.7	4.6	5.0
12	8.8	1.1	0.8	0.6	6.3	6.5
16	10.6	1.2	0.7	1.0	7.7	7.9

In conclusion, we compare the energy radiated by the arc with the energy released at the arc electrodes. The corresponding measurements were made calorimetrically, using the coolant water. In the pressure range 1.5 – 7.5 MN/m^2, the percentage ratio of the heat released on the electrodes and at the chamber walls remains approximately constant, being equal to 14 for the cathode, 29 for the anode, and 57 for the walls. This test was made with an arc stabilized by rotating screens; arc length 5 cm, current 100 A. Analogous tests were made with a nozzle-stabilized arc; the pressure was maintained constant, and the arc length varied. The experimental results for p = 1.5 MN/m^2 and I = 100 A are given in the table (l being the arc length, IU the total electric power, W_a, W_c the power

released at the anode and the cathode, respectively, W_{gas} the power carried away by the circulating gas, W_w the power released at the chamber walls).

The last column lists the power measured with a thermopile; integration along the arc was carried out numerically, using experimental curves of the type of curve 3 in Figure 4.

According to the data of the table, the quantity of heat released at the electrodes does not vary much with the increase in arc length; the quantity of heat released at the walls and carried away by the circulating gas, on the other hand, increases with arc length. The satisfactory fit of the data in the last columns of the table indicates that in our experiments the energy is mainly lost by radiation along the entire arc (the electrode space included).

BIBLIOGRAPHY

1. BOROVIK, E. S., R. V. MITIN, and Yu. R. KNYAZEV. – ZhTF, 31: 1329. 1961.
2. MITIN, R. V., Yu. R. KNYAZEV, and V. I. PETRENKO. – ZhTF, 34: 340. 1964.
3. MITIN, R. V. – ZhTF, 34: 1466. 1964.
4. ELENBAAS, W. – Physica, 4: 314. 1937.
5. NEUMANN, W. – Beitr. Plasma. Phys., 2: 252. 1962.

I. Yu. Adamov, L. A. Dushin, V. I. Kononenko and O. S. Pavlichenko

MICROWAVE RADIATION FROM AN ELECTRODELESS INDUCTIVE DISCHARGE

Intense epithermal microwave radiation is observed in various plasma-creating machines /1–3/. This radiation may originate in a nonequilibrium plasma which carries either currents or beams of charged particles. The plasma in this case is unstable with respect to oscillations. Large-amplitude plasma oscillations arising in a bounded inhomogeneous plasma may be converted into transverse electromagnetic waves: the plasma acts as a source of radio waves, much more powerful than any thermal source. The existence of this epithermal mechanism of microwave radiation in the plasma of a linear pinch discharge was reported in /4/, where it was suggested that this radiation was connected with collective interactions of electron streams with the plasma.

X-ray radiation indicatory of the presence of high-energy accelerated electrons is invariably observed in machines where the plasma is created by an electrodeless inductive discharge (theta-pinch). This distortion of the electron distribution function may excite plasma oscillations. Our experiments were made in order to test the suggestion that epithermal microwave radiation could originate in the plasma of an electrodeless inductive discharge, due to the same accelerated electrons whose bremsstrahlung registers as X-rays.

Equipment and technique

Microwave and X-ray radiation was studied using an electrodeless inductive discharge in hydrogen as the source of plasma. The alternating magnetic field was set up by a single-loop coil 11 cm in diameter and 20 cm long connected to a condenser bank (C = 18.6 μF, U = 30 kV) through a discharger. Peak amplitude of the magnetic field in the mirror was 1320 kA/m, mirror ratio 1.1, period of magnetic field 8.6 μsec. A ~ 200 W, 50 Mc/s generator was used in preliminary ionization of the gas.

The variation of the magnetic field inside and outside the plasma was recorded with magnetic probes. Plasma density and the rate of its growth were estimated from the attenuation of the microwave signals transmitted through the plasma (at wavelengths of 3.2, 0.8, 0.4, and 0.2 cm). The position of the plasma layers whose concentration exceeded the critical value for the corresponding wavelengths was determined from the amplitude and the phase of the reflected signal. Microwave radiation from the plasma was registered by detector receivers at wavelengths of 3.2, 0.8, and 0.4 cm (sensitivity, 10^{-5} W).

X-ray radiation was detected using a scintillation element and a photomultiplier. The average X-ray energy was estimated by the method of filters. The region of peak X-ray radiation was determined by photographing the discharge in X-rays with a camera obscura. The electron temperature was estimated from the relative intensity of helium lines (this gas was added in a small quantity).

Results of measurements

Microwave and X-ray radiation was recorded in the range of initial pressures $1.6-7.1 \cdot 10^{-2}$ N/m^2 for discharge voltages of 5—30 kV across the

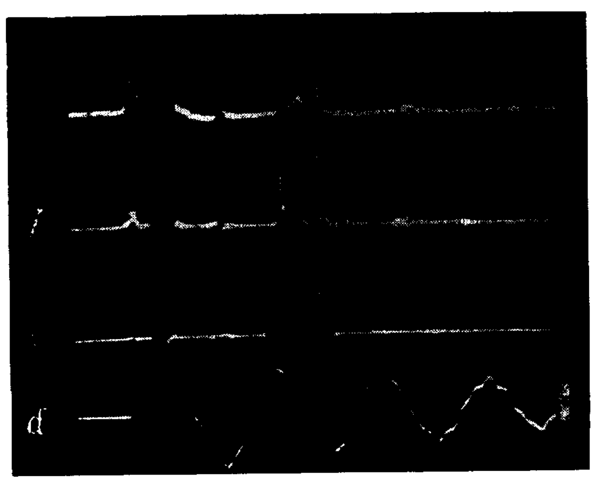

FIGURE 1. Oscillograms of microwave radiation at wavelengths of 0.4 cm (a), 0.8 cm (b), 3.2 cm (c); oscillogram of the external magnetic field (d).

condenser bank. The radiation was picked up from the plasma lying along the axis of the single-loop coil.

Typical oscillograms of the microwave radiation at various wavelengths and of the magnetic field (Figure 1) were obtained for an initial pressure of $0.86\,N/m^2$ and a discharge voltage of 20 kV. We see that the peak intensity of the microwave radiation corresponds to the third half-period of the magnetic field. The X-ray pulse registered under these conditions also corresponds to the third half-period (Figure 2).

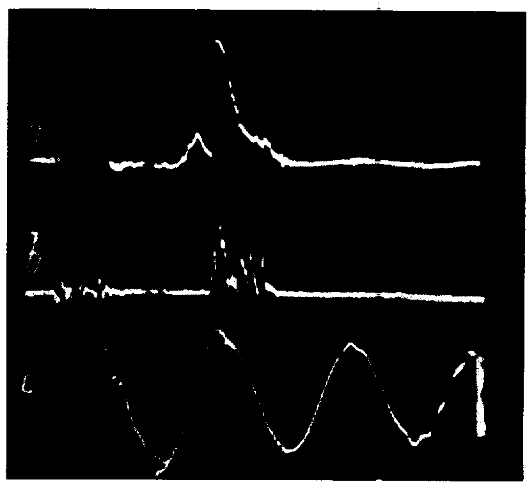

FIGURE 2. Oscillograms of X-ray radiation (a), 3.2-cm microwave radiation (b), and magnetic field (c).

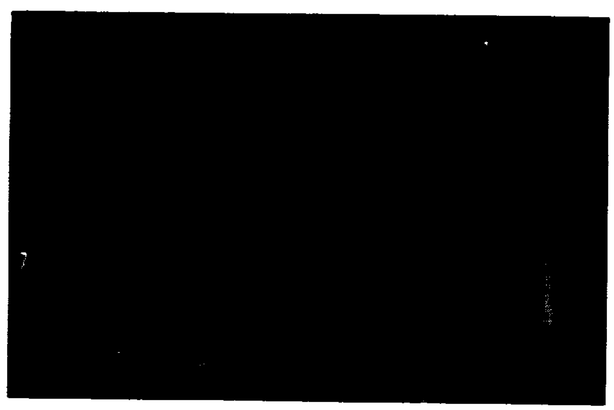

FIGURE 3. Oscillograms of the transmitted signal at 3.2 cm (a) and of the magnetic field (b).

The oscillogram of the transmitted signal (3.2-cm wavelength, $0.3\,N/m^2$ initial pressure, 20 kV discharge voltage) also shows pulses of the received

microwave radiation, which arise when the transmitted signal is cut off (Figure 3). Typical oscillograms of microwave radiation and of a signal reflected by the plasma at 3.2-cm wavelength are also given for the initial pressure of 0.86 N/m^2 and 20 kV voltage (Figure 4).

Comparison of oscillograms obtained under identical conditions shows that radiation, reflection, and transmission cutoff all occur simultaneously. A necessary condition for microwave radiation at a given frequency is thus the existence of a critical density of charged particles in the plasma, for which $\omega_{pe} = \sqrt{\frac{4\pi ne^2}{m}}$ is equal to the receiver frequency.

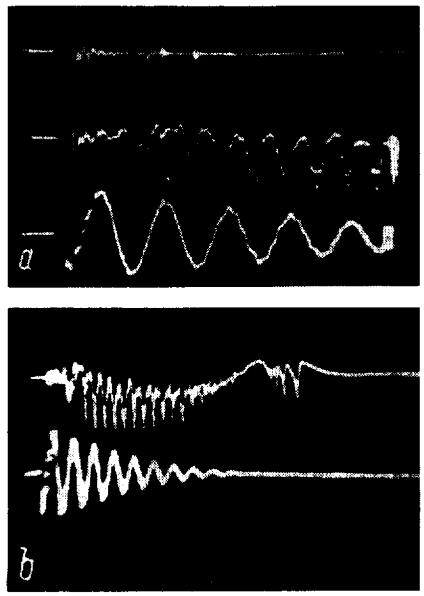

FIGURE 4. Microwave radiation and a reflected signal at 3.2-cm wavelength (a); reflected signal taken with a large time base (b). The bottom oscillogram in each plate corresponds to the magnetic field.

Figure 5 plots the microwave intensity at various frequencies as a function of the discharge voltage. Radiation whose power exceeds the receiver sensitivity threshold is observed at 3.2 cm for a voltage of 5 kV (1) and at 0.8 cm for a voltage of 10^{-2} kV (2); the intensity somewhat increases with voltage. Radiation at 0.4-cm wavelength is picked up at a voltage of 10 kV.

The microwave intensity as a function of the initial pressure (for 15 kV voltage) is plotted in Figure 6. Peak intensity corresponds to a pressure of 0.5—0.6 N/m^2. As the pressure increases further, the intensity decreases, the microwave and X-ray pulses shift to the earlier half-periods of the magnetic field, and all radiation vanishes at a pressure of 1.3—1.6 N/m^2. As the pressure decreases below 0.5 N/m^2, the intensity also decreases and the microwave and X-ray pulses shift to the later half-periods of the magnetic field. The occurrence of the critical density

of charged particles is similarly shifted in time. Microwave radiation vanishes at pressures which are insufficient to produce the critical density. At pressures of 0.3 N/m^2, no reception was possible at wavelengths of 0.8 and 0.4 cm, while at pressures of 0.13 N/m^2 the radiation at 3.2 cm stopped.

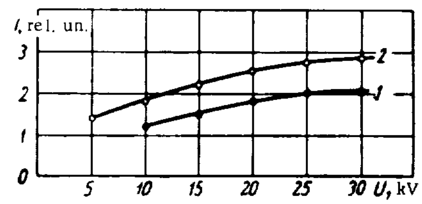

FIGURE 5. Intensity of microwave radiation as a function of discharge voltage for initial pressure of 0.6 N/m^2.

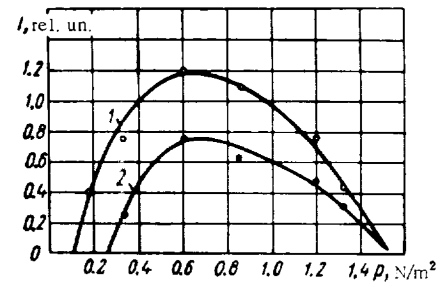

FIGURE 6. Intensity of microwave radiation as a function of initial pressure for discharge voltage of 15 kV.

It is difficult to decide what the polarization of the microwave radiation is, since the radiating plasma is screened by the coil. Observations show that varying the polarization of the receiving horns does not alter the power

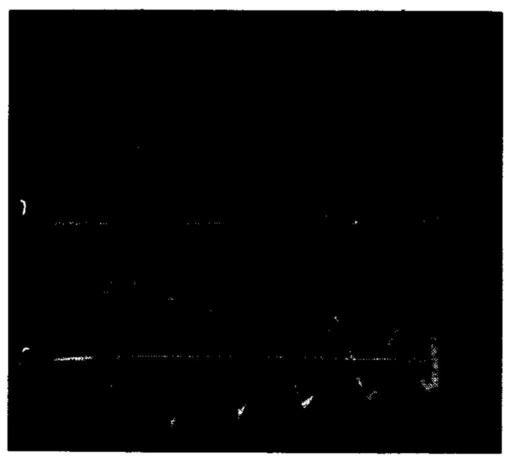

FIGURE 7. Oscillograms of microwave radiation at 3.2 cm (a), of the magnetic field on the plasma axis (b), and of the magnetic field outside the plasma (c); initial pressure 0.6 N/m^2, discharge voltage 20 kV.

of the signal received from the ends of the discharge tube. For reception through a window in the coil, with the electric field polarized along the external magnetic field, the amplitude of the signal is smaller than the amplitude of the signal received in the case of perpendicular polarization.

Analyzing the amplitude and the phase of the reflected signal, we see that the external magnetic field induces radial oscillations in the plasma cloud, with a frequency of 240 c/s (twice the frequency of the magnetic field). The maximal diameter of a plasma with a density of $1.2 \cdot 10^{12}$ el/cm^3 is 3.5—4 cm. It is also significant that microwave radiation precedes by one period the capture of the magnetic field of opposite sign by the plasma (Figure 7).

X-ray photographs taken in this range of pressures showed that the X-ray radiation originated mainly in the plasma under the coil, having a diameter of $\sim$ 3 cm; according to microwave measurements, this diameter corresponds to a plasma with a density of over 10^{12} el/cm^3. The X-ray energy measured by absorption in aluminum was of the order of $(3.2-4) \cdot 10^{-15}$ J. Estimates of the electron temperature from the relative intensity of helium lines gave $5 \cdot 10^5$ °K.

Discussion of results

Estimates of the thermal power radiated by the plasma, based on measurements of the relative intensity of helium singlet and triplet lines, are several orders of magnitude below the actually received power. Cyclotron radiation cannot be assumed either, since the received power is independent of the magnetic field, and furthermore the reception frequency is not equal to the gyromagnetic frequency. It has been shown in /4/ that this epithermal radiation may arise in the plasma of a high-current gas discharge due to the excitation of powerful electron plasma oscillations in the presence of drifting electrons. The electromagnetic radiation observed is the result of the conversion of longitudinal plasma oscillations into transverse modes.

The time correlation between the emission of microwave radiation and the occurrence of the critical density suggests that fairly intense electron plasma oscillations are excited, with a frequency $\omega \approx \omega_{pe}$. These oscillations may be connected with the onset of streaming instability, arising in the presence of groups of accelerated electrons in the plasma. The existence of these electrons is confirmed in our case by the detection of X-rays, which are radiated when the fast electrons interact with the plasma ions. The suggestion that the electrons are accelerated in the region where the magnetic field reverses its sign (the time of capture of the reverse magnetic field) has not been confirmed experimentally. It has been established that microwave and X-ray radiation are both emitted before the magnetic field is captured by the plasma (see Figure 7).

The mechanism of acceleration of electrons in an alternating magnetic field has been investigated experimentally /5/ and theoretically /6/. In /5/ it is shown that in a rapidly alternating magnetic field electrons arise with energies of the order of hundreds of kiloelectronvolts and this acceleration is tentatively attributed to the betatron mechanism. In /6/ the energy acquired by electrons in an alternating magnetic field is calculated. It is shown that if the magnetic field increases at a sufficiently fast rate, the electrons may gain several tens of kiloelectronvolts in a single cycle.

In our case, the fast electrons may form while moving in an accelerating magnetic field along a helical trajectory to the center of the system. The fast electrons then interact with the impurity ions in the relatively dense plasma near the axis, and X-rays are emitted. Furthermore, the velocity distribution function of the electrons at that time may be favorable for the onset of streaming instability, since initially $T_e > T_i$. As the plasma density increases, the prevailing oscillations shift to the region of higher frequencies, and when the density attains the critical value for the given wavelength, microwave radiation is registered — a result of the conversion of longitudinal plasma oscillations into transverse modes. This radiation is cut off subsequently due to the compression heating of the ions ($T_i > T_e$).

We are not in a position to establish the exact nature of the instability in this case, since the different acceleration mechanisms vary in their contribution to the excitation of longitudinal oscillations in the presence of a transverse magnetic field. It is hoped that future experiments will throw some light on the subject.

BIBLIOGRAPHY

1. DAWSON, J. and C. OBERMAN. – Phys. Fluids, 2:103. 1959.
2. FIELD, G. – Astrophys. J., 124:555. 1956.
3. BERNSTEIN, CHEN, HEALD, KRANZ. – Phys. Fluids, 1:430. 1958.
4. SUPRUNENKO, V. A. et. al. – Atomnaya Energiya, No. 7. 1963.
5. VOLKOV, Ya. F., V. T. TOLOK, and K. D. SINEL'NIKOV. – ZhTF, 3[?]:811. 1962.
6. ANKUDIMOV, V. A., V. M. KEL'MAN, and L. N. SYSOEVA. – ZhTF, 33:19. 1963.

Section Four

PLASMA STABILITY

V. D. Shapiro and V. I. Shevchenko

QUASILINEAR THEORY OF INSTABILITY OF A PLASMA WITH ANISOTROPIC ION VELOCITY DISTRIBUTION

Collective motions related with the ionic branch of oscillations are excited in a collisionless plasma with a fairly high temperature anisotropy (longitudinal and transverse temperatures) in the presence of a magnetic field /1/. In these collective motions, the longitudinal thermal energy of the plasma increases at the expense of the transverse energy (or vice versa), until the plasma reaches a state which is stable with respect to the collective interactions. In what follows, we consider this process in the quasilinear approximation.

A highly characteristic feature of these instabilities is their aperiodicity (the real part of the frequency ω' is zero). Generally (see, e.g., /2/), the quasilinear theory is applied in cases when the increment is small in comparison to the frequency, $\gamma_k \ll \omega'_k$. However, it will be shown that the quasilinear theory may be applied to aperiodic instabilities also, provided that $\gamma_k \ll k_z v_{t\parallel}$ ($v_{t\parallel}$ is the longitudinal thermal velocity of the ions). The last condition applied to these instabilities, whose very origin is connected with the anisotropy of the distribution function, implies that the initial deviation of the plasma parameters from the critical values corresponding to the onset of instability is small. Under this assumption we have found the temperature which is established in the plasma in the state of saturation and the energy of the magnetic field generated by the collective interaction in the plasma.

1. According to /3/, the dispersion equation of the ionic branch, having $|\omega| \lesssim \omega_{Hi}$, is

$$\cos^2\varphi n^4 - (\varepsilon_{11} + \varepsilon_{22}\cos^2\varphi) n^2 + \varepsilon_{11}\varepsilon_{22} + \varepsilon_{12}^2 = 0, \tag{1}$$

where $n = \frac{ck}{\omega_k}$, φ the angle between $\mathbf{k}$ and $\mathbf{H}_0$, $k_y = 0$.

In the following we shall consider low-frequency disturbances $|\omega| \ll \omega_{Hi}$, when $\varepsilon_{12} \sim \frac{|\omega|}{\omega_{Hi}}\varepsilon_{22} \ll \varepsilon_{22}$; we are dealing with collective motions where the electric field is perpendicular to the plane through $\mathbf{k}$ and $\mathbf{H}_0$. Then from (1)

$$c^2k^2 = \omega_k^2\varepsilon_{22}. \tag{2}$$

Inserting ε_{22} from /3/ and taking

$$k_z^2 v_{t\parallel}^2 \ll \omega_{Hi}^2; \quad k_\perp^2 v_{t\perp}^2 \ll \omega_{Hi}^2, \tag{3}$$

we write (2) in the form

$$c^2k^2 - \omega_k^2 - \frac{\omega_{0i}^2}{N\omega_{Hi}^2}\left\{\int d\mathbf{v} f_0\left[\omega_k^2 + k_z^2\left(v_z^2 - \frac{v_\perp^2}{2}\right) - k_\perp^2 v_\perp^2\right] - \right.$$
$$\left. - \frac{1}{4}\int d\mathbf{v} k_\perp^2 v_\perp^4 \frac{\partial f_0}{\partial v_z}\cdot \frac{k_z}{k_z v_z - \omega_k}\right\} = 0. \tag{4}$$

Following /1/, we shall consider two separate cases:
a) $k_\perp = 0$. For ω_k we have from (4)

$$\omega_k^2 = -\frac{k_z^2}{1 + \dfrac{H_0^2}{4\pi N M c^2}} \cdot \frac{T_\parallel - T_\perp - \dfrac{H_0^2}{4\pi N}}{M} = -\frac{k_z^2 T_\parallel Y}{M\left(1 + \dfrac{H_0^2}{4\pi N M c^2}\right)}, \tag{5}$$

where

$$T_\perp = \frac{M}{2N}\int v_\perp^2 f_0 d\mathbf{v}; \quad T_\parallel = \frac{M}{N}\int v_z^2 f_0 d\mathbf{v}; \quad Y = \frac{T_\parallel - T_\perp - \dfrac{H_0^2}{4\pi N}}{T_\parallel}$$

For $|Y| \ll 1$ (this is the case considered in all that follows), $\omega_k^2 \ll k_z^2 v_t^2$. Instability sets in ($\omega_k^2 < 0$) when $T_\parallel > T_\perp + H_0^2/4\pi N$;

b) $k_\perp \neq 0$. Only the terms linear in ω_k need be retained in the dispersion equation. Integrating with respect to v_z in (4) for the case $|\omega_k| \ll k_z v_{t\parallel}$, we find for ω_k

$$\omega_k = ik_z \frac{\dfrac{M}{8N}\displaystyle\int \frac{v_\perp^4}{v_z}\cdot\frac{\partial f_0}{\partial v_z} d\mathbf{v} + T_\perp + \frac{H_0^2}{4\pi N} - \frac{k_z^2}{2k^2}\left(T_\perp + \frac{H_0^2}{4\pi N} - T_\parallel\right)}{\dfrac{\pi M}{8N}\displaystyle\int v_\perp^4 \frac{\partial^2 f_0}{\partial v_z^2}(v_\perp, 0)\, d\mathbf{v}_\perp}. \tag{6}$$

Since for any function f_0 having a maximum at $v_z = 0$, $\int v_\perp^4 \frac{\partial^2 f_0}{\partial v_z^2}(v_\perp, 0) < 0$, the condition for the onset of instability is

$$-\frac{M}{8N}\int \frac{v_\perp^4}{v_z}\frac{\partial f_0}{\partial v_z} d\mathbf{v} > T_\perp + \frac{H_0^2}{4\pi N}.$$

In distinction from case a), instability sets in only when the transverse temperature is sufficiently high. The condition $\gamma_k \ll k_z v_{t\parallel}$, as it follows from (6), is met when

$$Y^* = \frac{\dfrac{M}{8N}\displaystyle\int \frac{v_\perp^4}{v_z}\cdot\frac{\partial f_0}{\partial v_z} d\mathbf{v} + T_\perp + \frac{H_0^2}{4\pi N}}{\dfrac{M}{8N}\displaystyle\int v_\perp^4 \frac{\partial^2 f_0}{\partial v_z^2}(v_\perp, 0)\, d\mathbf{v}_\perp} \ll 1.$$

From (6) it also follows that for $Y^* \ll 1$ the largest growth increment is characteristic of the modes with $k_z \ll k_\perp \left(\frac{k_z^2}{k_\perp^2} \sim Y^*\right)$. If the distribution function f_0 is Maxwellian with two different temperatures

$$f_0 = N_0 \frac{m^{3/2}}{(2\pi)^{3/2}} \cdot \frac{1}{T_\perp T_\parallel^{1/2}} \exp\left(-\frac{mv_\perp^2}{2T_\perp} - \frac{mv_z^2}{2T_\parallel}\right), \tag{7}$$

the growth increments obtained from (5) and (6) coincide with those calculated in /1/. In this reference, the dispersion equation was investigated retaining only terms of lowest order in $\frac{k_\perp v_{t\perp}}{\omega_{Hi}} \ll 1$. Introduction of the finite Larmor radius /4, 5/ showed that for $\frac{k_\perp^2 v_{t\perp}^2}{\omega_{Hi}^2} \gtrsim Y^*$ the plasma is stabilized with respect to the aperiodic instabilities. In our case, with $Y^* \ll 1$, we thus have $\frac{k_\perp^2 v_{t\perp}^2}{\omega_{Hi}^2} \ll 1$ in the entire unstable region of the spectrum.

2. Let us now proceed with the derivation of the quasilinear equations. The velocity distribution function of the ions — a solution of the Boltzmann—Vlasov nonlinear equation — is divided into two parts, one oscillating in space, which characterizes the collective plasma motions, and one homogeneous, which varies monotonically in time and describes the "background" against which these motions are set:

$$f = f_0 + f_1.$$

All the quantities describing the collective plasma motions are represented as a superposition of Fourier harmonics·

$$f_1 = \frac{1}{2}\sum_{\mathbf{k}} f_{\mathbf{k}} e^{i\mathbf{kr}} + \text{c.c.},\ \mathbf{E} = \frac{1}{2}\sum_{\mathbf{k}} E_{\mathbf{k}} e^{i\mathbf{kr}} + \text{c. c.},$$

$$\frac{c}{\omega_{\mathbf{k}}}[\mathbf{kE_k}] = \mathbf{H_k};\quad \frac{\partial E_{\mathbf{k}}}{\partial t} = \gamma_{\mathbf{k}} E_{\mathbf{k}}.$$

Averaging the Boltzmann—Vlasov equation over distances much greater than the oscillation wavelength, we obtain the following equation for $f_0 = \langle f \rangle$ (in averaging we make use of the equalities $\langle E \rangle = 0, \langle \mathbf{H} \rangle = \mathbf{H}_0 \parallel z$ and also remember that f_0 is independent of the azimuthal angle in the velocity space, ϑ):

$$\frac{\partial f_0}{\partial t} = -\frac{e}{2M}\sum_{\mathbf{k}}\left\{\mathbf{E}_{\mathbf{k}}^*\left(1 - \frac{\mathbf{kv}}{\omega_{\mathbf{k}}^*}\right) + \frac{\mathbf{k}}{\omega_{\mathbf{k}}^*}(\mathbf{vE}_{\mathbf{k}}^*)\right\}\frac{\partial f_{\mathbf{k}}}{\partial \mathbf{v}} + \text{c. c.} \tag{8}$$

In this equation we can conveniently pass to the polar coordinates $v_\perp$, v_z, Θ; $\Theta = \vartheta - \Phi$, where ϑ, Φ are the azimuthal angles of the vectors $\mathbf{v}_\perp$ and $\mathbf{k}_\perp$. If $E_{\mathbf{k}}$ is independent on Φ, integration with respect to Φ in the right-hand side of (8) is equivalent to averaging over Θ. The dependence on ϑ in the diffusive coefficients in (8) drops out, the axial symmetry of f_0 is conserved in time.

Equation (8) is written as

$$
\begin{gathered}
\frac{\partial f_0}{\partial t} = \left(\frac{\partial}{\partial v_\perp} + \frac{1}{v_\perp}\right) \sum_{\mathbf{k}} (I_1 \cos\Theta + I_2 \sin\Theta) + \frac{\partial}{\partial v_z} \sum_{\mathbf{k}} I_3; \\
I_1 = -\frac{e}{2M}\left(\frac{k_\perp v_\perp}{\omega_{\mathbf{k}}^*} E_{\mathbf{k}}^* f_{\mathbf{k}} \sin\Theta + \mathrm{c.\,c}\right); \\
I_2 = -\frac{e}{2M}\left[\left(1 - \frac{k_z v_z}{\omega_{\mathbf{k}}^*} - \frac{k_\perp v_\perp}{\omega_{\mathbf{k}}^*}\cos\Theta\right) E_{\mathbf{k}}^* f_{\mathbf{k}} + \mathrm{c.\,c.}\right]; \\
I_3 = -\frac{e}{2M}\left(\frac{k_z v_z}{\omega_{\mathbf{k}}^*} E_{\mathbf{k}}^* f_{\mathbf{k}} \sin\Theta + \mathrm{c.\,c}\right).
\end{gathered} \tag{9}
$$

Here we made use of the fact that $\mathbf{E_k}$ is perpendicular to $\mathbf{k}_\perp$ and $\mathbf{H}_0$; $f_{\mathbf{k}}$ depends on the "background" distribution function f_0.

To obtain the explicit form of this dependence, we shall have to make two assumptions, which are not new in the quasilinear theory.

We assume that f_0 varies adiabatically, i. e., $\left|\frac{1}{\omega - k_z v_\parallel + n\omega_H} \cdot \frac{1}{f_0} \cdot \frac{\partial f_0}{\partial t}\right| \ll 1$; $n = 0, \pm 1 \ldots$; $\omega = \omega' + i\gamma$ (see /6/). In our case, when the instability is aperiodic ($\omega' = 0$) and the thermal spread is small ($k_z v_{t\parallel} \ll \omega_{Hi}$), the strongest condition is obtained for $n = 0$. Since $\left|\frac{1}{f_0} \cdot \frac{\partial f_0}{\partial t}\right| \lesssim \gamma$, this condition can be written as $\gamma \ll k_z v_{t\parallel}$.* From (5) and (6) it follows that this condition is met when $Y, Y^* \ll 1$, i. e., when the deviation of the plasma parameters from the critical values corresponding to the onset of instability is small.

We also assume that the collective plasma motions can be adequately described in the linear approximation. In Section 5 we shall establish the conditions when the nonlinear coupling between the various harmonics of the collective motions is negligible.

Under these assumptions we write for $f_{\mathbf{k}}$ the ordinary formula of the linear theory:

$$
\begin{gathered}
f_{\mathbf{k}} = \frac{e}{2M} \sum_{n, n'} e^{-in'\Theta} J_{n'}(\lambda_2)\left[J_{n+1}(\lambda_2) - J_{n-1}(\lambda_2)\right] \frac{e^{in\Theta}}{n\omega_{Hi} - k_z v_z + \omega_{\mathbf{k}}} \times \\
\times E_{\mathbf{k}}\left[\frac{\partial f_0}{\partial v_\perp} - \frac{k_z}{\omega_{\mathbf{k}}}\left(v_z \frac{\partial f_0}{\partial v_\perp} - v_\perp \frac{\partial f_0}{\partial v_z}\right)\right].
\end{gathered} \tag{10}
$$

Substituting (10) in (9), we average over Θ and simplify the equation. Seeing that $\omega' = 0$ and conditions (3) are satisfied, we write

$$
\begin{gathered}
\frac{\partial f_0}{\partial t} = \frac{e^2}{2M^2}\left\{\frac{1}{v_\perp} \cdot \frac{\partial}{\partial v_\perp}\left[v_\perp \sum_{\mathbf{k}} \frac{|H_{\mathbf{k}}|^2}{c^2 k^2}\left(\frac{\gamma_{\mathbf{k}}}{\omega_{Hi}^2}\left(k_z^2 v_z^2 + \gamma_{\mathbf{k}}^2 + \frac{k_\perp^2 v_\perp^2}{2}\right)\frac{\partial f_0}{\partial v_\perp} - \right.\right.\right. \\
\left.\left. - \frac{k_\perp^2 v_\perp^2}{\omega_H^2} k_z^2 \frac{\gamma_{\mathbf{k}}}{k_z^2 v_z^2 + \gamma_{\mathbf{k}}^2} v_z \frac{\partial f_0}{\partial v_z}\right)\right] + \frac{\partial}{\partial v_z} \sum_{\mathbf{k}} \frac{|H_{\mathbf{k}}|^2}{c^2 k^2} \times \\
\left. \times \left[-\frac{2\gamma_{\mathbf{k}}}{\omega_{Hi}^2} k_z^2 v_z v_\perp \frac{\partial f_0}{\partial v_\perp} + \left(k_z^2 v_\perp^2 \frac{\gamma_{\mathbf{k}}}{\omega_{Hi}^2} + \frac{k_\perp^2 k_z^2 v_\perp^2}{\omega_{Hi}^2} \frac{\gamma_{\mathbf{k}}}{k_z^2 v_z^2 + \gamma_{\mathbf{k}}^2}\right)\frac{\partial f_0}{\partial v_z}\right]\right\}.
\end{gathered} \tag{11}
$$

* It is assumed that all velocity-averaged quantities need be considered in the region $v_\parallel \sim v_{t\parallel}$. This is true for all the averages, with the exception of $\int \frac{v_\perp^4}{v_z} \cdot \frac{\partial \delta f}{\partial v_z} dv$, where for $t \to \infty$ the region $v_\parallel \sim v_{t\parallel} \sqrt[4]{w^*} \ll v_{t\parallel}$ is relevant (see equation (28)). However, it is easily seen that for $t \to \infty$ the condition $v_\parallel \gg \frac{\gamma_k}{k}$ is satisfied for these velocities also.

3. Equation (11)*, like the dispersion equation, will be solved separately for the two cases $k_\perp = 0$, $k_\perp \gg k_z$.

For $k_\perp = 0$, the instability is connected with all the plasma particles, and not with a particular group of resonance particles: the growth increment is determined by the average temperatures $T_\parallel$, $T_\perp$ (see (5)) and the diffusive coefficients in (11) are smooth functions of v_z, $v_\perp$. In this case it therefore suffices to consider velocity-averaged quantities, i.e., moments of the velocity distribution function. From (11) we have $\int \frac{\partial f_0}{\partial t} d\mathbf{v} = 0$; $\int v_z \frac{\partial f_0}{\partial t} d\mathbf{v} = 0$, i.e., f_0 quite properly remains an even function of v_z.

For the second-order moments we have from (11) for $k_\perp = 0$

$$N\frac{dT_\perp}{dt} = \int \frac{Mv_\perp^2}{2}\cdot\frac{\partial f_0}{\partial t} d\mathbf{v} = \frac{1}{4\pi}\cdot\frac{\omega_{0i}^2}{\omega_{Hi}^2}\sum_k \gamma_k |H_k|^2 \frac{\gamma_k^2 + k^2\frac{T_\parallel}{M}}{c^2k^2} =$$

$$= N\sum_k \gamma_k \frac{|H_k|^2}{H_0^2}\left(2T_\parallel - T_\perp - \frac{H_0^2}{4\pi N}\right); \qquad (12)$$

$$N\frac{dT_\parallel}{dt} = \int Mv_z^2 \frac{\partial f_0}{\partial t} d\mathbf{v} = -\frac{1}{\pi}\frac{\omega_{0i}^2}{\omega_{Hi}^2}\sum_k \gamma_k |H_k|^2 \frac{T_\parallel - \frac{T_\perp}{2}}{Mc^2} = -4N\sum_k \gamma_k \frac{|H_k|^2}{H_0^2}\left(T_\parallel - \frac{T_\perp}{2}\right). \qquad (12')$$

The variation of the energy of the electromagnetic field is determined from the equation

$$\frac{d}{dt}\sum_k \frac{|E_k|^2 + |H_k|^2}{8\pi} = \frac{1}{4\pi}\sum \gamma_k |H_k|^2\left(1 + \frac{\gamma_k^2}{k^2c^2}\right). \qquad (12'')$$

From (12)—(12'') we have the law of conservation of energy

$$N\frac{dT_\perp}{dt} + \frac{N}{2}\cdot\frac{dT_\parallel}{dt} + \frac{1}{4\pi}\sum_k \gamma_k(|H_k|^2 + |E_k|^2) =$$

$$= \frac{1}{4\pi}\cdot\frac{\omega_{0i}^2}{\omega_{Hi}^2}\sum_k \frac{\gamma_k |H_k|^2}{k^2c^2}\left[\gamma_k^2\left(1 + \frac{H_0^2}{4\pi NMc^2}\right) - k^2\frac{T_\parallel - T_\perp - \frac{H_0^2}{4\pi N}}{M}\right] = 0. \qquad (13)$$

The electrons in this problem make no contribution to energy conservation. This is so because the highest electron current flows at right angles to the electric field (in this direction the electron current balances the ion current). The electron current along the electric field is small in comparison with the current of ions, the two longitudinal currents relating as $\mu = \frac{M_e}{M_i}$.** Therefore the energy absorbed by the electrons when instability sets in is $1/\mu$ of the energy absorbed by the ions. From (12)—(12'') we can easily find the variation of $T_\parallel$, $T_\perp$, and $W = \frac{1}{8\pi}\sum_k \frac{|H_k|^2}{H_0^2}$ with the onset of instability.

* In our derivation of (11) we neglected resonance particles with velocities $v \simeq \frac{\omega + \omega_{Hi}}{k_z} \gg v_{T\parallel}$. Introducing these particles in the dispersion equation, we obtain a new species of instabilities in an anisotropic plasma, which are considered in /7/. However, since the resonance particles are few ($v_{res} \gg v_T$), these instabilities cannot alter the plasma parameters to any considerable extent.

** It is assumed that the velocity distribution of the electrons is isotropic.

Dividing equation (12) by (12') and substituting the initial values $T_\perp^0$ and $T_\parallel^0$ for $T_\perp$ and $T_\parallel$ in the right-hand side of the resulting equation (this substitution corresponds to the omission of terms $\sim Y$), we find

$$\frac{dT_\perp}{dT_\parallel} = -\frac{T_\parallel^0}{2(2T_\parallel^0 - T_\perp^0)}.$$

Hence an equation for the variations of the longitudinal and the transverse temperatures with the onset of instability,

$$\delta T_\perp = -\delta T_\parallel \frac{T_\parallel^0}{2(2T_\parallel^0 - T_\perp^0)}. \tag{14}$$

On the other hand, on saturation, when $\gamma_k \to 0$,

$$T_\parallel^\infty = T_\perp^\infty + \frac{H_0^2}{4\pi N}, \tag{15}$$

whence follows another equation for the total variations of the longitudinal and the transverse temperatures:

$$\delta T_\parallel^\infty = \delta T_\perp^\infty - Y T_\parallel^0. \tag{15'}$$

For $\delta T_\parallel^\infty$ and $\delta T_\perp^\infty$ we find from (14) and (15')

$$\delta T_\perp^\infty = Y \frac{T_\parallel^{02}}{5T_\parallel^0 - 2T_\perp^0}; \quad \delta T_\parallel^\infty = -Y\frac{2T_\parallel^0 (2T_\parallel^0 - T_\perp^0)}{5T_\parallel^0 - 2T_\perp^0}. \tag{16}$$

Analogously, from (12') we have for W as $t \to \infty$

$$W^\infty = \frac{Y}{4\pi} \cdot \frac{T_\parallel^0}{5T_\parallel^0 - 2T_\perp^0} \tag{17}$$

(for $t \to \infty$, when $\gamma_k \to 0$, $|E_k|^2 = \frac{\gamma_k^2}{k^2c^2}|H_k|^2 \to 0$). For $Y \sim 1$, the quasilinear theory, as we have already observed, does not apply. However, for lack of a more rigorous theory, we shall try to extrapolate the solutions of (12) and (12') to the region $Y \sim 1$. In this case from (12) and (12') we have

$$\frac{dT_\parallel}{dT_\perp} = -2\frac{2T_\parallel - T_\perp}{2T_\parallel - T_\perp - \frac{H_0^2}{4\pi N}}. \tag{18}$$

Solving (18) with $T_\perp = T_\perp^0$, $T_\parallel = T_\parallel^0$ and seeing that for $t \to \infty$ relation (15) is satisfied, we obtain the following equation for the transverse temperature on saturation:

$$T_\perp^\infty - \frac{H_0^2}{30\pi N} \ln \frac{T_\perp^\infty + \frac{9}{20\pi}\cdot\frac{H_0^2}{N}}{2T_\parallel^0 - T_\perp^0 - \frac{1}{20\pi}\cdot\frac{H_0^2}{N}} = \frac{T_\parallel^0 + 2T_\perp^0 - \frac{H_0^2}{4\pi N}}{3}. \tag{19}$$

For $Y \ll 1$, equation (19) gives formula (16) for $\delta T_\perp^\infty$, but for $Y \sim 1$ formulas (16) and (19) also give fairly close results. For example, for $T_\perp^0 = 0.5T_\parallel^0$,

$Y = 0.4\delta T_\perp^\infty$, $\delta T_\perp^\infty$ calculated from (19) is equal to $0.12\, T_\parallel^0$, and that calculated from (16) is $0.1\, T_\parallel^0$.

4. Let us now consider instabilities with $k_\perp \neq 0$ setting in when the transverse temperature is fairly high. Retaining in the diffusive coefficients of (11) the contribution of the most stable spectral region, where $k_z \ll k_\perp$, $k_z^2 \sim k_\perp^2 Y^*$ (see (6)), we find an equation for the time variation of f_0:

$$\frac{\partial f_0}{\partial t} = \frac{1}{2}\sum_{\mathbf{k}} \frac{|H_{\mathbf{k}}|^2}{H_0^2}\left\{\frac{1}{v_\perp}\cdot\frac{\partial}{\partial v_\perp}\right| v_\perp < \gamma_{\mathbf{k}}\frac{v_\perp^2}{2}\cdot\frac{\partial f_0}{\partial v_\perp} - \\ - k_z^2 v_z v_\perp^3 \frac{\gamma_{\mathbf{k}}}{k_z^2 v_z^2 + \gamma_{\mathbf{k}}^2}\cdot\frac{\partial f_0}{\partial v_z} > \Bigg] + \frac{\partial}{\partial v_z}\left(\frac{k_z^2 v_\perp^4}{2}\cdot\frac{\gamma_{\mathbf{k}}}{k_z^2 v_z^2 + \gamma_{\mathbf{k}}^2}\cdot\frac{\partial f_0}{\partial v_z}\right)\Bigg\}. \tag{20}$$

Hence for the variation of the ion transverse temperature

$$N\frac{dT_\perp}{dt} = \int \frac{Mv_\perp^2}{2}\cdot\frac{\partial f_0}{\partial t}\,d\mathbf{v} = \sum_{\mathbf{k}}\gamma_{\mathbf{k}}\frac{|H_{\mathbf{k}}|^2}{H_0^2}\left[\int Mv_\perp^2 f_0 d\mathbf{v} + \right. \\ \left. + \frac{1}{2}\int Mv_\perp^4 \frac{k_z^2 v_z}{k_z^2 v_z^2 + \gamma_{\mathbf{k}}^2}\cdot\frac{\partial f_0}{\partial v_z}\,d\mathbf{v}\right]. \tag{21}$$

The last integral in (21)

$$\int Mv_\perp^4 \frac{k_z^2 v_z}{k_z^2 v_z^2 + \gamma_{\mathbf{k}}^2}\cdot\frac{\partial f_0}{\partial v_z}\,d\mathbf{v} = \int Mv_\perp^4 \frac{1}{v_z}\cdot\frac{\partial f_0}{\partial v_z}\,d\mathbf{v} - \gamma_{\mathbf{k}}^2\int\frac{Mv_\perp^4}{k_z^2 v_z^2 + \gamma_{\mathbf{k}}^2} \times \\ \times \frac{1}{v_z}\cdot\frac{\partial f_0}{\partial v_z}\,d\mathbf{v} = \int Mv_\perp^4\frac{1}{v_z}\cdot\frac{\partial f_0}{\partial v_z}\,d\mathbf{v} - \pi\frac{\gamma_{\mathbf{k}}}{k_z}\int Mv_\perp^4\frac{\partial^2 f_0}{\partial v_z^2}(v_\perp,\,0)\,d\mathbf{v}_\perp.$$

For $T_\perp$ we finally have

$$N\frac{dT_\perp}{dt} = \sum_{\mathbf{k}}\gamma_{\mathbf{k}}\frac{|H_{\mathbf{k}}|^2}{H_0^2}\left[2NT_\perp + \frac{1}{2}\int Mv_\perp^4\frac{1}{v_z}\cdot\frac{\partial f_0}{\partial v_z}\,d\mathbf{v} - \frac{\pi}{2}\frac{\gamma_{\mathbf{k}}}{k_z}\int Mv_\perp^4\frac{\partial^2 f_0}{\partial v_z^2}(v_\perp,\,0)\,d\mathbf{v}_\perp\right]. \tag{22}$$

Analogously, for the time variation of the longitudinal temperature we have from (20)

$$N\frac{dT_\parallel}{dt} = -\frac{1}{2}\sum_{\mathbf{k}}\gamma_{\mathbf{k}}\frac{|H_{\mathbf{k}}|^2}{H_0^2}\left[\int Mv_\perp^4\frac{1}{v_z}\cdot\frac{\partial f_0}{\partial v_z}\,d\mathbf{v} - \right. \\ \left. - \pi\frac{\gamma_{\mathbf{k}}}{k_z}\int Mv^4\frac{\partial^2 f_0}{\partial v_z^2}(v_\perp,\,0)\,d\mathbf{v}\right]. \tag{23}$$

From (22), (23) we can derive the law of conservation of energy: the change in the energy of the thermal motion of ions is equal to the energy of the magnetic field generated with the onset of instability,

$$N\frac{dT_\perp}{dt} + \frac{N}{2}\cdot\frac{dT_\parallel}{dt} + \frac{d}{dt}\sum_{\mathbf{k}}\frac{|H_{\mathbf{k}}|^2}{8\pi} = N\sum_{\mathbf{k}}\gamma_{\mathbf{k}}\frac{|H_{\mathbf{k}}|^2}{H_0^2}\left[2T_\perp + \frac{H_0^2}{4\pi N} + \right. \\ \left. + \frac{1}{4}\int Mv_\perp^4\frac{1}{v_z}\cdot\frac{\partial f_0}{\partial v_z}\,d\mathbf{v} - \frac{\pi}{4}\cdot\frac{\gamma_{\mathbf{k}}}{k_z}\quad Mv_\perp^4\frac{\partial^2 f_0}{\partial v_z^2}(v_\perp,\,0)\,d\mathbf{v}_\perp\right]. \tag{24}$$

Substituting $\gamma_{\mathbf{k}}$ from (6) in (24) and neglecting terms $\sim \frac{k_z^2}{k_\perp^2}$*, we write an expression where the integral in the right-hand side of (24) vanishes.

* These terms would introduce small corrections $\sim \frac{k_z^2}{k_\perp^2} \sim Y^*$ in the equations for $T_\perp$ and $T_\parallel$.

Neglecting the variation of the electric field energy $\sum\limits_{k}|E_k|^2 \sim \sum\limits_{k}\frac{\gamma_k^2}{k^2c^2}|H_k|^2$ in (24) is equivalent to neglecting the terms quadratic in γ_k in the dispersion equation (see (16)).

Let us now proceed with the solution of equation (20). For $v_z \sim v_{t\parallel}$ equation (20) can be solved by successive approximation. Writing f_0 as $f_0^0(\mathbf{v}) + \delta f_0\,(t,\,\mathbf{v})$, where $f_0^0\,(\mathbf{v}) = f_0\,(0,\,\mathbf{v})$ is defined by (7), and taking $\left|\frac{\delta f_0}{f_0^0}\right| \ll 1$, we find for δf_0

$$\delta f_0 = 2\pi W\left[\frac{1}{v_\perp}\cdot\frac{\partial}{\partial v_\perp}\left(\frac{1}{T_\parallel^0} - \frac{1}{2T_\perp^0}\right) - \frac{1}{2T_\parallel^0}\,\frac{\partial}{\partial v_z}\,\frac{1}{v_z}\right] M v_\perp^4 f_0^0. \tag{25}$$

In our case, with $Y^* \ll 1$, $W \ll 1$, and $v_z \sim v_{t\parallel}$, $\left|\frac{\delta f_0}{f_0^0}\right| \ll 1$. For $v_z \to 0$, the last term in (25), $\sim 1/v_z^2$, becomes large, and the foregoing technique is inadequate for the solution of (20). This is so because the third term in the transport equation (20) has a sharp maximum for $v_z \ll v_{t\parallel}$, so that in the region of small v_z, f_0 may vary considerably, although the velocity-average $T_\perp$, $T_\parallel$ remain fairly constant for $Y^* \ll 1$. In the region of small v_z, equation (20) must be solved exactly, retaining the third term only. In this case, changing over to the variable W, we obtain for f_0

$$\frac{\partial f_0}{\partial W} = \pi v_\perp^4\,\frac{\partial}{\partial v_z}\left(\frac{1}{v_z^2}\cdot\frac{\partial f_0}{\partial f_z}\right). \tag{26}$$

This equation is solved by Laplace transformation. Writing f_0 as $f_0 = f_0^0 + \delta f_0$, we obtain for the Laplace transform $f_p = \int\limits_0^\infty e^{-pW}\delta f_0\,dW$ the equation*

$$\frac{d^2 f_p}{dv_z^2} - \frac{2}{v_z}\cdot\frac{df_p}{dv_z} - \frac{p v_z^2}{\pi v_\perp^4} f_p = -\frac{1}{4}\left(\frac{d^2 f_0^0}{dv_z^2} - \frac{2}{v_z}\,\frac{df_0^0}{dv_z}\right) = -\frac{A}{p}\,. \tag{27}$$

where $A = n_0\frac{1}{(2\pi)^{3/2}}\left(\frac{m}{T_\parallel}\right)^{1/2}\frac{m}{T_\perp}e^{-\frac{mv_\perp^2}{2T_\perp}}$. This equation can be solved by the method of variation of arbitrary constants. The constants are determined from the condition that f_p is even in v_z and that f_p is bounded as $v_z \to \infty$. The result gives

$$f_p = \frac{A}{4p}v_z^{3/2}v_\perp^{1/2}\left\{I_{3/4}(z)\int\limits_z^\infty\frac{K_{3/4}(z')}{z'^{3/4}}dz' + \right.$$
$$\left. + K_{3/4}(z)\left[\int\limits_0^z\frac{I_{3/4}(z')}{z'^{3/4}}dz' - \frac{2^{3/4}}{\pi^{1/4}}\Gamma\left(\frac{3}{4}\right)\right]\right\}\left(\frac{4\pi}{p}\right)^{1/8}. \tag{28}$$

Here $z = \frac{v_z^2}{v_\perp^2}\sqrt{\frac{p}{4\pi}}$; f_p has a branching singularity at the origin: for $p \to 0$, $f_p \cong \frac{\alpha}{p^{5/4}} + \frac{\beta}{p} + \frac{\gamma}{p^{3/4}} + \ldots$, where $\alpha = -\pi A v_\perp^2\frac{\Gamma\left(\frac{3}{4}\right)}{\Gamma\left(\frac{1}{4}\right)}$, $\beta = \frac{Av_z^2}{2}$. Returning to the

* Equation (27) applies for small $v_z \ll v_{t\parallel}$, and therefore in the right-hand side $f_0^0(v_\perp,\,0)$ has been substituted for $f_0^0(v_\perp,\,v_z)$.

original variable W, we find

$$\delta f_0 = \frac{1}{2\pi i}\int_{\sigma-i\infty}^{\sigma+i\infty} f_p e^{pW} dp = -\frac{1}{2\pi i}\int_c f_p e^{pW} dp. \tag{28'}$$

The last integral in (28) is taken along the upper bank of the cut (Re $p < 0$, Im $p = 0$) from $-\infty$ to $-\varepsilon$, then along the circle of the radius ε enclosing the singularity at zero, and finally along the lower bank of the cut from $-\varepsilon$ to $-\infty$. The integrals over the sections $|p| \to \infty$, $\pi/2 < \arg p < \pi$ and $-\pi \arg p < -\pi/2$ make no contribution to δf_0, since for $|p| \to \infty$, $f_p \sim 1/p^2$. We thus have

$$\delta f_0 = \frac{A}{2} v_z^2 - A \cdot 2^{3/2} (\pi W)^{1/4} \frac{\Gamma\left(\frac{3}{4}\right)}{\Gamma\left(\frac{1}{4}\right)} v_z^{3/2} v_\perp^{1/2} \operatorname{epx}\left\{-\frac{v_z^4}{32\pi W v_\perp^4}\right\} \times$$
$$\times \left[M_{-\frac{1}{8},\ \frac{1}{8}}\left(\frac{v_z^4}{v_\perp^4} \cdot \frac{1}{16\pi W}\right) + \frac{v_\perp^2}{v_z^2} (\pi W)^{1/2} M_{\frac{3}{8},\ -\frac{3}{8}}\left(\frac{v_z^4}{v_\perp^4} \cdot \frac{1}{16\pi W}\right)\right]. \tag{29}$$

where $M_{\alpha,\beta}(z)$ are Whittaker's functions. Applying the well-known asymptotic expansions of Whittaker's functions for large z, we find that for $v_z \gg v_\perp W^{1/4}$, δf_0 reduces to the leading term in (25), equal to $\pi W \frac{M v_\perp^4}{T_\parallel^0 v_z^2} f_0^0(v_\perp, 0)$. All the other terms in (25) remain small as $v_z \to 0$, providing $W \ll 1$. Therefore, combining (25) and (29), we obtain for δf_0 a relation which applies for any $v_z\,(0 < v_z < v_{t\parallel})$, if $W^\infty \ll 1$:

$$\delta f_0^{tot} = \left\{2\pi W \frac{1}{v_\perp} \cdot \frac{\partial}{\partial v_\perp}\left(\frac{1}{T_\parallel^0} - \frac{1}{2T_\perp^0}\right) M v_\perp^4\right\} f_0^0 + \delta f_0, \tag{29'}$$

where δf_0 is determined from (29).

Having solved (20), we can find the variation of $T_\perp$, $T_\parallel$, and W with the onset of instability. Substituting f_0^0 for f_0 in the right-hand side of equation (22) for $T_\perp$, which is equivalent to retaining leading terms in Y^*, and omitting the last term $\sim \gamma_{\mathbf{k}}$, we find

$$\frac{dT_\perp}{dt} = 2\sum_{\mathbf{k}} \gamma_{\mathbf{k}} \frac{|H_{\mathbf{k}}|^2}{H_0^2} T_\perp^0 \left(1 - \frac{2T_\perp^0}{T_\parallel^0}\right). \tag{30}$$

For the time variation of W we have

$$\frac{dW}{dt} = \frac{1}{4\pi}\sum_{\mathbf{k}} \gamma_{\mathbf{k}} \frac{|H_{\mathbf{k}}|^2}{H_0^2}. \tag{30'}$$

Dividing (30) by (30'), we find a relation among the variations of the transverse temperature and of the magnetic field energy with the onset of instability:

$$\frac{dT_\perp}{dW} = 8\pi T_\perp^0\left(1 - \frac{2T_\perp^0}{T_\parallel^0}\right), \text{i. e.}, \delta T_\perp = 8\pi W T_\perp^0 \left(1 - \frac{2T_\perp^0}{T_\parallel^0}\right). \tag{31}$$

On the other hand, for $t \to \infty$, when $\gamma_k \to 0$,

$$\frac{1}{8}\int M v_\perp^4 \frac{1}{v_z} \cdot \frac{\partial f_0^\infty}{\partial v_z} d\mathbf{v} + NT_\perp^\infty + \frac{H_i^2}{8\pi} = 0.$$

Substituting $f_0^\infty = f_0^0 + \delta f_0^\infty$, $T_\perp^\infty = T_\perp^0 + \delta T_\perp^\infty$, we obtain another equation for $\delta T_\perp^\infty$:

$$\delta T_\perp^\infty + \frac{M}{8N}\int \frac{v_\perp^4}{v_z} \cdot \frac{\partial \delta f_0^\infty}{\partial v_z} d\mathbf{v} = Y^* \frac{T_\perp^{02}}{T_\parallel^0}. \tag{32}$$

Substituting $\delta T_\perp^\infty$ from (31) and δf_0^∞ from (29'), we obtain an equation for W^∞:

$$8\pi W^\infty T_\perp^0\left(1 - \frac{2T_\perp^0}{T_\parallel^0}\right) + \frac{15}{8} G \left(\frac{T_\perp^0}{T_\parallel^0}\right)^{3/4} T_\perp^0 (\pi W^\infty)^{1/4} = Y^* \frac{T_\perp^{02}}{T_\parallel^0}, \tag{33}$$

where G is a constant,

$$G = \int_0^\infty \frac{dz}{z^{1/4}} \cdot \frac{d}{dz}\left\{z^{1/8} - 4z^{5/8} e^{-\frac{z}{2}} \frac{\Gamma\left(\frac{3}{4}\right)}{\Gamma\left(\frac{1}{2}\right)} \times \right.$$
$$\left. \times \left[M_{-\frac{1}{8},\ \frac{1}{8}}(z) + \frac{1}{4z^{1/2}} M_{\frac{3}{8},\ -\frac{3}{8}}(z)\right]\right\} = 2^{1/2} \frac{\left[\Gamma\left(\frac{3}{4}\right)\right]^2}{\Gamma\left(\frac{1}{4}\right)}.$$

The region of small v_z ($v_z \sim v_t (W^\infty)^{1/4}$) is the most relevant in the integral with respect to v_z in (32), its contribution being $\sim (W^\infty)^{1/4}$. The region of large v_z ($v_z \sim v_t$) gives a small contribution $\sim W^\infty$, which can be neglected. With the same accuracy, we may neglect the first term in (33). Then

$$W^\infty = \frac{1}{20\pi} Y^{*4} \frac{T_\parallel^{02}}{T_\perp^{02}}. \tag{34}$$

Making use of equation (31), we obtain for the total variation of the transverse temperature

$$\delta T_\perp^\infty = -\frac{4}{5} Y^{*4} \frac{T_\parallel^{02}}{T_\perp^0}\left(\frac{2T_\perp^0}{T_\parallel^0} - \quad\right). \tag{34'}$$

Analogously, from (23) we find for the total variation of the longitudinal temperature

$$\delta T_\parallel^\infty = \frac{8}{5} Y^{*4} T_\parallel^0. \tag{34''}$$

5. To justify the application of the quasilinear approximation to our problem, we must show that for saturation amplitudes H_k^∞, determined by (17) and (34), the nonlinear coupling of the harmonics is negligible. Let

us consider this coupling. We shall start with the nonlinear kinetic equation for the electrons and the ions ($\alpha = e,\ i$) in the form

$$\frac{\partial f_{\mathbf{k}}^{\alpha}}{\partial t} + i\,(k_{\perp} v_{\perp} \cos\Theta + k_z v_z) f_{\mathbf{k}}^{\alpha} - \omega_{k\alpha} \frac{\partial f_{\mathbf{k}}^{\alpha}}{\partial \Theta} + \frac{e^{\alpha}}{M^{\alpha}} E_{\mathbf{k}} \left[\frac{\partial f_0^{\alpha}}{\partial v_{\perp}} \left(1 - \frac{k_z v_z}{\omega_{\mathbf{k}}}\right) + \right.$$
$$\left. + \frac{k_z v_{\perp}}{\omega_{\mathbf{k}}} \cdot \frac{\partial f_0^{\alpha}}{\partial v_z} \right] = - \frac{e^{\alpha}}{M^{\alpha}} \left\{ \left(\frac{\partial}{\partial v_{\perp}} + \frac{1}{v_{\perp}} \right) \sum_{\mathbf{k}'} E_{\mathbf{k}-\mathbf{k}'} f_{\mathbf{k}'}^{\alpha} \sin\Theta \left(1 - \right.\right.$$
$$\left. - \frac{(k_z - k_z') v_z}{\omega_{\mathbf{k}-\mathbf{k}'}} \right) + \frac{1}{v_{\perp}} \cdot \frac{\partial}{\partial \Theta} \sum_{\mathbf{k}'} E_{\mathbf{k}-\mathbf{k}'} f_{\mathbf{k}'}^{\alpha} \left[\cos\Theta \left(1 - \frac{(k_z - k_z') v_z}{\omega_{\mathbf{k}-\mathbf{k}'}} \right) - \right.$$
$$\left.\left. - \frac{|\mathbf{k}_{\perp} - \mathbf{k}_{\perp}'|\, v_{\perp}}{\omega_{\mathbf{k}-\mathbf{k}'}} \right] + \frac{\partial}{\partial v_z} \sum_{\mathbf{k}'} E_{\mathbf{k}-\mathbf{k}'} f_{\mathbf{k}'}^{\alpha} \sin\Theta \cdot \frac{(k_z - k_z') v_{\perp}}{\omega_{\mathbf{k}-\mathbf{k}'}} \right\}. \tag{35}$$

Here for simplicity we assume that $\mathbf{k}$, $\mathbf{k}'$ and $\mathbf{H}_0$ are coplanar.*

In the case of aperiodic instability, mode coupling alters the time dependence of the amplitude $H_{\mathbf{k}}$ already in the second order relative to the oscillation amplitude. To find $f_{\mathbf{k}}$ in this approximation, we substitute $f_{\mathbf{k}}^{\alpha}$ from (10) in the nonlinear terms, which are all collected in the right-hand side of (35). Solving this equation and simplifying (it is assumed that $|\omega_{\mathbf{k}-\mathbf{k}'}|,\ |\omega_{\mathbf{k}'}| \ll \omega_{Hi}$ and that conditions (3) are satisfied for $\mathbf{k}$ and $\mathbf{k}'$), we obtain after simple, though fairly tedious manipulations the following expression for the nonlinear correction to the distribution function $f_{\mathbf{k}}$:

$$f_{\mathbf{k}}^{(2)} = \frac{1}{4} \sum_{\mathbf{k}'} \frac{H_{\mathbf{k}'} H_{\mathbf{k}-\mathbf{k}'}}{H_0^2 k' |\mathbf{k} - \mathbf{k}'|} \left\{ \sum_{\pm} \frac{e^{\pm i\Theta} \omega_{Hi}}{k_z v_z \mp \omega_{Hi} - \omega_{\mathbf{k}-\mathbf{k}'} - \omega_{\mathbf{k}'}} \left[2\,|\mathbf{k}_{\perp} - \mathbf{k}_{\perp}'| \mp \right.\right.$$
$$\left. \mp \mathbf{k}_{\perp}' \frac{\partial}{\partial v_{\perp}} v_{\perp} \frac{\omega_{\mathbf{k}-\mathbf{k}'} - (k_z - k_z') v_z}{\omega_{\mathbf{k}'} - k_z' v_z} \mp \frac{\partial}{\partial v_z} \cdot \frac{k_{\perp}' (k_z - k_z') v_{\perp}^2}{\omega_{\mathbf{k}'} - k_z' v_z} \right] \times$$
$$\left. \times \left[\frac{\partial f_0}{\partial v_{\perp}} (\omega_{\mathbf{k}'} - k_z' v_z) + k_z' v_{\perp} \frac{\partial f_0}{\partial v_z} \right] + \sum_{s=0, \pm 2} A_s e^{is\Theta} \right\}. \tag{36}$$

We do not give here the highly cumbersome expressions for f_s, since they make no contribution to j_x, j_y.** Applying Maxwell's equations, we obtain for $H_{\mathbf{k}}$

$$\frac{1}{c^2} \cdot \frac{\partial^2 H_{\mathbf{k}}}{\partial t^2} + k^2 H_{\mathbf{k}} + \frac{4\pi}{c^2} \hat{\sigma}_{22} \frac{\partial H_{\mathbf{k}}}{\partial t} = - \frac{4\pi}{c}\, ik \sum_{\alpha} e^{\alpha} \int v_{\perp} \sin\Theta f_{\mathbf{k}\alpha}^{(2)} d\mathbf{v};$$
$$\frac{1}{c^2} \cdot \frac{\partial^2 \widetilde{H}_{\mathbf{k}}}{\partial t^2} + k_z^2 \widetilde{H}_{\mathbf{k}} + \frac{4\pi}{c^2} \hat{\sigma}_{11} \frac{\partial H_{\mathbf{k}}}{\partial t} = \frac{4\pi}{c}\, ik_z \sum_{\alpha} e^{\alpha} \int v_{\perp} \cos\Theta f_{\mathbf{k}\alpha}^{(2)} d\mathbf{v}, \tag{37}$$

where $H_{\mathbf{k}}$ is the magnetic field amplitude observed with the onset of instability in the plane through $\mathbf{k}$ and $\mathbf{H}_0$; $\widetilde{H}_{\mathbf{k}}$ is the amplitude of the magnetic field at right angles to this plane, contributed by mode coupling; σ_{11}, σ_{22} are the linear-theoretical components of the conductivity tensor ($\omega_{\mathbf{k}}$ should be replaced with $i\frac{\partial}{\partial t}$ in these quantities).

Substituting $f_{\mathbf{k}\alpha}^{(2)}$ from (36), we integrate with respect to $\mathbf{v}$ in the right-hand side of (37) setting $|\omega_{\mathbf{k}}| \ll k_z v_{T\parallel}$. We also assume that the velocity distribution function of the electrons is isotropic. Then it is only ions that

* This can be done without loss of generality, since we are concerned with evaluating the order of magnitude of mode coupling.

** The presence of a term with $s = 0$ in (36) implies that mode coupling in our case gives rise to j_z and, consequently, to $E \parallel \mathbf{H}_0$. However, since ε_{33} is large at low frequencies, $\mathbf{E}_{\parallel}$ is small.

contribute to $j_x^{(\mathrm{non})}$, $j_y^{(\mathrm{non})}$. Moreover, for $k_\perp = 0$, the terms proportional to $e^{\pm i\varphi}$ vanish in $f_{\mathbf{k}}^{(2)}$. Therefore, only one component of $\mathbf{j}^{(\mathrm{non})}$, viz., $j_z^{(\mathrm{non})}$, does not vanish: thus for $k_\perp = 0$ the coupling of two transverse modes may only produce longitudinal oscillations $\mathbf{E} \parallel \mathbf{H}_0$.* However, as we have previously observed, ε_{33} being large at low frequencies, the field in these oscillations is negligible. Therefore, for the second-order amplitude $H_{\mathbf{k}}$, mode coupling need be considered only when $k_\perp \neq 0$, i.e., for instabilities conditioned by a high transverse temperature. In this case, from (37),

$$\frac{\partial H_{\mathbf{k}}}{\partial t} = \gamma_{\mathbf{k}} H_{\mathbf{k}} - \frac{k_z^2}{\pi k_\perp} \sum_{\mathbf{k}'} \frac{k_z - k_z'}{|k_\perp - k_\perp'|} H_{\mathbf{k}'} \frac{H_{\mathbf{k}-\mathbf{k}'}}{H_0} \times \frac{3T_\perp - T_\parallel + \frac{M}{4} \int \frac{v_\perp^4}{v_z} \cdot \frac{\partial f_0}{\partial v_z}\, d\mathbf{v}}{\frac{M}{4} \int v_\perp^4 \frac{\partial^2 f_0}{\partial v_z^2} (v_\perp, 0)\, d\mathbf{v}_\perp}, \tag{38}$$

where $\gamma_{\mathbf{k}}$ is defined by (6);

$$-\frac{\partial^2 H_{\mathbf{k}}}{\partial t^2} \left(1 + \frac{H_0^2}{4\pi N M c^2}\right) + k_z^2 \frac{T_\parallel - T_\perp - \frac{H_0^2}{4\pi N}}{M} \widetilde{H}_{\mathbf{k}} = i k_z^2 \sum_{\mathbf{k}'} \frac{k_z'}{k_\perp'} H_{\mathbf{k}'} \frac{H_{\mathbf{k}-\mathbf{k}'}}{H_0} \cdot \frac{T_\perp - T_\parallel}{M}. \tag{39}$$

The quasilinear theory considers only the first term in the right-hand side of equation (38); it is of the order of $k_z v_{T\parallel} Y^* H_{\mathbf{k}}$. The second term is attributable to mode coupling. For the amplitudes $H_{\mathbf{k}}^{\infty}$ determined from (34) this term is small, of the order of $k_z v_{T\parallel} \frac{k_z^2}{k_\perp^2} \cdot \frac{H_{\mathbf{k}}^2}{H_0} \sim k_z v_{T\parallel} Y^{*3} H_{\mathbf{k}}$.

Mode coupling is thus insignificant over times $\sim 1/\gamma$, and it can actually be neglected when considering the growth of the instability to the steady-state amplitude (34).

From (39) it follows that mode coupling also produces a magnetic field at right angles to the $\mathbf{k}$, $\mathbf{H}_0$ plane, but the amplitude of this field is small in comparison with $H_{\mathbf{k}}$:

$$\widetilde{H}_{\mathbf{k}} \sim \frac{k_z}{k_\perp} \cdot \frac{H_{\mathbf{k}}^2}{H_0} \sim H_{\mathbf{k}} Y^{*^{3/2}}.$$

Hence, for $k_\perp \neq 0$, mode coupling may be neglected if $Y^* \ll 1$.

With $k_\perp = 0$ mode coupling is felt only for the third-order amplitude $H_{\mathbf{k}}$. Calculations follow the usual scheme: having found the nonlinear correction $f_{\mathbf{k}}^{(3)}$ to the distribution function, we calculate $j_x^{(\mathrm{non})}$, $j_y^{(\mathrm{non})}$ and substitute the results in Maxwell's equations. In this case the nonlinear mode coupling proves to be much more significant than for $k_\perp \neq 0$. This is so because with $k_\perp = 0$ small terms $\sim \gamma_{\mathbf{k}}^2$ must be considered in the left-hand side of equation (37), which more than compensates for the appearance of mode coupling as late as the third-order $H_{\mathbf{k}}$.

The nonlinearity of the collective plasma motions for $k_\perp = 0$ can be neglected if $\left|\frac{T_\parallel - T_\perp}{T_\perp}\right| \ll 1$. This condition is equivalent to $Y \ll 1$ for small magnetic fields H_0 only, when $\frac{H_0^2}{4\pi N T} \ll 1$. The quasilinear theory of instability thus applies for $k_\perp = 0$ if $Y \ll 1$, $\frac{H_0^2}{4\pi N T} \ll 1$.

* In accordance with previous results (see /9/).

BIBLIOGRAPHY

1. VEDENOV, A. A. and R. Z. SAGDEEV. – In: "Fizika plazmy i problemy upravlyaemykh termoyadernykh reaktsii", 3, p. 278. Moskva. 1958.

2. VEDENOV, A. A., E. P. VELIKHOV, and R. Z. SAGDEEV. – Nucl. Fusion, 2:465. 1962.

3. STEPANOV, K. N. and A. B. KITSENKO. – ZhTF, 31:167. 1961.

4. FURTH, H. – Nuclear Fusion, 1:169. 1962.

5. ZASLAVSKII, G. M. Doctorate thesis, Novosibirsk State University. 1963.

6. SHAPIRO, V. D. and V. I. SHEVCHENKO. –JETP, 42:1515. 1962

7. SAGDEEV, R. Z. and V. D. SHAFRANOV. – JETP, 39:181. 1960.

8. GRAY, E. and G. B. MATHEWS. – In: "Funktsii Besselya i ikh prilozheniya k fizike i mekhanike", Moskva. 1953.

9. TSINTSADZE, N. L. and N. P. GIORGADZE. – Izv. vuzov, Radiofizika, 7:262. 1964.

V. G. Makhan'kov and V. I. Shevchenko

QUASILINEAR THEORY OF APERIODIC INSTABILITIES FOR THE INTERACTION OF A BEAM WITH A PLASMA

The interaction of a beam of charged particles with a plasma in the absence of a magnetic field gives rise not only to electrostatic instabilities /1, 2/, but also to instabilities in the form of transverse electromagnetic waves propagating at right angles to the streaming velocity /3, 4/. Instabilities of this kind are connected with the anisotropy of the velocity distribution function in the plasma-beam system.

In /3, 4/ these instabilities were investigated in the approximation of linear oscillation amplitudes and the authors determined the spectrum of the collective motions, the conditions of their excitation, and the growth increments in the initial stage. It would be interesting to establish the variation of the macroscopic system parameters (the directional streaming velocity, the temperature of the beam and the plasma) resulting from this instability and to find the oscillation amplitudes on saturation. These problems are considered in the present paper in the quasilinear approximation.

A characteristic feature of these instabilities is their aperiodicity ($\omega = i\gamma$, γ the growth increment). The applicability of the quasilinear theory to these instabilities was considered in /5/. It was shown that the quasilinear theory can be applied to aperiodic instabilities if $\gamma_k \ll kv_t$ (v_t the thermal velocity in the direction of wave propagation).

1. Let us consider the case of a hot beam moving through a cold plasma, with an initial velocity $u_0 \parallel 0z$. The dispersion equation for the collective motions propagating at an angle of $\pi/2$ relative to the beam is

$$
\begin{aligned}
&\varepsilon_{11}\left(\varepsilon_{33}-\frac{c^2k^2}{\omega^2}\right)-\varepsilon_{13}^2=0;\\
&\varepsilon_{11}=1+\sum_{\alpha}\frac{4\pi e^2}{m^{\alpha}}\cdot\frac{1}{k}\int\frac{1}{\omega_k-kv_x}\cdot\frac{\partial f_0^{\alpha}}{\partial v_x}\,d\mathbf{v};\\
&\varepsilon_{33}=1+\sum_{\alpha}\frac{4\pi e^2}{m^{\alpha}}\cdot\frac{1}{\omega_k^2}\int\left(\frac{kv_z^2}{\omega_k-kv_x}\cdot\frac{\partial f_0^{\alpha}}{\partial v_x}-f_0^{\alpha}\right)d\mathbf{v};\\
&\varepsilon_{13}=\sum_{\alpha}\frac{4\pi e^2}{m^{\alpha}\omega_k}\int\frac{v_z}{\omega_k-kv_x}\cdot\frac{\partial f_0^{\alpha}}{\partial v_x}\,d\mathbf{v},
\end{aligned}
\tag{1}
$$

where $\alpha = 1,2$ refer to the beam and the plasma, respectively; $\mathbf{k}$ $(k,\ 0,0)$ is the wave vector of the oscillation. Taking $k^2v_t^{(1)2} \gg |\omega_k|^2$, $k^2v_t^{(2)2} \ll |\omega_k|^2$ in the expression for ε_{ik}, we easily find

$$
\frac{|\varepsilon_{13}|}{|\varepsilon_{11}\varepsilon_{33}|}\approx\frac{\Omega_1^2}{\Omega_2^2}\cdot\frac{mu_0^2}{mu_0^2+T_{\parallel}^{(1)}}\cdot\frac{|\omega_k|^2}{k^2\frac{T^{(1)}}{m}}\ll 1.
\tag{2}
$$

In the following we shall limit the analysis to collective motions having the electric field parallel to the streaming velocity $\mathbf{u}$. For this case we have from (1)

$$
\frac{c^2k^2}{\omega^2}=\varepsilon_{33}.
$$

Retaining in the dispersion equation (2) only those terms which are linear in ω_k, we find

$$
\omega_k=i\frac{k}{\pi}\cdot\frac{\frac{4\pi e^2}{m}\int\frac{v_z^2}{v_x}\cdot\frac{\partial f_0^{(1)}}{\partial v_x}\,d\mathbf{v}+c^2k^2+\Omega_2^2+\Omega_1^2}{\frac{4\pi e^2}{m}\int v_z^2\left(\frac{\partial^2 f_0^{(1)}}{\partial v_x^2}\right)_{v_x=0}dv_z\,dv_y}
\tag{3}
$$

Instability sets in if

$$
-\frac{4\pi e^2}{m}\int\frac{v_z^2}{v_x}\cdot\frac{\partial f_0^{(1)}}{\partial v_x}\,d\mathbf{v}>c^2k^2+\Omega_2^2+\Omega_1^2.
$$

The condition $\gamma_k \ll kv_t$ is satisfied when

$$
Y=\frac{\frac{4\pi e^2}{m}\int\frac{v_z^2}{v_x}\cdot\frac{\partial f_0^{(1)}}{\partial v_x}\,d\mathbf{v}+c^2k^2+\Omega_2^2+\Omega_1^2}{\frac{4\pi e^2}{m}\int\frac{v_z^2}{v_x}\cdot\frac{\partial f_0^{(1)}}{\partial v_x}\,d\mathbf{v}}\ll 1.
$$

If the distribution function of the beam particles has the form

$$
f_0^{(1)}=\frac{m}{2\pi T_{\perp}^0}\left(\frac{m}{2\pi T_{\parallel}^0}\right)^{1/2}e^{-\frac{m(v_z-u_0)^2}{2T_{\parallel}^0}-\frac{m(v_x^2+v_y^2)}{2T_{\perp}^0}}
\tag{4}
$$

the growth increment is

$$\gamma_k = k\left(\frac{T_\perp^0}{m}\right)^{1/2}\sqrt{\frac{2}{\pi}}\cdot\frac{\Omega_i^2\dfrac{mu_0^2+T_\parallel^0}{T_\perp^0} - c^2k^2 - \Omega_2^2 - \Omega_1^2}{\Omega_i^2\dfrac{mu_0^2+T_\parallel^0}{T_\perp^0}} \tag{5}$$

and the condition of excitation amounts to

$$\Omega_i^2\frac{mu_0^2+T_\parallel^0}{T_\perp^0} - c^2k^2 - \Omega_1^2 - \Omega_2^2 > 0.$$

For

$$k_0^2 = \frac{1}{3c^2}\left(\Omega_i^2\frac{mu_0^2+T_\parallel^0}{T_\perp^0} - \Omega_2^2 - \Omega_1^2\right) \tag{6}$$

the increment is maximal:

$$\gamma_{k\,\max} = k\left(\frac{T_\perp^0}{m}\right)^{1/2}\frac{2}{3}\sqrt{\frac{2}{\pi}}\cdot\frac{\Omega_i^2\dfrac{mu_0^2+T_\parallel^0}{T_\perp^0} - \Omega_2^2 - \Omega_1^2}{\Omega_1^2\dfrac{mu_0^2+T_\parallel^0}{T_\perp^0}}. \tag{7}$$

The condition $k\left(\frac{T_\perp^0}{m}\right)^{1/2} \gg \gamma_k$ is satisfied when

$$Y^* = \frac{\Omega_1^2\dfrac{mu_0^2+T_\parallel^0}{T_\perp^0} - \Omega_2^2 - \Omega_1^2}{\Omega_1^2\dfrac{mu_0^2+T_\parallel^0}{T_\perp^0}} \ll 1.$$

2. Let us now derive the equation in the quasilinear approximation. We write the velocity distribution function as $f^\alpha = f_0(t, \mathbf{v}) + f_1^\alpha(\mathbf{r}, \mathbf{v}, t)$, where $f_0(t, \mathbf{v})$ is the slowly varying (in time) function of the "background" against which the collective motions are set; $f_1(\mathbf{r}, \mathbf{v}, t)$ is the oscillating (in space) function which describes the collective motions.

All the quantities describing the collective motions are written as

$$f_1 = \frac{1}{2}\sum_k f_k e^{ikz} + \text{c. c}; \quad E_1 = \frac{1}{2}\sum_k E_k e^{ikz} + \text{c. c.}$$

Averaging the kinetic equation over distances large in comparison with the oscillation wavelength, we find for $f_0(t, \mathbf{v})$

$$\frac{\partial f_0^\alpha}{\partial t} = \frac{e^2}{m^2}\sum_k \frac{|H_k|^2}{c^2k^2}\left\{\frac{\partial}{\partial v_x}\left[\frac{\gamma_k}{k^2v_x^2+\gamma_k^2}\,k^2v_z^2\,\frac{\partial f_0^\alpha}{\partial v_x}\right] + \frac{\partial}{\partial v_z}\left[-2\gamma_k\frac{k^2v_xv_z}{k^2v_x^2+\gamma_x^2}\cdot\frac{\partial f_0^\alpha}{\partial v_z}\right]\right\}. \tag{8}$$

Applying equation (8), we easily obtain the relations

$$\int\frac{\partial f_0}{\partial t}\,d\mathbf{v} = 0; \quad \int v_x\frac{\partial f_0}{\partial t}\,d\mathbf{v} = 0$$

(the number of particles is constant in time, and the function f_0 remains even in v_x).

From (8) we have for the variation of the transverse temperature of the particles

$$N^{\alpha}\frac{dT_{\perp}^{\alpha}}{dt}=\int\frac{m}{2}(v_x^2+v_y^2)\frac{\partial f_0^{\alpha}}{\partial t}d\mathbf{v}=-\frac{e^2}{m}\sum_k\frac{|H_k|^2}{c^2k^2}\gamma_k\int\frac{k^2v_xv_z^2}{k^2v_x^2+\gamma_k^2}\cdot\frac{\partial f_0^{\alpha}}{\partial v_x}d\mathbf{v}. \qquad (9)$$

The expression for the variation of the longitudinal temperature is found analogously:

$$N^{\alpha}\frac{dT_{\parallel}^{\alpha}}{dt}=\int m(v_z-u^{\alpha})^2\frac{\partial f_0^{\alpha}}{\partial t}d\mathbf{v}=2\frac{e^2}{m}\sum_k\frac{|H_k|^2}{c^2k^2}\gamma_k\int\left[f_0^{\alpha}+2\frac{k^2v_xv_z(v_z-u^{\alpha})}{k^2v_x^2+\gamma_k^2}\cdot\frac{\partial f_0^{\alpha}}{\partial v_x}\right]d\mathbf{v}. \qquad (10)$$

The variation of the streaming velocity of the particles is given by

$$\frac{du^{\alpha}}{dt}=\int(v_z-u^{\alpha})\frac{\partial f_0^{\alpha}}{\partial t}d\mathbf{v}=2\frac{e^2}{m^2}\sum_k\frac{|H_k|^2}{c^2k^2}\gamma_k\int\frac{k^2v_xv_z}{k^2v_x^2+\gamma_k^2}\cdot\frac{\partial f_0^{\alpha}}{\partial v_x}d\mathbf{v}. \qquad (11)$$

The energy generated by the electromagnetic field varies as

$$\frac{d}{dt}\cdot\frac{1}{8\pi}\sum_k|H_k|^2=\frac{1}{4\pi}\sum_k\gamma_k|H_k|^2. \qquad (12)$$

Here and in what follows we neglect the energy of the alternating electric field, since

$$|E_k|^2\simeq\frac{\gamma_k^2}{c^2k^2}|H_k|^2\ll|H_k|^2.$$

Applying equations (9)–(12), we obtain the law of conservation of energy: the energy of the streaming motion lost by the beam is converted into the thermal energy of the particles and the energy of the magnetic field resulting from the instability,

$$\sum_{\alpha=1,2}\left[N^{\alpha}\left(\frac{dT_{\perp}^{\alpha}}{dt}+\frac{1}{2}\cdot\frac{dT_{\parallel}^{\alpha}}{dt}\right)+N^{\alpha}\frac{d}{dt}\left(\frac{mu^{\alpha 2}}{2}\right)\right]+\frac{\partial}{\partial t}\cdot\frac{1}{8\pi}\sum_k|H_k|^2=$$
$$=\frac{1}{4\pi}\sum_k\frac{|H_k|^2}{c^2k^2}\left[\Omega_1^2+\Omega_2^2+c^2k^2+\sum_{\alpha=1,2}\frac{4\pi e^2}{m}\int\frac{k^2v_xv_z^2}{k^2v_x^2+\gamma_k^2}\cdot\frac{\partial f_0^{\alpha}}{\partial v_x}d\mathbf{v}\right]. \qquad (13)$$

It is easily seen that

$$\int\frac{k^2v_xv_z^2}{k^2v_x^2+\gamma_k^2}\cdot\frac{\partial f_0^{\alpha}}{\partial v_x}d\mathbf{v}=\int\frac{v_z^2}{v_x}\cdot\frac{\partial f_0^{\alpha}}{\partial v_x}d\mathbf{v}-\frac{\gamma_k}{k}\pi\int v_z^2\left(\frac{\partial^2 f_0}{\partial v_x^2}\right)_{v_x=0}dv_ydv_z,$$

and the expression in brackets is therefore zero (see (3)).

3. Equation (8) for the beam distribution function is solved by the technique suggested in /5/. For $v_x\sim v_t$, the solution of (8) is obtained by

successive approximations, setting $f_0^{(1)}$ in the form $f_0(0, \mathbf{v}) + \delta f_0(t, \mathbf{v})$, where $f_0(0, \mathbf{v})$ is defined by (4). Taking $\left|\frac{\delta f_0}{f_0}\right| \ll 1$, we find

$$\delta f_0 = \frac{e^2}{2m}\sum_k \frac{|H_k|^2}{k^2c^2}\left\{\frac{\partial}{\partial v_z}\left[\frac{2v_z}{T_\perp^0} - \frac{(v_z - u_0)}{T_\parallel^0}\right] - \frac{\partial}{\partial v_x}\left(\frac{v_z^2}{T_\perp^0 v_x}\right)\right\} f_0(0, \mathbf{v}). \qquad (14)$$

For $v_x \to 0$, the last term in (14) becomes very large, and the equation cannot be solved by the method of successive approximations. In the region of small v_x, equation (8) should be solved exactly, retaining the leading term only.

Applying the results of (5), we have

$$\delta f_0 = \frac{A}{2} v_x^2 - A 2^{1/4} (\pi W)^{1/4} \frac{\Gamma\left(\frac{3}{4}\right)}{\Gamma\left(\frac{1}{4}\right)} v_x^{3/2} v_z^{1/2} \times$$

$$\times \exp\left\{-\frac{v_x^4}{32\pi W v_z^4}\right\}\left[M_{-\frac{1}{8},\ \frac{1}{8}}\left(\frac{v_x^4}{v_z^4} \cdot \frac{1}{16\pi W}\right) + \frac{v_z^2}{v_x^2}(\pi W)^{1/2} M_{\frac{3}{8},\ -\frac{3}{8}}\left(\frac{v_x^4}{v_z^4} \cdot \frac{1}{16\pi W}\right)\right], \qquad (15)$$

where

$$A = N_1 \frac{1}{(2\pi)^{3/2}}\left(\frac{m}{T_\parallel^0}\right)^{1/2}\left(\frac{m}{T_\perp^0}\right)^2 \exp\left\{-\frac{m(v_z - u_0)^2}{2T_\parallel^0} - \frac{mv_y^2}{2T_\perp^0}\right\};$$

$$W = \frac{1}{2\pi} \cdot \frac{e^2}{m^2} \sum_k \frac{|H_k|^2}{c^2k^2} \cdot \frac{1}{v_z^2};$$

$M_{\alpha,\beta}(z)$ Whittaker's functions. Applying (14) and (15), we derive for δf_0 a relation which holds true for any v_x $(0 < v_x < v_{t\perp})$,

$$\delta f^{tot} = \frac{e^2}{2m}\sum_k \frac{|H_k|^2}{c^2k^2} \cdot \frac{\partial}{\partial v_z}\left[\frac{2v_z}{T_\perp^0} - \frac{(v_z - u_0)}{T_\parallel^0}\right] f_0(0, \mathbf{v}) + \delta f_0, \qquad (16)$$

where δf_0 is substituted from (15).

4. Having solved equation (8), we can establish the variation of the streaming velocity, of the temperature ($T_\perp$ and $T_\parallel$) of the beam particles, and of the energy of the magnetic field generated with the onset of instability. For $t \to \infty$, when $\gamma_k \to 0$,

$$\frac{4\pi e^2}{m}\int \frac{v_z^2}{v_x} \cdot \frac{\partial f_0^{(1)\infty}}{\partial v_x}\, d\mathbf{v} + c^2k^2 + \Omega_2^2 + \Omega_1^2 = 0.$$

Substituting $f_0^{(1)\infty} = f_0(0, v) + \delta f_0$, we find

$$\frac{4\pi e^2}{m}\int \frac{v_z^2}{v_x} \cdot \frac{\partial f_0(0, \mathbf{v})}{\partial v_x} d\mathbf{v} + c^2k^2 + \Omega_2^2 + \Omega_1^2 + \frac{4\pi e^2}{m}\int \frac{v_z^2}{v_x} \cdot \frac{\partial \delta f_0}{\partial v_x}\, d\mathbf{v} = 0. \qquad (17)$$

Applying (6) and (16), we have

$$-Y\frac{mu_0^2 + T_\parallel^0}{T_\perp^0} + \frac{m}{T_\perp^0} \cdot \frac{e^2}{m^2}\sum_k \frac{|H_k|^2}{c^2k^2}\left[\frac{2(mu_0^2 + T_\parallel^0)}{T_\perp^0} - 1\right] +$$

$$+ \frac{2^{1/4}}{\pi^{1/2}} \cdot \frac{mu_0^2}{T_\perp^0} \cdot \frac{u_0^{1/2}}{(T_\perp^0/m)^{1/4}}\left(\frac{m}{T_\perp^0} \cdot \frac{e^2}{m^2}\sum_k \frac{|H_k|^2}{c^2k^2}\right)^{1/4} G = 0. \qquad (18)$$

where G is a constant,

$$G = \int_0^\infty \frac{dz}{z^{3/4}} \cdot \frac{d}{dz}\left\{z^{1/4} - 4z^{1/4}e^{-\frac{z}{2}}\frac{\Gamma\left(\frac{3}{4}\right)}{\Gamma\left(\frac{1}{4}\right)} \times \right.$$

$$\left.\times\left[M_{-\frac{1}{8},\ \frac{1}{8}}(z) + \frac{1}{4z^{1/4}} M_{\frac{3}{8},\ -\frac{1}{8}}(z)\right]\right\} = 2^{3/4}\frac{\left[\Gamma\left(\frac{3}{4}\right)\right]^2}{\Gamma\left(\frac{1}{4}\right)}.$$

Making use of (6), we can show that

$$\frac{m}{T_\perp^0} \cdot \frac{e^2}{m^2}\sum_k \frac{|H_k|^2}{c^2k^2} = \frac{3}{Y} \cdot \frac{\sum_k |H_k|^2}{\frac{1}{2}N_1(mu_0^2 + T_\parallel^0)}. \tag{19}$$

We shall take this quantity to be small in comparison with unity (this assumption is confirmed by the results). Then the second term in (18) may be neglected relative to the third term. For the energy of the magnetic field established toward the end of the growth process we have

$$\frac{1}{8\pi}\sum_k |H_k|^2 = \left(\frac{4}{2^{1/4}G}\right)^4 \frac{1}{6} Y^6 N_1 T_\perp^0 \frac{mu_0^2 + T_\parallel^0}{nu_0^2}. \tag{20}$$

The smallness of (19) is ensured by the smallness of Y.

Applying (9)—(11), we find the gain of the transverse thermal energy for the beam electrons:

$$N_1\delta T_\perp^1 = \frac{3}{Y};\quad w = \frac{1}{8\pi}\sum_k |H_k|^2 \tag{21}$$

for the longitudinal thermal energy

$$\frac{1}{2}N_1\delta T_\parallel^1 = w\frac{3}{Y} \cdot \frac{T_\perp^0}{mu_0^2 + T_\parallel^0}\left(1 - \frac{2T_\parallel^0}{T_\perp^0}\right). \tag{22}$$

The change in streaming energy is calculated from

$$N_1 mu\delta u = -w\frac{6}{Y} \cdot \frac{mu_0^2}{mu_0^2 + T^0}. \tag{23}$$

From equation (9) we can determine the energy expended in enhancing the transverse thermal motion of the plasma electrons:

$$N_2\delta T_\perp^{(2)} = \left(\frac{4}{2^{1/4}G}\right) Y^2 \frac{T_\perp^0}{mu_0^2} T^{(2)0} \tag{24}$$

The heating of the plasma is insignificant, if the initial plasma temperature $T^{(2)0}$ is low. Saturation in our problem is attained not for $\gamma_k \to 0$, but actually for $\gamma_k \sim ku_{t2}$. This factor introduces terms proportional to plasma temperature in equations (21)—(23). These terms, however, are neglected in the present analysis.

BIBLIOGRAPHY

1. AKHIEZER, A. I. and Ya. B. FAINBERG. – DAN SSSR, **64**: 555. 1949; JETP, **21**: 1262. 1951.
2. BOHM, D. and E. P. GROSS. – Phys. Rev. **75**: 1851. 1949.
3. NEUFIELD, J. and P. H. DOYLE. – Phys. Rev., **121**: 654. 1961.
4. MAKHAN'KOV, V. G. and A. A. RUKHADZE. – Nucl. Fusion, **2**: 177. 1962.
5. SHAPIRO, V. D. and V. I. SHEVCHENKO. – This volume, p. 149.

V. D. Shapiro and V. I. Shevchenko

VARIATION OF BEAM AND PLASMA PARAMETERS WITH THE ONSET OF CYCLOTRON INSTABILITY

When a beam of excited ion oscillators interacts with an electronic plasma immersed in a strong magnetic field ($\omega_{He}^2 \gg \Omega_e^2$), the so-called cyclotron instability may set in due to the energy of the transverse motion of the ions. The linear theory of this instability was considered in /1, 2/. An important problem that can be analyzed only in the framework of the nonlinear theory is the determination of the reciprocal effect of the oscillations on the macroscopic parameters of the beam ions and the plasma electrons. A considerable change in the thermal energy of a plasma with the onset of cyclotron instability was observed on the OGRA thermonuclear facility /2/.

In the present paper we consider the feedback from the oscillations excited when an ion beam, having an initial streaming velocity u_0 along the magnetic field and an initial transverse velocity $v_\perp^0$, interacts with a low-density cold electronic plasma ($\omega_{He}^2 \gg \Omega_e^2$); by feedback in this text we mean the variation of the beam and plasma parameters (streaming velocity and thermal energy).

The dispersion equation of the longitudinal oscillations propagating at an angle Θ to the direction of a constant magnetic field has the form /1–3/:

$$1 - \frac{\Omega_e^2}{\omega^2}\cos^2\Theta - \sum_{n=-\infty}^{\infty}\left[\frac{J_n^2\Omega_i^2\cos^2\Theta}{(\omega - n\omega_{Hi} - k_z u_0)^2} + \frac{2nJ_nJ_n'\Omega_i^2\sin^2\Theta}{a\omega_{Hi}(\omega - n\omega_{Hi} - k_z u_0)}\right] = 0 \qquad (1)$$

(it is assumed that $\frac{T^i}{M} \ll v_\perp^{0\,2}$; $\omega_{He}^2 \gg \Omega_e^2$; $|\omega - n\omega_{Hi} - k_z u_0| \gg k_z v_{ti}$; $|\omega| \gg k_z v_{te}$). Here Ω_i, Ω_e are the Langmuir frequencies of the ions and the electrons (the number densities of the ions in the beam and the electrons in the plasma are assumed equal for simplicity); $J_n(a) = J_n\left(\frac{k_\perp v_\perp^0}{\omega_{Hi}}\right)$ Bessel's function of n-th order; $\omega_{Hi} = \frac{eH_0}{Mc}$ the ion gyrofrequency.

The increments of the oscillations are maximal when the electron plasma frequency is equal to the frequency of the beam particles:

$$\omega_k = \Omega_e \cos\Theta = k_z u_0 + n\omega_{Hi} \tag{2}$$

and

$$\gamma_k = \frac{\sqrt{3}}{2^{4/3}} (\mu J_n^2)^{1/3} \Omega_e \cos\Theta, \tag{3}$$

where $\mu = \frac{m}{M}$ is the electron to ion mass ratio.

In our analysis of the feedback from the oscillations we shall apply the results of /3/, where the interaction of a monoenergetic beam with a plasma in the presence of a magnetic field was considered. In case of instabilities set up by the Vavilov—Čerenkov effect and the anomalous Doppler effect, an equation describing the change in the "background" distribution function is /3/

$$\frac{\partial f_0^\alpha}{\partial t} = \frac{\partial}{\partial v_i}\left(\alpha_{ik}^\alpha \frac{\partial f_0^\alpha}{\partial v_k}\right), \tag{4}$$

where α_{ik}^α is the tensor of coefficients of diffusion in the velocity space,

$$\begin{aligned}
\alpha_{\perp\perp}^\alpha &= \frac{e^2}{2\pi^2 m^{\alpha 2}} \iint k_\perp dk_\perp dk_z |E_{\mathbf{k}}|^2 \frac{k_z^2}{k^2} \sum_{n=1}^{\infty} \frac{n^2 J_n^2(\lambda_2^\alpha)}{\lambda_2^{\alpha 2}} [\Gamma_{-n}^\alpha + \Gamma_n^\alpha];\\
\alpha_{\perp z}^\alpha &= \frac{e^2}{2\pi^2 m^{\alpha 2}} \iint k_\perp dk_\perp dk_z |E_{\mathbf{k}}|^2 \frac{k_\perp^2}{k^2} \cdot \frac{k_z v_\perp}{\omega_H^\alpha} \sum_{n=1}^{\infty} \frac{n J_n^2(\lambda_2^\alpha)}{\lambda_2^{\alpha 2}} [\Gamma_{-n}^\alpha - \Gamma_n^\alpha];\\
\alpha_{zz}^\alpha &= \frac{e^2}{2\pi^2 m^{\alpha 2}} \iint k_\perp dk_\perp dk_z |E_{\mathbf{k}}|^2 \frac{k_z^2}{k^2} \left\{ J_0^2(\lambda_2)\Gamma_0 + \sum_{n=1}^{\infty} J_n^2(\lambda_0^\alpha)[\Gamma_{-n}^\alpha + \Gamma_n^\alpha] \right\};\\
\Gamma_{\pm n}^\alpha &= \frac{\gamma_{\mathbf{k}}}{(\omega_{\mathbf{k}}^2 - k_z v_z \pm n\omega_H^\alpha)^2 + \gamma_{\mathbf{k}}^2}; \quad \lambda_2^\alpha = \frac{k_\perp v_\perp}{\omega_H^\alpha}; \quad \omega_{\mathbf{k}} = \omega_{\mathbf{k}}^z + i\gamma_{\mathbf{k}}.
\end{aligned} \tag{5}$$

Here $\alpha = i, e$ refer to the beam ions and the plasma electrons, respectively. The integrals in (5) are taken in the region $k_z > 0$.

We shall now find the variation of beam parameters with the onset of instabilities conditioned by the Vavilov—Čerenkov effect and the anomalous Doppler effect. Assuming that the change in the streaming velocities and in the temperature of the beam ions is not large, so that

$$\frac{k_z \delta u}{\gamma_{\mathbf{k}}} \ll 1; \quad \frac{k_z^2 v_{t\parallel}^2}{\gamma_{\mathbf{k}}^2} \ll 1; \quad \frac{\delta v_\perp}{v_\perp^0} \ll 1; \quad \frac{k_z^2 v_{t\perp}^2}{\gamma_{\mathbf{k}}^2} \ll 1 \tag{6}$$

(δu, $\delta v_\perp$ are the variations in the streaming velocities (longitudinal and transverse) of the ions; $v_{t\parallel}$, $v_{t\perp}$ are the longitudinal and the transverse thermal velocities of the beam ions), and series-expanding α_{ik}^i in terms of $w = v_z - u_0$, $\zeta = v_\perp - v_\perp^0$, we obtain an equation for the variation of the "background" distribution function of the ions:

$$\begin{aligned}
\frac{\partial f_0}{\partial t} - \alpha_{\perp\perp}^0 \frac{\partial^2 f_0}{\partial v_\perp^2} - \alpha_{zz}^0 \frac{\partial^2 f_0}{\partial v_z^2} &= \frac{\partial \alpha_{\perp\perp}^0}{\partial u_0} w \frac{\partial^2 f_0}{\partial \zeta^2} + 2\frac{\partial \alpha_{\perp z}^0}{\partial u_0} w \frac{\partial^2 f_0}{\partial w \partial \zeta} + \\
&+ \frac{\partial \alpha_{zz}^0}{\partial u_0} w \frac{\partial^2 f_0}{\partial w^2} + \frac{\partial \alpha_{zz}^0}{\partial u_0} \cdot \frac{\partial f_0}{\partial w} + 2\alpha_{\perp z}^0 \frac{\partial^2 f_0}{\partial \zeta \partial w}.
\end{aligned} \tag{4'}$$

Here α^0_{ik} is the tensor of the ion diffusivities for $v_z = u_0$; $v_\perp = v^0$. Applying (4') we easily obtain two relations for the variations of the longitudinal velocity of the beam

$$\langle v_z \rangle = u_0 + \int_0^t \frac{\partial \alpha^0_{zz}}{\partial u_0}\, dt' \tag{7}$$

and of the transverse velocity of the beam

$$\langle v_\perp \rangle = v^0_\perp + \int_0^t \frac{\partial \alpha^0_{\perp z}}{\partial u_0}\, dt'. \tag{8}$$

For the variation of the temperature of the beam ions, we have from (4')

$$\begin{aligned} T_\parallel &= T^i_0\left(1 + \frac{2M}{T^i_0}\int_0^t \alpha^0_{zz}\, dt'\right); \\ T_\perp &= T^i_0\left(1 + \frac{2M}{T^i_0}\int_0^t \alpha^0_{\perp\perp}\, dt'\right), \end{aligned} \tag{9}$$

i.e., the onset of instability leads to an anisotropy in ion temperatures. Taking the integrals with respect to t and $\mathbf{k}$ in (7)—(9), we remember that

$$\frac{d}{dt}|E_\mathbf{k}|^2 = 2\gamma_\mathbf{k}|E_\mathbf{k}|^2$$

and the increment $\gamma_\mathbf{k}$ is maximal for some $\mathbf{k} = \mathbf{k}_0$. The values $\mathbf{k}_0$ are found from

$$k_z u_0 - n\omega_{Hi} = \Omega_e \cos\Theta \quad (n = 0,\ 1,\ 2,\ \ldots) \tag{10}$$

and the condition specifying the maximum of the quantity

$$\Omega_e \cos\Theta\left[\mu J_n^2\left(\frac{k_\perp v^0_\perp}{\omega_{Hi}}\right)\right]^{1/3}.$$

In OGRA $\omega_H = 1.4 \cdot 10^7$ sec^{-1}, $v^0_\perp = 3.8 \cdot 10^8$ cm/sec, $u_0 = 1.5 \cdot 10^8$ cm/sec, $n_0 = 3 \cdot 10^8$ cm^{-3}, $k_{z0} = 6.3$ cm^{-1}, $\sin\Theta_0 \simeq 0.01$ for the first cyclotron harmonic. The radiation in this spectral region was not investigated in the experiment.

Substituting for the pre-exponential factors in (7)—(9) their values for $\mathbf{k} = \mathbf{k}_0$, we can easily take the integrals with respect to $\mathbf{k}$ and t. From (7) we obtain an equation for the variation of the longitudinal streaming velocity resulting from the growth of the instabilities due to the anomalous Doppler effect or the Vavilov—Čerenkov effect,

$$\delta u = -\frac{1}{4\pi}\sum_n \frac{1}{N_0 M u_0}\left(\frac{k_z u_0}{\Omega_e \cos\Theta}\right)_{\mathbf{k}=\mathbf{k}_0} \sum_\mathbf{k} |E_\mathbf{k}|^2. \tag{11}$$

The sum is taken over n (0, 1, 2, . . .) for which instability may set in. As should have been expected, the longitudinal streaming velocity decreases

with the growth of instabilities associated with these elementary effects. For the variation of the transverse velocity of the ions in the beam we have from (8)

$$\delta v_{\perp} = \frac{1}{4\pi} \sum_n \frac{1}{N_0 M v_{\perp}^0} \left(\frac{n\omega_H}{\Omega_e \cos \Theta} \right)_{\mathbf{k}=\mathbf{k}_n} \sum_{\mathbf{k}} |E_{\mathbf{k}}|_2. \quad (12)$$

The transverse velocity of the beam ions thus increases with the onset of instability associated with the anomalous Doppler effect.

From (9) we analogously find an equation for the variation of the longitudinal and the transverse temperatures in the ion beam:

$$\begin{aligned} \delta T'_{\parallel} &= \frac{2^{3/2}}{4\pi} \sum_n \frac{1}{N_0} (\mu J_n^2)^{1/2}_{\mathbf{k}=\mathbf{k}_n} \sum_{\mathbf{k}} |E_{\mathbf{k}}|^2; \\ \delta T'_{\perp} &= \frac{2^{3/2}}{4\pi} \sum_n \frac{1}{N_0} \left[\frac{n^2 \omega_H^2 (\mu J_n^2)^{1/2}}{k_z^2 v_{\perp}^{02}} \right]_{\mathbf{k}=\mathbf{k}_n} \sum_{\mathbf{k}} |E_{\mathbf{k}}|^2. \end{aligned} \quad (13)$$

The change in the macroscopic parameters of the plasma electrons is computed seeing that the components of the diffusivity tensor for the plasma electrons are small in comparison with the corresponding quantities for the ions, with the exception of the component α_{zz}^e.

For $kv_t^e \ll \omega_k^r$,

$$\alpha_{zz}^e \simeq \frac{e^2}{2\pi^2 m^2} \iint k_{\perp} dk_{\perp} dk_z |E_{\mathbf{k}}|^2 \frac{k_z^2}{k^2} \cdot \frac{\gamma_{\mathbf{k}}}{\omega_{\mathbf{k}}^{r2}} \quad (14)$$

Therefore, as it is easily verified, the energy transmitted to the plasma electrons enhances the longitudinal thermal motion. The variation of the longitudinal temperature of the plasma electrons is

$$\delta T_{\parallel}^e = \frac{1}{4\pi} \cdot \frac{1}{N_0} \sum_n \sum_{\mathbf{k}} |E_{\mathbf{k}}|^2 \quad (15)$$

From (11)—(13) and (15) we have the following law of conservation of energy: the change in the kinetic energy of the beam ions and the plasma electrons is equal to the energy of the field generated with the onset of instability:

$$\begin{aligned} M N_0 u_0 \delta u + M N_0 v_{\perp}^0 \delta v_{\perp} + \tfrac{1}{2} N_0 \delta T'_{\parallel} + N_0 T'_{\perp} + \\ + \tfrac{1}{2} N_0 \delta T_{\parallel}^e = -\frac{1}{8\pi} \sum_{\mathbf{k}, n} |E_{\mathbf{k}}|^2. \end{aligned} \quad (16)$$

In the case of the normal Doppler effect, instabilities grow at the expense of the energy of transverse streaming. Two oscillation branches may be unstable in this case (see /4/): 1) $\omega_{\mathbf{k}}^{(1)} = k_z u_0 + n\omega_{Hi} (k_z > 0;\ n = 1, 2, \ldots)$: the waves are radiated in the downstream direction; 2) $\omega_{-\mathbf{k}}^{(2)} = -k_z u_0 + n\omega_{Hi}\ (k_z > 0;\ n\omega_H > k_z u_0;\ \omega_{-\mathbf{k}}^{(2)} > 0)$: the waves are radiated upstream.

The equation for the change in the distribution function of the beam ions is written as equation (4), where

$$\alpha_{ik}^a = \alpha_{ik}^a (\mathbf{k}, \omega_{\mathbf{k}}^{(1)}) + \alpha_{ik}^a (-\mathbf{k}, \omega_{-\mathbf{k}}^{(2)}); \quad \omega_{-\mathbf{k}}^{(2)} > 0.$$

Applying equation (4), we can find the variations of the streaming velocity and of the temperature of the ions and the electrons with the onset of instabilities associated with the normal Doppler effect.

For instabilities on the branch $\omega_{\mathbf{k}}^{(1)}$, applying (7)—(9), we find the change in the energy of transverse streaming:

$$N_0 M v_{\perp}^0 \delta v_{\perp} = -\frac{1}{4\pi} \sum_n \left(\frac{n\omega_{Hi}}{\Omega_e \cos\Theta} \right)_{\mathbf{k}=\mathbf{k}_0} \sum_{\mathbf{k}} |E_{\mathbf{k}}|^2 \tag{17}$$

($\mathbf{k}_0$ is obtained from $k_z u_0 + n\omega_{Hi} = \Omega_e \cos\Theta$ and the condition specifying the maximum of the quantity $\Omega_e \cos\Theta \left| \mu J_n^2 \left(\frac{k_\perp v_\perp^0}{\omega_{Hi}} \right) \right|^{1/3}$). The energy of the transverse streaming of ions thus decreases.

For the change in the energy of the longitudinal streaming of ions, we have

$$N_0 M u_0 \delta u = -\frac{1}{4\pi} \sum_n \left(\frac{k_z u_0}{\Omega_e \cos\Theta} \right)_{\mathbf{k}=\mathbf{k}_0} \sum_{\mathbf{k}} |E_{\mathbf{k}}|^2, \tag{18}$$

i.e., the beam is decelerated.

The growth of instabilities heats the beam ions and the plasma electrons. The change in the longitudinal and the transverse thermal energy of the ion beam is

$$\frac{1}{2} N_0 \delta T_{\parallel}^i = \frac{2^{2/3}}{8\pi} \sum_n (\mu J_n^2)_{\mathbf{k}=\mathbf{k}_0}^{1/3} \sum_{\mathbf{k}} |E_{\mathbf{k}}|^2;$$

$$N_0 \delta T_{\perp} = \frac{2^{1/3}}{4\pi} \sum_n \left[\frac{n^2 \omega_{H}^2}{k_z^2 v_\perp^{02}} (\mu J_n^2)^{1/3} \right]_{\mathbf{k}=\mathbf{k}_0} \sum_{\mathbf{k}} |E_{\mathbf{k}}|^2. \tag{19}$$

The gain of longitudinal thermal energy for the plasma electrons is

$$\frac{1}{2} N_0 \delta T_{\parallel}^e = \frac{1}{8\pi} \sum_n \sum_{\mathbf{k}} |E_{\mathbf{k}}|^2. \tag{20}$$

Applying (17)—(20) we can easily verify that the total energy is conserved.

For instabilities on the second branch

$$\omega_{-\mathbf{k}}^{(2)} = -k_z u_0 + n\omega_{Hi} \quad (k_z > 0, \quad \omega_{-\mathbf{k}}^{(2)} > 0),$$

the change in the energy of transverse motion is described by formula (17), with the only difference that $\mathbf{k}_0$ is now determined from $\Omega_e \cos\Theta = -k_z u_0 + n\omega_{Hi}$ and the condition of maximal increment $\gamma_{\mathbf{k}} \sim \Omega_e \cos\Theta (\mu J_n^2)^{1/3}$. The change in the energy of transverse streaming for instabilities on this branch is

$$N_0 M u_0 \delta u = \frac{1}{4\pi} \sum_n \left(\frac{k_z u_0}{\Omega_e \cos\Theta} \right)_{\mathbf{k}=\mathbf{k}_0} \sum_{\mathbf{k}} |E_{\mathbf{k}}|^2, \tag{21}$$

i.e., with the onset of instability on the branch $\omega_{-\mathbf{k}}^{(2)}$ the ion beam is accelerated in the longitudinal direction by the recoil it suffers when waves are radiated. The change in the energy of thermal motion of the ions and the plasma electrons is determined by formulas (19) and (20) with appropriate $\mathbf{k}_0$.

In OGRA, $\omega_{Hi} = 1.4 \cdot 10^7$ sec^{-1}, $v_\perp^0 = 3.8 \cdot 10^8$ cm/sec, $u_0 = 1.5 \cdot 10^8$ cm/sec, $N_0 = 3 \cdot 10^8$ cm^{-3}; for the first harmonic of the second branch $k_{z0} \simeq 10^{-3}$ cm^{-1}, $\cos\theta_0 \sim 0.014$, while for the fundamental harmonic of the first branch k_{z0} is somewhat higher, i.e., there is a net deceleration of ions. For $k_{z0} = 10^{-3}$ cm^{-1}, $k_z u_0 \simeq 1.5 \cdot 10^5$ sec^{-1}; $k_z u_0 \ll \omega_{Hi}$, i.e., in this case instabilities set in on the first and the second branches for $\omega \sim n\omega_H$, which is actually observed in the experiments of /2/. The instabilities grow at the expense of the energy of transverse motion, which is converted into the energy of thermal motion of the plasma electrons and the energy of the field generated when instability sets in. The beam ions are heated much less:

$$\frac{W_t^i}{W_t^e} \sim (\mu J_n^2)^{1/3}$$

(W_t^i, W_t^e is the thermal energy of the ions and of the plasma electrons, respectively).

The foregoing results apply in the initial stage of instability, when conditions (6) are satisfied. It is easily seen that the most rigid conditions under which relations (6) are met are

$$\frac{\frac{1}{8\pi}\sum_{\mathbf{k}} |E_{\mathbf{k}}|^2}{\frac{1}{2} N_0 M u_0^2 (\mu J_n^2)^{1/3}} \ll 1; \qquad \frac{\frac{1}{8\pi}\sum_{\mathbf{k}} |E_{\mathbf{k}}|^2}{\frac{1}{2} N_0 M v_\perp^{02} (\mu J_n^2)^{1/3}} \ll 1. \tag{22}$$

In OGRA, with $N_0 \sim 10^8$ cm^{-3}, $u_0 \simeq 1.5 \cdot 10^8$ cm/sec, $v^0 = 3.8 \cdot 10^8$ cm/sec, the maximal $E_{\mathbf{k}}$ was 50 V/cm. It is easily seen that conditions (22) are satisfied:

$$\frac{\frac{1}{8\pi}\sum_{\mathbf{k}} |E_{\mathbf{k}}|^2}{\frac{1}{2} N_0 M u_0^2 (\mu J_n^2)^{1/3}} \sim \left(\frac{1}{30} - \frac{1}{50}\right).$$

BIBLIOGRAPHY

1. STEPANOV, K. N. and A. B. KITSENKO. – ZhTF, 31: 167, 1961.

2. PISTUNOVICH, V. I. – Atomnaya Energiya, 14: 72, 1963.

3. SHAPIRO, V. D. and V. I. SHEVCHENKO. – JETP, 42: 1515, 196?.

A. N. Kondratenko

"DECAY" INSTABILITY OF WAVES IN A PLASMA WAVEGUIDE

1. The problem of "decay" instability of some wave modes in a plasma was considered in /1—3/. "Decay" instability is defined as the instability of a wave of frequency ω which excites two other waves differing from the initial wave in their frequencies, phase velocities, and sometimes even in their mode of oscillation. The decay is a strictly nonlinear phenomenon, leading to a transfer of energy between the wave modes.

The "decay" instabilities considered in /1—3/ refer to an infinite plasma. It would be interesting to consider the "decay" instability of wave modes in a bounded plasma also.

It has been shown in /1/ that decay may occur for waves whose dispersion curves display sections where two wave vectors correspond to one frequency, and also in cases when the decay curve possesses several branches.

From this point of view, an electromagnetic wave cannot decay in a cylindrical plasma waveguide in the absence of a magnetic field, since the dispersion curve in this case has a single branch and there is a one-to-one correspondence between frequencies and wave vectors. In a plasma waveguide immersed in a magnetic field, however, this decay is permitted, since the dispersion curves are branched and in some frequency intervals the function $k(\omega)$ is not single-valued /4/.

Let us consider the "decay" instability of waves in a cylindrical plasma waveguide immersed in an infinitely strong magnetic field ($\omega_e^2 \gg \Omega_0^2, \omega^2$). In this case, generally speaking, an infinity of wave vectors corresponds to any given frequency.

2. The hydrodynamic system of equations describing the propagation of electromagnetic waves in a cylindrical plasma waveguide immersed in an infinitely strong magnetic field has the form (the E -wave)

$$\frac{\partial v^{(0)}}{\partial t} + v^{(0)} \frac{\partial v^{(0)}}{\partial z} = -\frac{e}{m} E_z^{(0)}; \tag{1}$$

$$\frac{\partial^2 H_\varphi^{(0)}}{\partial z^2} + \frac{1}{c} \cdot \frac{\partial^2 E_z^{(0)}}{\partial r \partial z^2} = \frac{1}{c^2} \cdot \frac{\partial^2 H_\varphi^{(0)}}{\partial t^2}; \tag{2}$$

$$\frac{1}{r} \cdot \frac{\partial}{\partial r}\left(r \frac{\partial H_\varphi^{(0)}}{\partial z}\right) = \frac{1}{c} \cdot \frac{\partial^2 E_z^{(0)}}{\partial t \partial z} + \frac{4\pi e}{c} \cdot \frac{\partial H_\varphi^0}{\partial t}; \tag{3}$$

$$\frac{\partial n^{(0)}}{\partial t} = -\frac{\partial n^{(0)} v^{(0)}}{\partial z}, \tag{4}$$

where $v^{(0)}$ the velocity, $n^{(0)}$ the number density of the plasma electrons. The ions, whose number density is n_0, are at rest.

We seek a solution of equations (1)—(4) in the form $A^{(0)} = A_\sim + A$, where $A_\sim$ is the unperturbed solution (the "background"), A a perturbation. The analysis is conveniently made in the wave's own frame /1/. The unperturbed solution is then time-independent, and the linearized perturbation equations are

$$\left(\frac{\partial}{\partial t} - u \frac{\partial}{\partial z}\right) v = -\frac{e}{m} E_z - \varepsilon u I_0 (k_{\perp 0} r) \frac{\partial}{\partial z} (v \sin k_0 z); \tag{5}$$

$$\frac{\partial^2 H_\varphi}{\partial z^2} + \frac{1}{c} \cdot \frac{\partial^2 E_z}{\partial r \partial t} = \frac{1}{c^2} \cdot \frac{\partial^2 H_\varphi}{\partial t^2}; \tag{6}$$

$$\frac{1}{r}\cdot\frac{\partial}{\partial r}\left(r\,\frac{\partial H_\varphi}{\partial z}\right)=\frac{1}{c}\cdot\frac{\partial^2 E_z}{\partial t\partial z}+\frac{4\pi e}{c}\cdot\frac{\partial n}{\partial t};\tag{7}$$

$$\left(\frac{\partial}{\partial t}-u\frac{\partial}{\partial z}\right)n=-\frac{\partial v}{\partial z}-\varepsilon I_0(k_{\perp 0}r)\frac{\partial}{\partial z}\left[(v+nu)\sin k_0 z\right],\tag{8}$$

where u is the phase velocity of the wave, $\varepsilon=\frac{eE_0}{mu\omega_0}$, ω_0 the "background" frequency corresponding to $k_{0z}\equiv k_0$; $k_{\perp 0}^2=-\varepsilon_3 k_0^2(1-\beta_0^2)$; $\varepsilon_3=1-\frac{\Omega_0^2}{\omega_0^2}$; $\Omega_0^2=\frac{4\pi e^2 n_0}{m}$; $\beta_0=\frac{u}{c}$; I_0 Bessel's function of zero order.

Weak nonlinearity is assumed, so that the fundamental harmonic is adopted as the "unperturbed" solution, and equations (5)—(8) are solved by successive approximations.

3. We seek a solution of equations (5)—(8) as a sum of two waves (see /1/)

$$A=e^{-i\omega t}\left[A_1(r)\,e^{ik_1 z}+A_2(r)\,e^{ik_2 z}\right].\tag{9}$$

Here

$$k_2=k_0+k_1,\tag{10}$$

the frequencies ω_1 and ω_2 corresponding to k_1 and k_2 are equal in the moving frame, while in the laboratory frame they are related by

$$\omega_2=\omega_0+\omega_1.\tag{11}$$

For the radial variation of the E_z fields of the first and the second waves we obtain

$$\frac{1}{r}\cdot\frac{\partial}{\partial r}\left(r\,\frac{\partial}{\partial r}E_{z1,2}\right)-k_{\perp 1,2}^2E_{z1,2}=$$
$$=\varepsilon\psi I_0(k_{\perp 0}r)\,k_{\perp 1,2}^2(1-\beta_{1,2}^2)\,E_{z1,2},\tag{12}$$

where

$$k_{\perp 1,2}^{(2)}=-\varepsilon_{31,2}k_{1,2}^2(1-\beta_{1,2}^2)\,\beta_{1,2}=\frac{k_{1,2}}{\omega c},\ \varepsilon_{31,2}=1-\frac{\Omega_0^2}{\omega_{1,2}^2};$$
$$\psi=\frac{1}{2}\cdot\frac{\Omega_0^2}{\omega_1^2\omega_2^2}\left[\omega_1\omega_2+u\,(k_1\omega_2+k_2\omega_1)\right],\ \omega_{1,2}=\omega+k_{1,2}u.$$

The solution of equation (12) obtained by the method of successive approximations is

$$E_{z1}=C_1I_0(k_{\perp 1}r)+\frac{\varepsilon}{\varepsilon_{31}}k_{\perp 1}^2C_2\psi\left[I_0(k_{\perp 1}r)\int_0^r r'F_2(r')\,Y_0(k_{\perp 1}r')\,dr'-\right.$$
$$\left.-Y_0(k_{\perp 1}r)\int_0^r r'F_2(r')\,I_0(k_{\perp 1}r')\,dr'\right.,\tag{13}$$

where C_1, C_2 are constants, Y_0 Weber's function. E_{z2} is obtained from (13) by permutation of subscripts, $1\to 2$, $2\to 1$. The fields $H_{\varphi 1,2}$ are

determined from

$$H_{\varphi 1,2} = -i\frac{c}{\omega}\cdot\frac{\beta_{1,2}^2}{1-\beta_{1,2}^2}\cdot\frac{\partial E_{z1,2}}{\partial r}. \tag{14}$$

The radial functions of the fields in the vacuum

$$E_{z1,2} = E_{1,2}K_0(\varkappa_{1,2}r); \tag{15}$$

$$H_{\varphi 1,2} = -i\frac{c}{\omega}\cdot\frac{\beta_{1,2}^2}{1-\beta_{1,2}^2}\varkappa_{1,2}E_{1,2}K_1(\varkappa_{1,2}r), \tag{16}$$

where K_1 and K_0 are Macdonald's functions of first and zeroth order;

$$\varkappa_{1,2}^2 = k_{1,2}^2(1-\beta_{1,2}^2).$$

The continuity of E_z and H_φ fields at the waveguide boundary leads to a dispersion equation (a being the waveguide radius)

$$\Delta_1\Delta_2 = \frac{\varepsilon^2\psi^2N^2}{a^2I_0^2(k_{\perp 1}a)\,I_0^2(k_{\perp 2}a)}\cdot\frac{k_1^2k_2^2}{\varkappa_1\varkappa_2}, \tag{17}$$

where

$$\Delta_1 = \frac{\varkappa_1}{k_{\perp 1}}\cdot\frac{I_0(k_{\perp 1}a)}{I_1(k_{\perp 1}a)}\cdot\frac{K_1(\varkappa_1 a)}{K_0(\mu_1 a)} - 1;$$

$$\Delta_1 \to \Delta_2, \quad \text{if} \quad 1 \to 2;$$

$$N(a) = \int_0^a rI_0(k_{\perp 1}r)\,I_0(k_{\perp 0}r)\,I_0(k_{\perp 2}r)\,dr. \tag{18}$$

4. Let two waves exist for $\varepsilon = 0$, whose frequencies ω_1 and ω_2 are determined (for given k_1 and k_2) from the equations $\Delta_1 = \Delta_2 = 0$. These equations, for $|\varepsilon_{31,2}| \gg 1$, $\varkappa_{1,2}a \gg 1$, $\beta_{1,2}^2 \ll 1$, lead to a linear relation between ω and k:

$$\omega_{1,2}^{(0)} = \frac{\Omega_0 a}{\lambda_{p1,1}}k_{1,2}, \tag{19}$$

where λ_p is the root of Bessel's function of first order, $I_1(\lambda_p) = 0$.

We seek the solution of equation (17) in the form $\omega_{1,2} = \omega_{1,2}^{(0)} + \omega^{(1)}$, where $\omega_{1,2}^{(0)}$ is defined by (19) and $\omega^{(1)} \ll \omega_{1,2}^{(0)}$. For $\omega^{(1)}$ we find

$$\omega^{(1)\,2} = \frac{\varepsilon^2\psi^2N^2}{a^4I_0^2(\lambda_{p1})\,I_0^2(\lambda_{p2})}\cdot\frac{\omega_1^3\omega_2^3}{\Omega_0^4}. \tag{20}$$

The decay conditions take the form

$$\pm|\omega_2| = \omega_0 \pm |\omega_1|;$$

$$\pm|\lambda_{p2}\omega_2| = \lambda_{p0}\omega_0 \pm |\lambda_{p1}\omega_1|. \tag{21}$$

From (20) and (21) we see that the decay of an initial wave ($\omega^{(1)2} < 0$) into two waves of frequencies ω_1 and ω_2 is permitted if the waves propagate in opposite directions.

Since $k_{\perp}a \gg 1$, the upper limit in (18) can be taken as ∞. Let $k_{\perp 0}$, $k_{\perp 1}$, $k_{\perp 2}$ be such that they may form a triangle. Then the integral in (18) can be taken, and the growth increment has the order of magnitude

$$\nu \sim \frac{\varepsilon}{8\lambda_p}\omega_0. \tag{22}$$

BIBLIOGRAPHY

1. ORAEVSKII, V. N. and G. Z. SAGDEEV. – ZhTF, **32**: 1291. 1962.
2. GALEEV, A. A. and V. N. ORAEVSKII. – DAN SSSR, **147**: 1. 1962.
3. ORAEVSKII, V. N. – ZhTF, **33**: 251. 1963.
4. FAINBERG, Ya. B. and M. F. GORBATENKO. – ZhTF, **29**: 549. 1959.

R. V. Polovin

THE DIFFERENCE BETWEEN ABSOLUTE AND CONVECTIVE INSTABILITIES AND BETWEEN AMPLIFYING AND EVANESCENT WAVES

The instability of any system with respect to small perturbations is generally analyzed by representing an arbitrary disturbance as a superposition of monochromatic plane waves of the form $e^{ikx-i\omega t}$. The relation among ω and k is given by the dispersion equation

$$F(\omega, k) = 0 \tag{1}$$

If to some real k corresponds a complex ω with a positive imaginary part, instability sets in, i.e., the perturbations grow exponentially in time. However, the perturbations at any given point in space need not increase as $t \to \infty$. The perturbation may be carried away by the wave, so that at the point of origin it approaches zero* as $t \to \infty$. This instability is called convective, in distinction from the absolute (nonconvective) instability, when the perturbation increases indefinitely for $t \to \infty$ at the point of origin. The difference between these two kinds of instabilities was first defined by Landau and Lifshitz /2/.

Let us now consider amplifying oscillations. A perturbation $\varphi(x, t)$ is given at a certain point $x = 0$ for all t. This perturbation is representable as a Fourier integral with respect to all the frequencies ω. If for some real ω, k is complex, the oscillations are generally amplified. Note that a complex k sometimes implies evanescence, and not amplification. Evanescence occurs, e.g., in a cylindrical waveguide at subcritical frequencies.

* Here the perturbation indefinitely increases at a point moving with the group velocity of the wave /1/.

Sturrock /3/ was the first to define the distinction between amplification and evanescence. For amplification of oscillations it is necessary that at $x = \pm\infty$ the perturbation $\varphi(x, t)$ vanish for any finite t. Otherwise, perturbations are forbidden and we have a case of evanescent waves.

Taking the asymptotic expression for the perturbation $\varphi(x, t)$ at $x = 0$ and $t \to \infty$, we may distinguish between absolute and convective instabilities on the basis of definition alone. Fainberg, Kurilko, and Shapiro /4/ identified in this way the instabilities setting in when an electron beam interacts with a hot plasma, and also the instability of finite self-focusing beams (see also Kitsenko /5/, Fainberg /6/, and Feix /1/). Kurilko /7/ showed by the same technique that the reflection of an electromagnetic wave by a plasma moving in a waveguide is accompanied by evanescence.

Direct calculations, however, involve considerable mathematical difficulties due to the complex structure of the Riemann surfaces of the dispersion equation (1), and can be successfully completed for small parameters only. Sturrock /3/ recently proposed simple criteria for distinguishing between absolute and convective instabilities and between amplification and evanescence. Sturrock's criteria do not require any calculations. It suffices to examine the graph of the dispersion curve (1) (the graph clearly shows only those points which correspond to real ω and k).

The presence of complex ω for real k (instability band) is immediately obvious from the graph. Complex ω correspond to those real k for which the number of intersection points of the line $k = \text{const}$ with the dispersion curve is less than the degree of the dispersion equation (we assume that the dispersion equation is a polynomial). The real ω corresponding to complex k are located similarly.

Sturrock's criterion of absolute and convective instability is as follows. If k is real for all real ω, the instability is absolute (nonconvective); if, however, k is complex for some real ω, the instability is convective.

Let us now consider a criterion distinguishing between amplification and evanescence. If ω is complex for some real k, amplification occurs; otherwise, evanescence is observed.

In his proof of these criteria, Sturrock /8/ assumed that the Fourier amplitudes of the initial disturbance

$$a(k) = \frac{1}{2\pi}\int_{-\infty}^{\infty} \varphi(x,\ 0)\, e^{-ikx} dx \tag{2}$$

are other than zero only in a small neighborhood of some $k_0 : |k - k_0| < \varepsilon$. This assumption was necessary because in the determination of the asymptotic behavior of $\varphi(0, t)$ as $t \to \infty$ the contribution of the singular points in the integrand was neglected. It is more natural to assume that the initial perturbation is not zero in some finite region of space /9/. In this case, the Fourier amplitudes do not vanish for any value of the wave vector.

If Sturrock's approach is adopted, the integral describing the perturbation includes neither the singularities, as originally observed by Sturrock /8/, nor the infinitely large values of the wave vector. The latter would imply that the instability is invariably convective.

For Sturrock's criteria to apply, it suffices that the dispersion equation be a polynomial of n-th degree, which for $k \to \infty$ breaks up into n independent

branches $\omega = \beta_i k$, where all β_i are real, different, and take values other than zero or infinity.

The amplification of electromagnetic waves is of interest in radio physics and astrophysics. Various papers have dealt with this question. Neither Haeff /10/ and Pierce /11/, discussing the amplification of electromagnetic waves in a two-beam tube, nor Bailey /12, 13/ and Bohm and Gross /14/ dealing with the amplification of electromagnetic waves in sunspots give a precise definition of the initial and boundary conditions. This imprecision met with the criticism of Twiss /15/ and Piddington /16/.

Twiss observes that to establish the difference between amplification and evanescence, one must solve the problem with proper initial and boundary conditions; he suggests the Laplace transform as a convenient technique (see also /17–20/). This method is suitable if we want to distinguish between absolute and convective instability. In this case, the perturbations are taken to vanish identically for $t < 0$, and we thus have a rule for bypassing the singular points in the inversion of the Laplace integral. The initial-value technique, however, leads to the same results as Sturrock's much simpler method /3/.

We do not see, however, how the Laplace transform will help us with amplification and evanescence. We cannot take the perturbations to vanish identically for $x < 0$, since the waves from a source lying in the plane $x = 0$ may propagate both downstream and upstream /21/.

Unlike Twiss, Piddington came to the wrong conclusion that the linear theory of amplification is entirely in error. Piddington's paper /16/ contains some false statements, including the proposition that the allegedly unique mechanism of amplification is the entrapment of electrons in the potential wells of the traveling wave* (a nonlinear effect). A more detailed criticism of Piddington's papers will be found in Pierce and Walker /23/ and Bailey /13/.

An energy criterion for distinguishing between amplification and evanescence was suggested by Bailey /12, 13/ and Pierce /24/ (see also /25/). Amplification occurs only if the Umov–Poynting vector points in the direction of increasing amplitude of the electromagnetic wave. Sturrock's arguments /26/ indicate that for weak coupling between the various wave modes (i.e., low beam density), the energy criterion of amplification and evanescence coincides with Sturrock's criterion (see Figures 2 and 3 in /26/).

An amplification criterion connected with conductivity was proposed by Buneman /27, 28/. There is no proof, however, of the equivalence of Buneman and Sturrock criteria.

BIBLIOGRAPHY

1. FEIX, M. – Nuov. Cim., 27(5): 1130. 1963.

2. LANDAU, L. D. and E. M. LIFSHITS. Mekhanika sploshnykh sred (Mechanics of Continuous Media), p. 141. – Moskva, GITTL. 1953.

* Note that in the presence of a transverse magnetic field, no particles are trapped in the potential wells /22/.

3. STURROCK, P. A. – Phys. Rev., **112**: 1488. 1959.

4. FAINBERG, Ya. B., V. I. KURILKO, and V. D. SHAPIRO. – ZhTF, **31**(6): 633. 1961.

5. KITSENKO, A. B. – ZhTF, **31**(10): 1270. 1961.

6. FAINBERG, Ya. B. – Atomnaya Energiya, **11**: 313. 1961.

7. KURILKO, V. I. – ZhTF, **31**(8): 899. 1961.

8. STURROCK, P. A. – Plasma Phys. (Editor J. E. Drummond), p. 124. N. Y., McGraw-Hill Book Co. 1961

9. POLOVIN, R. V. – ZhTF, **31**: 1220. 1961; **33**: 255. 1963.

10. HAEFF, A. – Proc. IRE, **37**: 4. 1949.

11. PIERCE, J. R. – Proc. IRE, **37**: 980. 1949.

12. BAILEY, V. A. – Phys. Rev., **78**: 428. 1950; **106**: 1356. 1957.

13. BAILEY, V. A. – Phys. Rev., **83**: 439. 1951.

14. BOHM, D. and E. P. GROSS. – Phys. Rev., **75**: 1864. 1949.

15. TWISS, R. Q. – Phys. Rev., **80**: 767. 1950; **84**: 448. 1951; **88**: 1392. 1952; Proc. Phys. Soc., **B64**: 654. 1954.

16. PIDDINGTON, J. H. – Austr. J. Phys., **9**(1):31. 1956; Phil. Mag., **3**:1241. 1958; Phys. Rev., **101**(9):14. 1956.

17. LANDAU, L. D. – JETP, **16**: 574. 1946.

18. PIERCE, J. R. – Bell Syst. Tech. J., **30**: 626. 1951.

19. GOULD, R. W. – IRE Trans., **ED 2**: 37. 1955.

20. FILIMONOV, G. F. – Radiotekhnika i Elektronika, **4**: 75. 1959.

21. LUCHINA, A. A. – JETP, **28**: 17. 1955.

22. MORAWETZ, C. S. – Phys. Fluids, **4**(8): 488. 1961; **5**(11): 1447. 1962.

23. PIERCE, J. R. and L. R. WALKER. – Phys. Rev., **104**: 306. 1956.

24. PIERCE, J. R. – Bell Syst. Tech. J., **33**: 1343. 1954.

25. HAUS, H. A. – IRE Trans., **ED-5**: 225. 1958.

26. STURROCK, P. A. – Ann. of Phys., **9**: 422. 1960.

27. BUNEMAN, O. – Plasma Phys. (Editor J. E. Drummond), p. 143. N. Y., McGraw-Hill Book Co. 1961.

28. SWIFT-HOOK, D. T. – Phys. Rev., **118**: 1. 1960.

E. A. Sukhomlin, V. A. Suprunenko, and N. I. Reva

ELECTRICAL CONDUCTIVITY OF A PLASMA WITH ELECTROSTATIC INSTABILITIES

The variation of plasma conductivity is of considerable significance in the analysis of processes occurring in a plasma in the presence of electrical fields. Knowledge of conductivity, combined with other data, gives a fairly lucid picture of the interaction of electrons when a current flows through the plasma.

In small electric fields, where Coulomb collisions are significant, the conductivity of the plasma is independent on field and density: it is determined by the temperature alone /1/, $\sigma \sim T_e^{3/2}$. However, preliminary investigations of discharges /2/ have sufficed to establish that the conductivity is a sensitive function of the electric field. This is attributable to the high (from the viewpoint of Spitzer's theory) strength of the electric field. Dreicer /3/ showed that in intense electric fields the force of dynamic friction due to binary collisions rapidly decreases, if the streaming velocity of the electron gas is greater than its random thermal speed. The electron gas is accelerated by the electric field and forms a beam of "runaway" electrons.

Akhiezer and Fainberg /4/ and Bohm and Gross /5/ showed that the equilibrium in a plasma-beam system is unstable, whenever the streaming velocity is greater than the thermal velocity.

Analogous instabilities may occur in a plasma immersed in an intense electric field,

$$E > E_{cr} = 1.58 \cdot 10^{-2} \frac{n_0}{T_e},$$

where n_0 is the electron number density, m^{-3}; T_e the electron temperature, °K.

In this case, the electron beam is decelerated, and its energy is expended in the excitation of plasma oscillations. The calculations of Buneman /6/ and Shapiro /7/ show that this mechanism is highly effective, producing a substantial stopping already within the first 100 oscillations. In our case, this is equivalent to a time of some 10^{-10} sec.

The aim of this study was to investigate the electrical conductivity of a dense plasma immersed in an intense electric field, when processes associated with the generation of "runaway" electrons predominate.

The experimental setup comprised a linear pinch discharge stabilized by a magnetic field, which had been described in detail in /8/. The electric fields varied from 10,000 to 100,000 V/m, the external magnetic field reached strengths of $7 \cdot 10^{-1}$ T, the current in the plasma was close to 100 kA, current period 9 μsec. The starting pressure varied from $133 \cdot 10^{-1}$ to $133 \cdot 10^{-3}$ N/m². Working gas — hydrogen, helium. High vacuum conditions were created in the setup.

Figure 1 shows the electric diagram of the setup. The following quantities were measured: interelectrode voltage (using a low-resistance divider); total current (using Rogowsky loop); the "runaway" electron current through a hole in the electrode; the temperatures of the ions and the electrons and their densities (by spectroscopic methods). Microwave radiation at a wavelength of some 1.2 cm was also recorded.

The discharge resistance was found by measuring the interelectrode voltage and the total discharge current. Table 1 lists the resistance for

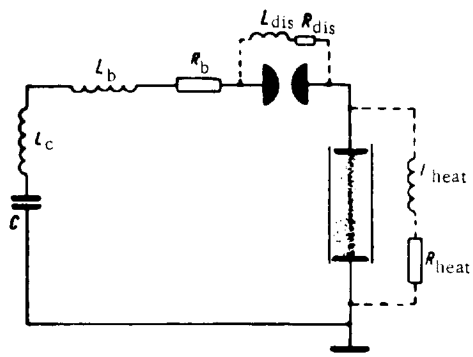

FIGURE 1. The electric circuit of the experimental setup.

various sections of the discharge circuit. The inductance of the arc gap was determined from the length of the period of the discharge current; it was found to be equal to 0.077 μH. The corresponding inductive reactance is 0.048 ohm at a discharge frequency of 100 c/s.

The reactive component in this case clearly accounts for a very minor fraction of the interelectrode impedance.

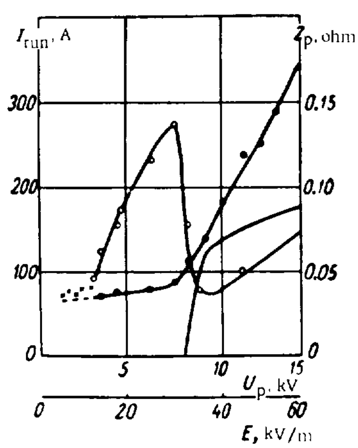

FIGURE 2. Discharge resistance, "runaway" electron current, and microwave radiation as a function of the electric field.

Figure 2 shows the discharge resistance, the "runaway" electron current, and the microwave plasma radiation as a function of the electric field in the plasma, for a starting pressure $p_0 = 266 \cdot 10^{-2}$ N/m^2 and an external magnetic field $H_0 = 0.4$ T. We see that the resistance remains fairly constant up to a certain field strength . For fields greater than this critical E, the resistance rapidly increases with the electric field in the plasma. The sharp growth of resistance near the critical field is accompanied by an abrupt drop in the "runaway" electron current and intense emission of microwave radiation from the plasma. All this indicates that as long as the drift velocity of the electrons does not exceed the thermal speed, the discharge resistance does not vary much with the field E. When the drift velocity becomes greater than the thermal velocity, the beam of "runaway" electrons excites electrostatic oscillations in the plasma and decelerates losing its energy to the oscillatory modes. In Figure 2 this is reflected in the abrupt drop of the "runaway" electron current. Electromagnetic radiation recorded by the microwave receiver is a consequence of the onset of streaming instability.

The rapid growth of the plasma resistance with the electric field is thus attributable to collective processes occurring in the discharge in the

presence of an electric field. These processes also explain the experimental dependence of the discharge resistance on the initial pressure p_0 (Figure 3).

TABLE 1

U_c, kV	I_{tot}, kA	U_p, kV	Z_p, ohm	Z_{tot}	Z_b
28	74.6	12.1	0.16	0.38	0.22
28	81.6	11.0	0.15	0.37	0.22
28	76.6	13.2	0.17	0.39	0.22
30	66.5	15.0	0.23	0.45	0.22
30	82.8	13.0	0.16	0.36	0.20
32	80.9	15.8	0.20	0.40	0.20
32	111.6	11.7	0.10	0.29	0.19
34	115.9	12.1	0.10	0.29	0.19

The curves correspond to a magnetic field H_0 = 0.7 T and an electric field E_0 = 40,000 V/m. If only Coulomb interactions are considered, the resistance should not vary with plasma density. The actual variation is easily explained by means of collective interactions: as the plasma density

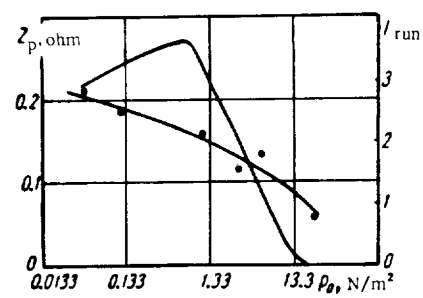

FIGURE 3. Discharge resistance and "runaway" electron current as a function of the initial pressure.

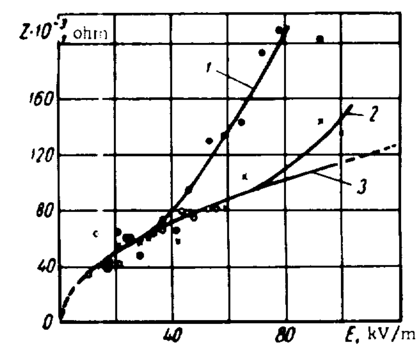

FIGURE 4. Discharge resistance as a function of the electric field for various constant initial pressures

increases in a constant applied electric field, the "runaway" electron current steeply drops, and excitation of electrostatic instabilities stops.

Figure 4 shows the variation of the discharge resistance with the electric field for various initial pressures. Curve 1 corresponds to $p_0 = 533 \cdot 10^{-3}$ N/m², curve 2 $p_0 = 266 \cdot 10^{-2}$ N/m². We see that each curve is characterized by its own critical field, when the steep growth of resistance begins. Curve 3 corresponds to p_0 = 13.3 N/m². The critical field has not been attained on this curve (in view of experimental limitations).

Combining the critical fields at the different pressures from Figure 4 with the data from Table 2 (the table is based on the results of spectroscopic measurements), we calculated the ratio $\frac{E_{cr1}}{E_{cr2}}$ using the formula

$$E_{cr} = 1.58 \cdot 10^{-2} \frac{n_0}{T_e}$$

and compared it with the ratio of the directly measured fields: calculated $\frac{E_{cr}}{E_{cr}} = 3$, from Figure 4 $\frac{E_{cr}}{E_{cr}} = 2.8$. This fairly close agreement indicates that the anomalous growth of resistance starts in critical fields associated with the onset of beam instabilities in a plasma.

TABLE 2

p_0, N/m^2	T_e, °K	n_e, m^{-3}	E_{cr}, V/m
10.66	$25 \cdot 10^4$	$2.8 \cdot 10^{21}$	—
2.66	$20 \cdot 10^4$	$7.1 \cdot 10^{20}$	$70 \cdot 10^3$
0.53	$12 \cdot 10^4$	$1.4 \cdot 10^{20}$	$25 \cdot 10^3$

Proceeding from our data on conductivity, we also considered the role of Coulomb interaction in the experimental conditions. If the plasma conductivity is known, we can calculate the effective frequency of interaction of the electrons with the plasma:

$$\nu_{eff} = 1.95 \frac{ne^2}{m_e \sigma}.$$

Since $\sigma \; \frac{l}{s}$, where l is the discharge length, s the cross section area, we can find the conductivity if the geometrical dimensions of the discharge are known. In our case, $s = 12.5$ cm^2 and $l = 25$ cm.

We can thus calculate the effective interaction frequency ν_{eff} corresponding to the experimental data. On the other hand, proceeding from the theory with Coulomb collisions, we can find the frequency of binary interactions ν_i. Furthermore, applying the results of Buneman /6/ and Shapiro /7/, who dealt with the theory of the onset of electrostatic instability, we can obtain the effective time of electron—plasma interaction, corresponding to a frequency ν_{coll}.

Table 3 gives the frequencies ν_i, ν_{eff}, ν_{coll} calculated for various initial pressures p_0.

TABLE 3

p_0, N/m^2	n_e, m^{-3}	ω_e, sec^{-1}	ν_i, sec^{-1}	σ, (ohm-cm)$^{-1}$	ν_{eff}, sec^{-1}	ν_{coll}, sec^{-1}
0.04	$6.6 \cdot 10^{19}$	$4.6 \cdot 10^{11}$	$0.8 \cdot 10^7$	$9.5 \cdot 10^2$	$2.2 \cdot 10^9$	$1.2 \cdot 10^9$
0.12	$2.0 \cdot 10^{20}$	$7.9 \cdot 10^{11}$	$2.5 \cdot 10^7$	$10.5 \cdot 10^2$	$6.2 \cdot 10^9$	$2.4 \cdot 10^9$
1.07	$1.8 \cdot 10^{21}$	$2.4 \cdot 10^{12}$	$3.3 \cdot 10^8$	$12.5 \cdot 10^2$	$7.3 \cdot 10^{10}$	$1.3 \cdot 10^9$
2.66	$4.4 \cdot 10^{21}$	$3.8 \cdot 10^{12}$	$5.0 \cdot 10^8$	$16.7 \cdot 10^2$	$8.4 \cdot 10^{10}$	$2.4 \cdot 10^{10}$
5.33	$8.8 \cdot 10^{21}$	$5.5 \cdot 10^{12}$	$1.1 \cdot 10^9$	$14.3 \cdot 10^2$	$1.9 \cdot 10^{11}$	$0.5 \cdot 10^{11}$

We see from Table 3 that the effective electron—plasma interaction time measured experimentally is roughly 1/100 of the Coulomb interaction time and is of the same order of magnitude as the time of growth of plasma

oscillations. This implies that in our experiment collective interactions predominate, whereas Coulomb interactions are of secondary importance.

In our study of the conductivity of plasmas in intense electric fields we established that the discharge resistance increases anomalously with the electric field. This growth was shown to be connected with the onset of electrostatic instabilities, limiting the electron drift velocities. Direct measurements established that the onset of beam instabilities is reflected in an abrupt drop of the "runaway" electron current and intense emission of microwave radiation in critical electric fields. It is also shown that in the conditions of our experiment Coulomb interactions are insignificant.

BIBLIOGRAPHY

1. SPITZER, L. Physics of Fully Ionized Gases. – N. Y., Interscience Publ. 1956.

2. BORISOV, M. D., V. A. SUPRUNENKO, E. A. SUKHOMLIN, and E. D. VOLKOV. – In: "Fizika plazmy i problemy upravlyaemogo termoyadernogo sinteza", Vol. 1, pp. 133–138. Kiev, Izdatel'stvo AN UkrSSR. 1962.

3. DREICER, H. – Phys. Rev., 115: 238. 1959.

4. AKHIEZER, A. I. and Ya. B. FAINBERG. – DAN SSSR, 69: 555. 1949.

5. BOHM, D. and E. GROSS. – Phys. Rev., 75: 1851. 1949.

6. BUNEMAN, O. – Phys. Rev., Lett., 1: 8. 1958.

7. SHAPIRO, V. D. – ZhTF, 31: 522–528. 1961.

8. SUPRUNENKO, V. A., Ya. B. FAINBERG, V. T. TOLOK, E. A. SUKHOMLIN, N. I. REVA, P. Ya. BURCHENKO, E. D. VOLKOV, and N. I. RUDNEV. – Atomnaya Energiya, 14: 349. 1963.

O. S. Pavlichenko, L. A. Dushin, I. K. Nikol'skii, and L. V. Brzhechko

MACROSCOPIC INSTABILITY OF THE PLASMA IN A REFLEX DISCHARGE

Anomalous diffusion of charged particles in the positive column of a low-pressure glow discharge, discovered by Lehnert /5/, was interpreted by Kadomtsev and Nedospasov /6/, Hoh and Lehnert /7/, while Paulikas and Pyle /8/ demonstrated a satisfactory quantitative agreement of experimental results with the predictions of Kadomtsev and Nedospasov's theory. This immediately suggested a study of diffusion processes in a plasma without any strong longitudinal electric fields E_z, which lead to a macroscopic instability of the plasma column in the presence of a high magnetic field. The experiments were made using a PIG reflex discharge in a magnetic field; this discharge has been studied in sufficient detail by various authors.

The first investigation of diffusion in a reflex discharge, carried out by Bonnal, Brifford, and Manus /1/, showed that the diffusion of the plasma in a discharge chamber with nonconducting walls increased when the magnetic field had risen above a certain critical strength. Emission of r-f noise (f = 1000 Mc/s) accompanied the enhanced diffusion.

Chen and Cooper /3, 4/ studied the discharge in a conducting chamber, emphasizing the aspect of the steady-state low-frequency ion oscillations arising in the plasma. They established the existence of several regions (depending on the magnetic field), characterized by different behavior of the ionic modes: in the region of medium magnetic fields, $(1.6-6)\cdot 10^4$ A/m, the oscillations have a stable sinusoidal form, but in higher fields incoherent hash is observed. Applying the correlation technique, they measured the phase velocity of waves of various frequencies in the hash and showed that it lied between the acoustic ($\sim 10^4$ m/sec) and the Alfvén ($\sim 10^7$ m/sec) speeds, being equal to $2\cdot 10^5$ m/sec. Chen and Cooper stress the fact that they did not observe an increase of diffusion as the magnetic field was raised to $3.2\cdot 10^5$ A/m.

In the present paper we describe the results obtained for the diffusion of charged particles in a discharge plasma with nonconducting walls in the range of pressures from $1.33\cdot 10^{-2}$ to 1.33 N/m^2.

Equipment and procedure

The setup is schematically shown in Figure 1. The plasma was created in a glass discharge tube of 5.0 cm diameter; external diameter of anodes and cathodes 4.4 cm, anode holes 3.6 cm in diameter. Cathode separation 70 cm, cathode—anode distance 8 cm. The discharge tube was mounted on the axis of a coil system generating a homogeneous (to within 0.5%) magnetic

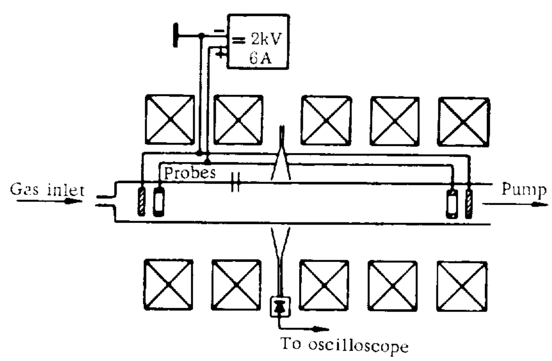

FIGURE 1. The experimental setup.

field of up to $2.7\cdot 10^5$ A/m along the entire tube length. A constant voltage of up to 2 kV was impressed on the electrodes; the current varied between 50—300 mA. The initial vacuum in the system was $1.3\cdot 10^{-4}$ N/m^2. The basic results were obtained with helium in the pressure range $6.6\cdot 10^{-2}$—1.3 N/m^2.

The discharge plasma was investigated by various techniques: current measurements with a probe maintained at a negative potential relative to the plasma; measurements of the density of the charged particles on the discharge axis with a double electric probe; transmission of a microwave signal (λ = 3 cm) through the plasma; electron temperature T_e and its radial distribution, measured from the relative intensities of the lines He II 4686 Å and He I 4921 Å; radial distribution of helium glow intensity; measurements of a signal with precision-collimated photomultipliers. The results give a figure of $5 \cdot 10^{11}$ cm^{-3} for the plasma density, and $(1.5-2) \cdot 10^5$ °K for the electron temperature.

Results of measurements

Observations of anomalous diffusion. Figure 2 gives the variation of the wall ion current with the magnetic field, measured by means of a probe having negative polarization relative to the plasma. The wall ion current at first decreased with the increase of the magnetic field, but started increasing above a certain critical strength H_{cr}. Characteristic curves having extrema near H_{cr} were also obtained for the density of the charged particles on the discharge axis and for the electron temperature (these measurements were made with a spectrograph ISP-51 and a photoelectric attachment FEP-1). Figure 3 plots the corresponding variations for the case p = 0.6 N/m^2, U_a = 1000 V. The critical magnetic field increases

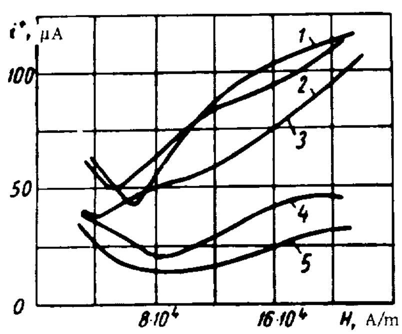

FIGURE 2. The wall ion current as a function of the magnetic field:
He; U = 1000 V; 1) p = 0.18; 2) p = 0.1; 3) p = 0.05; 4) p = 0.49; 5) p = 0.65 N/m^2.

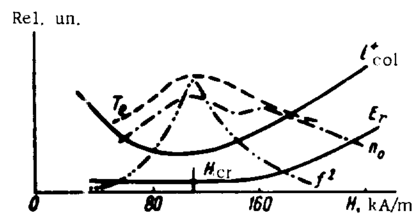

FIGURE 3. Wall ion current, density on discharge axis, electron temperature, radial electric field, and the square of the frequency of steady-state oscillations as a function of the magnetic field:
He; U = 1000 V; r = 2.5 cm.

with the increase of pressure. Figure 4 gives H_{cr} (obtained from the measurements of $i^+ = f(H)$) as a function of pressure.

Two probes on the discharge axis and near the wall measured the radial difference of potential, which proved to be highly sensitive to the magnetic field and the pressure. Figure 5 plots the variation of the radial electric field with the magnetic field for various pressures (in Figure 3 this

variation is shown simultaneously with the other parameters; we see that the radial electric field increases with the increase of plasma diffusion).

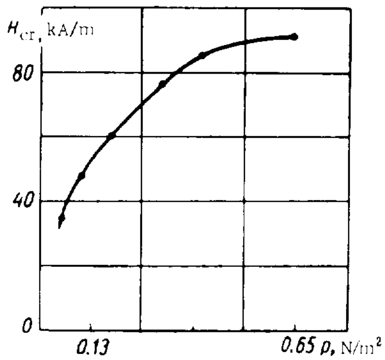

FIGURE 4. H_{cr} vs. pressure.

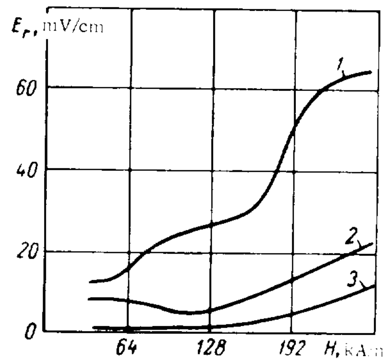

FIGURE 5. The radial electric field as a function of the magnetic field:
He; $U = 1000$ V; 1) $p = 0.06$; 2) $p = 0.39$; 3) $p = 0.65$ N/m^2.

Macroscopic nature of the anomalous diffusion. To establish the nature of the enhanced diffusion, we streak-photographed the plasma column through a slit perpendicular to the discharge axis, using a rotating mirror. Visual observations showed that a well-shaped plasma column with sharply outlined boundaries started curving into a helix when the magnetic field was increased

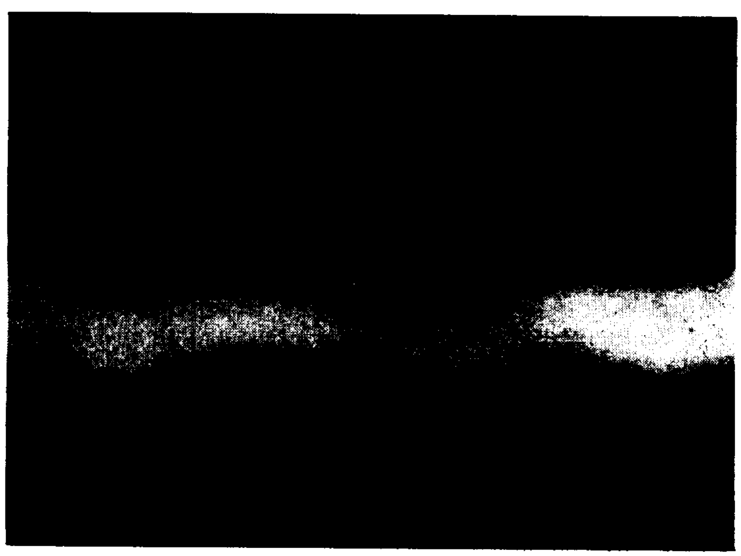

FIGURE 6. A streak photograph of the plasma column through a slit perpendicular to the discharge axis:
$p = 0.06$ N/m^2, $U = 1000$ V; 1 cm to 500 μsec.

above the critical value. Figure 6 is a streak photograph of the plasma column in this case; the column pulsations had a frequency of some 200—800 c/s. Observations were also made with a collimated photomultiplier receiving light from the region near the wall. The signal increased sharply when H_{cr} was crossed, i.e., the plasma moved to the walls.

We also measured the radial distribution of the helium glow intensity. The plasma column was projected onto the input slit of the spectrograph equipped with a long-focus camera UF-85. The spectrograms gave the distribution of the relative intensities of the He I and He II lines along the

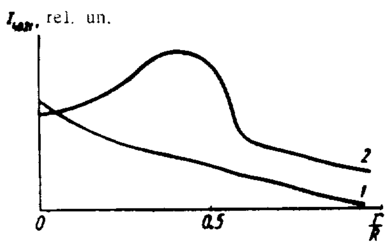

FIGURE 7. Radial distribution of the He I 4921 Å intensity:
$H_{cr} = 8 \cdot 10^4$ A/m; $p = 0.13$ N/m^2; $U = 1000$ V; 1) $H = 38$; 2) $H = 110$ kA/m.

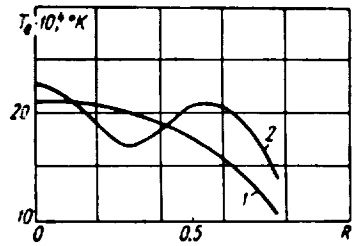

FIGURE 8. Radial distribution of electron temperature:
He; $H_{cr} = 8 \cdot 10^4$ A/m; $U = 1000$ V; $p = 0.13$ N/m^2; 1) $H = 3.8 \cdot 10^4$; 2) $H = 1.1 \cdot 10^5$ A/m.

height of the slit. The measurements were converted into the radial distribution across the plasma column by numerically solving an Abel equation, following the technique proposed by Dolgov and Mandel'shtam /8/. Figure 7 gives the variation of the intensity of the line He I 4921 Å for subcritical and supercritical magnetic fields. The intensity received from the peripheral plasma increases on crossing the critical field. Measurements of the radial distribution of the electron temperature T_e show that on passing through the critical field, the plasma column separates into a "hot pinch" on the tube axis and a "hot fur" at some distance from the axis (Figure 8).

Low-frequency plasma oscillations. The microwave probing of the plasma column ($\lambda = 3$ cm), and the oscillograms of the a.c. component picked up by the wall probe show that in subcritical magnetic fields the plasma sustains stable low-frequency oscillations of the density of charged particles. Our results are fully consistent with previous data /2, 9/. The frequency of these oscillations lies between 20--50 c/s and does not vary much with the discharge current. As the magnetic field increases in the subcritical region, the oscillations are distinctly sinusoidal and their frequency increases; near the critical field, the oscillations develop additional overtones. Above the critical field, the oscillations are random.

We measured the frequency of these oscillations as a function of the magnetic field (see Figure 3). The frequency varies with the magnetic field H approximately as the electron temperature does. Our result agrees with the measurements of Consoli et al. /10/, who identify these steady-state oscillations with ionic sound waves.

We also tried to study the relation of these low-frequency oscillations with the onset of the enhanced plasma diffusion by stimulating the

corresponding modes with the aid of an external source. An audio-frequency generator was coupled to one pair of electrodes; the cathode remained grounded, acting as the reflex. The amplitude of the low-frequency oscillations could be increased in this way by tuning the generator to

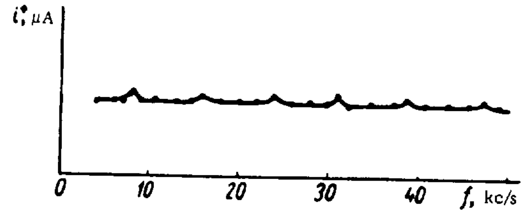

FIGURE 9. The probe ion current as a function of the generator frequency:
U_a= 1600 V; p= 0.06 N/m^2; $H = H_{cr}$; U_{gen} = 100 V.

resonance with the plasma oscillations. The wall ion current in a magnetic field $\sim H_{cr}$ increased, and the variation of the ion current with the generator frequency followed a periodically repeating resonant curve (Figure 9).

Discussion of results

The enhanced diffusion observed in high magnetic fields is consistent with the results of Bonnal, Briffod, and Manus /1/. The enhanced diffusion is accompanied by a decrease in the electron temperature in the plasma, at variance with the results obtained in the positive column of a glow discharge. This is apparently attributable to a difference in the corresponding mechanisms: in a positive column the current cannot be sustained unless the electric field and T_e increase to compensate for the accelerated rate of diffusion of the particles acorss the magnetic field. In a plasma with oscillating electrons, on the other hand, the enhanced diffusion results in an increase of thermal flow across the magnetic field, and the plasma cools.

The anomalous diffusion of charged particles is apparently a consequence of the macroscopic motion of the column ($m > 0$) observed in streak photographs and in measurements of the radial intensity distribution of helium. In this case, our results are at variance with those of Bonnal et al., although they were specifically looking for any macroscopic factors linked with the enhanced diffusion. The extremely low frequency of these oscillations possibly accounts for their failure to detect the column instability.

The rotation of the column is apparently a result of the instability of the azimuthal drift motion of the column in crossed fields E_r and H_z;* estimates of the rotation frequency based on measurements of E_r (see Figure 5) are in satisfactory agreement with the experiment: for E_r = 50 mV/cm and H_z = = 1.6·10^5 A/m, the column rotates with a frequency of 900 c/s.

* The significance of radial electric field in the process of enhanced diffusion in PIG-type discharge was pointed out by Bonnal, Gregoire, and Manus /1, 2/.

It is still not clear how the constant radial electric field is generated. A possible explanation can be sought in the charging of the nonconducting chamber walls attendant on the excitation of transverse ion modes in the magnetic field. The existence of these modes is suggested by the results of Chen and Cooper /4/, who studied the low-frequency oscillations in a reflex discharge. The high phase velocity of the low-frequency oscillations along the magnetic field observed by these authors ($v_{ph} = 2 \cdot 10^5$ m/sec and $v_{sound} = 10^4$ m/sec) is possibly a consequence of the excitation of "oblique drift waves" /10/ with a phase velocity

$$v_{ph} = -\frac{k_y}{k_z} \cdot \frac{c}{eHn}\left[T_e \frac{dn}{dz} + \frac{d}{dr}(nT_i)\right],$$

where k_y, k_z are projections of the wave vector. For a high $\frac{k_y}{k_z}$ ratio, this velocity may be greater than the velocity of sound, the waves propagating almost without damping. The ions in these waves will start vibrating also transversally to the magnetic field, which must charge the walls.

The presence of a radial field far from the anodes may also prove to be a trivial consequence of potential sagging from the region of the fast anode fall.

A remarkable feature is the absence of enhanced diffusion in a strong magnetic field in chambers with metallic walls (Chen and Cooper /3/). Although helical disturbances ($m = 1$) rotating with a speed of $c\frac{E_r}{H_z}$ were observed in the plasma column, they did not increase the diffusion, which is possibly due to the stabilizing influence of the metallic screen relative to the onset of large-amplitude hydromagnetic instabilities.

BIBLIOGRAPHY

1. BONNAL, J. F., G. BRIFFORD, and C. MANUS. – Phys. Rev. Lett., 6:665. 1961.
2. BRIFFORD, G., M. GREGOIRE, and C. MANUS. – Phys. Lett., 2:201. 1962.
3. CHEN, F. and A. COOPER. – Phys. Rev. Lett., 9:333. 1962.
4. BINGHAM, R. and F. CHEN. – Bull. Amer. Phys. Soc. Ser. II. 7:401. 1962.
5. LEHNERT, B. – Proceedings of the Second Geneva Conference on Peaceful Uses of Atomic Energy, Vol. 32, p. 349. Geneva. 1958.
6. KADOMTSEV, B. B. and A. V. NEDOSPASOV. – Journ. Nucl. Energy, Part C, 1:433. 1960.
7. HOH, F. and B. LEHNERT. – Phys. Fluids, 3:600. 1960.
8. PAULIKAS, G. and R. PYLE. – Phys. Fluids, 5:348. 1962.
9. DOLGOV, G. G. and S. L. MANDEL'SHTAM. – JETP, 24:691. 1953.
10. CONSOLI, F., R. Le GARDEUR, and L. SLAMA. – Compt Rend., 253(8):1923. 1961.
11. KADOMTSEV, B. B. – JETP, 43:1688. 1962.

METHODS AND DIAGNOSTICS OF PLASMOIDS. PLASMA INJECTORS

A. A. Kalmykov, A. D. Timofeev, Yu. I. Pankrat'ev, and V. I. Tereshin

A METHOD FOR MEASURING THE ENERGY AND THE MASS SPECTRA OF THE IONIC COMPONENT OF A MOVING PLASMA

Various papers have recently been published on the performance of different varieties of plasma guns and the interaction of the plasmoids created by these guns with magnetic fields. In these researches, and particularly in the interpretation of the results on the interaction of plasmoids with magnetic fields, knowledge of the energy spectra of the plasmoid particles and of the mass composition of the plasma is absolutely essential; the spectroscopic data are especially significant for the study of plasmoids injected into magnetic traps. Some works /1/ make use of the Thomson mass analyzer, but this instrument has several deficiencies: the energy spectra of the particles in the low-energy region cannot be obtained, the absence of time resolution makes it impossible to determine the structure of the plasmoids, the distribution of various particles along the plasmoids, etc.

In the present paper we describe an instrument which is free from these shortcomings and can be applied in various experiments with moving plasmas.

Operation and description of various component units

The apparatus schematically shown in Figure 1 is used in analyzing a beam of ions separated from a plasma. A low-density ion beam is cut from a plasma stream passing through a system of diaphragms D_1, D_2, D_3; the beam is then directed to the modulators M_1, M_2 which isolate a single, compact ion packet. Passing through the electric analyzer C_2 (a plate condenser), the beam is deflected through a preset angle and is picked up by the detector behind the diaphragm D_6. The distance between the modulator and the detector is the drift length. Ions of equal energy but different mass traverse this distance in different times, and if the length of the ion packet is less than the difference in times of flight, the screen of an oscilloscope coupled into the detector will display the mass spectrum of particles of given energy. The mass spectrum can be obtained only if the size of the diaphragm is less than the Debye radius for the plasma,

$$d < r_d.$$

If the plasma is dense and r_d is very small, several diaphragms must be applied in succession to reduce the density of the plasma, i.e., to increase

r_d. If a voltage is applied to the diaphragm, r_d has the form

$$r_d = \sqrt{\frac{eU}{8\pi n e^2}}.$$

Then, for a given diaphragm radius, the condition

$$d < r_d$$

can be met by altering U; in other words, complete separation of the plasma components can be achieved by adjusting the diaphragm potential. To avoid distortion of the energy spectrum, the voltage must be applied symmetrically. For example, if the particles are accelerated in the $D_2 - D_3$ gap and suitably accelerated in the $D_3 - D_4$ gap, the energy of the particles passing through the $D_2 - D_3 - D_4$ system will not change.

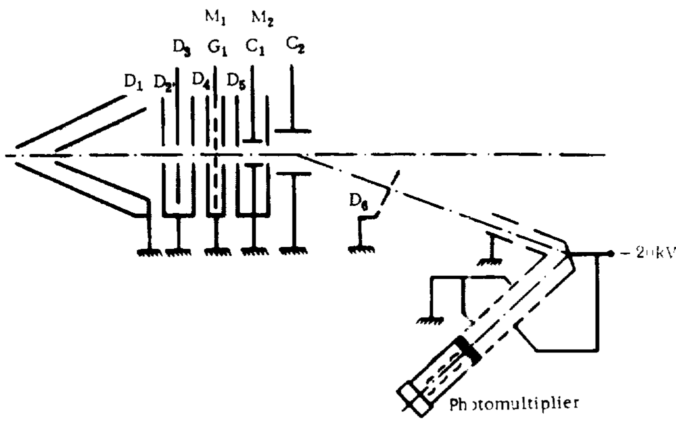

FIGURE 1. Schematic of the system.

In some cases, e.g., for plasmoids generated by different plasma accelerators, the process of separation is somewhat simpler. In /3/ it was shown that for plasmoids

$$W_{0i} \gg W_i, \; W_{0e} \ll W_e,$$

where W_{0i} and W_{0e} are the drift energies of the ions and the electrons, respectively; W_i and W_e are the mean thermal energies of these particles.

It follows from this relation that ions pass through diaphragms much more easily than electrons. Plasma separation thus occurs even if no voltage is applied, and the stream is simply channeled through several diaphragms.

In our setup, two modulators are used. The first modulator M_1 (see Figure 1) modulates low-energy ion beams. It comprises a grid G_1 between two diaphragms. The distance from the grid to either diaphragm is 2 mm. When a positive voltage U_M is applied to the grid,

$$U_M > W_i/Ze$$

(W_i the beam energy in eV, Ze charge of ions), the beam does not pass through the modulator. When the grid potential is compensated by a pulse fed from a square pulse generator, ions are transmitted for a time τ (the pulse length) through the modulator. An ion packet is thus formed.

The second modulator for high-energy ions is a plate condenser C_1 between two diaphragms. If positive voltage is applied to the condenser, the beam is deflected between the plates and does not pass through the diaphragm. If a compensating pulse is applied to the condenser plates, the beam passes through, so that the diaphragm gives an ion packet with a duration equal to the pulse length.

The introduction of two modulators is inevitable: the first modulates beams with energies of the order of magnitude of the applied voltage (when working with high-energy ions, this necessitates the application of large voltages, and insulation difficulties become formidable), while the second is inadequate for generating short pulses of low-energy ions on account of the limitations imposed by the deflection angle (the drift time between the condenser plates must be much less than the length of the modulation pulse).

The resolving power of the drift mass spectrometer is given by

$$\frac{M}{\Delta M} = \frac{t_{dr}}{2\tau},$$

where t_{dr} is the drift time, τ pulse length, or

$$\frac{M}{\Delta M} = 0.361 \frac{l_{dr}}{\tau} \sqrt{\frac{M}{W_i}}.$$

Here l_{dr} is the drift length in cm, τ pulse length in μsec, W_i particle energy in Ev, M the mass number.

In our instrument, the drift length was 40 cm, variable up to 150 cm. The square pulse generator gave pulses with $\tau = 0.2\,\mu$sec, $0.5\,\mu$sec, $1\,\mu$sec, so that satisfactory resolution could be obtained for particles of different energies.

The energy resolution of an electrostatic analyzer is determined from the system geometry:

$$\gamma = \frac{\Delta W}{W} = \frac{\Delta S}{S},$$

where ΔS is the geometrical width of the slit at the analyzer outlet, S beam deflection, W particle energy, ΔW the energy width of the slit.

Hence, $\Delta W = \gamma W$, i.e., the energy width of the slit increases in proportion to the particle energy. Therefore, the detected current pulse is given by

$$I_0 = f(W)\,\Delta W$$

and to obtain the energy spectrum $f(W)$ we must know the width of the energy slit. The energy distribution has the form

$$f(W) = \frac{I_0(W)}{W},$$

where $f(W)$ is the energy distribution function of the particles, $I_0(W)$ detector current for a given particle energy.

Ion currents were detected by the method descr bed in /4,5/. The ion beam was accelerated to 20 keV and then aimed at a target; the secondary electrons knocked out by the fast beam were accelerated by the same voltage and hit a plastic scintillator. The light pulses were picked up by a FEU-33 photc multiplier. This detector arrangement is fairly sensitive and has several advantages in comparison with a secondary electron multiplier. A shortcoming of this system is the dependence of the secondary emission coefficient on the mass o the ion, which may lead to errors in the determination of the relative composition of ions of different masses. Special experiments were therefore made to determine the coefficients of secondary emission for ions of various masses. The results are plotted in Figure 2. We see that in the working region, i.e., for detector voltage ~15 kV, the coefficient of secondary emission is insensitive to ion mass.

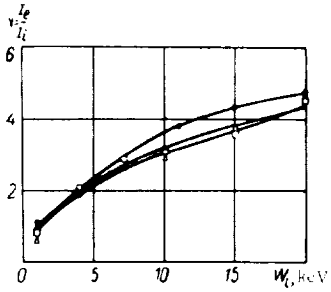

FIGURE 2. The coefficient of secondary electron emission as a function of the accelerating voltage for
● H^+ △ A^+ □ Ne^+.

We also measured the detector gain for pulsed currents and showed that the system was linear in a very wide range of currents.

Since only one multiplier stage in the detector (the ion-electron converter) comes in direct contact with the vacuum system, the gain factor will remain fairly constant even if the vacuum parameters are varied between wide limits; this can hardly be said of systems employing secondary electron multipliers.

Calibration and tests

The various units were calibrated and tested using a special ion source, comprising a hot cathode in a magnetic field in combination with a three-electrode le is. This system generated ion beams of different masses, depending on the atomic number of the gas injected intc the source, and beam energies of up to 5 keV.

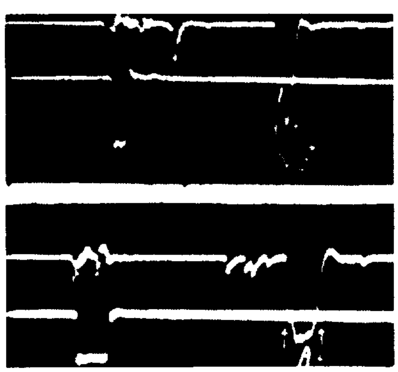

FIGURE 3. Current pulses with modulated Ne^+ (top) and A^+ (bottom) beams.

Figure 3 shows the oscillograms of the pulses obtained with modulated Ne^+ and A^+ beams. The calculated position of the pulses is indicated by arrows; the lower trace gives the modulation pulse. There is satisfactory agreement between the experimental results and the theoretically calculated pulse positions. An ion beam was used to calibrate the electrostatic analyzer, i.e., to plo the condenser voltage vs. particle energy curve. The calibration curve is shcwn in Figure 4. Figure 5 is the mass spectrum of the ions generated when hydrogen is injected into the source, as obtained with our drift analyzer. For purposes of comparison, Figure 6 gives the mass spectrum of the same source, taken

with a magnetic mass spectrometer. The performance of our instrument is seen to be acceptable.

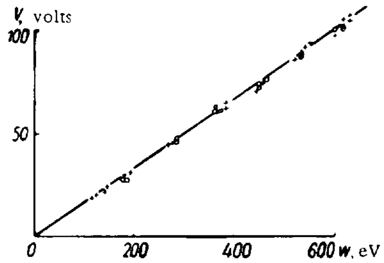

FIGURE 4. Calibration curve of the electrostatic analyzer for: O Ne^+; × A^+.

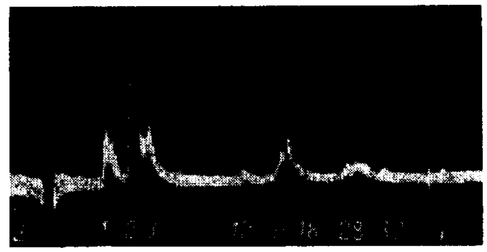

FIGURE 5. Mass spectrogram of an ion source taken with the drift mass spectrometer.

Since the performance of the separation unit is critical for the performance of the entire apparatus, we proceeded with special plasma separation tests. The ion source was replaced with Bostick's button-type source /7/, and we studied the energy spectra of some ions in two cases: with negative voltage applied to the central electrode of the separation system and without the application of negative voltage. Since the density of the plasma passing through all the diaphragms is low, the voltage applied to the central electrode should suffice for complete separation of ions and electrons in the plasmoid. No considerable difference was observed in the energy spectra taken in these tests. If a plasma stream is channeled into the analyzer, and the condition $r_d > d$ is not satisfied, the spectra should contain ions of various energies, depending on the potential applied to the separation electrode. The tests show that if a positive voltage is applied to the central electrode of the separation system, the energy spectrum contains only ions with energies corresponding to voltages higher than the applied voltage. The lower boundary of the energy spectrum rigidly follows any variation in the separation voltage. The results of these experiments support the suggestion that an ion beam can be separated from a plasmoid of given density ($\sim 10^{12}$ cm^{-3}) simply by passing the plasma through several diaphragms in succession.

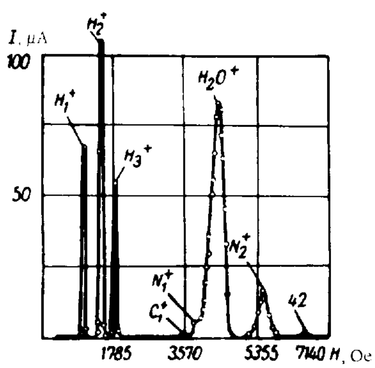

FIGURE 6. Mass spectrum of an ion beam taken with a magnetic mass spectrometer.

Our instrument is also suitable for determining the time characteristics of pulsed plasma sources. If ions of equal energy reach the detector, and the masses are adequately separated in the drift space, the length of the peak of each mass corresponds to the length of the ionization time in the pulsed source, with allowance for the time resolution of the system;

the time resolution in this case is defined by

$$\Delta t = t_{dr}\sqrt{\frac{m}{2W}}$$

The instrument was used to determine the mass and energy spectra of the ionic component of the plasmoids generated by Bostick's button source.

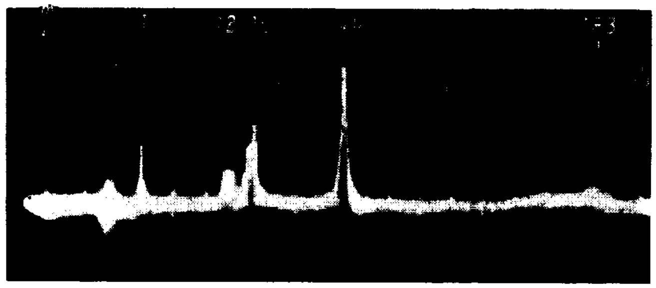

FIGURE 7. Mass spectrogram of 640 eV particles obtained in tests with the button-type source. Sweep 5 μsec/cm.

Figure 7 is a typical mass spectrum of the ionic plasma component. The mass spectrum corresponds to particle energy of 640 eV. Taking these spectra for different energies, we can plot the energy distribution of ions of various masses and charges.

BIBLIOGRAPHY

1. LUK'YANOV, S. Yu., I. M. PODGORNYI, and S. A. CHUVATIN. — ZhTF, **33**: 1026. 1961.
2. AGISHEV, E. I. and N. I. IONOV. — ZhTF, **26**: 203. 1956.
3. GILLIO, M. A. — Phys. Fluids, **4**: 210. 1961.
4. SCHÜTZE, W. and F. BERNHARD. — Zs. f. Phys., **145**: 44. 1956.
5. AFROSIMOV, V. V. et al. — ZhTF, **30**: 1447. 1956.
6. ROZMAN, I. M. — JETP, **28**: 251. 1955.
7. BOSTICK, W. H. — Phys. Rev., **104**(2): 292. 1956.

L. I. Krupnik and N. G. Shulika

PLASMA DIAGNOSTICS WITH A BEAM OF FAST PARTICLES

The modern techniques of plasma diagnosis in terms of atomic particles naturally fall into two broad groups:

a) plasma diagnostics based on the analysis of the atomic particles ejected by the plasma or withdrawn from the plasma;

b) plasma diagnostics by probing with beams of atomic particles (neutral atoms and ions).

The techniques under a) constitute the so-called passive diagnostics. They are discussed in a separate paper. The present paper deals with the development and the experimental application of the second group of techniques, the methods of the so-called active plasma diagnostics, based on the probing of the plasma with beams of fast particles.

The passage of a beam of ions (atoms) through matter alters the initial charge composition of the probing beam due to the collision of the beam particles with the target. The attenuation of the primary beam of ions (atoms) depends on the species of the colliding particles, their relative velocity, number of particles in the target, as well as the cross sections of the various processes contributing to the attenuation of the primary beam.

If it is assumed that the cross sections of the corresponding processes are all known, a method can be proposed for estimating the density (thickness) of the target by measuring the attenuation of the primary beam. However, in reality, it is not always possible to calculate the target density in this way, since many of the cross sections are unknown.

In the present paper we consider the possibility of measuring the parameters of a hydrogen plasma by probing with a beam of fast hydrogen atoms and ions. Seeing that the plasma is almost invariably immersed in a magnetic field, it is more reasonable to probe with a beam of neutral particles. Thus, let a beam of fast hydrogen atoms H_1^0 (beam energy must satisfy the condition $E_{H_1^0} \gg E_{pl}$, where E_{pl} is the energy of the particles in the plasma) cross a stream of plasma. If we assume that the degree of ionization of the plasma is fairly high, the main process responsible for the attenuation of the beam of probing neutrals is the process of resonance charge exchange,

$$H_1^0 + H_1^+ \rightleftarrows H_1^+ + H_1^0.$$

The cross section of this process has been studied in great detail by Fite /1/. The cross section sharply increases as the energy of the colliding particles decreases. For $E \approx 3-8$ keV, σ_{10} is approximately equal to 10^{-15} cm^2 (Figure 1).

The attenuation of the primary neutral beam is then given by

$$\Delta N^0 = N^0 (1 - e^{-\sigma_{10} n L}), \tag{1}$$

where n is the density of the plasma, L the path of the probing beam in the plasma, N^0 and ΔN^0 the intensity of the primary neutral beam and its attenuation after encounter with the plasmoid. If σ_{10} and L are known,

then by measuring N^0 and ΔN^0 we can easily calculate the plasma density n.*

It should be noted that the "plasmas" used in experimental work contain, besides the ionized component, also a certain amount of nonionized H_2^0 and H_1^0.

It is of course desirable to isolate the neutral component, thus eliminating undue interference in experimental work. This is possible when working with fast plasmoids with large drift velocities. However, we should always bear in mind that the cross section for the collision of atoms with neutrals is not resonant, remaining fairly small in the low-energy region: at $\sim 3-8$ keV, this cross section is $\sim 10^{-17}\,\mathrm{cm}^2$ /2/, i.e., roughly one-hundredth of σ_{10} (Figure 1). In highly ionized plasmas, the charge exchange of atoms with plasma neutrals can thus be neglected; this also applies to ionization by collision with plasma electrons in this energy range.

All the preceding applies to a pure hydrogen plasma. The accuracy of the technique is seriously impaired when the impurity content of the plasma is substantial.

A few words on the applicability of this technique. The lower boundary depends on the sensitivity of the measuring apparatus, detecting the attenuation ΔN^0 of the neutral beam (see (1)). The upper boundary is found by assuming complete charge exchange (with 100% participation of the beam particles), which in our case is achieved for plasma densities of $5\cdot 10^{15}\,\mathrm{cm}^{-3}$.

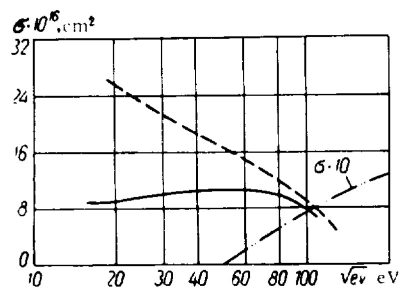

FIGURE 1. Reaction cross sections in a probing beam vs. energy: dashed line: $H_1^0 \to H_1^+$ in collisions with H_1^+ (σ_{10}); solid line: $H_1^0 \to H_1^+$ in collisions with H_2^+; dash-dotted line: $H_1^0 \to H_1^+$ in collisions with H_2^0.

If no magnetic field is impressed (or the plasma is immersed in weak magnetic fields), interesting results can be obtained by probing with a mixed beam of neutral and charged particles.

When hydrogen plasma is probed with a proton beam, no interactions are observed with the ionized plasma component (H_1^+ ions), since neither the probe nor the target particles carry any electrons. However, the proton beam will actively sense the neutral plasma component (H^0 and H_2^0). These collisions lead to charge exchange reactions $H_1^+ \to H_1^0$, with a cross section of $\sim 10^{-15}\,\mathrm{cm}^2$.

Combined application of charged and neutral beams will enable us to determine the density of the charged and the neutral components of a plasma and to measure its degree of ionization.

* In principle, the probing beam may also collide with the ions H_2^+ and H_3^+. If the relative content of the components H_1^+ and H_2^+ is known, this effect can be taken into consideration. However, the conditions in plasma are rather unfavorable for the existence of H_2^+ and H_3^+ ions, and they are therefore neglected. This is consistent with the experimental mass-spectroscopic data on the composition of some plasmas. The content of H_2^+ and H_3^+ ions never exceeds a few percent.

Apparatus

The proposed technique was experimentally applied on a setup, schematically shown in Figure 2.

The setup comprises two main units: a source of fast neutral and charged particles and a source of pure hydrogen plasma.

The fast beam was generated by an ion gun, comprising a high-frequency ion source 1 and a three-electrode electrostatic lens 2. The protons contaminating the beam were removed in the chamber of the magnetic mass monochromator 3. The intensity of the beam emerging from the mass monochromator could be measured with a trap 4. The protons from the mass monochromator were fed into the vacuum chamber 5, which was separated from the rest of the equipment by channels 6 and 7. In experiments with neutral beams, the vacuum chamber was filled with hydrogen to a pressure of $\sim 0.13\,N/m^2$.

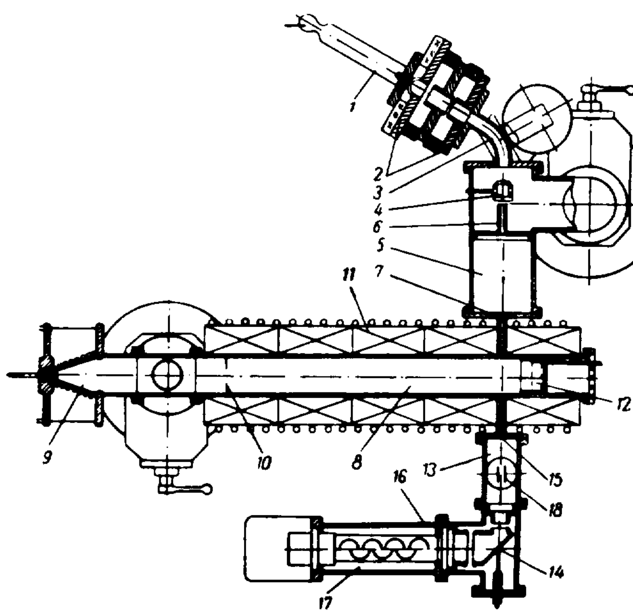

FIGURE 2. A schematic diagram of the setup.

The protons were neutralized to hydrogen atoms by collision with the gas. Through channel 7, the probing beam of fast particles was admitted into the plasma region 8.

The plasma was created by a conical source with pulsed gas inlet 9.

The plasmoid generated by this source was directed through the diaphragm 10 into the chamber 8, where it was intercepted by the fast probing beam. The chamber 8 was immersed in a magnetic field $H = 159{,}000\,A/m$ set up by the coils 11. The field H improved the transmission of the plasmoid and simultaneously removed the charged particles from the neutral beam.

The stream of neutrals, after encounter with the plasmoid, reached the detector chamber 13. The detection was based on the secondary electrons knocked out from the plate 14 by the neutral beam. The electrons were accelerated to 20 keV and then hit a plastic scintillator 15, whose luminescence was picked up by a photomultiplier 17. The photomultiplier was protected by a steel screen 16, and its signal was fed directly to an oscilloscope. The plasma was probed with a proton beam when the magnetic field in the chamber 8 was nil. The H_1^0 atoms produced by charge exchange with the plasma were detected, and the remaining passive protons were removed by the field of the electric condenser 18 interposed between the chamber 8 and the detector.

Procedure and results

The following conclusion can be drawn from the foregoing: no reliable data on the parameters of plasmoids can be obtained unless we are sure that these plasmoids are reasonably pure, i.e., contain no more than 20% of heavy ion impurities. To establish the impurity content of the plasmoid, a Thomson mass analyzer was provided at the outlet of the chamber 8. The procedure developed in our laboratory enabled us to determine with fair accuracy the percentage content of various ions in the plasmoids. The results are listed in the table. We see from these figures that for low plasma source voltages (~ 10 keV), the plasmoid contains $\sim 90\%$ of hydrogen ions. This purity is highly satisfactory. The procedure of mass spectroscopic analysis is described in detail in /3/. The source voltage in the probing of plasmoids with beams of fast particles was invariably 10–12 keV.

Content of ions in a plasmoid, %

H_1^+	H_2^+	H_3^-	C^+	O^+	N^+	Si^+	O^-	C^{2+}, Zn^+ and others
92	1.1	0.2	2.6	2.8	0.3	0.4	0.4	0.2

L is one of the basic parameters entering formula (1), from which the plasma density n is calculated. This parameter is in fact the diameter of the plasmoid traveling through the chamber 8. This quantity was determined experimentally using the plasmascope 12 fitted into the end wall of the chamber 8 (see Figure 2). This device, whose structure is described in detail in /4,5/, produces a visual display of the plasmoid. A photograph taken off the plasmascope screen is shown in Figure 3. The diameter of the plasmoid in various modes of source operation and in various magnetic fields can be found from these photographs.

The first series of experiments with probing beams of neutral atomic hydrogen H_1^0 was carried out in order to establish whether the fast plasmoid is separated from the trail of neutral gas (not ionized by the discharge) diffusing through the chamber.

Control oscillograms were taken for the case of a fast neutral beam probing a stream of nonionized gas forced through the chamber without sparking (Figure 4). The gas was injected into the source through a pulsed valve. The oscillograms indicate a certain attenuation of the neutral beam in the gas for various inflows from $0.5\,cm^3$ (curve b) to $2-3\,cm^3$ (curve a).* We see from the figure that the attenuation of the probing beam in the gas only starts some $300\,\mu sec$ after the zero point ($1200\,\mu sec$ time base), and reaches noticeable values only for a large inflow of gas into the source, after $500\,\mu sec$ (curve a).

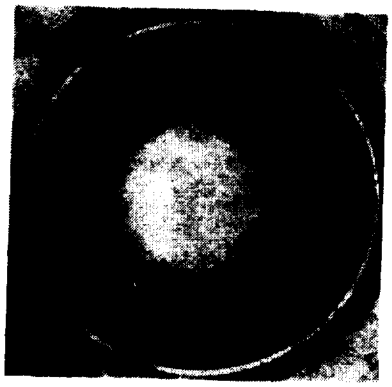

FIGURE 3. A photograph of the plasmascope screen.

The next series of curves (Figure 5, a, b, c) represents the encounter of a probing beam with a plasmoid. The previous time base was retained ($1200\,\mu sec$). The photographs were again taken with the valve opened in varying degrees. Figure 5,a corresponds to a small gas inflow, $\sim 0.5\,cm^3$. The hydrogen is then admitted in increasing amounts into the source, and Figure 5,c corresponds to an abnormally large inflow of gas, which is never realized under ordinary operating conditions. These

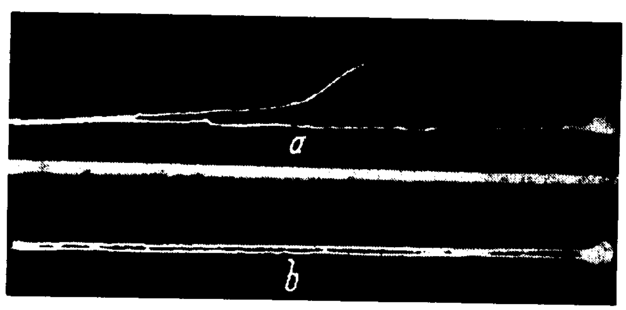

FIGURE 4. The attenuation of a probing H_1^0 beam in a gas: a) gas inflow $\sim 4-5\,cm^3$; b) gas inflow $\sim 0.5\,cm^3$.

experiments show that the fast plasmoid is essentially separated in space from the slow nonionized trail, which moves with a velocity $v \sim 10^3$ m/sec.

In the following, we concentrated on the parameters of the ionized head only.

Figure 6 traces the attenuation of a neutral probing beam intercepting the head of a plasmoid. This oscillogram was obtained with a smaller time base ($\sim 190\,\mu sec$), and it distinctly shows the signal front and the head of the plasmoid. Experiments with a beam of protons H_1^+ of the same energy intercepting a plasmoid in the absence of a magnetic field H constituted a valuable addition to the probing of a plasmoid with neutral

* [There seems to be some confusion in the Russian original; curve (a) in Figure 4 corresponds to a gas inflow $\sim 4-5\,cm^3$.]

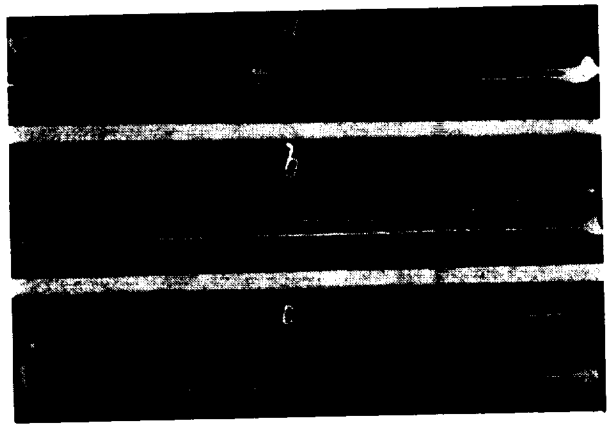

FIGURE 5. The attenuation of a probing H_1^0 beam in a plasmoid: a) gas inflow $\sim 1-0.5\,cm^3$; b) gas inflow $\sim 2\,cm^3$; c) gas inflow $\sim 4-5\,cm^3$.

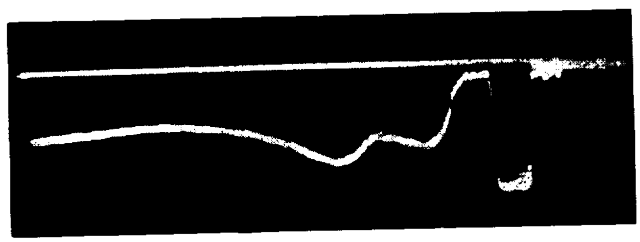

FIGURE 6. The attenuation of a neutral probing beam of H_1^0 atoms in a plasmoid.

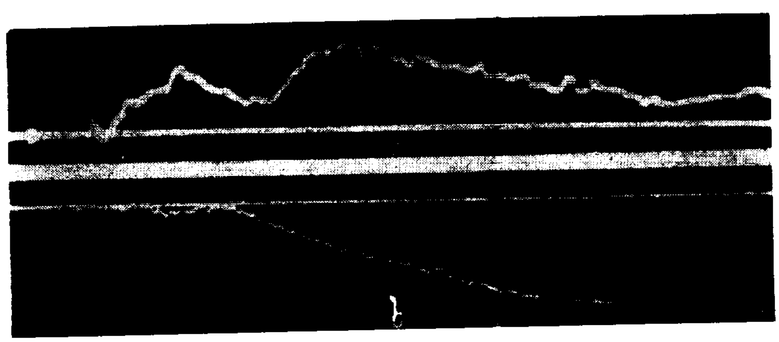

FIGURE 7. The attenuation of a probing beam of H_1^0 atoms and of a proton beam in a plasmoid.

beams. Figure 7 shows the attenuation of a charged beam of H_1^+ (curve b), as compared with the attenuation of a beam of neutrals (curve a). As we have previously observed, the proton beam penetrates through the ionized plasmoid without sensing the H_1^+ ions, and the attenuation is mainly due to charge exchange with the neutral components of the plasmoid (H_1^0 and H_2^0). The interaction with the ions H_2^+ and H_3^+ is neglected, since their content in the plasmoid is very low (1–2%). The following conclusions can be easily made from a comparison of the curves in Figure 7: the fast plasma ejected by the source breaks up into two plasmoids, a very fast, fully ionized head with a density peak after some 7 μsec, and a slower, very extended component grading into a characteristic "tail" with a density peak after 35–40 μsec. The degree of ionization in the second component falls off from "head" to "tail", where the plasmoid blends with a nonionized gas cloud propagating by diffusion (the signal from this cloud was registered in Figure 4). This structure is plotted in Figure 8. The ratio of the first and the second maxima depends on the source operating conditions and may be changed in either direction. Figure 9 shows the attenuation of a neutral beam for operating conditions characterized by different ratios of the two peaks. The density of the plasmoids may be made as high as 10^{15} cm^{-3}

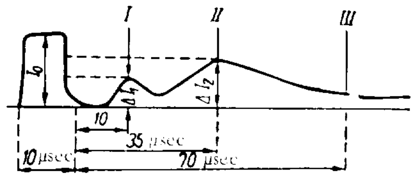

FIGURE 8. A typical attenuation curve of a probing H_1^0 beam intercepting a plasmoid.

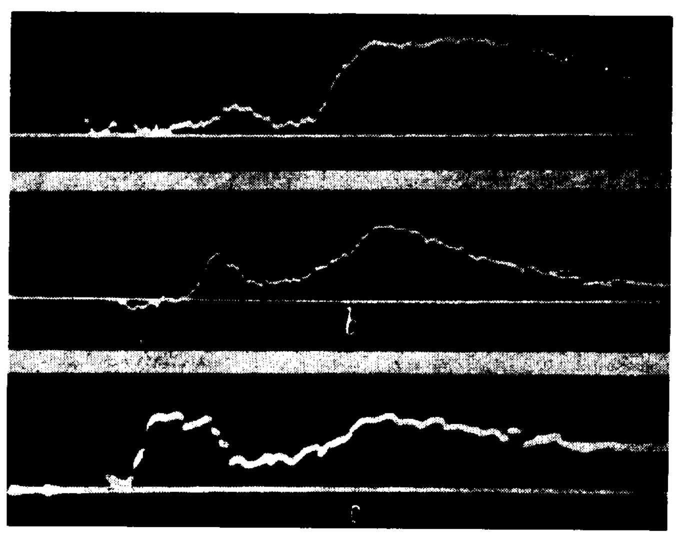

FIGURE 9. The attenuation of a probing beam of H_1^0 atoms by a plasmoid for different source operating conditions:
a) gas inflow ~ 0.5 cm^3; b) gas inflow ~ 1 cm^3; c) gas inflow ~ 2 cm^3.

Note that undesirable cutoff occurs when a plasmoid is probed with a beam of charged particles: very many of the beam particles collide with the plasmoid and are lost in the chamber without reaching the detector. This is possibly due to the interaction of charged particles with the plasma, induction of spurious fields, and deflection of the probing particles from their straight trajectory. The cutoff apparently cannot be attributed to ordinary scattering, since a neutral beam of the same mass and energy does not display considerable scattering.

It is fairly difficult to estimate the percentage penetration of the protons through the plasma, and without this datum it is impossible to obtain quantitative results on the attenuation of a proton beam in a plasmoid (the experiments are regretfully all qualitative).

It follows from the preceding that beams of neutral particles, unaffected by electric and magnetic fields, are clearly superior for purposes of plasma diagnostics.

BIBLIOGRAPHY

1. FITE, W. L. – Phys. Rev., 112: 1161. 1958.
2. FOGEL', Ya. M., V. A. ANKUDINOV, D. V. PILIPENKO, and N. V. TOPOLYA. – JETP, 34: 579. 1958.
3. KONOVALOV, I. I., L. I. KRUPNIK, I. N. ONISHCHENKO, and N. G SHULIKA. – In: "Diagnostika plazmy", p. 154. Moskva, Gosatomizdat. 1963.
4. ELIZAROV, L. I. and A. V. ZHARINOV. – Nuc. Fus. Suppl. Part 2, 4: 699. 1962.
5. ARTSIMOVICH, L. A. Upravlyaemye termoyadernye reaktsii (Controlled Thermonuclear Reactions). – Moskva, Fizmatgiz. 1961.

A. A. Kalmykov, A. D. Timofeev, Yu. I. Pankrat'ev,
and M. G. Nozdrachev

AN INVESTIGATION OF A PLASMA SOURCE WITH A DRIFT MASS SPECTROMETER

In /1/ a method was proposed for mass and energy analysis of the ions in plasmoids. This method is adequate for investigating in detail the performance of plasma sources, and in the present study we chose to deal with Bostick's button-type source. The choice of this particular source was mainly determined by the simplicity of its design; furthermore, the main features of acceleration by this source are common for all other types of sources. This was the first application of the new technique, and we therefore concentrated on problems connected with the applicability of the method to plasmoids.

Apparatus and procedure

The apparatus for the analysis of plasmoids is schematically shown in Figure 1. A button source /2,3/ made of plexiglas with tungsten electrodes was used. This source is very simple to make and to operate, and the main working characteristics of the button source are apparently common for other sources also, e.g., the coaxial plasma gun /4/. A condenser bank $C = 0.1\,\mu F$, $U = 18$ kV was discharged through the plasma source. The source was equipped with a rotating device 2, and its position relative to the system axis could be varied within ±90°.

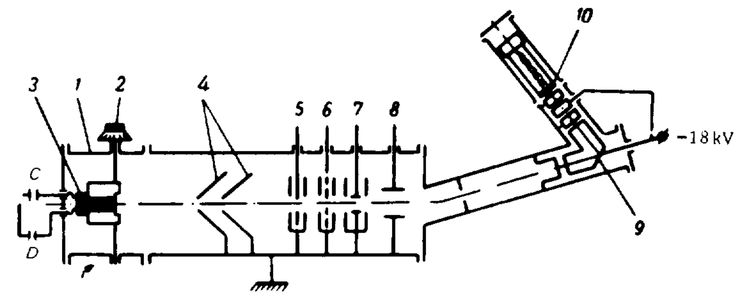

FIGURE 1. Schematic of the setup.

The mass and energy spectra were obtained with a drift mass spectrometer. The plasmoid ejected by the source first passes through inlet conical diaphragms 4, which admit a thin plasma beam. The plasma beam then passes through a separating device 5, where the ion component of the plasmoid is isolated; the beam is then directed to modulators 6,7 and is energy-analyzed in the electrostatic analyzer 8. The detector comprises an ion-electron converter 9 and a scintillation counter 10. The various units of the apparatus are described in detail in /1/.

The electrostatic analyzer admits ions of one energy only, and therefore if this category includes ions of different masses, they will traverse the drift space in different times (all having different velocities), so that ions of different masses are time-resolved at the analyzer outlet. To achieve satisfactory mass-resolution, the difference in drift times of ions of close masses should be greater than the length of the modulation pulse; we therefore decided on modulation pulses $0.2\,\mu$sec long for a drift length of 40 cm between the modulator and the detector.

The length of the ionic current signal, corresponding to the arrival of ions of a given energy at the detector, depends on the time of their formation in the source and on the time-resolution of the analyzer, which can be written as

$$\Delta t = \gamma l \sqrt{\frac{M}{W_i}}, \tag{1}$$

where Δt is the time-resolution of the system, γ the energy resolution ($\gamma = 6\%$ in our case), l drift length, M ion mass, W_i the energy of the ions.

The Δt was small in the range of relevant masses and energies, and the length of the ionic current signal was therefore mainly determined by the time of formation of the ions in the source.

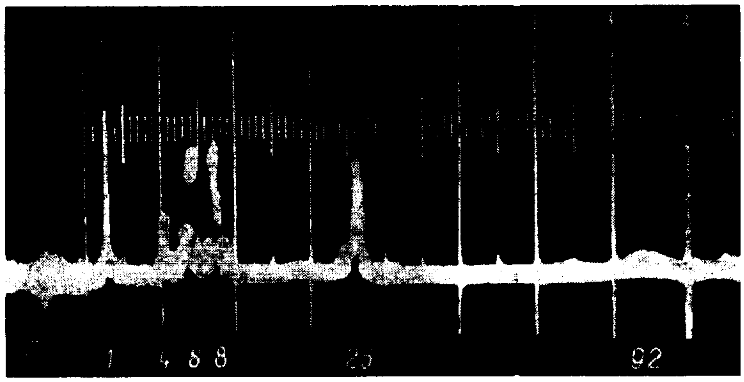

FIGURE 2. A typical mass spectrum of 320 eV ions from a plasmoid (sweep 5 μsec/cm).

A typical oscillogram of the current produced by 320 eV ions presents a succession of short peaks (Figure 2). The time of formation of the ions in the source, estimated from the half-width of these peaks, was found to be 0.1–0.2 μsec. The data indicate that the time of ionization in the source is much less than the discharge period (T = 1.6 μsec) and that the plasmoid is mass-resolved when actually moving from the source to the modulator.

The particle mass, or more precisely the ratio of the mass m to the charge Z, is determined from the expression

$$\frac{m}{Z} = \frac{2kU_a t^2}{l^2}, \tag{2}$$

where k is a proportionality coefficient relating the particle energy with the voltage applied to the plates of the electrostatic analyzer; U_a the voltage applied to the plates of the electrostatic analyzer; t the drift time of the particle; l the drift length.

Since the particles are formed in a very short time, no additional modulation is required and the distance from the plasma source to the detector may be regarded as the drift length. This, however, introduces some uncertainty in the determination of the drift time, since the exact time of plasmoid creation relative to the source discharge (the so-called start point) is unknown. A modulator eliminates this uncertainty. The time is then reckoned from the modulation pulse, and since the drift length is exactly known, the ratio $\frac{m}{Z}$ is unambiguously found from (2). On the other hand, given $\frac{m}{Z}$ and applying the same relation (2), we may calculate the drift time from the pulsed source to the detector, thus marking the start point of the various particles on the discharge current oscillogram. The start point is found to be the same for all the source

particles, corresponding to the first quarter of the discharge period. It is significant that the discharge current oscillogram (Figure 3) displays a singularity at this point.

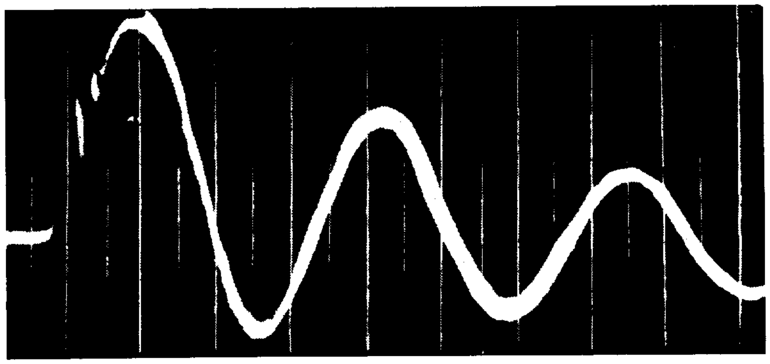

FIGURE 3. An oscillogram of the source discharge current (sweep 0.5 μsec/cm).

Relation (2) can also be applied to test the performance of the system. For constant $\frac{m}{z}$, k, and l, the drift time is a function of $U_a : t \sim U_a^{-\frac{1}{2}}$; this relation was observed with fair accuracy for all the ion masses studied.

Experimental results

By varying the voltage applied to the plates of the electrostatic analyzer, we may obtain mass spectra at any energy, thus recovering the energy spectra for particles of various masses. Figure 4 shows the energy spectra of hydrogen for various modes of source operation. The ordinate gives, in arbitrary units, a quantity which is proportional to the energy distribution function. Figures 5, 6 give the energy distribution for the ions of carbon and oxygen.

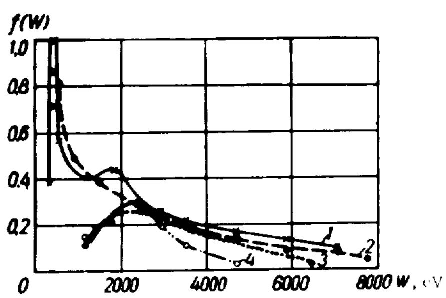

FIGURE 4. Energy distribution of H^+ for different source voltages:
1) $U = 17$ kV; 2) $U = 14$ kV; 3) $U = 10$ kV; 4) $U = 7$ kV.

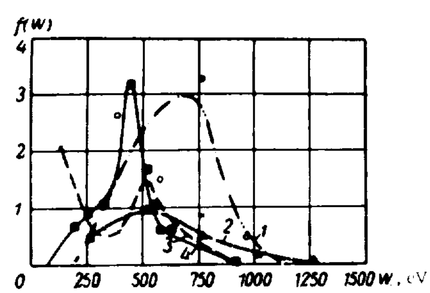

FIGURE 5. Energy distribution of carbon ions:
1) $C^{3+}, \frac{m}{z} = 4$; 2) $C^{4+}, \frac{m}{z} = 3$;
3) $C^{2+}, \frac{m}{z} = 6$; 4) $C^{+}, \frac{m}{z} = 12$.

It is remarkable that two groups of particles are distinguishable in these distributions: the main group, corresponding to an energy of some 100 eV, and a broad distribution of fast particles with energies of up to 10 keV. Source voltage is the parameter of the different curves. The spectra of fast particles contain no particles with energies greater than the applied voltage. The fast group of particles is not observed in the energy spectra of carbon and oxygen. Figure 7 plots the mean energy of various masses as a function of $\frac{m}{Z}$. We see that the mean energy does not depend on the particle species, being constant almost for all $\frac{m}{Z}$.

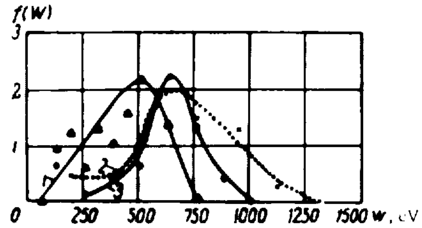

FIGURE 6. Energy distribution of oxygen ions:

1) O^{+}, $\frac{m}{Z} = 16$; 2) O^{3+}, $\frac{m}{Z} = 5.33$;
3) O^{2+}, $\frac{m}{Z} = 8$.

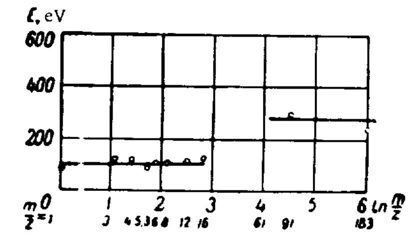

FIGURE 7. The mean particle energy vs. $\frac{m}{Z}$.

The rotating device was used to obtain the angular distributions of ions of various masses and energies. Some results are shown in Figure 8, which gives the angular distributions of hydrogen ions of different energies. Analogous results were obtained for other ions also. It is characteristic that fast ions form a narrower velocity cone than the slow ions. Therefore, in a chamber without a magnetic field, the ratio between the number of fast and slow ions will change continuously on account of the higher rate of loss of the slow ions to the chamber walls. The true energy spectrum should thus be reconstructed by measuring the angular distributions of the particles and integrating the number of particles of a given energy for all the angles. Otherwise, gross errors are introduced. Indeed, since the velocity cone of the fast particles is narrower than that of the slow particles, the penetration of the fast particles through the diaphragm is much higher.

We see from Figure 4 that the amount of fast particles decreases with the decrease of source voltage more slowly than the amount of slow particles does. This may point to a difference in the ionization mechanisms of fast and slow particles. Possible mechanisms of formation of fast particles are discussed, in particular, in /5,6/. Without going into this problem, we only note that in our experiments there always was high correlation between the detection of fast particles and the application of high source voltage; in other words, fast particles invariably form upon sparking, when a high voltage is maintained across the spark gap. Furthermore, no ions with energies higher than the applied voltage were observed, which contradicts the concepts of /5/.

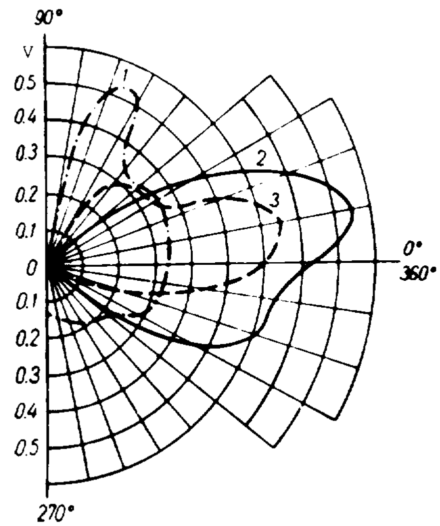

FIGURE 8. Angular distribution of H^+ for various energies:
1) $W = 590$ eV; 2) $W = 1770$ eV; 3) $W = 5900$ eV (scales of curves 2 and 3 stretched by a factor of 3 and 10, respectively).

To study the influence of the discharge length on the energy spectra, we measured the energy distributions of particles with the source triggered by the capacitor bank and by a pulse-forming line.

Figure 9 shows two energy spectra of tungsten ions obtained for equal source currents with the aid of the capacitor bank (curve 1) and a pulse-forming line (curve 2). Condenser parameters: $C = 0.1\,\mu$F, discharge period $1.6\,\mu$sec. The pulse-forming lines generated square pulses $0.7\,\mu$sec long. We see that the difference in the energy spectra is slight, and since the length of a plasmoid is mainly determined by the spread of particle velocities, application of short pulses of source current will not produce short plasmoids. This conclusion is consistent with magnetic probe measurements and transmission of 3-cm microwave signals.

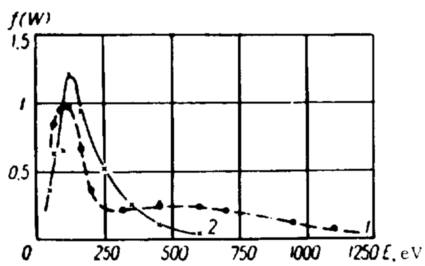

FIGURE 9. The energy spectra of tungsten with the source triggered by a condenser bank and by a pulse-forming line.

It is thus established that the creation and the acceleration of plasma in a button source occur simultaneously, both in a very short time. Since the particles have a broad spectrum of velocities, the plasmoid spreads in the longitudinal direction while traveling away from the source. The length of the plasmoid is determined by the spread of particle velocities only, and therefore does not depend on the length

of the source discharge. Since the mean velocities of different masses decrease as the mass increases a characteristic mass distribution is established along the plasmoid. Light ions, in particular hydrogen, predominate in the head, while the heavy ions concentrate in the tail. This space distribution of ions of different masses becomes more distinct as the drift length increases. When a plasmoid travels in a field-free space, the slow ions having a braod velocity cone are lost more rapidly.

We suggest that the picture of plasmoid creation and propagation emerging from the results of this work also applies to other plasma sources with electrodes, specifically to a coaxial plasma gun.

BIBLIOGRAPHY

1. KALMYKOV, A. A., A. D. TIMOFEEV et al. – This volume, p. 191.
2. BOSTICK, W. H. – Phys. Rev., 104(2): 292. 1956.
3. SINEL'NIKOV, K. D., B. G. SAFRONOV, I. T. GUZHOVSKII, and Yu. G. YAREMENKO. – In: "Fizika plazmy i problemy upravlyaemogo termoyadernogo sinteza", 1: 102. Kiev, Izdatel'stvo AN UkrSSR. 1962.
4. MARSHALL, J. – Phys. Fluids, 3: 134. 1960.
5. PLYUTTO, A. A. – JETP, 39(6): 1589. 1960.
6. HENDEL, H. W. and I. T. REBOUL. – Phys. Fluids, 5: 38. 1962.

Yu. S. Azovskii, I. T. Guzhovskii, and B. G. Safronov

MEASURING THE ENERGY OF PLASMOIDS WITH THERMOPROBES

The total energy and the radial energy distribution of plasmoids can be determined with a thermocouple probe /1–4/, comprising a pickup (a plane disk or a cylindrical tube) with a thermocouple soldered to it.

For fairly extended plasmoids*, energy measurements with a plane thermocouple probe are inaccurate. The reason is as follows. When the head of the plasmoid hits a plane pickup, a characteristic plasma "cushion" is formed, whose thickness increases in time; in other words, we have here a reflected shock wave which propagates upstream. This "cushion" screens the thermoprobe from the rest of the stream, and the energy readings obtained with the probe are too low. Energy measurements with a probe provided with a sufficiently long cylindrical pickup are much more accurate, since the reflected shock wave propagates over distances less than the cylinder length.

On the other hand, when a cylindrical thermoprobe immersed in a plasma is used to measure the radial energy distribution, the probe thermoelectric emf is determined not only by the probe cross section, but also

* All the existing plasma guns create plasmoids with a length of about 1 meter.

by the entire outer surface of the pickup in contact with the plasma. This is another source of errors in absolute energy measurements.

The aim of this work was to establish how the depth of the pickup and screening of its outer surface affect the accuracy of the measurements by the thermocouple method.

The experimental system comprised a plasma source with electrodes /5/ and a glass vacuum chamber (a tube 9 cm in diameter) through which the plasmoids traveled. The energy of the plasma stream was determined with probes along the axis of the vacuum system; probes with different pickup length-to-diameter ratios were used, namely a disk with $\frac{l}{d} = 0$ and cylinders with $\frac{l}{d} = 1, 2, 3$. The diameter of the disk and of the cylinders was 1.4 cm; the copper foil from which the pickups were fabricated was 0.1 mm thick. The outer pickup surface was protected by a streamlined (conical) screen.

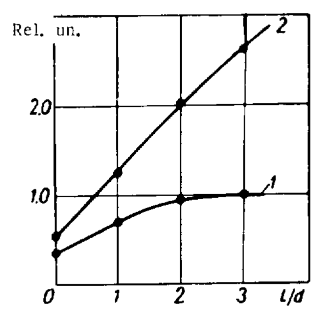

The energy registered by the thermocouple as a function of pickup depth.

The figure plots the energy registered by the thermocouple (in arbitrary units) as a function of the pickup depth (the probe was set at a distance of 20 cm from the source, initial source voltage 10 kV). With screened thermocouples, the energy registered by the probe first increases with $\frac{l}{d}$, and then levels off for $\frac{l}{d} > 2$. It seems that the energy readings obtained with $\frac{l}{d} = 3$ are exact for all practical purposes. The fractional energy picked up for $\frac{l}{d} = 2, 1, 0$ is 0.96, 0.70, and 0.36, respectively. With unscreened probes (curve 2), the energy monotonically increases with pickup length; this is attributable to the additional heating of the thermoprobes as the plasma hits the outer surface of the cylinder. The slight difference in readings taken with screened and unscreened disk thermocouples shows that the plasma also hits the reverse (relative to the stream) side of the disk or the bottom of the cylinder.

Similar curves were observed (to within 5–10%) in the entire range of plasma energies (with the source voltage varying from 6 to 18 kV, at distances of 5–50 cm from the source).

We thus see that in relative plasma energy measurements, a thermoprobe with any pickup geometry may be used, providing the range of energy values is not too large; in absolute measurements, however, screened probes with a deep pickup are required. Excessively deep pickups are nevertheless undesirable, since in this case the heat transfer from the walls to the bottom of the cylinder is impeded.

BIBLIOGRAPHY

1. MARSHALL, J. – Phys. Fluids, 3: 134. 1960.

2. LUK'YANOV, S. Yu., I. M. PODGORNYI, and A. S. CHUVATIN. – ZhTF, 31: 1026. 1961.

3. KLEBANOV, Yu. D. and V. I. SINITSIN. – JETP, 41: 1340. 1961.

4. KOVAL'SKII, N. G., S. Yu. LUK'YANOV, and I. M. PODGORNYI. – Nucl. Fusion, Suppl., Part 1, 81. 1962.

5. AZOVSKII, Yu. S., I. T. GUZHOVSKII, and B. G. SAFRONOV. – This volume, p. 239.

A. G. Belikov, V. P. Goncharenko, V. M. Mishchenko,
B. G. Safronov, and A. S. Slavnyi

CREATION OF FAST PLASMOIDS WITH A COAXIAL SOURCE

Previous papers studying the performance of coaxial sources /1–3/ reported the possibility of creating plasmoids with velocities of $(4-8) \cdot 10^7$ cm/sec. The present paper is a continuation of /3/. In distinction from /3/, we concentrated on the parameters of a fast plasmoid and the conditions of its creation. The variable parameters were the source voltage, the time delay between the admission of gas through the valve into the interelectrode gap and the application of voltage to the electrodes, and the inflow of gas.

Apparatus

The apparatus is schematically shown in Figure 1. Length of accelerating electrodes 17.5 cm. External diameter of the central electrode 32 mm, internal diameter of the outer electrode 72 mm. The energy is stored in a bank of nine IM 50/3 condensers with a total capacitance of 27 μF. Each condenser is coupled into the source through a spark gap by eight coaxial cables. Discharge period 9 μsec. The gas is admitted into the interelectrode gap by a high-speed valve through holes in the central electrode. The plasmoid travels in a glass tube 95 mm in diameter, where all the measurements are made.

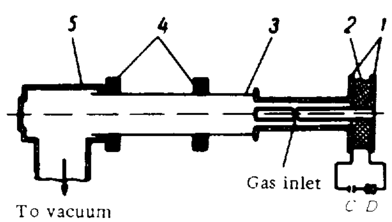

FIGURE 1. Schematic of the setup: 1) electrodes; 2) insulator; 3) glass tube; 4) diamagnetic probes; 5) vacuum chamber.

Previous measurements /3/ show that maximal speeds are obtained for the first plasmoid when the time between the triggering of the valve and the application of voltage to the electrodes is so small that the gas does not expand far from the point of inlet. In this case, however, the plasma carries a considerable content of impurities. This is so because the valve cannot admit a sufficient amount of gas in a comparatively short time. Special tests were made to ensure adequate gas inflow in a very short time. By adjusting the strength of the blow on the anvil and raising

the pressure in the plenum to $6 \cdot 10^5 N/m^2$, we ensured an inflow of $1-1.5$ cm^3 of gas (calculated for atmospheric pressure) in some 100μsec. Most of the measurements in this work were made for an inflow of 1 cm^3 ($3 \cdot 10^{19}$ particles). The valve remained open for 80μsec. The admission of the gas into the gap began some $\tau = 170 \mu$sec after the hammer blow which opened the valve. In the following, τ is interpreted as the time between valve triggering and the application of voltage to the source electrodes. Deuterium was used as working gas.

Measurements of plasmoid parameters

The ionic component of the plasma was mass and energy analyzed with Thomson's mass spectrometer with an extracting electric field set at a distance of 2.5 m from the source. The voltage on the extracting electrode was 17 kV. Ten firings sufficed to obtain spectrograms suitable for photometry. The particles were registered with MK nuclear photographic plates.

The velocity of the plasmoids was determined from their drift time between two diamagnetic probes. In our case, a diamagnetic probe was a 100-turn coil immersed in a constant magnetic field of $(5-8) \cdot 10^3$ A/m. Probe separation 120 cm. The first probe was set at a distance of 80 cm from the source, since at smaller distances the measurements were complicated by the strong interference due to plasma currents.

The plasmoid density was regulated by watching the cutoff of an 8-mm microwave signal at a distance of 80 cm from the source.

The total energy of the plasma was also tentatively estimated with a calorimeter.

All measurements were made without the driving magnetic field.

Results of measurements

The mass spectrometer was used to take spectrograms in different modes of source operation. Figures 2 and 3 give the distribution of photographic density along the deuterium parabolas. The source voltage U_s (Figure 2) and the delay τ (Figure 3) are used as the parameters. We see from Figure 2 that the energy of the ions E may reach 20 keV. As a characteristic quantity, we chose the energy of the ions producing maximum density on the photographic plates. Figure 4 gives the energy corresponding to maximum density as a function of delay. All the foregoing curves pertain to the first plasmoid. The peak energies are observed for delay times of $200-250 \mu$sec. If the delay is less than 170μsec, the voltage is maintained on the electrodes until enough gas has been admitted into the gap for sparking. In this case, the slow plasmoid prevails, and the amount of fast particles is negligible.

Diamagnetic probe measurements show that a slow plasmoid accompanies the fast one. Figure 5 is a sequence of diamagnetic signals from a probe set at a distance of 80 cm from the source. These signals give a picture of the variation of the amplitude ratio of the first and the second plasmoids

with delay time. The amplitude of the signal produced by the leading plasmoid for small delay times is several times higher than the amplitude of the trailing plasmoid. As the delay increases, the signals of the first

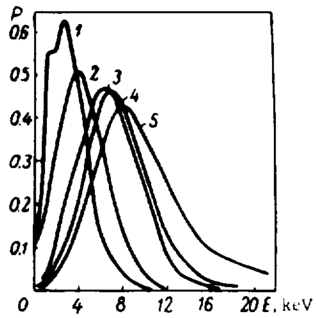

FIGURE 2. Distribution of density along the deuterium parabolas for various source voltages:
1) 10 kV; 2) 12 kV; 3) 15 kV; 4) 17 kV; 5) 20 kV.

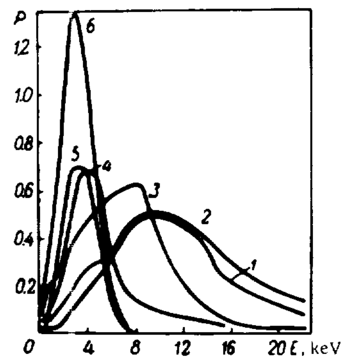

FIGURE 3. Distribution of density along deuterium parabolas for various delay times:
1) 220 μsec; 2) 240 μsec; 3) 270 μsec; 4) 300 μsec; 5) 350 μsec; 6) 400 μsec.

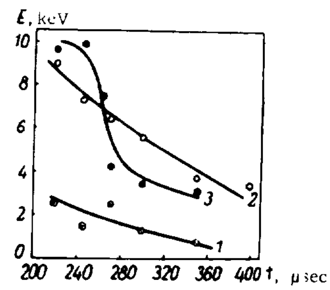

FIGURE 4. The energy corresponding to maximum photographic density as a function of delay for various source voltages:
1) 10 kV; 2) 15 kV; 3) 20 kV.

and the second plasmoids approach each other, merging into a single peak for large delay times. This behavior is qualitatively confirmed by mass-spectrometric results. The amount of slow ions increases with delay time; for small delay times, there are cases when only fast ions are observed, while for large delay times no fast ions are present at all.

Figure 6 gives the velocity v of the first plasmoid as a function of the voltage U_s applied to the source. This curve was calculated from the energy corresponding to maximum photographic density and measured independently from the half-fronts of the diamagnetic signals. Each point is an average of ten readings. The statistical error in diamagnetic measurements does

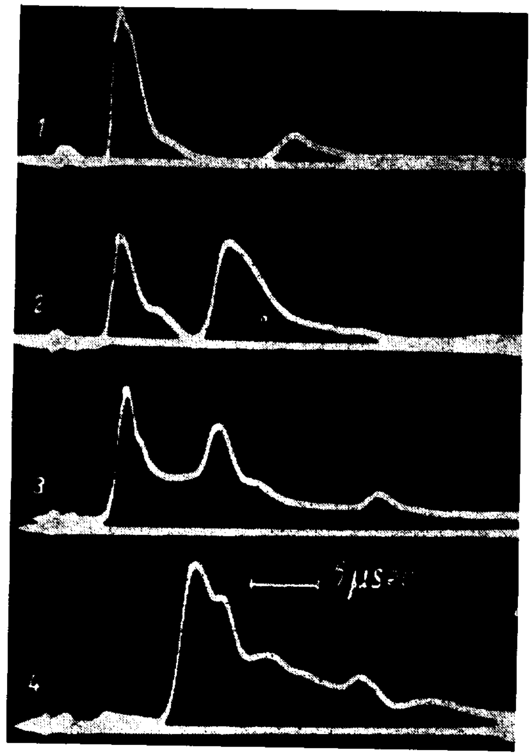

FIGURE 5. Diamagnetic signals for various delay times: 1) 240 µsec; 2) 270 µsec; 3) 350 µsec; 4) 700 µsec.

not exceed 10%. The velocity variation obtained from mass-spectroscopic measurements is thus confirmed by diamagnetic probes.

The velocity of the second plasmoid, as determined from diamagnetic measurements, varies from $5 \cdot 10^6$ cm/sec for small delay times to $(8-9) \cdot 10^6$ cm/sec for large delays.

A typical oscillogram of the diamagnetic signal for the first plasmoid, picked up by probes at distances of 80 and 200 cm from the source is shown in Figure 7. The first signal has a steep front, while the second signal is blurred, which points to a spread of the plasmoid in the direction of motion.

With small delay times, when the first plasmoid prevails, the energy of the impurity ions is greater than 50 keV. The content of impurities is difficult to determine since no calibration data are available for the photographic plates at these energies. The velocity of the impurities, however, is less than the velocity of deuterium; in particular, for deuterium ion velocities of $9 \cdot 10^7$ cm/sec, the velocity of carbon ions is $5 \cdot 10^7$ cm/sec and of copper ions $3.5 \cdot 10^7$ cm/sec. The head of the plasmoid is apparently fairly pure at some distance from the source.

As we have previously observed the total inflow of gas per one pulse is 1 cm^3 (atmospheric pressure). Reducing the gas inflow increases the

impurity content considerably, while an increase of gas inflow lowers the velocity: this is obviously due to the increase in the accelerating mass.

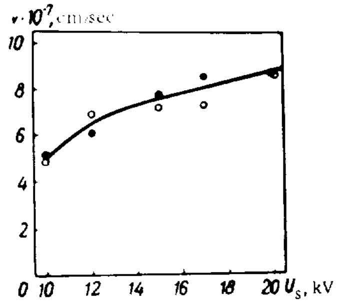

FIGURE 6. Plasmoid velocity vs. source voltage:
○ diamagnetic probes; ● mass-spectrograms.

The cutoff of the 8-mm signals occurs simultaneously with the diamagnetic signal from the first plasmoid.

The total energy of the plasmoids was measured with a calorimeter. To ensure maximal accomodation of energy by the calorimeter, it must have a large L/D ratio, where L is the length and D the diameter. The calorimeter was provided with a conical bottom, to reduce the effects connected with the shock wave which formed when the plasmoid was reflected. The calorimeter was made from copper foil 0.2 mm thick, weighing 125 g, $L = 20$ cm and $D = 9$ cm. Measurements were made at a distance of 90 cm from the source. The heating of the calorimeter was measured with a chromelcopel thermocouple. The results for a 240 μsec delay are listed in the table. Each figure is the average of numerous readings.

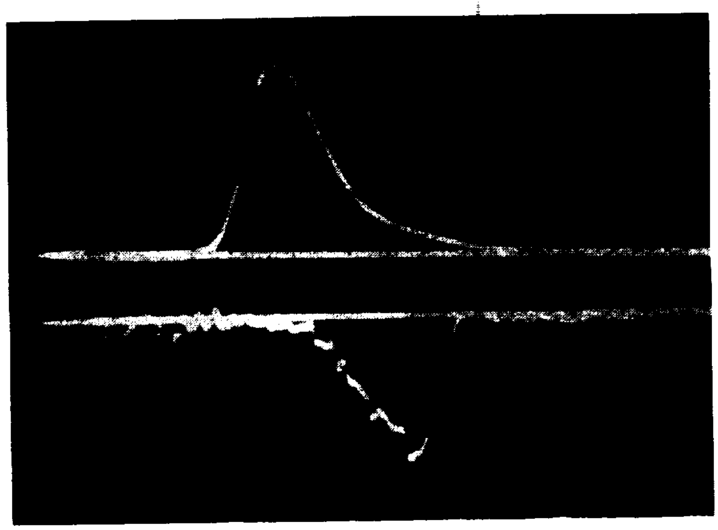

FIGURE 7. An oscillogram of diamagnetic signals from the first plasmoid: top – 80 cm from the source, bottom — 200 cm from the source.

U_s, kV	W, J
10	80
15	120
20	460

The variation of plasma energy with the distance from the source is plotted in Figure 8. The corresponding measurements were made with a small calorimeter along the system axis.

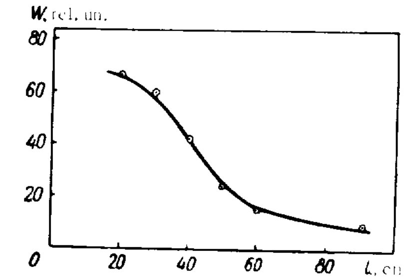

FIGURE 8. Plasma energy vs. distance between source and calorimeter.

Discussion of results

Measurements show that the first plasmoid may move with velocities of up to $(8-9) \cdot 10^7$ cm/sec. It is interesting to estimate the ratio of the number of particles in the first and the second plasmoids.

The methods used do not give an unambiguous answer. The mass spectrometer analyzes the plasma at a distance of 2.5 m from the source. If we remember that the velocities of the two plasmoids differ almost by one order of magnitude, and each plasmoid may have its own rate of spread, it is obvious that the ratio of the number of particles in the first and the second plasmoids measured at this distance from the source does not reflect the true picture. On the other hand, analysis at smaller distances may be complicated by the "cushion", which forms in a dense plasma and impedes the penetration of particles through the diaphragm. Note that the density of the first plasmoid at the position of the mass analyzer is less than 10^{12} cm^{-3}. The error introduced in the analysis of the first plasmoid is therefore insignificant.

The amplitude of the diamagnetic signal is mainly determined by the translational velocity of the plasmoid. The concentration of particles in the two plasmoids therefore cannot be estimated with the diamagnetic probes. As regards the second plasmoid, we know that the number of particles in it increases with the delay time. This follows from the mass spectrograms (a considerable increase in the content of slow ions) and from the diamagnetic signals (lengthening of the plasmoid).

The number of particles in the first plasmoid can be crudely estimated as follows. If we assume that the contribution of the second plasmoid and of the fast impurities to the total energy is negligible, then for $U = 15$ kV, $\tau = 240\,\mu$sec, we have $W = 120$ J, $v = 8 \cdot 10^7$ cm/sec. Hence,

$$N = \frac{W}{\frac{mv^2}{2}} = \frac{120 \cdot 10^7 \cdot 2}{1.67 \cdot 10^{-24} \cdot 10^{14} \cdot 64 \cdot 2} \sim 10^{17}.$$

The width of the diamagnetic signal at the point where the total energy is estimated, $\Delta t = 1.5-2\,\mu$sec. Plasma guide cross section $S = 60$ cm^2. Assuming that the particles are distributed over the entire cross section, we obtain for the volume occupied by the particles at a distance of 90 cm

$$V = \Delta t S v = 2 \cdot 10^{-6} \cdot 8 \cdot 10^7 \cdot 60 \sim 10^4 \text{ cm}^3.$$

Since the cutoff of the 8-mm microwave signal occurs at this point ($n = 1.7 \cdot 10^{13}$ cm^{-3}), the number of particles in the first plasmoid is

$$nV = 10^{13} \cdot 10^{4} = 10^{17}.$$

The density of the second plasmoid should be greater at least by one order of magnitude to make a noticeable contribution to the total energy. The amount of energy carried by the second plasmoid is variable, since its velocity may change between successive measurements. This is obvious from Figure 9, which is a superposition of five diamagnetic signals obtained in five successive firings. The signals of the first plasmoid overlap fairly well, although there is a certain spread of amplitudes.

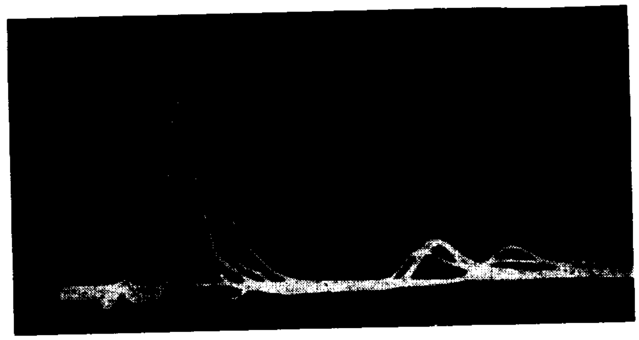

FIGURE 9. Diamagnetic probe signals.

Conclusions

1. Conditions have been established for the creation of plasmoids with velocities of $(8-9) \cdot 10^{7}$ cm/sec and densities of not less than 10^{13} cm^{-3} with a coaxial source.
2. Mass spectroscopy has established that the particles in the plasmoid are distributed in a wide range of energies, the mean energy of deuterium ions being 8 keV, the peak energy reaching 20 keV.
3. The total number of fast ions in the plasmoid has been estimated.

BIBLIOGRAPHY

1. MARSHALL, J. Plasma Acceleration, pp. 60–72. – Calif. Univ. Press. 1960
2. MARSHALL, J. and T. STRATTON. – Nucl. Fusion Suppl., Part 2, 663. 1962.
3. BELIKOV, A.G., V.P. GONCHARENKO, V.M. MISHCHENKO, B.G. SAFRONOV, and A.S. SLAVNYI. – In: "Fizika plazmy i problemy upravlyaemogo termoyadernogo sinteza", 3: 255. Kiev, Izdatel'stvo AN UkrSSR. 1963.

A. A. Kalmykov, S. A. Trubchaninov, V. A. Naboka,
and L. A. Zlatopol'skii

ENERGY SPECTRA AND THE STRUCTURE OF PLASMOIDS IN A COAXIAL PLASMA SOURCE

In /1,2/ a method was developed for taking the energy and mass spectra of ions in plasmoids and it was applied to investigate some properties of plasma guns, in particular conical and button sources. It would be interesting to make similar measurements for other sources, e.g., the coaxial plasma gun /3,4/.

These investigations give information on the mechanism of plasma acceleration in the source and, furthermore, provide detailed data on the composition and structure of plasmoids. All this is highly important for some problems connected with the injection of plasmoids into magnetic traps of various geometries.

Apparatus and procedure

The measurements were made with a coaxial gun having the following parameters:

$l = 17.5$ cm,	$b = 1.76 \cdot 10^7$ H/m,	$\tau = 7\,\mu$sec,
$D = 7.5$ cm,	$L_0 = 0.1\,\mu$H,	$W = 600–2400$ J,
$d = 3$ cm,	$U = 10–20$ kV,	$C = 12\,\mu$F,

where l the length of the gun; D, d the diameters of the external and the internal electrodes; b inductance per unit length; L_0 parasitic inductance of the circuit; U voltage applied to the condenser bank; τ the discharge period; W energy stored; C capacitance of the bank.

Hydrogen was admitted into the system through a pulsed valve, in amounts of 10^{-6} m^3 at atmospheric pressure (the pressure in the plenum was approximately $58.84 \cdot 10^4$ N/m^2). The energy and the mass spectra of the plasma ions were analyzed with a system described in /1/. The

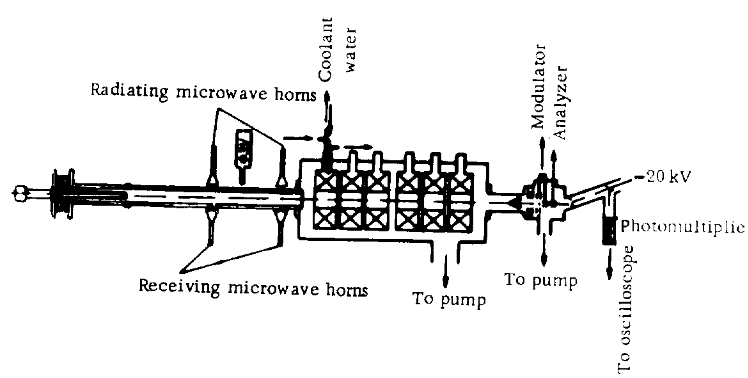

FIGURE 1. Schematic diagram of the setup.

velocity and the density of the plasma was controlled by probing with microwave signals at wavelengths of 3 cm and 8 mm and by recording the plasma glow with a photomultiplier.

The general layout of the apparatus is shown in Figure 1. The mass and the energy spectra were taken at various distances from the source. The plasmoids ejected by the source traveled down a glass tube 80 mm in diameter and 1.5 m long; no magnetic fields were impressed. The discharge current was picked up with a Rogowsky loop.

Analysis of mass and energy spectra

Since the system operates in a pulsed mode, the plasma is naturally modulated in time. If we separate particles of one energy and ensure satisfactory mass resolution in the drift space, the length of the peaks corresponds to the time of ionization and acceleration of the particles in source (provided no additional modulation is applied).

Figure 2 shows mass spectra of particles with energies $W_i = 600$ eV, $W_i = 3600$ eV, and an oscillogram of the discharge current. We see that the peaks are fairly narrow. To find the time of ionization in the source, we must consider the time-resolution of the apparatus. In the range of energies employed in our tests, the half-width of the peaks was of the same order of magnitude as the instrumental resolution, and we therefore could only determine the lower bound of the time of ionization. This lower bound gave approximately 0.3–0.5 μsec. Thus, given the energy and the mass of the particles, we can calculate the start point, i.e., the time of ejection of the particles from the source, from the drift time. The start point was found to be the same for ions of different masses and energies, coinciding with the singular point on the current oscillogram (Figure 2).

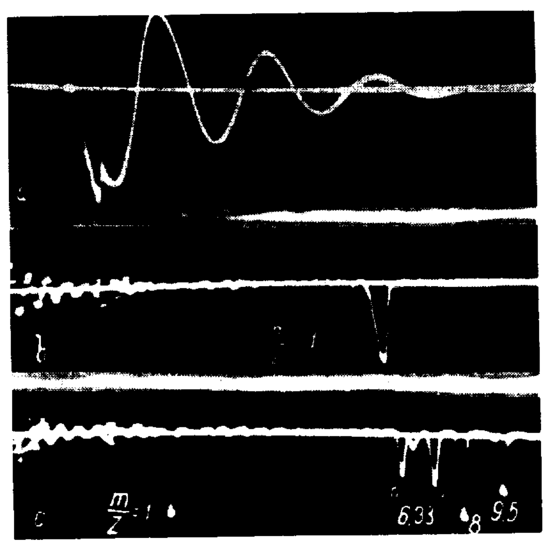

FIGURE 2. Mass spectra and the discharge current: a) discharge current, period 7 μsec; b) mass spectrum with $W_i = 600$ eV; c) mass spectrum with $W_i = 3600$ eV.

This singularity is very pronounced for small delays between the admission of gas and the sparking of the source. It therefore seems that ions of all masses and energies participating in the fast component of the plasmoid are formed in a very short time (that is, short in comparison with the discharge period of the source). Using a high-gain detector, we may pick up ions of low energies also, but no such time modulation is observed in this case: these ions apparently form in a time which is comparable with the total duration of the discharge.

Ions of different masses and charges were observed in the mass spectra, e.g., H^+, C^{3+}, C^{2+}, C^+, F^{3+}, F^{2+}, F^+, N^{3+}, N^{2+}, N^+, O^{2+}, O^+, and others. To be more precise, we could only determine the m/z ratio, while exact identification of the ions required additional analysis. The impurities are decomposition products of the diffusion pump oil and of the insulators (in the source and the pulsed valve). The content of impurities can apparantly be lowered by improving the design of the source. At present, the plasma carries as much as 20% of impurities.

The energy spectra of protons were studied as a function of the delay time between the triggering of the valve and the application of voltage to the source. Figure 3 plots the energy spectra of protons for various delay times (source voltage 12 kV). The distance between the source and the analyzer is 3.6 m. The peak of the distribution curve shifts in the

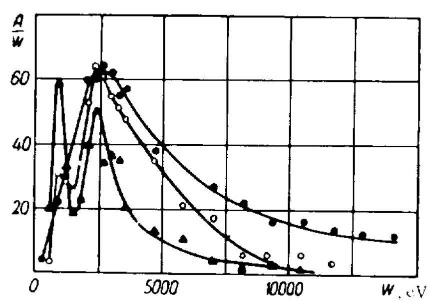

FIGURE 3. Energy spectra of protons for various delay times between gas admission and sparking: —●— 270 μsec; —○— 300 μsec; —△— 450 μsec;

direction of higher energies as the delay time decreases; the number of particles in the high-energy part of the spectrum increases. These changes are not too pronounced for delay times of 260–450 μsec, but for large delay times the entire spectrum above 200 eV is cut off. Figure 4 shows the energy spectra of protons for various source voltages (and a constant delay $\tau = 350\,\mu$sec). We see that the number of fast particles increases with voltage, but the peak of the distribution curve shifts only between 2 and 3 keV as the source voltage is raised from 10 to 18 kV.

A delay of 350 μsec is in a certain sense optimal, both as regards the number of fast particles and their energy.

It is remarkable that energy spectra taken at a distance of 3.6 m from the source show no particles with energy less than 600 eV, although these low-energy particles are detected by other methods.

In /2/ the angular distribution of ions of different energies was studied for a button source and it was shown that high-energy ions formed a narrow beam in the velocity space, while the slow ions moved in a very broad cone, virtually with an isotropic distribution. Therefore, when a plasmoid moves through a vacuum chamber, the slow ions are lost much faster, and the plasmoid is correspondingly enriched in fast ions. In our case we apparently have a similar situation. A study of energy spectra, taken at various distances from the source confirms this suggestion.

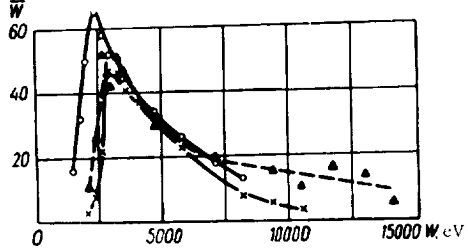

FIGURE 4. Energy spectra of protons for various source voltages:
—▲— 12 kV; —×— 14 kV; —○— 16 kV.

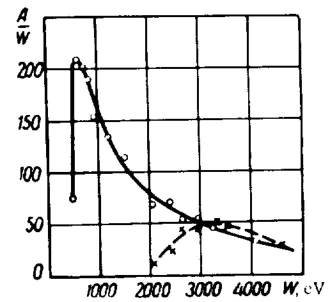

FIGURE 5. Energy spectra of protons at different distances from the source:
—○— 260 cm; —×— 360 cm.

Figure 5 shows energy spectra of protons ($U = 12$ kV, $\tau = 350\,\mu$sec) taken at different distances from the source. The spectra coincide in the high-energy region, sharply diverging in the range of low energies. This is obviously consistent with the above remarks on different angular distributions for ions of different energies.

An analysis of the impurity energy spectra shows that the spectra are peaked approximately around the same energy as the proton spectra, so that the protons and the impurity ions have widely different velocities. This spread of velocities leads to a separation of protons and impurity ions as the plasmoid travels along the system, which may become quite substantial if the drift space is large enough. This presents certain possibilities in connection with the separation of impurities from plasma.

Microwave measurements

The density of the plasma and the mean microscopic velocity were determined by probing with microwave signals Signals of 3-cm and 8-mm wavelengths were used. The oscillogram (Figure 6) shows the cutoff of the 8-mm signal for various distances of the microwave antennas from the source. The occurrence of two distinct cutoffs corresponding to two different plasmoids – the fast and the slow – is a characteristic feature of these oscillograms. For distances of ~1.5 m from the source, the two plasmoids constitute two separate entities in space, which produce two cutoffs at the 8-mm wavelength; this resolution, however, is not observed with the 3-cm signal. The velocity of the fast plasmoid measured by the microwave technique is in good agreement with the average velocity

of the particles obtained from the energy spectra at the same distance from the source. This comparison was made for several source-pickup distances. Microwave measurements show the plasmoid to be denser than 10^{19} m^{-3}. Measurements made with a photomultiplier show that the fast plasmoid is not luminous, which is apparently due to its being fully ionized; the slow plasmoid produces considerable glow.

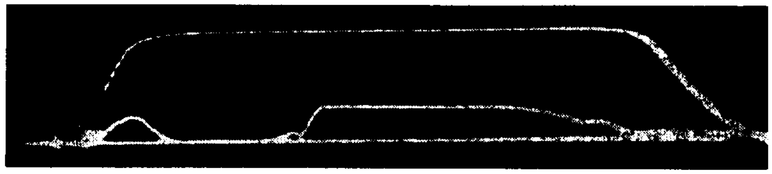

FIGURE 6. The cutoff of an 8-mm signal in a plasma.

The total number of particles in the fast plasmoid and its energy can be calculated from the energy spectra and the cutoff of microwave signals. Corresponding calculations give $(6-7) \cdot 10^{16}$ particles in the fast component, as compared with the 10^{19} gas particles injected into the source. Energy calculations show that the fast plasmoid is much more energetic than the slow one.

Discussion of results

Our results give the following picture of plasma creation and acceleration. The bulk of the gas is ionized and accelerated in a very short time (in comparison with the discharge period). Since the particles have a broad velocity spectrum, the plasmoid is stretched longitudinally; the fast particles concentrate in the head of the plasmoid, the slower particles move in a tail. The heavier ions are the slower ones, so that as the plasmoid moves through the plasma guide, the hydrogen ions are spatially separated from the impurities. The peculiar angular distribution of ions of different energies in a field-free space enhances the loss of slow ions. A weakly ionized stream of plasma trails behind the plasmoid with a velocity of some 10^4 m/sec. This plasma is ejected during the entire lifetime of the discharge in the source.

The source may operate in two radically different modes, which are mainly determined by the delay between the triggering of the valve and the sparking of the source. For large delay times, the source creates plasmoids with velocities of 10^5 m/sec, and the mechanism of acceleration is apparently consistent with the basic notions developed in /5/. For small delay times, the plasmoid has a velocity of $6 \cdot 10^5 - 10^6$ m/sec. The energy spectrum of the particles of the fast plasmoid is insensitive to source voltage or capacitance, the critical parameter being the delay time, i.e., the inflow of gas prior to sparking. This, taken in conjunction with the very short ionization time of the particles in the source, suggests

a slightly different acceleration mechanism from that proposed in /5/, which is apparently connected with the actual process of gas breakdown.

BIBLIOGRAPHY

1. KALMYKOV, A. A., A. D. TIMOFEEV, Yu. I. PANKRAT'EV, and V. I TERESHIN. – This volume, p. 191.

2. KALMYKOV, A. A., A. D. TIMOFEEV, Yu. I. PANKRAT'EV, and M. G. NOZDRACHEV. – This volume, p. 204.

3. MARSHALL, J. – Phys. Fluids, 3: 134. 1960.

4. BELIKOV, A. G., V. P. GONCHARENKO, V. M. MISHCHENKO, B. G. SAFRONOV, and A. S. SLAVNYI. – This volume, p. 212.

5. BURKHARDT, L. D. and R. H. LOVBERG. – Phys. Fluids, 5: 341. 1962.

A. A. Kalmykov, V. G. Marinin, F. V. Sivagin, and
A. D. Timofeev

THE GEOMETRY OF ELECTRODES AND ITS INFLUENCE ON THE PARAMETERS OF A PLASMA IN A COAXIAL GUN

Various papers have recently been published /1–5/ dealing with plasmoids created by coaxial guns. These investigations have shown that these plasmoids may contain $10^{17}-10^{19}$ charged particles, moving with velocities of $(1-8)\cdot 10^5$ m/sec. The plasmoids are highly ionized, but carry a substantial amount of impurities, especially in the slow component (up to 60%). The impurities are mainly decomposition products of the electrodes and the insulators. In all the studies dealing with coaxial sources, the electrodes are generally prepared from copper cylinders, although it is well known that brass and copper are among the materials which are very easily broken by discharge. Moreover, the sources have roughly constant geometrical dimensions, and the electric parameters of the discharge circuit vary but little from paper to paper, so that the discharge period is always approximately equal to $10\,\mu$sec. The insignificant variations in the geometrical and the electrical parameters clearly make it impossible to establish the influence of these factors on the properties of the plasmoids. It seems reasonable, however, that the qualitative and the quantitative composition of the plasmoids should change if the source is made of a different material or if the parameters of the condenser bank are altered.

With this point in view, we proceeded to investigate the influence of the above factors on the parameters of the plasmoids. The main emphasis, however, was placed on the effects due to the geometrical dimensions, in particular, the length of the central electrode.

Apparatus

A schematic diagram of the setup is shown in Figure 1. The plasma accelerator consisted of two coaxial stainless-steel cylinders. The internal diameter of the outer cylinder was 0.054 m, its length 0.25 m; the external diameter of the central electrode 0.02 m. The distance from the gas inlet to the end of the central electrode varied from 0.018 m to 0.1375 m. A capacitor bank of eight KIM-5 condensers with a total capacitance of 4 μF was discharged through the plasma accelerator. The bank was charged to a voltage of 20 kV. Working voltage 19 kV. The gas was admitted into the interelectrode gap through a hole in the inner electrode; a pulsed valve was used, ensuring inflow of 10^{-6} m^3 of gas at atmospheric pressure. Hydrogen was employed as the working gas in our experiments. The valve was actuated by a capacitor bank of two IM-150 condensers with a total capacitance of 300 μF. Valve voltage 2.5 kV. The plasmoids moved through a glass tube 0.1 m in diameter, joining the source with a Thomson mass spectrometer.

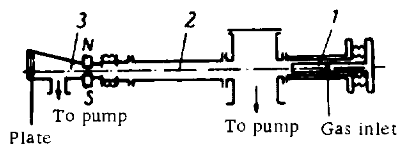

FIGURE 1. Schematic diagram of the apparatus: 1) coaxial gun; 2) tube joining the source with the mass analyzer; 3) mass analyzer.

Procedure and results

The plasmoid parameters were determined by mass spectroscopy with an extracting electric field and by microwave cutoff technique.

The former method gives the mass and the energy distribution of the ionic component of the plasmoid. In these experiments, the mass spectrograph was set at a distance of 1.5 m from the source, the voltage applied to the extracting electrode was 20 kV. The particles were recorded with MK photographic plates. The electron density was estimated from the cutoff of an 8-mm microwave signal probing the plasma at a distance of 0.7 m from the source. All measurements were made without any driving magnetic field.

Mass spectrograms of the ionic component were taken for different modes of source operation. The length of the inner electrode and the delay between the discharge of the valve-actuating bank and the discharge of the source capacitors were the variable quantities. The central electrode had the following lengths: 0.018, 0.0325, 0.0675, 0.1015, and 0.1375 m. The delay times varied from 220 to 600 μsec. The source displays two modes of operation in this interval of delay times. The first mode obtains for small delay times: it is characterized by the creation of two plasmoids with different velocities. The fast plasmoid moves with velocities of $(6-8) \cdot 10^5$ m/sec, and the slow plasmoid 10^5 m/sec. When the delay is

made greater than 300 μsec, the fast plasmoid vanishes, and only the slow component is observed. This interval of delay times represents the second mode of source operation. Since the creation of pure, fast plasmoids is the main object faced by the researchers, we concentrated on the first mode of source operation, where fast particles are generated. The delay times were chosen in the 220–300 μsec interval. The upper boundary of this interval corresponds to the longest delay for which fast particles are yet observed; the lower boundary is the smallest possible delay for which sparking occurs.

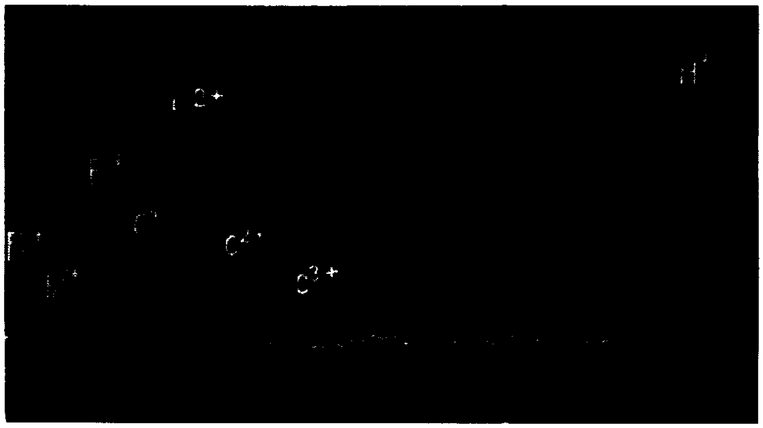

FIGURE 2. Photomicrogram of the ionic component of a plasmoid: 250 μsec delay, 0.0325 m electrode.

We studied the energy distribution, the mass composition, and the number of fast particles in plasmoids. Figure 2 shows typical photomicrograms of the ionic component of a plasmoid. We see that, besides hydrogen, the plasmoid carries impurity ions (F, Fe, C). The energy distribution of the hydrogen ions for electrode lengths of 0.0325 and 0.1375 m are shown in Figures 3 and 4. These curves are bimodal, the two peaks corresponding to the slow and the fast plasmoids, respectively. A comparison of the curve shows that the number of particles of any given energy decreases as the electrode is made longer (the delay being constant). Figure 5 plots the variation of the mean energy of hydrogen ions with the length of the central electrode, calculated from the energy distribution curves (see Figures 3,4). We see from Figure 5 that for short electrodes (less than 0.04 m), the mean particle energy increases as the delay is raised from 220 to 250 μsec. If the electrode length is changed, maintaining a constant delay time, the curve of the mean particle energy passes through a maximum for electrode lengths of 0.2–0.4 m, and then falls off smoothly. For a 250 μsec delay, the peak is slightly displaced in the direction of even smaller lengths, and the mean energy decreases fairly sharply with the increase of electrode length.

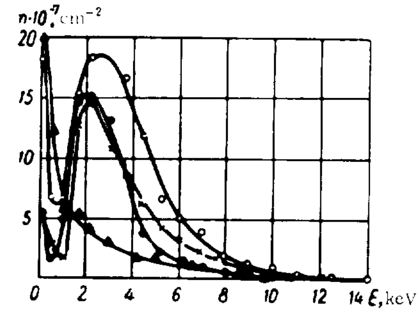

FIGURE 3. Energy distribution of hydrogen ions for 0.0325 electrode length and various delay times τ:
● - $\tau = 270\,\mu$sec; x - $\tau = 250\,\mu$sec;
O - $\tau = 230\,\mu$sec; ▲ - $\tau = 220\,\mu$sec;

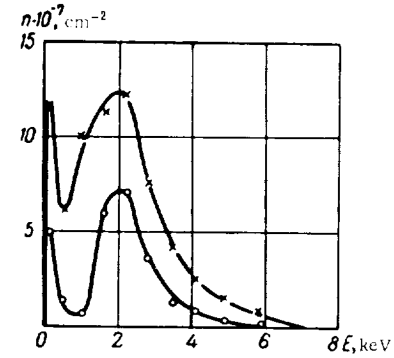

FIGURE 4. Energy distribution of hydrogen ions for 0.1375m electrode length and different delay times τ:
O — $230\,\mu$sec; x — $250\,\mu$sec.

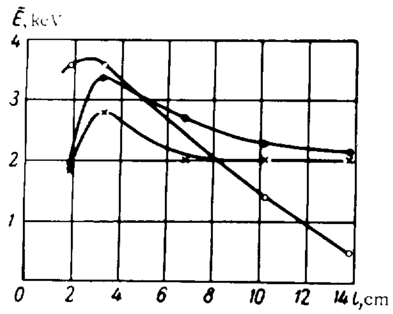

FIGURE 5. Mean energy vs. electrode length for various delay times τ:
x — $220\,\mu$sec; ● — $230\,\mu$sec; O — $250\,\mu$sec.

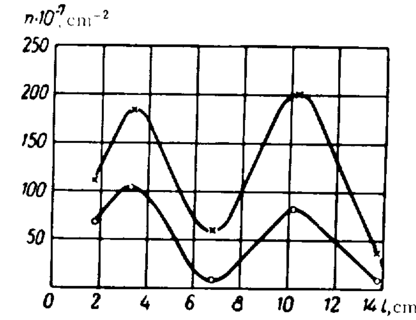

FIGURE 6. The total number of hydrogen ions as a function of the electrode length for various delay times τ:
x — $230\,\mu$sec; O — $250\,\mu$sec.

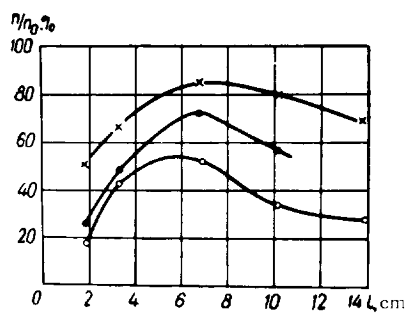

FIGURE 7. Percentage content of hydrogen as a function of the electrode length for various delay times τ:
● — $220\,\mu$sec; x — $230\,\mu$sec; O — $300\,\mu$sec.

Figure 6 gives the total number of hydrogen ions as a function of the electrode length. We see that the curves are bimodal, the amplitude of the peaks increasing as the delay time decreases. The number of fast particles as a function of the electrode length differs for different delay times. The fast particles are the most abundant for 220–250 μsec delay with an 0.0325 m central electrode. The percentage content of hydrogen as a function of the electrode length is shown in Figure 7 for various delay times. We see from this figure that the percentage content of hydrogen ions in the plasmoid reaches substantial values. It is only for the 300 μsec delay that it is less than 50%. As we have already observed, the principal impurities in the plasmoid are the ions detached from the insulator and the electrode. This in particular follows from the fact that in systems employing a plexiglas insulator the plasmoid contained ions of hydrogen, carbon, oxygen, nitrogen, and iron. When the plexiglas insulator was replaced with a Teflon insulator, virtually no nitrogen and oxygen impurities were observed. The remaining impurity ions were Fe, F, C.

Plasmoid densities of not less than $1.7 \cdot 10^{19}\ m^{-3}$ were obtained from the cutoff of an 8-mm signal. Figure 8 is an oscillogram of the cutoff for a 300 μsec delay.

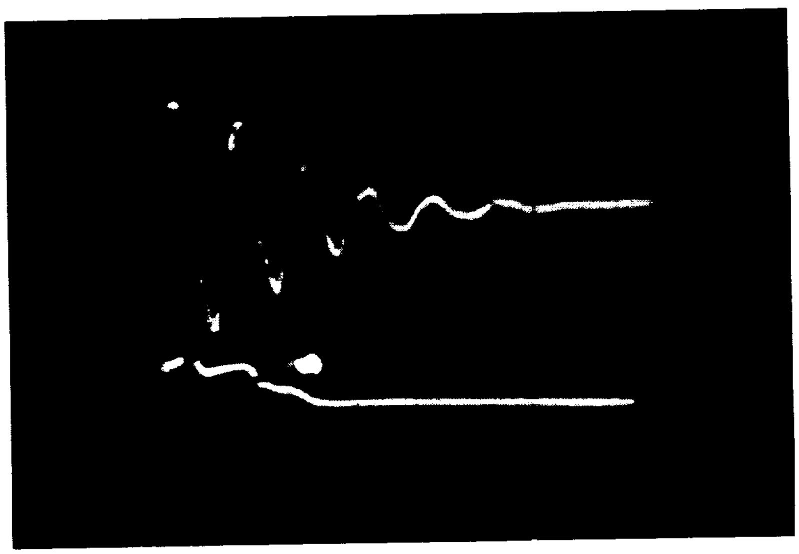

FIGURE 8. Oscillograms of the discharge current (top) and of the 8-mm signal cutoff at a distance of 0.7 m from the source (bottom).

Discussion of results

The energy of hydrogen ions measured in /3/ was 4–5 keV, the density of charged particles in the plasmoid was greater than $10^{19}\ m^{-3}$. In our experiments, the discharge period is 1/3 of that in /3/, and the capacitance

of the condenser bank is 1/6 of the corresponding parameter in the earlier work, but the plasmoids nevertheless have densities of over 10^{19} m^{-3} and a mean energy of 3 keV for hydrogen ions. We may thus conclude that at least this difference in the parameters of the discharge circuits has no influence on the properties of the plasmoids.

The plasma is contaminated with heavy ions because the electrodes and the insulators break on sparking. To reduce the impurity content, the source should apparently be redesigned so that the plasma does not touch the insulator. Furthermore, the source electrodes must be fabricated from a more durable material.

We have mentioned that the source may operate in two modes, characterized by different delay times between the triggering of the valve and the sparking of the source. In the second mode, when the delay is greater than 300 μsec, the source mainly creates slow plasma with velocities not exceeding 10^5 m/sec. In the first mode, with delay times of 220–330 μsec, the average velocity of the plasmoid reaches $8 \cdot 10^5$ m/sec for short accelerating electrodes (0.03 – 0.04 m). As the electrode is made longer, the average velocity decreases. The theoretical calculations of /6/ in application to our system with an 0.04 m electrode give a velocity of some $2 \cdot 10^5$ m/sec. This is approximately 1/4 of the experimental figure. We thus conclude that in the first mode of source operation the plasmoids are accelerated by a mechanism different from that proposed in /6/. The exact nature of this mechanism, however, is not clear.

BIBLIOGRAPHY

1. MARSHALL, J. – Phys. Fluids, 3: 134. 1960.
2. PODGORNYI, I. M., S. A. CHUVATIN, G. Z. BYKOV, and V. D. PISEMSKII. – In: "Fizika plazmy i problemy upravlyaemykh termoyadernykh reaktsii", 4: 222. Moskva, Izdatel'stvo AN SSSR. 1958.
3. BELIKOV, A. G., V. P. GONCHARENKO, V. M. MISHCHENKO, B. G. SAFRONOV, and A. S. SLAVNYI. – In: "Doklady III konferentsii po fizike plazmy i probleme upravlyaemykh termoyadernykh reaktsii", Khar'kov, FTI AN UkrSSR, BNTI. 1962.
4. OSHER, J. E. and D. E. HAGERMAN. – Bull. Am. Phys. Soc., Ser. II, 5: 350. 1960.
5. BURKHARDT, L. C. and R. H. LOVBERG. – Phys. Fluids, 5: 341. 1962.
6. LINHARD, J. G. – Nucl. Fusion, 1: 78. 1961.

I. M. Zolototrubov, V. A. Kiselev, and Yu. M. Novikov

INVESTIGATION OF PROCESSES IN A COAXIAL PLASMA SOURCE

The wide application of coaxial-type plasma guns led various specialists /1–5/ to investigate the mechanism of plasma acceleration in coaxial systems. In /1–4/ it is suggested that the ionized gas is driven by the force of magnetic pressure $\frac{H^2}{8\pi}$, where H is the magnetic field set up by the

current flowing in the center conductor. With this mechanism of acceleration, the plasma can be expected to leave the gun as a compact "blob" with an insignificant spread of particle velocities, whose density is higher than the original density of the neutral gas. Experiments show, however, that the plasmoids produced by coaxial sources have a considerable longitudinal extent.

On the other hand, in /5/ it is shown that sparking in the interelectrode gap produces a thin sheet current which is driven by electrodynamic forces through the neutral gas taking the form of a shock wave. All this indicates that the performance of the coaxial plasma gas, which is inherently a simple device, requires further study. In the present paper we give the results of an experiment carried out with the aim of establish ng what processes actually occur in a coaxial system.

Description of experiment

The experimental setup is shown in Figure 1; its principal parameters are listed below:

Diameter of external electrode	65 mm
Diameter of center electrode	30 mm
Length of electrodes.	660 mm
Total inductance of discharge circuit	0.211 μH
Maximum inductance of the gun	0.089 μH
Capacitance of condenser bank	12 μF
Voltage	20 kV
Maximum discharge current	105 kA
Half-period of current.	5.0 μsec
Initial vacuum	$133.322 \cdot 10^{-6}$ N/m^2
Volume of gas admitted into the gun (calculated for atmospheric pressure)	0.8 cm^3

The gun is made of two coaxial copper electrodes separated at one end by a ceramic insulator. Since we were interested in processes which occurred within a single half-period of the discharge current, we artificially increased the damping of the discharge circuit, comprising the capacitance C_1 and the sum inductance of the system. To this end, a serial resistance was coupled into the circuit, chosen so as to minimize the current amplitude in the second and later half-periods. The resistor was prepared from lengths of RK-50 coaxial cable, whose center conductor had been replaced with a nichrome wire 2 mm in diameter. The voltage from the condenser bank was impressed through a vacuum spark gap on the gun electrodes by means of twelve such lengths of cable, connected in parallel. Each length of cable measured 1.5 m, the total resistance was 0.077 ohn.

The interelectrode gap of the gun was filled with a gas, admitted in rated pulses through a high-speed electrodynamic vacuum valve, described in /6/. The valve was joined with the gun by a length of piping halfway along the external electrode. The distribution of gas density along the gun was not measured, but according to the data in /2,5, , the neutral gas probably expanded at a rate equal to the thermal velocity of its molecules. For hydrogen, the velocity is $1 \cdot 10^3$ m/sec; the delay between the time when the valve began to open and the application of voltage to the source electrodes was 200 μsec, so that the gas expanded some 20 cm in either

direction from the inlet. The sparking therefore occurred far from the insulator and far from the gun muzzle.

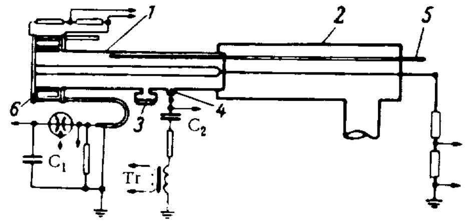

FIGURE 1. Schematic diagram of the setup:
1) gun; 2) vacuum system; 3) electrodynamic valve;
4) igniter electrode; 5) magnetic probe; 6) insulator.

An igniter electrode is fitted in the external electrode at a distance of 23 cm from the muzzle. The igniter electrode is maintained at a constant voltage relative to the external electrode, and its aim is to stabilize the discharge with respect to gas dissipation. For a certain gas density, a spark occurs between the igniter electrode and the external electrode of the gun. The current pulse transmitted by the spark is fed through the transformer Tr and ignites the vacuum spark gap. By altering the amplitude of the voltage applied to the igniter electrode, we can change between wide limits the delay between the triggering of the valve and the ignition of the vacuum spark gap. The point of sparking in the interelectrode gap is determined by the distribution of gas density along the gun at the time when voltage is applied to the electrodes, i.e., in the last analysis it depends on the delay time only.

Procedure and results of measurements

A magnetic probe measured the magnetic field inside the gun. The probe comprised a coil 4 mm in diameter. The coil was attached to a length of coaxial cable and the two components were enclosed in a glass tube 7 mm in diameter. The probe was inserted into the gun from the side of the muzzle and it could be freely moved along the surface of the external electrode. The probe was aligned so as to pick up the azimuthal magnetic field only. The probe signal was integrated by an RC-circuit and fed to an oscilloscope.

Figure 2 shows some oscillograms displaying the time variation of the magnetic field at various points along the gun. At points near the muzzle, the signal is delayed due to the finite velocity of discharge propagation. Moreover, the form of the oscillograms changes as the probe moves along the coaxial system. These oscillograms make it possible to reconstruct the distribution of the magnetic field along the gun at any time. These distributions for 1.8, 2.8, 3.8, and 4.8 μsec after sparking are shown

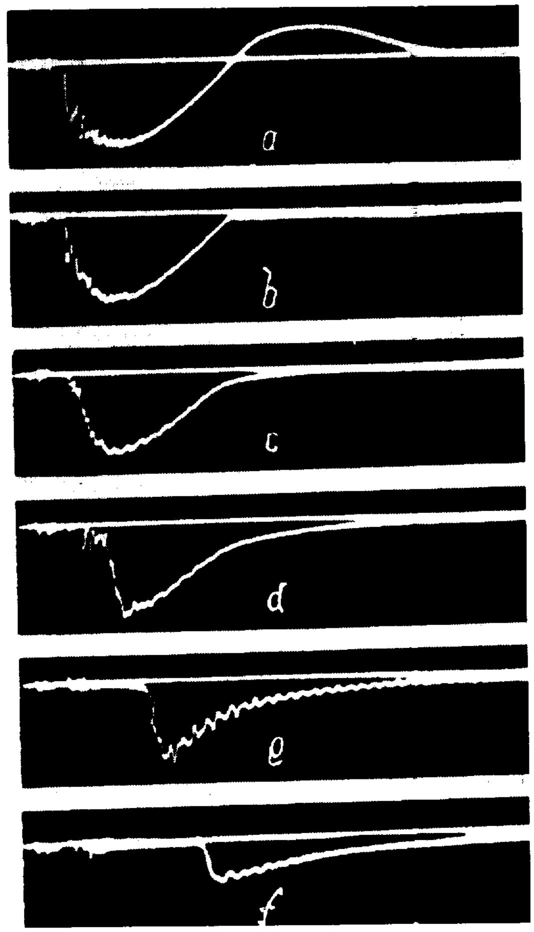

FIGURE 2. Oscillograms of the azimuthal magnetic field at various points along the gun:
a) 13 cm; b) 20 cm; c) 26 cm; d) 32 cm; e) 4· cm; f) 58 cm.

in Figure 3. We see from the figure that the discharge current flows through the gun in a thin sheet (that is, thin in comparison with electrode length) some 5 cm wide; this sheet propagates as one whole along the coaxial system toward the muzzle. Figure 4 plots the time of arrival of the leading edge of the current sheet for various points along the gun. The arrival time is also reckoned from sparking. This plot characterizes the velocity of the current sheet, which is found to be constant ($1 \cdot 10^5$ m/sec) over the entire gun length from 22 to 52 cm. The velocity slightly increases near the muzzle ($1.6 \cdot 10^5$ m/sec), apparently due to the decrease in the density of the neutral gas in this part of the gun

Field distribution after 3.8 and 4.8 μsec (Figure 3, curves 4 and 5) is distinguished from earlier field distributions by the appearance of a second current sheet due to the sparking in the interelectrode gap which

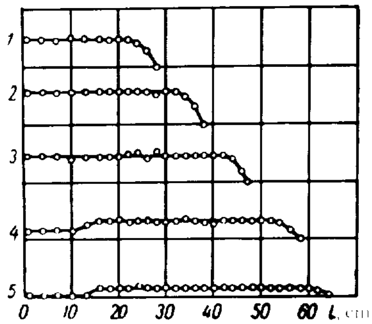

FIGURE 3. The distribution of the amplitude of the azimuthal magnetic field (in relative units) along the gun at various times:
1) 0.8 μsec; 2) 1.8 μsec; 3) 2.8 μsec;
4) 3.8 μsec; 5) 4.8 μsec.

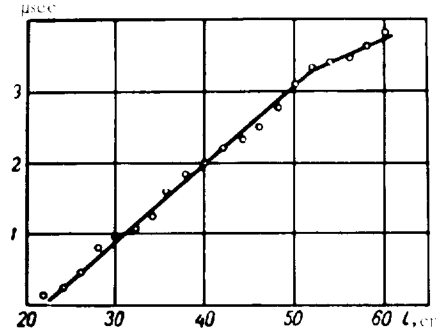

FIGURE 4. Time of arrival of the leading edge of the current sheet at various points along the gun.

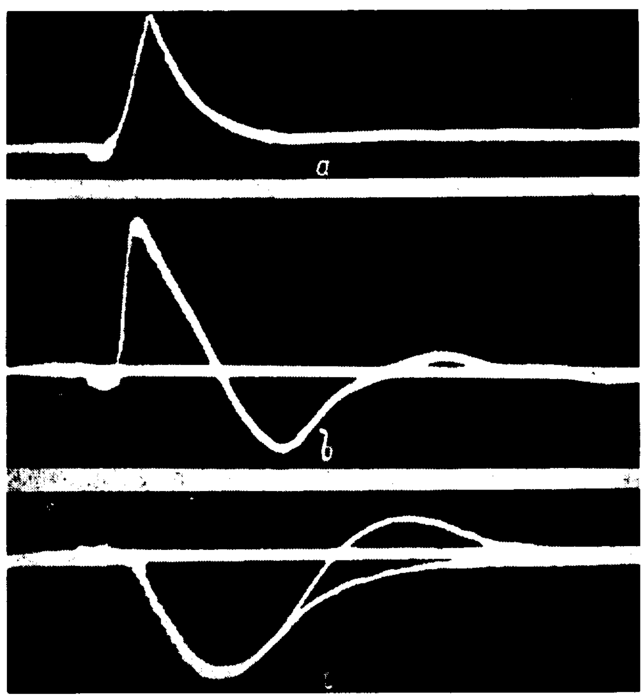

FIGURE 5. Oscillograms of electrode voltage:
a) muzzle side (peak amplitude 340 V); b) insulator side (peak amplitude 3.5 kV); c) superposition of azimuthal field oscillograms at points before and after the second spark.

occurs somewhat nearer to the insulator than the original spark. The current of this late spark also flows in a thin sheet, whose width is approximately equal to the width of the first current sheet; the second sheet, however, remains stationary. The second spark is distinctly observed by comparing the field oscillograms for points on either side of the second sparking position (Figure 5,c). These oscillograms are superimposed. The point at which the oscillograms diverge specifies with fair accuracy the time of second sparking. Figure 5 also gives oscillograms of the voltage fall on the gun electrodes on the side of the insulator (Figure 5,b) and on the side of the muzzle (Figure 5,a). The oscillograms were obtained with calibrated resistive dividers connected to the corresponding points of the gun. The voltage on the muzzle side is small; it apparently represents the voltage drop across the ohmic resistance of the plasma, while the voltage on the insulator side is equivalent to the sum of the drops of the resistive and the inductive voltages.

Measurements show that the inductive voltage drop is 10 times as large as the resistive drop.

The second sparking occurs when the interelectrode voltage is increased after the passage of the maximum current through the gun: the electrodes are then shorted near the insulator. The current produced by discharging the capacitor C_1 flows in this case in a new sheet, while inside the gun a closed coaxial circuit forms where the current and the magnetic field are exponentially damped in time. The damping constant is determined only by the parameters of this circuit, and is equal to $4\,\mu$sec.

To visualize the behavior of the discharge in the gun, we took some high-speed photographs through a longitudinal slit in the outer electrode. A longitudinal slit 4 mm wide should have no significant effect on the distribution of currents and fields in the coaxial system. The discharge starts at a distance of 22 cm from the insulator and propagates with a constant velocity, equal to $1 \cdot 10^5$ m/sec. These data are consistent with the results obtained in probe measurements. The time and position of the second spark also agree with magnetic probe measurements, but the second sparking is preceded by motion of plasma from the area of the first spark. Motion starts some $3\,\mu$sec after the first spark and terminates when the second sparking occurs. This result is somewhat unexpected and it can apparently be attributed to the behavior of a plasma in crossed electric and magnetic fields.

Discussion of results

Measurements show that the entire discharge current prior to the second sparking flows in a thin sheet moving with a velocity of $1 \cdot 10^7$ cm/sec through the neutral gas. The motion of this sheet current ionizes the gas in the gun and produces plasma. The effect of the current sheet in this case is equivalent to the effect of a shock wave /5/. The plasma in the wake of the current sheet is immersed in an azimuthal magnetic and a radial electric fields which produce longitudinal drift. Whether the plasma drifts toward the muzzle or in the opposite direction depends on the

particular orientation of the fields. The drift velocity in the laboratory frame is given by

$$\mathbf{u} = \frac{10^7}{4\pi} \cdot \frac{[\mathbf{E} \times \mathbf{H}]}{H^2} \text{ m/sec,} \tag{1}$$

where $\mathbf{E}$ is the electric field strength in V/m, $\mathbf{H}$ the magnetic field strength in A/m.

Let us estimate the drift velocity of a plasma in the initial sparking area; to this end we have to find the fields E and H entering (1). E is determined from the well-known expression of electrostatics, according to which the electric field in a gap between two coaxial cylinders is

$$E = -\frac{V}{r \ln \frac{R}{r_0}}, \tag{2}$$

where V is the potential difference between the electrodes, r the radial distance of the field point from the axis, $\frac{R}{r_0}$ the ratio of the radii of the outer and the inner cylinders.

As we have previously observed, the interelectrode voltage in the gun is mainly inductive; it can be defined as

$$V = -\frac{d}{dt}(LI), \tag{3}$$

where L is the inductance of the gun region between the sparking point and the current sheet, which is in turn expressible for any time t in terms of the inductance L_0 per unit length of the gun and the velocity of the current sheet v:

$$L = L_0 vt. \tag{4}$$

Seeing that $I = I_0 \sin \omega t$, where $\omega = \frac{2\pi}{T}$ and T the discharge period of the condenser bank, and assuming a constant v, we find

$$V = -\left(I\frac{dL}{dt} + L\frac{dI}{dt}\right) = -I_0 L_0 v (\sin \omega t + \omega t \cos \omega t). \tag{5}$$

Substituting (5) in (2),

$$E = \frac{I_0 L_0 v (\sin \omega t + \omega t \cos \omega t)}{r \ln \frac{R}{r_0}}. \tag{6}$$

The magnetic field is provided by the current flowing through the center conductor, and it can therefore be written as

$$H = \frac{I_0 \sin \omega t}{2\pi r}. \tag{7}$$

From (1), (6), and (7), we have

$$\frac{u}{v} = A(1 + \omega t \operatorname{ctg} \omega t), \tag{8}$$

where

$$A = \frac{L_0 10^7}{2 \ln \frac{R}{r_0}} = 0.948.$$

If $\frac{u}{v}$ is plotted as a function of time, we see (Figure 6) that at first the plasma drifts in the same direction as the current sheet, but with a somewhat higher velocity, then it starts lagging behind, and finally, after 3.2 μsec, its velocity is reversed and it accelerates in the direction of the insulator. This pattern of motion of the plasma in the wake of the current sheet is in satisfactory agreement with the results obtained from high-speed photographs. The motion of the plasma toward the insulator is observed in high-speed photographs 3.2 μsec after sparking

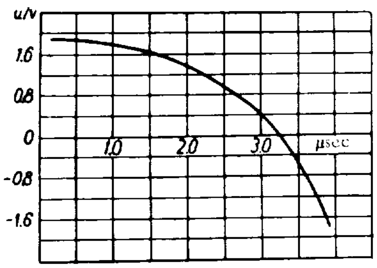

FIGURE 6. $\frac{u}{v}$ vs. time.

The experimental results thus show that inside the coaxial gun the plasma displays axial drift. This drift is attributable to the crossed electric (radial) and magnetic (azimuthal) fields behind the current sheet

A simple calculation shows that during most of the first half-period of the current the drift velocity points in the direction of motion of the current sheet, and the plasma is "raked" in this direction. The reversal of drift velocity after 3.2 μsec impels the plasma toward the insulator. The second spark through the interelectrode gap and the shorting of the electrodes near the insulator are connected with this reversed motion.

BIBLIOGRAPHY

1. DATTNER, A. Acceleration of plasma – "Proc. 4th Intern. Conf. Ionization Phenomena Gases, Uppsala, 1959", 2, pp. 1151-1155. 1960.

2. MARSHALL, J. Plasma Acceleration, p. 60 – Stanford University Press, Stanford, California. 1960.

3. LUK'YANOV, S. Yu., I. M. PODGORNYI, and S. A. CHUVATIN. – ZhTF, 31(9): 1026. 1961.

4. JENSEN, V. O., A. H. SILLENSEN, F. HIEKEL VINTHER, and C. F. WANDEL. – Conference of Plasma Physics and Controlled Nuclear Fusion Research, Salzburg. 1961.

5. BURKHARDT, L. C. and R. H. LOVBERG – Phys. Fluids, 5: 341. 1962.

6. UMAROV, G. Ya., A. K. ALIMOV, and N. F. OVECHKIN. – PTE, 1: 178. 1961

L. I. Krupnik and N. G. Shulika

MASS-SPECTROMETRIC INVESTIGATION OF A CONICAL SOURCE OF SIMPLIFIED DESIGN

The source of pure plasma used in all our experiments on the probing of plasma with beams of fast particles was developed by Azovskii's group /1/. This is a fairly simple facility whose structure has been studied in considerable detail and which creates high-purity plasma (~ 90%). One of the marginal shortcomings, which is nevertheless acutely felt in actual work with this apparatus, is the periodic breakage of the glass cones constituting the body of the source. The replacement of a broken cone is a rather unpleasant and difficult task. Our group therefore proceeded to the design of a slightly modified source, based however on the same operational principles.

Schematically, the source is identical with that described in /1/, but the conical body of thin glass has been replaced with a massive thick-walled cone cut from the neck of a bottle of 0.75 liter capacity.

The size of the new cone enabled us to simplify the source as a whole and to employ smaller support flanges. The assembled apparatus proved to be almost one and a half times smaller than the original design.

We studied the performance of this simplified source in great detail. It functioned without failure with voltages of 25 kV and higher, was highly durable, and did not break in any of the forced modes of operation.

A comparison of its mass-spectrometric characteristics with the parameters in /1/ gave highly satisfactory results. A Thomson mass spectrometer was applied to take the spectrum of the plasmoid ions in various modes of source operation, varying all the relevant parameters. Table 1 compares the mass spectra of the plasmoid with Azovskii's data for similar operating modes (delay $\tau = 270-280\,\mu$sec, gas inflow $g = 2$ cm^3).

TABLE 1

Ion composition of the plasmoid	Mass-spectroscopic characteristics of the plasmoid					
	in /1/	ours	in /1/	ours	in /1/	ours
	10 kV		15 kV		20 kV	
H_1^+	90	89	89	84.5	65	51.3
H_2^+	2	2 2	1	1.8	3	3.1
H_3^+	0,5	0.5	1	1.4	4	2.7
C^+	2	0.8	2.5	3	6	3.7
N^+Si^{2+}	—	1.6	0.5	0.8	1	1.9
O^+	3	3.5	—	1	8.5	4.2
C^{2+}	—	1.0	—	—	0.5	—
Na^{2+}	—	—	0.5	0.5	2	3.5
Si^+	0.5	1.5	1	2.3	6	12.5
Na^+	—	—	0.5	1	1.5	13.5

We see from the table that the results are in excellent agreement within the margin of experimental error.

The plasmoid created with our source had a purity comparable to that of the plasmoids from Azovskii's source ($\sim 90\%$). This high purity, however, was obtained only for certain modes of source operation, namely for a large delay between the admission of gas and the sparking of the source ($\tau = 270-300\,\mu$sec) and a comparatively low source voltage ($\sim 10-12$ kV).

In addition to the data in /1/, we give here the dependence of the plasmoid purity on the amount of gas admitted into the source for a delay $\tau = 300\,\mu$sec and a voltage $U = 15$ kV (Table 2). We see from the table that the content of hydrogen in the plasmoid is maximal for a gas inflow of $\sim 2-3\ \mathrm{cm}^3$, whereas further increase in gas inflow does not affect the ion composition of the plasmoid, sharply enhancing its neutral component (probing of the plasma with a fast neutral beam).

TABLE 2

Ion composition of the plasmoid	Gas inflow, cm^3			
	0.5	1.0	2.0	3.0
H_1^+	32.5	44	70	63
H_2^+	8.0	3	3	2.0
H_3^+	8.0	3.5	2.5	2.0
Impurities	51.5	48.5	24.5	32

To estimate the velocity of the plasmoids, we employed two double probes inserted at a certain distance from each other. The velocity of the plasmoid, as measured from the difference in its arrival times at the two probes, was found equal to $v = (5-7) \cdot 10^{-}$[illegible] cm/sec. This is fairly close to the velocity given in /1/.

In certain modes of source operation, however, we registered a group of faster particles. The Thomson spectrographic plates showed a parabola of hydrogen ions extending to energies of some 2–2.5 keV. The intensity of these fast particles was very low.

The operating modes in which these fast particles are ejected correspond to a very small delay between the triggering of the valve through which the gas is admitted into the source and the sparking of the source ($\tau = 150-170\,\mu$sec). In these modes, however, a very high impurity content was observed in the source. As an illustration, we give Table 3, which shows the variation of the impurity content in the plasmoid with the delay time to source sparking (gas inflow $g = 1-2\ \mathrm{cm}^3$).

TABLE 3

Ion composition of the plasmoid	Delay, μsec					
	150	170	230	280	330	370
H_1^+	4	7	54.5	56	70	60.5
H_2^+	1.5	1	12.0	1.0	2.8	1.5
H_3^+	2.0	9.5	2.0	3	2.5	3.0
Impurities	89.5	82.5	41.5	40	25	35

The conical source described in this paper is simple in design, reliable in operation, and has a long service life. By suitably choosing the mode of operation, high-purity hydrogen plasma can be obtained ($\sim 90\%$).

BIBLIOGRAPHY

1. AZOVSKII, Yu.S., I.T. GUZHOVSKII, and B.G. SAFRONOV. – This volume, p. 239.

Yu. S. Azovskii, I. T. Guzhovskii, and B. G. Safronov

A CONICAL PLASMA SOURCE WITH ELECTRODES AND PULSED GAS INLET

In /1/ two conical sources with electrodes were investigated, both having plexiglas discharge chambers. The plasmoids ejected from these sources contained plexiglas decomposition products, i.e., ions of hydrogen, oxygen and carbon; mass-spectrometric measurements /2/ showed that there was a mere 10% of hydrogen in the plasma.

In /3/ an inductive conical source was described, creating hydrogen plasma with less than 1% of heavy impurities.* Among the shortcomings of this source, however, is its complex supply circuitry.

A plasma source combining the advantages of these guns, i.e., simple electric circuitry and high-purity plasma, will be highly useful in various fields of plasma physics. To establish the feasibility of such a gun, we investigated a conical source with electrodes and a helical return conductor similar in its design to the source described in /1/, but with a pulsed gas inlet.

Apparatus

The plasma source is shown in Figure 1. This is a glass conical discharge chamber 2 with a cylindrical electrode 3 at the apex of the cone and a ring electrode 1 at the base of the cone. The diameter of the cylindrical electrode 1.5 cm, internal diameter of the ring electrode 9 cm, opening angle of the cone 50°. An eight-turn helix acting as the return conductor was wound on the outer surface of the discharge chamber. This helix, as shown in /1/, increases the source efficiency.

A high-speed valve is provided in the cylindrical electrode, admitting some 3 cm^3 of hydrogen into the discharge chamber. The design and the parameters of the electrodynamic valve are as in /3/. The plasma in the source was created by discharging a 6 μF condenser bank.** The inductance

* The 10% of impurities quoted in /3/ is not a source characteristic, since they intrude from the vapors of diffusion pump oil.

** The current was switched with a vacuum spark gap, similar to the spark gap described in /4/.

of the discharge circuit 0.34 μH (the source inductance accounting for half of this figure), discharge period 9 μsec. The plasma ejected from the source propagated along a glass tube with an i.d. of 9 cm. Residual gas pressure in the vacuum system $\sim 10^{-4}$ N/m^2.

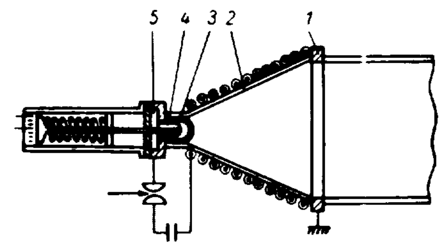

FIGURE 1. Conical source:
1) ring electrode; 2) discharge chamber; 3) cylindrical electrode; 4) valve head; 5) Teflon washer.

It has been established in /3/ that the performance of the plasma source and the parameters of the ejected plasmoids are highly sensitive to the inflow of gas into the source, i.e., the volume ΔV of the gas and the admission time, which in turn depend on the initial pressure in the valve plenum p_0, the voltage applied to the valve capacitors U_v, and the delay between the opening of the valve and the firing of the source. All subsequent measurements were made for $\Delta V = 2-3$ cm^3 ($p_0 = 4-6 \cdot 10^5$ N/m^2, $U_v = 1.5$ kV) and $\Delta\tau = 210$, 270, and 350 μsec. For $\Delta\tau = 210$ μsec, the gas just fills the source, while for larger $\Delta\tau$ the gas expands to distances of 10 and 40 cm from the source. The minimum delay which permits sparking in the source is approximately 170–180 μsec (it is determined by the time elapsing between the discharge of the valve condensers and the opening of the valve).

The following techniques were applied to determine the parameters of the plasma:

1. A Thomson mass analyzer (method of parabolas) was used to determine the mass composition of the plasmoids. The spectrograph analyzing the particles which moved along the axis of the vacuum chamber was set at a distance of 1.5 m from the source. The ions were detected with MK-type photographic plates. The spectra obtained characterize the mass composition averaged over the entire length of the plasmoid. The photometry of the plates was done on MF-4 microphotometer.
2. The visual glow of the plasma was picked up with a photomultiplier.
3. A magnetic probe (a coil 0.14 cm in diameter and 0.8 cm long) moving along the axis of the vacuum system measured the currents in the plasmoid. The signals of the photomultiplier and of the magnetic probe were fed to a pulsed oscilloscope OK-17. Typical oscillograms are shown in Figure 2, which also gives the signal of a one-turn loop representing the rate of change of the current through the discharge circuit.
4. The "cutoff" of microwave signals was used in estimating the density of the charged particles in the plasmoid. The probing was made at a frequency of $37.5 \cdot 10^9$ c/s, which corresponds to a critical density of $1.7 \cdot 10^{13}$ cm^{-3}.

5. Relative measurements of plasmoid energy were carried out with a thremocouple probe with a cylindrical pickup (4.2 cm length, 1.4 cm diameter). The probe was set on the axis of the vacuum system; its upper surface was screened to prevent contact with the plasma.

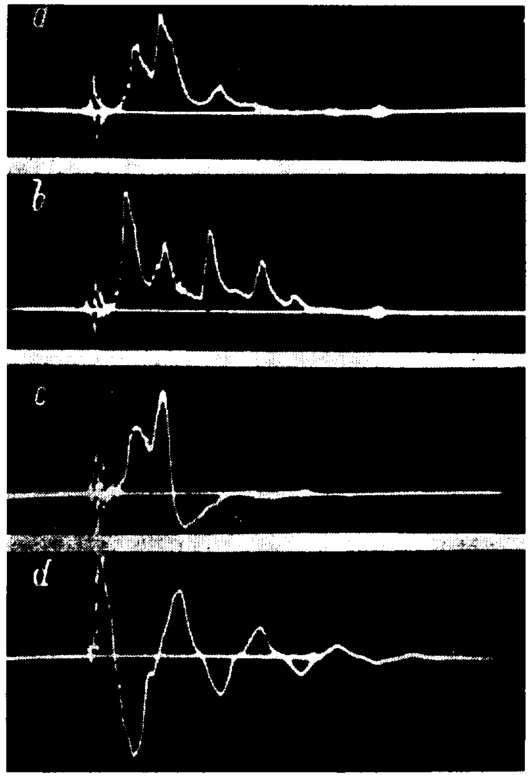

FIGURE 2. Typical signals:
a) photomultiplier signal, $U = 10\,\mathrm{kV}$; b) photomultiplier signal, $U = 15\,\mathrm{kV}$; c) magnetic probe signal, $U = 15\,\mathrm{kV}$; d) signal of the one-turn loop, $U = 15\,\mathrm{kV}$.

Results of measurements

The mass composition of the plasmoids was determined for various delay times and various source voltages. The table lists the relative content of ions in the plasmoid as a function of the delay $\Delta\tau$ and the source voltage for a constant gas inflow $\Delta V = 3\,\mathrm{cm}^3$. We see from the table that the amount of hydrogen in the plasma (the last row of the table) is between 70 and 90%, depending on the discharge conditions; besides atomic ions of hydrogen, there is also a certain amount of molecular ions, H_2^+ and H_3^+.* The plasma composition is approximately the same with a gas inflow of $\Delta V = 2\,\mathrm{cm}^3$; further reduction of gas inflow increases the relative impurity content.

* The analyzer does not separate H_3^+ and C^{4+}, but the presence of C^{4+} ions is little probable, since no C^{3+} ions are observed.

Delay $\Delta\tau$, µsec	Voltage U, kV	Cu^{2+}, Zn^{2+}	Si^{+}	Na^{+}, Cu^{3+}, Zn^{3+}	O^{+}, Cu^{4+}, Zn^{4+}	N^{+}, Si^{2+},	C^{+}	Na^{2+},	Si^{3+},	O^{2+},	C^{2+},	H_3^{+}	H_2^{+}	H_1^{+}	H_1^{+}, H_2^{+}, H_3^{+}
210	10	x	0.5	x	3.0	x	2.5	x	x	0.5	x	x	1.0	92.0	93.0
	15	x	2.0	x	3.5	0.5	3.0	0.5	x	0.5	x	0.5	2.0	86.0	88.5
	20	1.0	2.0	0.5	11.5	1.0	8.0	1.0	x	1.0	0.5	1.0	2.5	71.0	75.0
270	10	x	0.5	x	3.0	x	2.0	x	x	x	x	0.5	2.0	90.0	92.5
	15	x	1.0	0.5	3.5	0.5	2.5	0.5	x	x	x	1.0	1.0	88.5	90.5
	20	1.5	6.0	1.5	8.5	1.0	6.0	2.0	0.5	0.5	0.5	4.0	3.0	65.0	72.0
350	10	x	1.0	x	6.0	0.5	3.5	x	x	x	x	3.0	5.5	78.5	87.0
	15	0.5	2.0	x	6.5	1.0	4.5	x	x	x	x	2.5	3.5	77.5	83.5
	20	1.0	4.0	1.0	12.5	1.0	5.0	1.5	0.5	x	x	5.0	3.5	64.0	72.5

x — impurity content less than 0.5%.

The main heavy impurities, as with the inductive source /3/, are carbon and oxygen, which intrude from vapors of diffusion pump oil. They can be removed by substituting, say, absorption for diffusion pumps. Another group of impurities are the ions of silicon and sodium – from the glass of the discharge chamber, and the ions of copper and zinc – from the brass electrodes of the gun. The total content of these impurities is a small fraction of the carbon and oxygen content; the intrusion of electrode impurities can apparently be reduced by replacing brass with a more durable material, e.g., stainless steel.

Photomultiplier and probe signals lead to the following conclusion concerning the performance of the source.

Several plasmoids are ejected by the gun, corresponding to the later half-periods of the discharge current, but the first half-period creates, not one, but actually two (for $\Delta\tau = 240-310\,\mu$sec) or three (for $\Delta\tau = 210\,\mu$sec) plasmoids. The multiple plasmoids of the first half-period are apparently attributable to the onset of radial oscillations with the pinching of the discharge in the source. The increase in the number of oscillations for small delay times is apparently due to the smaller gas inflow and, correspondingly, the smaller inertia of the current sheath surrounding the discharge.

Currents circulate in the discharge, in the same direction as the azimuthal component of the source current. Magnetic signals also reveal the presence of two (or three) plasmoids with equally directed currents in the first half-period.

Microwave probing of plasmoids at right angles to the line of their motion led to complete "cutoff" of the signal for a few tens of microseconds, which apparently points to charged particle densities much higher than $1.7 \cdot 10^{13}$ cm^{-3}.

Figure 3 gives a typical plot showing the position of the plasmoids in the tube as a function of time (curves 1–5); these curves have been plotted from the maxima of the visual and the magnetic signals (the time is reckoned from the moment of sparking in the source, the distance from the cylindrical electrode; the dashed vertical lines mark the start of the successive half-periods). We see from the figure that measurements based on visual and magnetic signals coincide.

The muzzle velocity of the successive plasmoids can be determined from the slope of the curves, like those plotted in Figure 3. The results of velocity measurements for various delay times are shown in Figure 4.

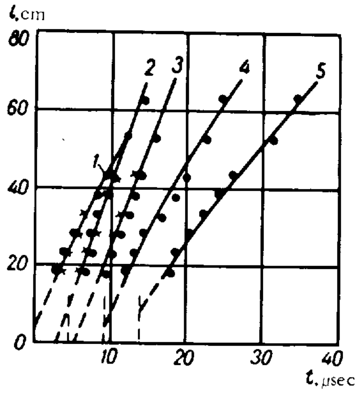

FIGURE 3. The position of plasmoids from successive half-periods as a function of time for $U = 15$ kV, $\Delta\tau = 270$ μsec; ● photomultiplier signals; x magnetic probe signals.

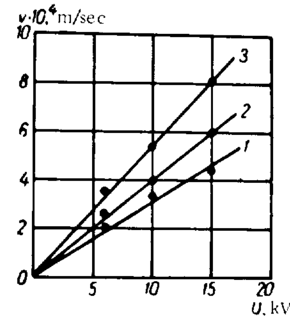

FIGURE 4. The velocity of the plasmoids as a function of the initial source voltage: 1) first plasmoid, $\Delta\tau = 310$ μsec; 2) second plasmoid of the first half-period and the plasmoid of the second half-period, $\Delta\tau = 310$ μsec; 3) first plasmoid, $\Delta\tau = 210$ μsec.

(accuracy 15%). For comparatively long delay times $\Delta\tau = 270-310$ μsec, the velocity of the second plasmoid from the first half-period and the velocity of the plasmoid from the second half-period are equal (curve 2), being somewhat higher than the velocity of the first plasmoid (curve 1). For short delay times $\Delta\tau = 180-210$ μsec,* the velocity of the first plasmoid (curve 3) is conversely higher than the velocities of the successive plasmoids, which are hardly affected by the change in the delay. This is not unlike the velocity-delay relation for the inductive source /3/, despite the considerable difference in the mechanisms of plasma acceleration in the two guns.

As with a plexiglas source /1/, the velocity of the plasmoids linearly increases with voltage, but the absolute values of the velocity are somewhat lower (for constant condenser capacitance and equal working voltage). This is apparently due to the discharge chamber of our source having a volume three times as large as the volume of the plexiglas gun, so that each unit volume contains less energy. Furthermore, the energy in our case is supplied at a lower rate on account of the higher inductance of the source and the additional inductance of the spark gap.

Figure 5 plots the energy of the plasmoids as a function of the source voltage (thermoprobe set at a distance of 20 cm from the source). We see that the experimental points closely follow the parabola $Q \sim U^2$ (solid curve). This is consistent with the plasmoid velocity being a linear function of voltage.

* For $\Delta\tau < 180$ μsec, the source performance became irreproducible.

The "damping" of the currents in the plasmoid is determined as the time of 1/e-folding of the magnetic signal amplitude as the plasmoid moves along the tube. The damping was found to be constant for $U = 10 - 15$ kV and $\Delta\tau = 270 - 310\,\mu$sec, being equal to $1.8 \pm 0.2\,\mu$sec for the second plasmoid of the first half-period and $1.1 \pm 0.2\,\mu$sec for the plasmoid of the second half-period. It is also remarkable that despite the difference in the damping time of the currents in the second and the third plasmoids, the distance over which this damping occurs is the same, being approximately equal to 7.2 ± 1.7 cm for both. Furthermore, the damping length for currents in plasmoids of the inductive source /3/ is also close to this figure, being

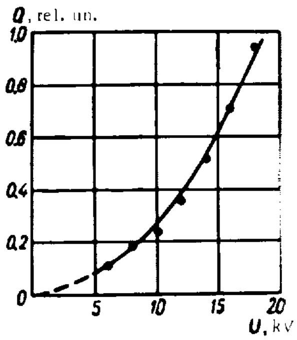

FIGURE 5. The energy of a plasmoid as a function of source voltage.

8.8 cm (the velocity of the plasmoids $22 \cdot 10^4$ m/sec, damping time $0.4 \cdot 10^{-6}$ sec). This coincidence for largely different plasma parameters apparently indicates that the damping is dominated not by the conductivity of the plasma, but rather by its expansion and interaction with the glass wall; we must assume, however, that the rate of expansion is proportional to the translational velocity of the plasmoid.

The experiments show that our source successfully combines the simple electrical circuitry of /1/ with the high purity of the plasma in /3/; the plasmoids, however, are somewhat slower and apparently have a smaller density.

BIBLIOGRAPHY

1. AZOVSKII, Yu. S., I. T. GUZHOVSKII, B. G. SAFRONOV, and V. A. CHURAEV. – ZhTF, 32:1050. 1962.

2. VOITSENYA, V. S., A. G. GORBANYUK, I. N. ONISHCHENKO, and B. G. SAFRONOV. – ZhTF, 34(2):280. 1964.

3. AZOVSKII, Yu. S., I. T. GUZHOVSKII, Yu. P. MAZALOV, V. V. MANK, B. G. SAFRONOV, and V. A. CHURAEV. – ZhTF, 33:1149. 1963.

4. AZOVSKII, Yu. S. and I. T. GUZHOVSKII. – PTE, 5:186. 1962.

A. A. Kalmykov, V. I. Tereshin, and N. S. Poltavtsev

ENERGY SPECTRA OF THE CONICAL PLASMA SOURCE WITH ELECTRODES

1. Plasmoids created by sources of various geometries were studied by many authors (there are numerous reports and papers on these experiments). A common feature of all these researches, however, is that the methods of investigation applied – magnetic and electric probes, microwave techniques, photomultipliers, etc. – reveal only some macroscopic characteristics of the plasmoid averaged over the entire plasma volume.

It is no less significant to establish the microstructure of the plasmoids, the energy distribution of ions of different masses in various fairly small parts of the plasmoid, etc. These researches will help us to find our way when interpreting the mechanism of plasma acceleration.

We investigated according to this program one of the many plasma guns, namely the conical source with a return conductor and a pulsed gas inlet /1/. The plasmoids created by this source were analyzed with the drift mass spectrometer that we had designed /2/ and which proved to be suitable for the measurements in question.

2. The experimental apparatus is schematically shown in Figure 1. The vacuum chamber was a copper tube 8 cm in diameter and 270 cm long. Coils fitted around this tube over a length of some 150 cm provided a uniform magnetic field with an induction of up to 0.2 Wb/m^2. The plasmoids were created by the conica source /1/. The parameters of the discharge circuit were as follows: total capacitance of condenser bank 6 μF, discharge period 9.6 μsec, condenser bank charged to 21–22 kV. Hydrogen was injected into the source in amounts of from 0.05 to 1.0 $cm^3 \cdot$ atm.

The drift mass spectrometer /2/ was set axially and it was used in basic measurements of plasma composition and of energy distribution of particles in the plasmoids. The spectrometer operates as follows: an ion beam is cut from the plasmoid by a system of diaphragms and is then directed to a modulator. The modulator transmits only part of this beam, having a preset length l_i. The transmitted ions are energy-analyzed with an electrostatic condenser; mass resolution is achieved in the drift space between the modulator and the detector, set at an angle to the axis of the system. The detector signals are fed to the oscilloscope OK-17M.

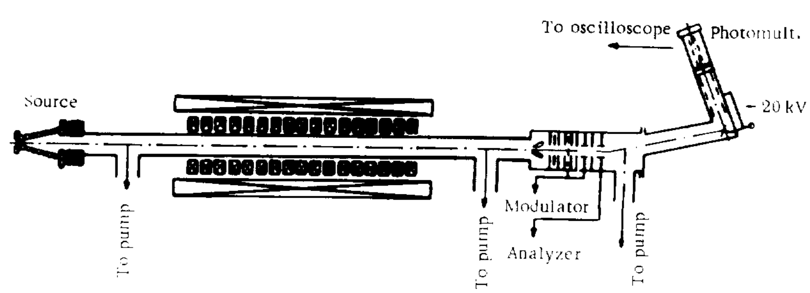

FIGURE 1. A schematic diagram of the apparatus.

Given the distance between the modulator and the detector and measuring the time of flight of particles of a certain energy, we can calculate the ionic mass-to-charge ratio:

$$\frac{m}{Z} = \frac{2W_i\tau^2}{l^2}, \tag{1}$$

where l is the drift length, τ the time of flight of the ions in the drift space, $W_i = kU$ the energy of the ions, U the deflecting voltage applied to the condenser plates, k a geometrical coefficient, which in our case is 6.38.

3. We established that the time of ionization of particles is characteristically small in comparison with the discharge period of the condenser bank. This point is illustrated by the oscillogram in Figure 2, which is the mass spectrum of 60 eV ions. This mass spectrum was taken without modulation, with the entire ion beam cut out by the diaphragms passing through the modulator. In this case the width of the peaks is determined only by the time of particle formation and acceleration in the source and by the time resolution of the instrument.

The time resolution can be written as

$$\Delta t = L\gamma \sqrt{\frac{m}{2W_i}}, \tag{2}$$

where L is the distance from the source to the analyzer, γ the energy resolution of the instrument, m_i the mass of the ions, W_i the energy of the ions. In our experiments

$$\Delta t = 12.4 \sqrt{\frac{m_i}{W_i}}. \tag{3}$$

The width of the peaks was invariably of the same order of magnitude as the instrumental time resolution; moreover, the dependence of the peak width on particle mass and energy is in satisfactory agreement with formula (3). The peak width thus sets an upper bound for the ionization time of the particles in the source. This limit is $\sim 1.5\,\mu$sec for protons with $W_i = 60$ eV and 0.4 μsec for $W_i = 1000$ eV, which is clearly much less than the discharge period.

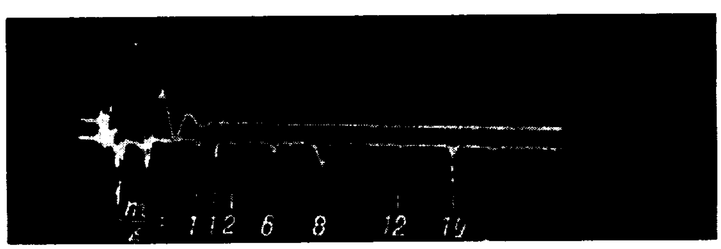

FIGURE 2. A mass spectrum of ions with $W_i = 60$ eV (upper trace, current variation dI/dt).

Independent measurements show that different peaks displayed on the oscillogram taken for ions of one energy correspond to different ionic masses. Given the mass of the ions, their energy, and the distance L from the source to the detector, we can find the time of flight τ_d of the particles in the drift space, assuming that the particles move with a constant velocity; this immediately gives the start point, i.e., the time of ejection of the particles from the source. The start point is found to "drift" relative to the sparking time, depending on the energy of the particles. For protons with energies of from 35 to 150 eV, the start point shifts with increasing energy from sparking to the third half-period. For protons with very low energies, less than 35 eV, we arrive at an absurd result: the particles are ejected from the source before sparking, the earlier the lower their energy (20 eV protons precede the spark by no less than 7 μsec). High-energy protons (with energies above 400–500 eV), however, are fired simultaneously (within the margin of experimental error), some 1–1.5 μsec after sparking.

It is noteworthy that almost all the oscillograms (Figure 2) display two peaks corresponding to the arrival of protons of a given energy (up to 150 eV) but separated by as much as 9.5–10 μsec, i.e., a time comparable with the discharge period. Part of the protons of the given energy apparently forms during a short time in the very first stages of sparking, while more protons of the same energy are produced after one period. The start point of these late protons displays the same energy shift relative to the voltage maximum in the third half-period.

Other ions, in particular C^{2+} and O^{2+}, show a similar double firing.

On the other hand, it does not seem likely that only particles of strictly constant energy are produced at any given time (as it follows from the preceding): particles of various energies should be expected. Furthermore, regardless of the interelectrode voltage and the polarity of the electrodes at any given time, ions of higher energy are generated at later times.

It is therefore our opinion that all the particles form simultaneously (or on several successive occasions), the ionization time being short in comparison with the discharge period. The drift of the start point with particle energy can be attributed to complex interactions of particles with other particles and with fields, taking place in the source and in the drift space. The time of formation of these particles can naturally be identified with the start point of the fast protons (with energies higher than 500 eV), which is independent of energy in this range. The next bunch of particles will then form in the voltage maximum of the third half-period. Identifying the characteristic points in the first and the third half-periods of the oscillograms (Figure 2), we can find the time of flight τ of the particles in the drift space. Comparison of these τ with the previously introduced τ_d (obtained from simple calculations) for various energies makes it possible to evaluate the deviation of the start point relative to the actual ionization time.

The relative change in the two times $\frac{\tau}{\tau_d}$ as a function of particle energy is plotted in Figure 3. The solid curve corresponds to protons generated in the first half-period, and the dashed curve to the protons of the third half-period. The ratio $\frac{\tau}{\tau_d}$ corresponding to protons with energies over 400 – 500 eV is also plotted in this figure.

The suggestion that the energy of the ions could vary in the drift space between the source and the spectrometer was verified with conical diaphragms inserted near the source and cutting a thin plasma stream 1.5–2 mm in diameter. This presumably reduced the density of the analyzed plasma. The measurements of τ and τ_d made under these conditions revealed similar displacement of the start point with energy almost for all the species of particles, with the exception of ions with energies less than 30–35 eV, whose start point was assumed to coincide with sparking time. Thus particles of very low energy may in all probability lose part of their energy in the drift space, so that the average energy of the particles over the entire trajectory will be higher than the measured energy and the time of flight will be correspondingly smaller.

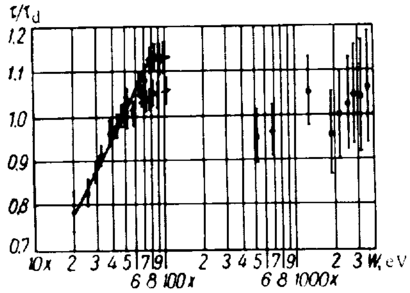

FIGURE 3. Relative change in the time of flight as a function of energy.

For all the other particles, this pnenomenon is possibly attributable to the presence of trapped magnetic fields in the plasma in the source, which prevent the immediate ejection of the particles retaining them in the gun or near it for some time (a few microseconds) after their birth. An analogous explanation was offered in /3/ for the observed delay in the ejection of plasmoids from a gun of similar design.

In connection with the determination of the ionization times, it is interesting to follow the variation of electrode voltage during the discharge. To this end we used a resistive voltage divider coupled into the circuit between the electrodes; the divider signal was fed to the oscilloscope OK-17M. Figure 4 shows some oscillograms of these signals taken for different voltages on the condenser bank. We see that in the very first stages of the discharge, on sparking, the interelectrode voltage is maximal, exceeding considerably the voltage amplitude in successive half-periods of the discharge. The length of this peak is close to 1–1.5 μsec. The smooth trace is then interrupted by the ejection in the third half-period. The singularities on the voltage oscillograms are in good agreement with the times of formation of particles as determined in the preceding. These oscillograms are observed for source voltages $U_s = 17-20$ kV. As the voltage applied to the condenser bank decreases, the third half-period singularity gradually diminishes, and it vanishes entirely for $U_s = 10$ kV. Note that for this voltage the mass spectrum never shows two hydrogen peaks, i.e., all the particles are created in a certain time during the first half-period. In this case the energy fed by the condenser bank into the source is apparently insufficient for secondary ionization.

It is remarkable that the appearance of singularities in the voltage oscillograms sharply interferes with the periodic variation of the electrode voltage.

The foregoing data concerning the ionization and the firing of the particles apparently explain the observed structure of the plasmoids. The plasmoids display space modulation in such a way that the light high-energy ions (protons) are concentrated in the head, the heavy ions of lower energies trailing behind.

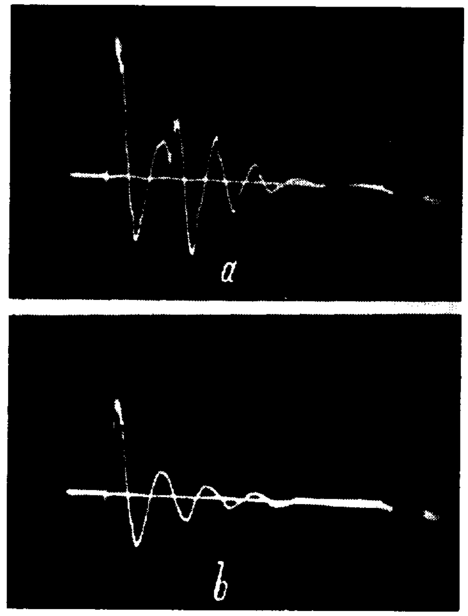

FIGURE 4. Electrode voltage in time:
a) $U_s = 18$ kV; b) $U_s = 10$ kV.

4. The mass analysis of plasmoid ions carried out with the drift mass spectrometer shows that, besides hydrogen ions (protons and H_2^+), the plasmoid also contains the impurity ions C^{3+}, C^{2+}, N^{2+}, O^{2+}, C^+, N^+, O^+, F^+, Si^+, Cu^+, whose presence is attributable to the erosion of electrodes and insulators, as well as the evaporation of diffusion pump oil during the discharge. This mass composition is in good agreement with the results obtained with a Thomson mass spectrograph, which give a proton content of 80–85% in the plasmoid.

The mass spectrometric data obtained for ions of various energies enabled us to plot the energy distribution of the protons and of the impurity ions for various modes of source operation (the variable quantities were the voltage applied to the source condensers U_s, the gas inflow ΔV, and the delay τ_s between the opening of the valve and the sparking). A comparison of the energy spectra obtained for various values of the parameters U_s, ΔV, and τ_s shows that the performance of the source substantially depends on whether the delay τ_s is greater or smaller than a certain critical τ_s^{cr}. The critical delay τ_s^{cr} is insensitive to the actual choice of U_s and ΔV, but it sharply changes with the polarity of the condenser bank relative to the source electrodes. We shall therefore consider the results pertaining to two radically different modes of source operation.

For the first case, when $\tau_s > \tau_s^{cr} = 200\,\mu$sec, no protons with energies higher than 150 eV were recorded in a fairly wide range of values of U_s (from 10 to 20 kV), ΔV (from 0.049 to 0.98 cm^3. atm), and τ_s (from 200 to 500 μsec), while the impurity ions were much more energetic (up to 1500 eV). It is remarkable that the mean energy of the protons and of the medium-weight impurity ions (e.g., C^{2+}, O^{2+}) is 30 – 40 eV under these conditions.

Figure 5 plots the energy distribution of protons for $U_s = 19$ kV, $\Delta V = 0.49\ cm^3 \cdot$ atm, $\tau_s = 260\,\mu$sec. Here the solid curve corresponds to the energy spectrum of the protons generated in the first half-period, while the dashed curve is the energy spectrum of the third half-period protons (the vertical axis gives the amplitude ratio of the signals picked up by the drift spectrometer in units relative to the width of the energy slit ΔW for a given particle energy W, $\Delta W = 0.06\,W$). In this case the mean energy was 30–35 eV ($v \simeq 8 \cdot 10^4$ m/sec) and 70–75 eV ($v \simeq 1.15 \cdot 10^5$ m/sec) for the first and the third half-period protons, respectively. An analysis of mass spectra obtained for different modes of source operation shows that the mean particle energy increases with the source voltage U_s. These data are in good agreement with the results obtained by other methods (magnetic probes, photomultipliers, etc.) in /1/. The mean proton energy also somewhat increases with the decrease of the delay time τ_s between fairly wide limits (from 500 to 200 sec). The increase of the mean particle energy is invariably accompanied by an overall broadening of the energy spectrum.

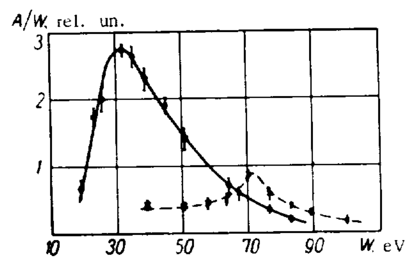

FIGURE 5. The energy spectrum of protons in plasmoids generated in the first mode of source operation ($\tau_s > \tau_s^{cr}$).

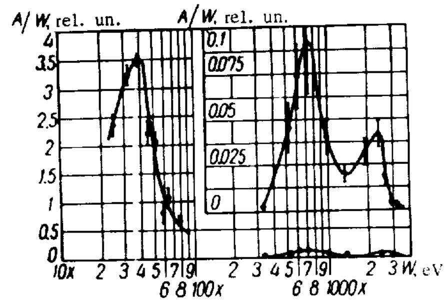

FIGURE 6. The energy spectrum of protons with the source operating in the second mode.

In the second case, with delay times $\tau_s < \tau_s^{cr} = 200\,\mu$sec and moderate gas inflow ($\Delta V < 0.196$–$0.294\ cm^3 \cdot$ atm), the plasmoids carry a considerable amount of protons with energies of a few kiloelectronvolts and even tens of kiloelectronvolts. The peak energies of the impurity ions are somewhat smaller in this case (by 30–40%) than the energy of the fastest protons. Figure 6 gives (in semi-logarithmic coordinates) the energy spectrum of protons generated for $U_s = 19$ kV, $\Delta V = 0.196\ cm^3 \cdot$ atm, $\tau_s = 180\,\mu$sec. On sparking, three distinct hydrogen plasmoids are seen to form in the gun, with mean energies of 40 eV ($v \simeq 0.85 \cdot 10^5$ m/sec), 700 eV ($v \simeq 3.7 \cdot 10^5$ m/sec) and 2.5 keV ($v \simeq 7 \cdot 10^5$ m/sec).

These results were obtained with the inner electrode (near the apex of the cone) maintained at a positive potential in the time of sparking. When the polarity of the source electrodes is reversed by switching the leads of the condenser bank, the outcome of the experiment is not affected provided the delay τ_s does not exceed $150\,\mu$sec (i.e., in this case $\tau_s^{cr} = 150\,\mu$sec). Note that in both cases the peak proton energies are twice as high as the energies of the charged particles accelerated by the interelectrode field

in the very first stages of the discharge, when this field is maximal (e.g., for $U_s = 10$ kV, protons with energies of ~ 18 keV were registered).

Crude estimates neglecting the different angular distributions of ions of different energies indicate that the slow hydrogen plasmoid ($W_i \sim 30-40$ eV) and the two fast plasmoids carry approximately the same number of particles.

Analogous results are obtained in the two operating modes if a driving magnetic field is impressed over a region of ~ 150 cm between the source and the analyzer.

The special conditions required for the formation of fast protons (with energies > 500 eV) and the constancy of the start point for these particles, in distinction from the group of slow particles (with energies of up to 150 eV), indicate that the slow and the fast particles are accelerated by two radically different mechanisms. A crucial condition for the formation of fast protons is that the gas admitted by the time of sparking does not fill the entire interelectrode space; the fast particles are possibly created in the spark. Further study is required to establish the detailed features of the acceleration mechanism of fast particles.

BIBLIOGRAPHY

1. AZOVSKII, Yu. S., I. T. GUZHOVSKII, and B. G. SAFRONOV. – This volume, p. 239.

2. KALMYKOV, A. A., A. D. TIMOFEEV, Yu. I. PANKRAT'EV, and V. I. TERESHIN. – This volume, p. 191.

3. BIEGER, W., H. GRESSER, P. NOLLAND, and H. TUCZEK. – Z. Naturforschung, 4(18a): 453. 1963.

A. A. Kalmykov, Yu. I. Pankrat'ev, and M. G. Nozdrachev

ON THE GENERATION OF FAST PARTICLES IN A PLASMA SOURCE

Two groups of particles were observed in the output of plasma guns of various types – a slow group with drift energies ~ 100 eV and a fast group with energies of up to 20–25 keV. In /1–5/ it has been shown that all these sources – coaxial gun, conical source, Bostick's button-type source – have much in common: the moving plasmoid forms simultaneously, in a time which is very short in comparison with the discharge period ($\sim 0.5\ \mu$sec). Ions of different masses have a broad velocity (energy distribution, and the moving plasmoid spreads continuously. The head of the plasmoid mainly contains plasma whose ionic component consists of fast protons, while the slow hydrogen ions and the heavier impurities concentrate midway along the plasmoid and in its tail. Over fairly large drift lengths, the hydrogen head may apparently separate from the bulk, moving as an individual bunch of plasma. This fast component is of considerable interest, since it mainly consists of hydrogen ions and carries the major part of the energy acquired by the plasmoid as a whole.

Since all plasma sources have much in common and the acceleration mechanism is apparently the same in all of them, it is only logical to choose the simplest, button-type source for investigating the influence of various factors, e.g., source geometry and electrical parameters of the discharge circuit, on the creation and acceleration of fast particles.

Basic results

The setup is described in /2/. A button-type source was used, with a capacitor $C = 0.1\,\mu F$, U up to 20 kV. A rotating device was provided, changing the position of the source axis relative to the axis of the analyzing system. The moving plasmoid was analyzed with a drift mass spectrometer with an electrostatic analyzer, whose operation is described in detail in /1,2/.

Energy distributions were plotted for plasma ions with different $\frac{m}{Z}$ (m the mass of the particle, Z its charge). All the energy distribution curves are peaked around the same energy /2/, but they are essentially different in the region of high energies. For $\frac{m}{Z} = 1$ (H^+ ions), the energy distribution extends up to ~20 keV, while for higher $\frac{m}{Z}$ the curves are truncated at much lower energies.

Typical distribution of H^+ ions are shown in Figure 1; the source voltage is the parameter of these curves. We see that the content of fast particles sharply decreases with the decrease of source voltage.

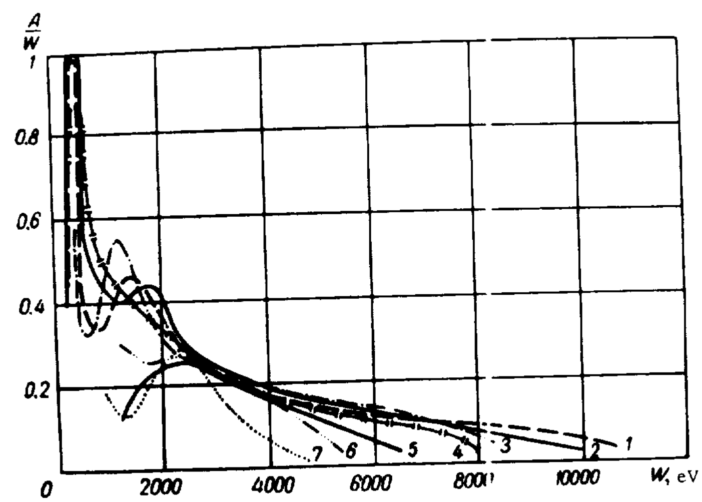

FIGURE 1. Energy distribution of H^+ ions for various source voltages U: 1) 18.7 kV; 2) 17 kV; 3) 15 kV; 4) 14 kV; 5) 10 kV; 6) 9 kV; 7) 7 kV.

In /2/ the angular distribution of the emerging particles was measured: particles of higher energies moved in a progressively narrow solid angle, while the slow particles displayed an almost isotropic angular distribution. As the plasmoid moves down the system, the losses of the slow particles to the walls are therefore much higher, and the energy distribution is highly sensitive to the distance from the source. In /5/ no particles with energies less than 1 keV were recorded at a distance of 300 cm. Furthermore, the fast particles emerging from the button source make a certain angle with the axis of the system; this deflection depends on the polarity of the voltage applied to the source electrodes: the exit velocity of the fast particles is parallel to the direction of the source electrode maintained at a positive potential.

These results are confirmed by measurements with an electrostatic probe. If the probe is set to intercept the fast particles, it registers the arrival of ions with velocities of 10^8 cm/sec. If the source is rotated through a certain angle relative to the initial axis, these particles are no longer picked up by the probe.

An important factor in the performance of plasma guns is the source geometry. The button source used in our experiments was prepared in four varieties shown in Figure 2. These sources differ in the following.

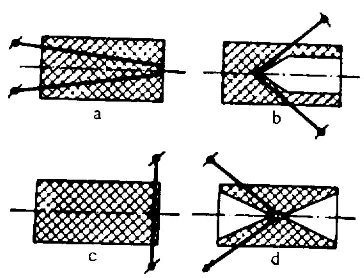

FIGURE 2. Different source geometries.

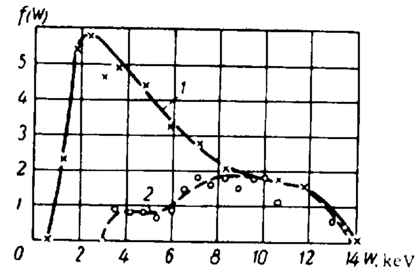

FIGURE 3. Energy distribution of H^+ ions (source geometry d).

According to Bostick /9/, the plasma is accelerated by the magnetic field set up by the current through the source electrodes, in the direction of decreasing magnetic pressure (Figure 2,a). We have established, however, that the plasma emerges from the source also in the opposite direction (Figure 2,d). The number of fast particles in all the four cases is almost constant; it is only the amount of slow particles that decreases in comparison with the output in Figure 2,a. For the source geometries in Figures 2c, d, we plotted the energy distribution of the plasma ions emerging in two opposite directions. The results are shown in Figure 3: curve 1 is the spectrum of particles whose motion is aided by the magnetic pressure, curve 2 the spectrum of particles opposed by the magnetic pressure. The two distributions overlap in the region of high energies. The main difference is observed for low energies: slow particles aided by the magnetic pressure are much more numerous.

The magnetic pressure for a given source geometry depends on the current flowing through the source electrode. The discharge current can

be varied by coupling additional active resistances or inductances into the discharge circuit. We plotted the energy distribution of H^+ ions for different additional resistances (30 and 60 ohm). Although the peak value of the discharge current changed considerably, the distribution curves were affected in a small degree (Figures 4, 5). When additional inductances were coupled into the discharge circuit, the upper bound of the particle energy increased, but the mean energy of the slow ions decreased (Figure 6). It is noteworthy that for fairly high inductances the plasma is generated multiply, on several successive occasions, which is at variance with the case of low inductances, when all the plasma is created at one time /2/. Independent probe measurements show that for a discharge period $T = 30\,\mu$sec and a length of $500\,\mu$sec (commonly, the discharge period was $\sim 1.6\,\mu$sec and the length $\sim 7\,\mu$sec), the probe registers a succession of plasmoids of decreasing amplitude during $\sim 300\,\mu$sec.

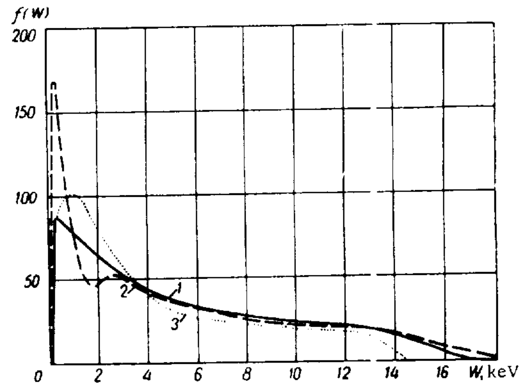

FIGURE 4. Energy distribution of H^+ ions for different resistances in the discharge circuit:
1) 60 ohm; 2) 32 ohm; 3) 0.1 ohm.

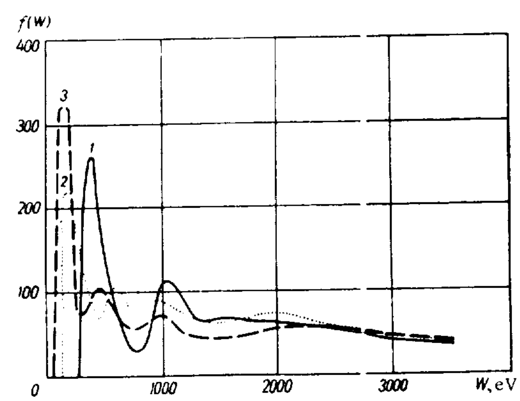

FIGURE 5. Energy distribution of H^+ ions for different resistances in the discharge circuit (the emphasis on the low-energy region):
1) 0.1 ohm; 2) 30 ohm; 3) 60 ohm.

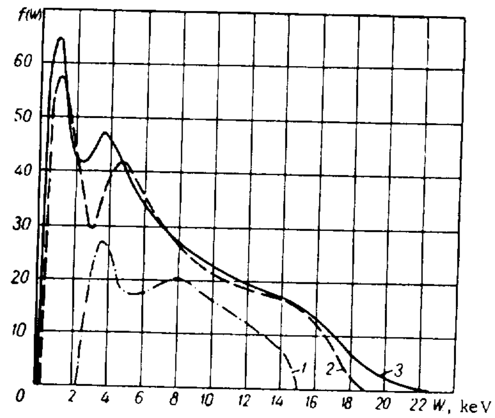

FIGURE 6. Energy distribution of H^+ ions for various inductances L in the discharge circuit, various oscillation periods T, and various discharge lengths t:
1) $L = l_1$, $T_1 = 1.6$ μsec, $t = 7$ μsec; 2) $L = l_2$, $T_2 = 2.2$ μsec, $t = 15$ μsec; 3) $L = l_3$, $T_3 = 30$ μsec, $t = 400$ μsec ($l_3 > l_2 > l_1$).

It is noteworthy that the introduction of additional resistances and inductances in the discharge circuit considerably reduced the content of ions with large $\frac{m}{Z}$; their mean energy also decreased, while the width of the H^+ peaks, characterizing the ionization time at a given energy /2/, increased.

Discussion of results

The electrodynamic model of plasma acceleration is commonly accepted /9,10/. Our results, however, show that at least the fast particles are unaccountable for within the framework of this model. In /10/ a formula is given for the energy acquired by the plasmoid under the electrodynamic acceleration model:

$$\frac{\varepsilon}{E} = \frac{bx}{L_0 + bx}, \qquad (1)$$

where ε the energy of the plasmoid, E the total energy stored in the condenser bank, b the inductance per unit length of the source, x length of accelerator electrodes, L_0 total inductance of condenser bank and leads.

We see from this formula that the total energy acquired by the plasmoid should increase with the effective source inductance. The source was provided with "rails" and we measured the energy distribution of H^+ ions as a function of their length (Figure 7). However, no increase in the mean energy was observed. The number of fast particles actually decreased with increasing "rail" length. Figure 8 plots the energy distribution of H^+ ions for a minute coaxial source (diameter of external cylinder 10 mm, internal cylinder 4 mm, plexiglas insulator). The distributions were taken for various lengths of the coaxial and various immersion depths of the inner electrode relative to the end faces. The measurements show that the number

of fast particles remained virtually constant in the energy interval between 3 and 18 keV: it is only the number of slow particles that changed.

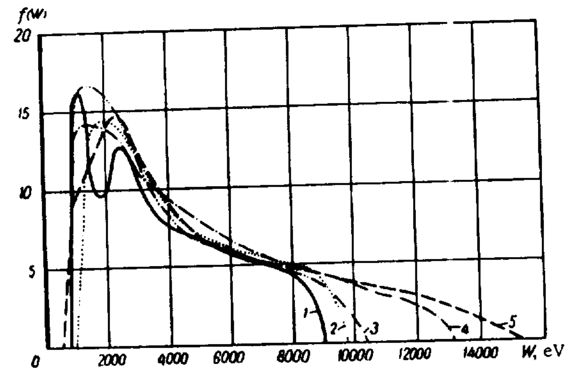

FIGURE 7. Energy distribution of H^+ ions for various lengths of source "rails":
1) 33 mm; 2) 30 mm; 3) 19 mm; 4) 10 mm; 5) 0 mm.

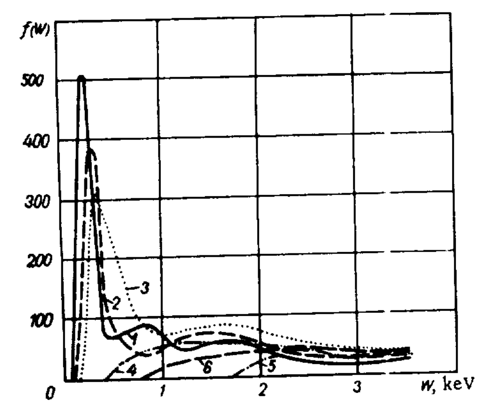

FIGURE 8. Energy distribution of H^+ ions in a minute coaxial source (the low-energy part of the distribution) for various distances of the insulator from the source end face a and of the end point of the central electrode from the source end face h:
1) $a = 0$, $h = 0$; 2) $a = 5$ mm, $h = 0$; 3) $a = 15$ mm, $h = 0$; 4) $a = 30$ mm, $h = 0$; 5) $a = 30$ mm, $h = 15$ mm; 6) $a = 30$ mm, $h = 33$ mm.

The energy corresponding to formula (1) can be compared with the energy obtained in measurements. The plasmoid energy in our experiments is estimated as follows. The number of particles in the energy distributions that we have plotted is given in arbitrary units. These distributions, however, can be converted, though crudely, into absolute figures. From the energy distributions for ions with various $\frac{m}{Z}$, we can reconstruct the waveform of the density and the current signals in time (at a certain point

along the path of the plasmoid); these signals are then compared with the cutoff of 3-cm microwave signals and with the probing signal at the same point. From the cutoff of the 3-cm signal we have the density of the plasma at a certain time. The density of the plasma is also known in arbitrary units for the same time, and we can thus calculate the arbitrary-to-absolute conversion factor.

The oscillogram of the probing signal can analogously be transformed to give the number of particles arriving at the probe as a function of time; the results are then compared with the relation calculated from the energy distribution in arbitrary units. The absolute values of one arbitrary unit obtained by these two techniques are in fairly good agreement.

Having thus "calibrated" the ordinate of the energy distribution curves, we can easily find the total number of particles in the plasmoid and the overall energy of the plasma. The total energy was found to be one and a half times as large as that predicted by (1).

Our experiments show that the creation and the acceleration of the fast particles are essentially independent of source geometry and the parameters of the discharge circuit. This is apparently possible if the plasmoid is created at the very first stage of the discharge, as suggested in /2/. The formation of fast particles is invariably reflected in a singularity in the discharge current oscillogram and in the presence of exceptionally high voltage on the source electrodes.

The high voltage on sparking may cause the appearance of fast particles. The source voltage is determined by the inductance and the resistance of the spark gap; if there are factors leading to a sharp change in the resistance or the inductance, the source voltage will also change radically. The resistance can be altered by the onset of two-stream instabilities in the plasma. The inductance will change considerably if the plasma density varies. Any of these factors may produce a high voltage in the discharge circuit, leading to effective acceleration of the particles.

Another probable mechanism is the rapid heating of electrons followed by acceleration of ions by the expanding electron gas. This mechanism was discussed in /6, 7, 8, 11, 12/.

The experimental data on hand, however, are still insufficient for unambiguously deciding in favor of any particular mechanism of plasma acceleration.

BIBLIOGRAPHY

1. KALMYKOV, A. A., A. D. TIMOFEEV, Yu. I. PANKRAT'EV, and V. I. TERESHIN. – This volume, p. 191.
2. KALMYKOV, A. A., A. D. TIMOFEEV, Yu. I. PANKRAT'EV, and M. G. NOZDRACHEV. – This volume, p. 204.
3. KALMYKOV, A. A., V. I. TERESHIN, and N. S. POLTAVTSEV. – This volume, p. 245.
4. KALMYKOV, A. A., S. A. TRUBCHANINOV, V. A. NABOKA, and L. A. ZLATOPOL'SKII. – This volume, p. 219.
5. MARSHALL, J. and T. F. STRATTON. – Nucl. Fusion Suppl., part 2, 663. 1962.
6. HENDEL, H. W. and T. T. REBOUL. – Phys. Fluids, 5(3): 363. 1962.

7. FOWLER, R.G., G.W. PAXTON, and H.G. HUGHES. – Phys. Fluids, **4**: 234. 1961.

8. NORINDER, H. and O. KARSTEN. – Ark. Mat. Astr. Fys., A. 36 Pt. 4. 1949.

9. BOSTICK, H.W. – Phys. Rev. **104** (2): 292. 1956; **106** (3): 404. 1957.

10. LINHART, J.G. – Nucl. Fusion, **1** (2): 78. 1961.

11. PAXTON, G.W. and R.G. FOWLER. – Phys. Rev., **128** (3): 993. 1962.

12. FOWLER, R.G. and J.D. HOOD. – Phys. Rev., **128** (3): 991. 1962.

INTERACTION OF PLASMA WITH MAGNETIC FIELDS. SHOCK WAVES IN PLASMA

I. I. Demidenko, V. G. Padalka, B. G. Safronov, and
K. D. Sinel'nikov

INTERACTION OF PLASMOIDS WITH TRANSVERSE MAGNETIC FIELDS

The results of experiments concerning the interaction of plasmoids with transverse magnetic fields have some bearing on the problem of plasma injection into magnetic traps.

Bostick et al. /1/ showed that plasmoids move at right angles to the magnetic field much more slowly than in a free space. Part of the plasmoid in this case will move in the direction of the magnetic field.

The interaction of plasmoids with transverse magnetic fields was also investigated in /2/, where the velocity of the plasmoids along the magnetic lines of force was measured.

The present paper analyzes in greater detail the interaction of a plasma with a transverse magnetic field: plasma parameters have been determined for transverse and longitudinal motions.

Apparatus and procedure

A schematic diagram of the experimental system is shown in Figure 1. The plasmoids were created by a conical source /3/ with a plexiglas discharge chamber 1. An eight-turn helix wound onto the outer surface of the chamber served as a return conductor. A 3 μF capacitor bank was discharged through the source when its voltage reached 15 kV. The period of the discharge current 8.0 μsec. The source was separated from the vacuum chamber by a copper grill of 0.7 mm^2 mesh. The plasmoids consisted of the ions of hydrogen, carbon, oxygen (plexiglas decomposition products), aluminum, and iron (the components of the ring and cylindrical electrodes). The time-constant magnetic field was set up by two solenoids 2 carrying equal currents; length of each solenoid 45 cm.

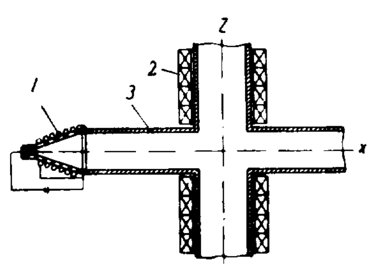

FIGURE 1.

A copper tube 3 with an i. d. of 8 cm transported the plasma from the source to the region with the transverse magnetic field; the distance from the plasma source to the axis of the solenoid was 70 cm. The field coils

were fitted around a copper tube 4 with an i.d. of 10 cm. Residual gas pressure in the system $\sim 1.3 \cdot 10^{-3}$ N/m^2.

Plasmascopes, magnetic and electric probes, and Thomson's mass analyzer were employed as diagnostic tools.

The magnetic and the electric probes could be moved longitudinally and transversally to the magnetic field. The magnetic probes were enclosed in a glass tube; they registered the variation of the magnetic flux through the probe section due to the flow of the plasma; an RC cell was used as an integrating unit, whose signal was fed through an amplifier 103-I to an oscilloscope OK-17M.

The electric probe in our experiments registered the ionic plasma component only: it was maintained at a negative potential ~ 50 V. To prevent excitation of the plasma by the electric field of the charged probe, the latter was screened by a fairly dense grounded net. These probes measured the longitudinal and the transverse motion of the plasmoids in the magnetic field.

Plasmascopes /4/ were applied to establish the configuration of the plasma penetrating through the transverse field and captured by it. A plastic scintillator was used as the luminescent screen of the scope, and not layers of zinc sulfide as in /4/. This arrangement is more convenient operationally, since it ensures higher reliability and greater uniformity of luminescence. The plasmascopes were moved on rods inside the system longitudinally and transversally to the magnetic field.

The mass composition of the plasma created by the conical source and of the plasma penetrating through transverse magnetic fields of various strengths and captured by them was determined with Thomson's mass analyzer (method of parabolas).

Results and discussion

Plasmascopes moving along the axes z and x were applied to determine the configuration of the plasma penetrating through the transverse field and captured by it. A diaphragm with a central hole 10 mm in diameter was provided at the inlet of the plasma into the transverse field ($x = -9$ cm); the plasma beam passing through the diaphragm was collimated with fairly high precision at right angles to the magnetic lines of force. Figure 2 shows some photographs taken with a plasmascope moving along the magnetic field (plasmoid configurations in the xy plane, injector to the right); the plasmascope was set in the position $z = 2$ cm. Photographs taken with a plasmascope moving across the magnetic field ($x = 5$ cm) are given in Figure 3, where the luminous distribution on the screen reflects the distribution of plasma density in the yz plane. The photographs in Figure 2 and 3 correspond to a magnetic field of $2.7 \cdot 10^{-2}$ T at the origin. The top photographs were obtained with the field pointing along the negative z axis, the bottom photographs with the field parallel to the positive z axis.

It follows from Figure 2 that a plasmoid injected into a transverse magnetic field is deflected toward the positive or the negative y axis, depending on the actual direction of the magnetic field. This is attributable to the longitudinal polarization setting in when the plasmoid enters a transverse field. The vector of this longitudinal polarization points against

FIGURE 2.

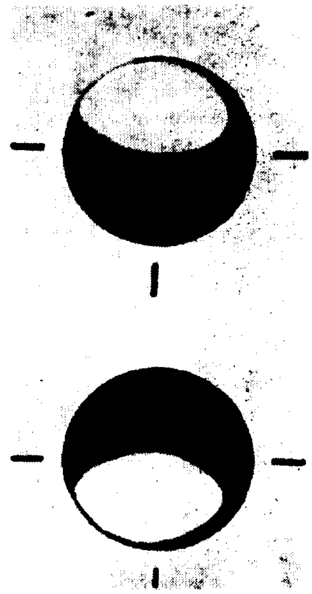

FIGURE 3.

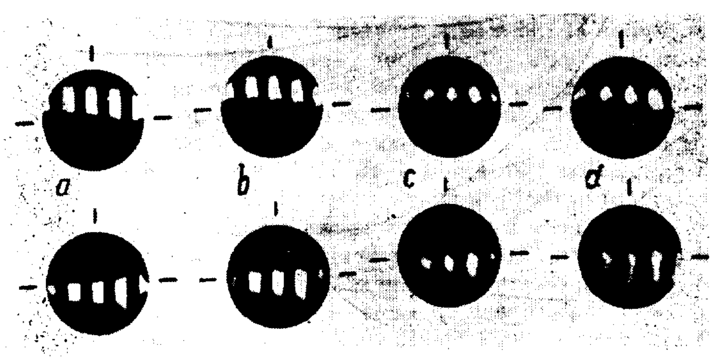

FIGURE 4.

the motion of the plasmoid, and the plasmoid drifts at right angles to its velocity vector with a speed $\sim \frac{E}{H}$. Longitudinal polarization is observed only when the plasmoid is injected into the transverse field; it does not occur when the plasmoid moves in a uniform magnetic field, and the lateral drift stops. Indeed we see from Figure 2 that the plasmoid traces a straight line at a certain angle to the x axis, since the magnetic field gradient along the x axis near the axis of the magnetic system is negligible (the diameter of the scope screen is 7 cm).

To determine the spatial distribution of the particle velocities in a plasma captured by the magnetic field, a fine reticular diaphragm was provided at z = 8 cm, splitting the plasma into several jets. The holes in the diaphragm are aligned with the y axis; their size and the separation between them are constant, being equal to 8 mm. The plasma passing through this diaphragm was recorded by a plasmascope moving along the magnetic field. The results are shown in Figure 4, where the top and the bottom rows of photographs correspond to oppositely directed magnetic fields; injector to the right. These photographs were taken at distances 1, 10, 20, and 30 cm from the diaphragm, respectively (magnetic field strength $2.7 \cdot 10^{-2}$ T). We see from Figure 4 that the plasma flowing in the direction of the magnetic field closely adheres to the lines of force: even at distances of 30 cm from the reticular diaphragm, the thin plasma jets 8 mm thick do not overlap, forming distinct traces on the scope screen. The spatial velocity distribution of the ions in a plasma captured by the magnetic field is thus highly directional, or beamed.

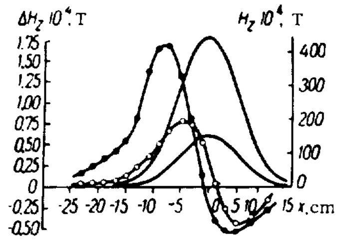

FIGURE 5.

Magnetic probes moving along x and z axes were applied to determine the displacement of the magnetic field by the moving plasmoids; the diaphragm inserted at the plasma inlet for the purpose of plasmascope measurements was removed. Figure 5 shows the peak amplitudes of the magnetic signal as a function of the position of the probe on the x axis. The probe registered the difference of the magnetic fields ΔH_z occurring in the absence of plasma and when a plasmoid passed by. This figure also gives the distribution of the transverse magnetic field H_z along the x axis. The variation of the magnetic field strength was measured for magnetic fields of $4.5 \cdot 10^{-2}$ T (the black dots in Figure 5) and $1.5 \cdot 10^{-2}$ T (circles) at the origin.

It follows from Figure 5 that the magnetic signal increases with the magnetic field strength, whereas its peak shifts in the direction of smaller x. However, the displacement of the magnetic field by the plasma is very slight (a similar situation was observed in /5/).

The magnetic probe signals point to two effects: compression of the magnetic field prior to the arrival of the plasmoid in the probe space, and subsequent expansion of the previously compressed magnetic field. These two effects are time-resolvable if they are of comparable magnitude; otherwise, the signal registered will correspond either to compression or expansion. Figure 6 shows typical oscillograms of the magnetic probe signal for a transverse magnetic field of $4.5 \cdot 10^{-2}$ T. The first oscillogram

(Figure 6, a) was taken at $x = -15$ cm; here the magnetic probe registered only expansion of the magnetic field (the preliminary field compression is slight). At $x = -1$ cm (Figure 6, b), the preliminary compression and the

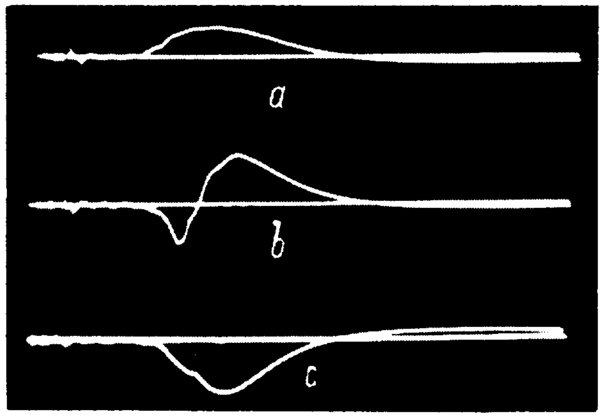

FIGURE 6.

subsequent expansion of the magnetic field are of comparable magnitude, and the two effects are resolved in time. At $x = 11$ cm (Figure 6, c) it is the compression that predominates.

The results obtained for the displacement of the magnetic lines of force by a plasma moving along the field are plotted in Figure 7. The measurements were made with magnetic probes set on the z axis at $x = -4$ cm (curve 1) and $x = +1$ cm (curve 2). The transverse magnetic fields at the origin

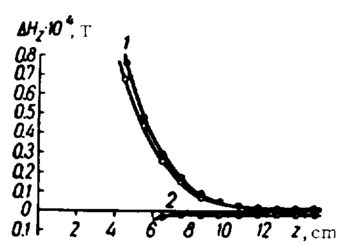

FIGURE 7.

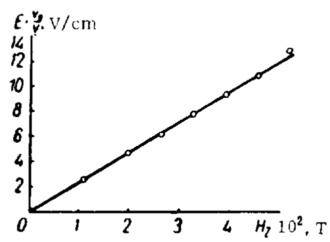

FIGURE 8.

were $4.5 \cdot 10^{-2}$ T (dark dots in Figure 7) and $1.5 \cdot 10^{-2}$ T (circles). The magnetic signal falls off very rapidly as the plasmoid moves along the magnetic field. The probe set at $x = -4$ cm shows that the magnetic lines of force are driven out by the plasmoid, while the probe at $x = +1$ cm registers compression of the magnetic field relative to the field geometry in the absence of plasma; the actual displacements are again very small.

Control tests were made by measuring the electric field of polarization setting in when the plasmoid crosses the transverse magnetic field. The polarization field is a function of the velocity of the plasmoid in the external

magnetic field and of the internal magnetic field in the plasma. Therefore, to find the magnetic field in the plasma, we must make independent measurements of the polarization field and of the velocity of the plasma along the x axis. Polarization measurements were carried out using two $4 \times 2.5 \text{ cm}^2$ plates separated by 2 cm. The plates were inserted in the plasma stream, and the polarization signal impressed on them was transmitted directly to the oscilloscope plates. The velocity of the plasma in various magnetic fields was determined with electric probes. In Figure 8, the straight line represents the polarization field calculated for a plasma whose velocity is equal to the velocity of a plasma without any external magnetic field and whose internal field is assumed to be equal to the field in vacuum (the circles in the figure correspond to the experimental values of the polarization field multiplied by $\frac{v_0}{v}$, where v_0 is the velocity of the plasma without external magnetic field, and v the velocity in a field of given strength). This automatically compensates for the deceleration of the plasma when the magnetic field strength is increased. The excellent fit between the experimental results, determined by the field in the plasma, and the calculated line plotted for the field in vacuum confirms the previous conclusion that the passage of plasma produces a negligible displacement of the magnetic field lines.

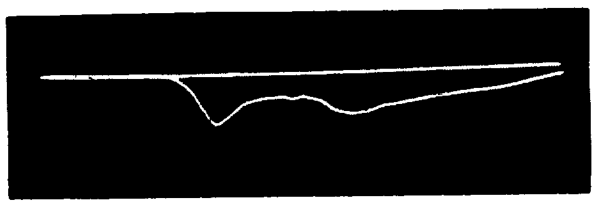

FIGURE 9.

The velocities of a plasma moving across the magnetic field and captured by the field were measured with electric probes registering the ionic component of the plasma. A typical oscillogram of a probe signal is shown in Figure 9. The two maxima on the oscillogram, the first of which hardly shows in magnetic signals (see Figure 6), can be identified with two plasmoids. The velocity of the plasmoids was determined from the slope of the straight line plotting the displacement of the probe as a function of the time between the occurrence of the first maximum and a certain point of the discharge current through the source. In our experiments, the velocity of the first plasmoid was $2.3 \cdot 10^4$ m/sec; the velocity of the second plasmoid was much less. This configuration is apparently attributable to the spontaneous velocity distribution of the particles. The first plasmoid apparently consists of hydrogen ions and multiply charged impurity ions, whereas the second, slow plasmoid is made up from singly charged ions of carbon, oxygen, and the components of the source electrodes.

The velocity of the plasma trapped by the magnetic field was measured with probes moving along the magnetic field at $x = -4$ cm and $x = +1$ cm. Figure 10 plots the results of these measurements for two values of the transverse magnetic field, $1.5 \cdot 10^{-2}$ and $4.5 \cdot 10^{-2}$ T (Δz the displacement

of the probes in cm; $\Delta\tau$ the time between the first maximum of the electric probe signal and a certain point of the discharge current, in μsec). The experimental points for the $1.5 \cdot 10^{-2}$ T magnetic field are marked by circles and those for the $4.5 \cdot 10^{-2}$ T field by dark dots. The linear dependences for the probe at $x = -4$ cm are given by curves 1, and those for the probe at $x = +1$ cm by curves 2. It follows from Figure 10 that the velocity of the plasma along the magnetic field is the same for the two probes, being equal to $4.8 \cdot 10^4$ m/sec in $1.5 \cdot 10^{-2}$ T fields and $6.3 \cdot 10^4$ m/sec in $4.5 \cdot 10^{-2}$ T fields; this is not much less than the velocity of the plasma created by the source. On the other hand, from the time delay of the signal of the $x = +1$ cm probe relative to the $x = -4$ cm probe, we can calculate the average velocity of the plasma across the magnetic field. For $1.5 \cdot 10^{-2}$ T fields, this velocity is $2.1 \cdot 10^4$ m/sec, and for $4.5 \cdot 10^{-2}$ T, it is $1.5 \cdot 10^4$ m/sec, which is less than the initial velocity of the plasma. The plasma propagating along the magnetic field is wedgeshaped; the perpendicular to the leading front of the plasma does not coincide with the direction of its motion.

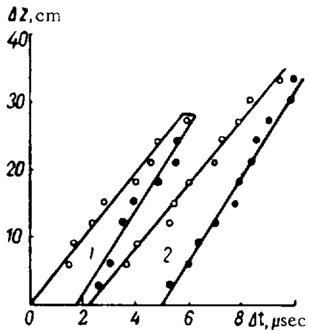

FIGURE 10.

TABLE 1

Ion	Percentage composition of plasma, $H=0$	Percentage composition ($H = 4.5 \cdot 10^{-2}$ T)	Percentage penetration ($H = 4.5 \cdot 10^{-2}$ T)	Percentage composition ($H = 7.25 \cdot 10^{-2}$ T)	Percentage penetration ($H = 7.25 \cdot 10^{-2}$ T)
H^+	11.5	5.2	30%	1.0	5%
C^{+4}	<1	<1	—	<1	—
C^{+3} O^{+4}	<1	<1	—	<1	—
O^{+3}	2.0	<1	—	<1	—
C^{+2}	7.8	4.2	37%	4.0	31%
O^{+2}	3.8	0.8	15%	<1	—
C^+	42.2	55.7	90%	58.6	82%
O^+	12.7	16.3	88%	18.0	84%
Al^+	7.7	5.7	50%	5.8	45%
Fe^+	11.5	11.1	70%	11.6	60%

The partial escape of the plasmoid along the magnetic field cannot be interpreted within the framework of the guiding center model. Indeed, all the particles injected into the magnetic field have velocities pointing at right angles to the field, without any component along the lines of force. The anisotropy of the magnetic pressure experienced by the plasmoid is much too small to account for the effect. The longitudinal drift of the plasmoid is possibly attributable to an electrostatic mechanism connected with the spread of the space charge arising on polarization. There is, however, no convincing proof of this, and the question remains open for the time being.

Thomson's mass analyzer (the method of parabolas) was applied to determine the composition of the plasmoids created by the conical source and of the plasma penetrating through the transverse magnetic field and captured by the field. We also determined the fraction of ions passing through magnetic fields of various strengths. The percentage composition of the plasma penetrating through the magnetic field and of the plasma generated by the source is listed in Table 1; the percentage of ions passing through the magnetic field is also given in the table. We see from Table 1 that the plasma emerging from a transverse magnetic field is noticeably depleted in hydrogen and multiply charged impurity atoms; the singly charged ions of carbon, oxygen, aluminum, and iron pass fairly well. An analysis of the composition of the plasma trapped by the magnetic field revealed hydrogen ions and singly ionized carbon; no other ions were detected. The percentage composition of the trapped plasma is given in Table 2. Note that the percentage content of hydrogen given in this table is too low, since measurements were made only after the plasma had left the magnetic field, so that it was depleted in light components. However, even if we neglect this depletion, the content of hydrogen is fairly high.

TABLE 2

Ion	Percentage composition of plasma	
	$H = 2.7 \times 10^{-2}$ T	$H = 4.5 \times 10^{-2}$ T
H^+	30	60
C^+	70	40

In conclusion we should note that the interaction of hydrogen plasma with a transverse magnetic field is highly sensitive to the content of the heavy impurities. A pure hydrogen plasma, whose impurities had all been removed in the field of a thoroidal solenoid, could not be injected into a transverse magnetic field. The pure hydrogen plasma was readily captured by very weak magnetic fields, and did not penetrate through. On the other hand, the plasma of a conical source containing all the heavy ion impurities fairly easily passed through the transverse fields applied in our experiments. The role of heavy ions in the interaction of a plasma with a transverse magnetic field requires further study.

BIBLIOGRAPHY

1. HARRIS, E.G., R.B. THEUS, and W.H. BOSTICK. – Phys. Rev., 105: 47. 1957.
2. SAFRONOV, B.G., V.P. GONCHARENKO, and D.K. GONCHARENKO. – In: "Fizika plazmy i problemy upravlyaemogo termoyadernogo sinteza", Vol. 1, p. 111. Kiev, Izdatel'stvo AN UkrSSR. 1962.
3. AZOVSKII, Yu.S., I.T. GUZHOVSKII, B.G. SAFRONOV, and V.A. CHURAEV. – ZhTF, 32: 1050. 1962.
4. SINEL'NIKOV, K.D., B.G. SAFRONOV, V.G. PADALKA, and I.I. DEMIDENKO. – ZhTF, 33: 1055. 1963.
5. ALIDIERES, M., R. AYMAN, Ph. T. JOURDAN, F. KOECHLIN, and A. SAMAIN. – Phys. Fluids, 6: 407. 1963.

A.A. Kalmykov and V.I. Tereshin

INTERACTION OF DENSE PLASMOIDS WITH A SPACE-PERIODIC MAGNETIC FIELD

1. Our previous investigations /1/ concerning the interaction of plasmoids with space-periodic magnetic fields were made with low-density plasmoids, $\sim 10^{15}-10^{16}\,\mathrm{m}^{-3}$. It was shown that when the condition of the characteristic parametric resonance of protons was satisfied,

$$\omega_{B_0} = \frac{eB_0}{m_p c} = \frac{2\pi}{L} v_{\parallel} \qquad (1)$$

(B_0 the magnetic induction of the uniform magnetic field region; L the period of the modulation field; $v_{\parallel}$ the translational velocity of the protons; m_p the mass of the protons), a considerable redistribution of energy between the components was observed: up to 50% of the energy of the translational motion of the plasmoid particles was converted to the energy of Larmor precession. The magnetic moment of the particles would in fact increase between fairly wide limits around the frequency (1), i.e., the resonance region is fairly broad. It is significant that almost all the results obtained with the low-density plasmoids are in satisfactory agreement with some calculations made in the one-particle approximation /2, 3/.

The aim of the experiments discussed in this paper was to investigate the interaction of comparatively dense plasmoids ($\sim 10^{20}-10^{21}\,\mathrm{m}^{-3}$) with space-periodic magnetic fields; these plasmoids are of applied significance, and if the experimental results prove to be positive, the dense plasmoids can be effectively employed for injection into various magnetic traps. One-particle approximation does not hold for high-density plasmoids, and the final outcome of the experiments is therefore by no means obvious.

2. The experimental setup is schematically shown in Figure 1. The uniform magnetic field with an induction of up to 0.2 Wb/m^2 could be generated over a region some 110 cm long. This field was space-modulated by a few magnetic coils in "head-on" coupling. The space-modulation period was 10 cm, and there were a total of 8.5 periods. The maximal value of the component b_z of the magnetic field reached 0.0175 Wb/m^2. The depth of modulation $\frac{b_z}{B_0}$ ranged between 0.10 and 0.20. The periodic

field geometry terminated with a magnetic mirror $B_{mir} \simeq 0.05-0.4\ Wb/m^2$ (the work was done for mirror ratios $\frac{B_{mir}}{B_0}$ not exceeding 4—4.5).

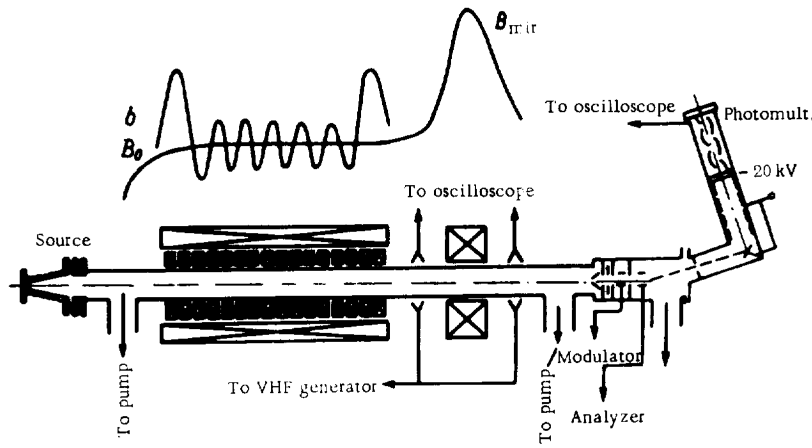

FIGURE 1. Schematic diagram of the experimental setup.

The plasmoids were created by a conical source with a return conductor /4, 5/ with pulsed gas inlet. The main parameters of the source discharge circuit: capacitance of condenser bank $6\mu F$, discharge period $9.6\mu sec$, voltage applied to the condenser bank ~ 17—2? kV, $\Delta V \simeq 0.49\ cm^3 \cdot atm$. The operation of this source is described in detail in /4, 5/. The conical source injects plasmoids with a density ~ $10^{20}-10^{21}\ m^{-3}$, whose ionic component contains up to 80—85% of hydrogen. The mean energy of the protons in the plasmoid at a distance of 2 cm from its axis is 40—45 eV. Ions of different masses and energies are distributed in space so that the fast light ions concentrate in the plasmoid head, the slower heavy ions trailing behind. Ions of a given mass and energy are concentrated in a region which is very small in comparison with the size of the plasmoid.

A copper pipe 8 cm in diameter and 300 cm long was used as a vacuum chamber. Over a length of 60 cm in the magnetic mirror region, a porcelain tube was substituted for the copper one, to permit microwave diagnostics.

At a distance of some 300 cm from the source a drift mass-spectrometer /6/ was set, displaced by 2 cm from the axis. This instrument cut a narrow ion beam from the plasmoid; the beam energies were analyzed using an electrostatic condenser, while mass analysis was based on the transit time of the ions in the drift space. Since ions of given mass and energy occupy a fairly tight region in the plasmoid (as we have previously observed), their detection is manifested in a sharp peak on the oscilloscope screen. Figure 2 is an oscillogram of the proton peak with the energy of ~ 40 eV (the source—analyzer drift time of impurity ions of this energy is somewhat greater than the time base employed). The analysis of these peaks recorded for protons of different energies gave the proton energy spectra of the plasmoids under various experimental conditions. The vacuum in the system was never worse than $2.66 \cdot 10^{-4} N/m^2$.

3. The experiments were intended to establish the existence of resonant interaction of plasmoids with a space-periodic magnetic field were based on the following principle. If in a certain group of plasmoid particles passing through a periodic system part of the longitudinal energy is converted into the energy of transverse motion, then with a fairly high mirror ratio, when $\frac{W_\perp}{W} > \left(\frac{B_{\mathrm{mir}}}{B_0}\right)^{-1}$, the particles will be reflected from the magnetic mirror. Whenever the particles pass through the system so that their initial transverse energy does not change, they freely penetrate through the magnetic barrier and reach the drift mass spectrometer.

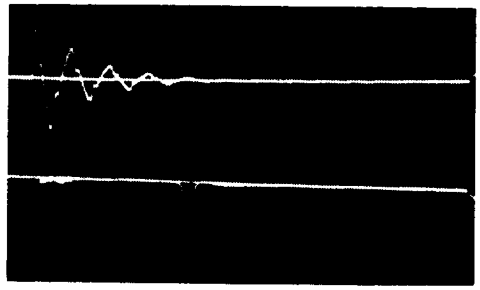

FIGURE 2. An oscillogram of the proton peak with the energy $W_i \sim 40$ eV (top trace—oscillogram of source current variation, $\frac{dI}{dt}$).

The following measurements were thus suggested.

The drift mass spectrometer was used to take the proton energy spectra of the plasmoids passing through the magnetic field configuration for various relations between the induction B_0 of the uniform magnetic field, the amplitude b_z of the axial modulation field, and the magnetic mirror field B_{mir}. For every given pair of values B_0 and B_{mir}, we took comparative proton spectra for plasmoids passing without field modulation and with field modulation of a certain depth $\left(\frac{b_z}{B_0}\right)$. These spectra differ to the greatest extent for modulation depths of $\sim 0.17-0.18$ and mirror ratios of $\sim 2-2.5$. All subsequent experiments were therefore carried out under the following conditions: $\frac{b_z}{B_0} = 0.177$, $\frac{B_{\mathrm{mir}}}{B_0} = 3$ (note that these optimal conditions are consistent with previous experiments /1/).

Figure 3 plots the energy distribution of protons in plasmoids passing through a modulation field (dashed curve) and without modulation (solid curve). These distributions were obtained for a uniform magnetic field $B_0 = 0.055\,\mathrm{Wb/m^2}$. A comparison of the two curves shows that near the energies of 45—55 eV ($0.93-1.02\cdot10^5$ m/sec) the difference in the energy spectra is the greatest: the deviation of the dashed curve from the solid curve clearly points to a resonant mechanism. The proton spectrum of the plasmoids passing through the modulation field "sags" apparently because a certain proportion of particles with energies in the 45—55 eV interval do not penetrate the magnetic mirror: the magnetic moment of

these particles sharply increases due to their interaction with the space-periodic magnetic field. A comparison of the ordinates in the two spectra (Figure 3) gives the relative number of these reflected particles. Some 40—45% of particles with energies in the 45—55 eV range resonate, redistributing not less than 20—25% of their energy (the numerical estimate is based on the condition of particle reflection from the mirror).

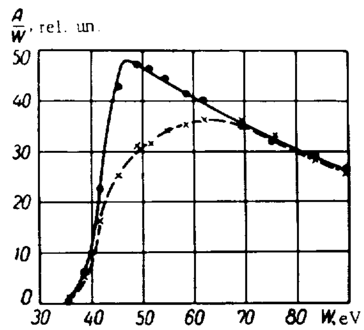

FIGURE 3. Proton energy spectra of plasmoids passing through a magnetic field configuration: solid line $\frac{b_z}{B_0} = 0.177$; dashed line $\frac{b_z}{B_0} = 0$.

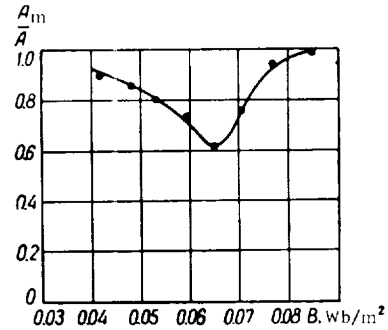

FIGURE 4. The change in the relative number of 54 eV protons penetrating through the magnetic mirror as a function of the uniform magnetic field B_0.

Note that the region of resonant energies for a given magnetic field B_0 shifts in the direction of higher energies as the uniform magnetic field decreases.

Somewhat different measurements were made under the following conditions. The drift mass analyzer was tuned to record protons of a certain energy (Figure 2), specifically $W_i = 54$ eV ($v \simeq 1.02 \cdot 10^5$ m/sec). The induction of the uniform magnetic field B_0 was chosen as the variable parameter. The amplitudes of the proton peaks obtained with (A_m) and without (A) modulation were compared for different magnetic inductions. The relative change in the number of particles of a given energy penetrating through the magnetic mirror, $\frac{A_m}{A}$, is plotted in Figure 4 as a function of the uniform magnetic field B_0. We see that the curve represents a distinct resonant dependence with a fairly wide resonance region, ~ 0.015—0.02 Wb/m^2; this is consistent with the width of the resonance region obtained in previous experiments (Figure 3). Similar results were obtained with the mass spectrometer tuned to protons of other energies, but the resonance region was somewhat displaced in accordance with (1).

Another series of experiments investigating the resonant interaction of plasmoids with magnetic fields called for the application of microwave techniques. All measurements were made under the same conditions as before, using a mass spectrometer. The cutoff of 8- and 4-mm electromagnetic waves by plasmoids before and after the magnetic mirror was measured with and without field modulation, for various magnetic fields B_0. The measurements show that for certain values of the magnetic induction, the cutoff becomes considerably longer (by as much as 50%) when modulation

is turned on (without modulation, the length of the cutoffs at 8- and 4-mm wavelengths for plasmoids before the mirror is 100 and 60 μsec, respectively, for $B_0 = 0.06\ \mathrm{Wb/m^2}$, varying with the strength of the driving magnetic field). Oscillograms of these signals are shown in Figure 5.

This cutoff lengthening is apparently observed when part of the particles with a density above the critical value at the given wavelength ($1.8 \cdot 10^{19}$ and $8 \cdot 10^{19}\ \mathrm{m^{-3}}$) is reflected from the magnetic barrier and again passes across the antenna with a certain time delay, i.e., this corresponds to the elongation of a plasmoid with a density greater than n_{cr}. The effect is most pronounced in magnetic fields where particles with energies close to the mean (Figure 3) resonate, since it is in this case that the number of resonance particles is greatest. Figures 6 and 7 plot the relative lengthening $\frac{\Delta\tau}{\tau}$ of the cutoffs when modulation is turned on, as a function of the uniform magnetic field B_0 (here $\Delta\tau$ is the difference in cutoff lengths measured with and without modulation). We see from the graphs that the relative change in cutoff length as a function of the magnetic field follows a resonance curve, and that the resonance regions in these curves are all correlated.

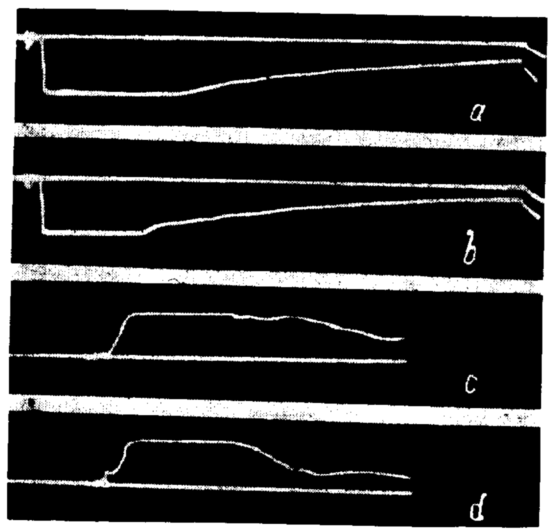

FIGURE 5. Microwave cutoff in plasmoids before the magnetic mirror: a, b) probing with 8-mm electromagnetic wave; c, d) probing with 4-mm electromagnetic wave; a, c) $\frac{b_z}{B_0} = 0.177$; b, d) $\frac{b_z}{B_0} = 0$.

Since we used beamed microwave antennas, the behavior of individual plasmoids could be investigated. In Figure 6, the solid line corresponds to the probing of the central part of a plasmoid 4 cm in diameter with an 8-mm electromagnetic wave, while the dashed curve has been obtained for the part of the plasmoid located on one side of the axial horizontal plane. In the latter case, the cutoff lengthening in resonance is more pronounced; this is apparently so because in the former case a large proportion of the protons in the axial region do not take part in the resonance, since the

radial component of the modulation field is zero on the axis, increasing along the radius toward the periphery.

The solid curve in Figure 7 plots the same dependence as the curves in Figure 6, but here a 4-mm electromagnetic wave is used (the microwave antenna is displaced by ~ 2 cm from the axis).

All the curves are peaked around $B_0 \approx 0.06\,\mathrm{Wb/m^2}$. This result is consistent with the previous data obtained in the one-particle approximation /1/. From (1) it follows that for $B_0 \approx 0.06\,\mathrm{Wb/m^2}$ particles with energies close to $W_i \approx 50\,\mathrm{eV}$ are in resonance, and in accordance with our experiments this energy corresponds to the peak in the energy distribution curve (Figure 3). As the field is further increased ($B_0 > 0.06\,\mathrm{Wb/m^2}$), the relative lengthening of the microwave cutoffs (Figures 6, 7) decreases, but without reaching the zero mark, it again increases in magnetic fields ~ 0.075—0.080 $\mathrm{Wb/m^2}$.

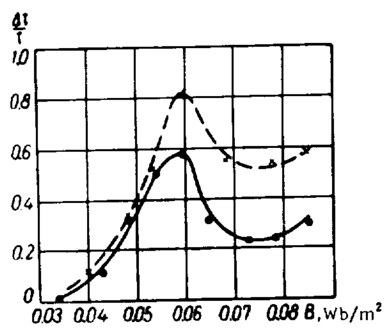

FIGURE 6. Relative lengthening of 8-mm signal cutoff as a function of the uniform magnetic field B_0 (before the magnetic mirror).

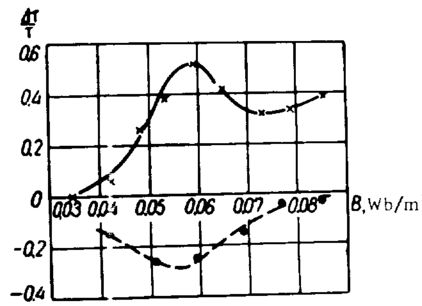

FIGURE 7. Relative change in the length of the 4-mm signal cutoff as a function of the uniform magnetic field B_0.

This trend can be interpreted as follows. In fairly strong fields ($B_0 > 0.06\,\mathrm{Wb/m^2}$), a considerable number of particles with energies above the mean will resonate, so that some plasmoid elongation is observed when these particles are reflected from the magnetic mirror. The growth of the relative cutoff lengthening in fields $B_0 \simeq 0.08\,\mathrm{Wb/m^2}$ is attributable to the resonance of the protons created in the third half-period of the source discharge /5/, whose mean energy is ~ 75 eV ($v \simeq 1.2 \cdot 10^5\,\mathrm{m/sec}$), so that the total number of resonance particles again increases.

Another experimental fact deserves special attention. Despite the very considerable length of the plasmoids (length of microwave cutoff without modulation ~ 70—100 μsec), they are further elongated by as much as 50%, although the resonance particles constitute but a minor fraction of the plasmoid (no more than a few tens of microseconds). Cutoff lengthening is apparently due to the following mechanism. The energy of the resonance protons is redistributed, and they are reflected from the magnetic barrier moving against the prevailing motion of the rest of the plasmoid. On the other hand, the density of the particles near the magnetic mirror may be much higher than the density of the plasmoid tail colliding with the reflected stream. The plasmoid may thus be elongated due to the reflection of its tail from this obstacle as from a rigid wall.

The dashed curve in Figure 7 represents the relative change in the length of 4-mm signal cutoff for a plasmoid penetrating through the magnetic mirror. We see from the graph that the plasmoid is somewhat foreshortened once it has passed through the modulation field; this is also a resonant curve, not unlike those obtained in the probing of plasmoids before the mirror. The maximum contraction of the plasmoid after the mirror is synchronized with its maximum elongation before the mirror, when a high proportion of the protons are reflected from the magnetic barrier.

4. In these experiments we operated with high-density plasmoids (10^{20}—10^{21} m^{-3}) having a large kinetic-to-magnetic pressure ratio, $\beta = \frac{nkT_i}{\frac{B^2}{8\pi}} = 0.5$. Under these conditions, the modulation magnetic field is highly screened, i.e., it cannot penetrate into the plasmoid to any substantial depth. But there is nevertheless a considerable conversion of the translational energy of the plasmoid particles into the energy of Larmor precession when the plasmoids interact with the space-periodic magnetic field. All the results of this study are in good agreement with earlier results /1, 2/, obtained in the one-particle approximation.

The observed resonant redistribution of the particle energy in a dense plasmoid makes these systems suitable for injection into magnetic traps. This technique, due to the substantial increase of the particle magnetic moment, should lead to an effective entrapment of the particles. Furthermore, the plasma accumulating in the trap should be stable. The injection of the plasma into the system makes it possible to avoid beam instabilities, arising when charged particles are injected. On the other hand, combination of these space-periodic fields with fields of trap geometry will apparently enable us to prevent the most harmful mode of instability, namely the convective instability, since the resultant magnetic field in the trap, like in /7/, will increase both along the axis and along the radius (from the center outward). Last, as we have previously observed /1/, this system should lead to resonance filtering of various plasma impurities.

BIBLIOGRAPHY

1. KALMYKOV, A. A., V. I. TERESHIN, S. A. TRUBCHANINOV, and B. G. SAFRONOV. -ZhTF, **32**(5): 579. 1962.

2. FEDORCHENKO, V. D., B. N. RUTKEVICH, and B. M. CHERNYI. - ZhTF, **29**(10): 1212. 1959.

3. SINEL'NIKOV, K. D., B. N. RUTKEVICH, and V. D. FEDORCHENKO. - ZhTF, **30**(3): 249. 1960.

4. AZOVSKII, Yu. S., I. T. GUZHOVSKII, and B. G. SAFRONOV. - This volume, p. 239.

5. KALMYKOV, A. A., V. I. TERESHIN, and N. S. POLTAVTSEV. - This volume, p. 245.

6. KALMYKOV, A. A., A. D. TIMOFEEV, Yu. I. PANKRAT'EV, and V. I. TERESHIN. - This volume, p. 191.

7. BAIBORODOV, Yu. T., M. S. IOFFE, V. M. PETROV, and R. I. SOBOLEV. - Atomnaya Energiya, **14**(5): 443. 1963.

I. I. Bakaev, Yu. G. Zalesskii, N. I. Nazarov, V. T. Tolok, and A. M. Ukrainskii

PENETRATION OF PLASMOIDS THROUGH A MAGNETIC BARRIER IN THE PRESENCE OF R-F FIELDS

The capture efficiency of a magnetic trap with mirrors for plasmoids injected along the trap axis is substantially determined by the transverse energy of the plasmoid particles. In this paper, we present some preliminary results on the penetration of plasmoids through a magnetic mirror in the presence of an r-f field.

The experiments were made on a setup (Figure 1, a) comprising a conical inductive plasma source 4, a plasma guide 1 (2.5 m long), a solenoid 3 setting up a quasistatic magnetic field, and an induction coil 2. When a $6 \cdot 10^{-3}$F condenser bank is discharged through the solenoid, the magnetic field increases to its maximum in 10 msec. Plasmoid injection and all the measurements were made when the magnetic field remained virtually constant. The magnetic field distribution along the solenoid was

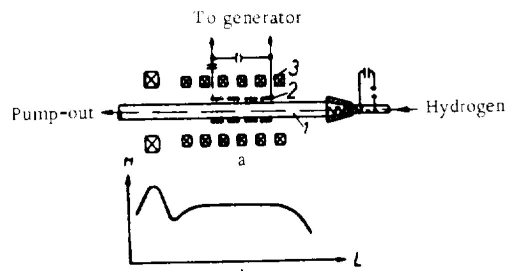

FIGURE 1.

measured by an improved variety of the conventional technique. The magnetic probe traveled on a resistor along the axis of the solenoid, which was fed by the main current. The d. c. voltage applied to the resistor was proportional to the distance along the solenoid. The probe signal was fed to the vertical plates of an oscilloscope (ENO-1), while the time base was connected with the resistor. The oscilloscope screen thus displayed the magnetic field configuration (Figure 2), a trap with two mirrors. The first mirror, the one inside the induction coil (Figure 1, b), had a uniform field region 50 cm long, with a field of up to 480 kA/m. The magnetic field in the second mirror was 720 kA/m, the field between the mirrors 240 kA/m. The absolute strength of the magnetic field was measured by the method of electron cyclotron resonance at 9370 Mc/s. The plasmoid was ejected from a region with a magnetic field close to zero. The parameters of the plasmoid penetrating through the inlet magnetic barrier and traveling in the uniform field region were as follows: velocity $v = 6 \cdot 10^6$ cm/sec, density $n \approx 1.7 \cdot 10^{13}$ cm^{-3}. An induction coil generating a space-periodic electromagnetic field with a wavelength $\lambda_z = 20$ cm fed the r-f energy into the plasmoid. This coil served as the inductance of an oscillator circuit supplied by a 10 Mc/s generator. Natural oscillations with the following

dispersion relation /1/ were excited in a plasmoid passing inside the coil:

$$\frac{k^2c^2}{\omega^2} + \frac{1}{2}\frac{\nu^2c^2}{\omega^2} = \frac{\Omega^2}{\omega\omega_{H_e}}$$

(the high-frequency branch of the fast magnetohydrodynamic wave), where $k = \frac{2\pi}{\lambda_z}$ is the longitudinal wave number, ν the radial wave number, ω the frequency, ω_{H_e} electron cyclotron frequency, Ω electron plasma frequency, c the velocity of light.

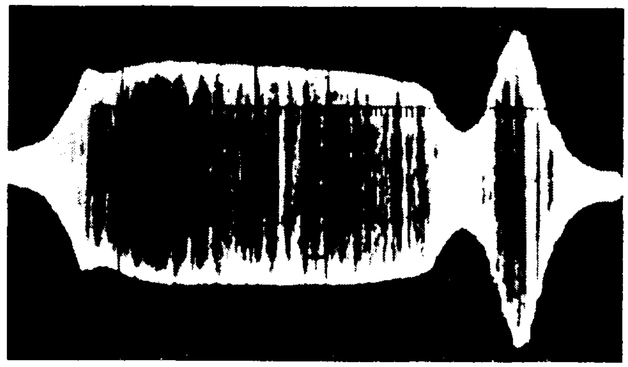

FIGURE 2.

Resonance excitation and damping of these oscillations in a plasma column was treated in detail in /1, 2/. Figure 3 plots the r-f voltage as a function of the magnetic field. This curve points to an effective resonant absorption of r-f energy by a plasma in magnetic fields of 120 kA/m. For the case of longitudinal wave propagation (k = 0.3, ν = 0), the density calculated from the dispersion relation is $2 \cdot 10^{13}\,\mathrm{cm}^{-3}$, which is in good agreement with the plasmoid density measured from 8-mm signal cutoff.

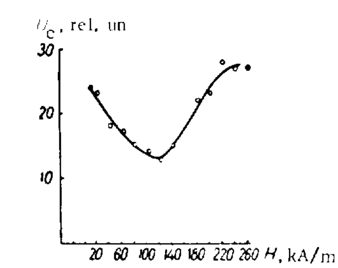

FIGURE 3.

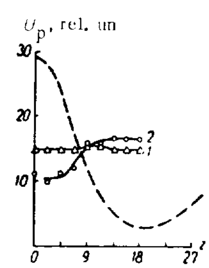

FIGURE 4.

Diamagnetic measurements were carried out to establish the influence of the r-f field on the penetration of the plasmoid through the magnetic mirror. The diamagnetic probe comprised a multiturn coil with an i.d. of 2 cm, enclosed in a glass envelope. The probe fitted around the plasma column, traveling along the solenoid axis. The sum signal was fed to an oscilloscope (OK-17). The results of measurements are shown in Figure 4. The origin corresponds to the position of the magnetic field maximum in the second mirror. During measurements, the probe traveled in the direction of decreasing magnetic field, into the trap.

The dashed curve in Figure 4 plots the distribution of the magnetic field along the z axis. Curve 1 gives the amplitude of the diamagnetic signal as a function of z when the r-f field is turned off. The pattern changes when an r-f field is impressed. Curve 2 shows a considerable attenuation of the diamagnetic signal in the mirror. Signal attenuation in the mirror and its amplification in the trap should be attributed to the reflection of the plasmoid from the mirror.

In this preliminary experiment with low r-f power we thus established that the absorption of r-f energy by a plasmoid had a considerable influence on its capture in a magnetic trap with mirrors.

BIBLIOGRAPHY

1. STIX, T.H. – Phys. Rev., 106 : 1146. 1957.

2. HOOK, W.M., M.A.ROTHMAN, P.AVIVI, and J.ADAM. – Phys. Fluids, 5(7): 864. 1962.

3. NAZAROV, N.I., A.M.ERMAKOV, V.D.DOLGOPOLOV, K.N.STEPANOV, and V.T.TOLOK. – Nucl. Fusion, 3 : 255. 1964.

L.I.Krupnik, N.G.Shulika, and P.A.Demchenko

THE BEHAVIOR OF DENSE PLASMOIDS IN A LONGITUDINAL MAGNETIC FIELD

We have previously proposed a method /1/ for the probing of a plasma by a beam of fast neutral hydrogen atoms. This technique makes it possible to measure with fair accuracy the density of the plasma intercepted by the beam, as well as its distribution in time and in space.

After the first satisfactory results had been obtained, the method of plasma probing with a neutral beam was applied to investigate the various modes of operation of the conical plasma source with pulsed hydrogen inlet used in experiments, and also the behavior of dense plasmoids moving in a longitudinal magnetic field.

The geometry

Experiments were made using the same setup as in /1/. The system consists of two basic units: a source of fast neutral particles and an ejector of pure hydrogen plasmoids moving in a longitudinal magnetic field. Figure 1 shows the geometry of the chamber where the plasmoid moves. The plasmoid generated by the source 1 is ejected into an extended chamber 2 immersed in a magnetic field set up by the coils 3. The chamber 2 is ~ 1.5 m long, 80 mm in diameter. To prevent free access of nonionized gas from the source, which trails by diffusion behind the plasmoid, and to eliminate, at least partially, the influence of the inlet geometry of the magnetic field on the plasmoid, a diaphragm 4 some 25 mm in diameter was provided in the region of the uniform magnetic field, at a distance of 15—20 cm from the coil entry position. At a distance of ~ 1.2 m from the source 1 and ~ 80 cm from the diaphragm 4, the plasmoid was intercepted by the probing neutral beam 5 with a diameter of 5 mm. A collecting iris 6 was provided directly before the beam; its diameter could vary continuously from 8 to 50 mm during the experiments. Depending on the particular experimental conditions, additional diaphragms 7 were interposed in positions I, II, III (either one of these, or all three together).

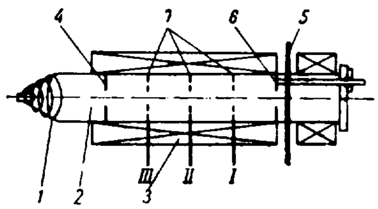

FIGURE 1.

Experimental results

The first series of experiments dealt with the various modes of operation of the conical plasma source with pulsed gas inlet used in our work. Its design and parameters are described in detail in /2/.

The operating mode of the pulsed valve through which the gas was admitted into the chamber was chosen so that the nonionized gaseous tail was reduced to the minimum without affecting the intensity of the plasmoid.

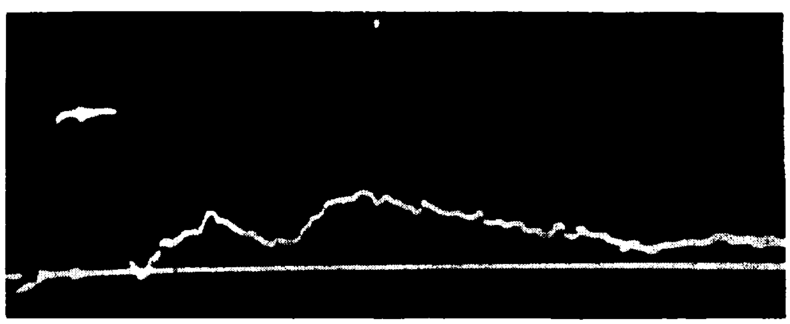

FIGURE 2.

Figure 2 is a typical oscillogram showing the attenuation of the neutral beam crossing a plasmoid. These oscillograms always distinctly show the leading fully ionized component with a maximum some 7 μsec after the signal start, and the second trailing component peaked around 35—40 μsec after the signal start, with the degree of ionization gradually falling off toward the plasmoid "tail". In all subsequent experiments we studied the behavior of the two plasmoid components.

Figure 3 gives the plasmoid density as a function of the voltage applied to the source condensers, as a characteristic of the source operating mode. We see from the figure that the plasma density increases steeeply with the discharge voltage, possibly reaching $10^{15}\,cm^{-3}$.

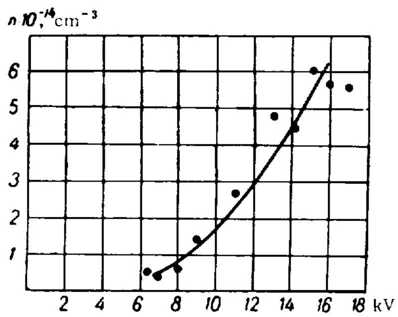

FIGURE 3.

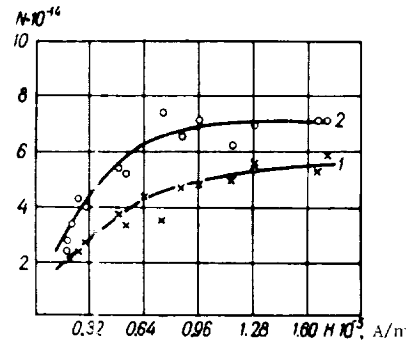

FIGURE 4.

In all subsequent experiments the plasma source was maintained in a constant mode of operation, allowing a moderate inflow of gas into the source (some 0.5 cm^3) and a voltage of 10—12 kV. High voltages entail high impurity content, which of necessity lowers the accuracy of our technique.

Figure 4 gives the transmission of the plasma through the chamber as a function of the longitudinal magnetic field. Curve 1 plots the number of ions in the first maximum (7 μsec after the signal start), and curve 2 the number of ions in the second maximum (35 μsec after the signal start). We see from the figure that in low magnetic fields the particle density increases sharply as the field rises to $(0.72-0.80)\cdot 10^5$ A/m; then the growth slows down and gradually levels off. In these fields almost the entire plasmoid passes through the inlet diaphragm, and further increase in magnetic field strength does not affect the density of the plasma.

The next series of experiments was concerned with the divergence of the plasmoid in various magnetic fields. We plotted several plasma density curves for various geometries of plasmoid propagation in the chamber 2 (Figure 1).

Figure 5 gives the plasmoid density as a function of the magnetic field in the following cases: curve 1 — inlet diaphragm 4 and free motion of the plasmoid along the chamber to interception with probing beam; curve 2 — additional diaphragm interposed in position I (30 mm in diameter) at a distance of 15 cm before the probing beam; curve 3 — three additional diaphragms interposed in positions I, II, III (each 30 mm in diameter).

An analysis of these curves shows that in weak magnetic fields the plasmoid spreads easily, possibly due to collision with chamber walls and subsequent reflection; this explains the initial trend of the curves, which do not coincide. As the magnetic field increases, the plasmoid is compressed: it is detached from the walls and moves along the chamber with a comparatively small spread. Almost the entire plasmoid passes through the diaphragm in position I, which is obvious from the merging of curves 1 and 2 in Figure 5 in high magnetic fields ($H = 1.6 \cdot 10^5$ A/m). Comparison of curves 2 and 3 indicates that in this geometry the plasmoid in the presence of a magnetic field does not follow the geometrical laws of divergence (otherwise curves 2 and 3 would have merged in high magnetic fields): interposing several diaphragms, we affect the motion of the plasmoid as a whole. This is apparently so because the particles trace helical trajectories in the magnetic field: the particles passing through a single diaphragm are therefore collected from a larger solid angle than that prescribed by the geometry of the diaphragms (oblique incidence of the particles moving in helixes). With three diaphragms, however, particles passing obliquely through one diaphragm are inevitably stopped by the next diaphragm. We must also consider another possibility, namely that the diaphragm introduces a certain perturbation into the plasma stream, causing additional divergence (flow of a fast stream past an obstacle). Anyhow, these distortions are insignificant, and the separation between curves 2 and 3 in the region of strong magnetic fields is not much greater than the margin of error.

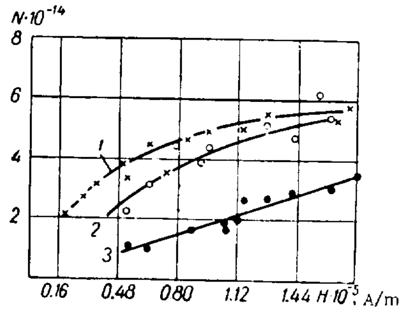

FIGURE 5.

Special experiments were carried out to find the radial distribution of plasma density.

Figure 6 gives the number of H_1^+ particles passing through the iris 6 with its diameter varying from 8 to 50 mm; the iris was interposed directly before the probing beam, no other intermediate diaphragms were used (curve 1). A diaphragm with a diameter equal to the inlet diameter 4 was then set in position I and alternately moved to positions II (curve 2) and III (curve 3). Differentiation of these curves gave the radial distribution of density in the plasmoid and its spread in the presence of a magnetic field. Figure 7 plots the results of this differentiation. We see from the figure that the plasmoid has a well defined dense component, spreading but insignificantly in the presence of a magnetic field. The mean plasmoid diameter changes from 20 to 25 mm between the two ends of the chamber, over a path some 80 cm long. All the foregoing applies to the fully ionized leading plasmoid. Analogous dependences were obtained for the second component also.

For the sake of comparison, Figure 8 gives the number of passing particles as a function of the iris diameter for the first (curve 1) and the second (curve 2) plasmoid components. They have the same slope, which corresponds to equal axial density. The derivatives of the two curves are shown in Figure 9 (curves 1 and 2, respectively). It follows that the two

plasmoids have different diameters. Their total diameters are 30 and 45 mm, respectively. The results of this experiment are in excellent agreement with plasmascope observations.

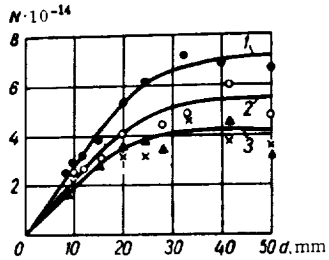

FIGURE 6.

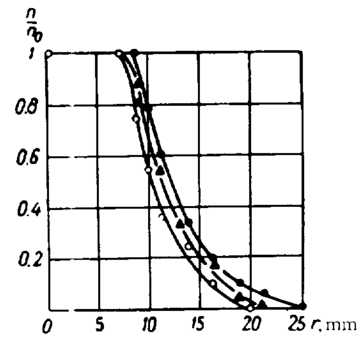

FIGURE 7.

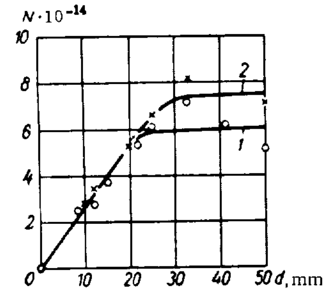

FIGURE 8.

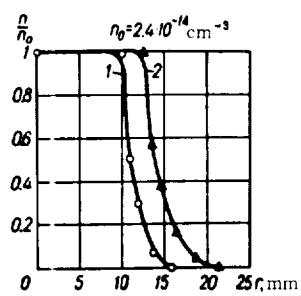

FIGURE 9.

The experiments studying the behavior of a plasmoid in a magnetic field lead to the following conclusions.

The plasmoid has two fairly well defined components. The two components behave identically in the presence of a magnetic field. The spread of the plasmoid is highly sensitive to the magnetic field up to $0.8 \cdot 10^5$ A/m. Further increase in magnetic field strength radically reduces the spread of plasma, and in a field of $1.2 \cdot 10^5$ A/m virtually no plasmoid divergence is observed over a distance of ~ 80 cm. The first and the second plasmoid components have slightly different diameters. The second plasmoid is approximately 1.5 times as broad as the first.

BIBLIOGRAPHY

1. KRUPNIK, L. I. and N. G. SHULIKA. – This volume, p. 197.

2. AZOVSKII, Yu. S., I. T. GUZHOVSKII, and B. G. SAFRONOV. – This volume, p. 239.

N. A. Khizhnyak

INTERACTION OF SMALL PLASMOIDS WITH EXTERNAL MAGNETIC FIELDS

The model of a flexible current-carrying loop is often applied to describe the interaction of small plasmoids with external magnetic fields /3/. This approximation was justified in /4/, where it was shown that the loop model could be obtained by averaging the Lagrangian of a system consisting of numerous positively and negatively charged particles.

The interaction of a plasma stream with external fields can also be described within the framework of magnetohydrodynamics. It would therefore be interesting to consider the advantages and the shortcomings of the two techniques as applied to the analysis of plasmoid interactions.

In this paper we show that the equations of the flexible loop model are equivalent to the magnetohydrodynamic equations, from which they can actually be derived; in some particular cases, however, they are much more convenient in application that the equations of hydrodynamics, as they reduce the problem to one in ordinary differential equations.

In the magnetohydrodynamic approximation, neglecting the dissipative terms, a plasma stream is described by the well known set of equations

$$\varrho\left(\frac{\partial \mathbf{v}}{\partial t} + (\mathbf{v}\nabla)\mathbf{v}\right) = -\nabla p - \frac{1}{4\pi}[\mathbf{H}\,\mathrm{rot}\,\mathbf{H}],$$
$$\frac{\partial \mathbf{H}}{\partial t} = \mathrm{rot}\,[\mathbf{v}\mathbf{H}],\quad \frac{\partial \varrho}{\partial t} + \mathrm{div}\,(\varrho\mathbf{v}) = 0,\quad \mathrm{div}\,\mathbf{H} = 0. \tag{1}$$

A bounded plasma configuration (a plasmoid) is more conveniently treated in terms of Lagrange variables, so that equations (1) take the form

$$\varrho\frac{d\mathbf{v}}{dt} = -\nabla p - \frac{1}{4\pi}[\mathbf{H}\,\mathrm{rot}\,\mathbf{H}],$$
$$\int\limits_S \mathbf{H}d\mathbf{S} = 0,\quad \varrho = \varrho_0\left(\frac{d\mathbf{r}_0}{d\mathbf{r}}\right),\quad \mathrm{div}\,\mathbf{H} = 0, \tag{2}$$
$$d\mathbf{r} = dxdydz.$$

In the second equation of (2), the integral is taken over the area of the plasmoid cross section at right angles to the velocity vector. In the third equation $\left(\frac{d\mathbf{r}_0}{d\mathbf{r}}\right)$ represents the change in the initial volume $d\mathbf{r}_0$ as the plasmoid moves.

The magnetic field $\mathbf{H}$ is the resultant of the field $\mathbf{H}_0$ set up by the coils and the field $\mathbf{H}_1$ of the currents induced in the plasmoid. Hence,

$$\frac{d}{dt}\left\{\int\limits_S \mathbf{H}_1 d\mathbf{S} + \int\limits_S \mathbf{H}_0 d\mathbf{S}\right\} = 0.$$

The integral $\int\limits_S \mathbf{H}_1 d\mathbf{S}$ is equal to the magnetic flux of the currents induced in the plasmoid. This quantity is easily expressible in terms of the total current in the plasmoid, I, and its self-inductance L:

$$\int\limits_S \mathbf{H}_1 d\mathbf{S} = k\frac{LI}{C}, \tag{3}$$

where the factor k is determined by the plasmoid geometry. If the plasmoid is annular, and the surface S is uniquely defined, then $k = 1$. The second equation of (2) thus reduces to the well known equation of electrical equilibrium in the loop approximation

$$\frac{d}{dt}\left\{k\frac{LI}{C^2}+\frac{1}{C}\int\limits_S \mathbf{H}_0 d\mathbf{S}\right\}=0\ , \tag{4}$$

and the total current in the plasmoid can be expressed in terms of a known magnetic field $\mathbf{H}_0$.

Given equation (4), we can proceed with a comparison of the two techniques. The magnetohydrodynamic description of the interaction of a plasmoid with the fields is complicated by the fact that the equations of motion contain the total magnetic field in the plasmoid, while only the field $\mathbf{H}_0$ is known (which is actually a certain function of position and time). The determination of the total field in accordance with equations (1) is a fairly complex problem. On the other hand, with the loop model, relation (4) immediately gives the total induced current in the plasmoid, providing the plasmoid self-inductance and the factor k are known. The difficulties encountered in the magnetohydrodynamic description of plasmoid-field interaction now reduce to the calculation of the plasmoid self-inductance. But, as shown in /4/, the self-inductance of a plasmoid is highly insensitive to such factors as particle density distribution within the plasmoid and the distribution of the induced currents. This implies that the magnetohydrodynamic approximation offers a much too detailed picture of the plasmoid-field interaction, whereas the loop model explains the more salient features of this phenomenon.

In what follows we shall show that the equations of motion of a plasmoid can also be expressed in terms of the total current in the plasmoid and its self-inductance, thus completely justifying the model of the flexible current-carrying loop within the framework of magnetohydrodynamics.

The second relation of (2) or its equivalent (4) are generally considered for the case of adiabatic motion of a plasma. This assumption is thought to simplify the qualitative analysis of plasma motion. In reality, however, this is an imagniary simplification, since the adiabatic conditions are associated with the total magnetic field, which is mostly unknown. It is only in cases when the total field virtually coincides with the externally impressed field, i.e., according to /4/, for low-density plasmoids $\left(n \ll \frac{10^{12}}{r_0^2},\right.$ where r_0 is the plasmoid radius), that the adiabatic conditions are indeed convenient for qualitative analysis of plasmoid motion.

To obtain the equations of motion of a plasmoid in terms of the total current and its self-inductance, we integrate the equation of motion over the plasmoid volume:

$$\int\limits_V \varrho\frac{d\mathbf{v}}{dt}\,d\mathbf{r} = -\int\limits_V \nabla p\,d\mathbf{r} - \frac{1}{4\pi}\int\limits_V [\mathbf{H}_0 \operatorname{rot}\mathbf{H}_1]\,d\mathbf{r} - \frac{1}{4\pi}\int\limits_V [\mathbf{H}_1 \operatorname{rot}\mathbf{H}_1]\,d\mathbf{r},$$

where we made use of the fact that rot $\mathbf{H}_0 = 0$.

Applying the equation of continuity (the third equation in (2)), we can

easily show that

$$\int_V \varrho \frac{d\mathbf{v}}{dt}\, d\mathbf{r} = \frac{d}{dt}\int_V \varrho \mathbf{v}\, d\mathbf{r}. \tag{5}$$

where $\varrho\mathbf{v}$ is the total flux of the plasma. It is made up from the motion of the plasmoid as one whole and from the motion due to the deformation of the plasmoid (radial displacement and longitudinal dilatation or compression).

The term $\int_V \nabla p d\mathbf{r}$ is associated with internal forces; it makes no contribution to the motion of the plasmoid as one whole and its significance is limited to deformation displacements. We therefore must establish the exact meaning of the terms containing the magnetic field.

The total current in the plasmoid is written as

$$\mathbf{I} = \frac{1}{l}\int_V \mathbf{j} d\mathbf{r}, \text{ i. e., } \int_V [\mathbf{j}\mathbf{H}_0]\, dv = l\,[\mathbf{I}\mathbf{H}_0], \tag{6}$$

where l is the length of the loop along the plasmoid periphery, at right angles to the velocity vector.

The total magnetic energy of the currents in the plasmoid is

$$W_{\text{mag}} = \frac{LI^2}{2C^2} = \frac{1}{2C^2}\int_V \mathbf{j}(\mathbf{r})\, d\mathbf{r} \int_V \frac{\mathbf{j}(\mathbf{r}')\, d\mathbf{r}'}{|\mathbf{r}-\mathbf{r}'|}, \tag{7}$$

where L is its self-inductance. In general, L is a tensor, but we shall consider the motion of a plasmoid in an axially-symmetric magnetic field, when only φ-currents are induced in the plasmoid, so that L may be regarded as a scalar. From (6) and (7), we have for the self-inductance

$$L = \frac{l^2}{\left[\int_V \mathbf{j}(\mathbf{r})\, d\mathbf{r}\right]^2} \cdot \int_V \mathbf{j}(\mathbf{r})\, d\mathbf{r} \int_V \frac{\mathbf{j}(\mathbf{r}')\, d\mathbf{r}'}{|\mathbf{r}-\mathbf{r}'|}, \tag{8}$$

where the integral is taken over the entire volume of the plasmoid.

Comparing this expression with the expression for the self-inductance of a plasmoid in /4/, we see that it is identical with the second part of the plasmoid self-inductance, which is of decisive significance in dense plasmoids. It is easily seen that the self-inductance (8) of a plasmoid is determined by its geometry, and not by the position in the interaction space, provided the distribution of currents inside the plasmoid remains constant as it moves in the magnetic field. Indeed,

$$\mathbf{j} = en\mathbf{u},$$

where $\mathbf{u}(\mathbf{r})$ is the velocity of the current-carrying component in the plasmoid. If $\mathbf{u} = \mathbf{u}_0\psi(\mathbf{r})$, where $\mathbf{u}_0$ characterizes the rotational velocity, and $\psi(\mathbf{r})$ is the distribution of these velocities in the plasmoid, we have

$$L = \frac{l^2}{\left[\int_V n(\mathbf{r})\psi(\mathbf{r})\, d\mathbf{r}\right]^2}\int_V n(\mathbf{r})\psi(\mathbf{r})\, d\mathbf{r}\int_V \frac{n(\mathbf{r})\psi(\mathbf{r}')\cos(\varphi-\varphi')\, d\mathbf{r}'}{|\mathbf{r}-\mathbf{r}'|} \tag{9}$$

depending on the plasmoid geometry only.

Let us calculate the quantity

$$\nabla \frac{LI^2}{2C^2}\Big|_{I=\mathrm{const}} = \frac{1}{2C^2}\nabla \int_V \varrho \mathbf{u}_0 \psi(\mathbf{r})\,d\mathbf{r} \cdot \int_V \frac{\varrho' \mathbf{u}_0 \psi(\mathbf{r}')\,d\mathbf{r}'}{|\mathbf{r}-\mathbf{r}'|}\Big|_{|\mathbf{u}_0|=\mathrm{const}}$$

or, applying the equation of continuity (the third equation in (2)), we reduce the integral to the initial volume of the plasmoid

$$\nabla \frac{LI^2}{2C^2}\Big|_{I=\mathrm{const}} = \frac{1}{2C^2}\nabla \int_{V_0} \varrho_0 \mathbf{u}_0 \psi(\mathbf{r}_0)\,d\mathbf{r}_0 \cdot \int_{V_0} \frac{\varrho_0' \mathbf{u}_0 \psi(\mathbf{r}_0')\,d\mathbf{r}_0'}{|\mathbf{r}_0-\mathbf{r}_0'+\vec{\xi}|}\Big|_{|\mathbf{u}_0|=\mathrm{const}}$$

By definition, $\psi(r)$ is invariant under this transformation, while the difference $|\mathbf{r}-\mathbf{r}'|$ acquires an additional term with $\vec{\xi}$ characterizing the deformation of the plasmoid. The gradient is therefore calculated with respect to the variable $\vec{\xi}$, so that

$$\frac{I^2}{2C^2}\nabla L = \frac{1}{2C^2}\int_{V_0} \varrho_0 \psi(\mathbf{r}_0)\,d\mathbf{r}_0 \left[\mathbf{u}_0 \,\mathrm{rot} \int_{V_0} \frac{\varrho_0' \mathbf{u}_0' \psi(\mathbf{r}_0')\,d\mathbf{r}_0'}{|\mathbf{r}_0-\mathbf{r}_0'+\vec{\xi}|}\right] + \frac{1}{2C^2}\int_{V_0} \varrho_0 \psi(\mathbf{r}_0)\,d\mathbf{r}_0 \left[\mathbf{u}_0 \,\mathrm{grad} \int_{V_0} \frac{\varrho_0' \psi(\mathbf{r}_0')\mathbf{u}_0'\,d\mathbf{r}_0'}{|\mathbf{r}_0-\mathbf{r}_0'+\vec{\xi}|}\right),$$

or in original variables

$$\frac{I^2}{2C^2}\nabla L = \frac{1}{C^2}\int_V \varrho(\mathbf{r})\psi(\mathbf{r})\,d\mathbf{r}\left[\mathbf{u}_0 \,\mathrm{rot}\int_V \frac{\varrho(\mathbf{r}')\psi(\mathbf{r}')\mathbf{u}_0'\,d\mathbf{r}'}{|\mathbf{r}-\mathbf{r}'|}\right] +$$

$$+\frac{1}{C^2}\int_V \varrho(\mathbf{r})\psi(\mathbf{r})\,d\mathbf{r}\left(\mathbf{u}_0 \,\mathrm{grad}\int_V \frac{\varrho(\mathbf{r}')\psi(\mathbf{r}')\mathbf{u}_0'\,d\mathbf{r}'}{|\mathbf{r}-\mathbf{r}'|}\right).$$

When the plasmoid moves in an axially-symmetric magnetic field, the velocity $\mathbf{u}_0$ has a φ-component only, while the angle φ enters the expression $|\mathbf{r}-\mathbf{r}'|$ only. On differentiation with respect to φ and subsequent integration between 0 and 2π, the second term vanishes. Hence,

$$\frac{I^2}{2C^2}\nabla L = \frac{1}{C^2}\int_V \left[\mathbf{j}(\mathbf{r})\,d\mathbf{r}\,\mathrm{rot}\int_V \frac{\mathbf{j}(\mathbf{r}')\,d\mathbf{r}'}{|\mathbf{r}-\mathbf{r}'|}\right] =$$

$$= \frac{1}{C}\int_V [\mathbf{j}(\mathbf{r})\,\mathrm{rot}\,\mathbf{A}]\,d\mathbf{r} = \frac{1}{4\pi}\int_V [\mathbf{H}_1 \,\mathrm{rot}\,\mathbf{H}_1]\,d\mathbf{r}. \qquad (10)$$

If the external magnetic field is fairly constant over distances comparable with the size of the plasmoid, the magnetic terms in the equation of motion can be written in the final form

$$\frac{I}{C}[\mathbf{lH}_0] + \frac{I^2}{2C^2}\nabla L.$$

The term with ∇L is associated with the deformation of the plasmoid, and it has no influence on the motion of its mass center. The motion of

the plasmoid as one whole is therefore described by the equation

$$MN\frac{d^2z}{dt^2} = \frac{2\pi r}{C}[\mathbf{IH}_0]_z. \tag{11}$$

The equation of radial motion is

$$MN\frac{d^2r}{dt^2} = \frac{2\pi r}{C}[\mathbf{IH}_0]_r + \frac{I^2}{2C^2}\frac{\partial L}{\partial r} - \int\limits_V \frac{\partial p}{\partial r}\,d\mathbf{r}, \tag{12}$$

and the equation of longitudinal dilatation or compression

$$MN\frac{d^2\xi}{dt^2} = \frac{I^2}{2C^2}\frac{\partial L}{\partial \xi} - \int\limits_V \frac{\partial p}{\partial \xi}\,d\mathbf{r}. \tag{13}$$

In the model of a flexible current-carrying loop $\frac{\partial L}{\partial \xi} = 0$ and $p = 0$. Equations (11)—(13) therefore reduce to ordinary equations of a flexible loop /1/.

For the set of equations (4) and (11)—(13) to be closed, we must show that the self-inductance defined by (3) is equivalent to the self-inductance defined by (8). To this end, applying (6) and (8), we calculate the quantity

$$\frac{LJ}{C} = \frac{I}{C}\cdot\frac{\int\limits_V \mathbf{j}(\mathbf{r})\,d\mathbf{r}\cdot\int\limits_V \frac{\mathbf{j}(\mathbf{r}')\,d\mathbf{r}'}{|\mathbf{r}-\mathbf{r}'|}}{\left|\int\limits_V \mathbf{j}(\mathbf{r})\,d\mathbf{r}\right|} = \frac{I\int\limits_V n\psi(\mathbf{r})A_\varphi(\mathbf{r})\,d\mathbf{r}}{\int\limits_V n\psi(\mathbf{r})\,d\mathbf{r}}.$$

On the other hand, for an axially-symmetric magnetic field

$$k\frac{LI}{C} = \int\limits_S \mathbf{H}_1 d\mathbf{S} = \int\limits_S \mathrm{rot}\,\mathbf{A}d\mathbf{S} = IA_\varphi\Big|_{r=r_{\text{bnd}}}.$$

Therefore

$$A_\varphi\big|_{r=r_{\text{bnd}}} = k\frac{\left(\int\limits_V n\psi(\mathbf{r})\,\mathbf{A}(\mathbf{r})\,d\mathbf{r}\right)_\varphi}{\int\limits_V n\psi(\mathbf{r})\,d\mathbf{r}},$$

and the factor k is determined from the equality. It is obvious that for a constant $\psi(\mathbf{r})$, the factor k is also constant, relating the volume-average vector potential $\overline{A_\varphi}$ with its value at the plasmoid periphery. It is also obvious that for $A_\varphi = \overline{A_\varphi}$, $k = 1$.

The equations of a flexible current-carrying loop thus follow directly from the equations of magnetohydrodynamics and give a fairly accurate description of the interaction of a small plasmoid with external magnetic fields. For extended plasmoids, the magnetic forces are essentially volume forces and the approximation of a single current-carrying loop is inadequate. It is however clear that by dividing the extended plasmoid into a finite number of small plasmoids and introducing the mutual inductance of the component plasmoids, we reduce the complex problem in partial differential equations to a simpler problem in ordinary differential equations.

BIBLIOGRAPHY

1. OSOVETS, S. M. — In: "Fizika plazmy i problemy upravlyaemykh termoyadernykh reaktsii", Vol. 2. Moskva, Izdatel'stvo AN SSSR. 1958.

2. OSOVETS, S. M. and I. I. SHCHEDRIN. — In: "Fizika plazmy i problemy upravlyaemykh termoyadernykh reaktsii", Vol. 3. Moskva, Izdatel'stvo AN SSSR. 1958.

3. SINEL'NIKOV, K. D., N. A. KHIZHNYAK, and B. G. SAFRONOV. — In: "Fizika plazmy i problemy upravlyaemogo termoyadernogo sinteza", Vol. 1. Kiev, Izdatel'stvo AN UkrSSR. 1962.

4. KHIZHNYAK, N. A. and B. G. SAFRONOV. — In: "Fizika plazmy i problemy upravlyaemogo termoyadernogo sinteza", Vol. 2. Kiev, Izdatel'stvo AN UkrSSR. 1963.

V. S. Voitsenya, B. P. Il'enko, E. M. Lats'ko, I. N. Onishchenko, B. G. Safronov, and V. T. Tolok

THE MOTION OF PLASMOIDS IN A HELICAL MAGNETIC FIELD

The motion of plasmoids along the magnetic field of a toroidal solenoid and the loss of particles to the walls of the plasma guide were studied experimentally in /1—6/. Transmission of dense plasmoids and filtering of impurities were observed in curved magnetic fields (in /5/, for densities $n > 10^{13}\,\mathrm{cm}^{-3}$). This is in contradiction with the theory /2/, which for the densities and the magnetic fields employed predicts electric polarization fields sufficient for ejecting the entire plasma to the walls of the plasma guide.

The motion of a dense plasma along a curved magnetic field and its purification from the heavy components is apparently governed by some additional effects which substantially attenuate the force of the polarization fields. A recent work /6/ suggests that the experimentally observed transmission of a dense plasma and its purification are due to the shorting of the polarization fields by currents, whose strength can be very small.

The transmission of plasmoids and the removal of the heavy impurities in helical magnetic fields should be investigated with a view to the newly established possibility of injecting plasma into closed magnetic traps /7/. The present paper discusses the results obtained in the magnetic field of a toroidal solenoid with a helical winding.

Apparatus and procedure

A schematic diagram of the setup is shown in Figure 1. A U-shaped vacuum chamber 1 was made of a copper pipe with an i.d. of 8 cm and a radius of curvature $R = 42$ cm; the length of each straight leg was 82 cm. Fourteen one-layer coils 2, eleven turns in each coil, set up a driving magnetic field from 0 to 80 kA/m in the entire chamber.

The curved section of the chamber was fitted with a three-turn helical winding 4, with a pitch of 134 cm. The radius of the helix $a = 5.4$ cm,

pitch angle $\alpha = 0.24$ rad, maximum current up to 2200 A. The curved base was joined to the straight legs by cylindrizers [circulizers] /8/, each 11.2 cm long with a tapering tangent of $\varepsilon = 0.5$. The helical winding and the driving field coils were made of water-cooled copper tubes, supplied by separate d.c. generators.

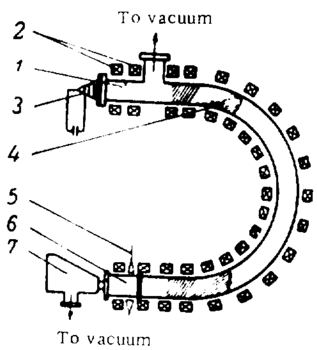

FIGURE 1. Schematic diagram of the experimental setup.

The field coils along the curved section were set using a rotating electron gun /8/. The geometry of the magnetic surfaces was displayed on a fluorescent screen.

The plasma was injected into the chamber by a conical source 3 with a return conductor /9/; the source generated plasmoids with a density $n > 10^{13}\,\mathrm{cm}^{-3}$ and a velocity of up to 10^5 m/sec. A length of glass tubing 6 was provided at the outlet, where the plasma was probed with a 3-cm electromagnetic wave 5 and then analyzed with a Thomson mass spectrometer 7.

The percentage content of the various components in the plasma and the degree of their transmission for various driving-to-helical field ratios could be determined using calibrated MK plates /10/ (for which the density vs. ion beam intensity is known for various ion masses and energies). The cutoff of the 3-cm signal provided information on the velocity and the density of the transmitted plasma.

Experiments and results

Preliminary density and velocity measurements showed that the best transmission of the plasmoid through the curved section was observed for $H_z = 48$ kA/m and $I = 2000$ A. The cutoff of the 3-cm signal shown in the oscillograms in Figure 2 indicates that in the optimal case ($H_z = 48$ kA/m, $I = 2000$ A) the amount of plasma with a comparatively low velocity ($v = 2\cdot10^4$ m/sec and less) and high density ($n > 10^{12}\,\mathrm{cm}^{-3}$) increases considerably. The fast head ($v = 1\cdot10^5$ m/sec) has a lower density.

For 17 kV discharge voltage, the plasma source used in our experiments gave, besides hydrogen, some 80% of impurities, including variously charged ions of carbon and oxygen /5/ (see Figure 3, which shows the mass spectrogram of the plasmoid generated by a source of this type and analyzed at a distance of some 40 cm from the source). Figure 4 gives mass spectrograms of plasmoids penetrating through a toroidal and a helical magnetic fields. We see that the helical field filters off the impurities, while the amount of transmitted plasma is substantially greater than in the case of a toroidal field. Hydrogen ions account for some 80% of the total number of particles at the output in both cases. The impurities remaining in the plasma (mostly C^+; the content of H_2^+, O^+, C^{2+} is less by one order of magnitude) apparently originate in the slow component of the plasmoid, which is just transmitted /6/. The suggestion that these impurities are derived from the films of diffusion pump oil bombarded by the plasmoid was disproved by the following experiment. A Teflon cone

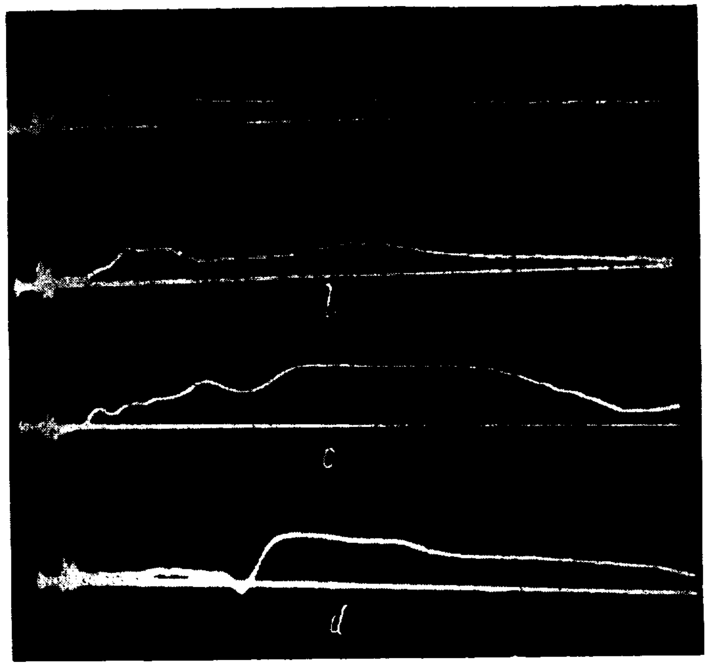

FIGURE 2. The cutoff of the 3-cm signal for various H_z and I:
a) $H_z = 48$ kA/m, $I = 0$; b) $H_z = 48$ kA/m, $I = 800$ A; c) $H_z = 48$ kA/m, $I = 2000$ A;
d) $H_z = 72$ kA/m, $I = 2200$ A.

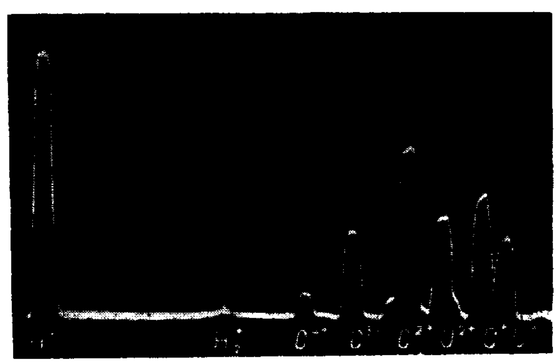

FIGURE 3. The mass spectrogram of a plasmoid ~ 40 cm from the conical source.

($F_2C = CF_2$) was inserted in the source with the purpose of injecting fluorine ions into the plasmoid. Fluorine impurities obviously could not intrude from the diffusion pump oil; they had almost the same percentage penetration as C^+ ions and were resolved simultaneously with the latter by the mass spectrometer. F^+ ions were observed to penetrate through the curved section, and this unambiguously proved that source impurities did pass through.

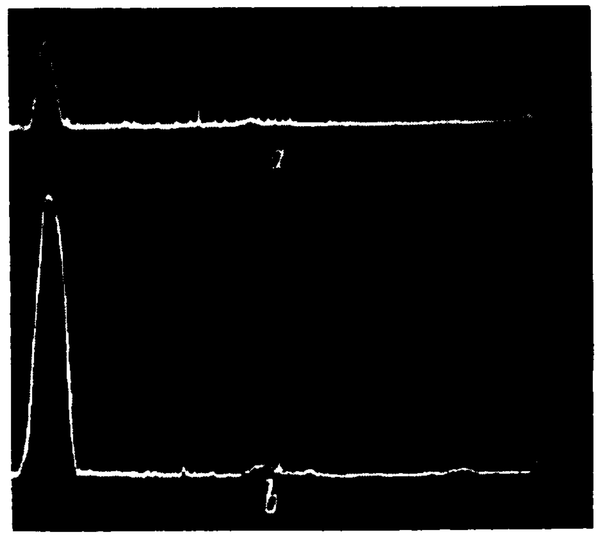

FIGURE 4. Mass spectrograms of transmitted plasmoids: a) toroidal magnetic field (H_z = 48 kA/m, I = 0); b) helical magnetic field (H_z = 48 kA/m, I = 2000 A).

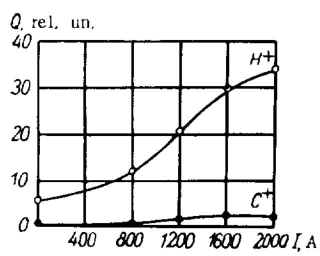

FIGURE 5. Transmission and purification of a plasmoid as a function of the current I through the helical winding.

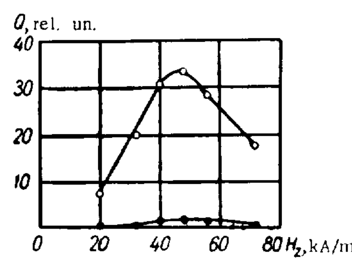

FIGURE 6. Transmission and purification of a plasmoid as a function of the driving magnetic field H_z.

For a driving magnetic field H_z = 48 kA/m, we plotted the transmission of the plasma and the filtering off of the impurities as a function of the current in the helical winding (Figure 5). These curves show that the percentage content of impurities does not increase with helix current, whereas the transmission of the plasmoid is improved considerably.

For a helix current $I = 2000$ A, we plotted the penetration of the plasma as a function of the driving magnetic field H_z (Figure 6). Highest penetration of hydrogen is observed approximately for $H_z = 48$ kA/m; the content of impurities does not increase.

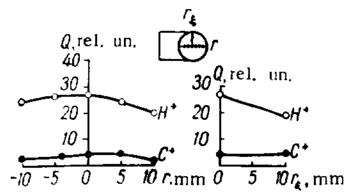

FIGURE 7. Particle distribution across a plasmoid, measured with a mass spectrometer: $H_z = 48$ kA/m, $I = 2000$ A.

The general trend of the curves does not change when the plasmoid density at the chamber inlet is varied (the density was altered by adjusting the voltage applied to the source condensers). The outlet density, however, was found to increase with the density of the injected plasma.

Figure 7 shows the cross sectional distribution of hydrogen ions and of the impurities for $H_z = 48$ kA/m and $I = 2000$ A. The density of the transmitted plasmoid slightly falls off away from the axis, and the plasmoid does not display a noticeable radial drift.

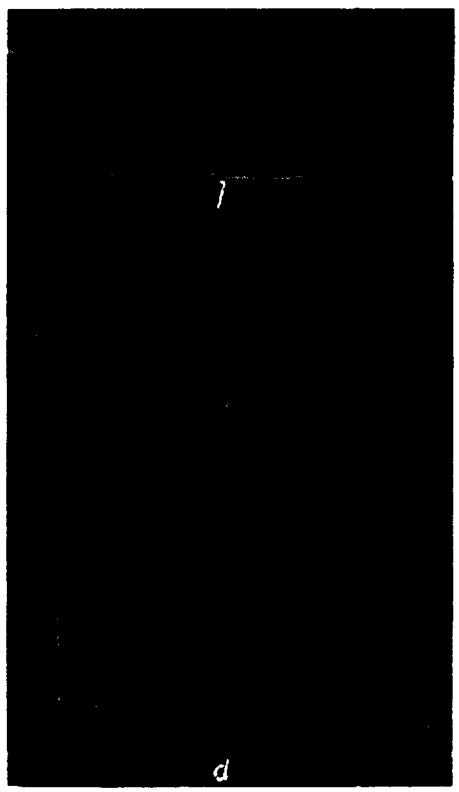

FIGURE 8. Mass spectrograms of plasmoids penetrating the curved section of the helical field for differently directed driving magnetic fields and different source polarities:

$\overset{+}{H_z}$ the field aids the plasmoid; $\overset{+}{V}$ the central source electrode is maintained at a positive potential.

In the course of our experiments we noticed that for a certain direction of the magnetic field $\vec{H}_z$ and a certain polarity of the source condensers $\vec{V}$, the plasmoid penetrated much better than in all other cases (Figure 8, d). All the curves are given for the optimal case (Figure 8, a—d). This behavior is apparently attributable to currents in the injected plasma, which interact with the driving magnetic field at the inlet and with the gradient along the curved section.

Discussion of results

The angle of rotation over a length z for the straight section of a helical magnetic field is given by /11/

$$i = \frac{16\pi}{\gamma^2}\left(\frac{r}{a}\right)^2,$$

where a is the radius of the helical winding; r the radius for which the angle of rotation is measured; $\gamma = \frac{a\varepsilon H}{0.2I}$; H the driving magnetic field; I the current in the helical winding; $\varepsilon = \frac{2\pi a}{L}$ the tangent of the pitch angle; L the pitch of the helix; z the distance along the chamber between turns with equally directed current.

In our case (H_z = 48 kA/m, I = 2000 A), we have a rotation angle i = 4.8 rad for a radius r = 2 cm. The angles of rotation in our experiments were thus large enough to prevent the drift of the particles to the chamber walls despite the combined action of the electric polarization field and the driving magnetic field, provided the plasmoid occupied the entire length of the chamber.

Without the helical field, the plasmoid penetrated through the curved section retaining a fairly high density (up to $10^{12}\,\mathrm{cm}^{-3}$), which either means that the polarization fields are very weak or that their effect is offset by other factors. The impurity content of the plasma at the outlet does not increase when the helical field is impressed. This seems to suggest that the helical field has but a negligible influence on the fast impurity components: they escape to the walls, as in a toroidal field. The cutoff of 3-cm signals also shows that the helical field restrains the radial drift of the slow component only. The substantial drop in the translational velocity of the plasmoid (Figure 2) when the helical field is turned on cannot be explained at present.

The transmission of hydrogen plasma and of some impurities is improved apparently because our magnetic-field geometry retains the plasma better than the toroidal field. The magnetic surfaces along the curved section, together with the longitudinal magnetic field in the straight legs, form a plasma guide of sorts, through which plasmoids pass hardly touching the walls. This model is useful for understanding why the transmission of hydrogen plasma and of the impurities depends on the driving-to-helical field ratio. Figure 4 shows that the transmission is considerably improved for H_z = 48 kA/m, I = 2000 A, i.e., when the separatrix (r_{max} = 2.3 cm) is inscribed in a chamber with a 4 cm radius. In higher magnetic fields, the separatrix touches the chamber walls, which leads to considerable losses

of plasma from the region enclosed by the separatrix. For magnetic fields $H_t < 48$ kA/m, the separatrix shrinks; the plasma lying outside the separatrix easily escapes to the walls. Since the magnetic field of the inlet cylindrizer acts as a diaphragm, the total amount of the driven plasma decreases in this case. The radial expansion of the plasma from the region enclosed by the separatrix in the cross sections where the r-f probes and the mass spectrometer were fitted lowered its density at the axis. Thus a large separatrix, which nevertheless does not touch the walls, ensures optimal transmission of the plasma through the curved section.

We have thus established that:

a) helical magnetic fields have no detrimental effect on the separation of heavy impurities from the plasmoids;

b) these fields considerably improve the transmission of the plasmoids (by as much as a factor of 6).

The magnetic-field geometry used gives pure hydrogen plasma of high density and may be described as highly retentive.

BIBLIOGRAPHY

1. WETSTONE, D.M., M.P. EHRLICH, and D. FINKELSTEIN. - Phys. Fluids, **3**: 617. 1960.

2. SCHMIDT, G. - Phys. Fluids, **3**: 961. 1960.

3. EUBANK, H.P. and T.D. WILKERSON. - Phys. Fluids, **4**: 1407. 1961.

4. SAFRONOV, B.G., V.S. VOITSENYA, and I.I. KONOVALOV. - ZhTF, **32**: 678. 1962.

5. VOITSENYA, V.S., A.G. GORBANYUK, I.N. ONISHCHENKO, and B.G. SAFRONOV. - ZhTF, **34**: 280. 1964.

6. KHIZHNYAK, N.A. Dvizhenie plazmennogo sgustka v magnitnom pole toroidal'nogo solenoida (The Motion of a Plasmoid in the Magnetic Field of a Toroidal Solenoid). - ZhTF, **35**: 847. 1965.

7. TOLOK, V.T. and K.D. SINEL'NIKOV. - ZhTF, **32**: 248. 1962.

8. ZYKOV, V.G., B.I. IL'ENKO, E.M. LATS'KO, I.A. STEPANENKO, A.M. TERNOPOL, V.T. TOLOK, and K.D. SINEL'NIKOV. - ZhTF, **32**: 1190. 1962.

9. AZOVSKII, Yu.S., I.T. GUZHOVSKII, L.A. DUSHIN, V.I. PRIVEZENTSEV, and V.A. CHURAEV. - In: "Fizika plazmy i problemy upravlyaemogo termoyadernogo sinteza", Vol. 3, p. 348. Kiev, Izdatel'stvo AN UkrSSR. 1963.

10. KRUPNIK, L.I. and N.G. SHULIKA. - In: "Diagnostika plazmy", pp. 154–162. 1963.

11. ALEKSIN, V.F. - ZhTF, **31**: 1284. 1961.

A. M. Kovalev and N. A. Khizhnyak

THE REFLECTION OF A PLASMA STREAM BY A MAGNETIC FIELD

The various papers dealing with the reflection of a plasma from a magnetic wall /1, 2, 3/ generally assume that in the region where the particle trajectories are reversed, the plasma remains quasineutral, and that the reflection plane is the same for both the electrons and the ions.

These two assumptions are contradictory. Indeed, the plane of reflection for the electrons and the ions is the same only if a fairly strong electric polarization field is impressed, so that the plasma in the boundary layer can hardly be regarded as quasineutral.

Furthermore, in writing $\frac{dH}{dx} = -\frac{4\pi}{c} j_y$ for the relation between the total magnetic field and the current density in the plasma, the authors of /1, 2, 3/ neglect the gradient of the magnetic field in the barrier, so that the solution of the equations of motion for the electrons and the ions does not contain the coordinate of the magnetic barrier surface (or boundary).

In the present work, a more careful approach is made to the reflection of plasma by a magnetic wall and a somewhat different technique is applied.

Fundamental equations

Consider a quasineutral plasma of density H_0 and velocity n_0 injected into a uniform magnetic field u_0. Interparticle collisions are neglected. The coordinate system is chosen so that the z axis points along the magnetic field H_0, while the plane $x = 0$ coincides with the plane of injection.

The reflection of the plasma by the magnetic field invariably produces an electric polarization field, pointing along the x axis (a one-dimensional problem is considered), and an additional magnetic field H' set up by the motion of charged particles in the boundary layer. It is assumed that the plasma is injected so that the induced magnetic field H' is negligible in comparison with the uniform field H_0. The steady-state equations of motion of the ions and the electrons in the magnetic field are then written as

$$m_i \frac{d^2x_i}{dt^2} = eE + \frac{ev_i}{c} H_0, \tag{1}$$

$$m_e \frac{d^2x_e}{dt^2} = -eE - \frac{ev_e}{c} H_0, \tag{2}$$

$$\frac{dv_i}{dt} = -\frac{eH_0}{m_i c} u_i, \tag{3}$$

$$\frac{dv_e}{dt} = \frac{eH_0}{m_e c} u_e, \tag{4}$$

$$n_i u_i = n_0 u_0, \tag{5}$$

$$n_e u_e = n_0 u_0, \tag{6}$$

$$\frac{dE}{dx} = -8\pi e (n_e - n_i), \tag{7}$$

$$\frac{dH'}{dx} = -\frac{8\pi e}{c} (n_i v_i - n_e v_e). \tag{8}$$

Here u and v are the velocities of the plasma particles along the axes x and y, respectively; m and n their mass and density; the subscript i qualifies ions, e electrons; c the velocity of light in vacuum; E the polarization field.

In (7) and (8) we made use of the fact that n_i and n_e are the number densities of the corresponding particles moving in one direction.

Equations (1)—(8) must be integrated with the following initial conditions

$$x_i = x_e = 0, \quad \frac{dx_i}{dt} = \frac{dx_e}{dt} = u_0$$

and boundary conditions

$$E(\infty) = E(-\infty) = 0,$$
$$|H'(\infty)| = |H'(-\infty)| = H'_{\max}$$

Solution of equations (1)—(8)

Integrating equations (3) and (4) with respect to time, and equations (7) and (8) with respect to x, we obtain, applying the boundary conditions

$$v_i = -\frac{eH_0}{m_i c} x_i,$$
$$v_e = \frac{eH_0}{m_e c} x_e,$$
$$E = -8\pi e n_0 u_0 [t_{i\max} - t_{e\max} - t_i(x) + t_e(x)]. \tag{9}$$
$$\frac{H'_{\max}}{H_0} = \frac{4\pi e^2 n_0 u_0}{m_i c^2}\left[\int_0^{t_{i\max}} x_i(t)\,dt + \frac{m_i}{m_e}\int_0^{t_{e\max}} x_e(t)\,dt\right]. \tag{10}$$

Here $t(x)$ is the time for an ion (electron) to move to a distance x away from the plane of injection; $t_{i\max}$ and $t_{e\max}$ are given by

$$t_{i\max} = t_i(x_{i\max}),$$
$$t_{e\max} = t_e(x_{e\max}).$$

Substituting the expressions for v_i, v_e and E in equations (1) and (2) and changing over to dimensionless variables, we obta n a set of two equations

$$\frac{d^2 y_i}{d\tau^2} + y_i = -\alpha[\tau_{i\max} - \tau_{e\max} - \tau + \tau_e(y_i)], \tag{11}$$
$$\frac{d^2 y_e}{d\tau^2} + \frac{m_i^2}{m_e^2} y_e = \frac{\alpha m_i}{m_e}[\tau_{i\max} - \tau_{e\max} - \tau_i(y_e) + \tau]. \tag{12}$$

The initial conditions are

$$y_i = y_e = 0, \quad \frac{dy_i}{d\tau} = \frac{dy_e}{d\tau} = 1,$$

and $\tau_{i\max}$ and $\tau_{e\max}$ are defined as

$$\tau_{i\max} = \tau_i(y_{i\max}), \tag{13}$$

$$\tau_{e\max} = \tau_e(y_{e\max}). \tag{14}$$

Here y and τ are the dimensionless variables, and α a parameter:

$$y = \frac{x}{R_i} \qquad \left(R_i = \frac{m_i u_0 c}{eH_0}\right),$$

$$\tau = \frac{eH_0}{m_i c} t,$$

$$\alpha = \frac{8\pi n_0 m_i c^2}{H_0^2}.$$

Equations (11) and (12) apply if $H'_{\max} \ll H_0$ or, as it follows from expression (1) for $H'_{\max}$, if

$$u_0^2 \ll \frac{c^2}{f(\alpha)}, \tag{15}$$

where $f(\alpha)$ is a function of the parameter α:

$$f(\alpha) = \frac{\alpha}{2}\left[\int_0^{\tau_{i\max}} y_i(\tau)\,d\tau + \frac{m_i}{m_e}\int_0^{\tau_{e\max}} y_e(\tau)\,d\tau\right].$$

As we shall show in the following, for very large values of the parameter α ($\alpha > 4 \cdot 10^2$), equations (11) and (12) can be solved numerically.

For the values of α compatible with the condition

$$\tau_{e\max} \ll \tau_{i\max}, \tag{16}$$

equations (11) and (12) are considerably simplified, and the motions of ions and electrons are independent of one another:

$$\frac{d^2 y_i}{d\tau^2} + y_i = \alpha\tau - \alpha\tau_{i\max}, \tag{17}$$

$$\frac{d^2 y_e}{d\tau^2} + \frac{m_i^2}{m_e^2} y_e = \frac{\alpha m_i}{m_e}\left[\tau_{i\max} - \tau_i(y_e)\right]. \tag{18}$$

Solving (17), we find the following expression for y_i:

$$y_i = (1-\alpha)\sin\tau - \alpha\tau_{i\max}(1-\cos\tau) + \alpha\tau. \tag{19}$$

Hence, applying (13), we obtain a relation among $\tau_{i\max}$ and α:

$$\alpha = \frac{\cos\tau_{i\max}}{\cos\tau_{i\max} + \tau_{i\max}\sin\tau_{i\max} - 1}. \tag{20}$$

From (19) it follows that at distances much less than $y_{i\max}$ from the plane of injection,

$$y_i(\tau) = \tau \text{ or } \tau_i(y) = y.$$

Therefore, if

$$y_{e\,\max} \ll y_{i\,\max} \tag{21}$$

equation (18) takes the form

$$\frac{d^2 y_e}{d\tau^2} + \frac{m_i^2}{m_e^2}\left(1 + \frac{\alpha m_e}{m_i}\right) y_e = \frac{\alpha m_i}{m_e}\,\tau_{i\,\max}$$

and the expression for y_e is

$$y_e = \frac{m_e}{m_i}\frac{1}{\sqrt{1+\frac{\alpha m_e}{m_i}}}\left[\sin\frac{m_i}{m_e}\sqrt{1+\frac{\alpha m_e}{m_i}}\,\tau + \right.$$

$$\left. + \frac{\alpha\tau_{i\,\max}}{\sqrt{1+\frac{\alpha m_e}{m_i}}}\left(1 - \cos\frac{m_i}{m_e}\sqrt{1+\frac{\alpha m_e}{m_i}}\,\tau\right)\right]. \tag{22}$$

Hence, applying (14), we can find $\tau_{e\,\max}$ if $\tau_{i\,\max}$ is known:

$$\tau_{e\,\max} = \frac{m_e}{m_i}\frac{1}{\sqrt{1+\frac{\alpha m_e}{m_i}}}\left(\pi - \operatorname{arctg}\frac{1}{\alpha\tau_{i\,\max}}\sqrt{1+\frac{\alpha m_e}{m_i}}\right). \tag{23}$$

For $\alpha \gg 1$, from (19)–(20) and (22)–(23)

$$\tau_{i\,\max} \approx \sqrt{\frac{2}{\alpha}},$$

$$y_{i\,\max} \approx \frac{1}{3}\sqrt{\frac{2}{\alpha}},$$

$$\tau_{e\,\max} \approx \frac{m_e}{m_i}\left(\frac{\pi}{\sqrt{1+\frac{\alpha m_e}{m_i}}} - \frac{1}{\sqrt{2\alpha}}\right),$$

$$y_{e\,\max} \approx \frac{m_e}{m_i}\,\frac{2\alpha}{1+\frac{\alpha m_e}{m_i}}\sqrt{\frac{2}{\alpha}}.$$

From (16) and (21) we see that our solution of equations (11)–(12) applies when

$$\alpha \ll \frac{m_i}{6m_e} \approx 3\cdot 10^2,$$

and condition (21) is the first to be violated.

For large values of the parameter α, when the penetration depth of the electrons in the magnetic field becomes comparable with the penetration depth of the ions, we have from (19), seeing that $\tau_{i\,\max}$ is small,

$$\tau_i(y) = \tau_{i\,\max}\left(1 - \sqrt[3]{1 - \frac{y}{y_{i\,\max}}}\right).$$

For the same α, as long as $y_{e\,\max} \leq y_{i\,\max}$, the equation describing the motion

of electrons in the magnetic field has the form

$$\frac{d^2 u_e}{d\tau^2} + \frac{m_i^2}{m_e^2} y_e = \alpha \tau_{i\,\max} \sqrt[3]{1 - \frac{y_e}{y_{i\,\max}}}. \tag{24}$$

Numerical solution of equation (24) for some values of the parameter α shows that $y_{e\,\max}$ is equal to $y_{i\max}$ for $\alpha \approx 4 \cdot 10^2$, and that condition (16) is satisfied up to $\alpha \approx 4 \cdot 10^2$.

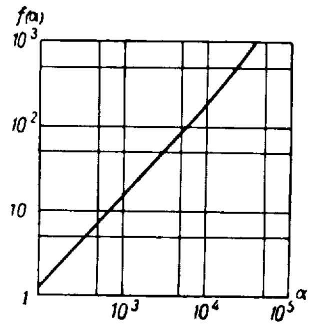

FIGURE 1. Graphical representation of $f(\alpha)$.

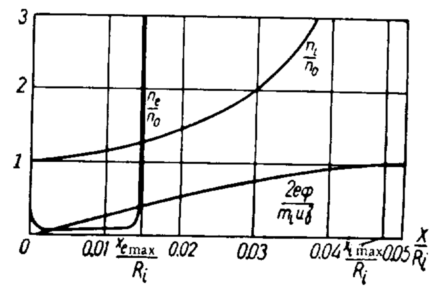

FIGURE 2. Ion and electron densities and the potential in the boundary layer for $\alpha = 10^2$.

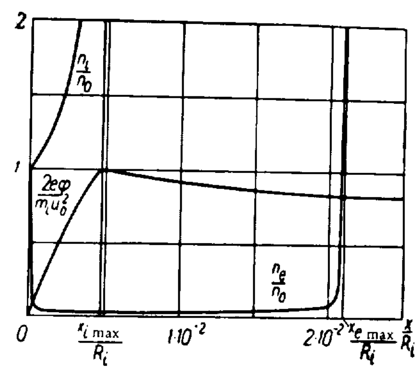

FIGURE 3. Ion and electron densities and the potential in the boundary layer for $\alpha = 10^4$.

Figures 1—3 show the results of the solution of equations (11)—(12) for some values of the parameter α.

It follows from Figure 1 that the induced magnetic field is indeed of no particular significance, provided the injection velocity of the plasma does not exceed a certain limiting value, dependent on α.

For example, for $\alpha = 10^2$, $f(\alpha) \approx 1$, and from (15) we see that the induced magnetic field is negligible if

$$u_0 \ll c.$$

$f(\alpha)$ increases with the parameter α, and the limiting velocity below which the induced magnetic field can be neglected decreases correspondingly.

For example, for $\alpha = 10^4$, $f(\alpha) \approx 120$ and the translational velocity should therefore be much less than $3 \cdot 10^9$ cm/sec.

Figure 2 gives the ion and electron densities, and also the polarization potential of the plasma as a function of depth in the magnetic field, for $\alpha = 2 \cdot 10^2$.

Figure 3 gives the same curves for $\alpha = 10^4$.

The graphs in Figures 2 and 3, as well as the solutions of equations (11) and (12) for $\alpha \ll 3 \cdot 10^2$, show that the plasma is by no means quasi-neutral in the boundary layer, where the particle trajectories are reversed.

The penetration depth of the plasma in a magnetic field for $\alpha \ll 4 \cdot 10^2$ is determined by the penetration depth of the ions

$$x_{\max} = x_{i\,\max} \approx \frac{1}{3}\sqrt{\frac{2}{\alpha}}\,R_i,$$

while for $\alpha > 4 \cdot 10^2$ it is determined by the penetration depth of the electrons, which remains fairly constant: as α increases from $4 \cdot 10^2$ to 10^4, the electron penetration depth drops roughly from $2.3 \cdot 10^{-2}$ to $2 \cdot 10^{-2}$.

BIBLIOGRAPHY

1. CHAPMAN, S. and V. FERRARO. – Geophys. Res., 57: 15. 1952.

2. ARTSIMOVICH, L. A. Upravlyaemye termoyadernye reaktsii (Controlled Thermonuclear Reactions). – Moskva, Fizmatgiz. 1961.

3. SHABANSKII, V. P. – JETP, 40: 1058. 1961.

L. I. Krupnik, N. G. Shulika, and P. A. Demchenko

REFLECTION OF PLASMOIDS FROM A METALLIC SURFACE

Having gained some experience in plasma probing with beams of fast charged and neutral particles, which is a fairly sensitive technique for recording plasma density variations, we made an attempt to investigate the reflection of plasmoids from a metallic surface. These experiments are still in their very first stages, and are very far from perfection. Further work is under way.

Experiments

The reflection of plasmoids was studied using a setup described in a previous paper /1/. The probing beam of fast neutral and charged particles intercepts a plasmoid, which is then directed to a metallic surface. The geometry of the experiments is schematized in Figure 1. A plasmoid moving through chamber 1 passes through diaphragm 2, where

it is intercepted by a beam of fast charged or neutral particles 3. After the encounter with the beam, the plasma stream is directed to a metallic screen, whose distance from the plasma—beam encounter can be varied continuously.

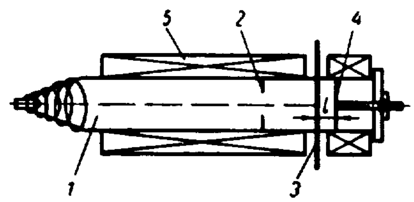

FIGURE 1. Schematic of the setup.

The reflected plasmoid was probed with a charged beam without external magnetic fields and with a neutral beam in the presence of a magnetic field; the magnetic field was set up by coils 5.

Results

In preliminary tests, a reflected signal was picked up by the particle detector, although no probing beam was aimed at the plasmoid. This signal decreased fairly rapidly as the reflector was moved away from the detector inlet. Figure 2 illustrates this spurious signal by three oscillograms taken at three different positions of the reflector 4: a — at a distance of 0.5 cm from the plasma—beam encounter; b — at a distance of 1 cm; c — at a distance of 1.5 cm.

This is hardly a reflected plasma signal, since it could be eliminated neither by a transverse magnetic field impressed in the region of the outlet channel nor by a system of three grids with various combinations of potentials interposed in front of the detector. We apparently have here a stream of neutral particles reflected from the screen. There is also a considerable likelihood of its being a photon signal. Since our aim was diagnostics of a reflected plasmoid with a beam, we did not try to elucidate the exact nature of the spurious signal picked up by the detector in the absence of a probing beam, and concentrated our efforts on suppressing this interference. By modifying the geometry of the outlet channel and of the particle detector, we reduced this signal until it became negligible in comparison with the amplitude of the signal produced by the probing beam.

Before proceeding with the analysis of the experimental results, we shall describe briefly the attenuation signal of a neutral beam intercepting a plasmoid, in a case when no reflection need be considered. It is hoped that this digression will help the reader to follow our arguments. Figure 3 is an oscillogram displaying the attenuation of the beam in the initial plasmoid. A plasmoid of course consists of a fully ionized head and a trailing component with a certain content of neutrals. The second component grades into a so-called "tail" with a high content of neutrals. These conclusions were confirmed by plasmoid probing with a proton beam

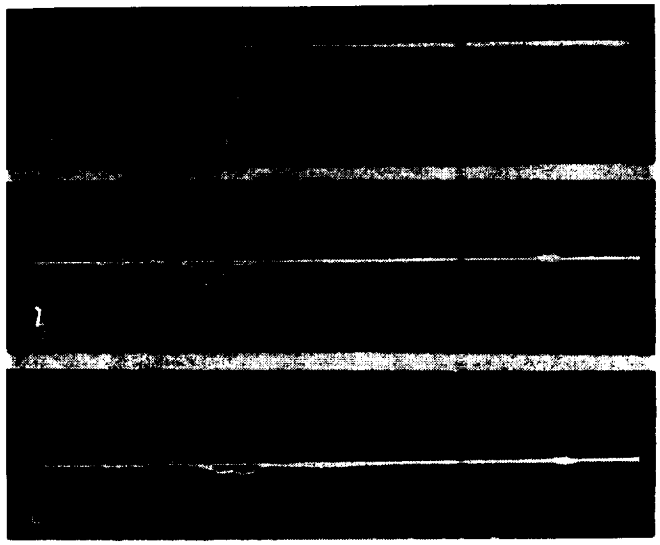

FIGURE 2. Signals picked up by the detector in the absence of a probing beam, for various positions of the reflector.

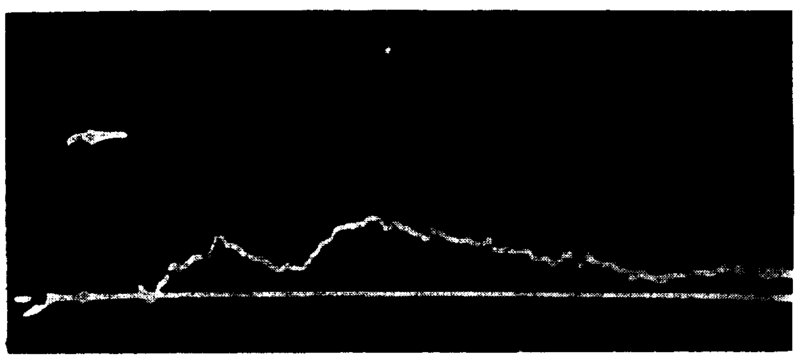

FIGURE 3. The attenuation of a probing beam of H_1^0 atoms intercepting a plasmoid.

FIGURE 4. The attenuation of a proton beam intercepting a plasmoid.

(Figure 4). The protons are attenuated by neutrals only. No neutrals are detected in the head; they appear in the rear portion (trailing the head by $20-25\,\mu$sec), reaching a high in the tail (after $100\,\mu$sec). The reflection of a plasmoid from a metallic screen can be traced on the oscillograms shown in Figure 5. This figure gives the attenuation signals of a proton beam intercepting a reflected plasmoid for four different positions of the screen 4: a — l = 0.5 cm, nearest to the beam; b — l = 1 cm; c — l = 2 cm; d — l = 3 cm. In case d, the initial plasmoid form was recovered (see Figure 4). It is obvious that the passage of the highly ionized plasmoid gives a strong reflection signal. Since this signal was obtained in probing with a proton beam, we are led to the conclusion that the ionized plasmoid is neutralized

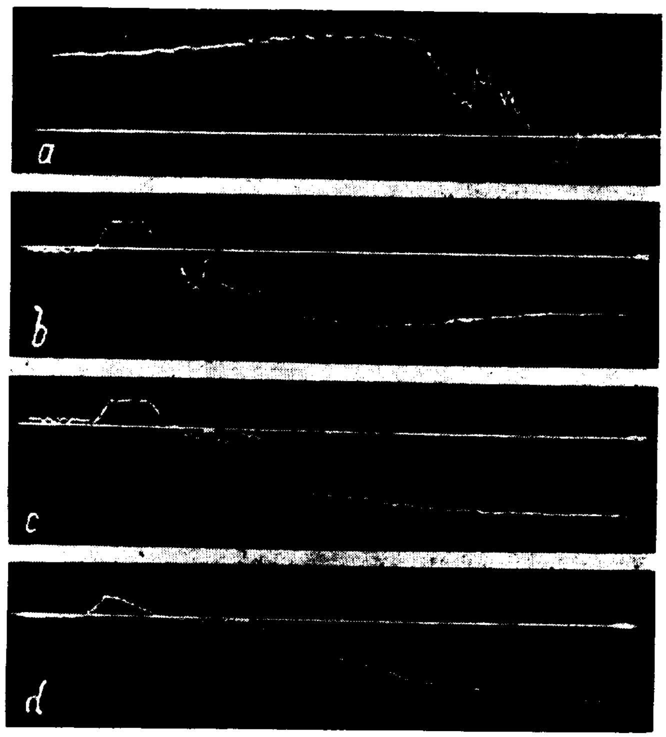

FIGURE 5. Detector signals for various screen positions.

on reflection. As the screen is moved away from the beam, the leading signal is suppressed and the initial form is restored. Figure 6 plots the amplitude of the leading signal as a function of the distance l between the screen and the probing beam. We see from the figure that the distortion produced by the plasmoid head rapidly decreases with the distance, vanishing for all practical purposes at $l = 3-4$ cm.

The probing of reflected plasmoids with a proton beam thus shows that even the head of the reflected plasmoid abounds in neutrals.

The next series of experiments was staged to investigate the attenuation of a neutral beam intercepting a reflected plasmoid. All these experiments

were made in the presence of a magnetic field. The oscillograms are somewhat less illustrative in this case, since the received signal represents the total attenuation of the neutral beam by the incident and the reflected plasmoid.

Before its encounter with the probing beam, the plasmoid was passed through the diaphragm 2 of 20 mm diameter; this was done to reduce the attenuation to a manageable level (~ 20 — 30%) and to keep it far from

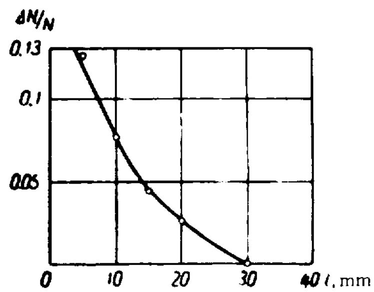

FIGURE 6. Proton beam attenuation vs. beam — screen distance.

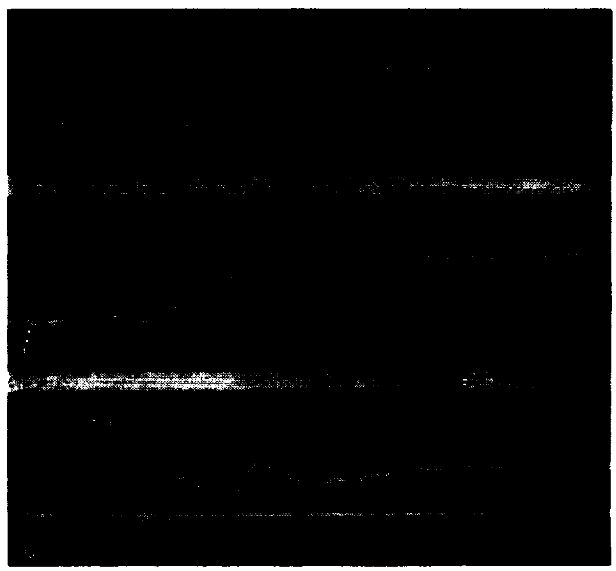

FIGURE 7. The attenuation of a probing beam of H_1^0 atoms intercepting a plasmoid.

complete charge exchange, in order that the attenuation contributed by the particles neutralized upon reflection should be felt. Figure 7 shows the attenuation signals of a neutral beam for various reflector positions. If the screen is located near the beam, l = 1 cm (Figure 7, a), the incident plasmoid is distorted (expanded) in all the three cross sections, whereas with the screen far off (l = 10 cm, Figure 7, b), the transit time of the reflected plasmoid is such that the head of the incident plasmoid is

registered by the beam without any distortion due to the reflected signal; for $l = 20$ cm (Figure 7, c), the reflection is distorted only by the tail, whose very existence is to a certain extent attributable to the reflection of the plasmoid from chamber ends. All these conclusions are consistent with the plots in Figure 8, which shows the number of particles in the first, second, and third plasmoid sections as a function of the beam—screen distance, 7 μsec, 35 μsec, and 100 μsec after signal start. The velocity of the reflected plasmoid can be estimated from the time shift of the reflection interference for various screen positions; estimates give $1-3 \cdot 10^6$ cm/sec, which is not far from the velocity of the incident plasmoid ($78 \cdot 10^6$ cm/sec). No unambiguous conclusions can be made from the foregoing results concerning the nature of the reflected plasmoid. It is clear that the reflected plasma, besides the charged component, also carries a high content of neutrals. The charged-to-neutral particles ratio of the reflected plasmoid has not been determined.

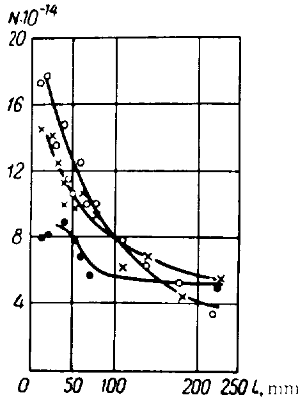

FIGURE 8. The attenuation of a probing beam of H_1^0 as a function of beam—screen distance: ••• in the first plasmoid maximum (7 μsec after signal start); x x x in the second plasmoid maximum (35 μsec after signal start); ooo 100 μsec after signal start.

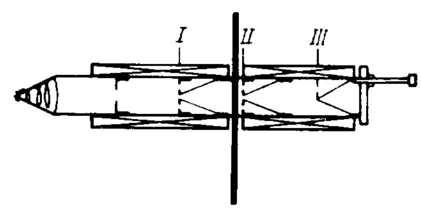

FIGURE 9. Illustrating the experiments with plasma penetration and reflection for plane and conical diaphragms of equal diameters.

In conclusion, we made some tests comparing the penetration and the reflection of plasmoids for a plane and a conical diaphragrams of equal diameters. According to the schematic diagram of Figure 8, a plane diaphragm 10 mm in diameter and a diaphragm of conical profile with an opening angle of 60° and a diameter of 10 mm were alternately interposed to intercept the plasmoid in three positions: before the beam (I), immediately after the beam (II), and at the outermost point of the plasmoid path (III). The experimental results are listed in the table, where N_1, N_2, N_3 is the number of particles after 7—10, 35—40, and 70—100 μsec, respectively. We see from the table that in the presence of a driving magnetic field the penetration of the plasmoid through the cone is somewhat worse than through a plane diaphragm, and that virtually no reflection occurs when a plasmoid hits the cone.

Our preliminary experiments with the reflection of plasmoids from a metallic surface reveal strong reflection at a distance of $\sim 10-12$ cm

Position of diaphragms		Number of particles in plasmoid ($N \cdot 10^{-14}$)		
		N_1	N	N_2
I	plane	1.3	3.[illegible]	1.5
	conical	0.9	2.[illegible]	3.2
II	plane	5.3	10.	20.0
	conical	1.5	7.8	5.4
III	plane	1.2	7.[illegible]	4.0
	conical	1.6	7.[illegible]	5.5

from the screen. The reflected plasmoid carries a large number of neutrals and has a fairly high velocity ($\sim 10^{9}$ cm/sec).

BIBLIOGRAPHY

1. KRUPNIK, L. I. and N. G. SHULIKA. — This volume, p. 197.

N. A. Khizhnyak and K. P. Cherkasova

SELF-INDUCTANCE OF AN ELLIPSOIDAL PLASMOID

The investigation of plasmoids impinging on a magnetic field is substantially simplified if the plasmoid self-inductance is known. The currents induced in the plasmoid, and consequently the internal magnetic field, are then easily expressed in terms of the external magnetic field and the plasmoid geometry.

In /1/, the self-inductance of a spherical plasma entity was calculated. It was also shown that for high densities $n \gg \frac{10^{12}}{r_0^2}$, where r_0 is the radius of the plasmoid, knowledge of the actual distribution of the rotational velocities in the plasmoid is irrelevant. However, when a plasmoid interacts with an external magnetic field, its geometry changes, and the model of an ellipsoidal plasmoid offers a more reasonable approximation.

In the present paper, we calculate the self-inductance of oblate and prolate ellipsoids of revolution (plasmoids in the shape of spheroids).

The general expression for the self-inductance of the electronic component of a plasmoid is /1/

$$L_{11} = \frac{4\pi^2 mc^2 N_e r_0^2}{e^2 \left[\int\limits_V n\psi_e(\mathbf{r})\, dV\right]^2} + \frac{8\pi^2 r_0^2 \lambda_1}{\left[\int\limits_V n\psi_e(\mathbf{r})\, dV\right]^2}, \tag{1}$$

where r_0 is the plasmoid radius; $\psi_e(\mathbf{r})$ characterizes the distribution of

electron angular velocities in the plasmoid,

$$N_e = \int_V n(\mathbf{r})\,\psi_e^2(\mathbf{r})\,dV,$$

$$\lambda_{11} = \int_V n(\mathbf{r})\,\psi_e(\mathbf{r}) \int_V \frac{n(\mathbf{r}')\,\psi_e(\mathbf{r}')\cos(\varphi-\varphi')}{|\mathbf{r}-\mathbf{r}'|}\,dV'dV.$$

We shall assume a constant plasmoid density,

$$n(\mathbf{r}) = n_0,$$

and a constant electron angular velocity in the entire plasmoid, i.e.,

$$\psi_e(\mathbf{r}) = \frac{h}{r_0},$$

where h is the distance of an electron from the rotation axis of the spheroidal plasmoid.

Then

$$N_e = \frac{n_0}{r_0^2}\int_V h^2 dV, \tag{2}$$

$$\lambda_{11} = \frac{n_0^2}{r_0^2}\int_V h \int_V \frac{h'\cos(\varphi-\varphi')}{|\mathbf{r}-\mathbf{r}'|}\,dV'dV. \tag{3}$$

From (1)–(3) we see that the calculation of self-inductance L_{11} reduces to the evaluation of the integrals

$$I_1 = \int_V h\,dV, \quad I_2 = \int_V h^2 dV, \quad I_3 = \int_V h \int_V \frac{h'\cos(\varphi-\varphi')}{|\mathbf{r}-\mathbf{r}'|}\,dV'dV.$$

It would be convenient to operate in spheroidal coordinates /2/. For a prolate spheroid, these coordinates are defined by

$$x = c\,\mathrm{sh}\,\eta\sin\theta\cos\varphi,$$

$$y = c\,\mathrm{sh}\,\eta\sin\theta\sin\varphi,$$

$$z = c\,\mathrm{ch}\,\eta\cos\theta,$$

$$0 \leqslant \varphi \leqslant 2\pi, \quad 0 \leqslant \theta \leqslant \pi, \quad 0 \leqslant \eta \leqslant \eta_0,$$

where

$$c = \sqrt{a^2 - r_0^2}, \quad \eta_0 = \mathrm{Ar\,th}\,\frac{r_0}{a}, \quad a > r_0,$$

where a and r_0 are the plasmoid half-length and radius, respectively.

Calculations give

$$I_1 = \frac{\pi^2}{4}\,ar_0^3, \tag{4}$$

$$I_2 = \frac{8\pi}{15}\,ar_0^4, \tag{5}$$

and the determination of self-inductance L_{11} reduces to the evaluation of the integral

$$I_3 = c^8 \int_0^{\eta_0} d\eta \int_0^{\pi} d\theta \int_0^{2\pi} d\varphi \Big\{ \mathrm{sh}^2\,\eta \cdot \sin^2\theta\,(\mathrm{ch}^2\,\eta -$$

$$- \cos^2\theta) \int_0^{\eta_0} d\eta' \int_0^{\pi} d\theta' \int_0^{2\pi} d\varphi' \left[\mathrm{sh}^2\,\eta'^2 \sin^2\theta' \frac{\cos(\varphi - \varphi')\,(\mathrm{ch}^2\,\eta' - \cos^2\theta')}{|\mathbf{r} - \mathbf{r}'|} \right]. \tag{6}$$

Let us expand the reciprocal distance in a series of spheroidal functions /2/

$$\frac{c}{|\mathbf{r} - \mathbf{r}'|} = \sum_{n=0}^{\infty} (2n+1)\,P_n(\cos\theta)\,P_n(\cos\theta')\,Q_n(\mathrm{ch}\,\eta)\,P_n(\mathrm{ch}\,\eta') +$$

$$+ 2\sum_{n=1}^{\infty}(2n+1)\sum_{m=1}^{n}(-1)^m \left\{\frac{(n-m)!}{(n+m)!}\right\}^2 \times$$

$$\times P_n^m(\cos\theta)\,P_n^m(\cos\theta')\,P_n^m(\mathrm{ch}\,\eta')\,Q_n^m(\mathrm{ch}\,\eta)\cos m(\varphi - \varphi') \tag{7}$$

$$(\eta' < \eta),$$

where $P_n^m(\mu)$, $Q_n^m(\mu)$ are the adjoint Legendre function of 1st and 2nd kind, respectively.

Substituting (7) in (6), we first integrate with respect to the angular variables φ', θ', φ, θ. Then, seeing that in (7) different spheroidal functions enter the expansion in the internal $(\eta' < \eta)$ and the external $(\eta' > \eta)$ regions, we divide the integral with respect to η' into two parts:

$$\int_0^{\eta_0} d\eta' \{\ \} = \int_0^{\eta} d\eta' \{\ \} + \int_0^{\eta_0} d\eta' \{\ \}.$$

We have

$$I_3 = -\frac{16\pi^2 c^7}{3}\left[\int_0^{\eta_0} \mathrm{sh}^2\,\eta\left(\mathrm{ch}^2\,\eta - \frac{1}{5}\right) f_1(\eta,\ \eta_0)\,d\eta\ - \frac{1}{5\cdot 5}\int_0^{\eta_0} \mathrm{sh}^2\,\eta\, f_2(\eta,\ \eta_0)\,d\eta\right],$$

where

$$f_1(\eta,\ \eta_0) = Q_1^1(\mathrm{ch}\,\eta)\int_0^{\eta} \mathrm{sh}^2\,\eta'\left(\mathrm{ch}^2\,\eta' - \frac{1}{5}\right) P_1^1(\mathrm{ch}\,\eta')\,d\eta' +$$

$$+ P_1^1(\mathrm{ch}\,\eta)\int_{\eta}^{\eta_0} \mathrm{sh}^2\,\eta'\left(\mathrm{ch}^2\,\eta' - \frac{1}{5}\right) Q_1^1(\mathrm{ch}\,\eta')\,d\eta',$$

$$f_2(\eta,\ \eta_0) = Q_3^1(\mathrm{ch}\,\eta)\int_0^{\eta} \mathrm{sh}^2\,\eta' P_3^1(\mathrm{ch}\,\eta')\,d\eta' + P_3^1(\mathrm{ch}\,\eta)\int_{\eta}^{\eta_0} \mathrm{sh}^2\,\eta' Q_3^1(\mathrm{ch}\,\eta')\,d\eta'.$$

Substituting $\mathrm{ch}\,\eta = t$ and integrating with respect to η', we find

$$I_3 = -\frac{16\pi^2 c^7}{3}\left\{\int_1^{t_0} (t^2 - 1)\left(t^2 - \frac{1}{5}\right) F_1(t,\ t_0)\,dt + \frac{4}{525}\int_1^{t_0} (t^2 - 1)\,F_2(t,\ t_0)\,dt\right\},$$

where

$$F_1(t, t_0) = r_1(t_0) + \frac{t^2}{5}, \quad F_2(t, t_0) = \frac{3}{2}(5t^2 - 1) r_2(t_0) - 6t^2,$$

$$r_1(t_0) = \frac{1}{10} t_0 (t_0^2 - 1)^2 \ln \frac{t_0 + 1}{t_0 - 1} - \frac{t_0^4}{5},$$

$$r_2(t_0) = \frac{3}{4} t_0 (t_0^2 - 1)^2 \ln \frac{t_0 + 1}{t_0 - 1} - \frac{3}{2}(t_0^2 - 1)^2 - \frac{t_0^2}{2} + \frac{3}{2}.$$

Finally, integrating with respect to t, we have

$$I_3 = \frac{16}{105} \pi^2 c^7 t_0^2 (t_0^2 - 1)^3 \left\{ 2t_0 - (t_0^2 - 1) \ln \frac{t_0 + 1}{t_0 - 1} \right\},$$

or substituting $t_0 = \operatorname{ch} \eta_0 = \frac{a}{\sqrt{a^2 - r_0^2}}$,

$$I_3 = \frac{16\pi^2}{105} \frac{a^2 r_0^6}{(a^2 - r_0^2)^{3/2}} \left\{ 2a \sqrt{a^2 - r_0^2} - r_0^2 \ln \frac{a + \sqrt{a^2 - r_0^2}}{a - \sqrt{a^2 - r_0^2}} \right\}. \tag{8}$$

Inserting (4), (5), and (8) in relations (1)—(3), we find an expression for the self-inductance of a prolate spheroid:

$$L_{11} = \frac{512}{15\pi} \frac{mc^2}{n_0 e^2 a} + \frac{2048}{105} \frac{r_0^2}{(a^2 - r_0^2)^{3/2}} \left\{ 2a \sqrt{a^2 - r_0^2} - r_0^2 \ln \frac{a + \sqrt{a^2 - r_0^2}}{a - \sqrt{a^2 - r_0^2}} \right\}.$$

Introducing the eccentricity $\varepsilon = \frac{\sqrt{a^2 - r_0^2}}{a}$, we write

$$L_{11} = \frac{512}{15\pi} \frac{mc^2}{e^2} \frac{1}{n_0 a} + \frac{2048}{105} (1 - \varepsilon^2) a \frac{\left[2\varepsilon - (1 - \varepsilon^2) \ln \frac{1 + \varepsilon}{1 - \varepsilon} \right]}{\varepsilon^3}. \tag{9}$$

For an oblate spheroid, the spheroidal coordinates are defined by

$$x = c \operatorname{ch} \eta \sin \theta \cos \varphi,$$
$$y = c \operatorname{ch} \eta \sin \theta \sin \varphi,$$
$$z = c \operatorname{sh} \eta \cos \theta,$$
$$c = \sqrt{r_0^2 - a^2}, \quad \eta_0 = \operatorname{Ar\,th} \frac{a}{r_0}, \quad a < r_0.$$

Proceeding as before, we find for the self-inductance of an oblate spheroid

$$L_{11}^{\bullet} = \frac{512}{15\pi} \frac{mc^2}{e^2 n_0 a} + \frac{4096}{105} \frac{r_0^2}{(r_0^2 - a^2)^{3/2}} \left[r_0^2 \operatorname{arctg} \frac{\sqrt{r_0^2 - a^2}}{a} - a \sqrt{r_0^2 - a^2} \right],$$

or, in terms of the eccentricity $\varepsilon = \frac{\sqrt{r_0^2 - a^2}}{r_0}$,

$$L_{11}^{\bullet} = \frac{512}{15\pi} \frac{mc^2}{e^2 n_0 a} + \frac{4096}{105} \frac{r_0}{\varepsilon^3} \left[\operatorname{arctg} \frac{\varepsilon}{\sqrt{1 - \varepsilon^2}} - \varepsilon \sqrt{1 - \varepsilon^2} \right]. \tag{10}$$

For $\varepsilon \to 0$, relations (9) and (10) both reduce to the well known expression for the self-inductance of a spherical plasmoid.

Let us consider some limiting cases.

Highly prolate spheroid ("needle"). In this case $\frac{r_0}{a} \ll 1$, $\varepsilon \approx 1$. From (9)

$$L_{11} \simeq \frac{512}{15\pi} \frac{mc^2}{e^2} \frac{1}{n_0 a} + \frac{4096}{105} \frac{r_0^2}{a},$$

whence it follows that, first, the two terms are proportional to r_0^2 and, second, for

$$n_0 \ll \frac{0.98 \cdot 10^{12}}{r_0^2},$$

L_{11} is determined by the first term, and for

$$n^0 \gg 0.98 \frac{10^{12}}{r_0^2},$$

by the second term.

Highly oblate spheroid ("disk"). In this case $\frac{a}{r_0} \ll 1$, $\varepsilon \approx 1$. From (10)

$$L_{11}^{\bullet} \simeq \frac{512}{15\pi} \frac{mc^2}{e^2} \frac{1}{n_0 a} + \frac{1024}{105} \pi r_0.$$

whence it follows that for

$$n_0 \ll 1.25 \frac{10^{12}}{a r_0},$$

$L_{11}^{\bullet}$ is determined by the first term, proportional to r_0^2, and for

$$n_0 \gg 1.25 \frac{10^{12}}{a r_0}$$

$L_{11}^{\bullet}$ is determined by the second term, proportional to r_0.

BIBLIOGRAPHY

1. KHIZHNYAK, N. A. and B. G. SAFRONOV. — In "Fizika plazmy i problemy upravlyaemogo termoyadernogo sinteza", Vol. 2, Kiev, Izdatel'stvo AN UkrSSR, 1963.

2. HOBSON, E. W. Theory of Spherical and Ellipsoidal Functions. — [Russian translation. 1952.]

R. V. Polovin

A CONTRIBUTION TO THE THEORY OF COLLISIONLESS SHOCK WAVES

In this paper we investigate the structure of a collisionless shock wave [quasi-shock] in a plasma immersed in a magnetic field. The thermal energy behind the shock wave is concentrated in ionic sound waves generated at the shock front by the reverse mechanism of Landau damping. Nonlinear interaction of waves leads to random, i.e., thermal, oscillations. The structure of the shock wave is ergodic. This means that infinitesimal fluctuations of the magnetohydrodynamic quantities in front of the shock wave first exponentially grow and then start pulsating at random, without returning to the initial state. Averaging over these pulsations, we find the effective heating. It is shown that this process enhances the rate of thermonuclear reactions. The relaxation length is found to be equal to the Debye radius.

Statement of the problem

In the kinetic approximation, the structure of a shock wave (in wave's own frame) is described by Vlasov's kinetic equations for the electrons and the ions

$$v_x \frac{\partial f_\mp}{\partial x} \mp \frac{e}{m_\mp}\left(\mathbf{E} + \frac{\mathbf{v}}{c} x\mathbf{H}\right)\frac{\partial f_\mp}{\partial \mathbf{v}} = 0 \tag{1}$$

(the wave moves along the x axis; $\frac{\partial}{\partial t} = \frac{\partial}{\partial y} = \frac{\partial}{\partial z} = 0$) and Maxwell's equations

$$\frac{dE_x}{dx} = 4\pi e \int (f_+ - f_-)\, d\mathbf{v}, \tag{2}$$

$$H_x = \text{const},$$

$$\frac{dH_y}{dx} = \frac{4\pi e}{c} \int v_z (f_+ - f_-)\, d\mathbf{v}, \tag{3}$$

$$\frac{dH_z}{dx} = -\frac{4\pi e}{c} \int v_y (f_+ - f_-)\, d\mathbf{v}. \tag{4}$$

The problem is to find a solution (or at least to prove its existence) where the hydrodynamic quantities E_x, H_y, H_z, $n_\pm \equiv \int f_\pm d\mathbf{v}$, $\mathbf{u}_\pm \equiv \int \mathbf{v} f_\pm d\mathbf{v}$ approach constant values in the region $x \to -\infty$ in front of the shock wave.

The existence of a collisionless shock wave is determined by the behavior of this solution in the region $x \to +\infty$ behind the wave. Four different cases should be distinguished.

1. For $x \to +\infty$ the hydrodynamic quantities approach a finite limit, different from the corresponding value for $x \to -\infty$. This solution describes a true shock wave. A true shock wave is impossible without collisions. These waves exist only in the presence of dissipative mechanisms (viscosity, heat conduction, Joule heating), which are all based on binary collisions /1-72/.

2. For $x \to +\infty$ the hydrodynamic quantities approach the same limit as for $x \to -\infty$. This solution is not a shock wave: this is a symmetric (solitary) wave /73–83/*.

3. For $x \to +\infty$ the hydrodynamic quantities assume arbitrarily large values /88/. This means that the problem has been improperly stated.

4. For $x \to +\infty$ the hydrodynamic quantities are bounded without approaching any limit. In this case, the random pulsations of the hydrodynamic quantities behind the shock wave can be identified with heating. This is the ergodic shock wave [quasi-shock] /89/.

Propriety

Since the shock wave moves with a velocity greater than the velocity of propagation of small perturbations, the medium in front of the shock wave is unperturbed. The intensity of the shock wave is determined by its velocity (or, equivalently, by the speed of the medium for $x \to -\infty$ in wave's own frame).

Therefore, regardless of the state of the medium in front of the shock wave and irrespective of the propagation velocity of the wave (as long as it is greater than the propagation velocity of small perturbations), the set of equations (1)–(4) is uniquely solvable.

If for some state of the medium in front of the shock wave ($x \to -\infty$) the set of equations (1)–(4) is unsolvable or has more than one solution, the problem has been improperly stated.

The proper statement of the problem is closely related with the topological characteristics of the set (1)–(4), since these characteristics are in fact the lines along which the different solutions are "matched" and the distribution functions $f_\mp$ retain a constant value.

The characteristics of the set (1)–(4) are described by the equations of motion of the electrons and the ions:

$$v_x \frac{d\mathbf{v}}{dx} = \mp \frac{e}{m_\mp}\left(\mathbf{E} + \frac{\mathbf{v}}{c} \times \mathbf{H}\right). \tag{5}$$

We shall first show that, despite reflection from potential barriers, all the particles travel from $-\infty$ to $+\infty$ (this proof was first suggested in /73/; for more details, see /90/).

Consider a moving frame of reference where the shock wave is at rest and, furthermore,

$$E_y = \text{const} \neq 0,\ E_z = \text{const} \neq 0 \ \text{and} \int^{\infty} E_x(\tau)\,d\tau = \infty \quad \left(d\tau = \frac{dx}{v_x}\right).$$

Setting $F(\tau) = \frac{1}{c}(v_y H_z - v_z H_y)$, we have from (5)

$$v_x = \mp \frac{e}{m_\mp}\left[\int_0^{\tau} E_x d\tau + \int_0^{\tau} F(\tau)\,d\tau\right] + \text{const}.$$

* Nonlinear collisionless plasma waves propagating along a magnetic field were investigated in some papers /78, 84–87/ for the case of Mach number less than unity. These waves are in no way related with shock waves, since here the magnetohydrodynamic quantities do not approach a constant limit for $x \to -\infty$.

Since v_x is bounded as $\tau \to \infty$, the following equality should be asymptotically satisfied for large τ:

$$\int_0^{\tau} E_x d\tau + \int_0^{\tau} F(\tau)\, d\tau = 0$$

Differentiating by τ, we find

$$E_x + \frac{1}{c}(v_y H_z - v_z H_y) = 0.$$

Analogous equalities are obtained for the other components.

We thus see that the equality

$$\mathbf{E} + \frac{\mathbf{v}}{c} \times \mathbf{H} = 0$$

is asymptotically satisfied for $\tau \to +\infty$. This relation shows that no particle may return to its point of origin ($x = -\infty$) when reflected from potential barriers. Nor may it be trapped in potential wells. All particles thus move from $x = -\infty$ to $x = +\infty$.

Since particle trajectories are the characteristics, the problem concerning the structure of a collisionless shock wave is mathematically proper and, moreover, the energy is conserved.

Ergodicity

To prove ergodicity, it suffices to show that the solution is not symmetric about $x = 0$, where $E_x = 0$.

Substituting $E_x = 0$ in (1), we see that $\frac{\partial f_\mp}{\partial x}$ vanishes at the point $x = 0$ only if

$$\mathbf{v} \times \mathbf{H} \cdot \frac{\partial f_\mp}{\partial \mathbf{v}} = 0$$

for $x = 0$ and an arbitrary $\mathbf{v}$.

The multipliers $\frac{\partial f_\mp}{\partial v_x}$, $\frac{\partial f_\mp}{\partial v_y}$, $\frac{\partial f_\mp}{\partial v_z}$ are not zero, since otherwise the function $f_\mp$ is not normalized. The factor $v_x H_y - v_y H_x$ does not vanish because, among other reasons, $H_x = \mathrm{const} \neq 0$. The vectors $\mathbf{E} + \frac{\mathbf{v}}{c} \times \mathbf{H}$ and $\frac{\partial f_\mp}{\partial \mathbf{v}}$ cannot be orthogonal, since this orthogonality is inconsistent with the symmetry of the problem. Orthogonality may obtain only sporadically, for some discrete values of the Mach number.

This means that the solution is asymmetric.

Infinitesimal fluctuations of the magnetohydrodynamic quantities in front of the shock wave first grow exponentially and then start pulsating at random, never returning to the initial state. Averaging over these pulsations, we find the effective heating.

Note that the temperature of ions and electrons behind the shock wave is the same as in front of the shock wave. However, the mean velocities at different points are different. This velocity spread may be interpreted as heating.

The width of the shock wave

Having proved the ergodicity of the shock wave, i.e., that the shock wave irreversibly transforms the uniform state u_0 in front of the wave into a pulsating state in its wake, we can estimate the relaxation length from the linear theory.

To this end, we should consider steady-state linear waves in plasma, moving with the velocity of the shock wave, u_0. In these waves, the disturbances are time-independent, all quantities varying as e^{ikx} with the coordinate x. The width L of the shock wave is expressed in terms of the imaginary part of k /89/

$$L = \frac{1}{\operatorname{Im} k}. \tag{6}$$

For the well-known kinetic dispersion relations to apply, the problem can be slightly modified: we consider perturbations of the form $e^{ikx-i\omega t}$, where $\omega = ku_0$, in a stationary plasma. The width of the shock wave is nevertheless determined from (6).

If the Alfvén speed and the velocity of the shock wave u_0 are non-relativistic, the dispersion equation for longitudinal ion waves has the form /91/

$$k^2D^2 = A\left(\frac{u_0}{v_{T_+}}\right) - i\frac{u_0}{v_{T_+}}\exp\left(-\frac{u_0^2}{v_{T_+}^2}\right), \tag{7}$$

where $D = \sqrt{\frac{T}{4\pi e^2 n}}$ is the Debye length; v_{T_+} is the thermal velocity of an ion; $A(\xi)$ a function equal in its order of magnitude to unity for any ξ; factors ~ 1 are omitted. It is assumed that the electron temperature is equal to the temperature of ions. In the linear theory of plasma waves the case $T_+ = T_-$ is rarely considered, since the wave is then highly damped. This case, however, is of the greatest interest to us, since wave damping leads to dissipation.

From (6), (7), we have

$$L = D\frac{v_{T_+}}{u_0}\exp\frac{u}{v_{T_+}^2}. \tag{8}$$

If the magnetic pressure $\frac{H^2}{8\pi}$ is of the same order of magnitude as the hydrostatic pressure p, the velocities of the fast and the slow magnetoacoustic waves are of the order of v_{T_+}, and the width of a shock wave of moderate intensity is therefore equal to the Debye length. At variance with the ordinary hydrodynamic situation, the width of the shock wave increases with the Mach number $M \equiv \frac{u_0}{v_{T_+}}$, and for large Mach numbers it becomes exponentially large. This is so because dissipation is governed by the reverse mechanism of nonlinear Landau damping.

The efficiency of heating for thermonuclear reactions

Since behind the shock wave the thermal energy is concentrated in waves, whereas the ions, strictly speaking, remain cold, it is not immediately obvious that this heating should enhance the rate of thermonuclear reactions.

In the wave's own frame, the ions revolve around the magnetic field vector tracing Larmor circles of the radius

$$r_+ = \frac{v_{T_+}}{\omega_+} \quad \left(\omega_+ = \frac{eH}{m_+ c}\right).$$

If the motion of the ions is ordered, i.e., they all move in phase, the number of collisions will not increase.

Collisions multiply if the wave correlation radius is less than the Larmor radius of the ions. It has been shown that the correlation radius is equal to the Debye length. The collision-dominated heating is therefore effective if $D \ll r_+$, i.e., the Alfvén speed must be nonrelativistic.

BIBLIOGRAPHY

1. BELOKON', V. A. —JETP, **36**:341, 1316. 1959.

2. BYKHOVSKII, E. B. —DAN SSSR, **146(4)**:751. 1962.

3. BURGERS, J. M. Magnetohydrodynamics. —[Russian translation. 1958.]

4. VVEDENSKAYA, N. D. —DAN SSSR, **111**:517. 1956; **136(3)**:532. 1961.

5. GALIN, G. Ya. —DAN SSSR, **121**:55. 1959.

6. GEL'FAND, I. M. —UMN, **14**:87. 1959.

7. GODUNOV, S. K. —DAN SSSR, **134**:1279. 1960; **136**:272. 1961.

8. GOLITSYN, G. S. and K. P. STANYUKOVICH. —JETP, **33**: 1417. 1957; **35**:828. 1958.

9. DOICH, R. V. —JETP, **40**:524. 1961.

10. ZHUMARTBAEV, M. T. —JETP, **37**:1000. 1959.

11. ZEL'DOVICH, Ya. B. —JETP, **16**:365. 1946; **32**:1126. 1957; Teoriya udarnykh voln i vvedenie v gazodinamiku (Theory of Shock Waves and Introduction to Gas Dynamics). —Moskva, Izdatel'stvo AN SSSR. 1946.

12. ZEL'DOVICH, Ya. B. and Yu. P. RAIZER. —UFN, **63**:613. 1957.

13. IMSHENNIK, V. S. —JETP, **42(2)**:236. 1962; Zhurnal Vychislitel'noi Matematiki i Matematicheskoi Fiziki, **2(2)**:206. 1962.

14. KAPLAN, S. A. —JETP, **38**:252. 1960.

15. KOGAN, M. N. —Izv. AN SSSR, series mechanics and machine engineering, No. 3:143. 1960.

16. KULIKOVSKII, A. G. —DAN SSSR, **137(4)**:810. 1961; PMM, **26(2)**:273. 1962; **26(4)**:631. 1962.

17. KULIKOVSKII, A. G. and G. A. LYUBIMOV. —DAN SSSR, **129**:52, 525. 1959; JETP, **37**:1173. 1959; Izv. AN SSSR, series mechanics and machine engineering, No. 4:130. 1959; PMM, **23(6)**:1146. 1959; **25(1)**:125. 1961; **26(4)**:791. 1962.

18. LADYZHENSKAYA, O. A. —DAN SSSR, **111**:291. 1956.

19. LANDAU, L. D. and E. M. LIFSHITZ. Mekhanika sploshnykh sred (Mechanics of Continuous Media), §87. —Moskva, GITTL. 1954.

20. LUN'KIN, Yu. P. —ZhTF, **27**:1276. 1957.

21. LYUBARSKII, G. Ya. —DAN SSSR, **140**:1255. 1961; JETP, **40**:1060. 1961; PMM, **26**(3):511. 1962; UMN, **17**(1):183. 1962; In "Fizika plazmy i problemy upravlyaemogo termoyadernogo sinteza", Vol. 1, p. 82. Kiev, Izdatel'stvo AN UkrSSR. 1962.

22. OLEINIK, O. A. —UMN, **12**(3):3. 1957.

23. SAGDEEV, R. Z. —ZhTF, **31**(10):1185. 1961; Proc. Symp. on Electromagnetic and Fluid Dynamics of Gaseous Plasma, Vol. 4, p. 443. Polytechnic Press, Brooklyn. 1962.

24. SIROTINA E. P. and S. I. SYROVATSKII. —JETP, **39**:746. 1960.

25. SYROVATSKII, S. I. —UFN **62**:247. 1957; Trudy FIAN SSSR, **8**:13. 1956.

26. SHAFRANOV, V. D. —JETP **32**:1453. 1957.

27. ANDERSON, N. S. —J. Acoust. Sos. Amer. **25**:529. 1953.

28. BECKER, R. —Z. Phys. **8**:321. 1922.

29. BERNARD, J. —J. Aeron. Sci., **18**:210. 1951

30. BLEVISS, Z. O. —Fluid. Mech. **9**(1):49. 1960.

31. BROER, L. J. F. —Appl. Sci. Res., **A3**:349. 1953.

32. COLE, G. H. A. —Advances in Phys. **5**:452. 1956.

33. COMISAR G. G. —Phys. Fluids **5**(12):1590. 1962.

34. DENISSE J. F. and Y. ROCARD. —Phys. Rad., **12**:911. 1951.

35. GEIGER W., H. J. KAEPPELER, and B. MAYSER. —Nucl. Fusion, Suppl., **2**:403. 1962

36. GERMAIN, P. —Rev. Mod. Phys., **32**:951. 1960.

37. GERMAIN P. and J. P. GUIRAND. —Compt. Rend., **250**:1960.

38. GILBARG, D. —Amer. Journ. of Math., **73**(2):256. 1951.

39. GILBARG, D. and D. PAOLUCCI. —J. Rat. Mech. Anal., **2**:617. 1953.

40. GOLDEN K. I., H. K. SEN, and Y. M. TRÈVE. —Proc. Fifth Int. Conf. on Ionization Phenomena in Gases, Münich, North-Holland Publ. Co., Amsterdam, **2**:2109. 1962.

41. GRAD, H. —Comm. Pure Appl. Math. **5**:257. 1952.

42. GREENBERG, O. W., H. K. SEN, and Y. M. TRÈVE. —Phys. Fluids **3**:379. 1960; Proc. Fourth Int. Conf. on Ionization Phenomena in Gases, Uppsala, North-Holland Publ. Co., Amsterdam, **2**:1098–1104. 1960.

43. GREENBERG O. W. and Y. M. TRÈVE. —Phys. Fluids, **3**:769. 1960.

44. GUSTAFSON, W. A. —Phys. Fluids, **3**:732. 1960.

45. HELLIWELL J. B. and D. C. PACK. —Phys. Fluids, **5**(6):738. 1962.

46. HERPIN, A. —Rev. Sci., **86**:35. 1948.

47. JUKES, J. D. —J. Fluid Mech., **3**:275. 1957.

48. KROOK, M. —Annals of Phys., **6**(2):188. 1959.

49. LIBBY, P. A. —J. Aeron. Sci., **18**:187. 1951.

50. LIEBER, R. S. L. —J. Aeron. Sci., **18**:55. 1951.

51. LIEPMANN, H. W., R. NARASIMBA, and M. T. CHAHINE. —Phys Fluids, **5**(11):1313. 1962.

52. LUDFORD G. S. S. —J. Fluid Mech., **5**(1):67. 1959; Quart. Appl. Math., **10**:1. 1952.

53. MARSHALL W. —Proc. Roy. Soc., **A233**:367. 1955; Phys. Rev, **102**:5. 1956.

54. MEYERHOFF, L. —J. Aeron. Sci., **17**:775. 1950.

55. MISES, R. —J. Aeron. Sci., **17**:551. 1950. Mathematical Theory of Compressible Fluid Flow, pp. 201, 436. Academic Press Inc., New York, 1958.

56. MORDUCHOV, M. and P. A. LIBBY. —J. Aeron. Sci., **16**:674. 1949.

57. MOTT-SMITH, H. M. — Phys. Rev., 82:885. 1951.

58. MUCKENFUSS, C. — Phys. Fluids, 3:320. 1960; 5(11):1325. 1962.

59. NEUMANN J. and R. D. RICHTMEYER. — J. Appl. Phys., 21:232. 1950.

60. OWENS O. G. — Actés IX Congr. internat. mécan. appl., Vol. 3, pp. 47–48, Bruxelles, Univ. Bruxelles. 1957.

61. PAI, S. I. — Actés IX Congr. internat. mécan. appl., Vol. 3, pp. 17–25, Bruxelles, Univ. Bruxelles, 1957.

62. PUCKETT, A. E. and H. J. STEWART. — Quart. Appl. Mech., 7:457. 1950.

63. RAYLEIGH, J. W. — Proc. Roy. Soc. A84:247. 1910.

64. ROY M. — Compt. Rend., 218:813. 1944; 251:178. 1960.

65. SEN, H. K. — Phys. Rev., 92:861. 1953; 102:5. 1956; Aust. J. Phys., 7:30. 1954.

66. SEN, H. K. and A. W. GUESS. — Phys. Rev., 108:560. 1957. Third Cosmic Gas Dynamics Symposium, p. 342. Moskva, IL. 1960.

67. SHERCLIFF J. A. — J. Fluid Mech., 9(4):481. 1961.

68. SHERMAN F. S. — J. Fluid Mech. 8(3):465. 1960.

69. THOMAS, L. H. — J. Chem. Phys., 12(11):449. 1944.

70. TIDMAN, D. A. — Phys. Rev. 111:1439. 1958.

71. WHITHAM, G. B. — Comm. Pure Appl. Math., 12(1):113. 1959.

72. ZOLLER, K. — Z. Phys., 130:1. 1951.

73. GARDNER, C. S., H. GOERTZEL, H. GRAD, C. S. MORAWETZ, M. H. ROSE, and H. RUBIN. — Second International Conference on Peaceful Uses of Atomic Energy, Geneva, 1958. Vol. 31, p. 230.

74. VEDENOV, A. A., E. P. VELIKHOV, and R. Z. SAGDEEV. — Nucl. Fusion, 1:82. 1961.

75. SAGDEEV, R. Z. — In: "Fizika plazmy i problema upravlyaemykh termoyadernykh reaktsii", Vol. 4, p. 384. Moskva, Izdatel'stvo AN SSSR. 1958; Proc. Fourth Int. Conf. on Ionization Phenomena in Gases, Uppsala, Vol. 2, p. 1081, North-Holland Publ. Co. Amsterdam. 1960.

76. SAGDEEV, R. Z., B. B. KADOMTSEV, L. I. RUDAKOV, and A. A. VEDENOV. — Second International Conference on Peaceful Uses of Atomic Energy, Geneva, 1958. Vol. 31, p. 151.

77. ADLAM, J. H. and J. E. ALLEN. — Phil. Mag., 3:448. 1958.

78. ALLEN, J. E. — Rend. Scuola Internat. di Fisica, 13:38. 1959.

79. AUER, P. L. and J. A. NATION. — Nuov Cim., 22:533. 1961.

80. BANOS A. and R. VERNON. — Nuov. Cim. 15:269. 1960.

81. DAVIS, L., R. LÜST, and A. SCHLÜTER. — Z. Naturforsch, 13a:916. 1958.

82. LÜST R. — Fortschritte d. Phys., 7:503. 1959.

83. LOLADZE, Ts. D. and N. L. TSINTSADZE. — ZhTF, 31:1298. 1961.

84. PATARAYA, A. D. — ZhTF, 32:139, 584. 1962.

85. TVERSKOI, B. A. — JETP. 42:833. 1962.

86. MONTGOMERY, D. — Phys. Fluids, 2:585. 1959.

87. SAFFMAN, P. G. — J. Fluid Mech. 11:16. 1961.

88. BERNSTEIN I. B., J. M. GREENE, and M. D. KRUSKAL. — Phys. Rev., 108:546. 1957.

89. SAFFMAN, P. G. — J. Fluid Mech., 11:552. 1961.

90. MORAWETZ, C. S. — Phys. Fluids, 4:448. 1961; 5:1447. 1962.

91. SITENKO, A. G. and K. N. STEPANOV. — JETP, 31:642. 1956.

V. G. Zykov, N. G. Sinitsa, I. A. Stepanenko, V. T. Tolok, and K. D. Sinel'nikov

THE INTERACTION OF PLASMA STREAMS IN A TRANSVERSE MAGNETIC FIELD

The interaction of colliding plasma streams is of applied interest with a view to thermalization of plasma. The streaming velocities provided by modern plasma guns (up to 10^6 m/sec) are quite sufficient for generating high-temperature plasmas when the fired plasmoids are slowed down to a complete stop.

The present work is a contribution to the study of the collision of fast plasma streams with thermalization of the kinetic energy of their streaming motion. The Coulomb interactions between colliding particles are apparently inadequate in this case, since plasmas with densities of 10^{18} cm^{-3} and stopping lengths of no more than 1 m are required to ensure sufficiently high temperatures (10^8 °K) by random motion only. The available plasma guns are incapable of producing these plasmas.

It is therefore interesting and advisable to consider the so-called polarization interaction of the plasma streams moving across a magnetic field.

The motion of plasmas in transverse magnetic fields was successfully studied in /1—4/. However, these experiments did not ensure proper collision of the plasmoids, and this had a detrimental influence on the efficiency of stopping.

Apparatus

The measurements were made on the setup shown in Figure 1. A chamber 5 with a diameter of 20 cm was immersed in a longitudinal magnetic field, provided by the coils 4 supplied by a d. c. generator. The field could be varied from 0 to 0.5 T. Eight conical plasma guns 1 with plexiglas cone insulators /5/ were arranged circumferentially midway along the gun. The plasma was created by discharging a 3 μF condenser through the central electrode in the apex of the gun and a ring electrode at its base. Discharge period 6 μsec. The plasma created by the gun 1 consisted of a fast and a slow components, with velocities of $8 \cdot 10^4$ and $3 \cdot 10^4$ m/sec, respectively, for 4 kV source voltage; the plasma contained ions of hydrogen, carbon, oxygen, and nitrogen

Depending on the experimental requirements the guns were fitted touching the chamber in the magnetic field region or were situated outside

the chamber, at the far end of plasma guides 2 (copper tubes of 5 cm diameter). The plasma guides were protected with iron screens 3, to prevent marginal infiltration of the magnetic field. The vacuum in the chamber was $1.33 \cdot 10^{-3} N/m^2$.

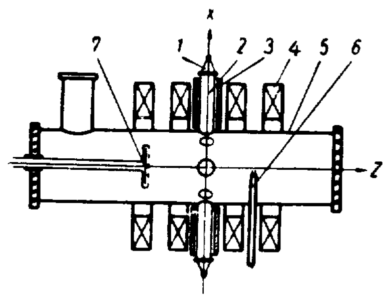

FIGURE 1. A schematic of the experimental apparatus.

The plasma was diagnosed with ultra-high speed photography, by photographing the integral-light visual glow, with double electrostatic probes 6, with a plane collector probe 7, with magnetic probes, and also with special targets whose surface darkened under the impact of plasma.

Motion of plasma across the magnetic field

Numerous experiments show that the plasma mostly traces a curved trajectory in a transverse magnetic field.

When the direction of the magnetic field is changed, the curvature of the plasma trajectory is also reversed. The plasma stream apparently carries a certain net charge, whose quantity and sign depend on the gun voltage.

Target measurements enabled us to study the motion of a plasma jet along the chamber. Figure 2 shows some photographs of targets set at different distances from the injection plane, at right angles to the magnetic lines of force. The targets were positioned at the following distances from the injection plane: a) $z = 4$ cm; b) $z = 7.5$ cm; c) $z = 15$ cm; d) $z = 23$ cm. The plasma was injected from a single gun in the direction marked with an arrow on each target. The magnetic field in these experiments was 0.25 T. We see from the photographs that the plasma, though injected across the magnetic field, also has a velocity component along the lines of force; the deflection of the plasma jet is also observed on these photographs.

The plasma propagates along the magnetic field symmetrically about the plane of injection. The plasma traces on the targets are highly extended along the z axis, symmetrically about the plane of injection.

Target measurements were made for a high source voltage ($U_s = 12$ kV, $n > 10^{14}\,cm^{-3}$), since with tenuous plasmas very high exposures were required. For dense plasmas and magnetic inductions of up to 0.5 T, a

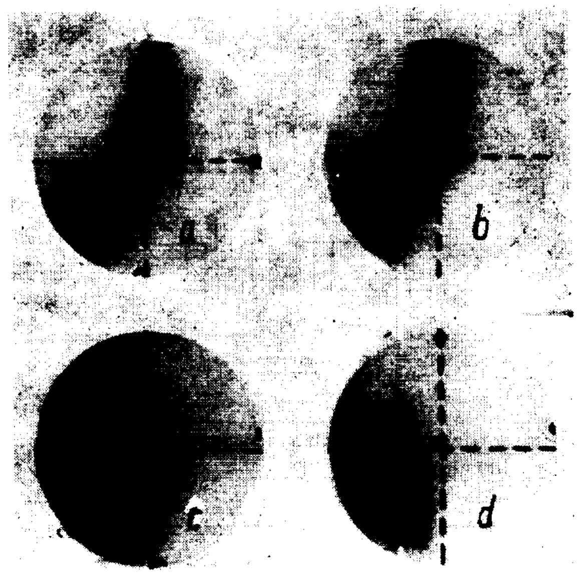

FIGURE 2.

considerable proportion of the plasma hits the opposite wall of the chamber. For lower densities ($n \approx 10^{12}\,cm^{-3}$ and $U_s = 4-5$ kV), however, the visual glow of the plasma column does not extend all the way to the opposite wall.

Plasma injection in opposite directions from several guns at right angles to the magnetic field

In previous experiments /6/ we investigated the collision of counter-streaming plasmas injected through a slit in cusped magnetic fields. The experimental conditions were adjusted so that the Coulomb interaction predominated (low velocity, high density of particles in colliding streams).

The aim of this work was to investigate the possibilities of complete stopping and thermalization of fast counterstreaming plasmas. It is quite obvious that the experimental conditions must be chosen so as to ensure strong interaction of the colliding plasma streams, other than the Coulomb interaction. The Coulomb mechanism is inadequate for stopping the fast, dense plasmoids generated by modern guns. We therefore decided to tackle the so-called polarization interaction.

Electric polarization fields of opposite signs are induced in two plasma streams moving across a magnetic field in opposite directions. When the

plasma collide, these fields mutually cancel, and the transversal drift should cease. The plasma thus stops on collision.

The experiments described in what follows were made with plasmoids for which Coulomb interactions had been rendered impossible (densities less than $10^{13}\ cm^{-3}$).

Figure 3 shows some photographs of the integral-light glow of the plasma taken for source voltages of 4 kV, i.e., plasma densities of the order of $10^{12}\ cm^{-3}$ (the density was estimated from the cutoff of 3-cm signals). The photograph in Figure 3,a was taken without a magnetic field. The plasma streams do not interact in this case. As the transverse magnetic field increases, the interaction is enhanced (see Figures 3, b, c, d, taken for 0.05, 0.35, and 0.48 T, respectively). The plasma streams stop on collision,

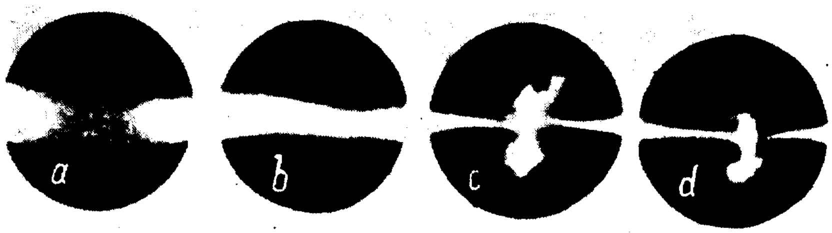

FIGURE 3.

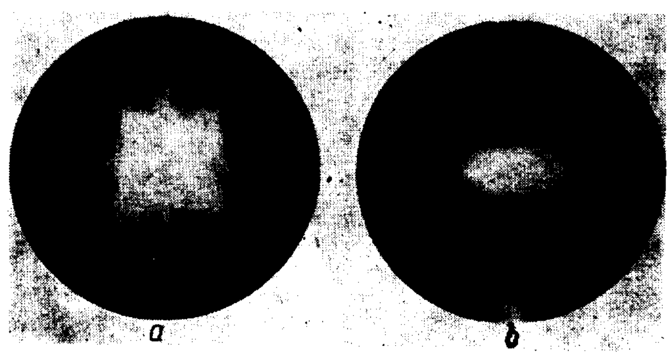

FIGURE 4.

ejecting lateral streamers and eddies. No such turbulent formations are observed with the ordinary Coulomb interaction (Figure 4). These streamers may or may not reach the chamber walls, depending on the source voltage, the magnetic field strength, and also the precision of hit. For a low source voltage and a high magnetic field, the streamers do not reach the walls (see Figures 3, c and 3, d), while conversely, with weak magnetic fields and strong source voltages, the streamers hit the chamber wall. In the case of a glancing collision, the streamers break at the point of contact and continue at an acute angle to their original direction.

Figures 5, a and 5, b show photographs of the integral-light glow of the plasma injected from four guns into a field-free space and across a magnetic field with an induction of 0.33 T (U_s = 4 kV). The plasmoids interact only in the presence of a magnetic field (Figure 5, b). If the plasma moves in a curved trajectory and no head-on collision occurs, a plasma-free space is formed near the axis in the case of injection from several guns. Typical photographs illustrating this configuration are shown in Figures 5, c and 5, d (gun voltage 5 kV, magnetic field 0.33 T, injection from four and eight guns).

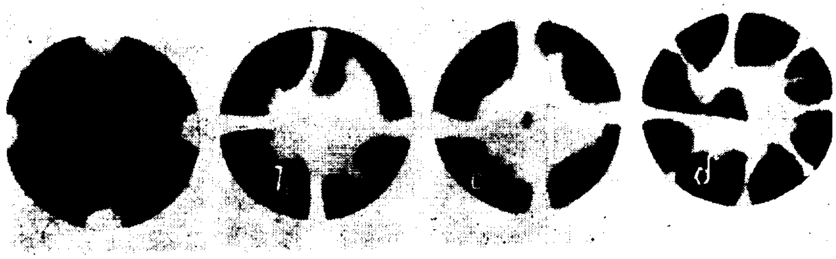

FIGURE 5.

FIGURE 6.

Figure 6 shows some high-speed photographs (taken at a rate of 250,000 frames a second) of the interaction of plasma streams injected from eight guns across the magnetic field. Comparing these photographs with the photographs in the case of Coulomb interaction (Figure 4), we see that the interaction here is spatial, rather than planar

The ring current induced in the plasma when the polarization fields were cancelled on collision was measured with a Rogowsky loop. The direction of this current was such that it increased the longitudinal magnetic field B_0 inside the forming plasma ring. This magnetic field enhancement was picked up by a magnetic probe, set in an axial position at the center of the ring in the plane of injection.

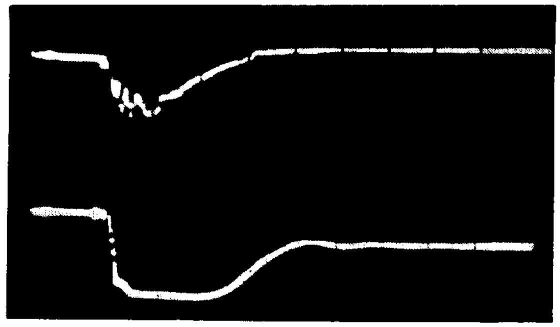

FIGURE 7.

Figure 7 shows some oscillograms of the integrated signals of the Rogowsky loop (top trace) and the magnetic probe (bottom trace), taken for $B_0 = 0.01$ T and injection from eight guns.

The graphs plotting the magnetic field increment ΔB_z and the azimuthal current I_φ as a function of B_0 in the case of eight-gun injection and $U_s = 8$ kV are shown in Figure 8. ΔB and I_φ linearly increase with B_0, reaching a maximum and then falling off as $\frac{1}{B_0}$. The peak of these curves shifts in the direction of higher B_0 when the source voltage increases. Enhancement of the axial magnetic field is observed for injection from eight, four and two guns. With injection from a single gun, the external magnetic field actually decreased in the plasma due to its diamagnetism.

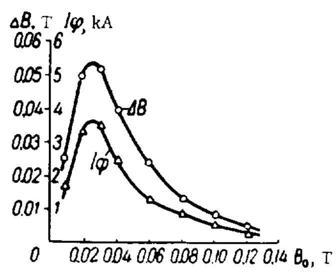

FIGURE 8.

The interaction of polarized plasma is also confirmed by measurements with a double electrostatic probe. The probe was inserted at a distance of 15 cm from the plane of injection and could be moved along the diameter of the chamber. Probe measurements showed that the glow line corresponded to the actual boundary of the plasma: outside the luminous region, the probe did not pick up significant signals.

The left half of Figure 9 shows photographs of plasma glow, the right half gives the saturation current of the double probe corresponding to these photographs. The lower trace of each oscillogram is a 200 kc/s sinusoidal timing signal. The oscillograms were taken for $B_z = 0.25$ T, $U_s = 4.7$ kV. The probe shows in all the photographs, since the plasma

was injected 15 cm behind the probe. The glow photographs and the oscillograms in Figure 9, a, b, c were obtained with the probe situated on the axis of the chamber, while Figure 9, d corresponds to a probe set at a distance of 2 cm from the wall opposite the plasma source.

Injection from a single gun (Figure 9 a, b) produces a much shorter probe signal than injection from two guns (Figure 9, c), with the probe situated near the axis. The amplitude of the signal for two-gun injection, however, is not larger than the amplitude for injection from a single gun. This apparently means that the plasma density in the interaction region does not increase with the volume of injected plasma.

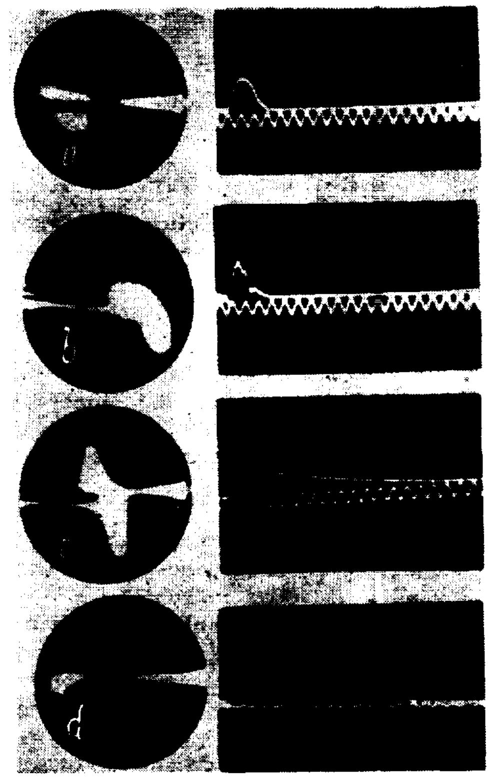

FIGURE 9.

Long signals are also recorded in the case of one-gun injection if the probe is inserted near the opposite wall (Figure 9, d). If the plasma is injected from two guns or from a single gun in the same wall where the probe is placed, the signal is short, like that in Figure 9, a, b. In other words, the probe picks up a long signal if it is immersed in an expanding cloud of plasma, and not in a narrow plasma jet.

We have seen from target measurements that the injected plasma moves longitudinally, as well as transversally, to the magnetic field. Proceeding from the experiments of Sinel'nikov and Padalka /7/, we suggest that the fast, light-weight component of the plasma moves along the magnetic field,

while the slower heavy component crosses the magnetic field, hits the opposite wall, and spreads near it. This explains why in single-gun injection a probe placed far from the plane of injection picks up a brief signal, produced by the fast component, while the wall signal is indicatory of the slow heavy plasma spreading along the opposite wall. When plasma is injected from two guns in opposite directions, the fast component continues along the magnetic field, while the slow plasma stops on collision without reaching the wall; in this case the plasma spreads near the axis. The axial probe, immersed in the plasma cloud, will therefore give a long signal, while the probe intercepting the thin jet produces a short blip.

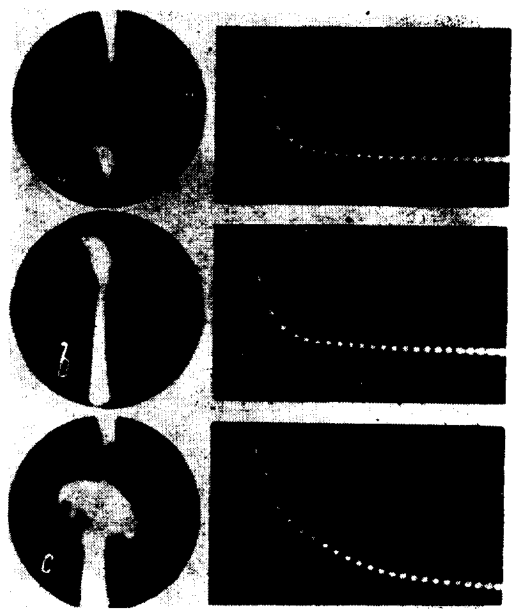

FIGURE 10.

A collector probe was also used, aside from the double probe. This is a disk 10 cm in diameter with a grid in front. A voltage of some 30 kV was applied between the grid and the disk, this being enough to saturate the probe current. The plane of the probe was set at right angles to the chamber axis, as shown in Figure 1. The probe could be moved along the axis, collecting the counterstreaming ions over an area $S = 78\ \mathrm{cm}^2$. The probe current I was assumed proportional to $envS$, where e the ion charge, n the density, v the velocity, S the probe area.

Typical probe current oscillograms and the corresponding plasma glow photographs (injection from one or two guns) are shown in Figure 10 ($U_s = 4.3$ kV, $B_z = 0.28$ T, probe distant 30 cm from injection plane, time markings each 20 μsec). The oscillograms show that for injection from a single gun the signal is much shorter than for two-gun injection. The amplitude of the signal in the case of two-gun injection is approximately equal to the sum of the signals from each gun separately, except in the

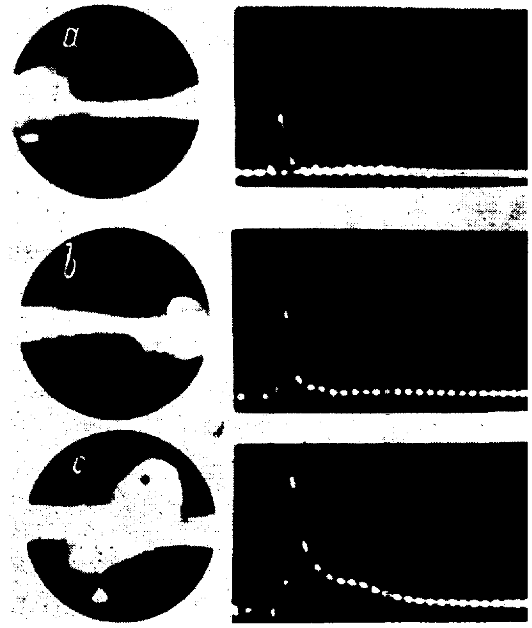

FIGURE 11.

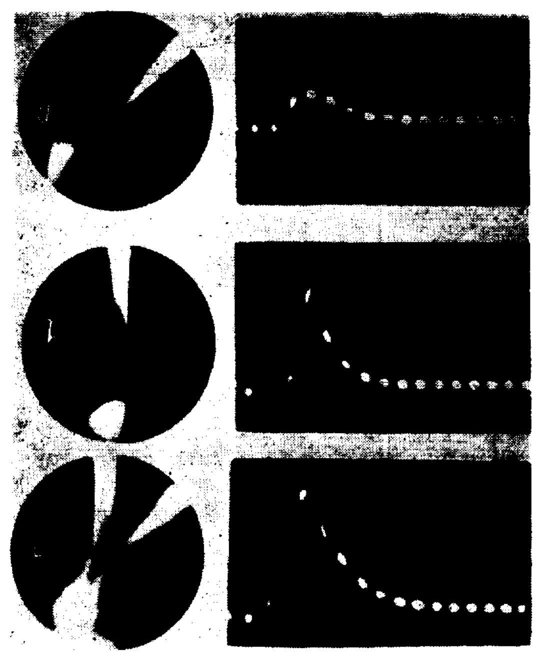

FIGURE 12

"tail", where the two-gun signal is substantially stronger than the sum of two single-gun signals.

It is noteworthy that unlike the double probe, which collects ions over its entire surface, so that its saturation current corresponds to the density of the ions at a given point, the large disk probe gives a current which is proportional, not only to the density, but also to the cross-sectional area of the plasma jet hitting the probe (providing, of course, that the probe is broader than the jet). Now, since the amplitude of the two-gun signal is equal to the sum of the amplitudes for injection from each gun separately, it seems that the fast plasma components moving along the magnetic field have almost parallel velocities and the two jets do not interact; this explains why the probe picked up twice the number of particles ejected by a single gun.

The slow component, which in the case of single-gun injection moved across the field without hitting the far probe, collided with its counterpart in simultaneous injection and spread along the magnetic field near the axis, thus producing the long "tail" of the probe signal.

The length and the height of the "tail" in glancing collision is much less than in head-on collision, as we see from Figure 11, c. The difference between one- and two-gun injection is even less pronounced if the plasma is fired from two sources making a small angle with each other. Typical oscillograms and integral-light photographs for this case are given in Figure 12. Adding the signals in Figures 12, a and 12, b, we obtain a curve which almost coincides with the oscillogram in Figure 12, c over its entire length.

Our experiments thus show that plasma streams in head-on collision in a transverse magnetic field experience intense stopping forces until all motion in the initial direction ceases. Unlike the Coulomb interaction, this interaction occurs, not inside the plasma jets, but at their leading fronts; it is distinctly turbulent, producing complex eddies and streamers.

In principle, this interaction should occur irrespective of the plasma parameters and the magnetic field strengths. For effective stopping, however, head-on collision of the plasmoids must be ensured. Similar experiments will be made in future employing pure hydrogen or deuterium plasmas.

BIBLIOGRAPHY

1. BOSTICK, W. H. — Phys. Rev., **104**: 292. 1956.

2. BOSTICK, W. H. — Phys. Rev., **106**: 404. 1957.

3. BOSTICK, W. H. — In: "Problemy sovremennoi fiziki", Vol. 3. 1958.

4. EUBANK, H. P. — Bull. Am. Phys. Soc., Ser. II, Vol. 6, p. 196. 1961.

5. AZOVSKII, Yu. S., I. T. GUZHOVSKII, B. G. SAFRONOV, and V. A. CHURAEV. — ZhTF, **32**: 1050. 1962.

6. ZYKOV, V. G., I. A. STEPANENKO, V. T. TOLOK, and K. D. SINEL'NIKOV. — In: "Fizika plazmy i problemy upravlyaemogo termoyadernogo sinteza", Vol. 3. Kiev, Izdatel'stvo AN UkrSSR. 1963.

7. DEMIDENKO, I. I., V. G. PADALKA, B. G. SAFRONOV, and K. D. SINEL'NIKOV. — This volume, p. 259. ZhTF, **34**: 7. 1964.

Ya. F. Volkov, V. A. Kornilov, and V. G. Dyatlov

INJECTION OF PLASMA IN A QUADRUPOLE MAGNETIC FIELD

We investigated the motion of a plasma stream injected by a coaxial gun into the magnetic field of a quadrupole lens. This is a field of cusped geometry, and the plasma in this field should be stable with respect to flutes. Some earlier experiments confirm this fact /1, 2/. The quadrupole field focuses charged particles of opposite signs in mutually perpendicular planes. However, the motion of a plasma in this geometry is hardly predictable. To interpret the interaction of a plasma jet with a quadrupole magnetic field, we determined the parameters of the plasma as a function of the operating mode of the gun.

Apparatus and procedure

The setup shown in Figure 1 is a molybdenum glass tube 100 mm in diameter with four rods 30 cm long fitted along the walls. The vacuum prior to the injection of hydrogen was $6.6 \cdot 10^{-4}\,N/m^2$. The amplitude of the current through the rods reached 23 kA, period 2 μsec. The current flowed in opposite directions in each pair of rods, providing a quadrupole magnetic field with a strength of 120 kA/m near the tube wall, in the magnetic slit. The plasma was injected along the axis from a coaxial-type gun. An 18 μF,

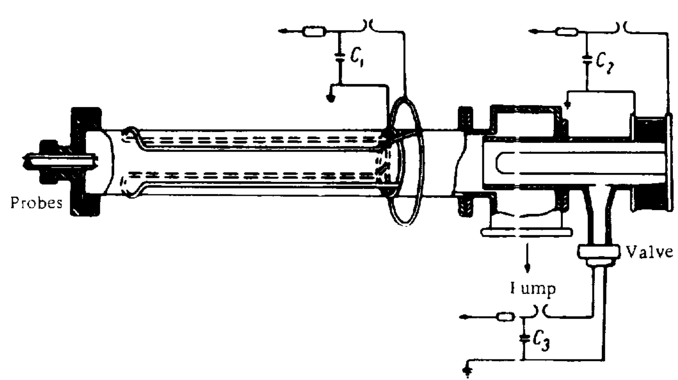

FIGURE 1. Schematic of the apparatus

17 kV condenser bank was discharged through the gun. The discharge was almost aperiodic. The first half-period was 12 μsec decrement of damping = = 4. The hydrogen was admitted through a pulsed valve described in /3/.

The operational sequence was as follows: the magnetic field was turned on, the valve was then triggered, and the gun was fired after a preset delay, approximately synchronized with the magnetic field maximum.

The density of the plasma was determined with double electric probes, whose plane was set at right angles to the plasma stream. Since the streaming velocity of the ions is much higher than their thermal velocity,

the probe current depends on the density and the drift velocity of the ions in the stream:

$$I = envs,$$

where I is the probe current, e the charge, n number density of streaming particles, v drift velocity, s the collecting surface of the probe.

The charge of the plasma stream was measured with a Faraday cup (l = 100 mm, D = 40 mm), which could be moved axially. The cage was grounded through a resistor, and the voltage across this load was picked up as a signal. Secondary electrons were suppressed by a transverse magnetic field.

The mass composition of the stream and the energy distribution of the ions were determined by Thomson's method of parabolas. By making photometry of the plate and applying the results of /4/, we could find the energy distribution of the ions in the stream.

Aiming ions of a certain mass at a CsI crystal coupled into a photomultiplier, we measured the time distribution of ions of various masses in the stream and the influence of the magnetic field on each component.

High-speed photographs taken through the end surface of the quadrupole displayed the spatial distribution of the plasma moving in the quadrupole field.

Results of measurements

Figure 2 shows some high-speed photographs taken through the end of the tube. The first three photographs correspond to a small delay between the opening of the valve and the triggering of the current (time between successive photographs, 0.5 μsec). The first photograph (Figure 2, a)

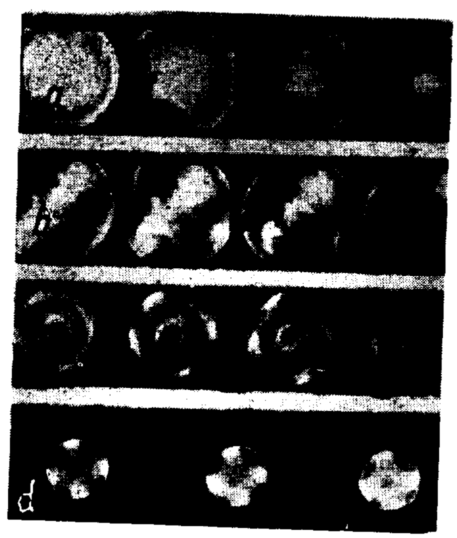

FIGURE 2. High-speed photographs:
a) no magnetic field; b) magnetic field of $6.4 \cdot 10^4$ A/m;
c) magnetic field of $1.2 \cdot 10^5$ A/m.

(no magnetic field) shows that the plasma moves as a cylinder through the tube, the glow intensity being maximal at the center.

When the quadrupole magnetic field is turned on, the plasma is compressed in the focusing plane of a positively charged beam (Figure 2, b). This pattern, however, disappears as the field strength increases (Figure 2, c). The fourth photograph was taken for a large delay between the gun current and the opening of the valve; here the plasma passes the quadrupole lens escaping through the magnetic slits (Figure 2, d). This behavior of the plasma stream in a quadrupole field can be attributed to the jet being neutral or carrying a space charge, depending on the operating mode of the gun.

Faraday cup measurements show that the plasma jet emerging from the gun can be divided into three components.

The first, fast component carries a negative charge. These are the electrons ejected by the gun on sparking. The second component is positively charged. This is the hydrogen plasma leaving the gun with a velocity of $(2-7)\cdot 10^7$ cm/sec (the lower bound of the velocity is determined from probe measurements, the upper bound is obtained from mass-spectrographic data). The third component is also positively charged. These are the heavy impurities, mainly copper. Their velocity is less than $7\cdot 10^6$ cm/sec.

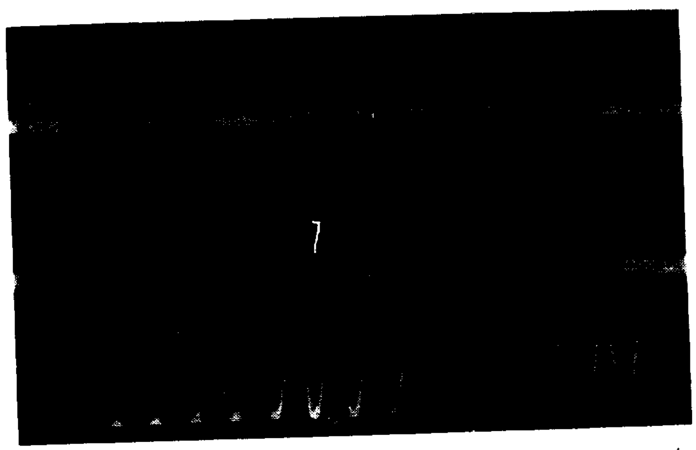

FIGURE 3. Gun current (a), double probe signal (b), timing signal $f = 200$ kc/s (c).

This structure of the plasma jet is very distinct for small delay times between the opening of the valve and the triggering of the gun. As the delay increases, the negatively charged component diminishes and eventually vanishes, while the velocity of the remaining components decreases.

Note that the plasma charge is generated inside the gun. This is so because the signal remains practically constant with the Faraday cup set at distances of 5 and 50 cm from the muzzle. The voltage across the $R = 2$ kohm resistor connected with the Faraday cup was $U = 50$ V for the leading plasma component ($v = 2-5\cdot 10^7$ cm/sec); this corresponds to an excess charge density $\Delta n \approx (1-0.45)\cdot 10^9$ cm^{-3}.

Figure 3 shows an oscillogram of the current produced by the double probes, which are incapable of picking up the electron component.

The first pulse corresponds to a hydrogen plasma with a density $n \approx 5 \cdot 10^{12}\,\mathrm{cm}^{-3}$, while the second pulse represents impurities with a density $n \approx 10^{14}\,\mathrm{cm}^{-3}$. The last figure is apparently too high by a factor of two, since the slow stream contains numerous multiply charged ions.

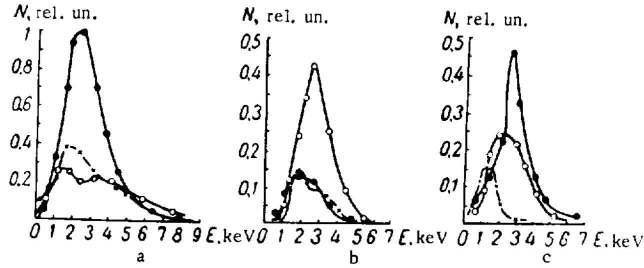

FIGURE 4. Energy distribution of ions for various delay times between the firing of the gun and the opening of the valve: ● 450 μsec; ○ 500 μsec; x 550 μsec.

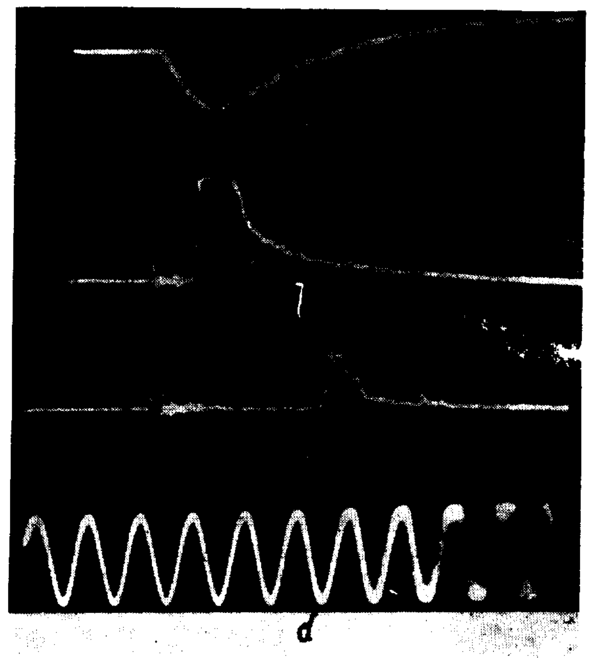

FIGURE 5. Gun current (a), H^+ peak (b), Cu^+ peak (c), timing signal $f =$ 200 kc/s (d).

Mass spectrography gives more accurate data on plasma densities. Figure 4 plots the results recovered from mass spectrograms. The first graph (Figure 4, a) corresponds to Cu^+ ions, the second (Figure 4, b) to H^+, and the third (Figure 4, c) to O^+. Different curves correspond to

different delay times between the firing of the gun and the opening of the valve. We see from Figure 4 that there is an optimal delay mode for which the peak content of hydrogen in the plasma is 60%, of copper 25 — 30%, and of other impurities 10 — 15%. The mean energy is the same for all the particles, being equal to 3 keV.

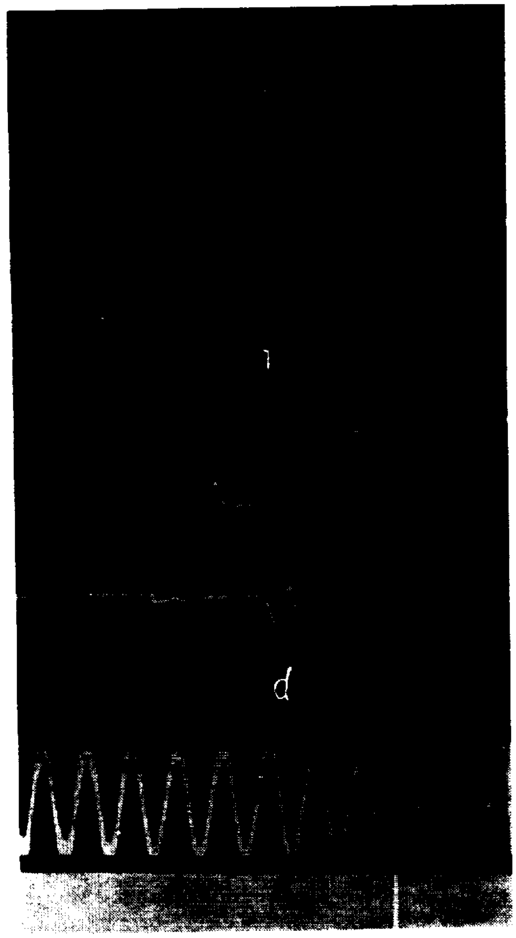

FIGURE 6. Gun current(a), Faraday cage signal for a small delay, no magnetic field (b), ditto, in the presence of a magnetic field(c), Faraday cage signal for a large delay, no magnetic field (d), timing signal f = 100 kc/s (e).

By aiming the ion beam through the mass spectrograph at a CsI crystal, we can establish the time distribution of the stream components. Figure 5 shows some oscillograms of the photomultiplier signals for Cu^+ and H^+. Comparing these oscillograms with probe measurements, we clearly see that the first component is a hydrogen plasma with a mean energy of 3 keV, while the second component comprises the slow impurities of the same energy. These components are resolved by 10 — 15 μsec in time.

Further investigations of the interaction of a plasma stream with a quadrupole magnetic field (Faraday cup set midway along the lens) showed that the fast electron component was not transmitted, while the charge of the two trailing streams was hardly affected (Figure 6).

The positive charge of the plasma at the quadrupole output increases by a factor of 20 — 30 with the magnetic field. Density measurements with double probes show, however, that the density is virtually constant along the quadrupole axis, irrespective of the magnetic field strength.

In conclusion, we suggest the following interpretation of the experimental results. When the gun is fired through a small quantity of residual gas, the discharge may contain electrons of energy eV, where V is roughly the voltage applied to the gun electrodes. These high-energy electrons apparently provide the negatively charged stream picked up by the Faraday cup. The next plasma should therefore carry a net positive charge. The absence of a neutral plasma (for small delay times) is apparently responsible for the bunching of the plasma transmitted through the quadrupole magnetic field into a plane stream.

The signal picked up by the Faraday cup at the quadrupole output increases apparently because the cold electrons in the plasma readily escape to the walls following the divergent magnetic lines of force, while the fast ions stick to the original course. The axial jet thus acquires a net positive charge, which sets up a potential difference of the order of $V = \frac{W}{e}$ across the stream boundary (W is the energy of the ions, equal to 3 — 4 keV).

Our experiments show that the plasma created by a coaxial source in the mode of a small delay is positively charged. As the delay increases, the charge is compensated, the stream velocity dropping from $(5-7)\cdot 10^7$ to $(7-10)\cdot 10^6$ cm/sec. The plasma jet enters the quadrupole field almost without any losses, it is bunched into a plane stream by the field, and emerges with a higher space charge.

BIBLIOGRAPHY

1. VOLKOV, Ya.F., S.M. KRIVORUCHKO, and V.T. TOLOK. — ZhTF, 33 : 9. 1963.

2. BAIBORODOV, Yu.T., M.S. IOFFE, V.M. PETROV, and R.I. SOBOLEV. — Atomnaya Energiya, 14(5) : 443. 1963.

3. ZOLOTOTRUBOV, I.M., V.A. KISELEV, and Yu.M. NOVIKOV. — In: "Fizika plazmy i problemy upravlyaemogo termoyadernogo sinteza", Vol.3. Kiev, Izdatel'stvo AN UkrSSR. 1963.

4. KRUPNIK, L.I. and N.G. SHULIKA. — In: "Fizika plazmy i problemy upravlyaemogo termoyadernogo sinteza", Vol.3. Kiev, Izdatel'stvo AN UkrSSR. 1963.

I. M. Zolototrubov, N. M. Ryzhov, I. P. Skoblik,
and V. T. Tolok

INJECTION OF PLASMA INTO A MAGNETIC TRAP WITH CUSPED FIELDS

An experiment is described with the injection of plasma into a magnetic trap with cusped fields /1, 2/. These traps are of particular significance since the theory predicts hydromagnetic stability of the plasma in these geometries /3/.

The experiment was carried out on the setup shown in Figure 1. A cylindrical chamber 0.30 m in diameter and 0.7 m long, made of stainless steel sheets 3 mm thick, was immersed in the field of two coils through which a 2400 μF condenser bank was discharged (the bank was charged to voltages of up to 4 kV). When the condensers were discharged, the magnetic field increased to its maximum in 4.4 msec, falling off with a decay constant of 16 msec (the coils were shunted with a shorted circuit). The magnetic field in the mirrors was $4 \cdot 10^5$ A/m; the field in the magnetic slits was $3.3 \cdot 10^5$ A/m. The initial vacuum in the chamber was $6.66 \cdot 10^{-4}$ N/m^2.

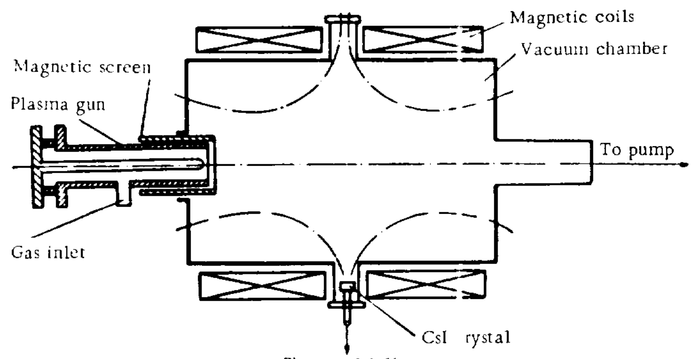

FIGURE 1.

An ordinary coaxial gun described in /4/ was used as the plasma source. The operating modes of the gun were studied separately as a function of the delay between the admission of the gas and the application of voltage to the source electrodes. The plasma in these tests was injected into a glass tube with two external magnetic probes, one placed at the muzzle, the other at a distance of 0.5 m. Figures 2, a and 2, c are oscillograms of probe signals characterizing two modes of source operation (Figure 2, a for a delay of 250 μsec, Figure 2, c for a delay of 100 μsec). The upper trace pertains to the first probe, the lower trace to the second. In the mode of a small delay, the gun ejects several plasmoids which move with different velocities. The velocity of the head is $8.8 \cdot 10^5$ m/sec, which corresponds to 3.9 keV hydrogen ions. Irrespective of the operating mode, 0.3 cm^3 of hydrogen (under standard conditions) was admitted into the gun.

The plasma was injected into the trap through the magnetic mirror when the magnetic field reached its maximum strength. We studied the time-

dependence of the X-ray radiation emitted on injection. The radiation was picked up with a CsI crystal coupled into a photomultiplier. The crystal was placed in a length of tube attached to the vacuum chamber in the plane of the magnetic slit (Figure 1). The crystal was protected from extraneous light by an aluminum foil 15 μ thick. Figures 2, b and 2, d are oscillograms of X-ray pulses (bottom trace) for two modes of operation: large delay (Figure 2, b) and small delay (Figure 2, d). The upper trace in both cases

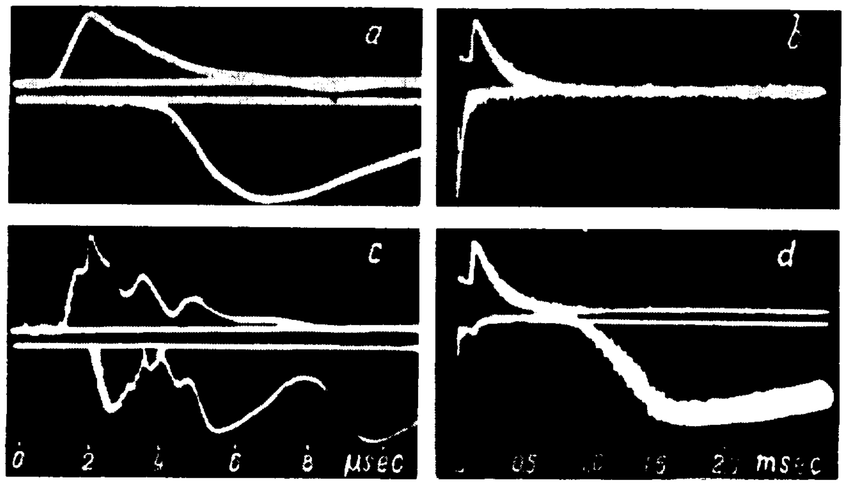

FIGURE 2.


FIGURE 3.

gives the visual glow of the plasma near the magnetic slit. The oscilloscope was triggered simultaneously with the firing of the gun. We see from the oscillogram in Figure 2, b that for large delay times the injection of the plasma is accompanied by a short X-ray blip. A similar starting blip is also observed for small delay times (Figure 2, d), but its amplitude is much

smaller than in the former case. Intense X-ray radiation is furthermore emitted in the small-delay mode 840 μsec after injection, falling off exponentially with a decay constant of some 3 msec.

This time variation of the pulse apparently indicates that part of the injected plasma escapes through the magnetic slit in the very first stage, while part of the plasma is trapped for the time between the first and the second pulses. The large decay constant of the second pulse (3 msec) shows that the trapped plasma escapes fairly slowly from its confinement.

The energy of the radiation picked up by the crystal was measured with an X-ray film, coplanar with the crystal; the film was covered with a graded absorber, a selection of aluminum foils 7 μ thick. A couple of X-ray pulses were sufficient for normal exposure of the film. The mean X-ray energy measured by this technique was 3.8 keV.

The film is darkened in a narrow strip (Figure 3), corresponding to the magnetic slit. This obviously proves that the X-ray radiation is in fact the bremsstrahlung of the charged particles escaping through the magnetic slit. It should be noted, however, that the film is not darkened when the gun operates in the large-delay mode.

The results of our experiments can be summarized as follows:

1) when plasma is injected into a trap with cusped fields from a coaxial gun operating with small delay times, intense X-ray radiation is observed 840 μsec after injection;

2) this radiation is the bremsstrahlung of charged particles escaping through the magnetic slit;

3) the X-ray energy (3.8 keV) is equal to the energy of hydrogen ions residing in the head of the injected plasmoid.

BIBLIOGRAPHY

1. KOVAL'SKII, N. G., S. Yu. LUK'YANOV, and I. M. PODGORNYI. — Nucl. Fusion, Suppl. Part 1, p. 81. 1962.
2. OSHER, J. E. —Phys. Rev. Letters, **8**: 305. 1962.
3. BERKOVICH et al. — Second International Conference on Peaceful Uses of Atomic Energy. Geneva, 1958.
4. ZOLOTOTRUBOV, I. M. et al. — ZhTF, **34**: 998. 1964.

Section Eight

MAGNETIC TRAPS

K. D. Sinel'nikov, N. A. Khizhnyak, N. S. Repalov,
P. M. Zeidlits, V. A. Yamnitskii, and Z. A. Azovskaya

MOTION OF CHARGED PARTICLES IN MAGNETIC TRAPS OF CUSPED GEOMETRY

The motion of charged particles in magnetic traps of cusped geometry has been investigated by various authors /1–3/, but we are still far from a comprehensive knowledge of the different features of this motion. To a certain extent, this inconclusiveness is attributable to the complicated analytical description of the magnetic fields inside the trap, as well as to difficulties encountered in the integration of the equations of motion. The magnetic field of a cusped trap in its simplest form is defined by the relations

$$H_r = ar; \quad H_z = -2az. \tag{1}$$

This field is maintained in the central region between two ring currents. The equations of motion of a particle are nonlinear even in this elementary field geometry, so that the particle trajectory can be determined by numerical methods only. Various properties of this motion, however, can be deduced from general considerations.

In the present paper we investigate the motion of charged particles in some axially symmetric magnetic fields of cusped geometry and discuss the particle trajectories obtained by numerical integration of the equations of motion.

Magnetic fields of cusped traps

The magnetic field inside the trap satisfies the equations

$$\operatorname{rot}\mathbf{H} = 0; \quad \operatorname{div}\mathbf{H} = 0$$

and it can be described in terms of the scalar magnetic potential Φ meeting the Laplace equation $\Delta\Phi = 0$. For axially symmetric cusped fields, the solution of the Laplace equation which is symmetric about the plane $z = 0$ has the form

$$\Phi = \sum_{n=0}^{\infty} A_n I_0(k_n r)\cos k_n z,$$

or

$$\Phi = \sum_{n=0}^{\infty} A_n J_0(k_n r)\,\mathrm{ch}\, k_n z, \tag{2}$$

where the amplitudes A_n and the separation-of-variables constants k_n are specified by the fields in the trap slits.

In the present paper it is assumed that the magnetic field in the entire trap is described by a single term in the sums (2).

Then in the first case, the magnetic field has the form

$$
\begin{aligned}
H_r &= H_0 I_1(kr)\cos kz,\\
H_z &= -H_0 I_0(kr)\sin kz,
\end{aligned}
\tag{3}
$$

and the line of force

$$
\frac{dr}{dz} = \frac{H_r}{H_z},
$$

i.e.,

$$
r I_1(kr)\sin kz = \text{const};
$$

in the second case

$$
\begin{aligned}
H_r &= H_0 J_1(kr)\,\text{ch}\,kz,\\
H_z &= -H_0 J_0(kr)\,\text{sh}\,kz
\end{aligned}
\tag{4}
$$

with the line of force

$$
(kr)\,J_1(kr)\,\text{sh}\,kz = \text{const}.
$$

Figures 1 and 2 are the field patterns of magnetic traps of the first and the second kind.

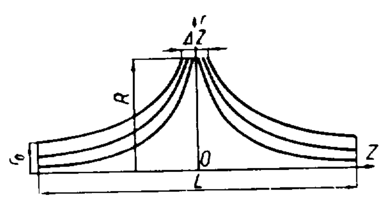

FIGURE 1.

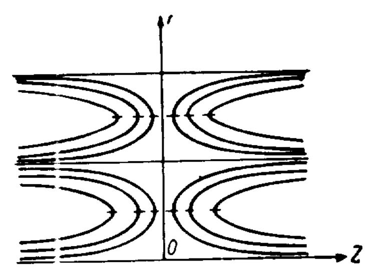

FIGURE 2.

The magnetic field in traps of the first kind is characteristic of the ordinary "picket fence" geometries. Traps of the second kind are planar, radially unbounded geometries terminating at "magnetic walls" with negative curvature of the magnetic field. This "magnetic wall" can be provided by a system of concentric conductors with alternate currents flowing in opposite directions.

The nonzero azimuthal component A_φ of the fields (3) and (4) has the form

$$
A_\varphi = -\frac{H_0}{k} I_1(kr)\sin kz,
$$

$$
A_\varphi = -\frac{H_0}{k} J_1(kr)\,\text{sh}\,kz.
$$

For $kr \ll 1$ and $kz \ll 1$, the fields (3) and (4) reduce to (1). However, unlike the field (1), they are characterized by two parameters H_0 and k, specifying the magnetic field in the mirrors and the geometrical size of the trap.

In the planes $kz = \pm\pi/2$, the magnetic field has one component only, H_z. If r_0 is the radius of the magnetic mirror, the flux of magnetic induction through the mirror is written

$$\Phi = \frac{2\pi H_0}{k} r_0 I_1(kr_0).$$

This flux also emerges through the corresponding half of the ring slit, having the width Δz and situated at a distance R from the axis of symmetry:

$$\Phi = \frac{2\pi H_0}{k} R I_1(kR) \sin\frac{k\Delta z}{2}.$$

The radius of the magnetic mirror and the slit width are thus related by the expression

$$\frac{r_0 I_1(kr_0)}{R I_1(kR)} = \sin\frac{k\Delta z}{2}. \tag{5}$$

This relation also follows from the equation of the line of force.

In the following we shall be concerned with magnetic traps of the first kind, although many of the relations can be easily generalized to traps with "magnetic walls" also.

The parameter k is related with the trap length L by the obvious expression

$$k = \frac{\pi}{L},$$

and (5) can therefore be written in the form

$$\frac{r_0 I_1\left(\frac{\pi r_0}{L}\right)}{R I_1\left(\frac{\pi R}{L}\right)} = \sin\pi\frac{\Delta z}{2L}. \tag{6}$$

The sizes of the mirror and of the ring slit are thus determined by the transverse and the longitudinal dimensions of the trap.

In the following we shall distinguish between two particular cases: for $\frac{\pi R}{L} < 1$ we shall speak of prolate traps, and for $\frac{\pi R}{L} > 1$ of oblate traps.

In a prolate trap, Bessel's functions entering the foregoing formulas can be approximated with their values for small arguments. Equation (6) takes the simple form

$$\frac{r_0^2}{R^2} = \frac{\pi}{2}\frac{\Delta z}{L}. \tag{7}$$

For a highly oblate trap, we may assume an asymptotic expression for $I_1(kR)$. Then, taking as before $kr_0 < 1$, we find

$$\frac{r_0^2}{R^2} = \frac{\pi}{2}\cdot\frac{\Delta z}{L}\frac{e^{\frac{\pi R}{L}}}{\sqrt{\frac{1}{2}\left(\frac{R}{L}\right)^3}}.$$

We see that with ring slits of equal width, the prolate trap has a smaller mirror radius than the oblate trap.

The above fields are symmetric about the plane $z=0$. Asymmetric magnetic fields can be described by a vector potential $(0, A_\varphi, 0)$ with the component A_φ:

$$A_\varphi = -\frac{H_0}{k}\left[I_1(kr)\sin kz + \alpha I_1\left(\frac{kr}{2}\right)\cos\frac{kz}{2}\right]$$

and

$$H_r = H_0 I_1(kr)\cos kz - \frac{\alpha H_0}{2} I_1\left(\frac{kr}{2}\right)\sin\frac{kz}{2},$$

$$H_z = -H_0 I_0(kr)\sin kz - \frac{\alpha H_0}{2} I_0\left(\frac{kr}{2}\right)\cos\frac{kz}{2}. \tag{8}$$

Direct calculations easily show that the foregoing relations describe a trap of length L displaced relative to the origin by $\Delta z = \frac{\alpha\sqrt{2}}{8k}$ in the direction of smaller fields (in this case, toward $z<0$). Setting $\alpha<1$, we find the magnetic field on the axes of the two mirrors:

on the axis of the right-hand mirror $\left(kz = \frac{\pi}{2} - \frac{\alpha\sqrt{2}}{8}\right)$

$$H_+ = -H_0\left(1 + \frac{\alpha}{2\sqrt{2}}\right);$$

on the axis of the left-hand mirror $\left(kz = -\frac{\pi}{2} - \frac{\alpha\sqrt{2}}{8k}\right)$

$$H_- = H_0\left(1 - \frac{\alpha}{2\sqrt{2}}\right).$$

Thus

$$\frac{H_-}{H_+} = \frac{1 - \frac{\alpha}{2\sqrt{2}}}{1 + \frac{\alpha}{2\sqrt{2}}}. \tag{9}$$

The surface of the zero z-component of the magnetic field is found directly from the second equation in (8). For a prolate trap, this surface is a plane (to within terms of second order of smallness in $\frac{r}{R}$) displaced relative to the plane of geometrical symmetry of the trap by the amount

$$\Delta(kz) = \frac{\alpha}{2}\left(1 - \frac{\sqrt{2}}{4}\right). \tag{10}$$

The motion of a charged particle in the magnetic field of a trap

Let us consider the motion of a particle in the magnetic field of an axially symmetric trap. The Lagrangian in this case is

$$L = \frac{m}{2}\left(\dot{r}^2 + r^2\dot{\varphi}^2 + \dot{z}^2\right) + \frac{e}{c} r\dot{\varphi}A_\varphi.$$

Since the coordinate φ is cyclic, the generalized momentum P_φ is an integral of motion:

$$P_\varphi = \frac{\partial L}{\partial \dot\varphi} = mr^2\dot\varphi + \frac{e}{c} rA_\varphi. \tag{11}$$

If the particle is created or injected at the point (r_0, z_0), with an initial azimuthal velocity $r_0\dot\varphi_0$, then according to (11)

$$\dot\varphi = \dot\varphi_0 \frac{r_0^2}{r^2} - \frac{e}{c}\left[rA_\varphi - (rA_\varphi)_0\right] \cdot \frac{1}{r^2}. \tag{12}$$

Making use of (11), we write for the Hamiltonian of the particle

$$H = \frac{1}{2m}(P_r^2 + P_z^2) + \frac{1}{2m}\left(\frac{P_\varphi - \frac{e}{c} rA_\varphi}{r}\right)^2, \tag{13}$$

and our problem can therefore be treated as dealing with the motion of a particle in the plane (r, z) in a field with the pontential energy /4/

$$U(r, z) = \frac{1}{2m}\left\{\frac{mr_0^2\dot\varphi_0 - \frac{e}{c}\left[rA_\varphi - (rA_\varphi)_0\right]}{r}\right\}^2. \tag{14}$$

Seeing that the Hamiltonian of a particle in a magnetic field is an integral of motion, we find the permitted region of motion of the particle:

$$\frac{1}{2m}\left\{\frac{mr_0^2\dot\varphi_0 - \frac{e}{c}\left[rA_\varphi - (rA_\varphi)_0\right]}{r}\right\}^2 \leqslant E_0, \tag{15}$$

where E_0 is the total energy of the particle (the equality sign in (15) defines the boundary of the permitted region). This inequality is *a priori* satisfied for $U = 0$, i.e., for

$$rA_\varphi = (rA_\varphi)_0 + \frac{mc}{e} r_0^2\dot\varphi_0. \tag{16}$$

Thus there is always a line of force, defined by (16), near which the particle may leave the trap unimpeded.

The surface describing the potential energy in three dimensions is determined by the coordinates of the particle injection point and the initial value of $\dot\varphi_0$.

However, from (15) it follows that, without loss of generality, we may take $\dot\varphi_0 = 0$. It suffices to assume that the particle has been created, not at some point (r_0, z_0), but at any point of the force line (16). The term $mr_0^2\dot\varphi_0$ in (14) is henceforth omitted.

In application to cusped magnetic fields, (14) takes the form

$$U(r, z) = \frac{m}{2k^2}\left(\frac{eH_0}{mc}\right)^2\left[I_1(kr)\sin kz + \frac{r_0}{r} I_1(kr_0)\right]^2, \tag{17}$$

where the particle is assumed to have been injected into the trap at the point $r = r_0$, $kz = -\pi/2$.

The surface describing the effective potential energy (17) in three dimensions is depicted in Figure 3. We see from the figure that slow particles, whose energy is less than U_b, are reflected from the opposite mirror and after several repeated collisions with the magnetic walls, escape through the ring slit or return to the original point of injection.

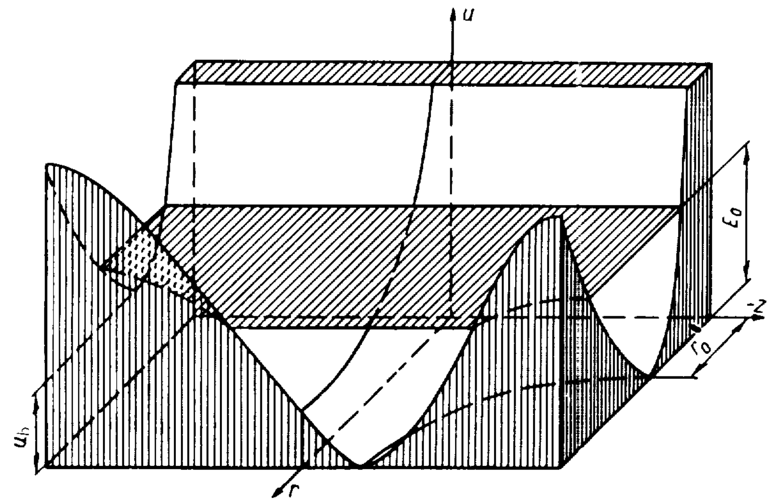

FIGURE 3.

The particles may escape through the opposite mirror only if their energy is greater than the threshold value U_b. Let us calculate this quantity. For $z = \frac{L}{2}$,

$$U(r) = \frac{m}{2k^2}\left(\frac{eH_0}{mc}\right)^2\left[I_1(kr) + \frac{r_0}{r}I_1(kr_0)\right]^2.$$

The potential energy is minimized for $r = r_1$, which is determined from the relation

$$k^2r_1^2I_1'(kr_1) = kr_0I_1(kr_0).$$

In the case of axial motion, $kr_1 \ll 1$ at the trap outlet, so that

$$r_1 \simeq r_0.$$

The particles will escape through the opposite mirror at a point whose distance from the axis is approximately equal to the distance of the injection point. The condition of mirror penetration can be written as

$$\frac{mv_0^2}{2} > \frac{2m}{k^2}\left(\frac{eH_0}{mc}\right)^2 I_1^2(kr_0).$$

If $kr_0 \ll 1$, this condition can be written as

$$R_L > r_0, \tag{18}$$

where $R_L = \frac{v_0 mc}{eH_0}$ is the Larmor radius of the particle in the field H_0.

To sum up, particles penetrating through the opposite mirror must have Larmor radii greater than the initial distance from the trap axis. Particles injected into the trap along the axis pass through irrespective of mass and velocity.

If particles of equal velocity but different masses are injected into the trap, all at the same distance from the axis, the heavier particles satisfying relation (18) will be the only ones to penetrate through the opposite mirror.

If the mass of the particles is such that

$$R_L > r_0,$$

where r_0 is the injection radius, they pass the trap without colliding with the magnetic walls, escaping through the opposite mirror. A beam of these particles injected with a velocity v_0 parallel to the trap axis has the following translational velocity upon emerging from the trap:

$$v = v_0 \sqrt{1 - \frac{r_0^2}{R_L^2}}. \tag{19}$$

This beam has been converted from a linear to a helical one. The rotational velocity of the beam about the trap axis is

$$v_\varphi = \frac{v_0 r_0}{R_L}. \tag{20}$$

The pitch of the helix

$$h = 2\pi R_L \sqrt{1 - \frac{r_0^2}{R_L^2}}. \tag{21}$$

If outside the trap the magnetic field is constant, homogeneous, and longitudinal, the emerging beam will trace a helix of radius r_0 with a pitch (21).

Let us now consider particles having a Larmor radius

$$R_L < r_0.$$

These particles are reflected from the mirror and oscillate inside the trap between the magnetic walls until they escape from the trap through the ring slit or through the inlet mirror.

Relation (15) defining the boundaries of the oscillatory motion takes the following form for cusped fields:

$$I_1(kr) \sin kz + \frac{r_0}{r} I_1(kr_0) = \pm kR_L. \tag{22}$$

For a prolate trap, $kr \ll 1$ and the equation takes on the simple form

$$r^2 \sin kr \pm 2R_L r + r_0^2 = 0.$$

The equations of the boundary surfaces are thus

$$r = \pm \frac{R_L}{\sin kz}\left[1 \pm \sqrt{1 - \frac{r_0^2}{R_L^2} \sin kz}\right]. \tag{23}$$

Expression (23) represents a system of four surfaces, two of which lie in the half-space $z < 0$, the other two in the half-space $z > 0$. Seeing that $r < 0$ is meaningless in cylindrical coordinates, we easily obtain the following relations for the boundary surfaces in the half-space $z < 0$:

$$\begin{aligned} r_1 &= \frac{R_L}{\sin kz}\left[1 - \sqrt{1 - \frac{r_0^2}{R_L^2} \sin kz}\right], \\ r_2 &= -\frac{R_L}{\sin kz}\left[1 + \sqrt{1 - \frac{r_0^2}{R_L^2} \sin kz}\right]. \end{aligned} \tag{24}$$

For $z \to 0$, the first boundary surface remains at a finite distance from the axis,

$$r_1(0) = \frac{r_0^2}{2R_L}, \tag{25}$$

while the second boundary surface escapes through the ring slit.

For $z > 0$, the equations of the corresponding surfaces are

$$\begin{aligned} r_1 &= \frac{R_L}{\sin kz}\left[1 - \sqrt{1 - \frac{r_0^2}{R_L^2}\sin kz}\right], \\ r_2 &= \frac{R_L}{\sin kz}\left[1 + \sqrt{1 - \frac{r_0^2}{R_L^2}\sin kz}\right]. \end{aligned} \tag{26}$$

The foregoing relations define the point of reflection of the particle from the opposite lateral mirror for $r_0 > R_L$. At this point characteristically $r_1 = r_2$, i.e.,

$$\sin kz = \frac{R_L^2}{r_0^2}. \tag{27}$$

It follows from (27) that as R_L decreases, the two boundary surfaces merge into the "natural" line of force, i.e., the line of force where the particle was created. The turning point, however, never recedes to the half-space $z < 0$. The permitted region of motion reduces with the decrease of R_L to a narrow strip enclosing the "natural" line of force, the particle moving almost adiabatically in this strip.

Classification of particles in terms of initial parameters

Let us consider the influence of the injection radius r_0 and of the initial angular velocity $\dot{\varphi}_0$ on the motion of a particle with constant R_L.

Particles injected into the trap fairly far from the axis cannot cross the plane $z = 0$, since their entire energy is converted into the energy of translational motion. Then for $r \approx R$, the lower boundary of the permitted region intercepts the ring slit at $z \leq 0$. According to (25), this occurs when

$$r_0 \geqslant \sqrt{2R_L R}.$$

All particles having equal Larmor radii R_L on injection can thus be subdivided into three categories:

1) for $0 < r_0 < R_L$, the particles penetrate through the trap, tracing a helix around the trap axis and escaping through the opposite mirror;

2) for $R_L < r_0 < \sqrt{2R_L R}$, the particles are reflected from the opposite mirror and, after several repeated reflections from the magnetic walls, they escape from the trap near the surface (formed by revolving the natural line of force) intercepting the ring slit, or through the inlet mirror;

3) for $r_0 \geqslant \sqrt{2R_L R}$, the particles move without oscillating along the magnetic line of force, escaping from the trap through the ring slit.

This triple classification of particles was first suggested by O. A. Lavrent'ev /3/. Note however that for $r_0 < R_L$ a particle may penetrate through the trap only if it hits the opposite mirror at a distance r_0 from the axis. If

it arrives at the mirror at a distance $r \neq r_0$ (greater or smaller), then, as we see from the topography of the effective potential energy at $kz = \pi/2$, it may be reflected. The condition $r_0 < R_L$ is therefore not without ambiguity.

The influence of the initial angular velocity of the particle on its motion can be considered with the aid of formula (12). In our fields, it takes the form

$$\dot{\varphi} = \left(\frac{eH_0}{mc}\right)\left\{\frac{I_1(kz)\sin kz}{kr} + \frac{r_0}{kr^2}\left[\left(\frac{mc}{eH_0}\right)kr_0\dot{\varphi}_0 + I_1(kr_0)\right]\right\}. \tag{28}$$

All the foregoing relations apply when the initial φ-velocity is not zero, if r_0 is replaced with a certain $r_0^{\bullet}$ defined by

$$kr_0^{\bullet} I_1(kr_0^{\bullet}) = kr_0\left[\left(\frac{mc}{eH_0}\right)kr_0\dot{\varphi}_0 + I_1(kr_0)\right]. \tag{29}$$

If $kr_0 \ll 1$ and $kr_0^{\bullet} \ll 1$, (29) takes the form

$$r_0^{\bullet} = r_0\sqrt{1 + 2\left(\frac{mc}{eH_0}\right)\dot{\varphi}_0}. \tag{30}$$

Hence, for particles with $\dot{\varphi}_0 > 0$, the conditions of penetration through the trap are the same as for particles with $\dot{\varphi}_0 = 0$ and a somewhat larger injection radius, while for particles with $\dot{\varphi}_0 < 0$ the equivalent radius is somewhat smaller. In particular, for $\dot{\varphi}_0 = -\frac{1}{2}\frac{eH_0}{mc}$, the particles pass through the trap without reflection from the magnetic walls. If outside the trap the magnetic field continuously grades into the uniform field of a solenoid, the particles having $\dot{\varphi}_0 = -\frac{1}{2}\frac{eH_0}{mc}$ will move into this field with $\dot{\varphi} \approx 0$.

The motion of a relativistic particle in a trap

For particles with relativistic velocities, the generalized momentum P_φ is

$$P_\varphi = \frac{mr^2\dot{\varphi}}{\sqrt{1-\beta^2}} + \frac{e}{c}rA_\varphi. \tag{31}$$

Therefore

$$\dot{\varphi} = \frac{eH_0}{mc}(1-\beta^2)^{1/2}\left[\frac{I_1(kr)\sin kz}{kr} + \frac{kr_0 I_1(kr_0)}{k^2r^2}\right].$$

The energy integral

$$\dot{r}^2 + \dot{z}^2 + \left(\frac{eH_0}{mc}\right)^2(1-\beta^2)\left[\frac{I_1(kz)\sin kz}{kr} + \frac{kr_0 I_1(kr_0)}{k^2r^2}\right]^2 = V_0^2. \tag{32}$$

Since all the results in the preceding sections have been derived on the basis of these integrals of motion, the previous results will apply if R_L is replaced with the relativistic Larmor radius

$$R_L = \frac{\varepsilon}{eH}.$$

For particles of fairly high energy, the condition $r_0 < R_L$ can always be satisfied, and some relativistic particles will pass through the trap without collision with the magnetic walls.

A magnetic trap of this kind can be applied to convert a linear current of relativistic electrons to a rotating beam with parameters described by (19)-(21). A small-pitch tight helix, however, is possible only for $\frac{\varepsilon}{eH_0} \simeq r_0$, and therefore fairly strong magnetic fields are required to produce reasonably slow rotating beams. For example, for electrons with $E = 50$ MeV and $r_0 = 10$ cm, the relation $r_0 = R_L$ is satisfied in magnetic fields of $B_0 \approx 20{,}000$ Oe.

The trajectories of trapped particles

The equations of radial and longitudinal motion have the form

$$\ddot{r} - r\dot{\varphi}^2 = \frac{e}{mc} r\dot{\varphi}H_z,$$

$$\ddot{z} = -\frac{e}{mc} r\dot{\varphi}H_r,$$

or, applying (3) and (28),

$$\ddot{r} - r\left(\frac{eH_0}{mc}\right)^2 \left[\frac{I_1(kr)\sin kz}{kr} + \frac{I_1(kr_0)\,kr_0}{k^2r^2}\right] \times$$

$$\times \left[\left(\frac{I_1(kr)}{kr} - I_0(kr)\right)\sin kz + \frac{I_1(kr_0)\,kr_0}{k^2r^2}\right] = 0,$$

$$\ddot{z} + r\left(\frac{eH_0}{mc}\right)^2 \left[\frac{I_1(kz)\sin kz}{kr} + \frac{I_1(kr_0)\,kr_0}{k^2r^2}\right] I_1(kr)\cos kz = 0. \quad (33)$$

In a prolate trap, or in the general case of axial motion, when $kr < 1$, equations (33) take the simple form

$$\ddot{r} + \frac{1}{4}\left(\frac{eH_0}{mc}\right)^2 r\left(\sin^2 kz - \frac{r_0^4}{r^4}\right) = 0, \quad (34)$$

$$\ddot{z} + \frac{1}{4}\left(\frac{eH_0}{mc}\right)^2 kr^2\left(\sin kz + \frac{r_0^2}{r^2}\right)\cos kz = 0.$$

Equations (34) were investigated numerically on a UMShN-type computer. The results are plotted in Figures 4-16 in the dimensionless coordinates $y_1 = kr$, $y_3 = kz$, where r is the radial displacement of a particle from the trap axis, z its longitudinal coordinate. The initial conditions of the problem are

$$y_2 = kR_\perp, \text{ where } R_\perp = \frac{mv_\perp c}{eH_0},$$

$$y_4 = kR_\parallel, \text{ where } R_\parallel = \frac{mv_\parallel c}{eH_0}.$$

Here $v_\perp$ and $v_\parallel$ are the transverse and the longitudinal velocity components of the particle on injection; H_0 the magnetic field strength on the axes of the trap mirrors. Figures 4-11 show the trajectories of particles injected into the trap through the left-hand mirror with the parameters

$$y_2 = 0; \quad y_4 = 0.1 \text{ and } kR = 0.78, \quad y_3 = -1.57.$$

In accordance with general considerations, particles with $y_1 \leq 0.1$ can be expected to move through the trap, while those with $y_1 > 0.28$ should move to the ring slit without crossing the plane $z = 0$.

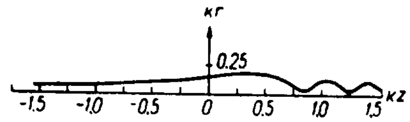

FIGURE 4.

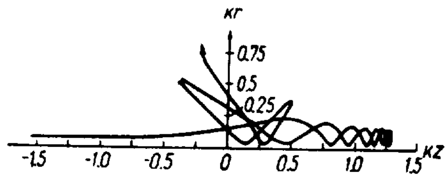

FIGURE 5.

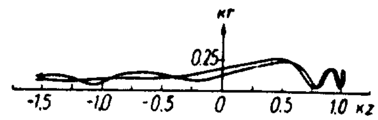

FIGURE 6.

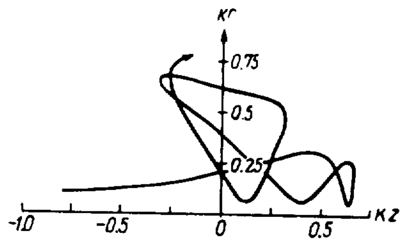

FIGURE 7.

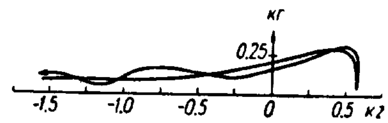

FIGURE 8.

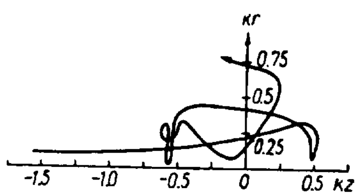

FIGURE 9.

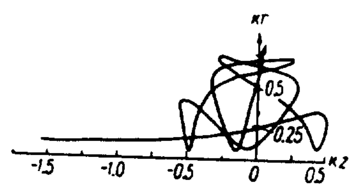

FIGURE 10.

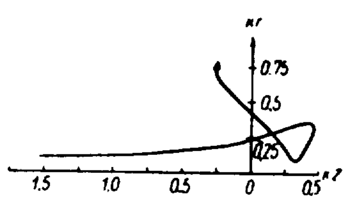

FIGURE 11.

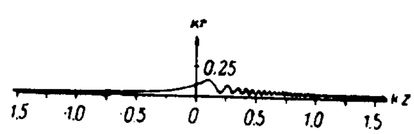

FIGURE 12.

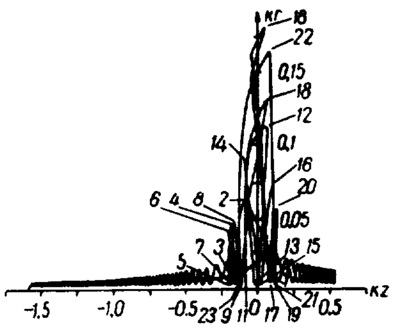

FIGURE 13.

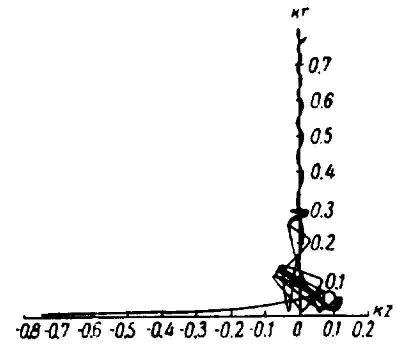

FIGURE 14.

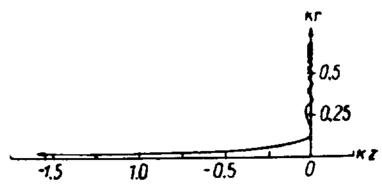

FIGURE 15.

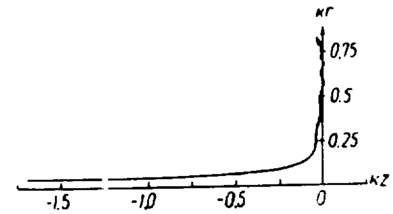

FIGURE 16.

Numerical calculations show that the y_1 of particles moving through the trap is somewhat smaller than the figure which follows from energy considerations. For $y_4 = 0.1$, particles pass through the trap only if $y_1(0)=0.07$ (Figure 4). The residence time of a particle in the trap $\tau = 0.460$.* As $y_1(0)$ increases, the following pattern is observed: for $y_1(0)$ close to the lower bound (e.g., $y_1 = 0.08$), the particles move in the half-space $z < 0$ slightly rotating in φ, but having crossed the plane $z = 0$ they start rotating around the axis $r = 0$ (Figure 17). This rotation is asymmetric with respect to the trap axis, and the particle therefore oscillates in the plane $\{r, z\}$. After reflection from the opposite mirror, the particle returns to the original site of injection and leaves the trap (Figures 5–8). The residence time of the particle in the trap is comparatively large in this case, since near the mirror the particle traces quite a few turns of a small-pitch helix (in Figures 5–8, $\tau = 1.236$, 0.782, 0.775, and 0.567, respectively). Repeated reflection of the particle is possible only if it approaches the inlet mirror far from the axis ($r \gg r_0$). In this case, the particle will in all probability escape through the ring slit. The number of oscillations performed by a particle between the magnetic walls is the highest for $y_1 = 0.105–0.110$ (Figures 9, 10, $\tau = 0.757$ and 1.10, respectively). As y_1 increases, the number of these oscillations decreases (Figure 11), and for $y_1 \geq 0.28$ the particles escape (after $\tau = 0.407$) through the ring slit without a single oscillation between the magnetic walls.

The particles are trapped in a certain sense only when y_1 is not much greater than y_4. This result is very obvious for particle injection into traps with $y_4 = 0.0044$, $y_2 = 0$, $y_3 = -1.57$ (Figures 12–16). This case corresponds to fairly high magnetic fields. The particles will penetrate through the trap only for $y_1 = 0.0022$ (Figure 12). The residence time of the particle

* The time τ is in units of $10^3 \frac{mc}{eH_0}$ (Figures 4–11) and $10^6 \frac{mc}{eH_0}$ (Figures 12–16).

in the trap $\tau = 0.0079$. For $y_1 \sim y_4$, some "trapping" of particles is observed ($\tau = 0.0243$). In this case they rotate tracing over 100 turns in the mirrors and undergo repeated reflection from the magnetic walls (over 23 reflections) (Figure 13). For $y_1 = 0.01$, the particle resides a fairly short time in the trap, and after no more than 15 reflections from the walls it escapes through the ring slit (Figure 14, $\tau = 0.015$). When the parameter y_1 is increased further, the particle escapes from the trap through the ring slit without crossing the plane of zero magnetic field (Figure 16, $\tau = 0.0049$). Figure 15 ($y_1 = 0.03$) illustrates a fairly improbable event, when a particle is reflected from the lateral slit and leaves the trap (after $\tau = 0.012$) precisely retracing its initial trajectory. Numerical integration with other values of the magnetic fields, $y_4 = 0.05$ and $y_4 = 0.15$, confirms the general pattern of particle motion as presented in Figures 4–17.

Our analysis of the trajectores leads to the following conclusions.

1. Particles injected along the trap axis escape freely if the injection radius is less than 0.7 R_L. For $r_0 = 0.7-0.75\,R_L$, they emerge from the trap rotating about the axis and tracing a comparatively tight helix. The axis of the helix is displaced relative to the geometrical axis of the trap, and this displacement increases with the decrease of injection radius (the injection velocity remaining constant). The displacement also increases if the particle is injected at an angle to the trap axis.

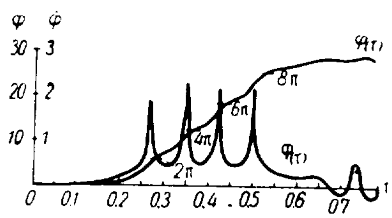

FIGURE 17.

For $0.7\,y_4 \lesssim y \lesssim y_4$, the particles injected along the axis are reflected from the opposite mirror, although particles injected at a certain angle to the axis may penetrate if they reach the opposite wall with a radius close to the injection radius.

Particles reflected from the opposite mirror may remain in the trap for a time of the order of $100/\omega_H$ residing mainly in the mirrors.

2. For $y_1 \lesssim y_4$, the particles are "trapped" in a certain sense. The trapped particle is repeatedly reflected from the magnetic walls and escapes mostly through the ring slit. The number of reflections essentially depends on the strength of the magnetic field. For $y_4 = 0.1$, the particle undergoes a few reflections (5–8) only, while for $y_4 = 0.0044$ the number of reflections is over 20.

3. For $y_1 > \sqrt{2y_4kR}$, the particles escape through the ring slit. The residence time of the particles in the trap is comparable with the free drift time.

BIBLIOGRAPHY

1. SCHMIDT. – Phys. Fluids, 5 (8) : 994. 1962.

2. Journal de Physique et le Radium, 23 (5) : 291 – 296. 1962.

3. LAVRENT'EV, O. A. – UkrFZh, 8 (4): 451. 1963.

4. ARTSIMOVICH, L. A. Upravlyaemye termoyadernye reaktsii (Controlled Thermonuclear Reactions). – Fizmatgiz. 1961.

K. D. Sinel'nikov and B. S. Akshanov

EXPERIMENTAL INVESTIGATION OF THE MOTION OF CHARGED PARTICLES IN MAGNETIC TRAPS OF CUSPED GEOMETRY

Various experimental studies have recently been published dealing with the behavior of plasmas in traps with cusped magnetic fields. However, the theoretical aspects relating to the behavior of a rarefied plasma in these magnetic-field geometries have been studied highly inadequately. This is not unexpected, since plasma particles whose energy is other than vanishingly small behave in a distinct nonadiabatic manner, so that the drift approximation does not apply. Some knowledge of the behavior of plasma in cusped fields can be gained by examining the separate trajectories of ions and electrons on the basis of the general equations of electron optices /4/, without resorting to the conventional paraxial approximation. The general equations of electron optics, however, are only solved numerically. The results of appropriate calculations /2/ made with an electronic computer show that when particles are injected along the system axis with a velocity v_0 from a region of uniform magnetic field B_0, it is only the particles having $r_0 > R_0$ which pass through the zero plane of the field B_r; here r_0 is the initial radial distance from the axis in the uniform field region and R_0 is the "effective" cyclotron radius

$$R_0 = \frac{v_0 mc}{eB_0}.$$

Injected particles having $r_0 < R_0$ escape through the ring slit in the midplane. For $r_0 > R_0$, the particles trace circular orbits around the system axis, and a judicious choice of parameters will ensure the formation of a hollow "electron cylinder", not unlike the Christophilos E-layer. The present paper deals with experimental verification of the numerical results of /2/.

Apparatus

The experimental setup (Figure 1) is a magnetic trap with cusped fields. The vacuum chamber 1 with an i.d. of 140 mm and a length of 500 mm is evacuated to a residual pressure of $1 \cdot 10^{-4}$ N/m^2. The magnetic system comprises two groups of alternating coils 2 set at a distance of 50 mm from each other; length of each coil group 120 mm. Additional coils can be switched in at the outlet mirror. The magnetic field in each coil group can be varied from 0 to 0.1 T. An electron gun 3 is provided at one end

of the chamber, near the vacuum system piping; it produces a focused beam 1–2 mm in diameter with energy varying from 0 to 4 keV. The gun can be easily moved along the axis z and along the chamber radius r without interfering with the vacuum; the inclination angle α of the gun to the axis can also be varied. Portable screens of various shapes and sizes are provided at the opposite end of the tube. These screens can be rotated or displaced axially down the chamber, until they virtually touch the gun. The following screens were used:

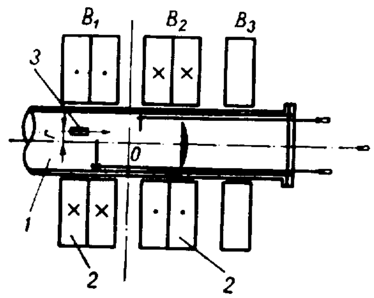

FIGURE 1. Experimental setup.

a) a solid screen coated on one side with a phosphorescent substance, screen diameter 130 mm;

b) a screen of 130 mm diameter with a slit 5 mm wide, aligned with the chamber radius; the slit admitted a straight beam, the screen was coated on the two sides with phosphors of different colors;

c) a half-screen (130 mm in diameter) with bilateral coating;

d) a small screen (60 mm in diameter) with bilateral coating;

e) a grid screen coated with a phosphor;

f) a convex or concave screen.

All the screens are transparent (with the exception of the grid screen). In some cases, additional metallic screens were used.

Procedure

The trajectories of the injected electrons were traced using various screen combinations. Electron paths, some showing five-fold reflection, were observed visually with satisfactory reproducibility. Figure 2 shows a trajectory photographed off a fixed half-screen set in the plane of reflection. If the screen is slightly displaced toward the gun (roughly by 1 mm), the photograph shows a small part of a second curve produced by doubly reflected particles (Figure 3). Doubly reflected particles are registered on the screen because a beam with the parameters $V = 3$ keV, $r_0 = 2$ cm, $B = 0.0085$ T slips past the thin half-screen, partially passing into the unscreened region. On reflection from the plane which is located somewhat deeper in the mirror, the particles return to the gun and after secondary reflection, they again arrive at the screen; now, however, they have a somewhat larger diameter and a new plane of reflection which is displaced toward the trap center. In some cases, for certain field ratios, as much as six or seven consecutive reflections can be registered (Figure 4).

The primary beam is best observed using the solid screen. By moving the screen from the gun to the reflection plane, we record the entire beam trajectory. The reflection plane can be pinpointed with high accuracy by the slitted screen. As this screen is displaced from the plane of reflection toward the trap center by a distance equal to its thickness, the reverse side of the screen shows bright luminescence attributable to the reflected beam.

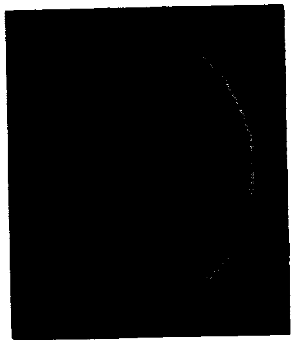

FIGURE 2. The trajectory of particles in the reflection plane of the second mirror.

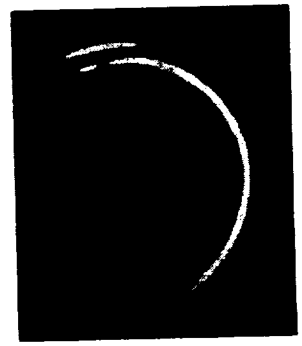

FIGURE 3. The trajectory of particles in the reflection plane of the second mirror; the primary beam is crescent-shaped; the reflected beam is represented by the small segment on top of the crescent.

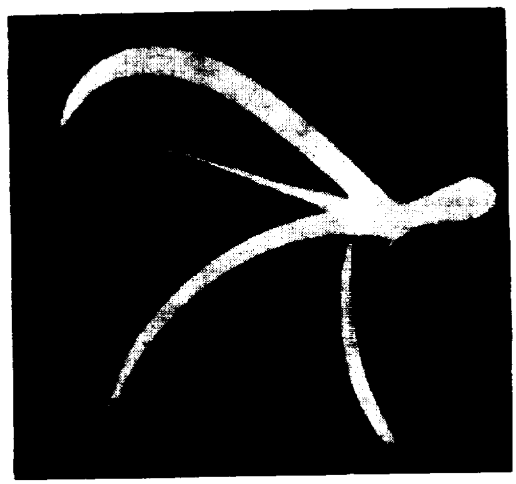

FIGURE 4. Trajectories of multiply reflected beams (photographed with a concave half-screen).

Since the electron helix pitch is sharply reduced in the plane of reflection, and the electrons as if spread over a circle, the application of two moving half-screens will enable us to register the primary and the reflected beams simultaneously. In this case, only part of the primary beam or the secondary beam reflected from the first mirror will be admitted through the slit into the gap between the two screens (Figure 5). The simultaneous existence of beams of different reflection multiplicities is easily verified as these beams are successively extinguished by moving the screen along the z axis.

This point is additionally confirmed when the beams are extinguished using a third half-screen provided near the gun. Various screen combinations were used in the experiments. Application of screens in a system

with an accurately calibrated length coordinate gives satisfactory qualitative and quantitative solutions to various important problems connected with charged particle injection.

FIGURE 5. Trajectories of the primary (bottom) and the reflected (top) beams obtained with two half-screens; beam parameters: $V = 3.6$ keV, $r_0 = 2.5$ cm, $B = 0.011$ T.

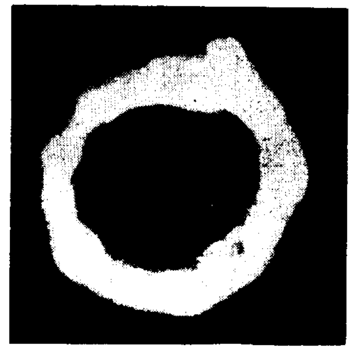

FIGURE 6. The trajectory of particles obtained with the screen moving from the gun to the reflection plane; beam parameters: $V = 3.8$ keV, $r_0 = 2$ cm, $B = 0.01$ T.

Experimental results

Figure 6 is a photograph of the trajectory of "extra-axial" and "paraxial" particles /1/, obtained as the screen moves from the gun to the reflection plane. Figure 7 (top) shows the projection of the trajectory on a plane parallel to the z axis. The same figure (bottom) gives the axonometric projection of this trajectory. The particles after first reflection move around the axis tracing a helix with an ever increasing pitch; between the neutral plane and the first plane of reflection, however, the particle trajectories do not embrace the axis.

Figure 8 shows beam trajectories of various reflection multiplicities photographed off a stationary half-screen provided in the gun region. The trajectories of the reflected particles in this case do not embrace the system axis. We thus see that the "extra-axial" particles existing to the left from the neutral plane are converted into an entirely different class of "paraxial" particles upon crossing the neutral plane (where the field is zero). In the reflection planes, the entire kinetic energy of translational motion $mv_0^2/2$ is converted into the energy of rotational motion $mv_0^2/2 = \psi$, where ψ is the meridian potential /1/. This feature is responsible for the reflection of particles from the magnetic mirrors, and the trajectory of a small-pitch beam of finite dimensions is displayed as a circle on the stationary screen.

The motion of particles in the trap is substantially influenced by the position of the gun. Displacement of the gun along the z axis toward the

neutral plane increases the helix pitch in the second mirror region and somewhat reduces the eccentricity Δr (see below).

Increasing the inclination α of the gun to the trap axis shifts the reflection plane toward the neutral plane. If the inclination is greater than 0.07–0.08 rad, no discrete beams are distinguished, and the screen glows continuously.

The distance r of the gun from the z axis has a very strong influence on the position of the plane of reflection and the trap volume (region of existence of reflected particles).

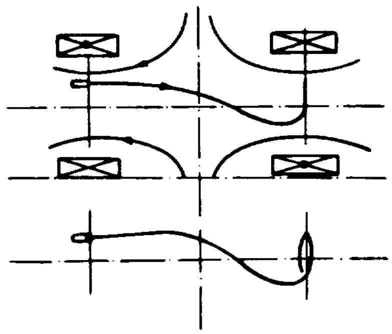

FIGURE 7. Particle trajectories.

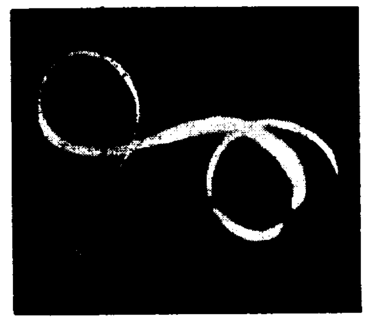

FIGURE 8. A photograph of "extra-axial" particles reflected from the first mirror.

The condition of trapping has the form $r > R_0/2l$. If the injection radius falls in the interval $0 < r < R_0$, the particles pass through the second mirror. When the gun is set on the axis ($r = 0$), the beam clearly moves unimpeded along the z axis. For r close to zero, particles are "trapped" only if the magnetic fields are large or the particle energy is correspondingly small. Figure 9 plots V_{cr} as a function of the injection radius r_0. This curve separates between the regions of reflected and transmitted particles. We shall see in the following that this curve is highly relevant for the correct choice of the parameters of helical beams.

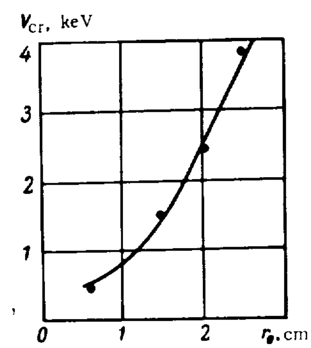

FIGURE 9. The critical energy of reflected particles V_{cr} as a function of the injection radius r_0.

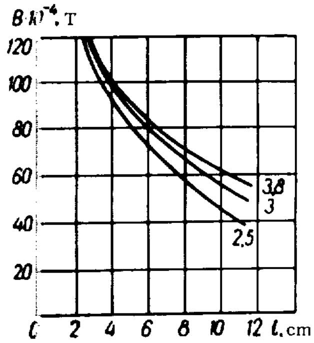

FIGURE 10. A family of curves plotting the position of the reflection plane as a function of the magnetic field for various injection energies (3.8, 3, and 2.5 keV).

As the magnetic field B increases, the plane of reflection moves toward the neutral plane. Figure 10 shows a family of curves which plot the position of the reflection plane as a function of the magnetic field for various injection energies.

A study of particle motion for various injection parameters shows that the conditions of multiple particle reflection are satisfied in a fairly wide range of parameters. Figure 11 plots the fields corresponding to adiabatic $(r \geqslant \sqrt{2R_0R})/2/$, reflected $(R_0 < r < \sqrt{2R_0R})$, and transmitted $(0 < r < R_0)$ particles as a function of injection energy. The curves are plotted for various injection radii.

If the field beyond the second magnetic mirror is uniform, and the beam energy is somewhat higher than the maximum reflection energy, the beam penetrates through tracing a very tight helix. The nearer the particle energy to reflection energy, the smaller the helix pitch.

Photographs of primary and reflected beams obtained in the second mirror point to a certain asymmetry of the beam relative to the z axis. This asymmetry is observed in the reflection plane, and also for helixes penetrating through the mirror. It is noteworthy, however, that the helix invariably embraces the axis, i.e., we are dealing with "paraxial" particles.

By reversing the field in the coils, we displace the emerging helix in the opposite direction. It is highly desirable that we should be able to control the helix, namely its pitch, diameter, and disposition relative to the axis.

These problems are solved as follows. The helix pitch is regulated by varying the field strength or the particle energy. By reducing the energy or correspondingly raising the field strength, we reduce the helix pitch.

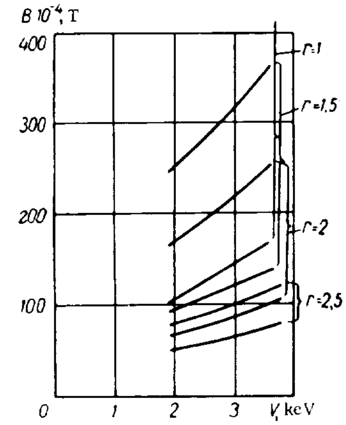

FIGURE 11. Fields corresponding to adiabatic, reflected, and transmitted particles as a function of injection energy for various distances of the gun from the z axis.

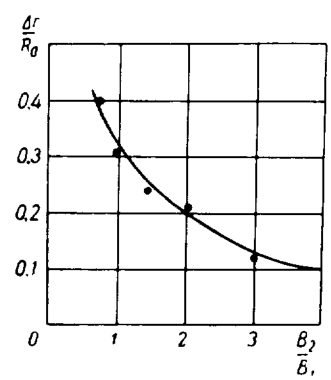

FIGURE 12. Helix eccentricity as a function of field ratio $\frac{B_2}{B_1}$.

A slight displacement of the helix center relative to the z axis can be achieved by increasing the field ratio $\frac{B_2}{B_1}$. Figure 12 plots the relative displacement of the helix as a function of the field ratio, $\frac{\Delta r}{R_0} = f\left(\frac{B_2}{B_1}\right)$.

The field B_1 in the first mirror remains constant, and it is the field B_2 in the second mirror which is increased. It follows from the curve that the increase in $\frac{B_2}{B_1}$ is effective up to a certain limit only (roughly up to $\frac{B_2}{B_1} = 3$). Further increase in field ratio gives a negligible contribution. Beam eccentricity can be somewhat reduced by moving the gun toward the neutral plane. An appropriate choice of parameters will actually ensure zero eccentricity.

We see from the preceding that special guns can be used to create transmitted helical beams with an extremely small pitch: these beams may in fact be regarded as solid-wall tubes composed of rotating electrons.

Preliminary experiments were made with injection of "helical" beams into a magnetic-mirror trap (the coils B_1, B_3). Effective particle trapping was observed for hydrogen pressures of $\sim 10^{-2}$ N/m^2, resulting in the creation of a plasma with fairly high parameters.

Conclusions

1. It is shown that, under certain conditions, transmitted "paraxial" beams can be produced, moving as a tightly wound helix.
2. Some relations are derived for the motion of particles in traps.
3. The experimental results are in satisfactory agreement with the theoretical conclusions in /2/ and with numerical calculations on an electronic computer.
4. Injection of "helical" beams into a magnetic-mirror trap is seen to produce a fairly dense ($n \approx 10^{12}$ cm^{-3}) long-lived ($\tau \approx 0.1$ sec) plasma.

BIBLIOGRAPHY

1. SINEL'NIKOV, K. D. and B. N. RUTKEVICH. – In: "Lektsii po fizike plazmy. Plazma v dreifovom priblizhenii". Khar'kov. 1963.

2. SINEL'NIKOV, K. D., N. A. KHIZHNYAK, et al. – This volume, p. 335

3. ARTSIMOVICH, L. A. Upravlyaemye termoyadernye reaktsii (Controlled Thermonuclear Reactions). – Moskva, Fizmatgiz. 1961.

4. SCHMIDT, G. – Phys. Fluids, 5: 994. 1962.

A. P. Slabospitskii, V. D. Fedorchenko, and B. N. Rutkevich

AN INVESTIGATION OF A NONADIABATIC MAGNETIC TRAP

In /1/ it is shown that a charged particle moving in a time-independent space-periodic magnetic field interacts with the field so that almost half of its longitudinal injection energy is converted to the energy of transverse motion. This phenomenon was observed when a characteristic "resonance"

condition $\omega_H = \frac{2\pi}{L} v_\parallel$ is satisfied. The total energy of charged particles in a time-independent magnetic field is conserved, and therefore any increase in the energy of transverse motion is offset by a decrease in the energy of longitudinal motion. As $v_\parallel$ decreases, the "resonance" conditions are no longer satisfied, and the particle ceases to be "resonant".

To ensure a more effective redistribution of energy, the particle must be maintained in "resonance" for a longer time. This can be achieved in two ways /2/:

1) by reducing the period L of the modulating magnetic field, while the guiding field remains constant;

2) by reducing the guiding magnetic field H_z along the trap axis, while the modulation period remains constant.

We adopted the second approach. To derive the variation of the guiding magnetic field which would ensure "resonance" conditions $\omega_H = \frac{2\pi}{L} v_\parallel$ in the entire space-periodic magnetic field region, we proceeded with a theoretical analysis of the motion of a charged particle in a magnetic field of the form

$$H_z = H_{0z}[1 + hI_0(\nu, r)\cos\nu z] \tag{1}$$

under the following assumptions: $\nu = \frac{2\pi}{L} = \text{const}$, $h = \frac{H_\sim}{H_z} = \text{const}$ and $\omega_H = \frac{2\pi}{L} v_\parallel$ along the entire space-periodic magnetic field region; h is the modulation ratio of the space-periodic field.

The equation of motion was written in the form

$$\ddot{r} + \frac{\omega_H^2}{4}[1 + 2hI_0(\nu, r)\cos\nu z]\, r = 0. \tag{2}$$

Simple substitution of variables reduced this equation to a canonical Mathieu equation, which was then solved by an asymptotic technique. The solution of this equation provided us with a relation describing the variation of the guiding magnetic field H_z necessary to establish the "resonance" $\omega_H = \frac{2\pi}{L} v_\parallel$ along the entire space-periodic field region:

$$H_z = \frac{mcv_0\nu}{e}\left\{1 - [1 + (r_0\nu)^{-2}]\, e^{\frac{h\nu z}{2}}\right\}^{\frac{1}{2}}, \tag{3}$$

where r_0 is the injection radius of the particle in the space-periodic field. We know from the theory of parametric resonance that small modulation factors ensure a narrow resonance curve. To ensure substantial interaction of the charged particle with the space-periodic magnetic field in systems with a low modulation factor (h= 5%), we set up a space-periodic field accomodating numerous periods.

Apparatus

A schematic diagram of the experimental setup (b) and the magnetic field geometry along the trap axis (a) are shown in Figure 1. The vacuum chamber is a tube 0.1 m in diameter and some 4 m long. Diffusion oil

pumps attached at both ends evacuated the chamber to a pressure of $1.33 \cdot 10^{-4}$ N/m^2. The guiding field solenoid was 3 m long. The guiding field varied in accordance with formula (3) from $9.3 \cdot 10^3$ AV/m to $4.8 \cdot 10^3$ AV/m. Space-periodic modulation of the guiding magnetic field was provided by a system of alternating coils. This coil system was set inside the guiding field solenoid. The modulating field strength varies according to formula (3), ensuring a constant modulation factor of 5% along the entire space-periodic field region. This region accomodated 19.5 magnetic field periods. The electrons were injected by a hot cathode electron gun mounted outside the magnetic field region. Deflecting plates were applied to ensure the required injection radius r_0. Electron injection energy was 1250 eV ($2 \cdot 10^{-16}$ J).

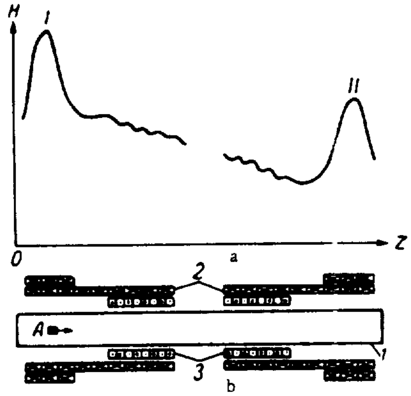

FIGURE 1. A schematic diagram of the setup and the magnetic field along the trap axis: I and II are the first and the second magnetic mirrors; 1) vacuum chamber; 2) guiding field coil; 3) modulation field coil; 4) electron gun.

In the first stages of our work, we had to solve the problem of producing a guiding magnetic field specified by formula (3). The required magnetic field variation along the axis was ensured by appropriately varying the current through each magnetic coil: the current was adjusted by coupling suitable resistances into each coil (Figure 2). The magnetic field was measured by a frequency-doubling magnetic modulation probe /3, 4/ and an EPP-09 recorder. The probe was moved along the magnetic system axis at a speed of 0.007 m/sec by an electromotor. The electric block-diagram of the probe is shown in Figure 3. The cores were fabricated from E-310 steel. Probe size, $0.01 \times 0.01 \times 0.008$ m. The probe was calibrated in the field of a long solenoid. The curves traced by the EPP-09 recorder were treated with the aid of a calibration graph (Figure 4). By adjusting the frequency and the amplitude of the magnetizing current, we hit on

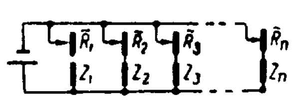

FIGURE 2. Guiding field coils.

the optimal operating mode of the probe, which was made to measure magnetic field gradients of $\sim 5\%$ to within 1.5%.

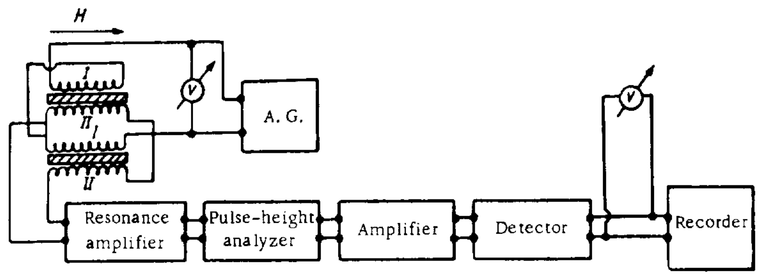

FIGURE 3. The electric block-diagram of the magnetic field probe.

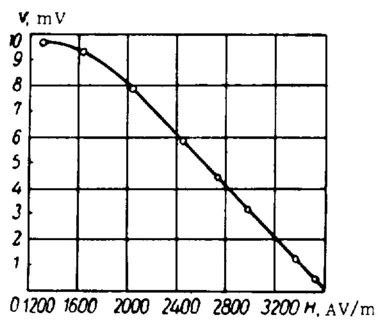

FIGURE 4. The voltage V of the second magnetic-probe harmonic as a function of the magnetic field H.

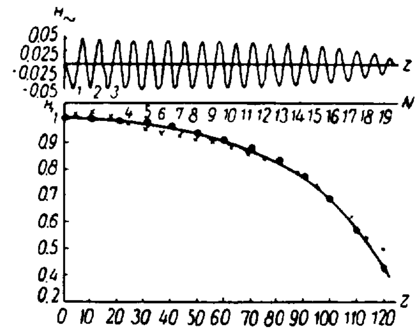

FIGURE 5. Magnetic field distribution along the trap axis: N is the period number of the modulation field; dots mark the magnetic field calculated from (3), crosses give the magnetic field set up in the trap.

Figure 5 shows the distribution of magnetic fields along the trap axis. The upper curve gives the axial variation of the modulation field $H_{\sim}$, and the lower plots the distribution of the guiding magnetic field H_z. We see from the figure that, to within 2%, the guiding field is identical with the magnetic field calculated from (3). By enclosing a space-periodic magnetic field region between magnetic mirrors, we created a magnetic trap. The magnetic field in the "mirrors" was not large.

Experimental results

The motion of charged particles in a space-periodic magnetic field was investigated using a phosphor-coated screen. This technique is fairly inaccurate (giving an error of some 10%), but it nevertheless revealed some very interesting features. Interacting with the space-periodic field,

the charged particles moved in an evolving helix touching the trap axis. This motion was observed when the "resonance" condition $\omega_H = \frac{2\pi}{L} v_\parallel$ was satisfied. The luminescent screen was set in a magnetic-field minimum position. By measuring the displacement of the beam image on the screen from the trap axis, we can find the transverse energy of the electrons (the magnetic field strength near the screen is of course known). On account of the partial phase defocusing of the beam, the image on the screen was crescent-shaped. A bright-up reticle was provided behind the screen, so that the beam displacement from the axis could be measured with an accuracy of 0.002 m. We thus established that in resonance, no less than 70% of the longitudinal energy of the particles was converted into the energy of transverse motion.

The transverse beam energy was also determined by an alternative technique. The transverse energy in the magnetic-field minimum H_0 was found from the condition of charged particle reflection from a magnetic "mirror": $\frac{W_{\perp 0}}{W_0} > \frac{H_0}{H_{\rm ref}}$. Having pinpointed the reflection plane and having measured the reflection magnetic field $H_{\rm ref}$, we could easily find the transverse-to-total beam energy ratio η (in %): $\eta = \frac{W_{\perp 0}}{W_0} \cdot 100\% = \frac{H_0}{H_{\rm ref}} \cdot 100\%$. The plane of reflection was not sharp, $H_{\rm ref}$ varying from $1.45 H_0$ to $1.25\ H_0$; hence $\eta = 69 - 80\%$.

The current collector with a small central hole (for the injection of the electron beam into the trap)which was provided in front of the first mirror outside the trap picked up the major part of the fast particles current at the time of resonance trapping. The phosphor coating of this collector displayed the trace of the fast particles emerging from the trap: they were seen to emerge near the axis.

All this shows that a system which is characterized by a highly effective "resonant" conversion of longitudinal energy into transverse energy is also most effective in converting the energy of transverse motion into longitudinal energy. This conclusion is confirmed by experiments dealing with the number of charged particle reflections from magnetic mirrors in a trap.

The number of charged particle reflections from the magnetic mirrors was determined by two methods. In the pulsed technique, a well-shaped square pulse was applied to the electron gun modulator to cut off the electron injection current. The electron collector provided in front of the first mirror outside the trap generated a current pulse which was induced by the fast electrons hitting the collector at the time of resonance trapping. The time of rise of the collector current gave the lifetime of the trapped particles, whereas the number of reflections could be evaluated from knowledge of the trap geometry. These measurements gave the figure 6 for the estimated number of reflections from the magnetic mirror. The pulsed technique is insufficiently accurate for small currents, since in this case we are dealing with small-amplitude pulses. On the other hand, if the electron injection current is raised above $10\,\mu$A, low-frequency oscillations are induced in the trap.

To check the results obtained with the pulsed technique, the number of charged particle reflections from the magnetic mirrors was determined

by measuring the ratio of the probe ionic current at the time of resonance trapping to the ionic current picked up as the electrons swept once across the probe. The probe ionic current was assumed to be proportional to the current of fast electrons. The collector surface of the wall ionic probe was large (some $0.6\,m^2$), which permitted working with small electron injection currents. The ions produced in dissociation processes drifted freely across the magnetic field. The probe ionic current picked up as the electron beam swept once across the probe (with the second magnetic mirror turned off) is $-I_1^+ \sim l$, where l is the electron path length; the probe ionic current under conditions of resonance trapping is $-I_t^+ \sim N_0 l$. The current ratio $\frac{I_t^+}{I_1^+} \approx \frac{N_0 l}{l} = N_0$ gives the number of electron reflections from the magnetic mirrors. The errors in these measurements are attributable to differences in trajectories under resonant and nonresonant conditions, which arise on account of the additional ionization by slow secondary electrons. Estimates show that the error is no greater than 35%. The measurements of probe current ratios give 23 as the number of reflections.

The initial phase of particles returning through the space-periodic magnetic field region was altered by raising the magnetic field strength in the second mirror, but the number of reflections did not increase noticeably. Raising the magnetic field strength in the first mirror, however, did increase the number of reflections, and saturation was reached for $\frac{H_{m}l}{H_{0z}} = 12$ and $\frac{H_{m}l}{H_{0z}} = 3$. The maximum number of reflections was 53. Changes in pressure did not affect the reflection of charged particles from the magnetic mirrors.

Our experiments show that a "resonant" magnetic field ensures effective conversion of longitudinal particle energy into transverse energy. The residence time of electrons in a magnetic trap with a "resonant" space-periodic field is not high, and it is mainly determined by the reverse process. Charged particles apparently escape from the trap after a very short time owing to the radial growth of the transverse magnetic field component. At a distance of 0.035 m from the axis, where the charged particles return to the space-periodic magnetic field region after reflection from the second mirror, H_R is large, the "resonant" curve is fairly broad, and the probability of the reverse process is high.

BIBLIOGRAPHY

1. FEDORCHENKO, V. D., B. N. RUTKEVICH, and B. M. CHERNYI. – ZhTF, 29: 1212, 1959.

2. SINEL'NIKOV, K. D., B. N. RUTKEVICH, and B. G. SAFRONOV – In: "Fizika plazmy i problemy upravlyaemogo termoyadernogo sinteza", 1: 113. Kiev, Izdatel'stvo AN UkrSSR, 1962.

3. ROZENBLAT, M. A. Magnitnye usiliteli (Magnetic Amplifiers). – Moskva, Izdatel'stvo Sovetskoe Radio, 1956.

4. PEREGUD, B. P. – PTE, 64, 1957.

A. P. Slabospitskii and V. D. Fedorchenko

EXPERIMENTAL INVESTIGATION OF A CLOSED MAGNETIC TRAP

In /1/ we showed that charged particles moving through a "resonant" space-periodic magnetic field convert some 70% of their initial longitudinal energy into the energy of transverse motion. The number of charged particle reflections from the magnetic mirrors, measured as the ratio of the probe ionic currents picked up in different trapping modes, was fairly small (up to 20). Special tests showed that most of the fast particles escaped through the injection mirror. A phosphorescent screen used for visual display of the charged beam showed a bright axial spot in the injection mirror, which was attributable to the emerging fast particles. It was suggested /2/ that this property of a "resonant" magnetic field can be applied to realize the reverse process, namely conversion of the transverse energy of charged particles into closed magnetic traps.

Apparatus

The vacuum chamber of the closed magnetic trap is shown in Figure 1. This is a racetrack with a perimeter length of some 10 m. Length of the straight legs 3.5 m, mean radius of the curving sections 0.35 m, effective trap aperture 0.06 m.

The magnetic field strength along the entire trap was close to $17 \cdot 10^3$ A/m; in the space-periodic field region, it varied as specified in /1/ from $9 \cdot 10^3$ to $4.8 \cdot 10^3$ A/m. Magnetic field modulation factor $h = 5\%$. In the linear parts of the trap the field was provided by multilayer coils, and in the curving sections by one-layer helical windings with a mean diameter of 0.13 m and a 0.04 m pitch.

The single-layer helical coil compensates for the toroidal drift of particles since its turns are slightly slanted /3/. This in turn determines the resonant properties of the single-layer helical coil: the toroidal drift is compensated only for particles of a certain energy $W_{\parallel 0}$. A point beam of electrons with various energies is stretched by the single-layer helical coil into a line which extends in the drift plane, i.e., for particles with $W_{\parallel} < W_{\parallel 0}$ the drift is overcompensated, while for particles with $W_{\parallel} > W_{\parallel 0}$ it is undercompensated.

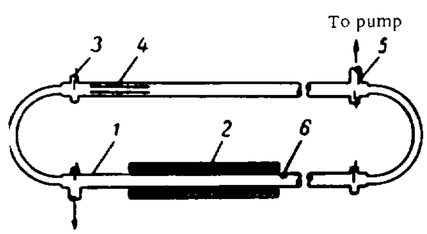

FIGURE 1. Schematic diagram of the vacuum components of a closed magnetic trap:
1) vacuum chamber; 2) modulation field coils; 3) flags; 4) plate condenser; 5) fast electrons collector; 6) electron gun.

The magnetic fields of the linear solenoid and of the single-layer helical coil were matched by slightly rotating (through nearly 10°) the end magnetic coils and doubling their field in comparison with the guiding magnetic field.

The electrons were injected from a region of minimum magnetic field. The injector was a three-electrode electron gun with a hot cathode. It

was provided at a distance of 0.035 m from the axis, injecting electrons at a 60° angle to the system axis. The optimal injection angle was adjusted by means of a plate condenser with its electric field parallel to the trap axis. The electron injection current on the trap axis reached 10 μA. Electron energy was 1400 eV.

Phosphor-coated grids and aperture limiters were used to record one revolution of the beam; nonphosphorescent flags served as electron current collectors. The flags were provided at the ends of the straight sections of the vacuum chamber. A diffusion oil pump evacuated the trap to a working pressure of $6.66 \cdot 10^{-4}$ N/m^2.

Experimental results

Experiments with a phosphorescent screen showed that appropriate choice of the distance from the space-periodic field region and of the angle between the particle velocity vector and the magnetic lines of force ensured effective conversion of the greater part of the transverse particle energy into longitudinal energy. The degree of conversion of $W_\perp$ to $W_\parallel$ was measured with an electrostatic analyzer immersed in a uniform magnetic field. Figure 2 shows two curves plotting the electron current I picked up by the analyzer collector as a function of the stopping potential U_s (total electron energy, 1380 eV). The two curves differ in the modulation factors of the space-periodic magnetic field $\eta = \frac{H_\sim}{H_0} \cdot 100\%$. An examination of these curves shows that the transverse-to-longitudinal energy conversion is a distinctly resonant process. No complete conversion of $W_\perp$ to $W_\parallel$ could be achieved; some 10% of the transverse energy remained in this mode. An important characteristic of a closed magnetic trap is the behavior of a beam with a certain η, moving through the space-periodic field from the direction of field minimum, where $\eta = \frac{W_\perp}{W_0} \cdot 100\%$ is the ratio of the transverse beam energy to the injection energy, in percent. To study this characteristic, a beam with $\eta = 10\%$ was created by a special electron gun and injected along the axis. The electrostatic velocity analyzer established that the η did not increase during beam passage through the space-periodic field. As the beam was displaced from the axis, the pattern changed, although the "resonance" condition $\omega_H = \frac{2\pi}{L} v_\parallel$ was not observed.

Figure 3 plots η as a function of the injection energy W_0 for $r = 0.17$ m, where r is the distance from the axis at which the beam enters the space-periodic field region; the inlet transverse energy is small ($\eta \leq 5\%$). An inspection of the curve shows that there is no "resonance". We may speak of a mean η for all energies. This property of the space-periodic field imposes rigid requirements on the motion of the electron beam in our closed trap.

The most interesting parameter of the closed magnetic trap is the number of revolutions N completed by a charged particle. N was determined by three methods as a ratio of the electron current circulating in the closed trap to the injection current. These methods are inherently inaccurate,

since all the injected electrons are assumed to circulate in the trap, and the intermediate electron losses are ignored.

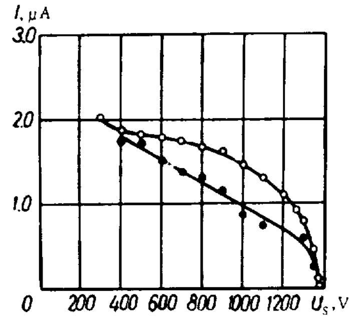

FIGURE 2. Analyzer current vs. stopping voltage U_s:
o — η = 4.9%; • — η = 4%.

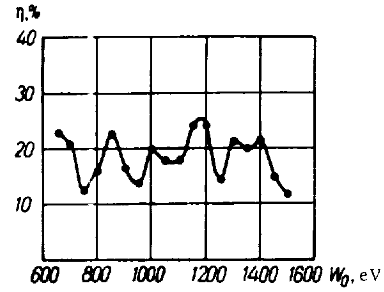

FIGURE 3. The ratio η vs. injection energy W_0.

An ionic probe with a large collecting surface (some 0.75 m^2) was provided in the straight legs of the vacuum chamber (the region of the uniform magnetic field). The large collecting surface made it possible to work with small injection currents. The number of revolutions N was obtained as the ratio of the probe ionic currents under different trapping conditions:

$$N = \frac{I_{+t}}{I_{+1}},$$

where I_{+t} is the probe ionic current in the mode of a closed circulating beam, I_{+1} the ionic current picked up when the electron beam swept once across the probe.

The slow secondary electrons interfered with ionic current measurements, and the probe was therefore maintained at a small negative potential. For optimal matching of the magnetic trap axes and for a probe potential of 20 V, the number of revolutions was 43. These experiments show that a closed electron beam is formed.

Pulsed pickup of the circulating current in the trap by a charged particle collector was applied to ensure more accurate measurements of the number of revolutions. In the straight sections with the uniform magnetic field, the ionic probe was replaced with a plate condenser 0.5 m long, with an 0.06 m gap. A pulsed electric field was provided between the condenser plates. The electron beam traveling through the condenser field drifted in the crossed electric and magnetic fields. The electric field strength was adjusted so that the beam would then hit the collector set at a distance of 0.03 m from the axis. If the collector pickup time t_p is made less than the period of revolution of the beam in the trap, t_r, the number of revolutions completed by the electron beam in the closed magnetic trap can be determined by comparing the circulating current with the current carried by a beam during a single revolution. A square pulse was applied to the condenser plates, having the parameters $t_p = 2.5 \cdot 10^{-7}$ sec, $t_{fr} = 0.5 \cdot 10^{-7}$ sec, $U_p \approx 1200$ V. Time to complete one revolution $t_r = 4 \cdot 10^{7}$ sec. Oscillographic comparison of the electron currents was hardly possible on account of the

small currents, the short pulses, and the comparatively high capacitances of the oscilloscope circuit. A condenser charging technique was therefore applied.

The electron beam was picked up by the collector with a frequency n, charging the output capacitance C_{out} of the collector and the electrostatic voltmeter. The number of revolutions N was calculated as the ratio of the electron currents in different trapping modes,

$$N = \frac{I_{-t}}{I_{-1}},$$

where I_{-t} is the circulating electron current of a closed trapped beam, I_{-1} is the electron current of a one-revolution beam. These electron currents can be easily related with measured electric parameters:

$$I_{-t} = \frac{C_{out}U_t}{t_p n_t}, \quad I_{-1} = \frac{C_{out}U_1}{t_p n_1}.$$

Hence for the number of revolutions

$$N = \frac{U_t n_1}{U_1 n_t},$$

where U_t and U_1 are the voltages to which C_{out} is charged by a circulating electron beam and by a one-revolution beam, respectively: n_t and n_1 are the frequencies at which the deflection pulse is applied to the condenser plates in the two trapping modes.

To ensure equal contributions from collector secondary emission in the different trapping modes, it is advisable to operate with close U_t and U_1, varying the train frequency of the deflection pulses. The measurements were made with the following parameters: $U_1 = 10$ V, $n_1 = 500$ pulses/sec, $U_t = 26$ V, $n_t = 50$ pulses/sec, $N = 26$ rev.

The number of revolutions was also estimated by the visual technique. A special movable electron gun injected a 1400 eV electron beam with $\eta = 10\%$ along the trap axis; the pressure in the closed magnetic trap was maintained constant. For a residual gas pressure of $2.7 \cdot 10^{-3}$ N/m^2 and an axial beam current of 80 μA, the residual gas was seen to glow. The axial gun was removed and electrons were then injected by the main gun. The injection current was chosen so that the circulating beam produced the same glow. The circulating electron current was found to be equal to 80 μA in this case. The current carried during a single revolution can be easily found; in our system I_{-1} was equal to 3.5 μA. The number of revolutions is given by the ratio $N = 80/I_{-1}$, so that $N = 23$ rev. The error of this technique is fairly large (some 20%). It is attributable to inaccuracies in the visual comparison of the glow intensities of the residual gas; N is also lowered by the poor vacuum. This technique is nevertheless suitable for estimating the number of revolutions N.

In our closed trap, the electron beam thus completed some 25 revolutions. This number is much too low to be attributable to the scattering of electrons by the residual gas. Estimates show that for the given working vacuum, the number of revolutions should be almost ten times as high. The circulation of charged particles in the closed trap is apparently governed by other factors, some of which are listed below.

1. Outward growth of the radial magnetic field component in the space-periodic field region. This should considerably broaden the "resonance" curve, enhancing the conversion of $W_{\parallel}$ to $W_{\perp}$.

2. The resonant property of one-turn helical coils. As the longitudinal particle energy varies, the particle is displaced from the axis in the drift plane.

3. Inadequate matching of the magnetic axes of the straight sections and the toroidal couplers.

4. During the $W_{\parallel}$-to-$W_{\perp}$ conversion, the injected beam is not precisely axial.

5. Slow secondary electrons are present in the trap.

BIBLIOGRAPHY

1. SLABOSPITSKII, A. P., V. D. FEDORCHENKO, and B. N. RUTKEVICH. — This volume, p. 354.
2. FEDORCHENKO, V. D. — Dissertation, FTI AN UkrSSR. 1963.
3. LINHART, J. G. Plasma Physics. — Amsterdam, North-Holland Publishing Company. 1960.

E. S. Borovik, F. I. Busol, V. A. Kovalenko, V. F. Yuferov, and E. I. Skibenko

A MAGNETIC TRAP WITH A STRONG MAGNETIC FIELD

A hot plasma can be created in magnetic traps by injecting high-intensity beams of fast neutral hydrogen or deuterium atoms, which are partly ionized and effectively trapped. This method of plasma creation started attracting attention especially after it had been proved /1, 2/ that excited hydrogen atoms could be dissociated by strong electric or magnetic fields. Measurements of the degree of ionization showed that the trapping efficiency of fast ions in this process may exceed by several orders of magnitude the trapping efficiency by residual-gas ionization at pressures of some 10^{-7} N/m^2.

In accordance with these new data, in summer 1962 we ceased work on the GVL-1 magnetic machine, which had been schematically described in /3/ and which had been originally intended for operation with central magnetic fields $B_0 = 2$ T, and switched over to a new project, the GVL-2 magnetic machine, which differed from GVL-1 mainly in the magnetic field strength.

From various published studies on the ionization of excited hydrogen atoms by electric and magnetic fields we know that the ionized fraction increases with field strength; from the data of /4/ it follows that the ionization growth is particular rapid in the range of $(1-2.5) \cdot 10^{-4}$ kV/m. It is thus obviously interesting to try to design a machine with a central magnetic field which will remain greater than 10 T for a sufficiently long time.

The previous experience gained in our laboratory with the generation of high magnetic fields in low-temperature coils /5-8/ indicates that this problem is solvable for machines with reasonable trapping volume, provided suitable power sources are available. Our power supply, however, was fairly limited (a condenser bank with $C = 1.75 \cdot 10^{-2}$ F, $U = 5$ kV, and a bank of 100 car batteries with a total e.m.f. of 1200 V), so that taking an internal trap diameter of 5 cm and a pulse length of nearly 1 sec, we could only generate fields which did not exceed 10 T at the center of each single coil. Without dwelling on this point in any detail, as these problems are discussed in a separate paper /9/, we can only note that the corresponding fields and times can be reached on account of the low temperature at which the coils are maintained. The cryogenic approach, as we shall see below, provides a successful solution to the problem of generating and sustaining ultrahigh vacuum and designing an injector of fast neutral hydrogen atoms. Before proceeding with the description of the layout and the main component units of the GVL-2 machine, we should note that the entire project was based on the previously developed vacuum system and injector of the GVL-1 machine, so that if necessary, one can easily pass from GVL-2 to GVL-1, or to a machine with other parameters, simply by replacing the magnetic field coils. It is noteworthy that the present machine, despite the small trapping diameter, is but slightly inferior to OGRA as regards the field-by-radius product /10/.

Apparatus

The first model of the GVL-2 magnetic machine which is at present in operation is shown in Figure 1. The main component units are the magnetic system, or the trap 1, a vacuum housing 2 with pumping facilities, and an injector of fast neutral hydrogen atoms comprising an ion source 3, a charge-exchange chamber 4, and a receptacle chamber 5 collecting the neutrals which pass through the entire system without dissociating. In principle, our machine does not differ from previously described installations /11, 2/, where the hot plasma is also created by injecting fast neutral hydrogen atoms into the trap; our approach to the solution of the technological problems, however, is essentially different. In the following description of the main units of the GVL-2 machine, we shall therefore concentrate mainly on the technological aspects of the project.

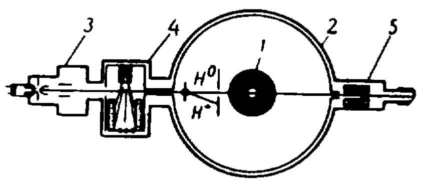

FIGURE 1. System layout – section through the axis of injected beam.

Magnetic system and trap parameters. The GVL-2 magnetic system comprises two serially connected coils fabricated from ordinary copper wire (PBD grade) 1.81 mm in diameter; the winding parameters:

$$a_1 = 2.5\,\text{cm};\ \alpha = 4.3;\ \beta = 4.4;\ B = 2.1 \cdot 10^{-2}\,I.$$

Here a_1 is the internal radius of the winding; α and β stand for the ratios $\frac{a_2}{a_1}$ and $\frac{b}{a_1}$ (a_2 and b are the external radius and the winding half-length,

respectively); B (T) is the field set up at the center of a single coil by a current I (A).

The coil design and disposition are schematically shown in Figure 2. Coil windings 1 are laid very tightly, almost continuously, with a filling ratio $\lambda = 0.6$; number of turns in each coil $N = 4280$. The calculated inductance of these coils $L = 0.8$ H; ohmic resistance at room temperature $R^{300} = 11$ ohm. The coils are held in stainless-steel air-tight jackets 2 with a wall thickness of 2 mm. Between the windings and the jacket walls, an insulating layer 3 is interposed, which is intended for working voltages of up to 5 kV, and which has been tested at voltages of 10 kV. When the magnetic field is turned on, considerable forces of attraction arise between the coils (calculations and special tests show that, for the maximum attainable fields and the small distances between the coils, these forces may be as high as a few hundreds of kilonewtons), so that stainless-steel support flanges 4 with a wall thickness of 8 mm are attached to the inner end surfaces of the coil jackets. Four double-end bolts 5 of 15 mm diameter are provided between the flanges. Part of the load is also shouldered by

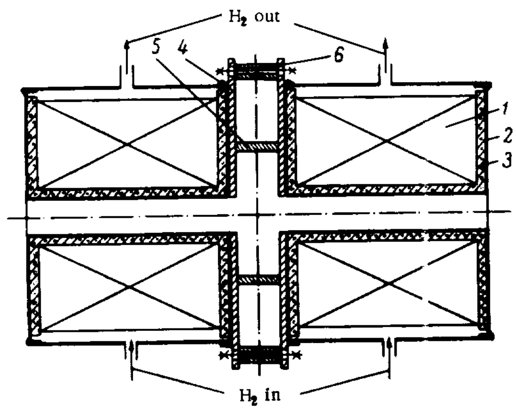

FIGURE 2. A schematic diagram of the magnetic trap system.

the cylindrical couplers 6 mounted on coupling bolts. By varying the length of the bolts 5 and the couplers 6, we can change the distance between the coils, i.e., the length of the trap and the magnetic mirror ratio. At present, the distance between the support flanges is 5 cm, between the winding edges 7.5 cm, and between the coil centers 29 cm. Seeing that the internal diameter of the tube on which the coils are wound is 4.5 cm, and the distance L_0 between the magnetic mirrors is somewhat less than the distance between the coil centers (approximately 27 cm), we have for the volume of plasma in the trap

$$V = 3.35 \cdot 10^{-4}\ \mathrm{m}^3 .$$

The arrangement of the coils inside the vacuum housing, whose design is briefly described in the following, is shown in Figure 3. The coils are connected axis to axis by the coupling bolts; they are mounted on stainless-steel supports which are rigidly fastened to the chamber walls. The height

of the mounts can be regulated within a few centimeters, so that the trap axis is displaced within the desired limits relative to the axis of the injected beam.

The coils, which are coupled in series, are supplied by carefully insulated wires laid in long nickel silver tubes 16 mm in diameter; the tubes emerge radically from the vacuum housing. The cross section of the copper leads is several times greater than the cross section of the winding wires; the quantity of heat transported by these wires to the coils is negligible, corresponding to evaporation of some $4 \cdot 10^{-6}$ kg of liquid hydrogen per second. In Figure 3, the tubes accomodating the supply wires are easily distinguishable, since they connect with the end surfaces of the coil jackets.

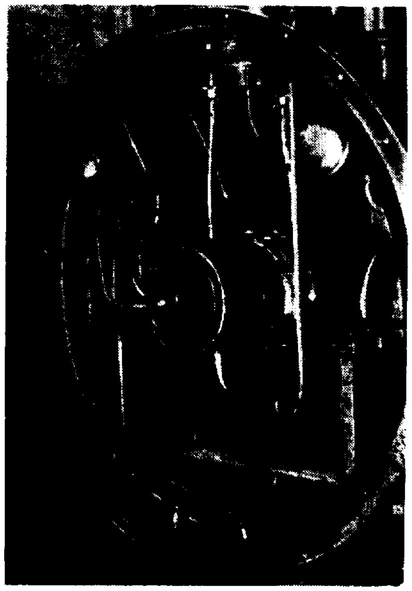

FIGURE 3. General view of the vacuum chamber and the coil arrangement.

The coils are cooled in two stages: first to 78°K with liquid nitrogen, and then to 20.4°K with liquid hydrogen. The liquid coolants reach the coil jackets from below through a single branching nickel silver tube, and evaporating they pass through an annular channel between the coil winding and the jacket wall; the vapors collect in a buffering space: N_2 vapors are ejected while H_2 vapors are fed into a gasholder. When the coils have been fully cooled to the required temperature, liquid N_2 and H_2 fill both the free coil volume and the buffering space. If necessary, the liquids can be evacuated through the same coolant feed tube. The volume of liquid nitrogen and hydrogen needed to cool the coils and the jacket walls is some 0.075 and 0.035 m^3, respectively. The rate of cooling of the coils was determined by measuring the variation in their ohmic resistance for continuous pumping, first, of liquid nitrogen and, then, of liquid hydrogen. Since the windings are thick and the coolant liquids do not circulate through the coil volume, the rate of cooling is slow, some 30° per hour. Fortunately, the cooling is twice as fast in the working temperature range of 50—20°K /9/. This means that in our machine the current pulses providing the maximum magnetic field can be applied at least with a frequency of two per hour.

The ohmic resistance of the pair of coils cooled to the liquid hydrogen point is 0.21 ohm, i.e., 1/105 of the resistance at room temperature. The initial power required to generate magnetic fields of some 10 T was thus of the order of 50 kW. These aspects are discussed in greater detail in /9/.

If the field at the center of one coil is known, the central field in the trap, and also the magnetic mirror ratio, are determined by the coil separation h. The axial field distribution was calculated from the usual

formulas, and it is plotted in Figure 4 for $h = 5$ cm and $h = 7.5$ cm. The abscissa gives the distance from the trap center to the outer coil edge, and the ordinate shows the total field B set up by the two coils, when the field in the center of one coil is precisely 10 T. We see from the figure that in both cases the mirror fields are fairly close, differing by a few percent only from the field at the center of one coil. The difference in the central trap fields, however, is more significant for the two values of h. The numerical values of the central trap field and of the magnetic mirror ratio which are plotted in the figure for the two values of h indicate that for $B_0 = 7$ T, which is the field strength used in calculations of the filling of our trap with plasma /12/, the mirror field should be $B_{mir} = 10.5$ T, when $h = 5$ cm.

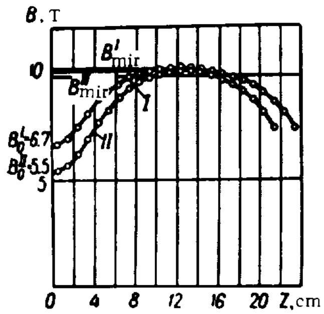

FIGURE 4. Axial field distribution in the trap: I) $h = 5$ cm; II) $h = 7.5$ cm.

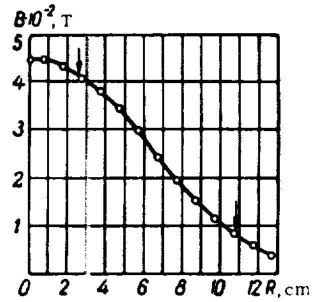

FIGURE 5. Radial field distribution in trap midplane for $h = 7.5$ cm.

The radial field distribution in the trap midplane was determined experimentally; the results for $h = 7.5$ cm are plotted in Figure 5. The values laid off the ordinate in Figure 5 were obtained in experiments with uncooled coils with a current $I = 4.5$ A. We were mainly interested in finding the field increment ΔB as the radius dropped from 2.5 cm to zero: it is known that this quantity determines the fraction of particles that can be ionized directly in the trap volume. From the graph we see that in this case

$$\frac{\Delta B}{B_0} \cong 7\%.$$

Vacuum housing and pumping techniques. The magnetic system of the GVL-2 machine is housed in a large vacuum chamber 2, whose design is obvious from Figure 3. The chamber is fabricated from ordinary soft steel, it is 1.8 m long and 1.2 m in diameter. The various joints and seams in the chamber are sealed with ordinary vacuum rubber, so that unlike most of the modern ultrahigh vacuum equipment, our system must not be heated to the high temperatures (400–450°) recommended in ultrahigh vacuum engineering. We nevertheless hope to achieve residual pressures of some 10^{-7} N/m^2; This will be done, first, by almost complete screening of the vacuum chamber walls by a copper screen 5 cooled to the liquid nitrogen point and, second, by establishing very high pumping spreads,

which are easily attained by the hydrogen 4 and the helium 3 condensation pumps. It has been proved in /13/ that in principle, vacuum of the order of $10^{-8} - 10^{-9}$ N/m^2 can be achieved in rubber-sealed systems.

To facilitate the assembly and the mounting of the coils, the vacuum chamber was designed, as shown in Figure 6, in three separate sections. The length of the central section, where the coils are accommodated, is 0.5 m, the length of the lateral sections, where the hydrogen and the helium condensation pumps are provided, is 0.4 m. Each section and the lids are protected by copper screens which are independently cooled by liquid nitrogen; the screens partly overlap when the chamber is assembled, sealing the chamber space from vapors of oil, rubber, etc.

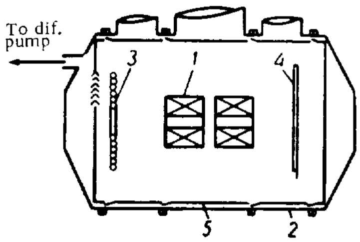

FIGURE 6. System layout – section through the vacuum chamber axis.

The hydrogen condensation pump, whose aim is mainly to pump out all the gases which do not liquefy at 78° K (when hydrogen is first admitted into the system), is a copper sheet welded with a copper tube of 30 mm diameter. The sheet is connected to a liquid-hydrogen container of 0.025 m^3 capacity which is mounted in a special length of piping in the upper part of the lateral section. The theoretical pumping speed for gaseous nitrogen is approximately 70 m^3/sec. This high pumping speed is absolutely essential, since in unheated systems residual gas inflow is possible even if no actual leaks occur: gas molecules are constantly desorbed from the walls. In our case, with the screen cooled to 78° K, the total leak is quite noticeable – close to $2.5 \cdot 10^{15}$ molecules/sec. A simple calculation shows that even in this unfavorable situation, the equilibrium pressure in the chamber will remain close to $1 \cdot 10^{-7}$ N/m^2 (ignoring all other pumping surfaces).

The helium condensation pump is a plane tightly wound copper-tube helix (tube i.d., 10 mm), through which low-pressure liquid helium is continuously pumped. The aim of this pump is to evacuate the hydrogen which leaks into the chamber during the firing of the ion source and the injection of the neutral beam into the trap. The external diameter of the helix 62 cm, the internal diameter some 10 cm. The total surface of the helium pump is approximately 0.6 m^2, i.e., hydrogen pumping rate is about 260 m^3/sec. However, if each H_2 molecule before condensation collides, at least once, with the nitrogen screen, the pumping speed will be approximately halved, to some 130 m^3/sec.

The large capacity of the vacuum housing and the enormous hydrogen pumping speed (it can be easily increased by a considerable factor) enable the charged component of the ion beam to be deflected directly in the trap, as shown in Figure 1, thus somewhat reducing the distance to the ion source. Since the population of the excited hydrogen levels rapidly fall off with the distance from the source /14/, this point may prove to be beneficial for increasing the proportion of neutrals ionized in the trap volume.

Applying the new data /15/ on the penetration factor of hydrogen ions in a heated stainless-steel target, we can easily show that even for the

given arrangement of the target and the helium pump, the equilibrium pressure in the chamber is maintained in the vicinity of the 10^{-7} N/m^2 mark for an injected ion current of up to 10 mA.

Injector of fast neutral hydrogen atoms. Ion source. Hydrogen ion beams were produced by an ion duplasmatron source attached directly to the charge-exchange chamber. This means that a mixed beam of hydrogen ions, containing H_2^+ and H_3^+ ions, as well as protons, hits the charge-exchange target. The beam of neutrals which emerges after charge-exchange also carries particles of different species. As it follows from the results of /16/, these particles are mainly hydrogen atoms with different energies: E, $E/2$, $E/3$, where E is the energy of the accelerated ions, equal in our case to 30 keV. It is known /17/ that mass composition of ion beams depends on the source operating conditions, and that an operating mode can be chosen with protons constituting the bulk of beam particles. In our case, we did not look for this optimal operating mode for the following reasons. It is shown in /1/ that the fraction of atoms ionized in a strong electric or magnetic field is highly sensitive to the particle origin: if the H^0 atoms are dissociation products of H_2^+ or H_3^+, the ionization is higher than in cases when the neutrals are produced by charge exchange. If we also remember that the yield of H^0 atoms per one charge-exchanging H_2^+ or H_3^+ ion is greater than unity, we see that under our conditions, despite the comparatively low efficiency of the electric field $\mathbf{E}^* = |\mathbf{v} \times \mathbf{B}|$ for 15 and 10 keV H^0 atoms, a much higher trapping efficiency can be expected than in experiments employing pure proton beams. It must be taken into consideration, of course, that the interpretation of the experimental results in "mixed-beam" cases is much more complicated, and a provision is therefore made in the original machine design for injection of beams with one-species particles.

Charge-exchange chamber. Charge exchange is achieved by intercepting the accelerated beam of hydrogen ions with a supersonic CO_2 jet. The behavior of supersonic gas jets injected into a vacuum and condensing on low-temperature surfaces has been investigated in some of our previous papers /18–20/. It has been shown that these jet targets have several obvious advantages, the main one being the low pressure maintained near targets of optimum thickness (as low as $1 \cdot 10^{-4}$ N/m^2); CO_2, A, and N_2 are also highly convenient for handling in this sort of work.

The charge-exchange chamber is of the same design as that employed in /18/, but the shape and the position of the condenser relative to the Laval nozzle have been altered: here the jet is directed downward, while in the previous experiments it was injected from bottom to top. This modification was introduced to neutralize the following effect: the solid condensate layer does not always remain stuck to the walls, it may crack and partly crumble. When the detached crystals fall on heated surfaces, they evaporate, and this clearly has a detrimental influence on the vacuum in the charge-exchange chamber. As regards the condenser geometry, it was found to have no influence on the vacuum in the charge-exchange chamber. This problem is discussed in greater detail in /20/.

Receptacle chamber. Its design is essentially simple (Figure 1). This chamber also was prepared taking into consideration the latest data on the penetration factor /15/: it comprises a heated stainless-steel target and a small condensation pump. It is assumed that the greater part of the neutral hydrogen beam hitting the target will penetrate into it for good. The part of the beam which is not absorbed by the target is removed by the condensation pump, whose pumping speed is somewhat

higher than $10\,m^3/sec$. If, say, the equivalent current of neutrals hitting the target is 10 mA, and the ion penetration factor is 90%, the equilibrium pressure in the receptacle chamber for this pumping speed is $2 \cdot 10^{-6}\,N/m^2$, (providing, of course, that the hydrogen vapor pressure at the condensation point is less than this figure). It can be easily shown, however, that this vacuum is unnecessarily high for a receptacle chamber of the given geometry (cooled channel diameter 5 cm, length 20 cm, distance to trap center, 80 cm), since already for pressures of $6 \cdot 10^{-5}\,N/m^2$, the equivalent pressure at the center, corresponding to the primary beam of hydrogen molecules emerging from the receptacle chamber, is less than $1 \cdot 10^{-7}\,N/m^2$.

In conclusion we should note that we have not yet completed the final tests of the machine components, but the preliminary experiments give quite satisfactory results. Pressures lower than $10^{-6}\,N/m^2$ were achieved in the vacuum chamber without any prolonged conditioning and even without turning on the helium condensation pump. The main difficulty at this stage was how to eliminate the so-called "cold" leaks, i.e., leaks arising when liquid nitrogen, hydrogen, or helium are poured into the coils or other vacuum-adjoining vessels.

The magnetic trap system was tested only with the condenser bank mentioned in the introduction. In the first experiments, the coils were cooled to the liquid nitrogen point, and later to the liquid hydrogen point. The maximum field in the magnetic mirrors produced at 20.4 °K for a condenser bank voltage of 5 kV was close to 10.5 T, i.e., nearly equal to the calculated figure. The growth time of current from 0 to I_{max} was 0.28 sec. In subsequent experiments, the coils will be supplied with power according to the scheme described in /9/.

BIBLIOGRAPHY

1. RIVIERE, A.C. and D.R. SWEETMAN. – Fifth Int. Conf. on Ionization Phenomena in Gases, Munich. August 28–September 1, 1961, preprint.
2. SWEETMAN, D.R. – Nucl. Fusion Suppl., **1**:279. 1962.
3. BOROVIK, E.S., F.I. BUSOL, and V.A. KOVALENKO. – In: "Fizika plazmy i problemy upravlyaemogo termoyadernogo sinteza", Vol. 1. Kiev, Izdatel'stvo AN UkrSSR. 1962.
4. KAPLAN, S.N., G.A. PAULIKAS, and R.V. PYLE. – Phys. Rev. Letters, **9**:347. 1962.
5. BOROVIK, E.S., F.I. BUSOL, and S.F. GRISHIN. – ZhTF, **31**:459. 1961.
6. BOROVIK, E.S. and A.G. LIMAR'. – ZhTF, **31**:939. 1961.
7. BOROVIK, E.S. and A.G. LIMAR'. – ZhTF, **32**:442. 1962.
8. LIMAR', A.G. and Yu. A. LITVINENKO. – ZhTF, **34**:344. 1964.
9. BUSOL, F.I., V.A. KOVALENKO, E.I. SKIBENKO, and V.G. YUFEROV. – This volume, p. 412.
10. KURCHATOV, I.V. – Atomnaya Energiya, **5**:105. 1958.
11. POST, R.F. – Proc. of the Fourth Int. Conf. on Ionization Phenomena in Gases, Uppsala, 17–21 August 1959, vol. II, p. 987, N.R. Nilson, ed. Amsterdam, North-Holland Publ. Co. 1960.

12. BOROVIK, E. S., F. I. BUSOL, and K. D. SINEL'NIKOV. – This volume, p. 372.

13. BOROVIK, E. S., S. F. GRISHIN, and B. G. LAZAREV. – PTE, 1:11. 1960.

14. HISKES, J. R. – Nucl. Fusion, 2:39. 1962.

15. BOROVIK, E. S., N. P. KATRICH, and G. T. NIKOLAEV. – This volume, p. 402.

16. FEDORENKO, N. V. – ZhTF, 24:769. 1954.

17. MOAK, C. D., H. E. BANTA, J. N. THURSTON, J. W. JOHNSON, and R. F. KING. – Rev. Sci. Instr., 30:694. 1959.

18. BOROVIK, E. S., F. I. BUSOL, V. B. YUFEROV, and E. I. SKOBENKO. – ZhTF, 33:973. 1963.

19. BOROVIK, E. S., F. I. BUSOL, and V. G. YUFEROV. – In: "Fizika plazmy i problemy upravlyaemogo termoyadernogo sinteza", 3. Kiev, Izdatel'stvo AN UkrSSR. 196:.

20. BUSOL, F. I., V. B. YUFEROV, and E. I. SKIBENKO. – This volume. p. 408.

E. S. Borovik, F. I. Busol, and K. D. Sinel'nikov

A CALCULATION OF THE FILLING OF THE G'/L-2 TRAP WITH PLASMA

In this paper we consider the filling with plasma of a small-capacity magnetic trap with a high magnetic field. The design of the magnetic machine is described in a separate paper /1/. Here we shall only give a schematic diagram of the magnetic system and some relevant data on magnetic field distribution which are needed in calculations.

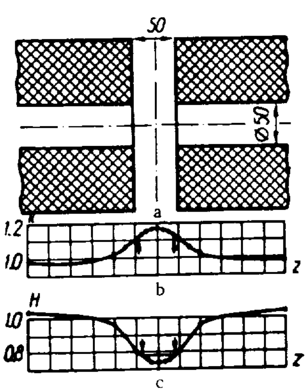

FIGURE 1. Magnetic system layout (a), paraxial line of force (b), and axial distribution of the magnetic field (c).

The magnetic trap system is schematically shown in Figure 1 (ξ is a quantity proportional to $\frac{1}{\sqrt{B}}$ in rel. un., H is the magnetic field strength in rel. un.). The magnetic field is provided by two long coils with a length-to-diameter ratio $\beta = 4.4$ and an external-to-internal diameter ratio $\alpha = 4.3$. The coils are fabricated from copper wire and are cooled by liquid hydrogen. It has been shown /2,3/ that fairly long pulses can be obtained under these conditions. For example, for a 10 T field at the center of one coil, the allowed field lifetime is close to 2 sec, and for a 20 T field, the lifetime is close to 0.5 sec. Copper coils with $\alpha = 4.3$ and $\beta = 4.4$ may sustain fields in excess of 20 T /3/.

Coil separation can be varied from 5 to 15 cm. The magnetic mirror ratio is a function of this distance. For coil separations of 5, 7.5, and 15 cm, the respective mirror ratio $\frac{B_{\mathrm{mir}}}{B_0}$ is approximately 1.5, 2.1, and 4.

Further calculations will be made for a central trap field $B_0 = 7$ T and a magnetic mirror field $B_{mir} = 10.5$ T. The two lower graphs in Figure 1 show the axial field distribution and the contour of the paraxial line of force for this case. We see that the lines of force in the greater part of the trap volume are convex toward the axis. The inflexion points, marked with arrows, are at a distance of some 2 cm from the midplane. We shall show in what follows that this peculiar field distribution is highly significant.

The entire magnetic system is enclosed in a large vacuum housing 1.2 m in diameter and 1.8 m long, which is evacuated by condensation pumps /4, 5/ to pressures of the order of $1 \cdot 10^{-7}$ N/m^2.

For purposes of comparison, the table below lists the principal parameters of different magnetic machines: OGRA /6, 7/, DCX-1 /8/, DCX-2 /9/, ALICE /10/, PHOENIX /11/, and our GVL-2 machine.

Parameters	OGRA	DCX-1	DCX-2	ALICE	PHOENIX	GVL-2
B_0, T	0.5	1	1.2	5	4.5	7
B_{mir}, T	0.8	2	4.2	7.7	9	10.5
r_0, cm	50	13	12.5	15	11	2.5
L, cm	1200	75	370	72	30	24
V_0, cm^3	10^7	$6 \cdot 10^3$	$2 \cdot 10^5$	$2.50 \cdot 10^4$	$6 \cdot 10^3$	$3 \cdot 10^2$
Injected particles	H_2^+	H_2^+	H_2^+	H_1^0	H_1^0	H_1^0
E, keV	160	600	600	20	30	30
I, mA	150	15	500	100	1	10
r_0/ϱ	4	1	2.5	35	20	7
$B_0 \cdot r_0$, T·cm	25	13	15	75	50	17

Aside from B_0, B_{mir} and r_0 (the radius of the plasma-filled volume), the table also gives the effective trap length L, the plasma-filled volume V_0, the energy E and the current I, of the injected particles, the ratio of the radius of the plasma-filled volume to the radius of the orbit $\frac{r_0}{\varrho}$, and also the product $B_0 \cdot r_0$ which may be regarded as a quality factor of the trap /6, 12/. We see from the table that, despite the very small capacity of our trap, its $B_0 \cdot r_0$ is fairly close to the corresponding factor of the largest magnetic machines in operation.

The small trap capacity enables us to reduce the injection current required to fill the trap to high densities. Indeed, in order to create a plasma with ion density of 10^{12} cm^{-3} for 1 sec, OGRA requires an injection current of no less than 1.6 A (even if perfect trapping is assumed), while our GVL-2 will fill to the same density with a current of $5 \cdot 10^{-5}$ A. A highly important factor is the smallness of the trapping ratio in the injection of neutral particles. As the trap volume is reduced, the field strength must of course be raised in order to maintain a constant $B_0 \cdot r_0$. The total magnetic energy, however, decreases, since it is proportional to $B_0^2 \cdot r_0^3$. It is always preferable to work with strong magnetic fields, since the plasma density is then additionally raised by the increased magnetic pressure. In OGRA, for example, the magnetic pressure is merely ~1 at, which corresponds to a maximum allowed density of $3 \cdot 10^{12}$ ions/cm^3. The actual density is of course much lower, since the magnetic pressure must be considerably smaller than the gas-kinetic pressure. The magnetic pressure in GVL-2 is 200 at, which for the injection of 30 keV particles corresponds to a maximum attainable density of $5 \cdot 10^{15}$ ions/cm^3. If we take $2 \cdot 10^{-3}$

as the allowed kinetic-to-magnetic pressure ratio, we see that densities of the order of 10^{13} ions/cm^3 can be achieved in principle in our magnetic machine. Let us consider to what extent the injection of fast neutral hydrogen atoms in GVL-2 is compatible with the attainment of these high densities.

The filling of the trap

Neglecting various secondary effects, we write the conventional expression for the variation in the number of trapped fast ions n:

$$V\frac{dn}{dt} = i_0\gamma + ln_0\sigma_i^0 i_0 + ln\,\sigma_i^- i_0 - nnv\sigma_e V - n^2\sigma_q vV\,\frac{\omega_0}{2\pi}. \qquad (1)$$

Here V is the volume of trapped plasma, l the path length of the injected beam of neutrals in the plasma (trap diameter), i_0 the number of neutral atoms injected per second, n_0 the density of neutral molecules in the plasma volume, γ the fraction of neutral atoms trapped due to ionization by the magnetic field, σ_i^0 and σ_i^+ ionization cross sections of fast neutral atoms in collision with the residual gas and with the trapped ions, respectively; σ_e is the cross section for the charge exchange of trapped ions with the residual gas, σ_q is the Coulomb collision cross section of the fast ions, v the velocity of the fast ions and neutrals, $\omega_0/2\pi$ is the probability that a particle experiencing a Coulomb collision will escape through the magnetic mirrors.

The first three terms in the right-hand side of (1) give the addition to the number of trapped particles due to the combined contribution from ionization of the injected neutral particles (a) by the magnetic field, (b) by residual gas molecules, and (c) by previously trapped ions. The last two terms represent particle losses by previously trapped ions. The last two terms represent particle losses by charge exchange with the residual gas and by penetration through magnetic mirrors on account of interparticle Coulomb collisions.

Differential equations analogous to (1) have been repeatedly solved /10–13/, and we shall not investigate it in the general form. We only propose to estimate the contribution from the different terms in various limiting cases, in application to our particular magnetic machine.

The following numerical values will be assumed for the constants entering equation (1). The equivalent current of neutrals will be taken equal to 10 mA, which corresponds to $i_0 = 6.25 \cdot 10^{16}$ particles/hour. A pressure of $1.3 \cdot 10^{-7}$ N/m^2 corresponds to a number density $n_0 = 3.5 \cdot 10^7$ molecules/cm^3. In estimating the plasma volume, we must remember that for ion number densities of less than 10^{11} ions/cm^3, Coulomb interactions hardly affect the velocity and the space distribution of particles in times of the order of 1 sec (this proposition will be proved in the following). Therefore, initially, the plasma occupies a limited volume at the center of the trap. This volume $V_1 \simeq 60$ cm^3, and only high-density plasmas occupy the entire volume between the mirrors, $V_0 \simeq 300$ cm^3. The trapping path length of the injected particles is approximately equal to the internal diameter of the coils, i.e., $l \simeq 5$ cm. Coulomb scattering cross section

for 30 keV hydrogen ions $\sigma_e = 6\cdot10^{-22}\,\mathrm{cm}^2$. Ion velocities $v = 2.4\cdot10^8$ cm/sec. The charge-exchange cross section with hydrogen molecules corresponding to this velocity is $\sigma_e \simeq 3.5\cdot10^{-16}$ cm^2. Ionization cross section of fast neutral hydrogen atoms by hydrogen molecules $\sigma_i^0 = 1.6\cdot10^{-16}$ cm^2 (for $E = 30$ keV). For velocities of $2.4\cdot10^8$ cm/sec, $\sigma_i^+ \sim 1.5\cdot10^{-16}$ cm^2. The last cross section should be averaged over the relative velocities of ions and neutrals, but this is hardly feasible, since no exact numerical data are available.

For γ we only have an approximate value. In published papers /14, 15/, only the total trapping ratio was measured for neutral particles passing through a magnetic or an electric field with a sharp boundary. It follows from the data in /15/ that a magnetic field of 7 T will ionize slightly over 1% of 30 keV particles. However, part of these ionized particles is not trapped in our case, since they dissociate in the weak magnetic field region between the coils. The magnetic field inside the coils varies approximately by 5%. If we assume that only particles corresponding to a 5% variation in the magnetic field are actually trapped, we have a trapping ratio close to 0.1%. There is however another helpful factor: part of the atoms which in principle can be ionized in regions adjoining the inner coil area will dissociate only in the working space, since their drift time through the coil region is much too short for ionization to occur. The trapping ratio may therefore rise to 0.2–0.5%. We henceforth take $\gamma = 10^{-3}$, and in some cases raise the estimate to $\gamma = 5\cdot10^{-3}$.

Let us first consider the filling of the trap without ionization by magnetic fields. If the concentration of fast ions is low, only the second and the fourth terms in (1) are significant. The equilibrium concentration of ions in this case is given by the formula

$$n_1 = \frac{i_0\sigma_i^0 l}{V_l v\sigma_e} \sim 0.6\cdot10^7 \text{ particles/cm}^3. \tag{2}$$

This number density is much less than n_0 and to achieve burn-out of the residual gas for the given injection current, the pressure must be lowered to $3\cdot10^{-8}$ N/m^2. In reality, however, this equilibrium is fairly meaningless, since trapping by the magnetic field is much more efficient than trapping due to ionization by the residual gas. Indeed,

$$l n_0\sigma_i^0 = 5\cdot3.5\cdot10^{+7}\cdot1.6\cdot10^{-16} = 2.8\cdot10^{-8}, \tag{3}$$

whereas the probability of ionization by the magnetic field, as we have previously observed, is of the order of 10^{-3}. At low concentrations, it is thus the first and the fourth terms in (1) that play the principal role; if these terms are assumed to be equal, we find the equilibrium concentration

$$n_2 = \frac{i_0\gamma}{n_0 v\sigma_e V_l} \simeq 3.6\cdot10^{11} \text{ ions/cm}^3. \tag{4}$$

Taking $\gamma = 5\cdot10^{-3}$, we have

$$n_2' \simeq 1.8\cdot10^{12} \text{ ions/cm}^3.$$

We see that the equilibrium concentration n_2 is enormous in comparison with the concentration of neutral molecules. It means, of course, that this equilibrium is not feasible either: neutral particles are burnt out and the loss of trapped ions is governed by Coulomb scattering.

Before proceeding with the analysis of processes after burn-out, let us first consider how burn-out occurs, estimating the characteristic times. In our trap, the concentration of the slow neutral particles in the plasma volume is altered mainly by the following two factors: ionization of neutral particles by the trapped ions and leakage of neutral molecules from the housing through the ring gap between the coils. The differential equation for the concentration of neutral particles is

$$V_1 \frac{dn_0}{dt} = (n_0' - n_0)\frac{1}{4}\bar{v}_t Sk - nn_0\sigma_i v V_1. \tag{5}$$

Here n_0' is the concentration of neutral molecules in the vacuum outside the trap, $\bar{v}_t$ the mean thermal speed of the residual gas molecules in the gap between the coils (equal to $4 \cdot 10^4$ cm/sec at 20 °K), S the ring gap area (approximately equal to 40 cm^2), $k \simeq 0.5$ the gap resistance coefficient, σ_i ionization cross section of hydrogen molecules by protons. For $E = 30$ keV, $\sigma_i = 1.7 \cdot 10^{-16}$.

To produce a substantial reduction in the concentration of neutral particles in the plasma volume, the following equality must be satisfied:

$$n_2\sigma_i v V_1 > \frac{1}{4}\bar{v}_t Sk. \tag{6}$$

Estimates give for the two sides of this inequality

$$n_2\sigma_i v V_1 \simeq 0.92 \text{ m}^3/\text{sec},$$
$$\frac{1}{4}\bar{v}_t Sk \simeq 0.20 \text{ m}^3/\text{sec}.$$

We see from these figures that the burn-out rate of the residual gas is much higher than the rate of leakage. Burn-out is an extremely fast process. This means that charge-exchange losses need not be taken into consideration and that all the ions trapped by the magnetic field will remain in the trap during the first stages. Thus, initially,

$$\frac{dn}{dt} = \frac{i_0 Y}{V_1} = 10^{12} \text{ ions/cm}^3\cdot\text{sec}. \tag{7}$$

As the concentration of ions increases, more and more particles are lost by Coulomb collisions. For the equilibrium defined by the equality of the first and the fifth terms in (1), we have

$$n_3 = \left(\frac{i_0 Y}{\sigma_q v V_1 \frac{\omega_0}{2\pi}}\right)^{1/2} \simeq 3 \cdot 10^{12} \text{ ions/cm}^3. \tag{8}$$

It is easily seen that this equilibrium is again infeasible, since for densities of the order of 10^{12} cm^{-3} the probability of ionization by previously trapped ions is comparable with the probability of ionization by the magnetic field. Indeed, for $n = 10^{12}$ cm^{-3}, we have

$$ln\sigma_i^+ = 5 \cdot 10^{12} \cdot 1.5 \cdot 10^{-16} = 0.7 \cdot 10^{-3}.$$

Therefore, already during the first second, the first and the third terms in (1) must not be neglected; if the losses are ignored, the rate of growth of particle concentration is described by the equation

$$\frac{dn}{dt} = \frac{i_0 Y}{V_1} + \frac{i_0 ln\sigma_i^+}{V_1}. \tag{9}$$

The second term in (9) represents exponential growth. The time constant of the exponent is

$$\tau_0 = \frac{V_1}{i_0 l \sigma_i^+} = 1.3\,\text{sec}. \tag{10}$$

However, for densities greater than $6 \cdot 10^{12}$ ions/cm^3, the time between Coulomb collisions is as low as one second, so that the plasma will spread through the entire volume between the magnetic mirrors, and in (9) V_0 should be substituted for V_1. The density will therefore increase at a lower rate, and the time constant of the exponential term takes the form

$$\tau_0' = \frac{V_0}{i_0 l \sigma_i^+} \simeq 6.5\,\text{sec}. \tag{11}$$

Losses through magnetic mirrors also become noticeable. Equilibrium is achieved when the losses become equal to the current gains, and the corresponding concentration of trapped particles is

$$n_4 = \frac{\frac{i_0\gamma}{n_4} + l\sigma_i^+ i_0}{\sigma_q v V_0 \frac{\omega_0}{2\pi}}. \tag{12}$$

For $\gamma = 10^{-3}$, $n_4 \simeq 4 \cdot 10^{12}$ cm^{-3}. Even when the density is highest ($4 \cdot 10^{12}$), only a negligible fraction of the injected particles is trapped: for this density, we have $ln\sigma_i^+ \simeq 3 \cdot 10^{-3}$.

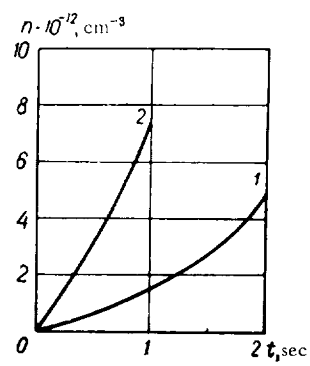

FIGURE 2. Plasma density vs. time for the initial build-up period: 1) $\gamma = 10^{-3}$; 2) $\gamma = 5 \cdot 10^{-3}$.

Curves plotting n as a function of the time t during the initial period, when the Coulomb interactions are negligible, are given in Figure 2 for two γ-values: 10^{-3} and $5 \cdot 10^{-3}$. Introduction of Coulomb collisions complicates the calculations, since the time growth of the magnetic field produces cross-sectional inhomogeneity of the plasma. The coefficient γ will change for the same reason, so that the curves plotted for the initial build-up period provide but a rough estimate for the variation of density in time. It nevertheless follows from this estimate that we can hope to reach densities of the order of 10^{12} ions/cm^3 in times of about 1 sec, provided the instabilities have been suppressed.

Suppression of instabilities

The foregoing description of the plasma build-up process is meaningless if instabilities set in and the plasma is ejected from the trap volume. Flutes constitute the most dangerous form of instability in this case. Although increasing the magnetic-to-kinetic pressure ratio is beneficial to plasma stability, the criterion for the onset of fluting instabilities does not contain the magnetic field strength in explicit form. However, the drift velocity in these relatively inhomogeneous fields is inversely proportional to field strength, so that charge accumulation in the flutes also decreases as the field is raised. If the rate of charge dissipation is assumed to be independent of field strength (e.g., the charge dissipating due to the motion of electrons along the field to a shorting metallic surface), plasma stability with respect to flutes should obviously increase with increasing magnetic field.

It also seems that the particular field configuration in the GVL-2 machine (the region with convex lines of force is geometrically small and it is also insignificant in comparison with the region of magnetic field variation) is further conducive to the suppression of flutes. Indeed, the field at the point of inflexion of a line of force is merely 5% greater than the central field. Therefore, if the particle velocities at the trap center follow a spherically symmetric distribution, merely 20% of the particles will be reflected from the field region with convex lines of force (thus displaying an adverse drift), while 40% will be reflected from regions with concave lines of force, and 40% will escape through the magnetic mirrors.

For the more conventional field distributions, with a magnetic mirror ratio $\frac{B_{\text{mir}}}{B_0} = 2$ and inflexion points corresponding to a field strength halfway between the central and the mirror fields, 58% of the particles are reflected from the field region with convex lines of force, 3% from regions with concave lines of force, and 29% escape through the mirrors. We see that the field geometry of the GVL-2 machine will apparently suppress the harmful drift even in isotropically distributed particles (the exact answer can be given only after numerical calculations with a computer). The expansion of the cone of solid angles with beneficial drift (this cone in our case is a certain fraction of 40%) promotes the anisotropic velocity distribution which suppresses the fluting instablities. Since up to densities of $\sim 10^{12}$ cm^{-3} Coulomb collisions are insignificant, a favorable particle distribution can be artificially created by injecting the particles into the trap after the inflexion points of the lines of force.

A second stabilizing factor is provided by the time growth of the magnetic field during plasma build-up. As the field increases, the initially trapped particles move to the center, and this establishes a favorable plasma distribution in the trap, the density increasing toward the center and the plasma volume possessing no sharp boundary. The radial field gradient is not large (the magnetic field varies by a mere $\sim$ [illegible]% along the trap radius), and therefore as the density rises and the thermal pressure becomes equal to a few percent of the magnetic pressure, the magnetic field in the entire plasma-filled region may, in certain cases, increase toward the periphery.

In conclusion we should note that the stability criterion proposed in /17/ applies for the GVL-2 up to densities of $\sim 10^{14}$ cm^{-3}. It therefore seems that the curves of Figure 2 can actually be realized in practice.

Enhancement of plasma build-up

The rate of plasma build-up and the maximum density can obviously be increased by raising the injection current. We shall consider, however, some alternatives to this trivial technique.

Enhancement of trapping by the magnetic field. As we have previously observed, on account of the extended magnetic-field boundary, only a small part of the particles are ionized in the magnetic trap, while the majority dissociate in the growing magnetic field in the gap between the coils. Application of magnetic screening for fields of some 10 T involves considerable difficulties. The ionizing influence of the magnetic field in the coil gap, however, can be eliminated by passing the neutrals through an electric field, such that

$$\mathbf{E} + [\mathbf{v} \cdot \mathbf{B}] < \mathbf{E}_i,$$

where $\mathbf{E}_i$ is the ionization onset field (in our case $\mathbf{E}_i \simeq 50\,\mathrm{kV/cm}$).

This field can be set up between plates of suitable geometry. The particles are then ionized in the trap only, so that the trapping ratio γ increases to 1%, i.e., by one order of magnitude. The deficiency of this method is that the particles are mostly ionized upon emerging from between the plates, i.e., an increased concentration of particles is obtained at the trap periphery. This shortcoming is fortunately offset by the central drift of charged particles in the fringes of the condenser field which penetrate into the trap.

Reduction of the effective Coulomb scattering cross section. The Coulomb cross section $\sigma_{ii} = 6 \cdot 10^{-22}\ \mathrm{cm}^2$ includes remote collisions which produce small-angle deflection. Coulomb collisions raise the longitudinal velocity component and enhance particle losses through the magnetic mirror. In a time-growing field, however, the transverse field component increases. The superposition of these two processes may conserve the perpendicular-to-longitudinal velocity ratio. The slow increase of the transverse energy obviously does not affect the outcome of close Coulomb collisions, when the direction of the velocity vector changes abruptly, but it may compensate for the adverse influence of remote collisions, when the velocity changes slowly.

Calculations show that in our case, with the field changing noticeably in one second, this compensation is possible up to number densities of the order of $10^{13}\ \mathrm{cm}^{-3}$. The effective Coulomb cross section is then reduced by the value of the Coulomb logarithm, i.e., approximately by one order of magnitude.

Reduction of charge-exchange cross section and increase of ionization cross section in a high magnetic field. In charge-exchange processes, most of the products are excited, and in a high magnetic field the proportion of excited states may possibly increase. These fast excited atoms may further dissociate in the magnetic field, without leaving the trap volume. In high magnetic fields, the ionization cross section may thus be increased, and the charge-exchange cross section reduced. The purpose of these purely qualitative observations is to focus the attention on this interesting and promising possibility and to urge all concerned to proceed with quantitative calculations or measurements of the corresponding cross sections. The effect may prove to be noticeable only in fields much greater than 10 T.

BIBLIOGRAPHY

1. BOROVIK, E.S., F.I. BUSOL, V.A. KOVALENKO, V.B. YUFEROV, and E.I. SKIBENKO. – This volume, p. 364.

2. BOROVIK, E.S. and A.G. LIMAR'. – ZhTF, 31:939. 1961.

3. BOROVIK, E.S. and A.G. LIMAR'. – ZhTF, 32:442. 1962.

4. BOROVIK, E.S., S.F. GRISHIN, and B.G. LAZAREV. – PTE, No. 1:115. 1960.

5. BOROVIK, E.S., F.I. BUSOL, and V.A. KOVALENKO. – In: "Fizika plazmy i problemy upravlyaemogo termoyadernogo sinteza", Vol. 1, p. 148. Kiev, Izdatel'stvo An UkrSSR. 1962.

6. KURCHATOV, I.V. – Atomnaya Energiya, 5:105. 1958.

7. GOLOVIN, I.N., L.I. ARTEMENKOV, G.F. BOGDANOV, D.A. PANOV, V.I. PISTUNOVICH, and N.N. SEMESHKO. – UFN, 73:685. 1961.

8. BARNETT, C.F., D.R. BELL, J.S. LUSE, E.D. SHIPLEY, and A. SIMON. – Proceedings of the Second International Conference on Peaceful Uses of Atomic Energy, 31:298. 1958.

9. GAUSTER, W.F. – Österr. Ingr.—Arch., 15:76. 1961.

10. POST, R.F. – Proc. of the 4th Int. Conf. on Ionization Phenomena in Gases, Uppsala, 17–21 August 1959. Vol. II, p. 987, N.R. Nilson, ed. North-Holland Publ. Co., Amsterdam. 1960.

11. SWEETMAN, D.R. – Nucl. Fusion Suppl., 1:279. 1962.

12. BUDKER, G.I. – In: "Fizika plazmy i problemy upravlyaemykh termoyadernykh reaktsii", Vol. 3. Moskva, Izdatel'stvo AN SSSR. 1958.

13. GIBSON, G., W.A. LAMB, and E.J. LAUER. – Proceedings of the Second International Conference on Peaceful Uses of Atomic Energy, 32:275. 1958.

14. RIVIERE, A.C. and D.R. SWEETMAN. – 5th Int. Conf. on Ionization Phenomena in Gases, Munich, August 28–September 1, 1961, preprint.

15. KAPLAN, S.N., G.A. PAULIKAS, and R.V. PYLE. – Phys. Rev. Letters, 9:347. 1962.

16. ARTSIMOVICH, L.A. Upravlyaemye termoyadernye reaktsii (Controlled Thermonuclear Reactions). – Moskva, Fizmatgiz. 1961.

17. DAMM, C.C., J.H. FOOTE, A.H. FURTH, and R.F. POST. – Phys. Rev. Letters, 10:323. 1963.

B.P. Il'enko, V.G. Zykov, E.M. Lats'ko, and V.M. Zalkind

POLARIZATION OF PLASMA MOVING IN A HELICAL MAGNETIC FIELD

The polarization of plasmoids moving in a transverse magnetic field was first studied by Bostick /1/ and later by other authors /2/. The study of plasmoids moving in toroidal magnetic fields is of considerable applied interest. As a plasmoid moves through a curved magnetic field, charge

separation is produced by the centrifugal force and by the perpendicularly oriented ∇B and B. This gives rise to an electric field component E_z at right angles to the magnetic-field gradient. On the other hand, according to /3/, charge separation produces an electric-field component E_r in a plane parallel to the magnetic-field gradient due to the difference in the Larmor radii of the ions and the electrons. The components E_z and E_r are considered in a cylindrical system of coordinates, with an axis through the center of curvature of the line of force at right angles to the plane of the drawing in Figure 2. Figure 1 shows the orientation of the components E_z and E_r for oppositely directed longitudinal magnetic fields in accordance with the theory of /3/.

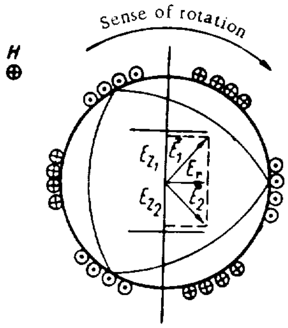

FIGURE 1. Vector diagram of the components E_z and E_r for oppositely directed magnetic fields.

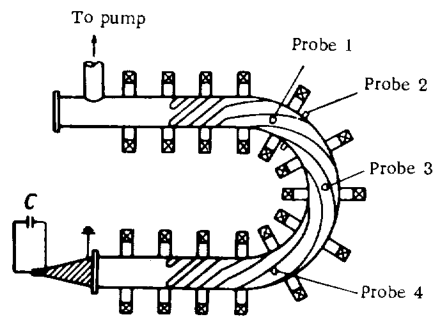

FIGURE 2. System layout.

The components E_z and E_r of the polarization field are perpendicular to each other and equal in magnitude. The resultant polarization vectors for the oppositely directed longitudinal magnetic fields are marked in Figure 1 by E_1 and E_2. The crossed magnetic and electric fields thus produce radial drift of the plasma to the chamber walls.

Several experimental works have been published /4, 5/ which show that plasma penetrates through a toroidal magnetic field for $n > 10^{12}$ cm^{-3} and $B \leq 80$ kA/m. These experiments are at variance with the theory /6/, which states that the penetration of plasma through a curved magnetic field is determined by its dielectric constant

$$K = 1 + \frac{mn}{\varepsilon_0 B^2}.$$

For $K \gg 1$, which corresponds to a dense plasma, the plasma moves in a straight line regardless of the magnetic-field curvature, whereas low-density plasmas follow the magnetic lines of force. The experimental studies /4, 5/ did not confirm this theoretical prediction, since the plasma was found to penetrate through curved magnetic fields even for $K \simeq 10^4$.

In /7/ it has been established experimentally that if the length of the plasmoid is less than the length of the curved magnetic-field region, the plasma experiences a strong radial drift due to the polarization electric field.

K. D. Sinel'nikov has suggested that we should also consider the electron currents flowing along the lines of force in a long plasmoid, which moves

partly in the curved magnetic field and partly in the uniform field. These currents short the polarization fields induced in the curved field region. The plasma passes through the curved section if the plasmoid is longer than the toroidal magnetic-field region. In this paper, we tried to determine experimentally the polarization electric field in a plasmoid moving in a stellarator-type combined toroidal and helical magnetic field.

Apparatus

Figure 2 gives the general layout of the system. A three-turn helical winding was fitted onto the vacuum chamber (copper tube of 8 cm diameter), bent into a semitorus with a 42 cm mean radius of curvature. The semitorus was joined to two straight sections, each 60 cm long. The longitudinal magnetic field was provided by 15 multiturn coils. The helical windings and the longitudinal field coils were supplied by separate d. c. generators.

The system parameters were as follows:

Vacuum chamber length l	254 cm
Internal diameter of the chamber $\varnothing$	8 cm
Maximum longitudinal magnetic field B	200 kA/m
Maximum current through helical winding I_{st} . .	3000 A
Pitch of helical winding L	134 cm
Effective radius of helical winding a	5.4 cm
Pitch angle of helical winding α	0.139 rad

The plasma was injected through the straight leg by a plexiglas conical source /8/. Capacitance of condenser bank 1 μF, voltage 8–12 kV. Discharge period 6.5 μsec. Density of plasma injected by the conical source, no less than 10^{13} cm^{-3}.

Results of measurements

The polarization field vector was measured with flat probes provided along the curved section, as shown in Figure 2. The flat probes measured the E_z and E_r components of the polarization electric fields between two points in a plane perpendicular to the lines of force of the longitudinal magnetic field. Figure 2 shows the setting of the probes 1,3,4 which measured the E_z component; probe 2 measured the E_r component. Separation of probe plates 4 cm. The probes were coupled into the plates of the OK-17M oscilloscope (insulated from the body) and were maintained at a floating potential. Figure 3 gives some oscillograms of the V_z signals for oppositely directed longitudinal magnetic fields and the gun discharge current (top trace).

The potential difference V_z between two points in the plasma was measured by probe 1. We see from the oscillograms that the V_z component reverses its sign when the longitudinal magnetic field is reversed.

Figure 4 gives oscillograms of the V_r component for oppositely directed longitudinal magnetic fields (field strength 150 kA/m). These oscillograms

show that the V_r component does not change its direction when the magnetic field is reversed; this point is strictly consistent with the theory /3/. The measurements were made with probe 2.

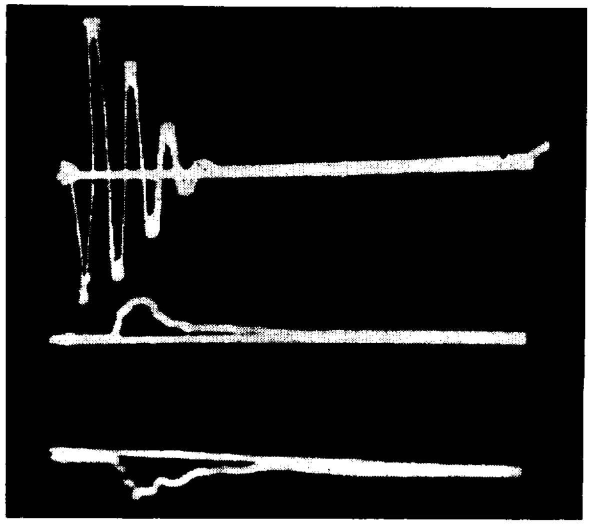

FIGURE 3. Oscillograms of the V_z polarization signals and the discharge current for oppositely directed magnetic fields.

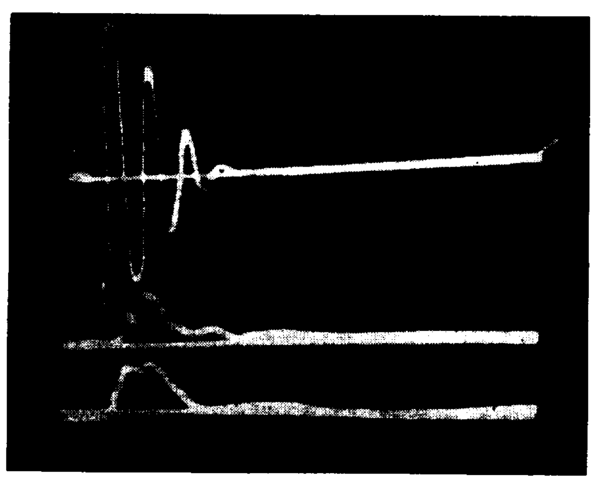

FIGURE 4. Oscillograms of the V_r polarization signals and the discharge current for oppositely directed magnetic fields.

Figure 5 plots the E_z component as a function of the magnitude and the direction of the longitudinal magnetic field; Figure 6 gives the same dependence for E_r. The magnitudes of E_z and E_r are the mean values obtained by dividing the potential difference by plate separation (4 cm in our case). The direction of the vectors $\mathbf{E}_1$ and $\mathbf{E}_2$ was determined experimentally as follows. Flat probes were provided at the outlet from the curved section; the probes could revolve in φ around the axis of the vacuum chamber. Plate separation, as before, 4 cm. Longitudinal magnetic field 160 kA/m. Figure 7 depicts two such curves obtained for oppositely directed longitudinal magnetic fields. We see from the figure that the maxima of curves 1 and 2 display a relative phase shift of some $\pi/2$ rad. According to the theory /3/, the angle between the vectors $\mathbf{E}_1$ and $\mathbf{E}_2$ is $\pi/2$ rad (see Figure 1).

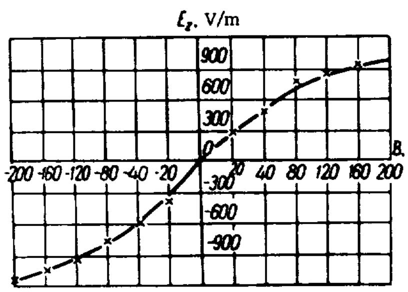

FIGURE 5. E_z vs. magnitude and direction of the magnetic field vector.

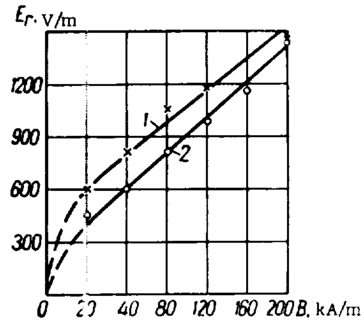

FIGURE 6. E_r vs. magnitude and direction of the magnetic field vector.

We also investigated the influence of the helical magnetic field on the polarization of plasmoids. In these measurements, the separatrix remained fixed, as indicated in Figure 1, since I_{st} reversed simultaneously with the reversal of the magnetic field.

The E_z component was measured with probe 1. Plate separation was reduced to 3 cm, to bring the probes inside the separatrix. Figure 8 plots E_z as a function of the current in the helical winding for $B = 160$ kA/m.

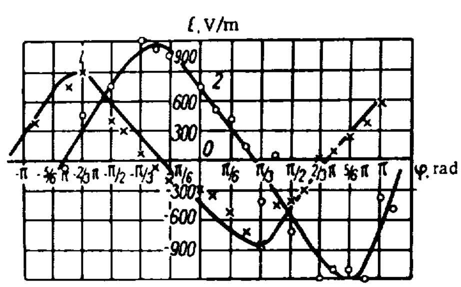

FIGURE 7. E vs. φ.

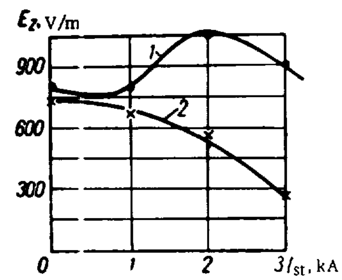

FIGURE 8. E_z vs. current in the helical winding.

We see from the figure that as the current in the helical winding increases (with B= const), the E_z component decreases (curve 2); if the longitudinal magnetic field and the helix current are reversed, E_z increases (curve 1). This variation of E_z with current for the given disposition of the probes can be interpreted by examining Figure 1, which shows the separatrix and the direction of the vectors $\mathbf{E}_1$ and $\mathbf{E}_2$.

If the polarization electric field is represented by the vector $\mathbf{E}_1$ for a certain direction of the magnetic field (see Figure 1), then superposition of the helical field will rotate the lines of force (clockwise in our case), and the charged particles moving along these lines will start rotating. The polarization vector $\mathbf{E}_1$ will also rotate, receding from the probe plates. The higher the current through the helical winding, the larger the angle of rotation of the lines of force and of the vector $\mathbf{E}_1$. The potential difference between the probes therefore decreases (curve 2, Figure 8).

In a reversed magnetic field, the E_z component points in the opposite direction, and the electric field vector goes over to $\mathbf{E}_2$. When the helical field is turned on, the lines of force and the vector $\mathbf{E}_2$ rotate in the same sense as in the previous case, i.e., clockwise. The vector $\mathbf{E}_2$ therefore approaches the probe; if the current through the helical winding increases further, the vector may pass clear through the probe and start receding from it. The potential difference between the probe plates first rises, and then diminishes (curve 1, Figure 8).

The following measurements were made to test these considerations.

Flat probes which could revolve in φ were provided at the outlet from the curved section. By revolving the probes, we established the positions of maximum or minimum potential difference.

The results of measurements made with revolving probes are depicted in Figure 9, which gives the polarization field vector as a function of φ for B= 160 kA/m, I_{st} = 0 and for B= 160 kA/m, I_{st}= 3000 A. We see from the graphs that the curve for I_{st} = 3000 A is displaced by $\pi/3$ rad relative to the initial curve; this is consistent with the theoretical results. The magnitude of the polarization field vector for B= 160 kA/m, I_{st} = 3000 A is almost the same as for B= 160 kA/m, I_{st} = 0. This supports our suggestion that the polarization vectors $\mathbf{E}_1$ and $\mathbf{E}_2$ do not diminish in the helical magnetic field; they only rotate. Measurements of the V_z component across the vacuum chamber were made with two probes. One of the probes was set near the wall, the other traveled across the chamber.

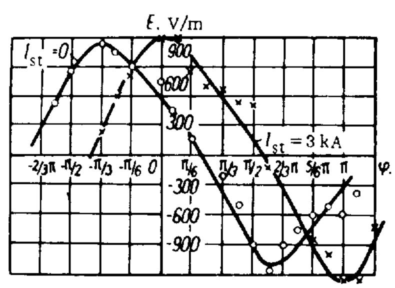

FIGURE 9. E vs. φ for B= 160 kA/m, I_{st} = 0, and B= 160 kA/m, I_{st}= 3000 A.

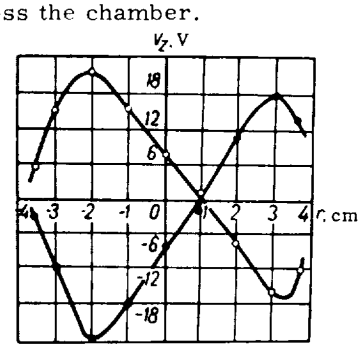

FIGURE 10. Variation of V_z across the vacuum chamber for B= 160 kA/m, I_{st} = 0.

Figure 10 plots the variation of $\mathcal{E}_r$ across the vacuum chamber. The longitudinal magnetic field was 160 kA/m.

The distribution of the polarization electric fields E_z and E_r across the vacuum chamber was measured with two probes separated by 1 cm. Both probes traveled across the chamber maintaining a constant separation. The longitudinal magnetic field was 160 kA/m.

Figure 11 plots the variation of E_z across the vacuum chamber for oppositely directed longitudinal magnetic fields. The zero points of the curves in Figure 11 are $r = -2.5$ cm and $r = 2-3$ cm. For larger radii, the sign of E_z is reversed. This indicates that the plasma jet moves mainly between $r = \pm 3$ cm, i.e., it is separated from the walls.

Figure 12 plots the same dependence for E_r. The intersection points of the curves with the r axis apparently specify the bounds of polarized plasma. On the outside, this component vanishes for $r = 3-3.5$ cm, and on the inside, for $r = 1.6-2.5$ cm, i.e., the plasmoid is slightly displaced toward the outside wall of the semitorus. Injection along the magnetic lines of force ensures a much higher E_r than injection against the lines of force (the curves show considerable vertical separation). The reason for this phenomenon is not clear.

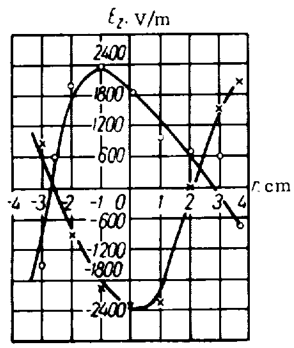

FIGURE 11. Variation of E_z across the vacuum chamber for oppositely directed magnetic fields.

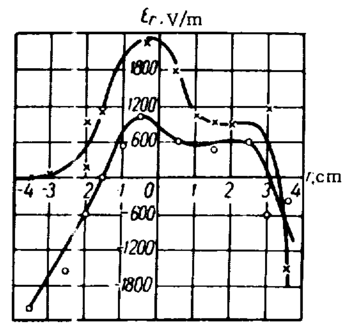

FIGURE 12. Variation of E_r across the vacuum chamber for oppositely directed magnetic fields.

Figure 13 shows the cutoff of a 3-cm wave and the V_z probe signal. The measurements were made at the outlet from the toroidal section. We see from the oscillograms that the front of the V_z signal leads the 3-cm cutoff front by 25 μsec. Length of the V_z signal, some 30 μsec. Front velocities of the 3-cm cutoff and of the V_z signal are $3 \cdot 10^4$ m/sec and $2.7 \cdot 10^5$ m/sec, respectively. From the oscillograms in Figure 13 we may conclude that the plasma in the low-density head (density less than 10^{12} cm^{-3}) is polarized, but there is hardly any polarization of plasma in the slow component (with a density $n \simeq 10^{12}$ cm^{-3}).

Figure 14 shows oscillograms of photomultiplier and V_z probe signals. We see that the front of the V_z signal leads the front of the photomultiplier signal, as in the case of the 3-cm cutoff.

In accordance with /3/, the polarization of a plasmoid moving in a curved magnetic field is a function of its translational velocity. In our case, the polarization is confined mainly to the fast component.

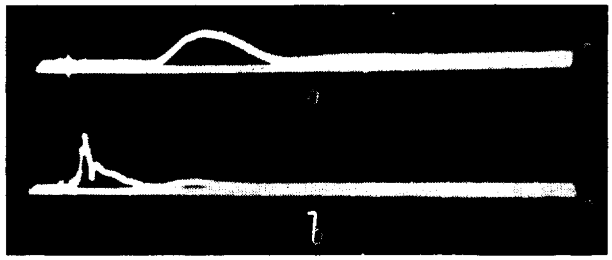

FIGURE 13. Oscillograms of 3-cm cutoff (a) and of the V_z probe signal (b).

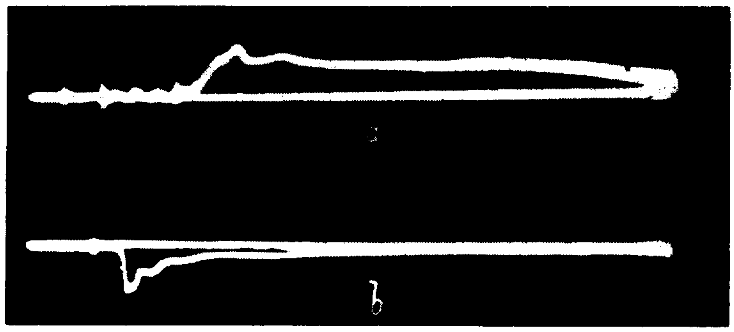

FIGURE 14. Oscillograms of photomultiplier signal (a) and V_z probe signal (b).

If we ignore the shorting of the polarization fields in the straight magnetic-field regions, we conclude that the polarization should apparently be greater than the measured figures both in the fast and the slow components, and that the plasma should not pass through the toroidal section.

If the plasma is highly conductive, on the other hand, the polarization fields are relieved by currents flowing along the magnetic lines of force. In our case, apparently, the fast plasmoid component is partly detached from the slow component, and the poor conductivity between the head and the tail is responsible for the retention of some residual polarization in the head.

BIBLIOGRAPHY

1. BOSTICK, W. H. – Phys. Rev., 101(2): 292. 1956.
2. EUBANK, H. P. – Bull. Am. Phys. Soc., 6: 196. 1961.
3. KHIZHNYAK, N. Y. – This volume, p. 281.
4. SAFRONOV, B. G., V. S. VOITSENYA, and I. M. KONOVALOV. – ZhTF, 6. 1962.

5. VOITSENYA, V. S., B. P. IL'ENKO, E. M. LATS'KO, I. N. ONISHCHENKO, B. G. SAFRONOV, and V. T. TOLOK. – This volume, p. 286.

6. SCHMIDT, C. – Phys. of Fluids, 3: 961. 1960.

7. SINEL'NIKOV, K. D., B. G. SAFRONOV, V. G. PADALKA, and I. I. DEMIDENKO. – In: "Fizika plazmy i problemy upravlyaemogo termoyadernogo sinteza", Vol. 3, p. 232. Kiev, Izdatel'stvo AN UkrSSR. 1963.

8. AZOVSKII, Yu. S., I. T. GUZHOVSKII, B. G. SAFRONOV, and B. A CHURAEV. – ZhTF, 9: 1051. 1962.

O. M. Shvets, S. S. Ovchinnikov, and V. F. Tarasenko

ROTATION OF PLASMA WITH SUPERCRITICAL VELOCITY

A considerable amount of rotational kinetic energy is deposited in a high-density plasma rotating in crossed fields (radial electric field and axial magnetic field). In the experiments /1/ the drift velocity of the hydrogen plasma never exceeded the critical value ($v_{cr} \approx 6 \cdot 10^4$ m/sec), although stable rotation persisted for comparatively long times (about 1 millisecond).

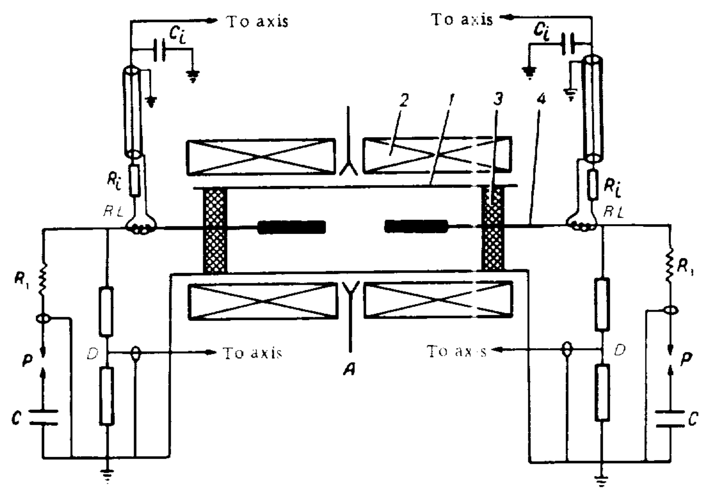

FIGURE 1.

Investigations of the magnetic containment of plasma and generation of high-temperature plasma by thermalization of the rotational kinetic energy require drift velocities. Preliminary experiments showed that high drift velocities could not be attained simply by increasing the radial field strength. The velocity did not rise above the critical value. Various hypotheses were advanced by both experimental and theoretical physicists to explain this curious phenomenon /2, 3/.

We made an attempt to attain supercritical rotation velocities of plasma in an improved machine /1/. Modified design of the center electrodes provided perfect separation of the plasma from the insulators (Figure 1), which sharply lowered the impurity content of the plasma and ensured full ionization of the plasma in the working volume.

The symmetry was improved by applying the radial electric field at the two ends of the chamber. Reduced gas pressures were employed to lower the volume of rotating plasma. This also ensured a high degree of ionization.

We do not intend to go into a theoretical description of the various processes obtaining in plasma machines of this kind: the reader is referred to special works /4, 5/.

Apparatus

Figure 1 is the functional diagram of the setup ($R_i C_i$ the integrating circuit, P spark gap, R_{li} limiting resistance, A microwave antenna). The vacuum chamber 1 is a copper cylinder 13 cm in diameter and 200 cm long. The chamber was initially evacuated to $1.33 \cdot 10^{-4}$ N/m^2; hydrogen was then forced in to pressures of $13.3 - 1.33$ N/m^2 and the chamber was conditioned by pulsed or continuous discharges produced by a high-frequency generator. The working vacuum depended on the temperature conditions of the palladium leak.

The magnetic field was provided by 24 coils around the vacuum chamber; the field geometry included two small magnetic mirrors separated by 120 cm. The field coils 2 were supplied by a 50 kW three-phase rectifier, which permitted smooth regulation of magnetic field strength at the axis from 0 to $2 \cdot 10^5$ A/m.

Two center electrodes 4 where set coaxially on insulators 3. These electrodes were coupled into separate condenser banks C of 150 μF capacity each.

The condenser bank current was measured with a Rogowsky loop RL, and the voltage with a resistive voltage divider D. Integrated plasma glow was picked up with a photomultiplier; the density of the plasma was inferred from the cutoff of a 3-cm signal modulated with 40 c/s frequency (modulation corresponds to the transmission of the signal through plasma).

Results of measurements

The following characteristic results were obtained for hydrogen pressure of 0.66 N/m^2, magnetic field strength of $(1.6 - 2) \cdot 10^5$ A/m, and radial voltage of $2000 - 2200$ V. It was found that the voltage between the coaxial electrodes did not drop substantially during the main ionizing discharge, remaining virtually constant for about 300 μsec (Figures 2, a, b).

Under these conditions, the plasma acts as a hydromagnetic condenser, and the entire voltage fall cannot be confined to a thin layer. The voltage may reach $1600 - 1900$ V, which is several times higher than the voltage corresponding to the critical rotation velocity of the plasma in our case ($U_{cr} = 550$ V).

It therefore seems that we have actually attained supercritical velocities in our machine: similar results are considered as a proof of supercritical rotation velocities in /6/. Comparison of our data with previous experiments /1, 2/ shows that the drift velocity exceeds the critical value.

We see from the oscillogram in Figure 2, b that the discharge current in the vacuum chamber falls off after the main ionizing pulse, and then increases, which is accompanied by a sharp drop of voltage across the coaxial. The 3-cm cutoff indicates that the density of the plasma between successive current pulses falls off appreciably (in some cases, the 3-cm signal is actually transmitted, as in Figure 2, c). Figure 2, d is an oscillogram of plasma glow obtained with a photomultiplier.

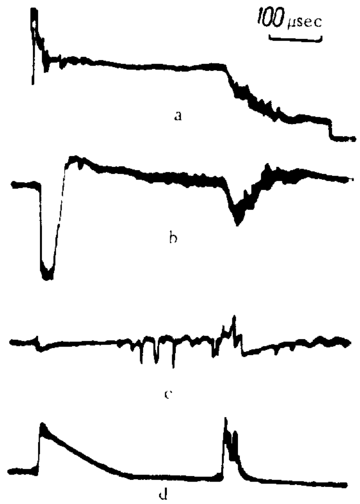

FIGURE 2.

Additional magnetic pressure should be created if all the plasma is to be retained in the machine. A check of the magnetic containment conditions for our experiment, made in accordance with /4/ for magnetic field strength of $1.6 \cdot 10^5$ A/m, hydrogen pressure of $0.66\,N/m^2$, and coaxial voltage of 1900 V, showed that the number density of the plasma was $n = 1.7 \cdot 10^{14}\,cm^{-3}$, whereas the maximum particle density that in principle can be contained by the magnetic field employed is $n_{cr} = 6 \cdot 10^{13}\,cm^{-3}$. The plasma density in our experiment is thus somewhat higher than the critical figure, which may result in a loss of particles. (Unfortunately, we could not achieve stable operating conditions with a subcritical number density.)

Additional plasma losses are incurred due to runaway phenomena in particles drifting near the wall, since their Larmor radii are fairly large.

The second current pulse in the oscillogram of Figure 2 is attributed to the ejection of the greater part of the ionized gas from the working chamber volume, where the density correspondingly decreases. Gas leak into the interelectrode space raises the density so as to permit second sparking, the energy stored by the condenser bank being sufficient.

To sum up, we could not attain supercritical velocities without incurring substantial losses of primary plasma. A modification of experimental procedure is apparently required to achieve this two-fold result.

BIBLIOGRAPHY

1. SHVETS, O. M., S. S. OVCHINNIKOV, V. F. TARASENKO, and V. T. TOLOK. —In: "Fizika plazmy i problemy upravlyaemogo termoyadernogo sinteza", Vol. 3, p. 184. Kiev, Izdatel'stvo AN UkrSSR. 1963.

2. LIN SHAO-CHI. —Phys. Fluids, 4(10): 123. 1961.

3. BAKER, D. A., J. E. HAMMEL and F. L. RIBE. —Phys. Fluids, 4(12): 1534. 1961.

4. BOYER, K., J. E. HAMMEL, C. L. LONGMIRE, D. NAGLE, F. L. RIBE, and W. B. RIESENFELD. —Proceedings of the Second United Nations International Conference on Peaceful Uses of Atomic Energy, 31: 319. 1958.

5. ALFVEN, H. —Rev. Mod. Phys., 12(4): 710. 1960.

6. HALBACH, K., W. R. BAKER, and R. W. LAYMAN. —Phys. Fluids, 5(11): 1482. 1962.

B. S. Akshanov, A. I. Strel'tsov, and Yu. N. Gurov

A STUDY OF MAGNETIC SURFACES IN A SYSTEM WITH TRIANGULAR WINDINGS

Stellarator-type machines are theoretically the most perfect magnetic trap available at present. The magnetic surfaces, set up by the longitudinal field coils (B_z) and by helical windings, together with compensation coils /1/ offsetting the effect of field nonuniformity in the curved sections, are clearly expected to retain the charged particles for a fairly long time.

The first stellarator had a figure-of-eight configuration. It prevented toroidal drift and was thus superior to machines with toroidal field geometry. In other words, the electric field set up by charge separation in the plasma along the curved sections was cancelled by twisting the torus into a figure-of-eight solid (the field had opposite signs and was relieved by equalizing currents flowing along the chamber axis). A line of force going once around the system does not close on itself as in torus geometry: there is a certain terminal displacement of the line. The rotation of the force line depends on the twisting of the chamber. A deficiency of the figure-of-eight configuration is the onset of exchange instabilities. These instabilities are eliminated if the rotation angle of the line of force possesses a certain gradient along the chamber radius. The required gradient is established if the rotation is provided by helical windings fitted onto the curved sections of the racetrack. The helical windings ensure that the rate of change in the pitch of the magnetic lines of force increases with the distance from the axis.

Racetrack machines with helical windings are fairly perfect, but they also have some shortcomings: 1) the magnetic field in the chamber is not "pure"; 2) a considerable fraction of the magnetic field energy is wasted due to imperfect coupling of the distant field coils; 3) the fitting of the helical coils involves considerable practical difficulties.

British scientists proposed an interesting modification of the stellarator magnetic system /3/, the NOVA machine. A so-called "magnetic molding" technique was proposed for shaping the inner toroidal surface into any stellarator-type geometry in this pulsed-operation machine.

It would be interesting to try the method of magnetic molding in continuous-operation systems. In the present paper, we describe the results obtained for a magnetic machine which comprises a solenoidal coil wound onto a triangular-shaped base frame. The base was axially twisted to provide the desired pitch and then shaped into a torus.

Apparatus and procedure

Two windings were prepared for comparative tests: a triangular-shaped arrangement and a conventional three-turn helical coil. These windings had identical parameters: the maximum separatrix radius of the common stellarator winding corresponded to the maximum separatrix radius of the triangular winding. Figure 1 shows some photographs of the straight (a) and the curved (c) sections of the triangular winding, as well as the straight (b) and the curved (d) sections of the conventional helical winding. The straight sections had a length of 500 mm each, with windings completing one revolution over 1 m. The internal diameter of the stellarator winding was 180 mm. The radius of the circle circumscribing the triangular winding was 90 mm. The major radius of the curved windings $R = 400$ mm.

Model measurements included magnetic measurements of the magnetic field components and electron beam probing. The magnetic field components were determined by the inductive technique, which is widely accepted, fairly simple, and sufficiently accurate. The measurements were made in one section, with field probes which revolved in circles of 25.5 and 15 mm radius. The components B_z, B_φ, and B_r were measured.

Results of measurements

The measurements in triangular and stellarator-type windings gave close results. Figure 2 plots the variation of the field components B_z, B_φ, B_r in concentric circles normal to the winding axis. These components correspond to the straight sections of the conventional stellarator system (Figure 2, a) and of the triangular-shaped winding (Figure 2, b). Figure 3 plots the field components for the curved sections of the stellarator (a) and the triangular (b) windings. We see from Figures 2 and 3 that the trend of the field components is identical in the two windings. B_φ and B_r display an identical phase shift of $\pi/2$ rad in the two windings.

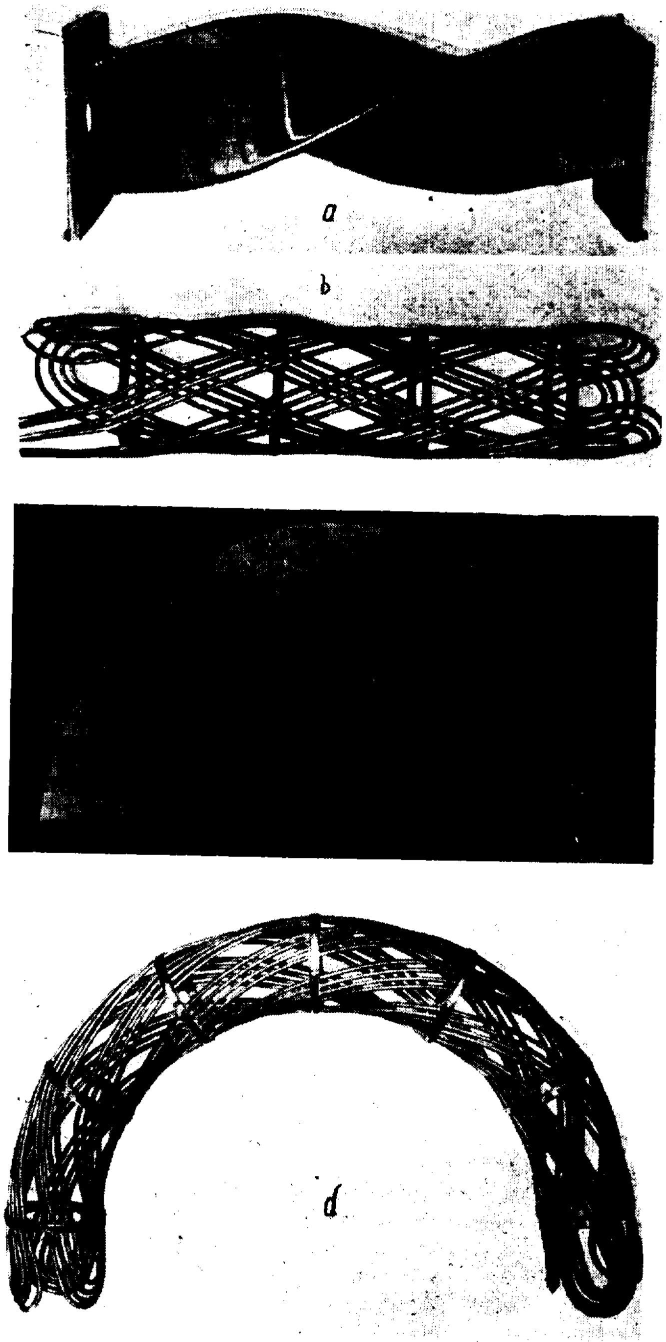

FIGURE 1.

If we accept that the field components B_φ and B_r vary as $\frac{1}{r^2}$ in the conventional stellarator geometry (falling off from the periphery to the axis), we obtain the same variation for the triangular-shaped model. The difference in the rates of change is insignificant: the rate of change in the triangular-shaped model is a mere 5% less than in the conventional stellarator. If the winding profile is further adjusted, this discrepancy will probably be eliminated.

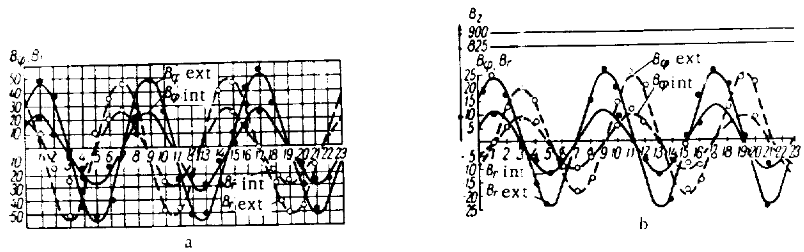

FIGURE 2.

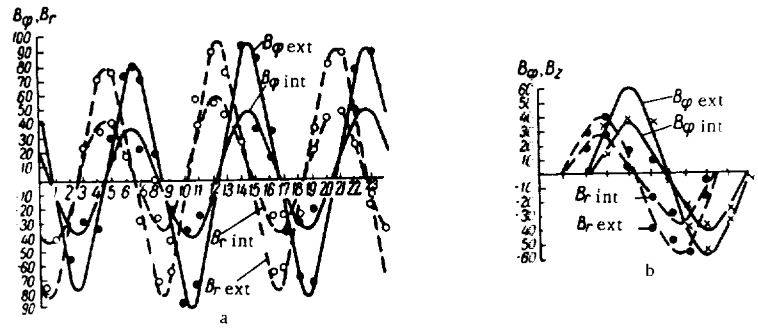

FIGURE 3.

Rotating electron beams were applied to trace the magnetic surfaces of the stellarator and the triangular windings. Since we could hardly expect to obtain an axially twisted triangular-shaped vacuum chamber, the triangular winding was placed directly in an ordinary vacuum chamber. This is obviously much better than fitting a cylindrical vacuum chamber inside the triangular-shaped winding. The latter course entails a reduction of the effective aperture, and considerable difficulties are to be expected in the tracing of the magnetic surfaces near the winding vertices. In this case the probing beams penetrate only through the central part of the triangular winding, which is insufficient. By placing the triangular winding inside the vacuum chamber, we avoided this difficulty, since the measurements could be made at any point near the winding surface. The triangular-shaped winding was fabricated in this case from water-cooled copper pipes wound onto a metallic base frame. The winding was insulated from the body with fiber glass. Fairly flimsy insulation was needed, since the winding was supplied by a high-current low-voltage source ($U = 6$ V).

The high vacuum properties of the components enabled us to carry out the experiments at pressures of some $1 \cdot 10^{-4}$ N/m^2. The results show that the triangular-shaped winding presents the same geometrical pattern of magnetic surfaces as the conventional stellarator winding. Figure 4 is a photograph of the magnetic surfaces of the triangular winding as displayed on a fluorescent screen.

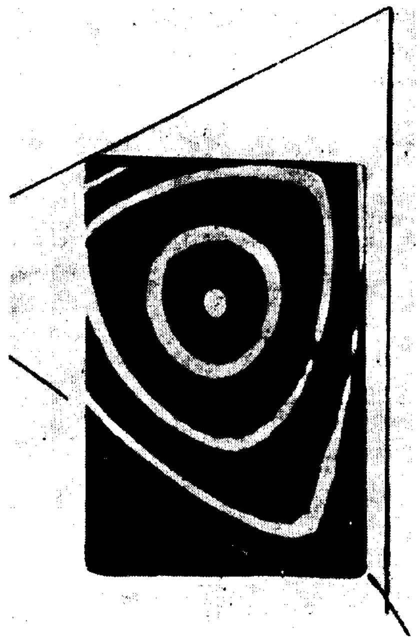

FIGURE 4.

Magnetic measurements and electron beam probing reveal that the triangular and the stellarator windings have closely similar characteristics in the straight and the curved sections.

If we examine a closed system with triangular-shaped windings, we detect a closed longitudinal current-carrying loop. The field set up by this current loop is highly dangerous. Appropriate coupling of the winding sections, however, will easily eliminate this closed current.

Conclusions

1. Magnetic fields in the component sections of the triangular winding are very similar to the magnetic fields in a conventional stellarator with a three-turn helical winding.
2. The high coupling between the triangular winding and the working volume permits effective utilization of the magnetic energy.

3. The magnetic field in the triangular winding is comparatively "pure": there are no flutes, the penetration of external fields is reduced, etc.

4. The triangular winding, particularly if fitted inside the vacuum chamber, is much simpler to assemble.

5. Since the application of these windings in experimental work is most promising, additional tests should be made with closed models.

BIBLIOGRAPHY

1. MEL'NIKOV, V. K. —DAN SSSR, 149(5): 1056-1059. 1963.

2. ALEKSIN, A. F. —In: "Doklady na 2-oi konferentsii FTI AN UkrSSR po fizike plazmy". 1961.

3. TAYLOR, J. B. and K. Y. ROBERTS. —Phys. Rev. Letters, 8(2): 52-53. 1962.

VACUUM TECHNIQUES. LOW-TEMPERATURE PROPERTIES OF METALS

E. S. Borovik, G. T. Nikolaev, and B. A. Sharevskii

PRODUCTION OF ULTRAHIGH VACUUM WITH A HEATED HYDROGEN CONDENSATION PUMP

Hydrogen condensation pumps have been applied more than ten years ago /1/ to create high vacuum in large unheated systems. The vacuum obtainable with these pumps, however, did not exceed $6.6 \cdot 10^{-7}\,N/m^2$, a limit set by outgassing. It has been later established /2/ that a vacuum of $1.6 \cdot 10^{-8}\,N/m^2$ (a figure very close to the saturated vapor pressure of nitrogen at 20.4 °K, which is $1.1 \cdot 10^{-8}\,N/m^2$ /3/) can be created by a hydrogen condensation pump inside a volume screened from the walls of the unheated vacuum system by a hydrogen baffle (eliminating outgassing).

The efficiency of hydrogen condensation pumps being high, it seems reasonable that a vacuum of $\sim 10^{-8}\,N/m^2$ can be expected for sufficiently short times in large volumes in heated systems.

We designed an experimental heated vacuum system with a hydrogen condensation pump and proceeded to investigate its vacuum characteristics.

Apparatus

The schematic diagram of the setup is shown in Figure 1.

The hydrogen condensation pump is provided inside the triplet 2, which is coupled into the evacuated volume 1 on one side and into an oil diffusion pump MM-40 on the other; the oil pump communicates with the triplet through a length of tubing 11 and a valve 7, and it is intended for preliminary pumping: system conditioning and evacuation of noncondensing gases.

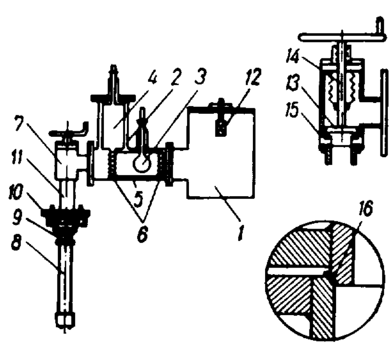

FIGURE 1.

A water-cooled trap 9 and a liquid-nitrogen-cooled trap 10 are provided to prevent leakage of oil vapor and its decomposition products from the diffusion pump to the vacuum system. We used an improved version of the MM-40 pump, the one with an abbreviated water jacket. This modification had been shown /4/ to reduce substantially the total quantity of decomposition products forming in the pump in unit time.

The hydrogen condensation pump 3 is a $220\,cm^2$ spherical surface cooled by liquid hydrogen. To minimize hydrogen consumption, the sphere was enclosed in a cold cylindrical baffle 5 cooled by liquid nitrogen from container 4. Chevrons 6 were provided in places in the baffle, to permit pumping.

The metallic valve 7, whose cutaway is shown in the upper right-hand corner of Figure 1, comprised a steel disk which could be moved up and down by a coupling rod 14. A sharp annular projection along the lower rim of the disk cuts into the silver ring seat 15 when the valve is closed, to form a vacuum-tight seal. The valve aperture is 60 mm in diameter.

The evacuated volume 1 and the triplet 2 were manufactured from stainless steel, to ensure clean interior surfaces and to minimize outgassing.

The fixed components of the system were argon-arc welded or brazed. Flange tightening was achieved by interleaving 0.5 mm annealed sheet copper 16. The leaves were held between two conical surfaces provided on both ends of the matched pipes (conical tapering, 10°), as is shown in the lower right-hand corner in Figure 2. This is a perfect vacuum seal which permits repeated and lengthy heating at 400 C without developing any leaks. The overall leakage in the system (after heating and degassing the interior surfaces) did not exceed $2.8 \cdot 10^{-10}\,N/m^2$, which could not possibly interfere with proper functioning of the setup up to a vacuum of $\sim 10^{-10}\,N/m^2$.

The ionization pressure gage comprised a molybdenum rod soldered in molybdenum glass. These glass leads were fixed to the stainless-steel flanges by special Kovar cartridges. The flange holding the ionization pressure gage was fitted into the upper wall of the evacuated volume and vacuum tightened with sheet copper as all the other flange joints.

The pressure in the system was measured at two points: near the diffusion pump, above the nitrogen trap 10, and inside the evacuated volume 1, using the ionization pressure gage 12.

The system was heated electrically by nichrome coils which were wound externally on special cores surrounding the evacuated volume and the triplet.

We have described here the first experimental metallic setup with a heated hydrogen condensation pump which is far from being perfect. Because of various technological difficulties, the vacuum pump was too large and could not be dismantled rapidly if the need arose.

Production of ultrahigh vacuum and the characteristics of the hydrogen condensation pump

Ultrahigh vacuum was created as follows: the system, initially at atmospheric pressure, was first subjected to forevacuum pumping. Valve 7 was then closed and the diffusion pump was started. The trap 10 was filled with liquid nitrogen; when the pressure above the trap dropped to $10^{-5}\,N/m^2$, valve 7 was opened and the entire system was pumped down to $\sim 10^{-5}\,N/m^2$.

The heating was then turned on. The temperature of the evacuated volume and the triplet, together with the condensation pump, was raised to 400 °C. The working temperature was commonly reached in 1.5 — 2 hrs (starting at room temperature).

The gas released by the interior walls upon heating was continuously pumped out by the diffusion pump with the nitrogen-cooled trap 10. By the end of the conditioning stage, the initial pressure ($\sim 10^{-5}\,N/m^2$) was restored in the system.

The elevated temperature (400 °C) was maintained for some time, this period varying from experiment to experiment. The heating was then turned off, and the system allowed to cool. Liquid nitrogen was poured into container 4 and the ionization gage 12 was switched on to measure the pressure in the evacuated volume.

Liquid-nitrogen conditioning took a few hours (2 — 4 hrs), in which time the pressure in the evacuated volume was reduced approximately by one order of magnitude.

The valve 7 was then closed and the hydrogen pump was filled with liquid hydrogen. The leak being small (less than $2.8 \cdot 10^{-10}\,N/m^2$), the diffusion pump was not turned on when the hydrogen condensation pump was running. The principal noncondensing gas in the air is hydrogen, and its content is 0.01%; a simple calculation shows in our case that more than 10 hours are required to raise the pressure in the evacuated volume by $1 \cdot 10^{-8}\,N/m^2$ in our case.

During the first minutes after the admission of liquid hydrogen, the pressure fell off very rapidly, and then leveled off until it reached the limit value. The maximum vacuum was maintained in the system to complete evaporation of the liquid hydrogen.

The pressure in the evacuated volume was generally measured by a Bayard-Alpert ionization gage 12. Since small ionic currents were involved, the collector had to be carefully protected against all possible current leaks. We noticed that if the ionization pressure gage 12 was turned on during the heating period, increased sputtering of the filament obtained and a conducting film formed between the leads, naturally raising the ionic current leak. The ionization gage 12 was therefore turned on only after a sufficiently high vacuum had been created (generally no less than $3 - 4 \cdot 10^{-5}\,N/m^2$ with the heating turned off). Alternative pressure measurements were carried out with a magnetron-type ionization gage with a cold cathode, manufactured and investigated in our laboratory /5/. The results obtained by the Bayard-Alpert and the cold-cathode ionization gages were identical.

During the heating stage, the pressure was controlled with an ordinary ionization gage (LM-2) provided above the diffusion pump MM-40 (above the trap 10).

In our investigations of the heated hydrogen condensation pump, we measured the pressure as a function of heating time and also the pump speed.

Figure 2 plots the time variation of pressure ($p = f(t)$) in an unheated system. For $t = 0$, the system is at atmospheric pressure. Arrow 1 marks the admission of liquid nitrogen, arrow 2 the admission of liquid hydrogen. The ultimate vacuum is attained 8 hours after the startup, and is approximately $4 \cdot 10^{-7}\,N/m^2$.

The curves $p = f(t)$ obtained after heating are shown in Figure 3. The heating time ($T = 400$ °C) was 3 hrs for curve I and 15 hrs for curve II.

In either case, pumping was started after the system had been maintained at atmospheric pressure for 15 hrs. The time from pump start to working temperature (400 °C) was 4 hrs.

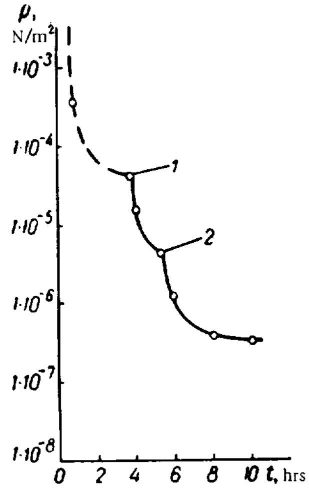

FIGURE 2.

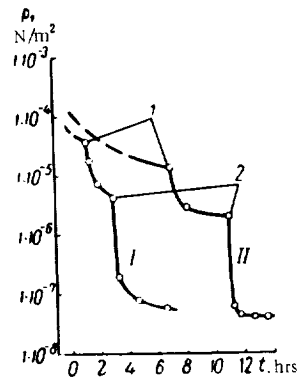

FIGURE 3.

In experiments with prolonged heating (curve II) the setup was allowed to cool for 7 hrs (to 40 °C), when liquid nitrogen was poured in (admission time marked by 1 in Figure 3); liquid hydrogen was admitted after another 4 hrs (2). Once liquid hydrogen had been poured in, the pressure dropped in a few minutes to $6.6 \cdot 10^{-8}\,N/m^2$, and then gradually (in 1.5 hrs) decreased to its limit of $4 \cdot 10^{-8}\,N/m^2$.

In the brief-heating experiment (curve I), the cooling time and also the time between the admission of nitrogen and hydrogen were correspondingly shorter. Here again the pressure dropped steeply in the first minutes after the admission of liquid hydrogen, reaching the minimum of $5 \cdot 10^{-8}\,N/m^2$ in 4 hrs.

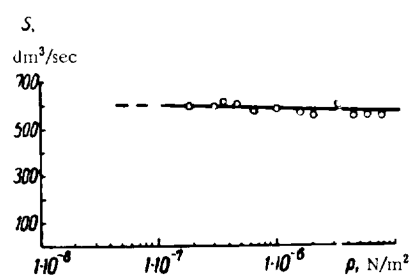

FIGURE 4.

Comparison of the curves in Figures 3 and 4 shows that the heated system is characterized by a very rapid drop of pressure in the first minutes after

the admission of hydrogen. In the unheated system, the initial time rate of change of pressure is approximately 1/5 of that in heated systems.

It also follows from these curves that the time required to attain pressures of $\sim 10^{-8}\,N/m^2$ in large metallic systems with heated hydrogen condensation pumps is much less than the time for diffusion pumps with heating /6/. If the vacuum of $6-8\cdot 10^{-8}\,N/m^2$ is regarded as the limit, the heating time (at 400 °C) can be as low as 1.5 – 2 hrs.

The speed of the hydrogen condensation pump was determined by the conventional technique /7/. The gas was admitted into the evacuated volume from an auxiliary vacuum chamber through a pipe of known carrying capacity. The pump speed was calculated from the partial pressure of the gas admitted into the evacuated volume. The pump speeds were measured in the range of pressures $2\cdot 10^{-7}-1\cdot 10^{-5}\,N/m^2$ and were found to be $600\,dm^3/sec$ (see Figure 4).

The consumption of liquid hydrogen is small, $1.2\,dm^3$ per day. Liquid hydrogen is therefore reordered from external suppliers when necessary, and the evaporated hydrogen can be released into the atmosphere.

Conclusions

1. The heated hydrogen condensation pump (a sphere 85 mm in diameter) creates an ultimate vacuum of $4-5\cdot 10^{-8}\,N/m^2$ in clean chambers several dm^3 in diameter.
2. The pump speed is $600\,dm^3/sec$. The pumping time to a vacuum of $5\cdot 10^{-8}\,N/m^2$ in a $60\,dm^3$ chamber can be reduced to 13 – 14 hrs.
3. The small consumption of liquid hydrogen ($1.2\,dm^3$ daily) renders this pump particularly suitable for laboratories without liquid hydrogen production facilities.

BIBLIOGRAPHY

1. LAZAREV, B.G., E.S. BOROVIK, M.F. FEDOROVA, and N.M. TSIN. — UFZh, 2(2): 175. 1957.
2. BOROVIK, E.S., S.F. GRISHIN, and B.G. LAZAREV. — PTE, 1: 115. 1960.
3. BOROVIK, E.S., S.F. GRISHIN, and E.Ya. GRISHINA. — ZhTF, 30: 540. 1960.
4. NIKOLAEV, G.T. and B.A. SHAREVSKII. — UFZh, 6(5): 697. 1961.
5. SHAREVSKII, B.A. and G.T. NIKOLAEV. — UFZh, 9(1): 66. 1964.
6. HUBER, W.K. and E.A. TRENDELENBURG. — Annual Meeting of Am. Vacuum Soc., Philadelphia. 1959.
7. DUSHMAN, S. Scientific Foundations of Vacuum Technique. — New York, Wiley. 1949. [Russian translation. 1950.]

E. S. Borovik, N. P. Katrich, and G. T. Nikolaev

TRAPPING OF H_1^+ IONS IN STAINLESS-STEEL SURFACES

The trapping of gas ions by various materials has recently attracted the attention of many physicists working with hot plasma. This is quite understandable since in magnetic devices with fast particle injection the ultrahigh vacuum is acutely sensitive to the trapping efficiency. The trapping efficiencies have been so far measured by few researchers only: for He^+ ions with energies of from 150 to 2600 eV /1/ and for He^+ and D^+ ions with energies of from 7 to 25 keV /2/. Some quantitative characteristics of trapping have been deduced by studying the desorption of particles imbedded by preliminary ion bombardment /3, 4, 5/ and also in connection with the development of techniques for the preparation of solid gas targets and separation of isotopes /6, 7/.

None of these studies, however, has been carried out in a vacuum, which is essential if the target is to remain sufficiently clean. We therefore proceeded with first measurements of the trapping efficiency η of 35 keV hydrogen ions H_1^+ in a target of 1 Kh 18 N 9 T stainless steel. The measurements were made in a vacuum, which ensured satisfactory purity of the target surface.

Apparatus

A photograph of the experimental setup is reproduced in Figure 1. A schematic diagram of the principal elements along the path of the H_1^+ beam

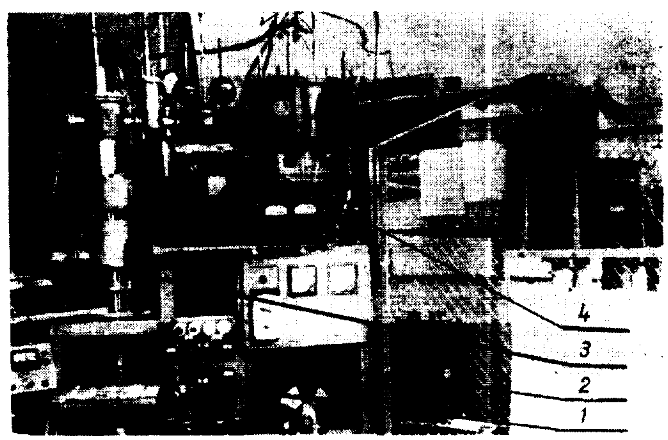

FIGURE 1.

is shown in Figure 2. A hydrogen ion beam was extracted from a high-frequency ion source 1 through an extracting electrode with an internal

diameter of 1 — 1.2 mm and a length of 5 — 6 mm; the beam was focused by the electrostatic lens 2, accelerated in the accelerator tube 3 to 35 keV, and delivered into the magnetic analyzer 11 through the first collimating system 8, 9. In the magnetic analyzer chamber the H_1^+ beam changed its direction by 60° and passed through the second collimating system 15, 17 into the measuring chamber 18, where it hit the target 21.

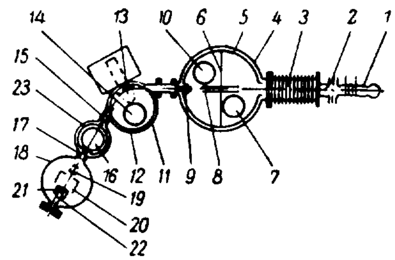

FIGURE 2.

The high-frequency ion source with the electrostatic lens provided a well focused beam of H_1^+ ions of up to 120 μA, which ensured a target current density of 160 $\mu A/cm^2$. Hydrogen requirements of the high-frequency ion sources were determined by the geometry of the extracting electrode and did not exceed 1.5 cm^3 per hour. This is a fairly low consumption in comparison with other types of ion sources, and yet it is much too high if a vacuum of the order of 10^{-7} N/m^2 is to be maintained in the system, since the corresponding pumping rates must exceed $3 \cdot 10^5$ dm^3/sec.

The pumping rate can be reduced to a few tens of thousands of cubic decimeters per second by applying a differential pumping technique. However, even these speeds are too high for diffusion pumps, not to mention the contamination of the manifold. We therefore employed multistage condensation pumping /8/ which ensured the required pumping rates, high stability of the vacuum, and sufficient purity of the target. The diagram of Figure 2 shows the arrangement of the helium condensation pumps (HCP) 10, 14, 16, each of which is a copper vessel of 0.5 dm^3 capacity with a calculated pumping speed of $1.2 \cdot 10^4$ dm^3/sec. The ultimate HCP vacuum (it is determined by the saturated vapor pressure of hydrogen) is fairly low if the pumps are cooled below the boiling point of liquid helium. The required cooling is easily attained by pumping out the vapors above the liquid helium. In our pumps, the vapors were pumped down approximately to 18 N/m^2, which corresponds to an ultimate vacuum of some $1 \cdot 10^{-10}$ N/m^2 /9/. The HCP running time was determined by the thermal loads and the quantity of helium in the pumps. The conventional liquid helium filling system using a float gave unsatisfactory results. Too little helium was admitted into the condensation pumps, and the pumping time was correspondingly short.

We therefore prepared specially designed floats which permitted liquid helium filling with continuous pumping of vapor above the liquid surface. The HCP running time was considerably increasing and reached 8 — 10 hrs.

Aside from the HCP, the system also contained two hydrogen condensation pumps 7, 20 of 0.5 dm^3 capacity each and two oil diffusion pumps M-500 and M-2500 (1 and 2 in Figure 1). The M-2500 pump was used in vacuum system conditioning and in preliminary evacuation of the hydrogen leaking from the high-frequency ion source into the chamber 4 during the experiment; the M-500 pump was intended for the conditioning of the measuring chamber 18. Both pumps are provided with water- and nitrogen-cooled baffles and, if necessary, they can be sealed off by a bakeable (3) and an unbakeable (4) vacuum valves shown in Figure 1. A chevron-type nitrogen baffle is provided at the bottom of chamber 4. A copper screen 5 is soldered to the baffle, and partition 6 divides the volume into two. The right-hand compartment is a chamber communicating with the diffusion pump through the chevrons. A hydrogen condensation pump 7 is provided in this compartment for pumping out the background gases. The left compartment is a sealed chamber which communicates with the right compartment and with the magnetic analyzer by means of collimating tubes 8, 9. The collimating tube 8 (14 mm diameter, $l = 250$ mm, inlet aperture diameter 12 mm) is brazed to the partition 6. The collimating tube 9 (11 mm diameter, $l = 150$ mm, inlet aperture diameter 9 mm) joins the left compartment with the magnetic analyzer. This collimation geometry ensures a sufficiently low exchange between the chambers and has but a negligible influence on the hydrogen ion beam. A helium condensation pump 10 with a speed of $1.2 \cdot 10^4$ dm^3/sec is provided inside the left-hand compartment. Two condensation pumps are thus provided inside a comparatively small volume, and they carry the main burden in the course of the experiment; penetration of impurity gases from the unbakeable part of the setup into the measuring chamber has been practically eliminated.

The magnetic analyzer chamber 11 is made of 1 Kh 18 N 9 T stainless steel and is vacuum sealed with Teflon. Only the magnetic pole tips 13 are inside the chamber; the rest of the magnet is held outside. The magnetic analyzer chamber is provided with a nitrogen-cooled baffle 12 accommodating the helium condensation pump 14. Hydrogen ions H_2^+, H_3^+ and fast neutral particles from the high-frequency ion source are partially trapped by the nitrogen baffle in the magnetic analyzer chamber, and the rest are pumped out by HCP. H_1^+ ions are transmitted through the collimating tube 15, the hole 23 in the nitrogen baffle, and the tube 17 into the measuring chamber, where they hit the target. The nitrogen baffle is a cylindrical chamber communicating with the measuring volume by tube 17 of known carrying capacity. The helium condensation pump 16 is provided in the upper part of the nitrogen baffle, above the path of the ion beam; this HCP evacuates the measuring chamber and protects it from leakage of hydrogen from the magnetic analyzer. The measuring chamber 5 and the adjoining components are fabricated from stainless steel; they are vacuum sealed by copper interleavings gripped between conical surfaces. The system can thus be baked out at 400 — 500 °C without developing any leaks. A bakeable mechanical valve (Figure 1) is provided under the measuring chamber, sealing it off from the diffusion pump M-500.

The target is supported on a copper block, which is in turn attached to a holder tube 22. The open end of the holder permits cooling the target during bombardment. The current of H_1^+ ions is measured with a moving Faraday cup 19. The vacuum in the measuring chamber is measured with

an open Bayard-Alpert ionization gage inserted into the chamber. The hydrogen condensation pump with the screen 20 enclosing the target shields it from background gases.

Conditioning

The measuring chamber and the valve sealing off the diffusion pump were baked out for 3—4 hrs at 400—450 °C before the actual experiment. During this stage, the oil diffusion pumps with nitrogen traps and the hydrogen condensation pump 7 were running. By the end of the bakeout period, the vacuum in the measuring chamber was $1.3 \cdot 10^{-5}\,N/m^2$.

When the heaters were turned off, liquid hydrogen was poured into the hydrogen condensation pump 20. The temperature of the chamber and the condensation pump was still close to 400 °C at that time. The total consumption of liquid hydrogen was close to $5\,dm^3$. The measuring chamber was simultaneously sealed off from the oil diffusion pump with the nitrogen baffle. This prevented leakage of oil decomposition products into the chamber and minimized the residual gas background. The vacuum in the measuring chamber immediately after liquid hydrogen filling was $4 - 5 \cdot 10^{-7}\,N/m^2$. The admission of liquid helium into HCP 16 improved the vacuum in the chamber to $1.3 \cdot 10^{-7}\,N/m^2$ almost instantaneously; further improvement was more gradual, so that at the end of an hour or an hour and a half the pressure in the measuring chamber was $6 \cdot 10^{-8}\,N/m^2$. The actual experiments, however, were generally begun immediately after liquid helium filling, in a vacuum of $1.3 \cdot 10^{-7}\,N/m^2$. Hydrogen was regarded as the main residual gas in the chamber. This assumption is justified, if we remember that the high-speed hydrogen condensation pump provided in the measuring chamber evacuates all the impurity gases, with the exception of those which do not condense readily at 20.4 °K. The conditioning procedure ensures satisfactory purity of the target surface and virtually eliminates any possibility of its contamination by adsorption after bakeout.

Results and discussion

The trapping efficiency is measured as follows. The H_1^+ beam is driven into the target. The flow of recovered hydrogen, attributable to the reflected component of the beam and the diffusive reemission of molecules from the target, affects the vacuum in the measuring chamber. A typical curve of vacuum vs. target bombardment time is shown in Figure 3 for an H_1^+ beam of 35 keV energy and 110 μA intensity. The change in pressure due to the ion beam reaching the magnetic analyzer is negligible. The pressure in the measuring chamber is altered only when the target is actually bombarded. Given the ion beam current, the vacuum in the measuring chamber, and the rate of pumpout of hydrogen from the measuring chamber, we can find the trapping efficiency from

$$\eta = 1 - \frac{n\,(p - p_0)\,W}{\frac{10^5 i^+}{c}},$$

where n is the number of particles in 1 dm^3 under standard conditions, p the working pressure in N/m^2, p_0 the initial pressure in N/m^2, W the pumping rate in dm^3/sec, i^+ the ion beam current in A, e the electron charge in C; 10^5 is the atmospheric pressure in N/m^2.

In the first experiments, the trapping efficiency of H_1^+ ions calculated for the pumping rate as determined by the carrying capacity of the tube 17 (8 dm^3/sec) was very high, initially reaching values close to unity (0.99). As the density of the trapped particles increased, the trapping efficiency dropped to 0.94 and then remained constant. This high trapping efficiency was obtained for the first time, and it was therefore suggested that the hydrogen was additionally pumped out by the clean wall surfaces and by the hydrogen condensation pump 20. To test this suggestion, we measured the pumping rates by admitting a constant flow of hydrogen through a capillary leak of known carrying capacity. The measurements showed that clean stainless-steel and copper surfaces did not possess a noticeable pumping in the range of temperatures from standard to 78 °K.

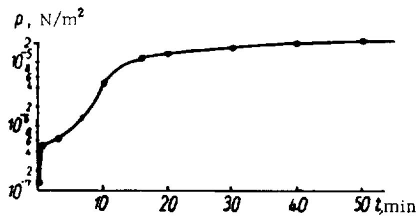

FIGURE 3.

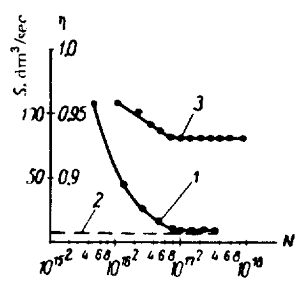

FIGURE 4.

The clean copper surface of the hydrogen condensation pump, however, was found to pump hydrogen at 20.4 °K. The pumping rate rapidly drops as the amount of pumped hydrogen increases, and it is virtually zero at concentrations equal to 0.01 monolayer. This effect has never been observed before, and it is quite unexpected at such low pressures. In Figure 4, curve 1 plots the experimental pumping rate as a function of hydrogen inflow. The dashed line marks the calculated rate of hydrogen pumping by the helium condensation pump 16, as determined by the carrying capacity of the tube 17 ($8 \pm 1.5\ dm^3/sec$).

The divergence between the experimental (10 dm^3/sec) and the theoretical ($8 \pm 1.5\ dm^3/sec$) pumping rates in the $N > 10^{17}$ range lies within the experimental margin of error. During bombardment, atomic hydrogen is present in the measuring chamber, and its adsorption may differ from that of molecular hydrogen. We therefore proceeded to determine the amount of hydrogen adsorbed in bombardment at 20.4 and 78 °K by defreezing the screen and measuring the pressure of the desorbed gas. It was established that atomic and molecular hydrogen were adsorbed only at temperatures below 30 °K and that all adsorption virtually ceased when the adsorbed hydrogen had reached concentrations of 0.01 monolayer. The total amount of desorbed hydrogen is consistent with the theory. The experiments furthermore showed that a certain amount of heavier gases was released from the target during bombardment (1 − 2% of the number of impinging ions).

The dependence of pumping rate on hydrogen inflow introduces some difficulties in the calculation of the trapping efficiency. Indeed, the pumping rate is required in calculation of the trapping efficiency, but the pumping rate depends on the amount of hydrogen admitted into the chamber, i.e., on the trapping efficiency. The coefficient η was therefore calculated by successive approximations, taking a speed of $10\,dm^3/sec$ as the zeroth approximation. The measurements of the trapping of H_1^+ ions by a clean stainless-steel surface for ion energies of 35 keV and beam currents of $110\,\mu A$ (current density $150\,\mu A/cm^2$) are plotted in Figure 5 as a function of the concentration of imbedded hydrogen. Curve 3 in Figure 4 plots the same results as a function of the amount of hydrogen in the chamber. Note that the greater part of the curve passes in a region of constant pumping rate. The trapping efficiency is therefore calculated without correcting for the speed of the hydrogen condensation pump. We see from the curve in Figure 5 that the trapping efficiency drops from 0.96 to 0.93 as the concentration of trapped atoms rises to $N \simeq 10^{18}\,cm^{-2}$. Further increase in the concentration of trapped atoms up to $N \simeq 2 \cdot 10^{19}\,cm^{-2}$ does not result in any reduction of the trapping efficiency; it apparently remains constant at much higher concentrations also.

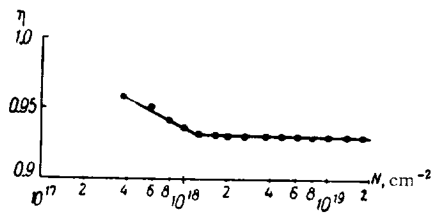

FIGURE 5.

The number of trapped hydrogen atoms was also determined by weighing. It was established that the concentration of trapped hydrogen reached $2 \cdot 10^{19}$ atoms/cm^2. Determinations of the trapping and reemission efficiencies by this technique are of independent interest and the results will soon be published in a separate paper.

Our results are radically different from those obtained in /2/. In this paper, the trapping efficiency of D^+ ions in a stainless-steel target is reported to vary from 0.2 to 0.35 in the energy interval from 7 to 25 keV. Saturation was observed in this energy interval, with the deuterium fluxes to an from the target mutually balancing. For example, the saturation for 15 keV D^+ ions was reached at concentrations of $3 \cdot 10^{17}$ trapped particles per cm^2.

The discrepancy between our results and those of /2/ apparently cannot be explained either by the difference in mass or by the difference in energy. Vacuum conditions governing the purity of the target surface probably make some contribution. Although we did not make any experiments to prove that the surface cleanup affected the trapping efficiency, there is some evidence that the efficiency decreases if the surface is contaminated. In /2/, the vacuum in the measuring chamber was $1.3-4 \cdot 10^{-6}\,N/m^2$, with some 30% impurities. This is clearly insufficient for maintaining a clean

target. For example, if the partial pressure of the active impurities in the measuring chamber is over $1 \cdot 10^{-7} N/m^2$, up to 0.1 monolayer may accrue on the target in 1 min after bakeout. The difference in vacuum conditions, however, can hardly be held responsible for entire discrepancy in results. Further experiments will help to establish the exact reasons for this divergence.

Conclusions

We have established that the trapping efficiency of 35 keV H_1^+ ions by a clean surface of 1 Kh 18 N 9 T stainless steel is over 93%. This value is retained up to concentrations of $2 \cdot 10^{19}$ trapped particles per cm^2, and no downward tendency is observed.

Our results indicate that in magnetic traps the rate of pumping of slow neutral particles may be reduced at least by one order of magnitude in comparison with the figures obtained from the runaway of fast particles from the plasma volume.

BIBLIOGRAPHY

1. VARNERIN, L. J. and J. H. CARMICHAEL. — J. Appl. Phys., 28 : 913. 1957.
2. SIMONOV, V. A., G. F. KLEIMENOV, A. G. MILESHKIN, and K. A. KOCHNEV. — Nucl. Fusion, Suppl., Part 1 : 325. 1962.
3. CARMICHAEL, J. H. and E. A. TRENDELENBURG. — J. Appl. Phy., 29 : 1570. 1958.
4. CARMICHAEL, J. H. and P. M. WATERS. — J. Appl. Phys., 33 : 1 70. 1962.
5. BROWN, E. and J. H. LECK. — Br. J. Appl. Phys., 6 : 161. 1955
6. KOCH, J. — Nature, 161 : 566. 1948.
7. FIEBIGER, K. — Zs. Angew. Phys., 9 : 213. 1957.
8. BOROVIK, E. S., S. F. GRISHIN, and B. G. LAZAREV. — PTE, No 1 : 115. 1960.
9. BOROVIK, E. S., S. F. GRISHIN, and E. Ya. GRISHINA. — ZhTF, 30 : 639. 1960.

F. I. Busol, V. B. Yuferov, and E. I. Skibenko

VACUUM IMPROVEMENT NEAR SUPERSONIC GAS JETS IN A CHARGE-EXCHANGE CHAMBER

In /1, 2/, a vacuum of nearly $5.2 \cdot 10^{-3} N/m^2$ was obtained in the charge-exchange chamber near a gas jet of optimal thickness. This is clearly an achievement, but the vacuum conditions must be further improved by one

or two orders of magnitude /2/. It has been shown in the previous works that the vacuum in the charge-exchange chamber with a supersonic jet is determined by three factors: the flux of particles escaping from the boundary layers at an angle $\theta > \theta_{theor}$ when the jet is ejected from the nozzle into the vacuum, the flux from all over the surface of the jet due to interparticle collisions, and the backstreaming from the condenser due to imperfect condensation of the jet.

In the present paper we discuss the results of experiments which have been staged to explore the deterioration of vacuum due to the nonideal nozzle geometry.

The quantitative contribution from each particle flux can be determined by screening off the ionization gage from different directions. The results for a CO_2 jet are plotted in Figure 1, which gives the pressure p_k in the charge-exchange chamber as a function of the nozzle discharge q under various conditions. Curve 1 was obtained with an open ionization gage LM-2, exposed to all the scattered particle fluxes. Curve 2 was obtained with the gage so screened that the particle flux originating in the nozzle was eliminated. From the pressure increment Δp_k between curves 1 and 2 at the corresponding q we can infer the flux of particles diverging at an angle $\theta > \theta_{theor}$ from the nozzle. Curve 3 was obtained with a covered gage, none of the particle fluxes reaching it directly. The deterioration of vacuum in this case is attributable to impurities which do not condense at the particular temperature, and also to CO_2 molecules which reach the tube without colliding with the condenser or the baffle after several reflections from the warm walls. The pressure difference between curves 2 and 3 gives the sum total of backstreaming plus the flux of particles diffusing from the jet due to interparticle collisions.

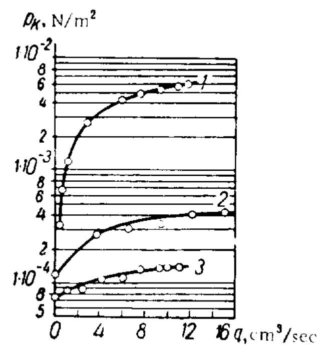

FIGURE 1. Pressure in charge-exchange chamber as a function of the flow rate q of the supersonic jet with variously screened pressure gage:
1) open gage; 2) screened from nozzle fluxes; 3) fully covered.

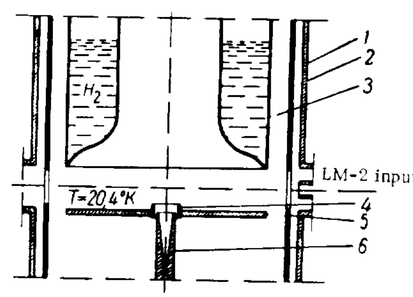

FIGURE 2. Schematic diagram of the baffling arrangement for the determination of the scattered flux from a nonideal nozzle:
1) chamber; 2) nitrogen-cooled baffle; 3) condensing element; 4) baffle tube; 5) nozzle; 6) disk.

We see from the curves in Figure 1 that the pressure in the charge-exchange chamber is determined mainly by the flux of particles with scattering angles $\theta > \theta_{theor}$, which is greater at least by one order of magnitude than all the other particle fluxes. We should note at this point that the baffle used in /1/ to cut off the backstreaming also partly eliminated

the flux of particles from the nozzle. The conclusion that backstreaming is the main factor influencing the vacuum in the charge-exchange chamber is therefore in error.

To attain the ultimate aim (a vacuum of $10^{-4}-10^{-5}\,N/m^2$), the effect of all the three fluxes should be eliminated, but in the present work we only explored the possibility of cutting off the scattered flux from the nozzle. A specially designed nozzle was used, which preserved the basic advantages of supersonic jets, namely large inlet and outlet diaphragms for the beam.

The scattered fluxes can be eliminated by screening the jets with cold pumping walls. One of the possible variants is described in the following, and the parametrs of the jets obtained under the new conditions are given.

The experiments were carried out on the setup described in /1, 2/. The baffled nozzle used in determining the scattered flux is schematically depicted in Figure 2. Supersonic jets of A and CO_2 were investigated. To reduce the scattered flux, the nozzle 5 was surrounded by a copper tube 4 with an i. d. of 26 mm, whose height relative to the plane of the outlet orifice varied from 0 to 8 mm. The clearance between the nozzle and the baffle tube was some 3 mm. The tube was held by the disk 6, coplanar with the outlet orifice. The condenser 3 and the tube with the disk were cooled with liquid hydrogen. The LM-2 gage and the axis of the ion beam, as in the previous experiments, were both in a plane distant 15 mm from the nozzle edge. The distances from the gage inlet to the jet axis and from the outlet orifice to the condenser were 150 and 50 mm, respectively.

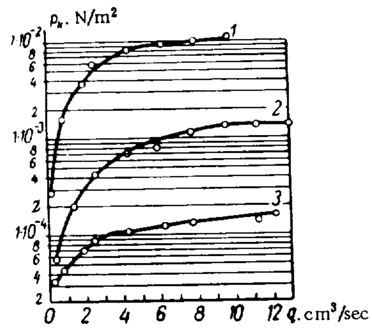

FIGURE 3. Pressure in charge-exchange chamber vs. flow rate for a supersonic argon jet:
1) $\delta = 0$; 2) $\delta = 5$; 3) $\delta = 8$ mm.

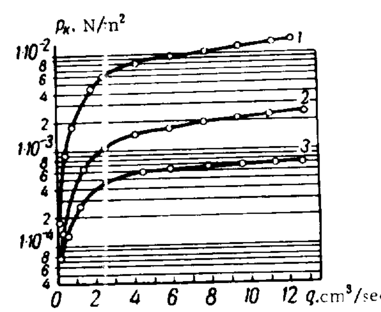

FIGURE 4. Pressure in charge-exchange chamber vs. flow rate for a supersonic CO_2 jet:
1) $\delta = 0$; 2) $\delta = 5$; 3) $\delta = 8$ mm.

Using this baffling device, we measured the pressure p_k as a function of the gas flow rate q in the jet. Typical curves are plotted in Figures 3 and 4 for A and CO_2, respectively. The parameter of the $p_k = f(q)$ curves is δ, the height of the baffle tube. We see that as δ increases, the vacuum in the charge-exchange chamber is substantially improved, which is attributable to the gradual screening off of the scattered flux from the nozzle and possibly to the partial elimination of the scattered flux produced by interparticle collisions in jet sections near the nozzle (where it is greatest because the jet density there is highest). Comparison of the graphs in Figure 1 and Figures 3–4 shows that the vacuum measured with an open

gage was somewhat poorer in the later experiments. As we were mainly interested in the relative change of pressure in the charge-exchange chamber with the elevation of the baffle tube, no special attempts were made to eliminate this divergence.

The variation of the pressure p_k with δ is plotted in Figure 5 in the entire range of δ values for A and CO_2 jets. We see from the figure that for the largest $\delta = 8$ mm, the vacuum recorded with the CO_2 jet is $6.7 \cdot 10^{-4}$ N/m^2 and that obtained with the A jet is $1.3 \cdot 10^{-4}$ N/m^2.

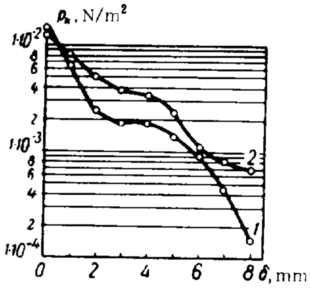

FIGURE 5. Pressure vs. δ for A (1) and CO_2 (2) jets.

Qualitatively, the trend of these curves can be characterized as follows. For $\delta = 0$, the ionization gage collects the three fluxes in their entirety. As δ increases (from 0 to 3 mm), the particles scattered from the nozzle at angles close to $\pi/2$ condense on the baffle tube. In the region $\delta = 3-4$ mm, p_k drops at a reduced rate, since for these δ the particles scattered at the nozzle do not all reach the gage. The LM-2 gage registers, as before, the scattered fluxes from the jet and from the condenser, plus the fractional flux of the nozzle-scattered particles which reach the gage after colliding with the warm walls. Starting with $\delta = 5$ mm, p_k again drops fairly steeply, since the flux of nozzle-scattered particles hits only the cold walls in the gap between the condenser and the nitrogen baffle, where the particles are pumped by the baffle or the external surface of the condenser.

As we see from Figure 5 the A curve falls off more steeply than the CO_2 curve. This is apparently so because the CO_2 molecules have a greater transverse velocity component than the A atoms, i.e., the scattering of the CO_2 jet is higher than that of the A jet.

The amount of gas condensing on the baffle tube determines the "service life" of the jet, i.e., the time in which, given optimum flow rates, the vacuum does not deteriorate. For example, with $\delta = 8$ mm and optimum flow rates, the A or CO_2 jets function properly for 30 min without affecting the vacuum. The clearance in the baffle tube progressively diminishes from 16 to 10 mm. Now, if the running time is stretched further, the condensate layer on the baffle tube becomes inordinately thick, its surface temperature increases, and full condensation can no longer be expected. Particle aggregates may moreover be knocked out from the condensate film which, reaching warm surfaces, have a highly detrimental effect.

Since the effective target thickness is the jet diameter plus the span of the scattered fluxes, the elimination of the scattered fluxes may require increased flow rates in the jet. Control experiments concerned with the target thickness under the new conditions hardly revealed any change in the charge-exchange curve of /1, 2/, i.e., the percentage of charge exchange on A and CO_2 jets reached its maximum for the same flow rates q as in the previous experiments.

Our results thus suggest that the vacuum near supersonic gas jets in a charge-exchange chamber can be substantially improved by fairly simple means. This conclusion is highly significant with a view to simplifying the shielding /2/ between the working volume and the charge-exchange chamber.

BIBLIOGRAPHY

1. BOROVIK, E. S., F. I. BUSOL, V. B. YUFEROV, and E. I. SKIBENKO. -- ZhTF, 33: 973. 1963.

2. BOROVIK, E. S., F. I. BUSOL, and V. B. YUFEROV. — In: "Fizika plazmy i problemy upravlyaemogo termoyadernogo sinteza", Vol. 3. Kiev, Izdatel'stvo AN UkrSSR. 1963.

F. I. Busol, V. A. Kovalenko, E. I. Skibenko, and V. B. Yuferov

OPTIMAL PARAMETERS OF THE GVL-2 MAGNETIC MACHINE AND SOME FEATURES OF LOW-TEMPERATURE SOLENOIDS

The magnetic field of the GVL-2 machine /1/ is provided by two solenoids which are fabricated from ordinary copper wire and cooled to the boiling point of liquid hydrogen. The geometrical parameters of these solenoids are the following: internal and external diameters $2a_1$ and $2a_2$ equal to 5 and 21.5 cm, respectively; length $2b = 22$ cm. The parameters α and β, defined as the ratios $\frac{a_2}{a_1}$ and $\frac{b}{a_1}$, are therefore 4.3 and 4.4, respectively. The choice of these parameters was mainly determined by the available power supply: a condenser bank with $U_0 = 5$ kV and $C_0 = 1.75 \cdot 10^{-2}$ F and a bank of 100 car batteries with a total e.m.f. of nearly 1.2 kV and a short-circuit current of 1780 A.

Magnetic fields B of the order of 10 T are virtually inconceivable under continuous-operation conditions in copper coils with an i.d. of 5 cm and reasonable values of α and β, even though the coils are cooled to liquid hydrogen point. This immediately follows from a comparison of the Joule heat generated in the coils with the maximum allowed thermal load per unit area, as determined in /2/.

On the other hand, the experience accumulated in our laboratory with long-lived pulsed magnetic fields /3/ suggests that the coils with the above values of a_1, α, and β may provide a field of some 10 T with a lifetime of the order of 1 sec if they are cooled to $T = 20.4$ °K. The experiments were therefore made under adiabatic conditions of solenoid operation. Since a high magnetic field should be maintained for as long as possible, we had to decide on optimal coil parameters, i.e., such that would ensure a maximum τ for the given a_1 and B and known power requirements. The solution of this particular problem proved the approach to be quite general and suitable for the choice of optimal α and β in different solenoids: pulsed and continuously operating, low-temperature and conventional. Some interesting features of low-temperature solenoids also follow from an inspection of the various modes of power supply of the GVL-2 magnetic machine. These in short are the problems discussed in the present paper.

1. Under adiabatic conditions, the field B and its lifetime τ are determined /3/ by the integral of the c-to-ϱ ratio (the specific heat and the electrical resistivity of the coil material, respectively) taken in the entire range of coil temperature variation. Since at low temperatures (20—80 °K) the electrical resistivity of pure metals (copper, in particular)

increases rapidly with rising temperature, the heating ΔT of the coils clearly should not exceed a few tens of degrees; otherwise, only a minor fraction of the energy stored in the power sources will be deposited in the magnetic field. Moreover, the rapid growth of resistance will complicate the conditions of power supply, especially if a constant or a growing field is required. Let $\Delta T = 32\,°K$ ($20-50\,°K$). The resistance of common electrical-engineering copper increases roughly 5-fold in this temperature interval.

The "cold reserve" of the coil winding is determined, besides ΔT, also by the size of the coil, or simply by the weight of copper. Therefore, in order to maximize, for the given $\Delta T = T_2 - T_1$, the product $B^2\tau$ in a coil with an internal radius a_1, the coil dimensions — its external diameter and length — must be increased. Indeed, let us write, for example, the balance of energy in the adiabatic case /3/:

$$B^2\tau = \mu_0^2 c_1^2 a_1^2 \int_{T_1}^{T_2} \frac{c}{\varrho}\, dT. \tag{1}$$

where c_1 is a shape factor depending on α and β as follows:

$$c_1 = \eta\beta \ln \frac{\alpha + \sqrt{\alpha^2 + \beta^2}}{1 + \sqrt{1 + \beta^2}}, \tag{2}$$

η is the filling ratio, $\mu_0 = 4\pi \cdot 10^{-7}$ Wb/A·m is the magnetic permeability in vacuum. The other quantities have been defined in the preceding. From (1) and (2) we see that by increasing α, we can reach arbitrarily large $B^2\tau$. An increase of β for $\beta > \alpha$ and $\alpha = \text{const}$ is hardly profitable, since c_1 approaches a limit in this case. The coil size clearly cannot be increased indefinitely keeping the internal diameter constant: in each particular case, the upper bound is set primarily by the parameters of the power source.

Our problem is therefore formulated as follows: what should be the shape of the coil to ensure a maximum $B^2\tau$ for given coil volume or weight; or alternatively, what α and β should be taken to ensure a maximum pulse length for given B, a_1, and ΔT.

From equation (1) we see that τ in this case is determined by the square of the shape factor c_1. If η is also known, we have

$$\tau = \text{const}\, \beta^2 \ln^2 \frac{z_1}{z_2}, \tag{3}$$

where

$$z_1 = \alpha + \sqrt{\alpha^2 + \beta^2}; \quad z_2 = 1 + \sqrt{1 + \beta^2}. \tag{4}$$

The function $\tau = \tau(\alpha, \beta)$ is extremized assuming the weight of the conductor P or the volume of the coil V to be known in advance. Since

$$P = 2\pi\beta(\alpha^2 - 1)\, a_1^3 d_0 \eta = V\eta d_0, \tag{5}$$

where d_0 is the specific weight of the coil material, we see that

$$\beta(\alpha^2 - 1) = \frac{P}{2\pi a_1^3 d_0 \eta} = \frac{V}{2\pi a_1^3} \equiv c_2, \tag{6}$$

i.e., constant.

Treating β as a function of α and differentiating τ with respect to α, we arrive at the following condition for a maximum of the function τ:

$$\left(\frac{z_1'}{z_1} - \frac{z_2'}{z_2}\right) - \frac{2\alpha}{\alpha^2 - 1} \ln \frac{z_1}{z_2} = 0. \qquad (7)$$

Here z_1' and z_2' are the derivatives of z_1 and z_2 with respect to α. Although this equation cannot be solved analytically for α or β, numerical solution can be obtained without difficulty.

Less accurate, but simpler and more illustrative is the alternative technique of optimizing α and β by a direct construction of the τ vs. α or β curves, subject to the condition (6). These curves for four values of c_2 (16 in curve 1, 76.3 in curve 2, 128.4 in curve 3, and 190 in curve 4) are plotted in Figure 1. The corresponding weights of copper wire are 8.35, 40, 67.5, and 100 kg. The numerical values of τ are calculated for $B = 10\,\mathrm{T}$, $a_1 = 2.5 \cdot 10^{-2}\,\mathrm{m}$, $T_1 = 20\,°\mathrm{K}$, $T_2 = 52\,°\mathrm{K}$, $\eta = 0.6$. The integral $\int_{T_1}^{T_2} \frac{c}{\varrho} dT\,(\mathrm{J/m^4 \cdot ohm})$ is evaluated taking account of the increase of the resistance of copper in a magnetic field and is found equal to $2.8 \cdot 10^{16}$. The magnetic field is assumed

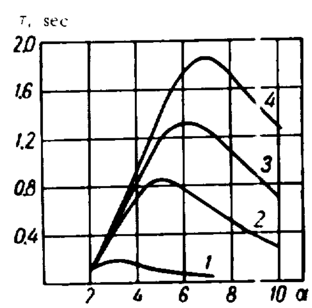

FIGURE 1.

to fall off linearly along the coil radius to zero for $r = a_2$. We see from the figure that the τ vs. α curves with $\beta(\alpha^2 - 1) = \mathrm{const}$ display a fairly pronounced maximum which is displaced in the direction of higher α as $\beta(\alpha^2 - 1)$ increases. The ratio $\frac{\alpha}{\beta}$, however, is remarkably constant at the maxima of all the curves, being equal approximately to 1.63. The fact that for any $\beta(\alpha^2 - 1)$ the maximum is attained with $\frac{\alpha}{\beta} \simeq 1.63$ is easily verified by solving the simultaneous system of equations

$$\begin{gathered} \beta(\alpha^2 - 1) = c_2, \\ \frac{\alpha}{\beta} \simeq 1.63 \end{gathered} \qquad (8)$$

and substituting the α and β in equation (7). This equation is satisfied with fair accuracy.

This empirical rule considerably simplifies the determination of the optimal coil parameters. For example, taking $a_1 = 2.5$ cm and $P_{Cu} = 67.5$ kg ($\beta(\alpha^2 - 1) = 110$) and applying the equation

$$\alpha^3 - \alpha - 1.63 \cdot 110 = 0,$$

we easily find $\alpha_{opt} \simeq 5.7$ and therefore $\beta_{opt} \simeq 3.5$.

Another important consequence of condition (6) is that the product $W\tau$ (where W is the power required to provide the field B at the center of the coil) is constant, being independent of α and β. Therefore, for the optimal values of α and β satisfying the condition $\beta(\alpha^2 - 1) =$ const, the active losses in the coil are minimal.

There is one additional point which merits consideration. In our solution, the role of the low-temperature cooling of the coils is manifested in the single fact that, for moderately strong magnetic fields, the integral $\int\limits_{T_1}^{T_2} \frac{c}{\varrho} dT$ in the given temperature interval ΔT is considerably greater at low temperatures than at room temperature. $B^2\tau$ is correspondingly larger at low temperatures. It is clear, however, that the magnitude of the integral does not affect the position of the maximum τ or the minimum W. Our conclusions therefore remain in force for solenoids operating at any temperature. The method for the determination of the optimum α and β is moreover valid for continuous-operation solenoids. In this case we seek the shape of the coil which ensures minimum ohmic losses for a given field strength or a maximum field strength for a given power.

It has been commonly assumed that Bitter's coil /4/ with $\alpha = 3$ and $\beta = 2$, i.e., $\frac{\alpha}{\beta} = 1.5$, satisfies this condition. If, however, we take the α and β from equations (8) with $c_2 = 16$ and substitute the results in the expression for the shape factor G_1 /4/

$$G_1 = \frac{\sqrt{2\pi}}{5} \sqrt{\frac{\beta}{\alpha^2 - 1}} \ln \frac{\alpha + \sqrt{\alpha^2 + \beta^2}}{1 + \sqrt{1 + \beta^2}}, \tag{9}$$

we easily find $G_1 \simeq 0.180$, whereas with $\alpha = 3$ and $\beta = 2$, $G_1 \simeq 0.179$. According to Bitter, this G_1 is the maximum for solenoids with constant current density over the cross section. We verified, and it is proved analytically, that the maximum G_1 occurs for $\frac{\alpha}{\beta} = 1.63$ in this case also. The difference in G_1 values is insignificant and hardly deserves to be mentioned.

It is interesting to consider to what extent the condition $\beta(\alpha^2 - 1) =$ const is general and necessary. We have shown that for pulsed-operation coils, knowledge of $\beta(\alpha^2 - 1)$ is decisive in obtaining the desired $B^2\tau$. It also seems that in most other cases, having selected a_1 and B from physical considerations, we may wish to find the optimal parameters for coils of different volumes. For example, if $a_1 = 10$ cm, the volume of Bitter's coil ($\alpha = 3$, $\beta = 2$) is about 0.1 m^3. Note that the true α_{opt} and β_{opt} for $\beta(\alpha^2 - 1) = 16$ are ~ 3.1 and ~ 1.9, respectively. Making use of (8), we find these optimal parameters without difficulty. All this substantially simplifies the choice of coil shape in various particular cases.

2. While the maximum τ for given magnetic fields B is attained by appropriately choosing the shape of the coil, the fundamental problem of generating the field B with the available power sources in turn depends on the choice of optimal coil geometry. We have already mentioned that our power supply was highly limited, and we therefore had to select a winding which would meet the following basic requirements:

(a) the field in the magnetic mirrors is not less than 10 T;

(b) the lifetime of this field is of the order of 1 sec.

The active resistance of clean low-temperature solenoids is characteristically a very small fraction of the resistance of wires of the same cross section at room temperature. The ratio of the coil inductance L to its ohmic resistance R, which in coils of any given shape is independent of wire cross section or the number of turns, varying only with the electrical resistivity ϱ of the coil material, is therefore very large in this case. The resulting effect in capacitive circuits or in circuits with d.c. sources will emerge from our analysis of the GVL-2 machine coils, which require $2.08 \cdot 10^6$ ampereturns (with a filling ratio $\eta = 0.6$) to provide a magnetic field of 10 T at the center.

Calculations with familiar relations show that our condenser bank with a discharge halfperiod $\frac{T}{2} = 2-3$ sec cannot produce magnetic fields B greater than 7–8 T, which is obviously at variance with condition (a) above. These calculations, as well as those which follow, take account of the increase of coil resistance with increasing current due to liberation of Joule heat and the effect of the magnetic field.

Car battery is effectively used if the growth time of the magnetic field to a prescribed level is less than the coil heating time. The current growth time in a circuit with an inductance and a resistance, supplied by a d.c. source, is given by the familiar relation

$$t_I = -\frac{L_n}{R_n} \ln\left(1 - \frac{I}{I_0}\right),$$

where L_n and R_n are the lumped inductances and resistances of the circuit, I_0 the maximum current through the circuit, I the current intensity under consideration. The time t_I should therefore be less than the time τ' in which the coil heats up and the resistance increases to such an extent as to suppress the current before the field has reached the prescribed strength.

Three different operating modes were considered in choosing the coil windings for the GVL-2 machine:

(1) The coil resistance R_c is substantially greater than the internal resistance of the source R_s ($R_c \gg R_s$), which in our case was close to 0.7 ohm. For continuous-operation coils, this represents a gain of energy at low temperatures;

(2) $R_c = R_s$; the power of the car battery is utilized most effectively, and, if the coils are not heated, the maximum field is attained;

(3) $R_c < R_s$ (the case chosen by us); when the coils heat, $R_c \to R_s$, so that maximum power can be fed into the coils, thus offsetting the growth of resistance.

Figure 2 plots the calculated fields vs. time curves for coils of identical shape ($a_1 = 2.5$ cm, $\alpha = 4.3$, $\beta = 4.5$) with windings representing the three cases above. The ordinate gives the field strength (in T) at the center of one of the series-connected coils, the abscissa marks the time in seconds. For curve 1, $R_c = 10\,R_s$(7 ohm), $L = 52.2$ H; for curve 2, $R_c = R_s$(0.7 ohm) and $L = 5.22$ H; for curve 3, $R_c = 0.3\ R_s$(0.21 ohm) and $L = 1.6$ H.

We see from the figure that under adiabatic conditions our power source (a bank of car batteries with an e.m.f. of 1200 V) provides the best approximation to the above conditions with coils having $R_c < R_s$. The maximum field for $R_c = 0.3\,R_s$ is $B_{max} = 11.75$ T with a lifetime of $\tau = 1.35$ sec. Coils with $R_c = R_s$ are somewhat inferior for our purposes, since the maximum field in this case is 9.6 T. Moreover, the equality $R_c = R_s$ does not help much, since the coil resistance will have increased considerably by the time the peak current is attained (in our case, a 6-fold increase in resistance is observed). Finally, with $R_c \gg R_s$, the field provided by heating coils grows much too slowly, and with $R_c = 10\,R_s$ the peak field strength is a mere 6.15 T.

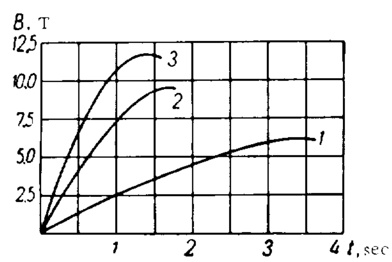

FIGURE 2.

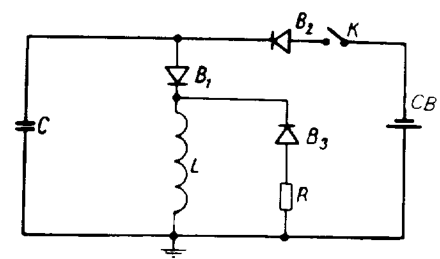

FIGURE 3.

The case $R_c < R_s$ ensures a magnetic field of desired strength for a period which is fairly long in relation to any process in the plasma.

On the basis of our calculations, the coils of the GVL-2 machine were fabricated from PBD-grade copper wire 1.81 mm in diameter. Number of turns in each coil $N = 4280$, resistance at $T = 20.4$ °K 0.105 ohm, and calculated inductance $L = 0.8$ H. The coils were coupled in series.

The field strength and its lifetime can be both increased by using the two power sources simultaneously, as shown by the circuit in Figure 3. The circuit functions as follows: the condenser bank C is discharged through the coils L and in approximately 0.2 sec the field rises to ~ 10 T.

After the discharge, field growth is sustained for some time by the car battery CB which energizes the coil through the closed switch K and the diode B_2. When B_{max} is attained, the switch K is opened and the energy stored in the coils is dissipated in the resistor R: the growing negative voltage across the coil triggers the diode B_3.

Among the advantages of this circuit we should mention the fact that a comparatively low power battery is required to reach fields of 10 T.

We have experimented with magnetic fields generated only by a single condenser bank. The maximum field strength was ~ 10.5 T. The time

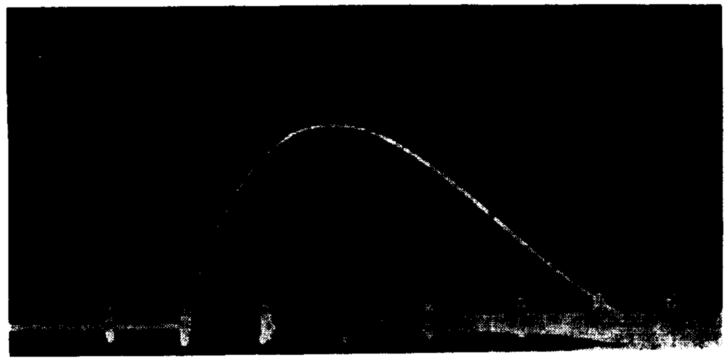

FIGURE 4.

variation of the field strength B is displayed by the oscillogram in Figure 4 (the abscissa markings correspond to 0.1 sec intervals).

BIBLIOGRAPHY

1. BOROVIK, E. S., F. I. BUSOL, V. A. KOVALENKO, V. B. YUFEROV and E. I. SKIBENKO. — This volume, p. 364.

2. BOROVIK, E. S., F. I. BUSOL, and S. F. GRISHIN. — ZhTF, 31: 459. 1961.

3. BOROVIK, E. S. and A. G. LIMAR'. — ZhTF, 31: 939. 1961.

4. BITTER, F. — Rev. Sci. Instr., 7: 479, 482. 1936.

E. S. Borovik, M. Sh. Mamedov, and V. G. Volotskaya

LOW-TEMPERATURE STRENGTH OF METALS UNDER PULSED LOAD

It has been shown /1/ that in coils providing pulsed magnetic fields the coil material is subjected to brief load pulses. In this paper we present the results of our measurements on the strength of aluminum wire $3.1 \cdot 10^{-4}$ m in diameter with pulse lengths $\tau = 0.3 \cdot 10^{-4}$ sec, at temperatures of 293, 77, and 20 °K, and the resistance increment of copper wire observed with loads of different magnitude and different repetitiveness.

Experimental results and comparison with published data

The strength of aluminum under pulsed load was studied on a setup described in /1/. We measured the temperature dependence of the impact strength σ_1 and the variation of strength σ_n with the number of pulses.

The results obtained for the impact strength σ_1 are given in Table 1 and Figure 1. In the Table, T is the initial temperature, j the current density, T_1 the temperature toward the end of the pulse, assuming an adiabatic process, δ the difference in loop lengths before and after breaking, related to the initial length.

TABLE 1

T, °K	$\sigma_1 \cdot 10^{-7}$, N/m²	δ, %	$j \cdot 10^{-9}$, A/m²	T_1, °K
293	22.2	10.4	1.95	—
77	53.3	14.6	4.52	85
20	59.6	14.8	5.25	32

TABLE 2

n	$\sigma_n \cdot 10^{-7}$, N/m²	
	293°K	20°K
2	22	59.5
10	17.3	39.6
50	9,6	29.7
100	—	25.8
190	7.7	23.8

We see from the above results that the σ_1 and δ both increase as the temperature decreases.

The measurements were made at 77 and 20 °K; Figure 1 gives the values of σ_1 at 85 and 32 °K, since we took account of specimen heating toward the end of the pulse.

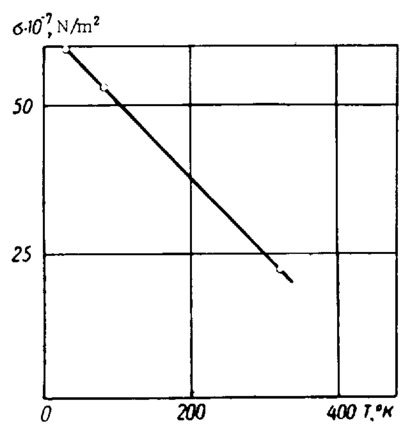

FIGURE 1. Strength σ_1 vs. temperature.

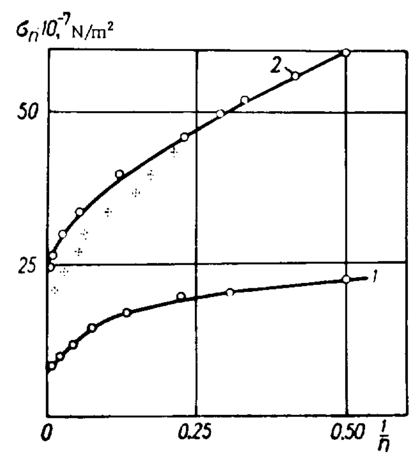

FIGURE 2. σ_n vs. the number of pulses: 1) T = 293 °K; 2) T = 20 °K.

The values of σ_n for various n and T are listed in Table 2.

In static tests /2, 3, 4/, the strength of aluminum increases approximately by a factor of 2 — 3.5 as temperature drops from 77 to 20 °K, while under pulsed conditions, the strength increases mainly as the temperature is lowered from 293 to 77 °K: further reduction of temperature to 20 °K has a negligible effect. Figure 2 plots the strength under pulsed load at liquid hydrogen point; the values obtained for T = 77 °K are marked by dots. Table 3 compares our data with the published results /2, 3, 4/.

We see from Table 3 that the impact strength under nonrepeating load, σ_1, is almost 1.5—2 times as great as the figure obtained in static tests. The strength obtained for multiple pulsed loading by extrapolating $n \to \infty$ is somewhat less than the static figure.

TABLE 3

Tests		$\sigma \cdot 10^{-7}$, N/m²			References
		293 °K	77 °K	20 °K	
Static		12	21	3[illegible]	/2/
Static		14	26	4[illegible]	/3/
Static		12	22	4[illegible]	/4/
Pulsed	σ_∞	7.5	20	2[illegible]	This work
	σ_1	22.2	53.3	59.[illegible]	

To obtain the residual deformation of copper we also measured the relative resistance increment of the specimens as a function of the number of pulses for various loads and pulse lengths ($\tau = 0.8 \cdot 10^{-4}$ and $2 \cdot 10^{-3}$ sec).

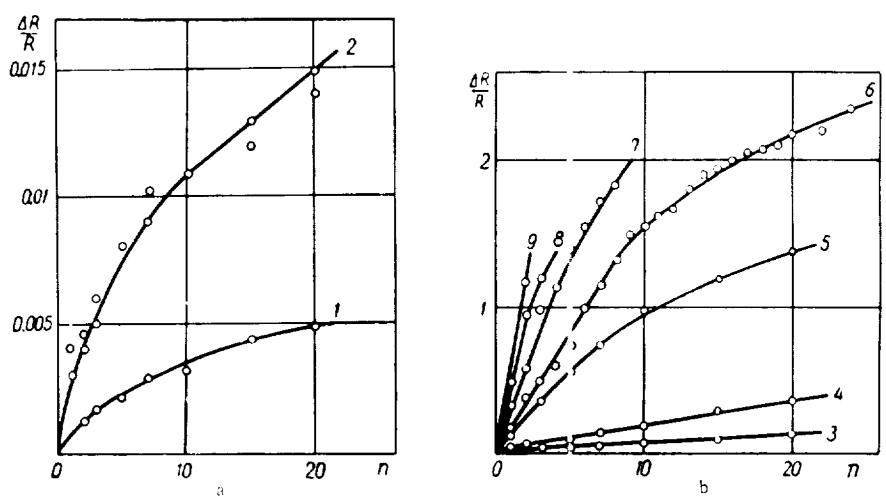

FIGURE 3. $\frac{\Delta R}{R}$ vs. number of pulses, $\tau = 0.8 \cdot 10^{-4}$ sec:

a — 1) $\sigma = 9.7 \cdot 10^7$ N/m²; 2) $\sigma = 14.5 \cdot 10^7$ N/m²; b — 3) $\sigma = 2[illegible].2 \cdot 10^7$ N/m²; 4) $\sigma = 36.3 \cdot 10^7$ N/m²; 5) $\sigma = 48.5 \cdot 10^7$ N/m²; 6) $\sigma = 53.5 \cdot 10^7$ N/m²; 7) $\sigma = 58.2 \cdot 10^7$ N/m²; 8) $\sigma = 72.6 \cdot 10^7$ N/m²; 9) $\sigma = 77.4 \cdot 10^7$ N/m².

The resistance was determined potentiometrically. The measurements were carried out at $T = 20$ °K for PEV-2 copper wire $2 \cdot 10^{-4}$ m in diameter. The resistance changed 100-fold as the temperature dropped from room temperature to the liquid hydrogen point.

We plotted the relative increment $\frac{\Delta R}{R}$ ($\Delta R = R_n - R$, where R_n is the resistance after the n-th pulse, R the initial resistance at the liquid hydrogen point) as a function of the number of pulses for various loads and different pulse lengths ($\tau = 0.8 \cdot 10^{-4}$ and $2 \cdot 10^{-3}$ sec). We see from Figure 3, a, b and Figure 4 that $\frac{\Delta R}{R}$ increases with increasing load magnitude and with the number and length of pulses.

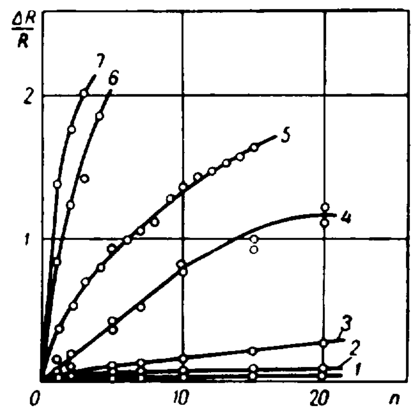

FIGURE 4. $\frac{\Delta R}{R}$ vs. number of pulses, $\tau = 2 \cdot 10^{-3}$ sec:
1) $\sigma = 14.3 \cdot 10^7$ N/m^2; 2) $\sigma = 15.4 \cdot 10^7$ N/m^2;
3) $\sigma = 20.6 \cdot 10^7$ N/m^2; 4) $\sigma = 28.6 \cdot 10^7$ N/m^2;
5) $\sigma = 32.6 \cdot 10^7$ N/m^2; 6) $\sigma = 36.8 \cdot 10^7$ N/m^2;
7) $\sigma = 38 \cdot 10^7$ N/m^2.

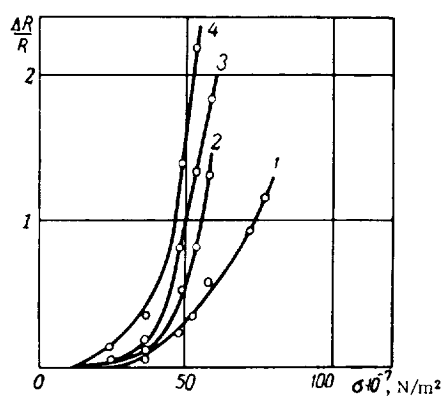

FIGURE 5. $\frac{\Delta R}{R}$ vs. σ, $\tau = 0.8 \cdot 10^{-4}$ sec:
1) $n = 2$; 2) $n = 5$; 3) $n = 8$; 4) $n = 20$.

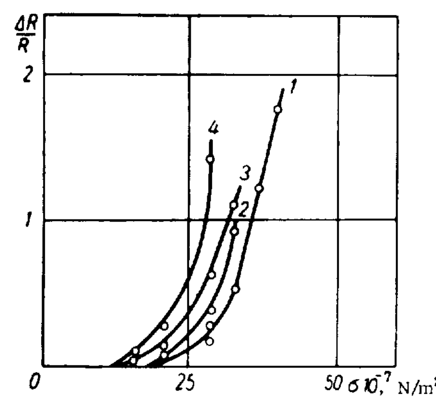

FIGURE 6. $\frac{\Delta R}{R}$ vs. σ, $\tau = 2 \cdot 10^{-3}$ sec:
1) $n = 2$; 2) $n = 5$; 3) $n = 8$; 4) $n = 20$.

From our data we plotted $\frac{\Delta R}{R}$ as a function of σ for various n (Figures 5 and 6). We see from the figures that for $\sigma = 14.5 \cdot 10^{-7}\,N/m^2$ the resistance increment does not exceed 0.01%; to $\sigma = 20-30 \cdot 10^{-7}\,N/m^2$ ($\tau = 2 \cdot 10^{-3}$ sec) and $\sigma = 30-40 \cdot 10^{-7}\,N/m^2$ ($\tau = 0.8 \cdot 10^{-4}$ sec), the resistance increment does not exceed 30–40%; starting with $\sigma = 50 \cdot 10^{-7}\,N/m^2$, the resistance increases substantially. Low-load conditions are therefore preferable for coils which are required to function for a long time.

BIBLIOGRAPHY

1. BOROVIK, E. S., M. Sh. MAMEDOV, and V. G. VOLOTSKAYA. — FMM, in print.
2. KOSTENETS, V. I. — ZhTF, 16(5): 515. 1946.
3. GINDIN, I. A., V. I. KOTKEVICH, and Ya. D. STARODUBOV. — FMM, 7(5): 794. 1959.
4. McCAMMON, R. D. and H. M. ROSENBERG. — Proc. Roy. Soc., 242: 204. 1956.

V. M. Lunev

SYNTHETIC ZEOLITES FOR THE PRODUCTION OF CLEAN VACUUM

Purity requirements in experimental work have lately become quite stringent. Special vacuum pumps have been developed which do not employ any contaminating fluids, and are thus suitable for producing comparatively clean, uncontaminated vacuum. Under this category we have the ionic sorption pumps, condensation pumps, adsorption pumps, etc. /1–4/.

The adsorption method of pumping is based on the ability of a porous substance, e.g., coal, to absorb large quantities of gases at low temperature, thus creating low pressures in the manifold. Finely porous silica gel and natural zeolites — faujasite, chabazite, etc. — are also suitable for this purpose. The application of synthetic zeolites, whose absorbing power is much superior to that of their natural analogs, should also be explored. Zeolites make it possible to create clean vacuum, and also provide high-purity forevacuum for other noncontaminating pumps which require preliminary evacuation.

Data have been published on zeolite adsorptivities in the range of high pressures only (from 13,332 to 101,323 N/m^2) /5–7/; hardly any data are available on low-pressure adsorption.

In this paper, we describe some experiments which have been staged to determine the adsorbing power of zeolites in the range of low pressures (at $T = 77.5\,°K$) and to explore the possibilities of zeolite application for the production of clean vacuum.

Structure of zeolites

The tetrahedral anion SiO_4, with four oxygens surrounding a silicon, is the basic structural unit of zeolites. Silicon can be replaced with aluminum, having a similar ionic radius. The lower valence of the aluminum ion leaves one negative charge uncompensated. In alumosilicate tetrahedra, part of the SiO_4 groups are replaced with AlO_4 groups. Eight tetrahedra join vertex to vertex to form a cuboctahedron, enclosing comparatively large free interstices. Separate cuboctahedra are joined by oxygen bridges. Lattices of these composite anion radicals carry a certain net negative charge, and the structure therefore contains interstitial metal ions compensating the residual charge of the anionic lattice. The porous structure of the zeolites can be visualized as molecule-sized interstices of nearly spherical shape. These interstices communicate by narrow apertures or windows.

Type A zeolites contain large interstices with a diameter of $1.14 \cdot 10^{-9}$ m and windows which, according to X-ray data /8/, measure $4.2 \cdot 10^{-10}$ m in diameter; there are also small interstices $6.6 \cdot 10^{-10}$ m in diameter with windows $2.5 \cdot 10^{-10}$ m in diameter.

Type X zeolites contain large interstices $1.16 \cdot 10^{-9}$ m in diameter and windows $(8-9) \cdot 10^{-10}$ m in diameter.

The large interstices are the vacancies between nearby cuboctahedra and the joining oxygen bridges. In type A zeolites, the cuboctahedra are joined by four-membered oxygen bridges, and in type X zeolites by six-membered oxygen bridges. The main difference between A and X zeolites is thus the size of the communicating windows.

Window diameters are not precisely equal to the results obtained in X-ray analysis; they depend on the nature of the ion-exchanging cation (mostly Ca^{2+} or Na^{2+}) in the alumosilicate lattice of the zeolite.

Zeolites are characterized by highly selective adsorption properties: a molecule of a certain species either will or will not pass through the window in the zeolite lattice. We thus have here a characteristic molecular-sieve effect. A distinctive feature of zeolites is that the fields set up by the opposite walls in the adsorbing interstices overlap, so that the adsorption potentials rise and the adsorptivity increases considerably. This effect is particularly pronounced at low concentrations of the adsorbate. In technology, zeolites are used in granular form, as crystalline powders with some binding agent added. The zeolite granules should possess sufficient mechanical strength to resist crushing and rubbing.

To sum up, the main properties of zeolites are the following:

(a) regular primary porous structure which is not affected by dehydration;

(b) nearly spherical interstices communicating by regular windows;

(c) highly pronounced molecular-sieve properties;

(d) an increase of the adsorption potentials in the interstices on account of the overlapping of the fields set up by the opposite walls.

Some 70 species of various zeolites have been synthesized by now, and four species are produced on a regular commercial scale; these are NaA, NaX, CaA, and CaX which are characterized by the following sieve window diameters: NaA $4 \cdot 10^{-10}$, NaX $1.3 \cdot 10^{-9}$ m, CaA $5 \cdot 10^{-10}$ m, CaX $1 \cdot 10^{-9}$ m.

Adsorption characteristics of zeolites

The pressure dependence of adsorptivity is the principal characteristic of zeolites which decides the question of their applicability, or otherwise, for the binding of gases in closed systems. This dependence can be inferred from gas adsorption isotherms in a wide range of pressures at constant temperature.

Adsorption isotherms of the gases N_2, A, H_2 were plotted for the zeolites NaA, NaX, CaA, CaX in the range of pressures from $1.333 \cdot 10^{-3}$ to 13,332 N/m^2 at the liquid notrogen point. These data enabled us to choose the optimal zeolite for the production of low pressures, and to determine the total quantity of adsorbed gas. This total adsorption sets a limit to the service life of the zeolite pump.

The zeolites were synthesized at the Khar'kov NIOKhIM*. The CaA zeolite was additionally procured from Groznyi.

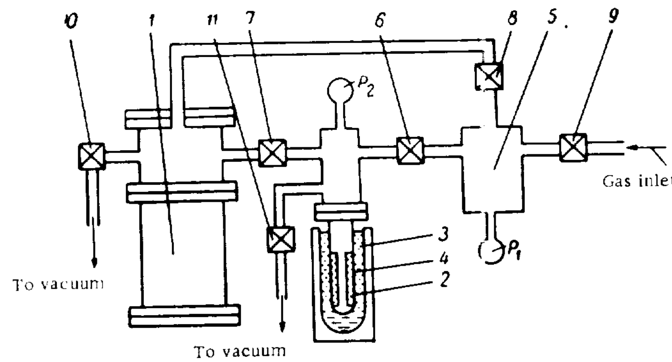

FIGURE 1. Schematic diagram of the setup for plotting the adsorption isotherms by the volumetric method:
1) high-vacuum titanium pump; 2) zeolite granules; 3) liquid nitrogen; 4) quartz flask; 5) volumetric container; 6, 7, 8, 10, 11) metallic valves; 9) leak.

Montmorillonite clays were mainly used as binding agents, but different zeolites contained different binders in amounts of 10 – 15%. The zeolites used in our experiments contained the following binders in crystalline powder form:

(a) CaA synthesized at NIOKhIM with Pyzhev bentonite as binder;
(b) CaX with Latnaya clay (NIOKhIM);
(c) NaA with Na_2SiO_3 (NIOKhIM);
(d) NaA with Khar'kov bentonite (NIOKhIM);
(e) NaX with Askaniya clay (NIOKhIM).

The adsorption isotherms were plotted by the volumetric method using the setup depicted schematically in Figure 1. Zeolite granules 2 were placed between the internal wall of a quartz flask 4 and a cylindrical grid. The quartz flask was immersed in a container with liquid nitrogen. The adsorbent-containing volume communicated through valves 6, 7 with a volumetric container 5 and a high-vacuum titanium pump 1; separate forepumping was provided.

* [Nauchno-Issledovatel'skii Institut Osnovnoi Khimii – Scientific Research Institute of Basic Chemistry.]

The artificial zeolite granules contain a large amount of adsorbed water. The low discharge capacity of the valves is an obstruction to rapid evacuation in the first stages. The bulk of gas during regeneration was therefore removed by forepumping; the valve between the adsorbent volume and the high-vacuum titanium pump was then opened and regeneration was carried out at a pressure of $1.333 \cdot 10^{-2}\,N/m^2$ and temperature of 588 °K. The curves in Figure 2 plot the variation of pressure and temperature during regeneration. The regeneration of freshly prepared zeolite took about three hours. Repeated regeneration after adsorption tests was much faster, and could be performed at pressures not exceeding $1.333 \cdot 10^{-2} - 6.666 \cdot 10^{-3}\,N/m^2$.

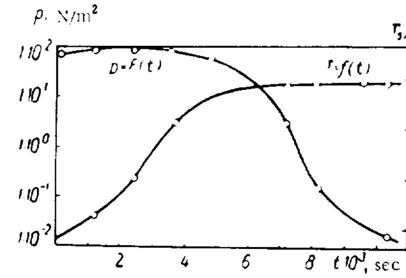

FIGURE 2. Time variation of regeneration.

After regeneration, the gas is admitted into the volumetric container 5, and valve 6 is opened to permit contact with the adsorbent. When adsorption appears to have stopped, a pressure reading is taken. By admitting various gas portions, we covered the entire pressure range from $13{,}332\,N/m^2$ to $1.333 \cdot 10^{-3}\,N/m^2$ and obtained the pressure dependence of the quantity of adsorbed gas. Adsorption isotherms were plotted from these data. The measurements were made simultaneously with mercury, thermocouple, and ionization pressure gages. The equilibrium takes a fairly long time to achieve, since internal diffusion is of decisive significance here. Observations of the adsorption process in the zeolites CaA, CaX, and NaX showed that the bulk of the gas was adsorbed in the first 2 — 3 min. The subsequent lengthy process occurs at a low pressure, and its quantitative contribution to overall adsorption is slight: it mainly reflects the dynamics of equilibrium. The poor adsorptivity of the zeolite NaA is connected with the very long time to equilibrium, which could not be realized in practice in our tests.

The adsorption quantity was calculated in m^3 of gas reduced to standard conditions (273 °K, $101{,}323\,N/m^2$), per 1 kg of hydrated zeolite. The elimination of water of crystallization in regeneration reduced the weight of the granules by 25%. The zeolite granules also contain a binder, which accounts for 10 — 15% of the weight. This point must be taken into consideration when the adsorptivity of the granules is compared with that of pure dehydrated crystals.

We see from Figure 3 that nitrogen is preferably adsorbed by CaA zeolites synthesized in Groznyi and at NIOKhIM. Zeolites of one grade fabricated in different places, under conceivably different conditions, possess different adsorptivities.

Unlike CaA, the zeolite NaA adsorbs nitrogen much less vigorously, since despite the geometrical accessibility of the NaA pores (window diameter $4 \cdot 10^{-10}$ m) for nitrogen molecules ($3 \cdot 10^{-10}$ m in diameter), the rate of sorption was very low on account of the low temperature maintained during the tests.

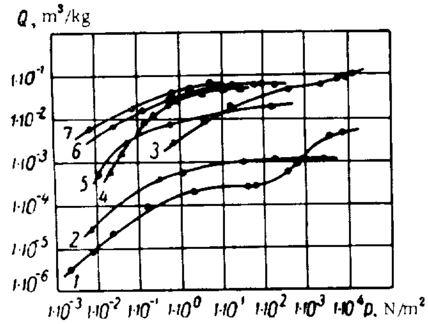

FIGURE 3. Adsorption isotherms of nitrogen (at 77.5°K) for zeolites of various grades: 1) NaA (glass); 2) NaA (Khar'kov bentonite); 3) silica gel; 4) NaX; 5) CaX; 6) CaA (NIOKhIM); 7) CaA (Groznyi).

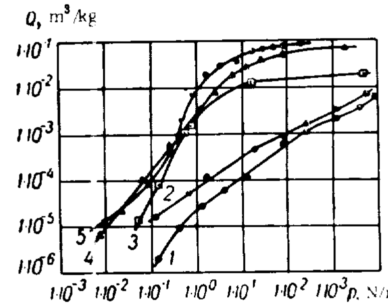

FIGURE 4. Adsorption isotherms of argon (at 77.5°K) for zeolites of various grades: 1) NaA (glass); 2) NaA (Khar'kov bentonite); 3) CaX; 4) NaX; 5) CaA (NIOKhIM).

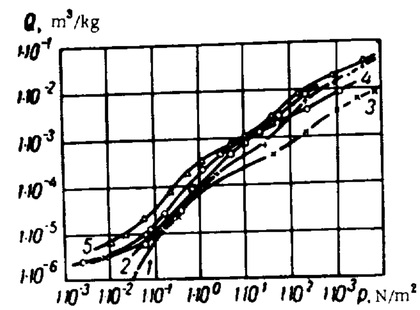

FIGURE 5. Adsorption isotherms of hydrogen (at 77.5°K) for zeolites of various grades: 1) NaX; 2) NaA (glass); 3) CaX; 4) NaA (Khar'kov bentonite); 5) CaA (NIOKhIM).

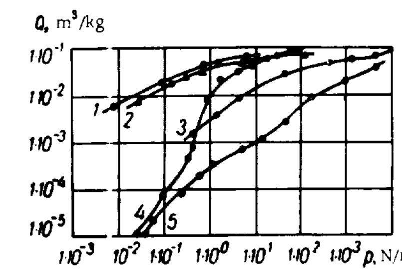

FIGURE 6. Adsorption isotherms of nitrogen, argon, and hydrogen for the zeolite CaA (at 77.5°K): 1) CaA from Groznyi, nitrogen; 2) CaA from NIOKhIM, nitrogen; 3) silica gel, nitrogen; 4) CaA (NIOKhIM), argon; 5) CaA (NIOKhIM), hydrogen.

We see that at any pressure the adsorption of nitrogen decreases in the following sequence: CaA > NaX > CaX > NaA.

Figure 3 also gives the adsorption isotherm of nitrogen by silica gel. Inspection of the curves shows that at low pressures silica gel is inferior to the zeolite CaA as far as nitrogen adsorption is concerned.

The same general trend is observed for argon (Figure 4). The difference in adsorption between low and high pressures is considerably greater in argon than in nitrogen.

Adsorption of hydrogen is small regardless of the particular zeolite employed, and is approximately equal to $5 \cdot 10^{-3}\, m^3/kg$ at $133.32\, N/m^2$ (Figure 5). Effective adsorption of hydrogen molecules under these conditions is precluded, since their critical temperature is lower than the temperature maintained in our adsorption tests.

The zeolite NaA with Khar'kov bentonite as the binder has a higher adsorptivity than the same zeolite doped with Na_2SiO_3.

Comparison of the adsorption of nitrogen, argon, and hydrogen by our specimens suggests that CaA is the optimal zeolite for the creation of low pressures; further experiments under controlled conditions are indicated.

Figure 6 gives the adsorption isotherms of N_2, A, H_2 at $T = 77.5\,°K$. The adsorptivity of the zeolite CaA decreases in the following order: $N_2 > A > H_2$.

Comparison of the capacity of the various zeolites for gas molecules at low pressures and temperatures leads to the conclusion that the best of the zeolites used in our tests are superior to all the conventional adsorbents, except coal, as far as atmospheric gases are concerned.

The adsorptivity of BAU-grade coal /3/ is greater by a factor of 1.5 — 2 than the adsorptivities of the best zeolites in our tests. The zeolites, however, cannot explode, unlike coal; they do not give off as much dust, and in general they are mechanically stronger. The application of coal may contaminate the vacuum manifold with carbon, which is sometimes undesirable.

Studies are under way, aimed at a synthesis of new zeolites whose low-pressure adsorptivities will exceed those of coal and of hitherto synthesized zeolites.

BIBLIOGRAPHY

1. Atomnaya Energiya, 5(4): 471. 1958.
2. LAZAREV, B. G. and M. F. FEDOROVA. — ZhTF, 29(7): 862—865. 1959.
3. LAZAREV, B. G. and M. F. FEDOROVA. — ZhTF, 30(7): 865— 867. 1960.
4. JEPSEN, R. L. — Le Vide, 80: 80. 1959.
5. KISELEV, A. V., Ya. V. MIRNYI, L. F. PAVLOVA, and R. S. PETROVA. — Khimiya i Tekhnologiya Topliv i Masel, 8: 7— 12. 1962.
6. NEIMARK, I. E., M. A. PIONTKOVSKAYA, A. E. LUKASH, and R. S. TYUTYUNNIK. In: "Sinteticheskie tseolity", pp. 49— 58. Moskva, Izdatel'stvo AN SSSR. 1962.
7. TSITSISHVILI, G. V. and T. G. ANDRONIKASHVILI. — In: "Sinteticheskie tseolity", pp. 117— 128. Moskva, Izdatel'stvo AN SSSR. 1962.
8. DUBININ, M. M. — In: "Sinteticheskie tseolity", pp. 5 — 6. Moskva, Izdatel'stvo AN SSSR. 1962.

Section Ten

PLASMA DIAGNOSTICS

I. A. Akhiezer, I. A. Daneliya, and N. L. Tsintsadze

A CONTRIBUTION TO THE THEORY OF TRANSFORMATION AND SCATTERING OF ELECTROMAGNETIC WAVES IN A NONEQUILIBRIUM PLASMA

Different modes of weakly damped oscillations may propagate in a plasma: isothermal plasma sustains transverse and high-frequency longitudinal (Langmuir) waves, nonisothermal plasma propagates low-frequency acoustic waves as well. On account of fluctuations, different wave modes are invariably present in a real plasma; in a state of thermodynamic equilibrium, their amplitude is determined by the temperature of the plasma (we shall use the term "fluctuation waves" to describe these modes).

In a nonequilibrium plasma, the amplitudes of the fluctuation waves can be found if the distribution functions of the particles of the plasma are known /1, 2, 3/. Plasmas may also propagate waves excited by external sources, which we call extraneous.

The equations describing a plasma are inherently nonlinear, and this nonlinearity leads to an interaction between the waves and causes scattering and conversion of some wave modes into other modes. There is an extensive literature dealing with the scattering and transformation of extraneous waves (see, e.g., /4, 2, 5/). Equilibrium and nonequilibrium plasmas are considered in connection with these subjects, but the state of the plasma is always assumed to be fairly far from instability.

It has been recently established /6, 7/ that the fluctuations in a plasma grow rapidly near the instability threshold. The coefficients of scattering of the transverse waves therefore become anomalously large /6/, a phenomenon analogous to critical opalescence. The coefficients of scattering in interactions of longitudinal wave modes should also be very high. One of the aims of the present paper is to investigate the scattering of an extraneous longitudinal wave, as well as its conversion into a transverse wave by critical plasma fluctuations.

Another characteristic effect observed in a nonequilibrium plasma is the spontaneous "glow" connected with the conversion of two longitudinal fluctuation waves into a transverse wave. (In an equilibrium plasma, only Rayleigh radiation is emitted, since the additional effect resulting from mode interaction vanishes in virtue of the detailed balance.) We shall find the intensity of this spontaneous glow (which in some cases is anomalously high) for plasmas fairly far from instability.

Intensity of secondary wave

Let us first find the amplitude of the secondary wave produced by the interaction of two waves propagating in a plasma. We shall start with the complete set of equations describing a plasma: the Boltzmann kinetic equation for particles of each species and Maxwell's equations. Assuming small amplitudes for the interacting waves and series-expanding the particle distribution functions and the electric and magnetic fields in terms of these amplitudes, we obtain for n-th order terms

$$\left(\frac{\partial}{\partial t}+\mathbf{v}\nabla\right)f_a^{(n)}+\frac{e_a}{m_a}\left(\mathbf{E}^{(n)}+\frac{1}{c}[\mathbf{v}\mathbf{H}^{(n)}]\right)\frac{\partial}{\partial \mathbf{v}}f_a^0=$$

$$=-\frac{e_a}{m_a}\sum_{n'=1}^{n-1}\left(\mathbf{E}^{(n')}+\frac{1}{c}[\mathbf{v}\mathbf{H}^{(n')}]\right)\frac{\partial}{\partial \mathbf{v}}f_a^{(n-n')}; \tag{1}$$

$$\operatorname{rot}\mathbf{H}^{(n)}=\frac{1}{c}\frac{\partial}{\partial t}\mathbf{E}^{(n)}+\frac{4\pi}{c}\sum_a e_a\int \mathbf{v}f_a^{(n)}d\mathbf{v},$$

$$\operatorname{div}\mathbf{E}^{(n)}=4\pi\sum_a e_a\int f_a^{(n)}d\mathbf{v}, \tag{2}$$

$$\operatorname{rot}\mathbf{E}^{(n)}=-\frac{1}{c}\frac{\partial}{\partial t}\mathbf{H}^{(n)};\quad \operatorname{div}\mathbf{H}^{(n)}=0,$$

where f_a is the distribution function of particles of the species a, having the mass m_a and the charge e_a; $\mathbf{E}$ and $\mathbf{H}$ are the electric and the magnetic fields. The non-linear effect of wave interaction is obviously represented by terms entering the right-hand sides of the kinetic equations (1).

Solving (1), (2) for the particular case when the two primary waves are longitudinal, we obtain an expression for the field of the secondary wave,

$$E_i^{(2)}(\mathbf{k},\omega)=-iD_{ij}(\mathbf{k},\omega)\int\frac{d\mathbf{k}_1d\omega_1}{(2\pi)^4}C_j(\mathbf{k}_1,\omega_1;\ \mathbf{k}-\mathbf{k}_1,\ \omega-\omega_1)\times$$

$$\times\varphi^{(1)}(\mathbf{k}_1,\omega_1)\varphi^{(1)}(\mathbf{k}-\mathbf{k}_1,\ \omega-\omega_1), \tag{3}$$

where $\varphi^{(1)}(\mathbf{k},\omega)=\frac{i}{k^2}\mathbf{k}\mathbf{E}^{(1)}(\mathbf{k},\omega)$ is the potential in the field of the primary wave,

$$C_i(\mathbf{k}_1,\omega_1;\ \mathbf{k}_2,\omega_2)=\frac{-4\pi}{\omega_1+\omega_2}\sum_a\frac{e_a^3}{m_a^2}\times\int\frac{v_i dv}{(\omega_1+\omega_2)-(\mathbf{k}_1+\mathbf{k}_2)\mathbf{v}}\left(\mathbf{k}_1\frac{\partial}{\partial \mathbf{v}}\right)\frac{\left(\mathbf{k}_2\frac{\partial}{\partial \mathbf{v}}\right)f_a^0}{\omega_2-\mathbf{k}_2\mathbf{v}}, \tag{4}$$

for a transverse secondary wave the tensor D has the form

$$D_{ij}^t(\mathbf{k},\omega)=\left(\delta_{ij}-\frac{k_ik_j}{k^2}\right)\left(\frac{c^2k^2}{\omega^2}-\varepsilon^t(\mathbf{k},\omega)\right)^{-1}, \tag{5}$$

and for a longitudinal secondary wave

$$D_{ij}^l(\mathbf{k},\omega)=-\frac{k_ik_j}{k^2}(\varepsilon^l(\mathbf{k},\omega))^{-1} \tag{6}$$

(ε^l, ε^t are the longitudinal and the transverse permittivities of the plasma).

The intensity of scattering and transformation of waves will be described in terms of the change in the square of the amplitude of the secondary wave in unit time, Σ:

$$\Sigma\equiv\frac{d}{dt}<E^{(2)2}>=\int d\Sigma \tag{7}$$

(the symbol $< \ldots >$ denotes averaging over fluctuations).

Let us first deal with the case of two longitudinal waves interacting to produce a transverse wave. For collision of two fluctuation waves, we have from (3) and (5)

$$d\Sigma = U(\mathbf{k}) \frac{d\mathbf{k}}{(2\pi)^3},$$

$$U(\mathbf{k}) = \frac{\Omega^2 + c^2k^2}{8k^2} \int \frac{d\mathbf{k}_1 d\omega_1}{(2\pi)^4} [\mathbf{k}\mathbf{C}(\mathbf{k}_1, \omega_1; \mathbf{k} - \mathbf{k}_1, \omega - \omega_1)]^2 \times \tag{8}$$
$$\times <\varphi^2>_{\mathbf{k}_1, \omega_1} <\varphi^2>_{\mathbf{k}-\mathbf{k}_1, \omega-\omega_1},$$

where $<\varphi^2>_{\mathbf{k}, \omega}$ is the Fourier component of the potential correlation function

$$<\varphi^2>_{\mathbf{k}\omega} = \int d\mathbf{r} dt \exp\{-i\mathbf{k}\mathbf{r} + i\omega t\} <\varphi(\mathbf{r} + \mathbf{r}_0, t + t_0)\varphi(\mathbf{r}_0, t_0)>$$

and $\Omega^2 = 4\pi e^2 \frac{n_0}{m}$ is the square of the electron plasma frequency. In deriving (8), we made use of the fact that, without higher correlations, the four-correlation function is representable in the form $(\omega_1 + \omega_2 \neq 0)$

$$<\varphi(\mathbf{k}_1, \omega_1)\varphi(\mathbf{k}_2, \omega_2)\varphi^*(\mathbf{k}_3, \omega_3)\varphi^*(\mathbf{k}_4, \omega_4)> =$$
$$= (2\pi)^8 <\varphi^2>_{\mathbf{k}_1\omega_1} <\varphi^2>_{\mathbf{k}_2\omega_2} \{\delta(\mathbf{k}_1 - \mathbf{k}_3)\delta(\omega_1 - \omega_3) \times$$
$$\times \delta(\mathbf{k}_2 - \mathbf{k}_4)\delta(\omega_2 - \omega_4) + \delta(\mathbf{k}_1 - \mathbf{k}_4)\delta(\omega_1 - \omega_4)\delta(\mathbf{k}_2 - \mathbf{k}_3)\delta(\omega_2 - \omega_3)\}.$$

If one of the colliding waves is extraneous $(\varphi^{(1)}(\mathbf{r}, t) = \varphi_0 e^{i\mathbf{k}_0\mathbf{r} - i\omega_0 t})$, then for the conversion ratio

$$d\sigma = \frac{d\Sigma}{|\mathbf{E}_0|^2}$$

we find

$$d\sigma = \frac{\Omega^2 + c^2k^2}{16k^2k_0^2} [\mathbf{k}\mathbf{C}(\mathbf{k}_0, \omega_0; \mathbf{k} - \mathbf{k}_0, \omega - \omega_0)]^2 <\varphi^2>_{\mathbf{k}-\mathbf{k}_0, \omega-\omega_0} \frac{d\mathbf{k}}{(2\pi)^3}. \tag{9}$$

Let us now consider the case of a longitudinal secondary wave. For the collision of two fluctuation waves, we have from (3) and (6)

$$d\Sigma = U(\mathbf{k}) \frac{d\mathbf{k}}{(2\pi)^3};$$

$$U(\mathbf{k}) = \frac{1}{2k^2} \left| \frac{\partial}{\partial\omega} \varepsilon^l(\mathbf{k}, \omega) \right|^{-2} \int \frac{d\mathbf{k}_1 d\omega_1}{(2\pi)^4} \times \tag{10}$$
$$\times (\mathbf{k}\mathbf{C}(\mathbf{k}_1, \omega_1; \mathbf{k} - \mathbf{k}_1, \omega - \omega_1))^2 <\varphi^2>_{\mathbf{k}_1\omega_1} <\varphi^2>_{\mathbf{k}-\mathbf{k}_1, \omega-\omega_1}.$$

In the collision of a fluctuation wave with an extraneous wave we have for $d\sigma$

$$d\sigma = \left| 2kk_0 \frac{\partial}{\partial\omega} \varepsilon^l(\mathbf{k}, \omega) \right|^{-2} (\mathbf{k}\mathbf{C})\, \mathbf{k}_0, \omega_0; \mathbf{k} - \mathbf{k}_0, \omega - \omega_0))^2 \;\; <\varphi^2>_{\mathbf{k}-\mathbf{k}_0, \omega-\omega_0} \frac{d\mathbf{k}}{(2\pi)^3}. \tag{11}$$

In conclusion of this section we give an expression for the function $\mathbf{C}$ in the collision of a high-frequency $(\omega_1 \sim \Omega)$, and a low-frequency $(\omega_2 \ll \Omega)$ wave. From (4),

$$\mathbf{C}(\mathbf{k}_1, \omega_1, \mathbf{k}_2, \omega_2) = \frac{e}{T_e} \left(\frac{\Omega}{\omega_1 + \omega_2}\right)^2 \mathbf{k}_2, \tag{12}$$

where T_e is the electron temperature of the plasma.

Transformation and scattering of waves in a plasma
with net electron drift

Let us consider scattering and transformation of waves in a nonisothermal plasma with electrons moving relative to the ions. We shall particularly be concerned with the case of critical fluctuations, when the drift velocity $\mathbf{u}$ of the electrons is close to the phase velocity of a two-temperature sound, $s = \left(\frac{T_e}{M}\right)^{1/2}$, M being the mass of the ion. The singularity attributable to critical fluctuations occurs in this case in the term corresponding to the propagation of acoustic waves, in the expression for the potential correlator /6, 7/:

$$<\varphi^2>_{\mathbf{q}\omega} = \frac{2(2\pi)^2 (T_e s q)^2}{\Omega^2 m (\omega - \mathbf{q}\mathbf{u})} \delta(\omega^2 - q^2 s^2). \tag{13}$$

Substituting (13) and (12) in (9), we find for the coefficient of conversion of an extraneous Langmuir wave into a transverse wave

$$d\sigma = \frac{\pi^2 e^2 (qs)^2}{2m\,|\Delta\omega - \mathbf{q}\mathbf{u}|} \frac{[\mathbf{k}\mathbf{k}_0]^2}{k^2 k_0^2} \delta(\Delta\omega^2 - q^2 s^2) \frac{d\mathbf{k}}{(2\pi)^3}, \tag{14}$$

where $\Delta\omega = \sqrt{\Omega^2 + c^2k^2} - \Omega - \mathbf{k}_0\mathbf{u} - \frac{3}{2}\Omega(ak_0)^2$ is the change in frequency and $\mathbf{q} = \mathbf{k} - \mathbf{k}_0$ is the change in wave vector due to transformation (a being the electron Debye radius). It is easily seen that for $\mathbf{q}\mathbf{u} \to \pm qs$, the coefficient preceding the delta-function in the expression for $d\sigma$ is anomalously large.

Integrating (14) with respect to the magnitude of the vector $\mathbf{k}$, we can find the coefficient of conversion of Langmuir waves into transverse waves propagating in unit solid angle. For $u \approx s$ and $\sin\theta_0 \ll 1$, we have

$$\frac{d\sigma}{do} = \frac{e^2 k_0 \Omega}{16\pi m c^2} f(\theta_0, \theta), \tag{15}$$

where

$$f(\theta_0, \theta) = \begin{cases} \frac{\sin^2\theta}{|\cos\theta|}\left[\sqrt{1 + \frac{2c^2k_0}{\Omega s\cos^2\theta}\left(1 + \frac{u}{s}\cos\theta_0\right)} - 1\right]^{-1} (\cos\theta < 0) \\ \frac{\sin^2\theta}{\cos\theta}\left\{\left[\sqrt{1 + \frac{2c^2k_0}{\Omega s\cos^2\theta}\left(1 + \frac{u}{s}\cos\theta_0\right)} - 1\right]^{-1} + \right. \\ \left. + \left[1 - \sqrt{1 - \frac{2c^2k_0}{\Omega s\cos^2\theta}\left(1 - \frac{u}{s}\cos\theta_0\right)}\right]^{-1}\right\} (\cos\theta > 0) \end{cases}$$

(Here and in what follows θ, θ_0 are the angles between the vectors $\mathbf{k}$, $\mathbf{k}_0$ and the vector $\mathbf{u}$.) It is easily seen that $\frac{d\sigma}{do}$ is anomalously large when $1 \pm \frac{u}{s}\cos\theta_0 \ll \frac{\Omega s}{c^2k_0}\cos^2\theta$. Note that this condition imposes very rigid restrictions on the angle θ_0 and the ratio $\frac{u}{s}$.

Let us calculate the amplitude increment, in unit time, of the transverse waves generated when Langmuir fluctuation waves are scattered and transformed by critical fluctuations. Seeing that the term representing Langmuir waves in the expression for the potential correlator is /1, 2, 3/

$$<\varphi^2>^L_{\mathbf{q}\omega} = \frac{2(2\pi)^2 \Omega \bar{T}_e}{q^2} \delta(\omega^2 - \Omega^2 - 3\Omega^2 a^2 q^2) \tag{16}$$

($\bar{\omega} = \omega - \mathbf{qu}$ is the frequency in the frame of reference where the electrons are at rest) and applying relations (8), (12), (13), we find

$$U(\mathbf{k}) = \frac{e^2 T_e \Omega}{m} \int d\mathbf{k}_1 d\omega_1 \frac{|\mathbf{k}\mathbf{k}_1|^2}{k^2 k_1^2} \frac{(qs)^2}{|\Delta\omega - \mathbf{qu}|} \times \delta(\Delta\omega^2 - q^2 s^2)\, \delta(|\omega_1 - \mathbf{k}_1 \mathbf{u}|^2 - \Omega^2), \tag{17}$$

where $\Delta\omega = \sqrt{\Omega^2 + c^2 k^2} - \omega_1$ and $\mathbf{q} = \mathbf{k} - \mathbf{k}_1$.

It is easily seen that the function $U(\mathbf{k})$ approaches infinity for $u \approx s$, if $\cos\theta \rightarrow \frac{c^2 k}{2\Omega u}$. The coefficient of the resonance factor $\left(\frac{c^2 k^2}{2\Omega} - \mathbf{ku}\right)^{-1}$ can be estimated by integrating equation (17) with respect to k_1 up to $k_1 = \tilde{a}^{-1}$, where $\tilde{a}$ is a quantity equal in its order of magnitude to a few Debye lengths. Then

$$U(\mathbf{k}) = \frac{e^2 T_e \sin^2\theta}{m\tilde{a}^3} \left| \frac{c^2 k^2}{2\Omega} - \mathbf{ku} \right|^{-1}. \tag{18}$$

Note that according to (15) and (18) the radiation from the plasma due to the conversion of a Langmuir wave (fluctuation or extraneous) into a transverse wave is anomalously large in the long-wave region only, where $k \sim \frac{\Omega u}{c^2}$.

Let us now consider the scattering of Langmuir waves by sound waves, generating secondary Langmuir waves. Applying (11), (12), (13), we find for the coefficient of scattering

$$d\sigma = \frac{\pi^2 e^2}{2m} \frac{(qs)^2}{|\Delta\omega - \mathbf{qu}|} \cos^2\vartheta\, \delta(\Delta\omega^2 - q^2 s^2) \frac{d\mathbf{k}}{(2\pi)^3}, \tag{19}$$

where $\Delta\omega = \frac{3}{2}\Omega a^2 (k^2 - k_0^2) + \mathbf{qu}$ is the change in frequency on scattering and ϑ is the scattering angle (the angle between the vectors $\mathbf{k}_0$ and $\mathbf{k}$). Integrating $d\sigma$ with respect to the magnitude of the vector $\mathbf{k}$, we see that $\frac{d\sigma}{do}$ is infinite when

$$(\cos\theta - \cos\theta_0)^2 = \left(2\frac{s}{u}\sin\frac{\vartheta}{2}\right)^2. \tag{20}$$

Near the directions specified by relation (20), $\frac{d\sigma}{do}$ has the form

$$\frac{d\sigma}{do} = \frac{e^2 k_0^2}{16\pi m} \frac{\sin\frac{\vartheta}{2}\cos^2\frac{\vartheta}{2}\,|u\cos\theta_0 + 3\Omega a^2 k_0|^{-1}}{\left|\frac{u}{s}(\cos\theta_0 - \cos\theta) \pm 2\sin\frac{\vartheta}{2}\right|}. \tag{21}$$

Transformation of waves in a plasma with a beam

Let us consider the transformation of waves in a plasma with a beam. The most important case is when the velocity of the beam is close to the critical velocity for which the Langmuir waves with a wave vector equal to the change in the wave vector on scattering become unstable. The

potential correlation function in this case contains a term /7/*

$$<\varphi^2>^L_{q\omega} = \frac{2(2\pi)^2\Omega^2 T_1}{q^2|\omega - \mathbf{qu}|}\delta(\omega^2 - \Omega_q^2), \tag{22}$$

which may be anomalously large. Here $\Omega_q^2 = \Omega^2 + 3\Omega^2(aq)^2 - (\Omega\Omega_1)^2\frac{m}{q^2T_1}$, $\Omega_1^2 = \frac{4\pi e^2 n_1}{m}$; $\mathbf{u}$, T_1, and n_1 are the mean velocity, temperature, and density of the beam (to avoid ambiguity, a hot beam is assumed).

Let us first deal with the "glow" resulting from the conversion of two longitudinal fluctuation waves into a transverse wave. This "glow" is attributable to processes of two kinds: mutual scattering of two Langmuir waves and scattering of a Langmuir wave by low-frequency fluctuations.

In the low-frequency region $\left(\omega \ll q\sqrt{\frac{T}{M}}\right)$, the correlation function of potential fluctuations is /1, 2, 3/

$$<\varphi^2>^D_{q\omega} = \frac{T^2}{4e^2 n_0 q}\left(\frac{2\pi M}{T}\right)^{1/2}, \tag{23}$$

where T is the temperature of the plasma. Substituting this expression in (8) and applying (12), we find

$$U^D(\mathbf{k}) \sim 0.4\frac{e^2\Omega^2 T_1}{m}\int d\mathbf{k}_1\frac{[\mathbf{kk}_1]^2}{k^2k_1^2}\frac{\delta(\omega^2 - \Omega_{k_1}^2)}{\Omega_{k_1} - \mathbf{k}_1\mathbf{u}}, \tag{24}$$

where the integral is taken in the region $|\mathbf{k}_1\mathbf{u}| < \Omega_{k_1}\left(1 - \frac{1}{\Delta}\right)$; Δ is a large parameter characterizing the maximum permissible amplitude of critical fluctuations (this "cutoff" parameter may be determined only in the framework of the nonlinear theory). From (24) we see that transformation produces long-wave transverse radiation, $k \ll \frac{\Omega}{c}$. Taking $\frac{ck}{\Omega} \gg \left(\frac{n_1 T}{n_0 T_1}\right)^{1/4}$, we find for the coefficient of transformation

$$U^D(\mathbf{k}) \sim 0.3\cdot\frac{e^2 T_1}{mua^2}\ln\Delta. \tag{25}$$

Let us now find the contribution to $d\Sigma$ from the scattering of Langmuir waves by Langmuir waves. The function $\mathbf{C}$, according to (4), is

$$\mathbf{C}(\mathbf{k}_1, \omega_1; \mathbf{k}_2, \omega_2) = \frac{e}{m}\left(\frac{\Omega}{\omega_1 + \omega_2}\right)^2\frac{\mathbf{k}_1}{\omega_2}\left(\frac{k_2^2}{\omega_2} - \frac{k_1^2 - k_2^2}{\omega_1 + \omega_2}\right). \tag{26}$$

Substituting (22) and (26) in (8), we find

$$U^L(\mathbf{k}) = \frac{e^2\Omega^8 T_1^2}{2m^2\omega^2}\int\frac{d\mathbf{k}_1 d\omega_1[\mathbf{kk}_1]^2}{(\mathbf{k} - \mathbf{k}_1)^2(\omega - \omega_1)^2 k^2k_1^2}\times$$
$$\times\left|\frac{(\mathbf{k} - \mathbf{k}_1)^2}{\omega - \omega_1} - \frac{2\mathbf{kk}_1 - k^2}{\omega}\right|^2\frac{\delta(\omega_1^2 - \Omega_{k_1}^2)\,\delta(|\omega - \omega_1|^2 - \Omega_{\mathbf{k}-\mathbf{k}_1}^2)}{|\omega_1 - \mathbf{uk}_1|\cdot|(\omega - \omega_1) - \mathbf{u}(\mathbf{k} - \mathbf{k}_1)|}. \tag{27}$$

* Neglecting the nonlinear effects of the interaction between fluctuations, we may use formula (22) in the region of frequencies ω and wave vectors $\mathbf{q}$, where the plasma oscillations do not grow.

where the integral is taken in the region $\widetilde{a}k_1 < 1$, $|\mathbf{uk}| < \Omega_{k_1}\left(1 - \frac{1}{\Lambda}\right)$, $|\mathbf{u}(\mathbf{k} - \mathbf{k}_1)| <$ $< \Omega_{k-k_1}\left(1 - \frac{1}{\Lambda}\right)$.

It can be verified that U^L, like U^D, has no poles attributable to critical fluctuations. In orders of magnitude, U^L is equal to

$$U^L(\mathbf{k}) \sim 0.1 \frac{e^2 T_1^2}{m^2 u \widetilde{a}^4} \ln \Delta \delta (c^2 k^2 - 3\Omega^2). \tag{28}$$

Let us determine the coefficient of conversion of an extraneous Langmuir wave into a transverse wave. Applying (9), (22), (26), we find

$$d\sigma = \frac{\pi^2 e^2 (\Omega^2 + c^2 k^2) T_1 (3q^2 - k_0^2)^2}{128 m^2 \Omega^2 q^2 |\Delta\omega - \mathbf{qu}|} \sin^2\vartheta \times \delta(\Delta\omega^2 - \Omega_q^2) \frac{d\mathbf{k}}{(2\pi)^3}, \tag{29}$$

where $\Delta\omega = \sqrt{\Omega^2 + c^2 k^2} - \Omega_{k_0}^2$ and $\mathbf{q} = \mathbf{k} - \mathbf{k}_0$.

It is easily seen that for $|\mathbf{qu}| \to \Omega_q$, the coefficient of the delta-function in this expression increases indefinitely.

Integrating (29) with respect to the magnitude of the vector $\mathbf{k}$, we find

$$\frac{d\sigma}{do} = \frac{\sqrt{3} \cdot e^2 \Omega T_1}{64 \pi m^2 c^3} \frac{k_0^2 \sin^2\vartheta}{\Omega + \mathbf{k}_0 \mathbf{u}} \tag{30}$$

(it is assumed that $\Omega \ll ck_0$). We see that if the projection of the wave vector of an extraneous Langmuir wave on the direction $\mathbf{u}$ is close to $\kappa - \frac{\Omega}{u}$, the ratio $\frac{d\sigma}{do}$ characterizing the amplitude increment, in unit time, of the transverse waves propagating in a certain direction is anomalously large.

BIBLIOGRAPHY

1. SALPETER, E. E. – Phys. Rev. 120: 1528. 1960.
2. AKHIEZER, A. I., I. A. AKHIEZER, and A. G. SITENKO. – JETP, 41: 644 1961.
3. ROSTOKER, N. – Nuclear Fusion, 1: 101. 1961.
4. DOUGHERTY, J. P. and D. T. FARLEY – Proc. Roy. Soc., A259: 79. 1960.
5. ICHIMARU, S., D. PINES and N. ROSTOKER. – Phys. Rev. Letters, 8: 231. 1962.
6. BOGDANKEVICH, L. C. A. A. RUKHADZE, and V. P. SILIN. – Izv. vuzov, Radiofizika, 5: 1093. 1962.
7. [Not given.]

O. S. Pavlichenko and L. A. Dushin

PLASMA DIAGNOSTICS UTILIZING THE SCATTERING OF ELECTROMAGNETIC WAVES

The interaction of electromagnetic waves with plasma is one of the most effective tools of plasma diagnostics. Various methods of active probing of a plasma with centimeter and millimeter radio waves have been developed, and they yield extensive information on the properties of the plasma in different plasma-generating facilities. However, active probing is suitable for measuring macroscopic plasma characteristics only: its maximum density, from the cutoff of a microwave signal, or the density averaged over the path of the signal, by interferometric techniques (with fairly dense plasmas, the measurements should be made in the optical region, with an optical interferometer). A reflected microwave signal establishes the position and the speed of a plasma layer having a certain critical density.

There is, however, another technique of active plasma probing, namely the analysis of the incoherent scattering of electromagnetic waves in a plasma. The spectral characteristics of an electromagnetic signal scattered at a certain angle in a plasma yield much more information. In particular, under certain conditions, the spectrum of the scattered signal is broadened by the thermal motion of the ions (although the electrons are responsible for the actual scattering) and is thus indicatory of the ion plasma temperature. Weak satellites appear, having the frequencies $\omega = \Omega_0 \pm \omega_p$, where Ω_0 is the probing frequency, and ω_p is the electron plasma frequency.

In this paper we consider the experimental possibilities of scattering of electromagnetic waves in the microwave and the optical region and deal with the optimal choice of probing frequency and power.

Intensity and spectrum of scattered radiation

Consider a plane wave incident on a plasma volume V. The frequency Ω_0 of the wave is chosen so that the wave is transmitted through the plasma, i.e., $\Omega_0 > \omega_p$. The electric field $\mathbf{E}_{scat}$ of the scattered wave should satisfy Maxwell's equation. Integrating this equation by parts and seeing that $\operatorname{div} \mathbf{J} + \frac{\partial n}{\partial t} = 0$, we write for the scattered wave in the wave zone /4/

$$\mathbf{E}_{scat}(\mathbf{x}, t) = -\frac{1}{c^2} \int dt' \int_V d\mathbf{x}' \frac{\delta\left[t' - t + \frac{|\mathbf{x} - \mathbf{x}'|}{c}\right]}{|\mathbf{x} - \mathbf{x}'|} \left\{\frac{\partial \mathbf{J}(\mathbf{x}', t')}{\partial t'} - \frac{\mathbf{x}\left(\mathbf{x}\frac{\partial \mathbf{J}}{\partial t'}\right)}{|\mathbf{x} - \mathbf{x}'|^2}\right\}. \tag{1}$$

The current density in the plasma may be written as

$$\mathbf{J}(\mathbf{x}, t) = \sum_n q_n \mathbf{v}_n(t) \delta[\mathbf{x} - \mathbf{x}_n(t)],$$

then

$$\frac{\partial \mathbf{J}}{\partial t} = \sum_n [q_n \dot{\mathbf{v}}_n \delta(\mathbf{x} - \mathbf{x}_n) - q_n \mathbf{v}_n \mathbf{v}_n \nabla \delta(\mathbf{x} - \mathbf{x}_n)], \tag{2}$$

where $\dot{\mathbf{v}} = \frac{q_n}{m_n} \mathbf{E}(\mathbf{x}_n, t)$, and $\mathbf{E}(\mathbf{x}_n, t) \sim \mathbf{E}_0 \cos(\Omega_0 t - \mathbf{k}\mathbf{x}_n)$, E_0 the field of the incident wave, q_n and m_n the charge and the mass of the particles.

The second term in (2) is omitted, since it is not dependent on E and is of no relevance in connection with the scattered wave. In the first term, the contribution of the electrons prevails, since $m_e \ll m_i$. Hence

$$\frac{\partial \mathbf{J}}{\partial t} \simeq \frac{e^2}{m} \mathbf{E}_0 \cos(\Omega_0 t - \mathbf{k}\mathbf{x})\, n_e(\mathbf{x}, t), \tag{3}$$

where $n_e(\mathbf{x}, t) = \Sigma_n \delta\,[\mathbf{x} - \mathbf{x}_n(t)]$ is the electron density.

It can be shown that in the wave zone, a receiver placed at a distance x from the scattering volume and having a passband $\left(\omega - \frac{1}{2}\Delta\omega,\ \omega + \frac{1}{2}\Delta\omega\right)$ will receive signals of amplitude

$$\Delta\mathbf{E}_{\mathrm{scat}}(\mathbf{x}, t) = -\frac{e^2}{mc^2}\frac{1}{|\mathbf{x}|}[\mathbf{E}_0 - \mathbf{N}(\mathbf{N}\cdot\mathbf{E}_0)] \int\limits_{\omega - \frac{1}{2}\Delta\omega}^{\omega + \frac{1}{2}\Delta\omega} \frac{d\omega}{2\pi} \cdot \mathrm{Re}\Big[e^{i\omega\left(t - \frac{|\mathbf{x}|}{c}\right)} \times$$
$$\times\, n_e\left(\mathbf{k} - \frac{\omega}{c}\mathbf{N},\ \omega - \Omega\right)\Big].$$

Let us consider the variation of the mean square of this quantity:

$$\lim_{T\to\infty} \frac{1}{T}\int \left|\Delta\mathbf{E}_{\mathrm{scat}}(t)\right|^2 dt = \frac{nVa_0^2}{|\mathbf{x}|^2}\left|\mathbf{E}_0\right|^2 \cdot [1 - \sin^2\alpha\,\cos(\varphi - \varphi_0)] \times$$
$$\times\, S\left(\mathbf{k} - \frac{\omega}{c}\mathbf{N},\ \omega - \Omega_0\right)\cdot\frac{\Delta\omega}{2\pi},\quad a_0 = \frac{e^2}{mc^2}, \tag{4}$$

where $S(\mathbf{k}, \omega) = \lim\limits_{\substack{V\to\infty\\ T\to\infty}} \frac{2}{VT}\left[\frac{|\mathbf{n}_e(\mathbf{k}, \omega)|^2}{n}\right]$ is the spectral density of electron density fluctuations — the dynamic formfactor of the electrons; n the electron density; α the angle between the directions of the incident and the scattered waves; φ and φ_0 angles defining the position of $\mathbf{N}$ and $\mathbf{E}_0$. For a nonpolarized wave, averaging over φ_0 gives the angular factor $\left(1 - \frac{1}{2}\sin^2\alpha\right)$.

The differential cross section for the scattering of electromagnetic waves by electron density fluctuations is thus

$$\frac{d^2\sigma}{d\Omega d\omega} = \left(\frac{e^2}{mc^2}\right)^2 NS(\mathbf{k}, \omega)\left(1 - \frac{1}{2}\sin^2\alpha\right), \tag{5}$$

where N is the total number of electrons interacting with the wave. Calculation of the scattering cross section reduces to the determination of $S(\mathbf{k}, \omega)$.

The dynamic formfactor of electrons

The electron dynamic formfactor was calculated by various authors /1—5/ for plasmas in thermal equilibrium and with an arbitrary ratio $\frac{T_e}{T_i}$.

Detailed calculations were also made for electron distribution functions unstable with respect to electron plasma oscillations, i.e., electrons drifting with a velocity V_d relative to the ions /5/ and plasma—beam systems /6/.

The simplest expression for the electron dynamic formfactor is obtained by the superposition of "dressed" particles /4, 5/. This method analyzes the screening of a test particle injected into a plasma by the charged particles clustering around it. The underlying principle of the superposition method asserts that if the particle is "dressed", i.e., the screening effects are properly introduced, its motion can be treated as the motion of a free particle. In particular, density fluctuations of "dressed" electrons in a two-component plasma of electrons and protons have the form /4/

$$\Delta n(\mathbf{k}, \omega) = \left|1 - \frac{4\pi\alpha_e(\mathbf{k}, \omega)}{\varepsilon(\mathbf{k}, \omega)}\right| 2\pi\delta(\mathbf{k}\mathbf{v}_e - \omega) + \frac{4\pi\alpha_i(\mathbf{k}, \omega)}{\varepsilon(\mathbf{k}, \omega)} 2\pi\delta(\mathbf{k}\mathbf{v}_e - \omega),$$

where $\alpha_{e,i}(\mathbf{k}, \omega)$ is the electron and ion polarizability,

$$\alpha_{e,i}(\mathbf{k}, \omega) = \lim_{\psi\to 0} \frac{ne^2}{m_{e,i}k^2} \int \frac{k\nabla_v f_{e,i}(\mathbf{v})}{kv - \omega - i\psi}\, d\mathbf{v},$$

m electron and ion mass, $f_{e,i}(\mathbf{v})$ electron and ion velocity distribution function, $\varepsilon(\mathbf{k}, \omega)$ longitudinal permittivity.

The dynamic formfactor is obtained as the Fourier transform of the even correlation function and has the form

$$S(\mathbf{k}, \omega) = \frac{N}{k} \cdot f_e\left(\frac{\omega}{k}\right)\left|\frac{1 + 4\pi\alpha_i(\mathbf{k}, \omega)}{\varepsilon(\mathbf{k}, \omega)}\right|^2 + \frac{N}{k} f_i\left(\frac{\omega}{k}\right)\left|\frac{4\pi\alpha_e(\mathbf{k}, \omega)}{\varepsilon(\mathbf{k}, \omega)}\right|^2. \tag{6}$$

The fluctuation spectrum can be calculated as soon as the distribution functions and $\varepsilon(\mathbf{k}, \omega)$ are known. Note that the formfactor may take very large values near points having $\varepsilon(\mathbf{k}, \omega) = 0$, i.e., near the roots of the dispersion relation for the collective oscillations. This quantity is limited only by the nonlinear effects.

Let us consider some estimates of $S(\mathbf{k}, \omega)$ for different cases.

Plasma with $T_e = T_i = T$. For a plasma in thermal equilibrium

$$S(\mathbf{k}) = \frac{k^2 + k_D^2}{k^2 + 2k_D^2},$$

where $k_D^2 = \frac{4\pi ne^2}{T}$,

$$S(\mathbf{k}) = \begin{cases} \frac{1}{2} & \text{for } k^2 \ll k_D^2 \text{ (long waves)}, \\ 1 & \text{for } k^2 \gg k_D^2 \text{ (short waves)}. \end{cases}$$

In this case $S(\mathbf{k}, \omega) = S_1(\mathbf{k}, \omega) + S_2(\mathbf{k}, \omega)$, where

$$S_1(\mathbf{k}, \omega) = \frac{N}{k} f_e\left(\frac{\omega}{k}\right) \cdot \left|\frac{1 + 4\pi\alpha_i(\mathbf{k}, \omega)}{\varepsilon(k, \omega)}\right|^2,$$
$$S_2(\mathbf{k}, \omega) = \frac{N}{k} f_i\left(\frac{\omega}{k}\right) \cdot \left|\frac{4\pi\alpha_e(\mathbf{k}, \omega)}{\varepsilon(k, \omega)}\right|^2.$$

The function $S_1(\mathbf{k}, \omega)$ is proportional to $f_e\left(\frac{\omega}{k}\right)$ and the width of its spectrum is $\Delta\omega \approx kv_{T_e} = k\sqrt{\frac{T}{m}}$; neglecting the ion polarizability $S_1(\mathbf{k}) = \frac{k^2}{k^2 + k_D^2}$ and assuming long wavelengths, we see that the contribution of $S_1(\mathbf{k})$ in $S(\mathbf{k}) \approx \frac{k^2}{k_D^2}$ is very small; in the case of short wavelengths, $S_1(\mathbf{k})$ dominates. The spectrum has the form $S(\mathbf{k}, \omega) = \frac{N}{k} f_e\left(\frac{\omega}{k}\right)$ with a width $\Delta\omega \approx k\ v_{T_e}$.

The function $S_2(\mathbf{k}, \omega)$ is associated with the electrons forming the screening cloud around the ions, and it is proportional to $f_i\left(\frac{\omega}{k}\right)$ with a width $\Delta\omega \sim kv_{T_i}$; $S_2(\mathbf{k}) = \frac{k_D^4}{(k^2 + k_D^2)\cdot(k^2 + 2k_D^2)}$, and for long wavelengths $S_2(\mathbf{k}) = \frac{1}{2}$ makes the main contribution in $S(\mathbf{k}, \omega)$. For $k^2 \gg k_D^2, S_2(\mathbf{k}) = \frac{k_D^4}{k^4}$ and its contribution is vanishingly small.

Summing up the results for a plasma with $T_e = T_i$ in the two extreme cases of long and short wavelengths, we may say that in the long-wave case the width of the spectrum $S(\mathbf{k}, \omega)$ characterizes the ion plasma temperature and $S(\mathbf{k}) = \frac{1}{2}$, while in the short-wave case the spectrum $S(\mathbf{k}, \omega)$ is representative of the electron temperature and $S(\mathbf{k}) = 1$.

Nonequilibrium plasma $(T_e \gg T_i)$. In a nonequilibrium plasma, with $T_e \gg T_i$, fairly stable acoustic waves may propagate, having the frequency

$$\omega_k = \sqrt{\frac{T_e}{M}}\, k = kv_s$$

Near acoustic resonances, the permittivity has the form $(k^2 \ll k_D^2)$

$$\varepsilon(\mathbf{k}, \omega) = \frac{k_D^2}{k^2}\left\{1 - \frac{\omega_k^2}{\omega^2} + i\pi\frac{\omega}{k}\left[f_e\left(\frac{\omega}{k}\right) + \frac{T_e}{T_i} f_i\left(\frac{\omega}{k}\right)\right]\right\}$$

and $S(\mathbf{k})$ is written as

$$S(\mathbf{k}) = \frac{f_e(v_s) + f_i(v_s)}{f_e(v_s) + \frac{T_e}{T_i} f_i(v_s)} \approx 1$$

We see that $S(\mathbf{k})$ is twice as great as in the first case. The spectrum $S(\mathbf{k}, \omega)$ in the long-wave region thus consists of two satellites with $|\Delta\omega| \approx kv_s$. The integral expression for $S(\mathbf{k})$ in each satellite amounts to half the total $S(\mathbf{k})$; since the satellites are narrow, they stand out from the general spectrum of the fluctuations.

Current-carrying plasma. In a plasma with $T_e \gg T_i$, in the presence of net electron drift, one of the acoustic plasma waves $\omega = kv_s$ may grow in amplitude, while the other is highly damped. If the drift velocity is fairly high, the sound wave becomes unstable, the fluctuations grow rapidly, and this growth is limited only by nonlinear effects. An analysis shows /5/ that the spectrum $S(\mathbf{k}, \omega)$ is the same as in the second case, but now it displays a certain asymmetry: the unstable wave will sharply raise the formfactor only for a single value $\Delta\omega \simeq kv_s$.

Plasma with a "beam". A plasma with an electron velocity distribution

$$n(v_z) = n_0 \sqrt{\frac{m}{2\pi T\varkappa}} \exp\left(-\frac{mv_z^2}{2T\varkappa}\right) + n_1 \sqrt{\frac{m}{2\pi T\varkappa}} \exp\left[-\frac{m}{2T\varkappa}(v_z - u)^2\right],$$

($n_1 \ll n_0$, u the velocity of the "beam") is unstable relative to electron plasma oscillations if $u > v_{Te} = \sqrt{\frac{T}{m}}$. This instability, even for small frequency increments $\left(\frac{\gamma}{\omega} \ll 1\right)$ may sharply increase the scattering cross section near $\Delta\omega \sim \omega_p$. The cross section increases since the energy lost by the beam to the plasma waves, though small in comparison with the thermal energy, may be much higher than the energy of plasma waves in thermal equilibrium.

This case was considered by W. Drummond /6/. He showed that for a plasma with a weak beam the scattering cross section increases due to the onset of instability at the frequency $\omega \approx \omega_p$ by

$$\beta = \frac{8\pi^2 R}{\left(\frac{k}{k_D}\right)^3} \frac{\gamma}{\omega_p} \bigg| \frac{n}{k_D^3},$$

where

$$R \approx \frac{1}{2} \ln \frac{8\pi^2}{\left(\frac{k}{k_D}\right)^3} \left(\frac{\gamma}{\omega_p}\right) \frac{n}{k_D^3},$$

γ the frequency increment.

Numerical estimates for a typical case of experiments with electron beams in a plasma /7/ show that for signals of λ = 3 cm the scattering cross section may increase by as much as 10^{12}.

Experimental investigation of scattering of electromagnetic waves

The scattering of electromagnetic waves can be investigated experimentally in the optical and the microwave regions, where sufficiently powerful generators are now available: quantum optical generators (lasers) and powerful masers are eminently suitable for scattering experiments. Let us consider the experimental possibilities in the two regions separately.

Optical region. A ruby laser can be applied: it generates radiation at a wavelength of 6943 Å and has an intrinsic line half-width of 0.1 Å. The simplest lasers have a yield of ≈ 1 joule per pulse, which for pulse lengths of ≈ 10^{-3} sec ensures a power output of 1 kW. Pulsed Q modulation gives a power output of up to 10^7 W over times of ≈ 10^{-7} sec with the same specimens.

When a laser beam is scattered in a plasma, the collective effects become noticeable only for $k^2 \lesssim k_D^2$; the spectrum of the scattered signal in this case has a Doppler width which is indicatory of the temperature of the ions. The condition $k^2 \lesssim k_D^2$ imposes restrictions on the parameters of the probed plasma. Figure 1 shows the region (n, T) where scattering is governed by collective effects (the region limited by the triangle).

Scattered radiation can be observed only if the natural radiation from the plasma near the probing frequency is less powerful than the reflected

signal. In a fully ionized hydrogen plasma near $\lambda = 7000\,\text{Å}$ it is only the bremsstrahlung and the recombination radiation that need be considered. Let us estimate the power of the bremsstrahlung and the recombination radiation in a spectral interval equal to the width of the scattered laser line. The expression for the spectral power density of bremsstrahlung and recombination radiation is /8/

$$W(T,\ \nu)\,d\nu = \frac{4\pi N_i N_e h}{\varkappa T} R \sqrt{\frac{8\varkappa T}{\pi m}}\, e^{-\frac{h\nu}{\varkappa T}} [\bar{g}(T,\ \nu) + f(T,\ \nu)]\,d\nu,$$
$$f(T,\ \nu) = 2\Theta \sum_{n=m(\nu)}^{\infty} n^{-3} e^{\Theta/n^2} g_n(\nu), \tag{7}$$

where $R = \frac{4\pi e^4}{3\sqrt{3} m h c^3}$; $\Theta = \frac{h\nu_0}{\varkappa T}$; $g_n(\nu)$ is the Gaunt factor for free-bound transitions; $h\nu_0 = E_i$ hydrogen ionization energy.

Applying this expression, we calculated (Figure 2) the power radiated by the plasma in the spectral interval corresponding to the scattering line ($\lambda = 7000\,\text{Å}$, dashed line), for plasma temperatures of 1, 10, and 100 eV. The function lg P vs. lg N is nonmonotonic, since the scattered line becomes narrower as we move to the $(n,\ T)$ region where the collective processes determine the width of the Doppler maximum. To permit comparison with the scattered laser power, the same figure gives (solid line) the corresponding results for lasers with a power output of 1 kW, 100 kW, and 10 MW (for a one-way passage of the light beam through the plasma).

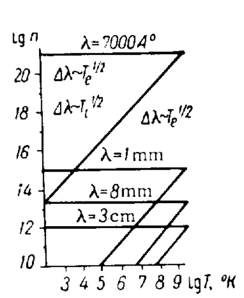

FIGURE 1.

The total power of the light scattered by the plasma can be substantially increased if the beam is allowed to pass several times through the plasma volume. One of the schemes for multiple passage of the laser beam through the plasma is shown in Figure 3: 1 is the ruby, 2 dielectric reflectors, 3 plane-parallel glass plates, 4 the volume with the plasma. This arrangement is superior to the scheme which calls for the introduction of the plasma directly into the resonant cavity: here the defocusing influence of the glass vessel confining the plasma and the enhanced scattering by the glass have no detrimental effect on the Q of the system. Multiple passage of the light beam through the plasma increases the scattered power by one order of magnitude and thus improves the signal-noise ratio for the same power output.

There are certain difficulties involved in light-scattering experiments, connected with the powerful scattering by extraneous objects (the plasma vessel): this spurious scattering may exceed by several orders of magnitude the power of the signal scattered by the plasma proper. In this case the signal-noise ratio can be improved by making use of the constant spectral composition of the spurious scattered light. Since the intrinsic line width of a laser is of the order of 10^{-9} cm, presumably with a Gaussian profile, it can be shown that at a sufficient distance from the line peak the intensity of the radiation scattered from the plasma is substantially higher than the intensity of the spurious line at the same point. For example, at a distance

$\Delta\lambda = \Delta\lambda_D$ determined by the Doppler temperature of the plasma electrons $(\Delta\lambda_D = \lambda_0 \frac{v_{Te}}{c})$, the signal-noise ratio is

$$\frac{I_{\text{scat}}(\Delta\lambda)}{I_{\text{spur}}(\Delta\lambda)} = \sigma_0 N \frac{\Delta\lambda_0}{\Delta\lambda_D} e^{\left(\frac{\Delta\lambda_D}{\Delta\lambda_0}\right)^2},$$

where $\sigma_0 = a_0^2$ is the scattering cross section; N the total number of particles interacting with the light wave; $\Delta\lambda_0$ the intrinsic width of the laser line; $\Delta\lambda_D$ Doppler width of the scattered line.

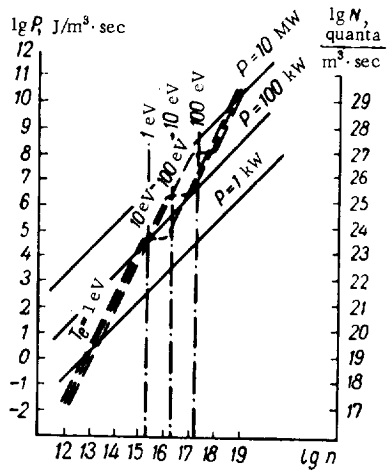

FIGURE 2.

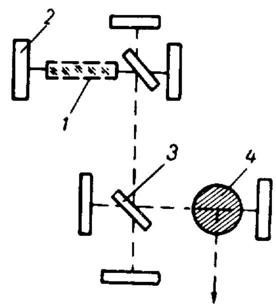

FIGURE 3.

We thus see that for sufficient spectral resolution, at a sufficient distance from the line peak, the intensity of the spurious signal is much less than the intensity of the radiation scattered by the plasma.

Summing up, we may say that application of lasers in the 100 kW range and schemes with multiple passage of the light beam through the plasma give an acceptable signal-noise ratio for experiments in a wide range of plasma parameters.

Microwave region

Experiments in the microwave region are feasible with the aid of fairly powerful centimeter- or millimeter-wavelengths generators. Figure 1 depicts the regions where collective effects prevail for radio waves of various wavelengths. We see that under the relevant conditions in plasmas, the scattering of millimeter waves is governed by the collective effects.

In the microwave region, "noise" constitutes the thermal equilibrium radiation from the plasma. It is known /9/ that the power of the equilibrium radiation emitted by a plasma per unit of its surface is

$$P(\omega, T)\, d\omega = \frac{\omega^2}{8\pi^3 c^2} kT_e \Delta\omega,$$

provided that the plasma volume is large enough for blackbody radiation. The power radiated by the plasma in the spectral interval corresponding to the scattered line is $\left(\Delta\omega - \omega \frac{v_{Ti}}{c}\right)$

$$P(\omega,\ T)\,d\omega = \frac{1}{\lambda^3} \cdot \frac{(\varkappa T_e)^{3/2}}{M^{1/2}}.$$

If the plasma volume is not large enough to sustain equilibrium, the main contribution is due to bremsstrahlung, which is calculated from formula (7) above (here $h\nu \ll \varkappa T_e$). The results of these calculations are shown in Figure 4; for plasma temperatures of 1 and 10 eV, we have plotted the power radiated by the plasma at λ = 3 cm. The horizontal sections represent transition to blackbody radiation (for plasma volumes of 1 cm^3). The same figure gives the scattered power for a 1 W signal; the vertical line indicates the "cutoff" of the probing signal at the given wavelength.

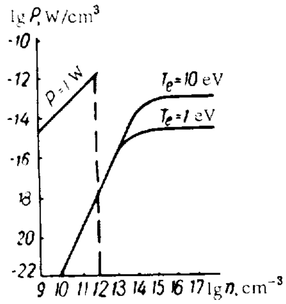

FIGURE 4.

We thus see that in experiments with microwave scattering the natural radiation of the plasma is of no practical significance, and the various experimental difficulties are confined to coping with spurious scattering.

BIBLIOGRAPHY

1. AKHIEZER, I. A., A. I. AKHIEZER, and A. G. SITENKO. – JETP, **41**: 644. 1961.

2. DOUGHERTY, J. and D. FARLEY. – Proc. Roy. Soc., **A259**: 79. 1960.

3. SALPETER, E. – Phys. Rev., **122**: 1663. 1961.

4. ISHIMARY, S. – Annals of Physics, **20**: 78. 1962.

5. ROSENBLUTH, M. and N. ROSTOKER. – Phys. Fluids, **5**: 776. 1962.

6. DRUMMOND, W. – Phys. Fluids, **5**: 1133. 1962.

7. KHARCHENKO, I. F. et al. – In "Fizika plazmy i problemy upravlyaemogo termoyadernogo sinteza", Vol. 2, p. 118. Kiev, Izdatel'stvo AN UkrSSR. 1963.

8. BRUSSAARD, P. and H. van de HULST. – Rev. Mod. Phys., **34**: 507. 1962.

9. BEKEFI, G. and S. BROWN. – Amer. Journ. Phys., **29**: 404. 1961.

L. A. Dushin, V. I. Privezentsev, and A. I. Skibenko

PLASMA DIAGNOSTICS UTILIZING THE EXTRAORDINARY TRANSVERSE WAVE

It is only the ordinary transverse wave that has been previously applied for purposes of microwave plasma diagnostics, probably because the dispersion properties of the plasma in this case are not dependent on the external magnetic field. The extraordinary wave has been used only in studies of the electron cyclotron resonance /2, 3/.

However, if we examine the variation of permittivity and of the phase and damping coefficients as a function of plasma density, it becomes obvious that the extraordinary wave is highly suitable for estimating both the plasma density and the collision frequency. The most successful technique calls for simultaneous application of the ordinary and the extraordinary transverse waves, where the measurements are mutually complementary. This is also convenient in technical respects, since the plasma is in fact probed with waves of one frequency, but different polarizations.

Microwave cutoff measurements

Analyzing the propagation of the extraordinary wave across a collisionless plasma, we find for the dielectric constant /1/

$$\varepsilon = 1 - \frac{v(1-v)}{1-u^2-v}, \tag{1}$$

where

$$v = \frac{\omega_0^2}{\omega^2}; \quad \omega_0^2 = \frac{4\pi n e^2}{m};$$

$$u = \frac{\omega_H}{\omega}; \quad \omega_H = \frac{eH}{mc}.$$

Cutoff occurs when $\varepsilon = 0$. Hence it follows that the critical density for $u < 1$ can be found from

$$v_{1,3} = 1 \pm u. \tag{2}$$

Cutoff is also possible for $1 - u^2 - v = 0$, where ε is discontinuous (Figure 1) and the critical density at that point can be obtained from

$$v_2 = 1 - u^2. \tag{3}$$

For $u > 1$, there is but one cutoff at

$$v_1 = 1 + u. \tag{4}$$

Applying the extraordinary wave, we can thus take three density readings at a constant frequency if $u < 1$, and one density reading if $u > 1$. Characteristic oscillograms of the amplitude of the transmitted signals are

given in Figures 2 and 3. Measurements were made using the decaying plasma of the pulsed reflex discharge /4/. Ordinary wave probing was simultaneously applied for control purposes.

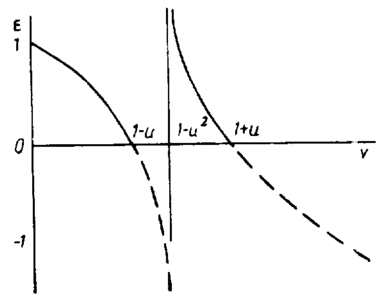

FIGURE 1. Dielectric constant vs. density.

In Figure 2 ($u < 1$), the cutoff times t_1, t_2, t_3, and t_4 correspond to the densities $v_1 = 1 + u$, $v_2 = 1 - u^2$, $v_3 = 1 - u$, and $v_4 = 1$, respectively. Since the measurements were made at 8-mm wavelength, in a magnetic field of 310 kA/m, the corresponding number densities are $n_1 = 2.2 \cdot 10^{13}$, $n_2 = 1.5 \cdot 10^{13}$, $n_3 = 1.2 \cdot 10^{13}$, and $n_4 = 1.7 \cdot 10^{13}$ el/cm^3. Hydrogen pressure 0.5 N/m^2. Time base 430 μsec.

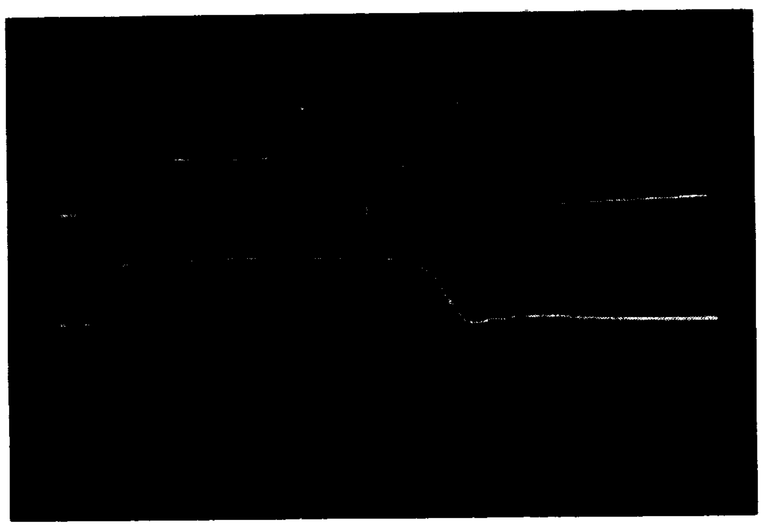

FIGURE 2. The amplitude of the extraordinary (top) and the ordinary (bottom) waves transmitted through the plasma:
H = 310 kA/m, λ = 8 mm, pressure 0.5 N/m^2.

In Figure 3 ($u > 1$), for a probing signal of 3.2-cm wavelength and a 600 kA/m magnetic field, the cutoff times t_1 and t_2 correspond to the

number densities $n_1 = 3.7 \cdot 10^{12}$ and $n_4 = 1.2 \cdot 10^{12}$ el/cm^3, respectively. Pressure 2 N/m^2. Time base 1800 μsec.

Under laboratory conditions, one sometimes deals with a plasma where collisions are not negligible. In this case, the transmission of the signal is altered considerably. No proper cutoff occurs here, since the refractive index cannot assume negative values, but the damping is so strong that the observed effect is equivalent to a cutoff. On certain approximation, we may therefore consider the influence of collision frequency on cutoff.

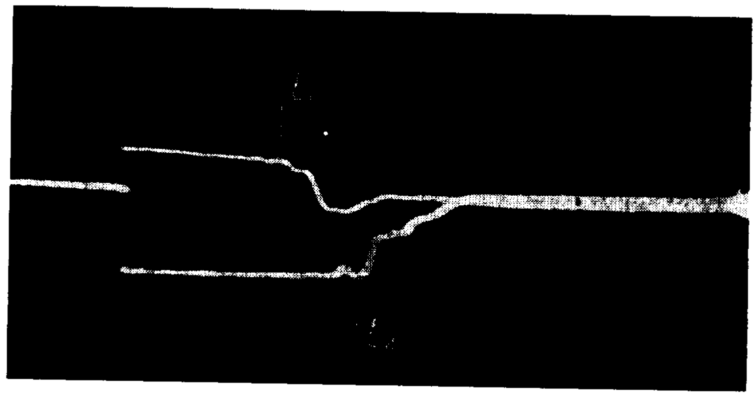

FIGURE 3. The amplitude of the extraordinary (top) and the ordinary (bottom) waves transmitted through the plasma:
$H = 600$ kA/m, $\lambda = 3.2$ cm, pressure 2 N/m^2.

The influence of collision frequency on the critical density in the case of the ordinary wave can be found fairly easily. Taking the permittivity equal to zero for $s' = \frac{\nu}{\omega} \ll 1$, we find for the critical density

$$\varepsilon' = 1 - \frac{v'}{1 + s^2}, \tag{5}$$

i.e.,

$$v' = 1 + s^2. \tag{6}$$

In the case of the extraordinary wave, the expression for ε is fairly complex:

$$\varepsilon = 1 - \frac{v\,[(1 - v)^2 - u^2 (1 - v) + s^2]}{(1 - v - u^2 - s^2)^2 + s^2 (2 - v)^2}; \tag{7}$$

it may have several solutions, depending on the relation among v, u, and s. The critical values of v are determined from the equality

$$v^3 - (3 - u^2 + s^2)\, v^2 + 3\,(1 - u^2 + s^2)\, v - [4s^2 + (u^2 - 1 + s^2)^2] = 0, \tag{8}$$

which after simple manipulations and the substitution $y = v - \frac{3 - u^2 + s^2}{3}$ is written as

$$y^3 + 3py + 2q = 0, \tag{9}$$

where

$$p = \frac{(s^2 - u^2)(3 - s^2 + u^2)}{9},$$

$$q = -\frac{1}{27}[9(s^4 + 4u^2s^2 + u^4) + (s^2 - u^2)^3]. \tag{10}$$

Equation (9) is best solved graphically. The intersections of the parabola $z = y^3$ with the straight line $z = -3py - 2q$ give the roots of the equation. The elegance of this approach is that the roots are found by plotting a single parabola and a family of straight lines corresponding to various u and s. One of the roots can be determined for the case of no collisions from the discontinuity of $\varepsilon(v)$, i.e., by setting the denominator in (1) equal to zero. Analysis shows that collisions make $\varepsilon(v)$ a continuous function for all real v, and its zeros are determined by (8) and (9).

The critical value of v is difficult to establish in the general case, and the result is fairly cumbersome. Investigation of equation (8) showed that for $s < 0.5$ application of the collisionless equations (2)—(4) did not lead to excessive errors.

The cutoff plasma density can thus be easily determined. To find the collision frequency, we must consider the damping of the wave in the plasma.

Damping measurements

The damping of the extraordinary wave propagating in a plasma is a function of the collision frequency, the magnetic field, and the density. The damping ratio is

$$\varkappa = \left\{-\frac{\varepsilon}{2} + \left[\left(\frac{\varepsilon}{2}\right)^2 + \left(\frac{2\pi\sigma}{\omega}\right)^2\right]^{1/2}\right\}^{1/2}, \tag{11}$$

where

$$\frac{4\pi\sigma}{\omega} = \frac{sv[(1-v)^2 + u^2 + s^2]}{(1 - v - u^2 - s^2)^2 + s^2(2 - v)^2};$$

σ the conductivity of the plasma; ε the dielectric constant (see (7)).

Figure 4 plots the damping ratio as a function of density for various magnetic fields and collision frequencies. We see that the damping decreases as the magnetic field and the collision frequency increase.

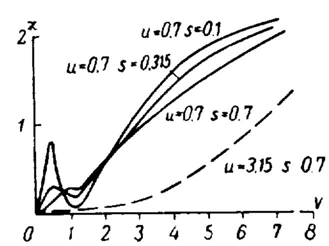

FIGURE 4. Damping ratio as a function of density.

For low collision frequencies, a damping minimum is observed in the region of densities $v_1 = 1 + u$ and $v_2 = 1 - u^2$. As the collision frequency

increases, the minimal damping becomes higher, and for large s the damping curves do not dip at all.

In certain limiting cases, the damping can be determined from relatively simple approximate relations. When s is small in comparison with other quantities, we have

$$\varepsilon = \frac{(1-v)^2 - u^2}{1 - v - u^2}, \tag{12}$$

$$\frac{4\pi\sigma}{\omega} = \frac{sv[(1-v)^2 + u^2]}{(1-v-u^2)^2}, \tag{13}$$

$$\varkappa = \frac{sv[(1-v)^2 + u^2]}{2(1-v-u^2)^{3/2}[(1-v)^2 - u^2]^{1/2}}. \tag{14}$$

For simultaneous application of the ordinary and the extraordinary waves, when $v = 1$, we have

$$\varepsilon = 1 - \frac{s^2}{(u^2+s^2)^2+s^2} = \frac{(u^2+s^2)^2}{(u^2+s^2)^2+s^2}, \tag{15}$$

$$\frac{4\pi\sigma}{\omega} = \frac{s(u^2+s^2)}{(u^2+s^2)^2+s^2}, \tag{16}$$

$$\varkappa = \sqrt{-1 + \sqrt{1 + \frac{s^2}{(u^2+s^2)^2}}} \cdot \frac{u^2+s^2}{\sqrt{2[(u^2+s^2)+s^2]}}. \tag{17}$$

When the ordinary wave is cut off, the extraordinary wave is transmitted with a certain attenuation η. Measuring this attenuation, we can find the

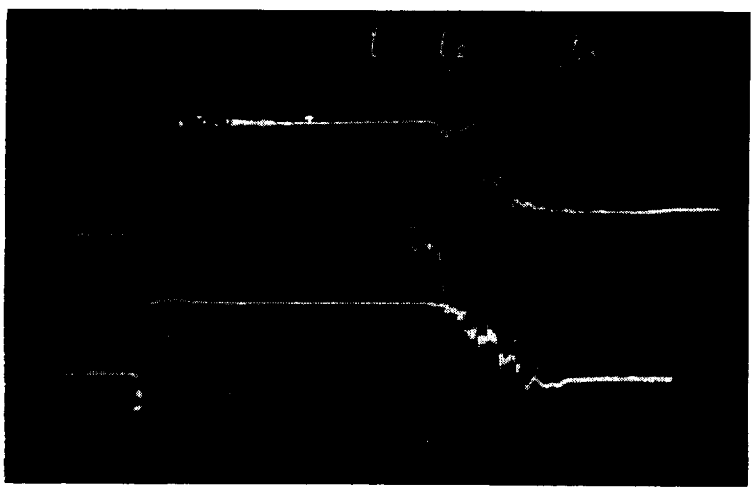

FIGURE 5. The amplitude of the extraordinary (top) and the ordinary (bottom) waves transmitted through the plasma; $H = 860$ kA/m, $\lambda = 8$ mm, pressure 0.5 N/m^2.

collision frequency if u is known. The calculations are particularly easy for $\frac{s}{u^2} \ll 1$, which is almost invariably true for transverse probing with

waves shorter than 3 cm. Then

$$\frac{4\pi\sigma}{\omega} \approx \frac{s}{u^2}, \tag{18}$$

$$\eta = \frac{\omega s}{cu^2}, \tag{19}$$

so that

$$s = \frac{\eta c u^2}{\omega}. \tag{20}$$

This formula, however, cannot be applied unless $s \ll 1$, which is necessary for the cutoff of the ordinary wave at $v = 1$.

Experimental measurements were made again in the decaying plasma of the pulsed reflex discharge. The characteristic oscillograms are shown in Figures 2, 5, 6. Figure 2 is an oscillogram of the amplitude of the transmitted signal for $u = 0.29$. The collision frequency for the ordinary wave cutoff time t_2 was calculated from (20) and found equal to $\nu = 3 \cdot 10^8\,\mathrm{sec}^{-1}$.

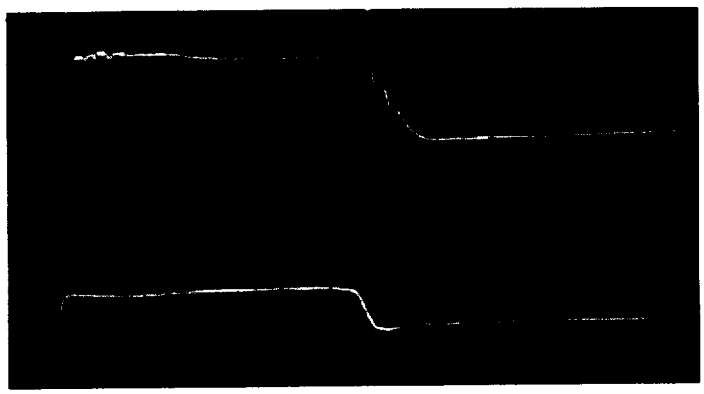

FIGURE 6. The amplitude of the extraordinary and the ordinary waves transmitted through the plasma:
$H = 620$ kA/m, $\lambda = 8$ mm, pressure 3 N/m^2.

Figure 5 is an oscillogram of the amplitude of the signal for the same pressure, but for a higher magnetic field and $u = 0.83$. The cutoff densities are $3 \cdot 10^{13}\,\mathrm{el/cm^3}$ for t_1, $4 \cdot 10^{12}\,\mathrm{el/cm^3}$ for t_2, $2.5 \cdot 10^{12}\,\mathrm{el/cm^3}$ for t_3, and $1.7 \cdot 10^{13}\,\mathrm{el/cm^3}$ for t_4. The collision frequency at the ordinary wave cutoff is $3 \cdot 10^9\,\mathrm{sec}^{-1}$. Time base $710\,\mu$sec. Figure 6 is a similar oscillogram for $u = 0.6$, pressure $3\,\mathrm{N/m^2}$, and time base $620\,\mu$sec. Increasing the pressure raised the collision frequency, and the signal was blanked in the interval of densities $1 + u$ and $1 - u^2$. Cutoff occurred at $v_3 = 1 - u$, i.e., for $n_3 = 6.8 \cdot 10^{12}\,\mathrm{el/cm^3}$.

Phase shift measurements

If the wave is transmitted through the plasma, its parameters can be determined from the refractive index

$$n = \sqrt{\frac{\varepsilon}{2} + \sqrt{\left(\frac{\varepsilon}{2}\right)^2 + \left(\frac{2\pi\sigma}{\omega}\right)^2}}. \tag{21}$$

when s is small, the collision frequency has a negligible effect on the refractive index, and its value is approximately equal to that for $s = 0$:

$$n = \sqrt{1 - \frac{v(1-v)}{1-u^2-v}}. \tag{22}$$

When s is comparable with v and u, the collision frequency must be taken into consideration. The graph of the refractive index is shown in Figure 7. We see that the refractive index varies sharply for small s in the range of densities $v_3 = 1 - u$ and $v_2 = 1 - u^2$. This complicates the phase measurements in the corresponding region.

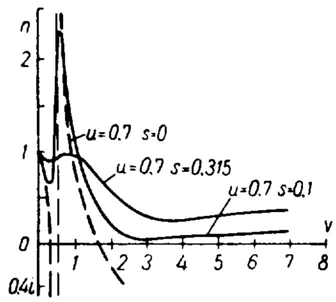

FIGURE 7. Refractive index as a function of density for low collision frequencies.

At higher collision frequencies, the refractive index varies smoothly, remaining close to unity in the entire range of densities. Phase measurements can be treated to determine the collision frequency (from the departure of the phase coefficient from unity), but damping must also be considered in this case. The damping ratio increases with density, but decreases with increasing magnetic field. Phase and damping measurements are therefore effective in high magnetic fields only.

BIBLIOGRAPHY

1. GINZBURG, V. L. Rasprostranenie elektromagnitnykh voln v plazme (Propagation of Electromagnetic Waves in Plasma). – Moskva, Fizmatgiz. 1960.

2. KELLY, C., H. MORGENAU, and S. BROWN. – Phys. Rev., 108 : 1367. 1957.

3. DUBOVOI, L. V. and A. G. PONOMARENKO. – In: "Fizika plazmy i problemy upravlyaemogo termoyadernogo sinteza", Vol. 2, p. 335. Kiev, Izdatel'stvo UkrSSR. 1963.

4. DUSHIN, L. A., V. I. KONONENKO, and A. I. SKIBENKO. – In "Fizika plazmy i problemy upravlyaemogo termoyadernogo sinteza", Vol. 2, p. 315. Kiev, Izdatel'stvo AN UkrSSR. 1963.

L. A. Dushin, V. I. Privezentsev, and A. I. Skibenko

MICROWAVE PLASMA DIAGNOSTICS UTILIZING LONGITUDINAL PROPAGATION OF RADIO WAVES

The application of longitudinal propagation of radio waves for the diagnostics of a plasma in the presence of an external magnetic field considerably expands the measurable range of some plasma parameters.

The theoretical studies /1, 2/ give a detailed treatment of this mode of propagation. The experimental papers /3, 4/ neglected the effect of collision frequency, and we concentrated on the influence of the collision frequency on the measurements of plasma parameters.

From the refractive index of a collisionless plasma

$$n_{1,2}^2 = 1 - \frac{v}{1 \pm u}, \tag{1}$$

we can determine the frequency range of the radio waves being used, as a function of plasma density and magnetic field. Figure 1 shows that in the presence of magnetic fields stronger than the resonance field ($u > 1$), the plasma may propagate extraordinary waves at any density. The influence of collisions is thus felt in the range of low frequencies (in comparison with the plasma frequency). The applicability of the ordinary wave is much more restricted, and it does not differ much from the applicability in the case of transverse propagation.

Interaction of longitudinal electromagnetic waves with a plasma

The propagation of electromagnetic waves in a magnetoactive plasma is characterized by a complex refractive index, which in the general case is written as

$$(n - i\varkappa)_{1,2}^2 = 1 - \frac{2v(1 - is - v)}{2(1 - is)(1 - is - v) - u^2 \sin^2\alpha \pm \sqrt{u^4 \sin^4\alpha + 4u^2(1 - is - v)^2 \cos^2\alpha}}, \tag{2}$$

where n is the refractive index, $\varkappa$ the absorption coefficient, ν the collision frequency, α the angle between the direction of the external magnetic field and the wave vector, $s = \frac{\nu}{\omega}$, $v = \frac{\omega_0^2}{\omega^2}$, $u = \frac{\omega_H}{\omega}$, $\omega_H = \frac{eH}{mc}$, e and m electron charge and mass, ω the frequency of the probing signal, c the velocity of light, N the density of electrons in the plasma, 1, 2 subscripts referring to the ordinary and the extraordinary wave, H the magnetic field.

In this paper we consider the case of longitudinal propagation, with $\alpha = 0$, when

$$(n - i\varkappa)_{1,2}^2 = 1 - \frac{v(1 \pm u)}{(1 \pm u)^2 + s^2} - \frac{ivs}{(1 \pm u)^2 + s^2}. \tag{3}$$

From this relation we can easily find the two quantities which are

measured experimentally, namely the phase shift and the damping

$$\varphi_{1,2} = \frac{\omega}{c} n_{1,2} = \frac{\omega}{c\sqrt{2}} \left\{ 1 - \frac{v(1 \pm u)}{(1 \pm u)^2 + s^2} + \right.$$
$$\left. + \left[\left(1 - \frac{v(1 \pm u)}{(1 \pm u)^2 + s^2} \right)^2 + \left(\frac{sv}{(1 \pm u)^2 + s^2} \right)^2 \right]^{1/2} \right\}^{1/2}, \tag{4}$$
$$\eta_{1,2} = \frac{\omega}{c} \varkappa_{1,2} = \frac{\omega}{c\sqrt{2}} \left\{ -1 + \frac{v(1 \pm u)}{(1 \pm u)^2 + s^2} + \right.$$
$$\left. + \left[\left(1 - \frac{v(1 \pm u)}{(1 \pm u)^2 + s^2} \right)^2 + \left(\frac{sv}{(1 \pm u)^2 + s^2} \right)^2 \right]^{1/2} \right\}^{1/2}. \tag{5}$$

Application of equations (4) and (5) in experimental calculations is permissible only if the waves are propagated in the plasma. This implies that $n > 0$. The values of the refractive index for the case $\nu \ll \omega$ and $s^2 \ll (1-u)^2$ show that $n_2 = 1 - \frac{v}{1-u}$ is positive in the region $u > 1$ for all v, and $n_1 = 1 - \frac{v}{1+u}$ is positive in the region $u > v - 1$ for $v > 1$ and for all u when $v < 1$. Hence, ordinary and extraordinary waves are propagated at different plasma densities, depending on n.

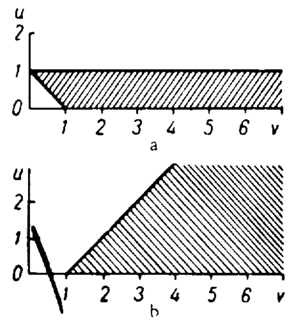

FIGURE 1. Transmission regions of radio waves as a function of density and magnetic field: a extraordinary wave; b ordinary wave.

Propagation at any density is only observed for the extraordinary wave with $u > 1$. The ordinary wave is propagated only when $v < u + 1$. Figure 1 shows the transmission zones for the two waves (the cross-hatched areas correspond to evanescence).

Measurements are of course best made with a single wave, choosing conditions when the damping of the probing signal is not excessive. The damping $\varkappa$ as a function of the density v is plotted in Figure 2. We see that the damping of the ordinary wave sharply increases for $v > 1 + u$. The damping of the extraordinary wave, on the other hand, increases more slowly. An increase of the magnetic field reduces the damping of the two waves.

Figure 3 plots the refractive index as a function of density (n vs. v curves) for various magnetic fields and collision frequencies

The refractive index of the ordinary wave decreases with increasing v, and reaches a minimum for $v > 1$; then it smoothly increases. The refractive index of the extraordinary wave has a minimum for $v < 1$ if $u < 1$; if, however, $u > 1$, it monotonically increases with density, remaining greater than unity.

The propagation of a signal in an ionized medium may also be characterized by its group velocity. For small collision frequencies,

$$V_{\text{gr}} = \frac{c}{\frac{d(\omega, n_{1,2})}{d\omega}}. \tag{6}$$

The group velocity of the extraordinary wave propagating in a homogeneous plasma is

$$V_{\text{gr}} = c\,\frac{(1-u)^{3/2}(1-u-v)^{1/2}}{(1-u)^2 + \frac{1}{2} vu}. \tag{7}$$

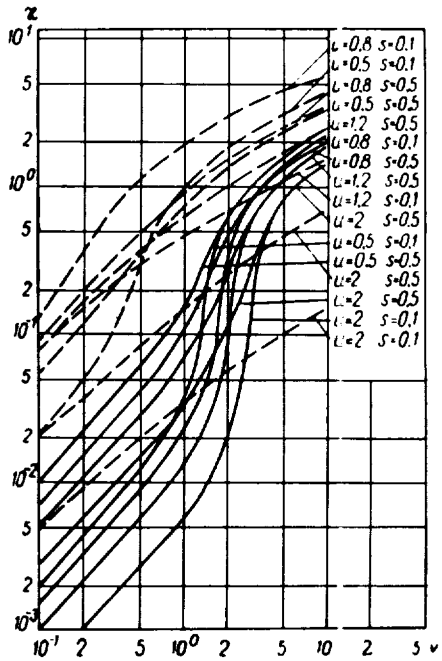

FIGURE 2. Damping as a function of density for various magnetic fields and collision frequencies: dashed lines – extraordinary wave; solid curves – ordinary wave.

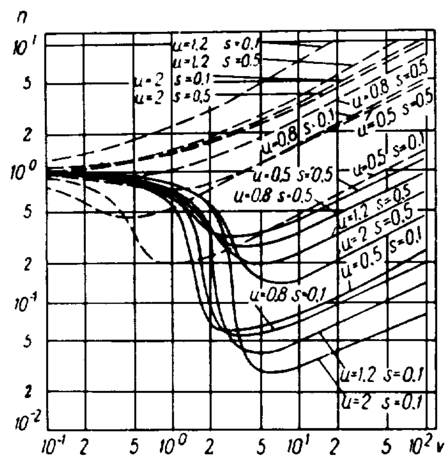

FIGURE 3. Refractive index as a function of density for various magnetic fields and collision frequencies: solid curves – ordinary wave; dashed curves – extraordinary wave.

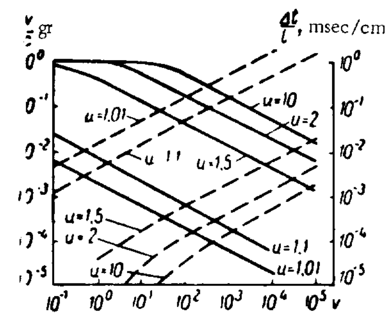

FIGURE 4. Group velocity (solid lines) and delay time (dashed lines) as a function of density for various magnetic fields.

Since the delay time of a signal transmitted through a plasma is

$$\Delta t = \frac{l}{V_{\mathrm{gr}}},$$

where l is the length of the path in the plasma, we may write

$$\Delta t = \frac{l}{c}\,\frac{(1-u)^2 + \frac{1}{2}u\cdot v}{(1-u)^{3/2}(1-u-v)^{1/2}}. \tag{8}$$

Hence for the density

$$v = \frac{2(1-u)^2\left[u(1-a^2) - 1 + \sqrt{(1-a^2)(u^2-2u)+1}\right]}{a^2u^2}. \tag{9}$$

Here

$$a = \frac{V_{\mathrm{gr}}}{c} = \frac{l}{c\Delta t_{\mathrm{gr}}},$$

so that by measuring Δt_{gr} we find the refractive index of the plasma and the instantaneous density of the electrons. Figure 4 plots $V_{\mathrm{gr}} = f(v)$ and $\Delta t = f(v)$ for various magnetic fields.

Experimental studies

Density and collision frequencies were measured using a PIG-type discharge immersed in a longitudinal external magnetic field of up to 796 kA/m /5/. Cathodes in the form of circular waveguides with aluminum flanges (introduced to increase the cathode surface) served as microwave antennas. Cathode separation 120 cm. Vacuum tube diameter 10 cm. The antennas could be adjusted relative to each other and relative to the discharge axis. A schematic diagram of the apparatus is shown in Figure 5.

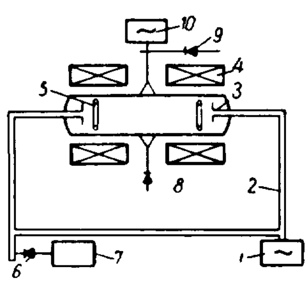

FIGURE 5. Schematic of the apparatus: 1) generator; 2) interferometer; 3) cathode; 4) magnetic field; 5) anode; 6) phase detector; 7) indicator; 8) detector of transmitted transverse signal; 9) phase detector for reflected transverse signal; 10) generator of transverse signal.

The plasma parameters were determined by a) measuring the phase shift of the wave; b) measuring the damping of the wave; c) measuring the delay time of the r-f pulse.

The phase shift was measured by a simple interferometer; a typical oscillogram is shown in Figure 6. The lower trace shows the cutoff of the ordinary transverse wave. Measurements were made at 3.1-cm wavelength. Applying (4) and calculating the density v from the cutoff at the time t_2, we can find s characterizing the collision frequency. The parameters v and s for the time t_1 are found by solving equations (4) and (5). The damping η is determined by measuring the amplitude of the wave transmitted through the plasma. The following

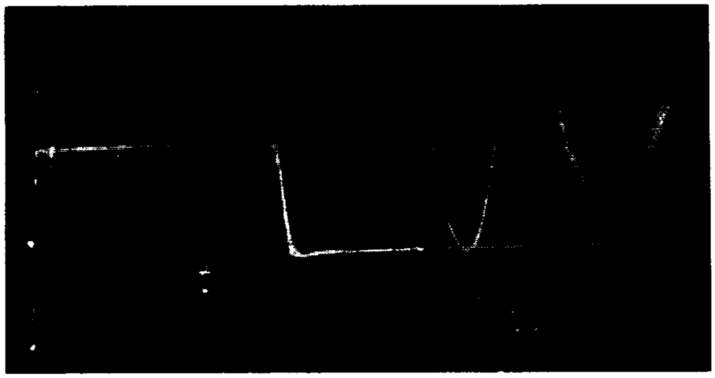

FIGURE 6. An interferogram of the longitudinal signal and the amplitude of the transmitted transverse signal; wavelength 3.1 cm, H = 320 kA/m, pressure 3 N/m^2.

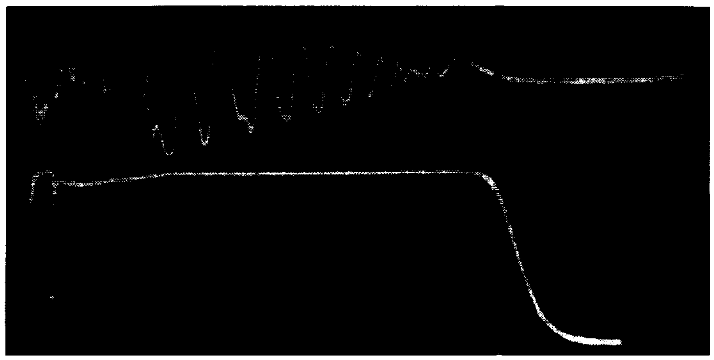

FIGURE 7. An interferogram of the reflected transverse signal of 8-mm wavelength and the amplitude of the transmitted longitudinal signal of 3.1-cm wavelength; H = 320 kA/m, pressure 3 N/m^2.

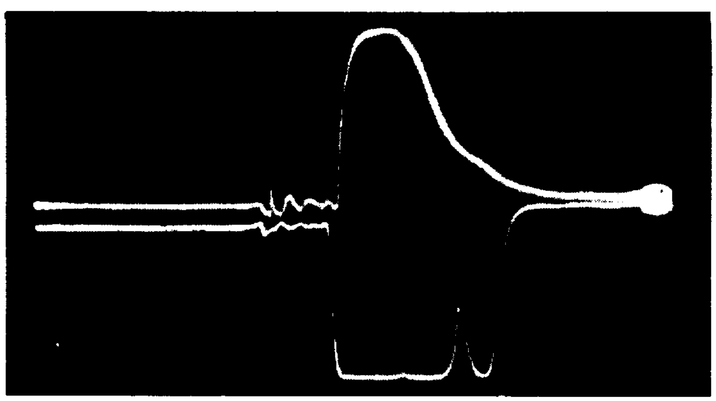

FIGURE 8. Oscillograms of pulses transmitted through the plasma (top) and supplied by the generator (bottom); wavelength 3.1 cm, pulse length 7.5 μsec, H = 320 kA/m, pressure 3 N/m^2.

values were obtained during the life of a plasma with a density exceeding 10^{12} el/cm^3 (300 μsec), for a magnetic field H = 320 kA/m and hydrogen pressure of 3 N/m^2:

$$t_1 = 84\,\mu\text{sec},\ v = 10\ (N = 1.25\cdot 10^{13}\ \text{el/cm}^3),\quad s = 0.3\ (\nu = 2\cdot 10^{10}),$$
$$t_2 = 290\,\mu\text{sec},\ v = 1\ (N = 1.25\cdot 10^{12}\ \text{el/cm}^3),\quad s = 0.17\ (\nu = 1.0\cdot 10^{10}).$$

In treating the results, we must remember that for small densities ($v < 1$) the plasma propagates ordinary and extraordinary waves. However, when collisions are introduced, the extraordinary wave is damped much faster. Already for s = 0.1, the damping of the two waves differs by as much as one order of magnitude. Therefore, for $v < 1$, the plasma may be regarded as transparent for the ordinary wave only, while for $v > 1$ it is only the extraordinary wave that is transmitted.

For purposes of comparison, the plasma was additionally probed with an 8 mm transverse signal under identical conditions. Figure 7 gives oscillograms of the reflected signal with a wavelength λ = 8 mm and of transmitted signals with a wavelength of 3.1 cm (bottom).

We see that the density of the plasma exceeds $1.7\cdot 10^{13}$ el/cm^3. From the interferogram of the reflected signal we find that at t_1 = 84 μsec a plasma column exists having a diameter of 68 mm and a density of over $1.7\cdot 10^{13}$ el/cm^3. The longitudinal signal transmitted by this column gives an average density of $1.25\cdot 10^{13}$ el/cm^3. The measured average and peak densities are thus in close agreement.

The same interferometer was used in group velocity measurements, but the compensator arm was replaced with two detector heads which picked up the pulses from a generator operating in a pulsed mode. The oscillogram in Figure 8 shows the delay of the pulse transmitted through the plasma. For a total time base of 30 μsec, the delay time Δt = 0.9 msec, which corresponds to an electron density of 10^{14} cm^{-3} at a time t = 55 μsec after plasma ignition. We see that the pulse transmitted through the plasma is distorted owing to the difference in the phase velocities of its spectral components.

Measurements made with a probing signal at 3.1-cm wavelength gave density readings much higher than the critical density corresponding to this frequency (from 10^{12} to 10^{14} el/cm^3), which demonstrates the expediency of applying longitudinal waves. The experiments gave collision frequencies of the order of 10^{10} sec^{-1} (high-pressure cold plasma), so that the plasma cannot be regarded as collisionless.

BIBLIOGRAPHY

1. GINZBURG, V. L. Rasprostranenie elektromagnitnykh voln v plazme (Propagation of Electromagnetic Waves in Plasma). – Moskva, Fizmatgiz. 1960.

2. GERSHMAN, B. N. and Yu. S. KOROBKOV. – Izvestiya vuzov. Radiofizika, No. 2: 51. 1958.

3. GALLET, R., J. RICHARDSON, B. WIEDER, and G. WARD. – Phys. Rev. Lett., **4**: 7. 1960.

4. CONSOLI, T., M. DAGAI, and O. LEPECHINSKI. – Proc. of the 5th International Conf. on Ionization Phenomena in Gases, V. I, 465, North – Holland Publ. Co., Amsterdam, 1962.

5. DUSHIN, L. A., V. I. KONONENKO, and A. I. SKIBENKO. – In: "Fizika plazmy i problemy upravlyaemogo termoyadernogo sinteza", Vol. 2, p. 315. Kiev, Izdatel'stvo AN UkrSSR. 1963.

L. A. Dushin, V. I. Kononenko, O. S. Pavlichenko,
V. K. Nikol'skii, and L. V. Brzhechko

MICROWAVE AND SPECTROSCOPIC INVESTIGATION OF AN ELECTRODELESS INDUCTIVE DISCHARGE

The heating of a plasma by a rapidly growing magnetic field was studied in fairly great detail at Los Alamos /1/, Aldermaston, and also by the Kolb group /2/. These researches were concerned with the fundamental processes accompanying rapid magnetic compression of plasmas; the instability of the plasma column which breaks up into two pinches rotating helically about a common axis was discovered and investigated; the capture of the magnetic field by the plasma and its relation to plasma heating was studied. Record parameters were obtained with the PHAROS machine: a plasma with a density of over $10^{16}\,cm^{-3}$ and a temperature of ions $10^7\,°K$ was sustained for a few microseconds. Researches carried out on less powerful facilities of this kind dealt with the various peculiarities of theta-pinch plasmas /4/. In /5/ epithermal microwave radiation from the plasma of a theta-pinch was discovered in the region of comparatively low pressures ($1.6 \cdot 10^{-2}$ to $7.1 \cdot 10^{-2}\,N/m^2$).

This paper investigates the parameters of a plasma emitting intense microwave radiation.

Apparatus

The plasma was created by discharging an $18.6\,\mu F$ capacitor bank charged to 30 kV voltage through a single-loop coil 11 cm in diameter and 20 cm long, wound onto a quartz tube 1 m long and 10 cm in diameter. The coil generated an alternating magnetic field with a maximal amplitude of $1.3 \cdot 10^6\,A/m$ and a period of $8.6\,\mu sec$; mirror ratio 1.1. Initial vacuum $1.33 \cdot 10^{-5}\,N/m^2$. The main results were obtained for hydrogen in the pressure range from 8 to $0.4\,N/m^2$. Preliminary ionization of the gas in the discharge tube was achieved with a ~ 200 W, 50 Mc/s r-f generator.

Microwave measurements

The plasma created by the coil and escaping from the coil enclosure along the tube axis was probed with microwave signals of various frequencies: $9.4 \cdot 10^9\,c/s$, $37 \cdot 10^9\,c/s$, and $140 \cdot 10^9\,c/s$. Typical oscillograms of the microwave signals ($E \parallel H$) transmitted through the plasma at right angles to the tube axis are shown in Figures 1 and 2 (initial pressure $1.6\,N/m^2$, discharge voltage $U = 10\,kV$). We see that the plasma with a density of over $2.4 \cdot 10^{14}\,cm^{-3}$ has a life of $60\,\mu sec$ inside the coil. Almost simultaneously with the creation of the dense plasma inside the coil, plasma is generated along the tube axis over considerable distances from the coil, the density outside the coil falling off at a slower rate than inside the coil. From measurements of the "cutoff" times of signals of various frequencies, we plotted the variation of the charged particle density in time inside the

coil and at a distance of 44 cm from its midplane (Figure 3), for various capacitor discharge voltages. The rapid decrease of density inside the coil

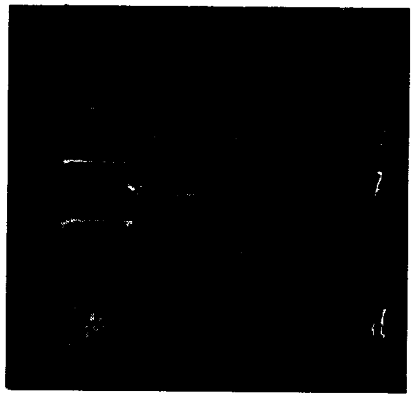

FIGURE 1. Oscillograms of the signal transmitted through the plasma region inside the coil: a) λ = 2.15 mm; b) λ = 8.1 mm; c) λ = 3.1 cm; d) current through discharge coil.

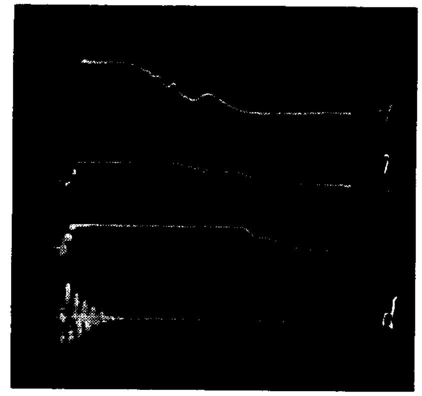

FIGURE 2. Oscillograms of the signal transmitted through the plasma region outside the coil: a) λ = 2.15 mm; b) λ = 8.1 mm; c) λ = 3.2 cm; d) discharge current.

may be due to the axial ejection of the plasma by the pinching field; outside the coil, the density decreases mainly due to recombination and diffusion. When the discharge voltage is raised from 5 to 25 kV, the life of plasmas of various concentrations increases. The largest increase in lifetime is observed for a plasma with a density of $2 \cdot 10^{14}\,cm^{-3}$. This apparently

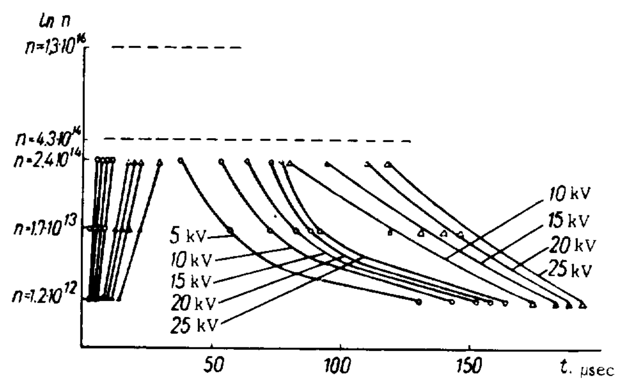

FIGURE 3. Peak density as a function of time for various discharge voltages and initial pressure of 1.6 N/m^2:
o inside the coil; Δ outside the coil.

implies that a plasma of higher density is created in the discharge (Figure 4). The insignificant increase in lifetime for a plasma with a density $\sim 10^{12}\,cm^{-3}$ and the leveling off of the lifetime vs. voltage curves indicate that a certain mechanism drives the particles outside the coil even in very

weak magnetic fields. The plasma outside the co l has a much longer life under the same conditions (Figures 3, 4). It is also noteworthy that the density decay curves outside the coil correspond :o a diffusive mechanism

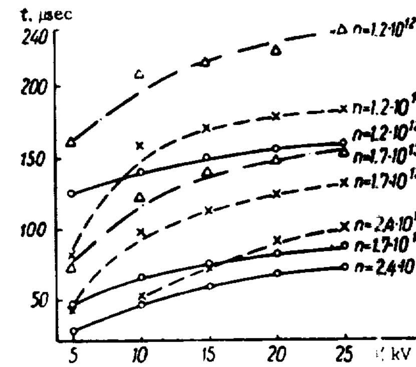

FIGURE 4. The lifetime of various electron concentrations in the plasma as a functio i of the discharge voltage for an initial pres.ure of 1.6 N/m²:
o inside the coil; x outside the coil; Δ pro)ing along the discharge tube.

($\ln n \approx -\alpha t$), while the escape mechanism inside tl e coil is considerably faster.

Probing of the plasma column at various di stances from the coil showed that plasma layers of different concent ·ations move away from the coil with different velocities. We measure l this velocity (Figure 5) and showed that low-density layers move faste·, with a velocity of some $7.6 \cdot 10^6$ cm, sec (for 25 kV voltage). This fact had been previously observed for the generatio 1 of plasma in various plasma injectors /6/. The rapid decrease of plasma densit·' inside the coil may thus be due to tl e axial ejection of the plasma from the coil space in the growing magnetic field.

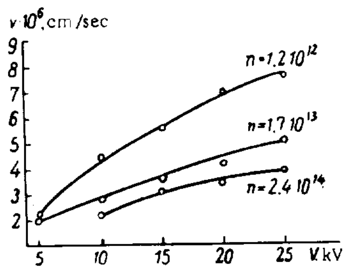

FIGURE 5. The velocity of plasma layers of various concentrations as a function of discharge voltage.

We also investigated the spatial distribution of charged partic e density inside and outside the coil by measuring the amplitude and the phase of reflected microwave signals at various waveleng.hs. An analysis of the oscillograms of ıeflected signals shows that in the preser ce of a magnetic field, the plasma inside the coil oscillates in the radial direction with twice the frequency of the ıagnetic field, ~ 240 kc/s. The maximal diameter of the plasma cloud with a density of over $10^{12}\,cm^{-3}$ was 4 — 8 cm in the range of experimental pressures. It is difficult to draw any definite conclusions concerning the radial distribution in this case. This density inside the coil is characteristic of the plasma near the walls, and it linearly increases toward the axis.

Spectroscopic measurements

The emission spectrum of the discharge in the visual region comprised a hydrogen line and lines of the Si and O impurities representative of the discharge tube, in the form Si III and O II. The oscillograms of the lines emitted by the plasma inside the coil show hydrogen emission at the minimum magnetic field position only; this indicates that the hydrogen is considerably ionized when the magnetic field increases. The impurities also emit near the minimum magnetic field positions. As the pressure is raised to $13.3\,N/m^2$, an intense continuum is observed. Measurements of the H_β line width made it possible to estimate the peak density of charged particles in the entire range of working pressures, $8-0.9\,N/m^2$. The charged particle density was estimated on the basis of the hydrogen line width theory proposed in /7/. The measurements are plotted in Figure 6,

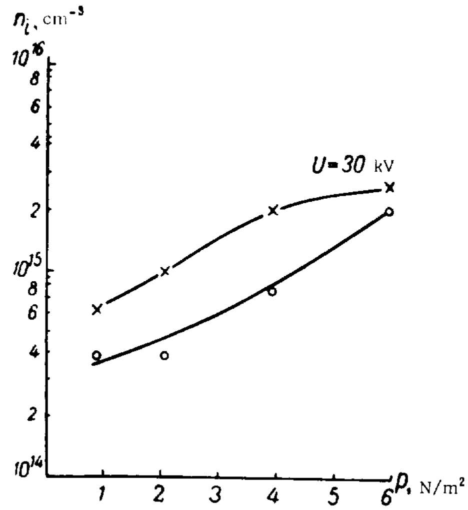

FIGURE 6. Plasma density vs. pressure: x theoretical curve; o experimental.

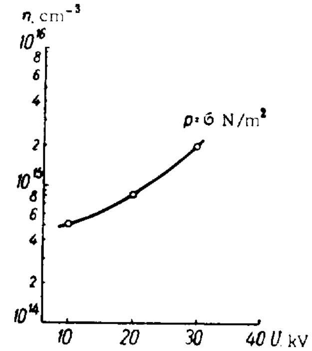

FIGURE 7. Plasma density vs. discharge voltage.

which gives the density as a function of pressure, assuming a fully ionized gas and neglecting the pinch effect. Comparing these results with the oscillograms of H_β we see that the measured plasma density is a time average for the zero magnetic field positions, so that the plasma is indeed not pinched (this justifies the comparison of the two curves in Figure 6) and the measured density is minimal. We made an attempt to estimate the upper bound of plasma density from the high-speed photographs used to determine the amount of pinch of the plasma column. The resulting figure $5 \cdot 10^{16}\,cm^{-3}$ (25-fold pinch) is apparently exaggerated, since the escape of plasma through the mirrors has been neglected.

The density increased almost linearly with discharge voltage (Figure 7), which is consistent with the results of microwave measurements.

The electron temperature of the plasma was measured from the intensity ratio of the singlet and triplet lines of helium, which was present in the system in small amounts (~ 5%). The measurements were made

photoelectrically, and they gave the time dependence of T_e in the plasma inside the coil. Figure 8 plots a typical $T_e = f(t)$ dependence. It is remarkable that the electron temperature increases in the maximum electric field position, as well as in the maximum magnetic field: the electrons are thus heated when gas breakdown occurs and also when the plasma column is pinched by the growing magnetic field. The electron temperatures in the two cases are correlated: the higher the temperature of the electrons at gas breakdown, the hotter the plasma is when subsequently pinched by the magnetic field. This is possibly due to better field skinning and magnetic field capture by the plasma (a captured magnetic field of opposite sign was detected in these cases with magnetic probes). The peak electron temperature was observed for a pressure of 1.6 N/m² (20 kV voltage) at the maximum position of the third magnetic-field half-period, being equal to $\sim 10^6$ °K.

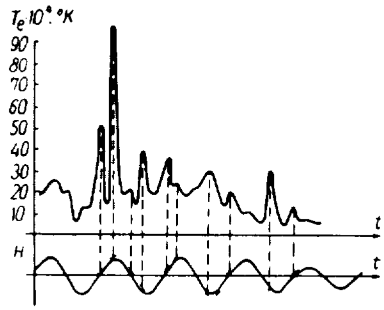

FIGURE 8. T_e vs. time, $p = 1.3\,N/m^2$, $U = 20$ kV.

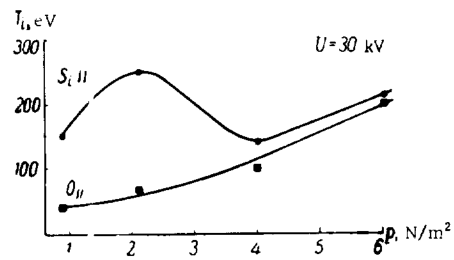

FIGURE 9. Temperature of ions vs. pressure.

The ion temperature of the impurities was measured from the Doppler width of O II and Si III lines. Figure 9 plots the measured temperature as a function of pressure. The temperatures of ions with different Z and M differ considerably. This is apparently a reflection of the acceleration mechanisms acting on the ions of the plasma. In particular, in the presence of fluctuation electric fields in the plasma, ions with different $\frac{Z^2}{M}$ ratio will have acquired different amounts of energy in these fields. That these fluctuation fields exist follows from the results on the reflection of the epithermal microwave radiation in the low-pressure region /5/. At elevated pressures, ionic sound oscillations may be excited in the plasma, just as electron plasma oscillations are excited at low pressures. This question is being investigated at present.

BIBLIOGRAPHY

1. LITTLE, E., W. QUINN, F. RIBE, and G. SAWYER. – Conf. Plasma Phys. and Controlled Nucl. Fusion Res., Salzburg. 1961.

2. GRIEM, H., A. KOLB, W. LUPTON, and D. PHILLIPS. – Conf. Plasma Phys. and Controlled Nucl. Fusion Res., Salzburg. 1961.

3. BODIN, H., T. GREEN, G. NIBLETT, J. QUINN, and J. REYNOLDS. – Conf. Plasma Phys. and Controlled Nucl. Fusion Res., Salzburg. 1961.

4. ZOLOTOTRUBOV, I. M., N. M. RYZHOV, I. P. SKOBLIK, and V. T. TOLOK. – In: "Fizika plazmy i problemy upravlyaemogo termoyadernogo sinteza", Vol. 1. Kiev, Izdatel'stvo AN UkrSSR. 1962.

5. ADAMOV, I. Yu., L. A. DUSHIN, V. I. KONONENKO, and O. S. PAVLICHENKO. – This volume, p. 142.

6. SINEL'NIKOV, K. D., B. G. SAFRONOV, I. T. GUZHOVSKII, and Yu. G. YAREMENKO. – In: "Fizika plazmy i problemy upravlyaemogo termoyadernogo sinteza", Vol. 1, p. 102. Kiev, Izdatel'stvo AN UkrSSR. 1962.

7. GRIEM, H., A. COLB and C. SHEN. – Phys. Rev., 116: 1. 1959.

V. G. Zykov, I. A. Stepanenko, L. A. Dushin,
I. K. Nikol'skii, O. S. Pavlichenko, and V. T. Tolok

SPECTROSCOPIC INVESTIGATION OF COLLIDING PLASMOIDS

The present paper is a continuation of a series of researches devoted to processes of capture and retention of plasma injected into a system with oppositely directed magnetic fields; the interactions of plasmoids colliding in the absence of a magnetic field are also studied.

In a previous paper /1/ we showed that when the plasma created by a conical source with an insulating plexiglas cone was injected in opposite directions through the slit and along the Z axis of a cusp-geometry trap, the lifetime of the trapped plasma was longer than its life without plasmoid collisions. We also showed that the interaction of the colliding plasmoids results in a rapid stopping of the plasma and its accumulation at the collision site, followed by plasma flow along the magnetic lines of force.

Previous experiments /1/ showed that the plasma of a conical source mainly consists of ionized carbon with a peak density $\approx 2 \cdot 10^{14}\,\mathrm{cm}^{-3}$; electron temperature in the plasmoid $5 \cdot 10^4\,°\mathrm{K}$. Probe measurements revealed the structure of the plasmoids, which comprise a fast component, having a velocity $\approx 1.4 \cdot 10^5\,\mathrm{m/sec}$, and a slow "tail".

In the present paper, we deal with the spectroscopic phenomena attendant on plasmoid interaction, and also give measurements of the ion temperature of the plasma created by plasmoid collision.

Apparatus and procedure

A schematic diagram of the apparatus and the position of the spectroscopic equipment are shown in Figure 1. The system parameters are given in /1/. Spectroscopic measurements consisted of two parts: 1) photographic recording of the emission spectrum of the plasma of free and

colliding plasmoids at right angles to the direction of their injection (part of the measurements were made along the injection line); 2) photoelectric recording of the emission in the plane of injection (Figure 2).

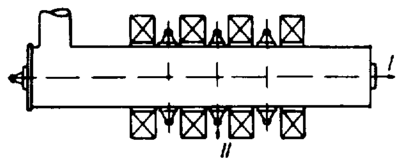

FIGURE 1. Position of spectroscopic equipment in the experimental system:
I to ISP-28 spectroscope with UF-85 camera;
II to ISP-51 spectroscope with FEP-1 photoelectric attachment.

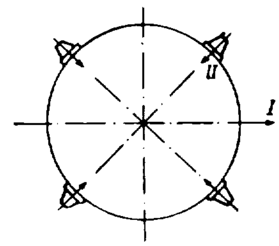

FIGURE 2. Photographic recording of the plasma emission spectrum:
I measurements; II injection.

The time-average emission spectrum of the plasmoids in the 2000 — 6000 Å interval was photographed through the quartz window at the end face of the system, using an ISP-28 spectrograph; line width and shift measurements were made with an ISP-51 spectrograph; photographs were taken with UF-85 long-focus camera on RF-3 film. Photoelectric measurements were made using the ISP-51 spectrograph with a photoelectric attachment FEP-1. The signal generated by the FEU-17 photomultiplier was fed through a cathode follower either to the amplifier of the OK-17 oscilloscope or to the IO-4 oscilloscope.

Experimental results

Photographic observations of the spectrum. The spectra photographed were those of the plasma injected by a single gun and of the plasma created in the collision of plasmoids from two and four guns (Figure 3). Gun voltage was 8 kV. Since the volume of plasma ejected by four guns was four times as large as that fired by one gun, equal-exposure technique was employed,

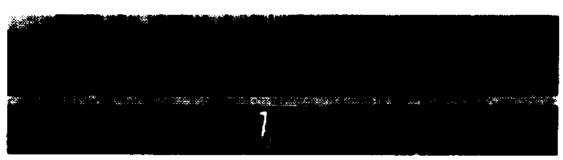

FIGURE 3. Emission spectrum of plasmoids:
a) one plasmoid; b) collision of plasmoids from four injectors.

i.e., the product of the number of guns by the number of collisions was always the same. The spectrograms differ considerably: the four-gun spectrum displays more features than the one-gun spectrum. For purposes

of comparison, the table lists the lines in one-gun and four-gun spectra.

Spectral composition of the plasma of colliding plasmoids

Wavelength and identification	One gun	Four guns	Wavelength and identification	One gun	Four guns	Wavelength and identification	One gun	Four guns
2746.5 CII		+	4172.1 OII		+	4414.0 OII	+	+
2743.3 CII		+	4074.5 CII		+	4621 NII		+
2836.8 CII		+	4089.3 OII		+	4634 NIII		+
3590.6 CI		+	4097.2 OII		+	4647.4 CIII		+
3712.7 OII		+	4103.4 NIII		+	4648.0 CIII		+
3727.3 OII		+	4132.8 OII		+	4673 OI		+
3750.1 H_{ε}		+	4156.5 OII		+	4678.8 CI		+
3832.1 CII		+	4267.0 CII		+	4694.5 NII		+
3863.5 OII		+	4291.2 OII	+	+	4705.3 OII	+	+
3861.7 CI		+	4294.0 OII	+	+	4710 OII		+
3876.0 CII	+	+	4296.1 CII		+	4861 H_{β}	+	+
3911.8 OII		+	4318.9 CII		+	5019.3 OII		+
3918.9 CII		+	4340 H_{γ}	+	+	5025.6 NII		+
3945.0 OII		+	4349.4 OII		+	5067.8 CII		+
3954.6 OII		+	4365.2 CI		+	5073.6 NII		+
3970 H_{δ}	+	+	4369.3 OII		+	5168.2 NII		+
4069.0 OII		+	4371.3 CI		+	5662.2 CII		+
						6563 H_{α}	+	+

We see from the table that the emission of the plasmoids is mainly attributable to the elements entering the composition of the insulating plexiglas cone: carbon, oxygen, hydrogen, and nitrogen. We see that at a distance ~ 10 cm from the site of plasma creation, excited C, N, O, H atoms are fairly abundant.

It is also noteworthy that some lines in the spectrum of colliding plasmoids (C II 4267 Å, 20.9 eV; C II 3876 Å, 27.4 eV; C III 4648 Å, 32.2 eV) have higher ionization potentials than those in the single-gun spectrum, where the strongest lines have ionization potentials ~ $1.6 \cdot 10^{-18}$ J. The common lines in the two spectra are considerably more intense (approximately by one order of magnitude) in the case of colliding plasmoids.

Photoelectric measurements

Line intensity oscillograms were taken for hydrogen H_{β} 4861 Å and carbon C I 4371 Å, C II 4267 Å at the midplane of the plasma region for different injection conditions. Typical oscillograms (injector voltage 12 kV) are shown in Figure 4; the upper trace gives the line intensity, the lower trace the injector discharge current (current period 6 μsec). The velocities of the plasmoid components were determined by treating the oscillograms.

The zero time in velocity measurements was taken as the time when the emission line first appeared in line-of-sight injection of the plasma; the time of arrival of the plasma at the axis of the system was identified with the appearance of this emission for plasma injection at right angles to the line of sight; the direct breakdown emission of the source thus did not interfere with our spectroscopy. To increase the accuracy of velocity

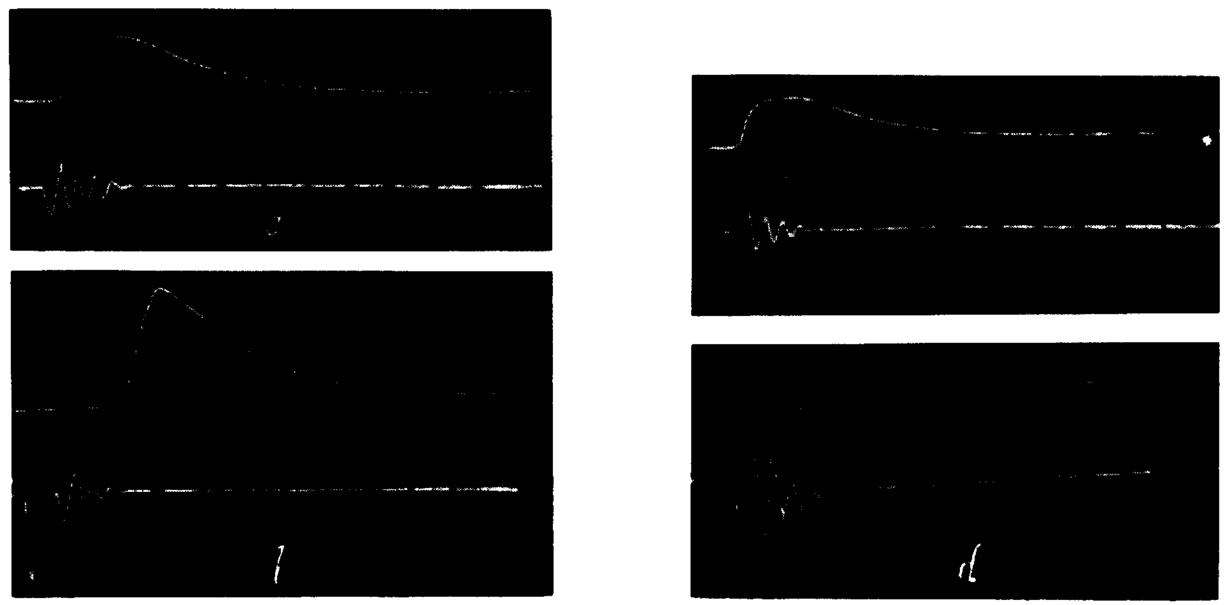

FIGURE 4. The intensity of the spectral lines emitted by a single plasmoid: a) H_β 4861 Å, 10 cm from the injector; b) H_β 4861 Å, 70 cm from the injector; c) CII 4267 Å, 10 cm from the injector; d) CII 4267 Å, 70 cm from the injector.

measurements, the plasma source was removed to a distance of 70 cm from the chamber axis. The results are shown in Figure 5, where the velocity was determined from the time of appearance of emission in the oscillograms. We see that the velocities of the different plasmoid components are distinctly different, but the velocity of all the components increases linearly with injector voltage. Singly ionized carbon moves faster than atomic carbon; hydrogen atoms move faster than carbon atoms. The velocity corresponding to C II ions is $3 \cdot 10^4$ m/sec for 12 kV gun voltage.

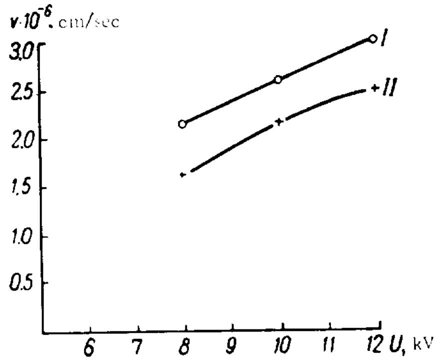

FIGURE 5. Plasmoid component velocities as a function of injector voltage.

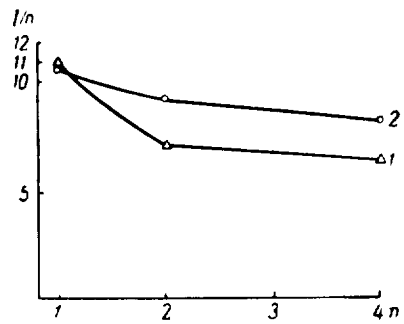

FIGURE 6. Reduced intensity of C II 4267 Å line as a function of the number of guns: 1) 8 kV gun voltage; 2) 12 kV gun voltage.

The intensity of the C II 4267 Å line was measured in the plane of injection at the time of peak emission for different numbers of guns. The results are plotted in Figure 6, which gives the intensity of C II 4267 Å, reduced to the number of guns, as a function of the number of guns. We see that the reduced line intensity $\frac{I_e}{n}$ (I_e line intensity, n number of guns) is almost constant, slightly decreasing with the number of injectors.

Photographic measurements of ion temperature

A long-focus camera UF-85 coupled with an ISP-51 spectrograph was used in measuring the width and the shift of the C II 4267 Å line for one plasmoid and for four colliding plasmoids, at right angles to the plane of injection. Line width measurements were made in the usual way. The shift of C II 4267 Å was measured relative to the position of this line in the one-gun spectrum for injection at right angles to the line of sight. The longitudinal component of plasmoid velocity had no effect in this case. The spectrograph dispersion in this region 2.8 Å/mm; instrumental line width measured for Hg 4358 Å excited in a low-pressure mercury lamp with water-cooled liquid electrodes was found to be equal to 0.15 Å and was allowed for in the usual way. Figure 7 gives the photometric results for C II 4267 Å profiles for different injection conditions. Assuming that the line width was mainly attributable to Doppler broadening, we calculated the

temperature of C II ions in a single plasmoid ($8.8 \cdot 10^4$ °K) and in four colliding plasmoids ($2.7 \cdot 10^5$ °K), for 8 kV gun voltage. The line emitted

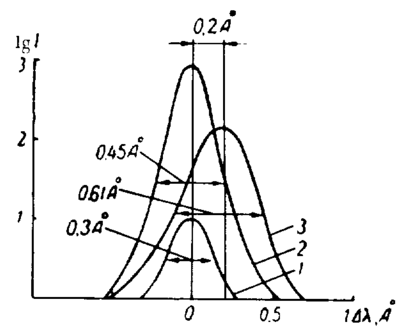

FIGURE 7. The width and the shift of C II 4267 Å for various conditions of injection: 1) one gun perpendicular to line of sight; 2) four guns perpendicular to line of sight; 3) one gun parallel to line of sight.

by a plasmoid moving toward the spectrograph shows a blue shift of 0.2 Å, which corresponds to a velocity of $1.3 \cdot 10^4$ m/sec for C II ions.

Discussion of results

It is highly significant for the understanding of plasmoid interactions that the densest part of the plasmoid, carrying the bulk of its mass, has a comparatively low velocity. This velocity, equal to $2-3 \cdot 10^4$ m/sec, is roughly one-tenth of the velocity of the low-density head ($v = 1.7 \cdot 10^5$ m/sec at 12 kV), as registered by double electric probes. This is a well known fact for plasma guns of this type /2/.

It is also noteworthy that there is a fairly high concentration of excited impurity atoms in the plasmoid, all moving with a velocity close to that of the plasma ions.

The presence of a considerable number of excited atoms and ions at a comparatively large distance from the source (> 10 cm) is also of interest, particularly if we remember that the transition probability for the C II 4267 Å line is $2.3 \cdot 10^8$ sec^{-1} /3/, so that deexcitation occurs in some $5 \cdot 10^{-9}$ sec. If preliminary excitation is discontinued, the number of excited ions or atoms should be negligible at distances which are traversed in a time of the order of $10\,\text{cm}/10^6\,\text{cm} \cdot \text{sec}^{-1} = 10^{-5}$ sec. It is little probable that continuous excitation in the moving plasmoid is sustained by the electrons, whose temperature according to probe measurements /1/ is $T_e = 4-5 \cdot 10^4$ °K, since in our case the strongest lines in the plasmoid emission spectrum have the excitation potentials of $27-30$ eV, while the $10-12$ eV lines are much weaker. The excited particles are formed in all probability due to charge exchange with the fast ions accelerated by the gas breakdown in the injector. In this process, a certain fraction of

the kinetic energy of the fast particle is expended in ionization and excitation. For example, in the charge exchange scheme

$$C^{+}_{fast} + C_2 \rightarrow C^{exc}_{fast} + C^{+} + C$$

we have

$$E^{C^+}_{kin} = E^{C}_{kin} + E_{exc} + E_{diss},$$

or

$$E^{C^+}_{kin} = E^{C}_{kin} + 13.6\,eV.$$

If the carbon ions C^+ have velocities of $2.7 \cdot 10^4$ m/sec, the velocity of carbon atoms should be $2.2 \cdot 10^4$ m/sec. For charge exchange with oxygen, the velocity of C^+ should be $2.3 \cdot 10^4$ m/sec, and with nitrogen, $2.3 \cdot 10^4$ m/sec.

In our case, charge is exchanged with the molecular nitrogen and oxygen of the air, with oil vapor, and, when plasmoids collide, also with the other plasmoid components — hydrogen and carbon. All these processes are apparently simultaneous, and the observed difference in the velocities of C and C^+ can be interpreted within the framework of this mechanism.

Measurements of ion velocities in plasmoids, in conjunction with probe measurements of ion density, show that the strong interaction of plasmoids observed in /1/, which stops the plasma and makes it flow transversally, is attributable to the stopping forces produced by Coulomb interaction of the plasmoids. Estimates of the stopping length of plasmoid ions give 3 cm for ion velocities $v_i = 3 \cdot 10^4$ m/sec, ion densities $2 \cdot 10^{14}\,cm^{-3}$, and electron temperatures $5 \cdot 10^4$ °K.

The weak dependence of the reduced intensity of C II 4267 Å on the number of injectors observed in photoelectric measurements in the plane of injection and the rapid variation of the reduced exposure for this line in photographic observations at right angles to the plane of injection (along the axis) is attributable to the substantial longitudinal (axial) spread of the plasma volume on collision. The flow of plasma at right angles to the line of injection is confirmed by probe measurements, which reveal motion of plasma in this direction.

The collision heating of ions points to partial thermalization of the energy of streaming motion of the plasmoids, which is equal to 32 eV for 8 kV gun voltage.

To sum up briefly:

1) we measured the velocities of the plasmoid components and showed that excited ions and atoms are present in a considerable concentration in the moving plasmoid;

2) the emission from plasmoids seems to be a result of charge exchange with the participation of the excited levels of the plasmoid ions;

3) plasmoid collisions raise the temperature of the ions;

4) the strong interaction of plasmoids observed in /1/ is attributable to the Coulomb mechanism.

BIBLIOGRAPHY

1. ZYKOV, V.A. et al. — This volume, p. 316.

2. SINEL'NIKOV, K.D., B.G. SAFRONOV, I.T. GUZHOVSKII, and Yu.G. YAREMENKO. — In: "Fizika plazmy i problemy upravlyaemogo termoyadernogo sinteza", Vol. 1, p. 102. Kiev, Izdatel'stvo AN UkrSSR. 1962.

3. ALLEN, C.W. Astrophysical Quantities. — London, Athlone Press. 1955. [Russian translation. 1960.]

EXPLANATORY LIST OF ABBREVIATIONS OF USSR INSTITUTIONS AND PERIODICALS APPEARING IN THIS BOOK

Abbreviation	Full name (transliterated)	Translation
AZh	Astronomicheskii Zhurnal	Astronomical Journal [Soviet Astronomy — AJ]
DAN SSSR	Doklady Akademii Nauk SSSR	Proceedings of the USSR Academy of Sciences [Soviet Physics—Doklady]
FTI	Fiziko-tekhnicheskii institut	Physicotechnical Institute [of the Ukrainian Academy of Sciences]
Izv. vuzov	Izvestiya vysshikh uchebnykh zavedenii	Bulletin of the Institutions of Higher Education
JETP	Zhurnal Eksperimental'noi i Teoreticheskoi Fiziki	Journal of Experimental and Theoretical Physics [Soviet Physics—JETP]
PTE	Pribory i Tekhnika Eksperimenta	Instruments and Experimental Techniques
UFN	Uspekhi Fizicheskikh Nauk	Advances in Physical Sciences [Soviet Physics—Uspekhi]
UFZh	Ukrainskii Fizicheskii Zhurnal	Ukrainian Journal of Physics
UMN	Uspekhi Matematicheskikh Nauk	Advances in Mathematical Sciences
ZhTF	Zhurnal Tekhnicheskoi Fiziki	Journal of Technical Physics [Soviet Physics—Technical Physics]